The Influence of Fault Geometric Uncertainty on Hydrocarbon Reservoir and Simulation Models

Alan Michael Wood

Submitted in accordance with the requirements for the degree of

Doctor of Philosophy

The University of Leeds

School of Earth and Environment

August 2013

I confirm that the work submitted is my own and that appropriate credit has been given where reference has been made to the work of others.

Acknowledgements

I'd firstly like to thank Richard Collier and Chris Townsend for conceiving the original project and securing funding for it. Shell are kindly thanked for providing said funding along with subsequent employment. My supervisors in Leeds, Douglas Paton and Richard Collier, are gratefully thanked for allowing me the freedom to control the direction that the project took. I'd also like to thank a large number of staff at Shell, especially Simon Price, Kachi Onyeagoro and John Marshall. A special mention must go to Richard Rigby, without whom I would have been buried in IT woe, and field assistants Dan Morgan and Ben Jervis. Infinite thanks go to my office mates and friends for making my PhD (almost) entirely enjoyable, especially Jo Venus, Rachael Dale, Steve Banham, Jess Ross, Rachael Spraggs, Hollie Romain and Sarah Southern: your humour was invaluable. I'd like to thank my dad, Geoff Wood, for teaching me that there is no substitute for hard work. The biggest thanks of all must go to my wife Viki. She has supported me (financially, emotionally and scientifically), through the last 5 years of MSc and PhD. I couldn't have done it without her.

Abstract

The impact of uncertainty in the geometry of normal faults upon hydrocarbon reservoir models has been assessed at the exploration-, field- and individual fault scale.

At the exploration-scale synthetic 2D seismic sections generated using mapped geometries from the Gulf of Corinth rift illustrate the uncertainty in along strike fault geometry and displacement continuity when correlating between disparate seismic lines. This uncertainty has implications for pore pressure prediction, spill point identification and calculation of hydrocarbon column heights.

At the hydrocarbon field-scale, incorporation of sub-seismic structure has been quantified using reservoir production simulations. Although the inclusion of sub-seismic fault tips often leads to increased reservoir segmentation, this does not necessarily imply a detrimental impact upon hydrocarbon production. Earlier onset of oil production decline for more segmented reservoirs is offset by a lower rate of decline due to an enhanced sweep pattern as well as a lower volume of produced water when compared to less segmented cases.

3D seismic forward modelling highlights the discrepancies between realistic, outcrop-derived fault geometries and those geometries resolvable in seismic data, with seismically resolvable faults significantly simplified in comparison to those observed at outcrop. Complex geometries such as displacement partitioning across multiple slip surfaces are hence not incorporated within reservoir models leading to the area of across-fault reservoir:reservoir juxtaposition being severely underestimated. In turn faults are modelled as overly retardant to flow, with the influence of fault rock properties being overstated. Where realistic (i.e. larger) areas of across-fault juxtaposition are modelled, the fault rock properties have less impact upon across-fault hydrocarbon flux. Juxtaposition is therefore the first order control on hydrocarbon flow across faults.

Table of Contents

List of Tables

List of Figures

Chapter 1

Thesis Introduction, Aims and Background Literature

1.1 Thesis Introduction

Within this section a brief outline of the rationale behind this thesis is presented, along with the aims of the project. To aid the reader a short explanation of the thesis structure is also given.

1.1.1 Thesis Structure

The thesis is structured such that each technical chapter can be read as a stand-alone document. As a result, much of the relevant background literature is referred to and critiqued within each individual chapter. For the sake of brevity repetition has been kept to a minimum, hence this literature review chapter mainly focuses on the principal concepts of the thesis regarding fault growth and linkage. In addition, the chapters are ordered by the scale to which they refer, starting at the rift-scale and progressing through field-scale to individual fault scale.

1.1.2 Thesis Rationale

Faults, across a range of scales within the upper brittle crust can be described as being ubiquitous within the geologic record, be this as observed at the surface or within the sub-surface. There is hence a high probability that the majority of hydrocarbon reservoirs contain or are influenced by faults. This influence may be at the 'exploration' scale, where large faults form structural traps and can influence reservoir facies distribution, or at the 'field' or 'reservoir' scale, where intra-reservoir faults may influence fluid flow and hydrocarbon recovery. Consequently, understanding the geometry and properties of faults within the sub-surface is critical when attempting to predict the magnitude of their effect upon reservoir volumes, compartmentalisation, integrity and performance. However, the methodologies available for characterising fault geometries (i.e. 2D/3D seismic data) have limited spatial resolution, and hence a significant uncertainty exists surrounding the precise geometry of faults in the sub-surface. By integrating data from outcrop analogues, where detailed fault geometries can be captured, it is possible to quantify the effect of fault geometric uncertainty on reservoir and simulation models at a range of scales, and derive predictive relationships for certain aspects of fault growth.

1.1.3 Thesis Aims

The broad aims of the thesis are the characterisation of the influence of uncertainty in the geometry of faults on hydrocarbon reservoirs, with additional aims being applicable at different scales.

At the exploration scale, construction of a high resolution, field data-based 3D model allows for an improved understanding of the evolution Gulf of Corinth rift. This model also facilitates an enhanced understanding of the limitations and potential uncertainties associated with correlating faults between disparate data, such as 2D seismic sections.

At the scale of hydrocarbon reservoirs and fields it is the intention to assess the different approaches for incorporating sub-seismic fault tips within reservoir models. An additional ambition is to develop a mechanism for predicting the presence or absence of sub-seismic breaching faults across relay zones. The influence of incorporating these features will be quantified in terms of reservoir segmentation and the effect on sub-surface fluid flow during hydrocarbon production.

Characterising the impact of geometric uncertainty at the scale of individual faults and fault relay zones, in relation to both fluid flow and the potential for fault reactivation, is a further objective. The aim here is to reconcile fault growth processes, and the resulting fault architectural heterogeneity, with a faults fluid flow properties. Since fine scale fault geometric heterogeneity cannot be observed in seismic data, or incorporated within typical reservoir and simulation models, the disparity between the influence on across-fault flow of realistic and seismically resolvable geometries is also investigated.

The impact of a number of structural uncertainties on hydrocarbon exploitation can be broadly separated into exploration and production scale. These uncertainties, and the chapters within which they are investigated are summarised in table 1.1.

	Structural Uncertainty	Chapter(s)
EXPLORATION	● Linkage Geometry	(Chapters 3, 4)
	● Along-Strike Displacement Continuity	(Chapters 3, 4)
	● Syn-Rift Reservoir Facies Distribution	(Chapter 4)
	● Fault Rock Properties	(Chapter 4)
PRODUCTION	● Linkage Geometry	(Chapters 5, 6, 7, 8)
	● Sub-Seismic Fault Tips	(Chapters 5, 6)
	● Sub-Seismic Fault Complexity	(Chapter 8)
	● Juxtaposition Uncertainty	(Chapters 7, 8)
	● Fault Rock Properties	(Chapters 6, 8)
	● Presence of Relay Zones	(Chapters 5, 6, 7, 8)
	● Fault Stability	(Chapter 9)

Table 1.1. The structural uncertainties investigated within this thesis can be broadly separated into whether they are relevant at the hydrocarbon exploration or production scale.

1.2 Literature Review

Here, a brief review of the existing literature pertinent to the main concepts explored within the thesis is presented.

1.2.1 Fault Geometry

A large amount of research into the evolution and linkage of extensional fault systems has been conducted over the last two decades (Larsen, 1988; Peacock and Sanderson, 1991; Dawers et al., 1993; Cartwright et al., 1996). The focus of much of this work has been on reconciling our effectively temporally static observations of faults and fault systems with a more complete understanding of their dynamic evolution through time. The use of four dimensional modelling techniques such as computer based numerical approaches (Cowie, 1998; Cowie et al., 2000) and sandbox modelling (Marchal et al., 2003; McClay et al., 2005) have complemented and helped to constrain and explain the 2D and 3D observations from outcrop and seismic data (Walsh and Watterson, 1988; Trudgill and Cartwright, 1994; Dawers and Underhill, 2000; Frankowicz and McClay, 2010). As a result of this research it is now widely recognised that in rift settings faults systems develop through a combination of growth, interaction and linkage of individual fault segments (Cartwright et al., 1996; Childs et al., 1996; Cowie et al., 2000; Walsh et al., 2003) across a range of scales.

Prior to developing models describing the growth, interaction and linkage of fault systems it is useful to first define the observable characteristics of an isolated normal fault growing in response to an extensional stress field. Barnett et al (1987) describe the geometry of an idealised isolated planar fault in terms of its displacement field, both parallel and normal to strike. Increasing displacement is coupled with increasing length of the fault during growth so that a broadly elliptical form is maintained (in the case of a blind fault), with the edge of this ellipse defining a contour of zero displacement. Displacement increases from this zero contour towards the centre of the ellipse where it reaches a maximum value, with the relationship between maximum displacement and fault length being termed the displacement ratio, d:L. Normal to strike displacement decreases with distance from the fault resulting in ductile deformation in the form of reverse drag (figure 1.1 A). For a blind fault geometrical constraint necessitates that additional ductile or small scale brittle deformation occurs due to the vertical displacement gradient between the maximum displacement in the centre of the fault and the point where displacement reaches zero at the tip (Barnett et al., 1987). This is manifested as compression at the top of the footwall and base of the hangingwall and extension at the base of the footwall and top of the hangingwall (figure 1.1 B).

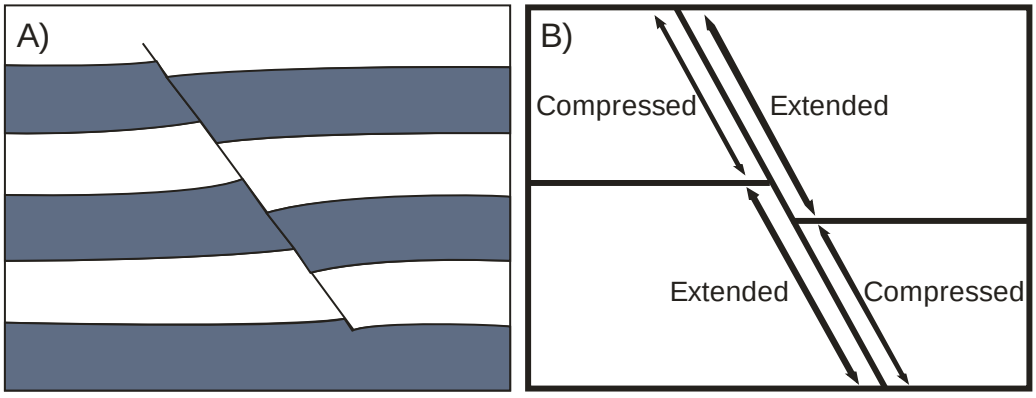

Figure 1.1. (A) View of an idealised blind normal fault in cross section. Decreasing vertical displacement away from the fault results in reverse drag, or rollover, in the hangingwall, and corresponding footwall uplift as the beds deform. (B) Geometric conservation of volume for a blind fault requires extension of beds in the top of the hangingwall and base of the footwall and compression in the top of the footwall and base of the hangingwall. Modified from Barnett et al (1987).

Several studies have been conducted investigating the relationship between fault length and maximum displacement for normal faults (Dawers et al., 1993; Cartwright et al., 1996; Walsh and Watterson, 1988). Although a positive correlation is observed, the variation in the displacement:length ratio spans up to two orders of magnitude (figure 1.2), indicating that no single relationship for the geometry of normal faults exists as suggested for a single fault under idealised conditions by Watterson (1986). This is partially attributable to heterogeneities in the deforming medium (Gross et al., 1997) as well as lithosphere scale controls (Ebinger et al., 1999), and the timing of observation relative to the growth and linkage history of the fault system (Cartwright et al., 1995).

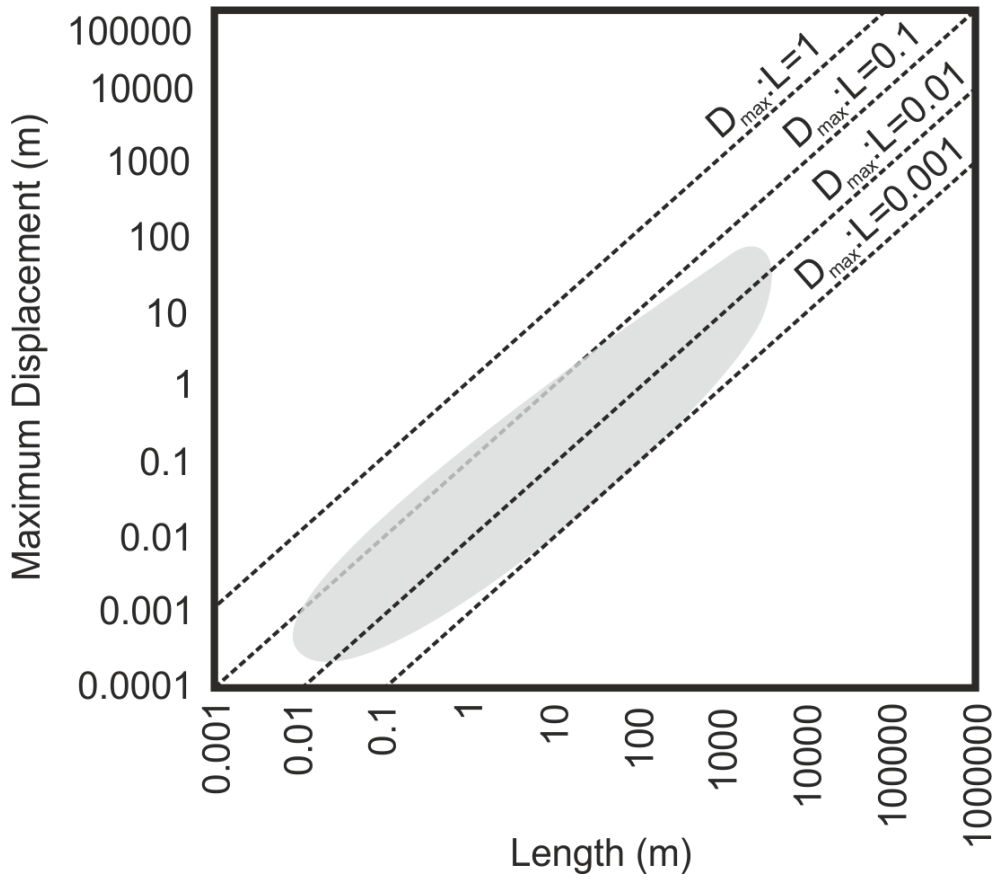

Figure 1.2. Log-log plot of maximum fault displacement against fault length. The majority of measured faults fall within the grey shaded area. Although a D_{max}:L relationship of 0.01 appears to be a reasonable best fit, the variability still covers two orders of magnitude. The reasons for this variability in fault dimensions include fault growth and linkage processes, the mechanical properties of the faulted stratigraphy and observational bias. Modified from Kim and Sanderson (2005).

1.2.2 Fault Growth and Linkage

The transfer of displacement through segment linkage in the form of relay ramps and connecting faults (Larsen, 1988) is observed to distort both the displacement length profiles of the resulting linked fault, and its individual components (Peacock and Sanderson, 1991, 1994). As the tips of two faults begin to overlap they become kinematically linked, with subsequent growth being accommodated by both faults acting as an individual structure (figure 1.3). At this stage the overlap zone has a dip sub-parallel to the strike of the faults and is termed a relay ramp. The cumulative displacement of the two faults at the zone of overlap may initially appears lower than that which would be expected for a single fault of comparable length. This is a result of a portion of the total displacement being accommodated through rotation and internal deformation of the relay ramp itself (Walsh et al., 2003; Long and Imber, 2010). This relative deviation from the displacement profile is reduced as displacement gradually increases on the overlapping tips. Interaction of the stress fields of the two faults within the zone of overlap prevents continued lateral propagation of the tips leading to an increase in the displacement gradient, hence resulting in a re-adjustment of the displacement profile towards that expected for an individual fault. As displacement continues the dip of the relay ramp increases. This is accompanied by an increase in stress which may be accommodated by fracturing and small scale faulting. Eventually a through going fault is established and the relay becomes breached forming a physical, or hard, linkage.

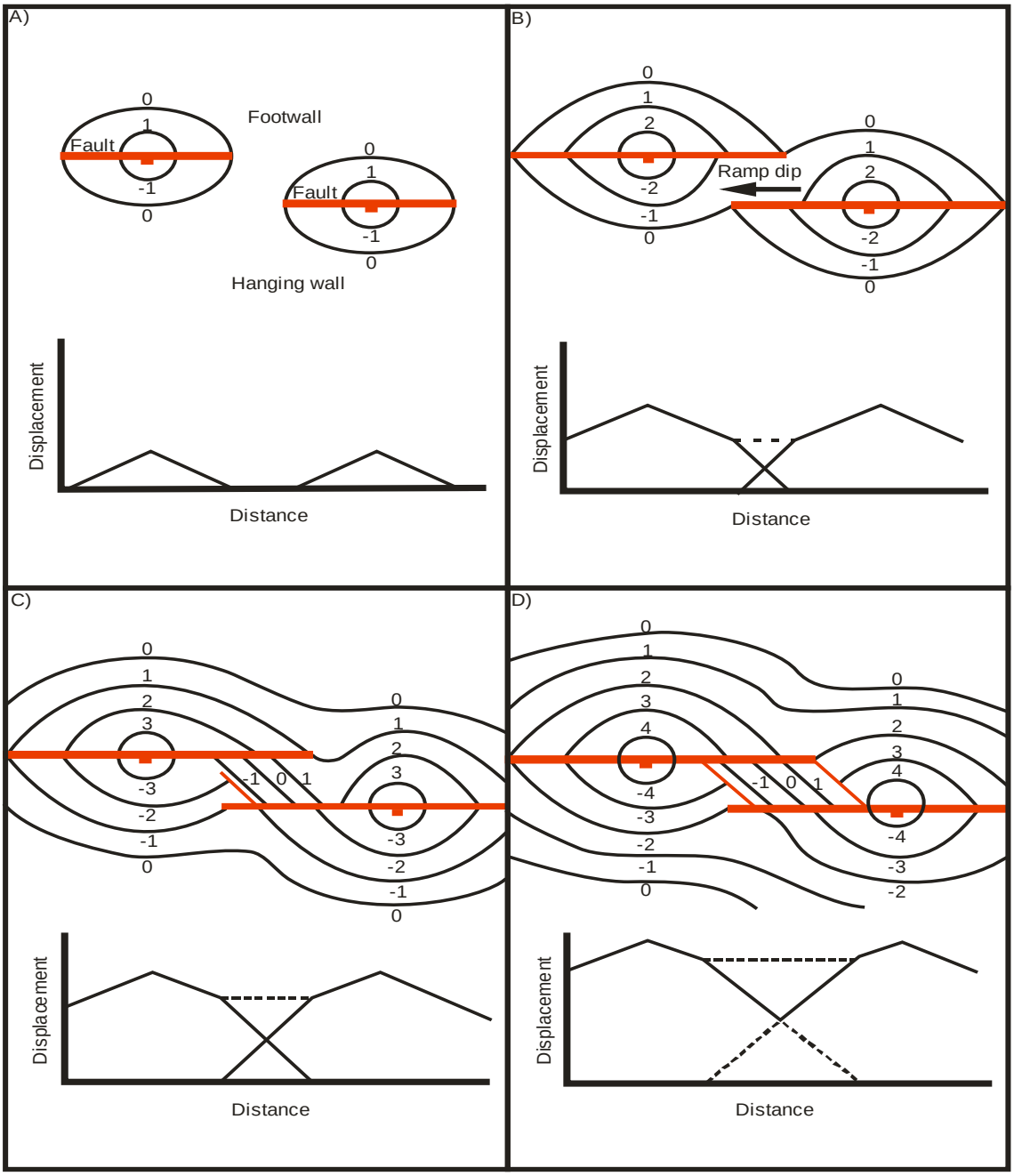
A)
Fault
Footwall
Fault
Hanging wall
Displacement
Distance
B)
Ramp dip
Displacement
Distance
C)
Displacement
Distance
D)
Displacement
Distance

Figure 1.3 (Previous page). Schematic diagram describing the evolution of contour patterns and displacement length (d:L) plots during relay ramp development and breaching. Contours are relative to a horizontal datum, with the downthrown side of the fault marked by a tick. (A) Initially the faults do not interact either kinematically or physically with the linear d:L profiles reflecting this. (B) As the fault tips grow towards each other they begin to kinematically interact with displacement accommodated by both faults acting as single structure. Displacement is transferred between the two faults by the rotation of beds parallel to the strike of the faults in the form of a relay ramp. The overlap of the fault segments limits lateral propagation of the fault tips hence increasing the displacement gradient whilst leading to a displacement minima. (C) As displacement increases the displacement gradient across the relay ramp begins to exceed the limit at which deformation can be accommodated in a ductile manner. This results in fracturing and the development of cross faults within the area of overlap. (D) Cross faults develop across the whole of the overlap zone, breaching the relay ramp. Initially a displacement minima remains, however this diminishes as deformation increases. Modified from Peacock and Sanderson (1994).

Cartwright et al, (1995) recognised that variations in the ratio of fault length to maximum displacement can be explained by the process of fault growth through linkage of individual fault segments. Their model suggests that physical linkage occurs early in a fault systems growth. In the period following linkage of two or more individual fault segments the resulting fault set will have a low overall displacement relative to its length. Post linkage accumulation of throw results in readjustment of the displacement profile.

Peacock and Sanderson (1994) and Gupta and Scholz (2000) suggest a subtly different model where individual segments interact kinematically prior to physical linkage occurring. This interaction results in modification of the displacement profiles of the individual segments, with migration of the point of maximum displacement and steepening of displacement gradients at interacting fault tips. This results in the displacement profiles of the individual segments becoming asymmetric with their d:L ratios also increasing. Increased displacement leads to stress being concentrated in relay zones with physical linkage eventually ensuing followed by re-adjustment of the displacement profile of the resultant fault.

Numerical modelling by Cowie et al (2000) produced characteristics of both models, suggesting additional factors affect fault behaviour. Position and orientation of the fault segments may not be conducive to early linkage due to occurrence of stress shadow zones in the vicinity of

the faults (Willemse, 1996; Cowie, 1998; Gupta and Scholz, 2000). Stress perturbations in the volume of rock surrounding a fault following slip can be positive or negative (Figure 1.3). This can lead to stress accumulation or dissipation on adjacent faults leading to either negative or positive feedback. Faults with overlapping positive stress fields tend to experience increased stress and hence slip can accumulate more rapidly. This is in contrast to faults with overlapping negative stress perturbations, which tends to lead to cessation of fault activity. Gupta et al (1998) suggest that this latter geometry favours the growth of en echelon fault arrays, whilst Ackermann and Schilsche (1997) also observe that the same stress distribution results in the formation of a 'stress shadow' in the immediate footwall and hangingwall to a fault leading to restriction of fault growth and nucleation within this zone.

In both models the interaction of individual fault segments is implied to occur coincidentally from within an array of randomly distributed discontinuities. This would suggest that faults are originally isolated and that growth through linkage initially occurs by chance ('Isolated Fault Model' - terminology from Walsh et al., 2003).

An alternative model proposed by Walsh et al (2003) acknowledges that although the implicit notion of coincidental linkage occurring is possible, it is more realistic that individual fault segments are kinematically related from early in their growth history ('Coherent Fault Model'- figure 1.4). This may be manifested by linkage to a more coherent structure at depth, for example in the case of reactivated fault systems, or as a series of isolated segments which in three dimensions form a kinematically linked array displaying an aggregate displacement profile approaching that of an idealised isolated fault.

The differences between the 'Isolated' and 'Coherent' models of fault interaction and linkage (figure 1.5) can be reconciled by the position and scale of observation. The concept of the Isolated Fault Model is for the most part based upon analysis on a single plane of observation (e.g. horizontal i.e. outcrop, vertical i.e. cross section) which is unlikely to be located at the point of maximum displacement (Figure 1.5), with the potential for out of plane interaction therefore being high. Despite this simple observation it is often unconsciously assumed that the observation plane is fortuitously located at the fault centre (Walsh et al., 2003). In turn this leads to the notion of isolated faults propagating towards each other and interacting by chance. Whether the 'isolated' or 'coherent' model applies to a particular fault set can be determined by examining the displacement profiles of the faults. In the isolated model (figure 1.4 a, b), where faults grow towards each other and interact by random, a displacement deficit will exist at all stages of growth, even when deformation due to rotation of the relay zone is accounted for. In contrast, where the coherent model is applicable (figure 1.4, c, d, e), a fault

set will be described by a continuous profile, with only minor displacement minima at relays, attributable to rotation of the rock mass of the relay zone.

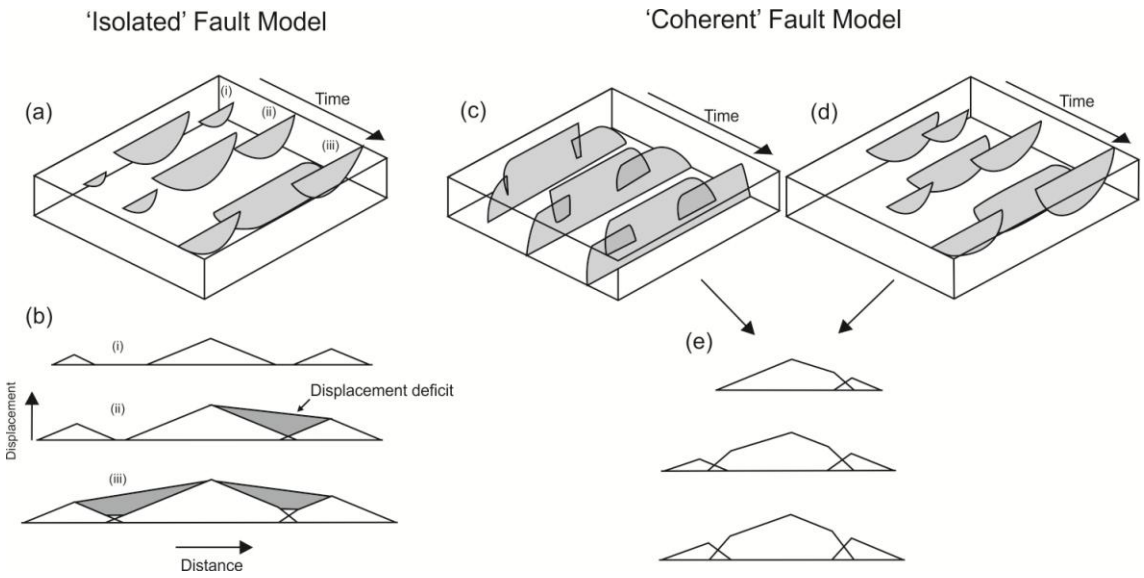

Figure 1.4. Figure illustrating the differences between the 'Isolated' and coherent fault growth models. Block diagrams (a), (c) and (d) show the 3D fault geometries, whilst (b) and (e) show the d:L profiles at the top surface of the block diagrams. The isolated growth model (a, b), where faults have coincidentally overlapped, maintains displacement deficits at all stages of growth, whilst in the coherent model (c, d, e) only minor deficits exist, and are accounted for by rotation of relay zones. This is the case for both hard-linked (c), and soft linked (d) geometries. Modified from Walsh et al (2003).

Figure 1.5 (Next page) Schematic illustrating how the position of the plane of observation (red) influences the perceived geometry of a fault relay zone. (A) Map view. The plane of observation coincides with the maximum displacement (D_{max}) on two faults. The observation that the faults are not interacting is therefore correct. (B) The plane of observation does not correspond with the position of D_{max} (yellow). In this scenario the faults are observed to be non-interacting, but are in fact interacting at depth to form a horizontal relay zone. (C) Section view. Plane of observation coincides with D_{max}. (D) The plane of observation does not coincide with D_{max}. Faults interpreted as non-interacting based upon their observable geometry in fact form a vertical relay zone away from the plane of observation. The likelihood that any single observation plane coincides with the maximum displacement on a fault is relatively unlikely, therefore 2D observations are generally unreliable when quantifying 3D fault geometries.

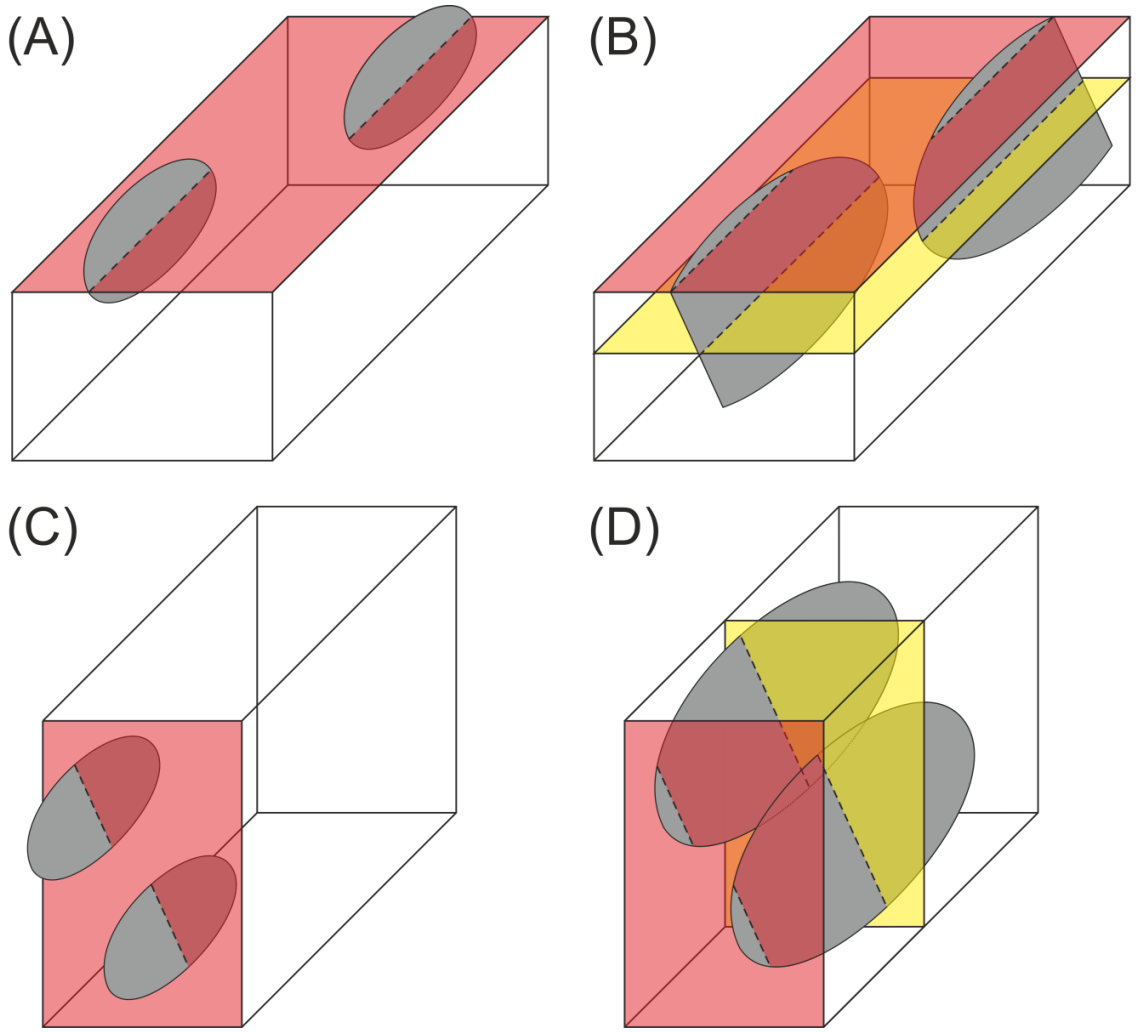
(A)
(B)
(C)
(D)

Growth of fault systems through the dynamic processes of interaction and linkage of their individual components occurs at all scales of observation, from micro-cracks (Wibberley et al., 2000) through to plate boundaries (Peacock et al., 2000), with relay zones also being ubiquitous at all scales. Generally though, our observations of faults consist of temporally instantaneous snapshots. Consequently when observing, for example, outcrop scale faults it is perhaps unintuitive to visualise what may appear to be a single fault plane as a product of its individual components. This leads to faults being identified as single isolated structures when in fact they are composed of a multitude of kinematically and/or physically interacting segments across a range of scales. The different scales of structure involved may not necessarily be evident for two reasons. Firstly the resolution of observation may exclude differentiation of the smallest structures and secondly, as the individual segments physically link they tend to become obscured by the through-going array.

1.2.2.1 Kinematics of Fault Growth and Linkage

The initial overlapping of two or more small scale discontinuities may or may not be entirely random, but irrespective it leads to modification of the local stress field (the 'stress shadow', figure 1.6) with strain subsequently becoming localised onto the interacting discontinuities. This strain localisation leads to an enhanced strain rate, in turn resulting in increased displacement accumulation and 3D propagation of the now kinematically linked faults (Gupta et al., 1998; Cowie et al., 2000). The increased propagation (both fault normal and fault parallel) increases the probability of further interaction with other individual segments, as well as broadening the stress shadow zones in the footwall and hangingwall leading to the abandonment of smaller structures. Through this mechanism faults which, by chance, interact early in their growth history will continue to grow and eventually become dominant, whilst smaller, isolated faults and discontinuities become inactive. Strain continues to accumulate in the form of fault displacement, with the associated profile re-adjustment of the interacting fault set leading to stress intensification at relay zones where the individual fault segments overlap. This ultimately leads to the breaching of relay ramps and hard linkage occurring across a broad range of scales.

Irrespective of which mechanism for linkage is operating within a rift system, the temporal variation in the geometry of fault systems implies that any observed relationship between displacement and length is valid only at the scale of observation and the relative timing of observation (Peacock, 2002).

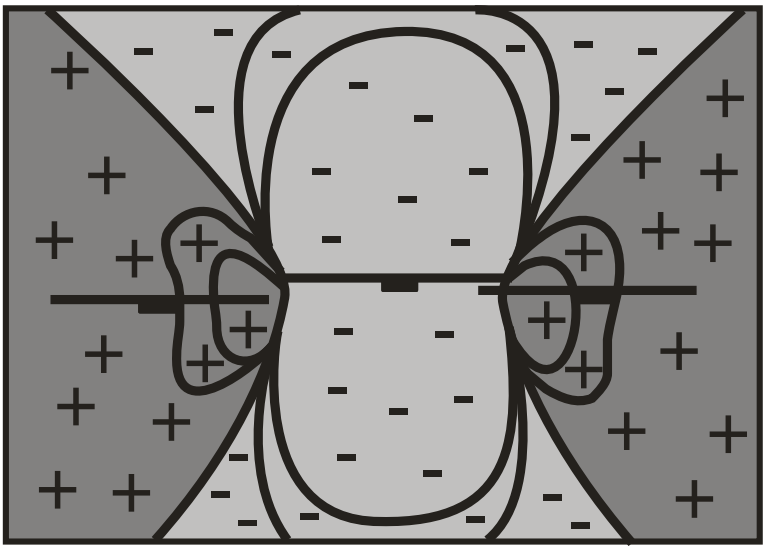

Figure 1.6. Coulomb stress changes due to deformation on a normal fault dipping at 60 degrees. This leads to stress enhancement (+) or relaxation (-), with a reduced likelihood of faulting in the negative perturbations and an increased likely hood in the positive perturbations. The areas of stress relaxation are often termed 'stress shadows'. Modified from Gupta et al (1998).

A number of authors have recognised the importance of fault linkage with respect to earthquake recurrence (Jackson, 1999; Cowie et al., 2000; Gupta and Scholz, 2000). Sieh et al., 1993 describe how the Landers earthquake cluster event in 1992 resulted in rupture on a number of faults that were linked but previously thought to be separate. It has been suggested that behaviour such as this is indicative of fault linkage processes (Cowie et al., 2000; Gupta and Scholz, 2000). Clustering of earthquakes may occur as a fault set previously composed of two or more segments interacts, links and re-establishes a characteristic displacement profile via displacement across the linkage zone (Gupta and Scholz, 2000). In this instance earthquake foci will be clustered around the previously soft linked relay zone between overlapping faults. In the same way earthquake foci may be observed to migrate laterally as the displacement profiles of kinematically linked faults become skewed in response to growth on the fault set as a whole (Peacock and Sanderson, 1994; Gupta and Scholz, 2000). As stress increases in the relay zone the faults begin to become physically linked through propagation of one or both of the fault tips or the development of cross faults. Co-seismic displacement is hence concentrated in the vicinity of the linkage zone as the displacement profile re-adjusts (Gupta

and Scholz, 2000). This leads to a clustering of earthquake activity as observed by Jackson (1999).

Cowie et al (2000) note that the differing mechanisms for fault linkage evolution will result in different geometries of the resulting hangingwall basins (figure 1.7). Model A ('early linkage') results in the formation of a number of small sub-basins prior to fault linkage, followed by the establishment of a shallow basin spanning the width of the system following linkage. This basin then undergoes rapid subsidence in its central portion until the original displacement:length ratio of the component segments is reached. In model B ('late linkage'), the component faults are kinematically but not physically linked during sub-basin development. This kinematic linkage results in migration of the fulcrum of the sub-basins towards the centre of the linked system, with the central sub-basin experiencing higher rates of subsidence and intrabasin highs developing at displacement minima between the segments. Eventually hard linkage occurs with the relatively deep sub-basins overlain by a broad basin which then subsides in response to movement along the entire length of the fault. Dawers and Underhill (2000) demonstrated this model for basin evolution using high resolution seismic data. They showed that the Statfjord East fault in the Northern North Sea evolved through linkage of a series of en-echelon segments, with early separate depocentres coalescing into a single large basin following linkage.

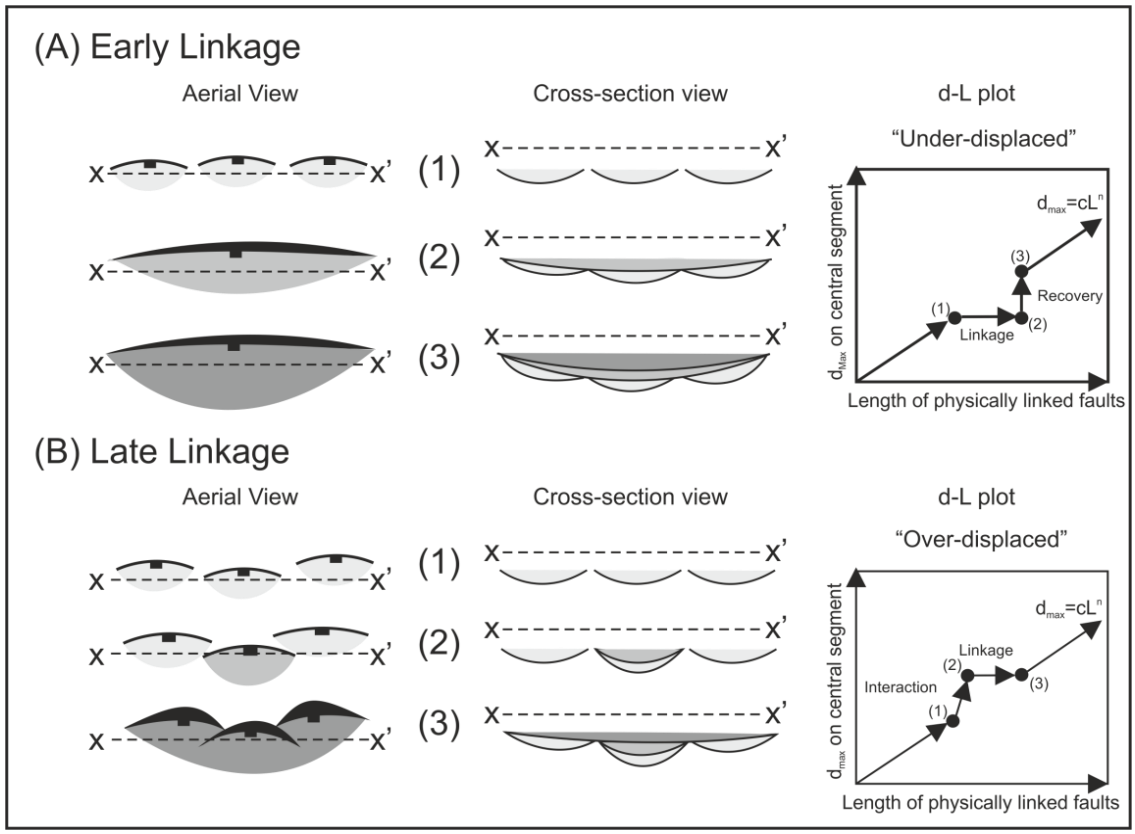

Figure 1.7 (Previous page). Schematic figure of the different hangingwall basin geometries formed as a result early (A) and late fault (B) linkage models. Early fault linkage (A) results in a broad, shallow hangingwall depocentre which subsides as a single basin. Late physical linkage results in narrower, deeper depocentres which initially subside separately. Following linkage the basins coalesce and subside as a single entity. Modified from Cowie et al (2000).

Cowie et al (2000) proposed a four stage model for fault growth and evolution within rift settings (Figure 1.8). Early rift initiation is characterised by nucleation and growth of individual fault segments in relative isolation with associated hangingwall depocentres. As extension continues individual faults begin to link, creating larger depocentres in their hangingwalls. Nucleation of new faults and growth of pre-existing faults is restricted due to stress reductions in the footwalls and hangingwalls to these larger faults. In the third stage deformation begins to localise onto larger fault segments, with adjacent faults becoming inactive and little nucleation of new structures. Smaller depocentres coalesce to form major basins. The final stage is characterised by the development of a single linked fault system with a large depocentre in its hangingwall. Displacement is localised onto this system and it begins to subside more uniformly. This focussing of displacement leads to an increase in the subsidence rate of the basin, without the need for an associated increase in the rate of extension.

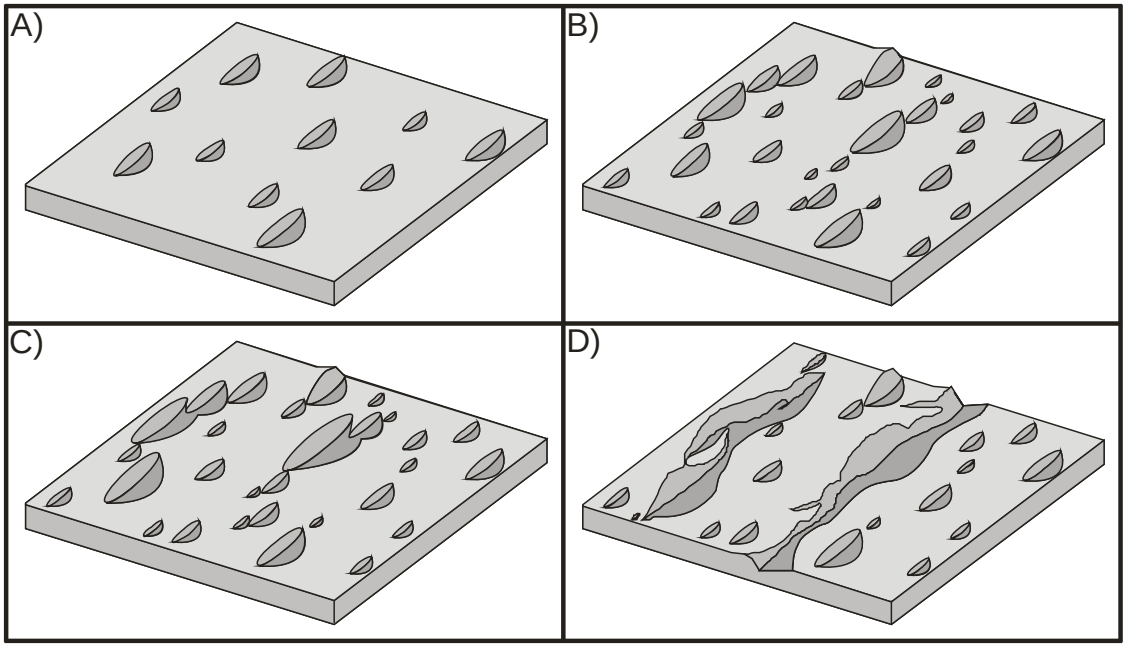

Figure 1.8 (Previous page). Four stage model for fault growth, linkage and rift evolution. (A) Initiation of rifting leads to nucleation of isolated fault segments developing along with hangingwall basins. (B) Continued fault nucleation leads to the onset of segment linkage and rapid enlargement of the linked fault sets. Major depocentres develop in the hangingwalls to theses linked fault sets. (C) Strain is concentrated onto the larger fault segments with smaller faults becoming inactive due to stress perturbations. The major depocentres grow through coalescence of smaller depocentres, with subsidence ceasing adjacent to inactive faults. (D) Continued extension leads to linkage across the rift and the formation of a through going fault set(s) with more uniform subsidence rates along strike. Modified from Cowie et al (2000).

Cowie and Roberts (2001) used field observations from a number of localities to suggest that slip rates along strike of normal fault sets vary significantly depending on the stage of linkage of the individual fault segments. This variation is explained by the general requirement of faults to maintain a characteristic d:L ratio. This ratio itself is dependent on numerous physical properties, however it is believed to be relatively constant for a given stratigraphy in a homogenous regional stress field. Cowie and Roberts (2001) suggest that as individual fault segments link the length of the fault set is correspondingly rapidly increased. To maintain the geomechanically desired d:L ratio slip rates increase, both at linkages and towards the centre of the new fault set. This increase in slip rate may be manifested as a decrease in earthquake re-occurrence period, an increase in the magnitude of co-seismic slip, or as an increase in the non-co-seismic (elastic) deformation rate. McLeod et al (2000) were able to constrain the timing of segment linkage and deformation rate using 3D seismic data from the North Sea. They observed an increase in the slip rate at the centre of a fault correlating to the time of linkage. The temporal variation in slip rate attributable to segment linkage suggests that d:L data derived from structurally immature regions may tend to overestimate the characteristic fault length due to insufficient time for profile re-adjustment (McLeod et al., 2000).

If regional extension and hence strain rates remain constant, any increase in strain localisation associated with linkage of fault segments must be accompanied by a decrease in activity in the footwall or hangingwall (Gupta et al, 1998). This has been identified by McLeod et al (2000), where an increase in slip rate due to segment linkage across the Strathspey-Brent-Statfjord fault coincided with reduced activity on faults in its hangingwall.

Although the regional strain rate may influence the maximum amount of strain that a system can accommodate, the distribution of this strain may also be influenced by local stress perturbations surrounding active fault segments (Gupta et al, 1998). Strain accommodation due to displacement across a fault results in a drop in the stress magnitude of the local stress field in the immediate hangingwall and footwall. If however displacement is limited to an individual segment of a fault set, the along strike stress field may in fact be intensified, especially in the vicinity of fault linkages where displacement gradients may be anomalously high or low (Cowie, 1998). If co-seismic slip and subsequent stress reduction in the fault-normal direction extends a significant distance then activity on any faults located within the reduced stress field may be restricted. This may have the effect of influencing the minimum fault spacing, especially in the early stages of rift evolution where strain is accommodated on a large number of small isolated faults, rather than fewer linked faults. Conversely, where large faults have nucleated and propagated a stress reduction shadow will exist to a distance away from the fault proportional to the local displacement. This shadow will limit the nucleation and growth of later faults within its boundaries (Ackermann and Schilsche, 1997). This can be a very powerful concept for populating reservoir models with sub-seismic scale faults when relative fault timing can be constrained (e.g. Maerten et al., 2006).

An additional factor stems from the three dimensional geometry of a fault. Willemse (1997) modelled the effect of fault aspect ratio (fault length: fault height) on stress perturbation (figure 1.9). They found that low aspect ratio (tall) faults had a larger negative stress perturbation field than high aspect ratio (short) faults. Hence high aspect ratio faults can have larger overlap for a given separation before kinematiaclly interacting when compared to low aspect ratio faults. This introduces the proposition that fault propagation direction, potentially controlled by the mechanical properties of the stratigraphy, alters the stress field perturbation dimensions and geometry. The inference is that it may be possible that vertically restricted, laterally propagating faults reduce the areal extent of their negative stress perturbation fields, and hence display a *decrease* in the minimum spacing between faults (Soliva et al., 2006). Conversely if faults are laterally rather than vertically restricted, for example by interaction with a pre-existing structural fabric, then their stress reduction fields may tend to extend further in a fault-normal direction into the footwall and hangingwall as their aspect ratio decreases. This may potentially lead to cessation of activity on smaller subordinate faults, and prevention of nucleation of additional faults within this region. The dimensions of the stress perturbation field also affect the proximity at which additional faults may nucleate, since faulting is less likely to occur in areas which have experienced a stress reduction compared to areas which have experienced an increase in stress. In general this increases the likelihood of

along strike propagation and linkage. The shape of the stress perturbation field controls the degree to which faults can overlap. Interaction of negative stress fields from two faults growing towards each other leads to tip restriction (Willemse et al., 1996). This is manifested as low displacements and low displacement gradients at fault tips compared to high displacement gradients at the point of overlap. A displacement anomaly may be observable where faults overlap (Gupta and Scholz, 2000). This is due to the negative stress perturbation field preventing lateral propagation of the fault tip. Stress is therefore accommodated in this portion of the fault by increased displacement relative to the characteristic d:L profile, hence increasing the displacement gradient. It is this increasing stress with increasing segment displacement at this point that eventually leads to hard linkages developing.

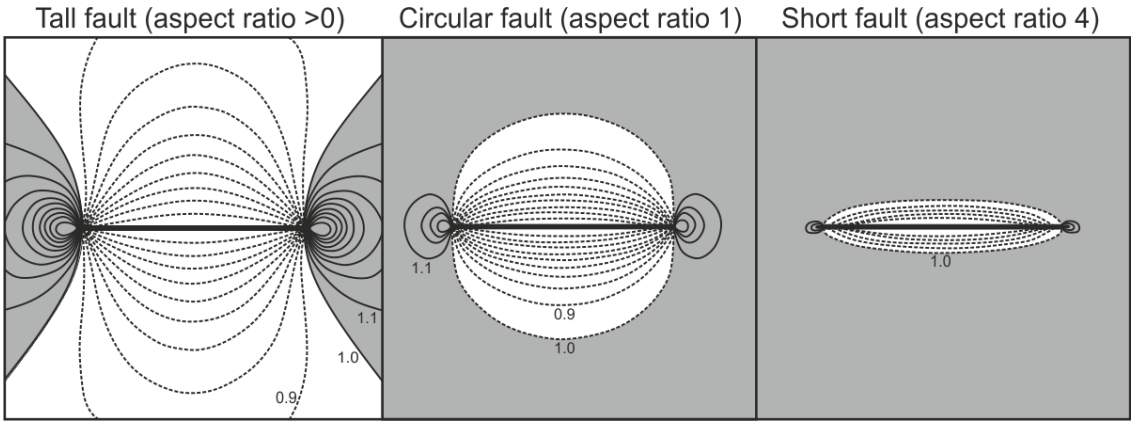

Figure 1.9. Influence of three dimensional fault shape on local shear stress perturbations for vertical normal faults. Stress is reduced in non-shaded areas and enhanced in shaded areas. Since faults can only form when stress exceeds the shear strength of the host, additional faults are less likely to form in areas of reduced stress. The aspect ratio of the fault at a given time plays a major role in determining the geometry of the altered stress field. As aspect ratio increases, the area of the decreased stress reduces. Modified after Willemse, 1997.

1.2.3 Fault Growth and Linkage: Summary

Early interpretations of the kinematics of fault growth through the linkage of initially separate segments relied upon the assumption that the plane at which observations were made were representative of the entire 3D fault geometry (e.g. Cartwright et al, 2005). This assumption leads to the model of fault growth and linkage at relay zones occurring coincidentally, through the independent propagation of isolated faults. The alternative model of fault growth proposed by Walsh et al (2002, 2003) recognises that the plane of observation will rarely be located at the position of maximum displacement on a fault, and that as a result out of plane

linkage is entirely possible. This implies that the growth of faults occurs through the evolution of a coherent array of fault segments, rather than coincidental linkage. Given that the majority of early fault growth models (Peacock and Sanderson, 1994; Cartwright et al., 1995; Cowie et al., 2000) are based upon 2D rather than 3D observations, the 'Coherent' growth model of Walsh et al (2003) seems to be more applicable to the majority of situations.

1.2.4 Mechanical Stratigraphy

Soliva et al (2006) used field observations coupled with numerical modelling to infer mechanical layer thickness as a controlling factor on both fault spacing and maximum relay separation (figure 1.10). They show that the mechanical thickness, T, of a layer constraining vertically restricted faults is proportional to the fault-normal width, S*, of the region of stress drop around a fault (Figure 1.10). In turn this controls the minimum spacing between faults, as well as the maximum separation between overlapping fault tips that will allow linkage. For a given amount of extension across a brittle layer strain is accommodated through faulting. If the brittle deformation (i.e. a fault) cannot propagate vertically due to the layer being contained between ductile units then additional faults must form to accommodate the horizontal extension. The minimum spacing between faults is controlled by the field of reduced stress associated with each fault, providing that the fault has not healed through, for example, cementation (e.g. Yasuhara et al., 2005). This area of stress reduction is itself controlled by the amount of strain (extension) accommodated by the fault, and hence by the thickness of the mechanical layer in which the fault is constrained (e.g. Ackermann and Schlische, 1997). Once a fault has propagated to the vertical limits of the mechanical layer there must be a stress intensification at its lateral tips. This is due to the regional strain having only been accommodated across the brittle portion of the fault (assuming no interaction with, or accommodation of strain by, other structures). It is intuitive to believe that this stress intensification must lead to an increase in the rate of lateral fault tip propagation, hence increasing the aspect ratio of the fault (i.e. decreasing the d:L) and consequently modifying the stress reduction field (Willemse, 1997). This may lead to modification of the critical fault spacing as described by Soliva et al., (2006).

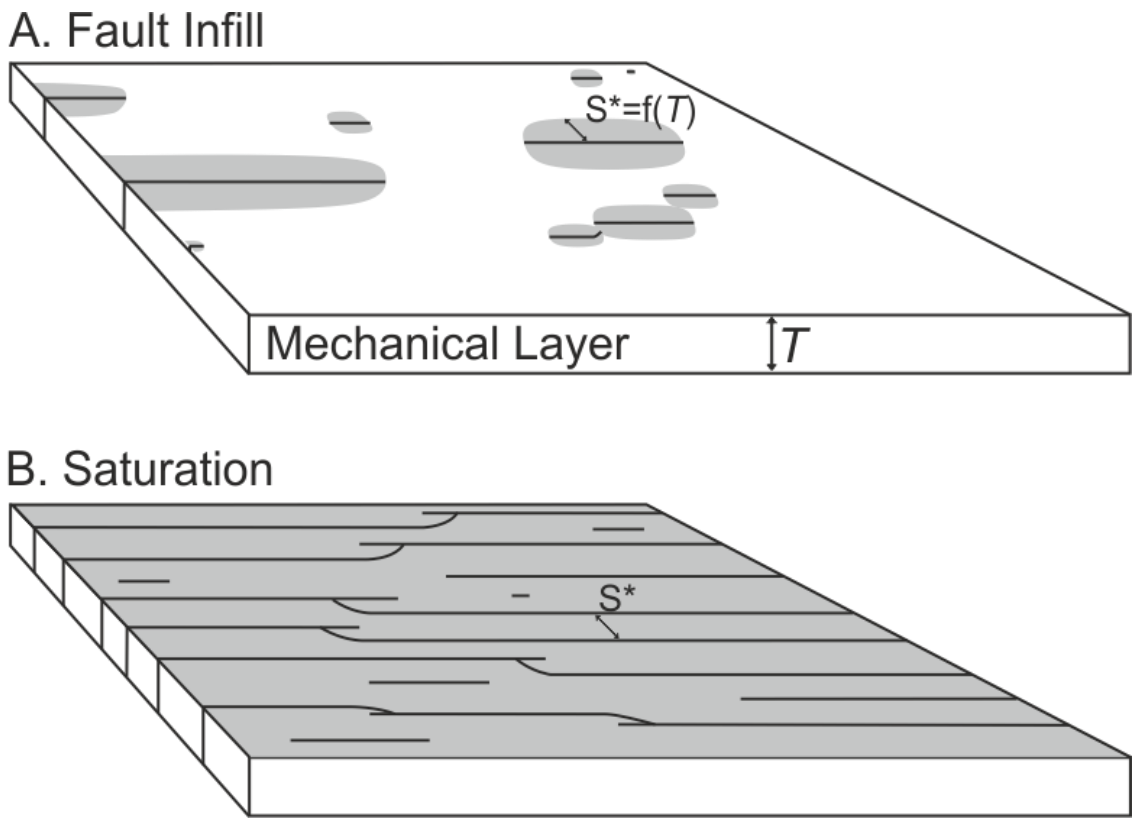

Figure 1.10. Idealised sketch describing the development of normal faults within a mechanical layer of restricted thickness, *T*. A. Initial faults are randomly distributed owing to minor heterogeneities in the stress field and mechanical properties of the host. The critical spacing S* is a function of the mechanical layer thickness, *T.* This dimension refers to the width of the stress reduction shadow around faults. This dimension controls the minimum spacing of faults and the maximum separation allowed for faults to be able to link. B. Faults have grown through nucleation (outside of stress shadows), lateral tip propagation and linkage. A relatively regular fault spacing has now developed since the mechanical layer is saturated. Modified from Soliva et al (2006).

It must be noted that this work relates to a mechanically brittle layer between two ductile layers, hence the degree of saturation (defined by the average spacing between faults) will be higher to accommodate strain. This could potentially be used as a tool for estimating sub-seismic fault populations and spacing, as well as constraining whether overlapping faults in

active extensional provinces are likely to become hard linked, with implications for seismic hazard management.

A consideration when determining the relative timing of activity on a number of fault sets is the ability of a specific fault set to remain active given a constant orientation of the regional extensional stress field. The dip of faults may be altered due to mechanical compaction of the media through which the fault is formed, rotation due to activity on synthetic faults in the hangingwall or footwall or regional scale isostatic or thermal subsidence or uplift. The implication of this is that faults may become rotated to such a degree so as to be unfavourably orientated for accommodating extension (e.g. Jackson, 1999). This may occur when the dip of a fault is reduced so that the stress required for continued movement is greater than the applied stress, leading to the preferential formation of a new, more favourably orientated fault.

1.2.5 Fault Rock Properties

The properties of faults pertinent to the flow fluid in the subsurface can be grouped into two classifications, geometric and petrophysical. The geometry is dependent on the processes of fault growth, which control the distribution of displacement and the resulting across-fault juxtapositions. The petrophysical properties of faults, or rather fault rock, determine the permeability of a fault, and hence the rate at which a fluid can flow across the fault under a specific pressure gradient. It is these petrophysical properties, and their representation in geological and simulation models that is outlined herein.

1.2.5.1 Fault Rock Forming Processes and Classification

The movement on faults leads to the formation of fault rock via a number of different processes (Yielding et al., 1997; Fisher and Knipe, 1998). The permeability of fault rock is dependent on the mechanism(s) of deformation, which in turn depend on a number of factors including the degree of lithification, clay content and burial depth (Fisher and Knipe, 1998). In general poorly indurated (and/or shallowly buried), clean sediments with less than 15% clay content will display disaggregation and rotation of grains rather than the cataclastic deformation and grain fragmentation seen for more indurated (and/or more deeply buried) rocks (figure 1.11). The fragmentation of grains associated with cataclasis results in the formation of nucleation sites for quartz cementation at temperatures above 90°C (Fisher et al., 2000), leading to significantly reduced local permeability. If cementation were to be continuous horizontally and vertically along a fault it could provide a major barrier to across-

fault flow, although forecasting the distribution and also the degree of cataclasis and cementation is difficult, the latter without local sample calibration.

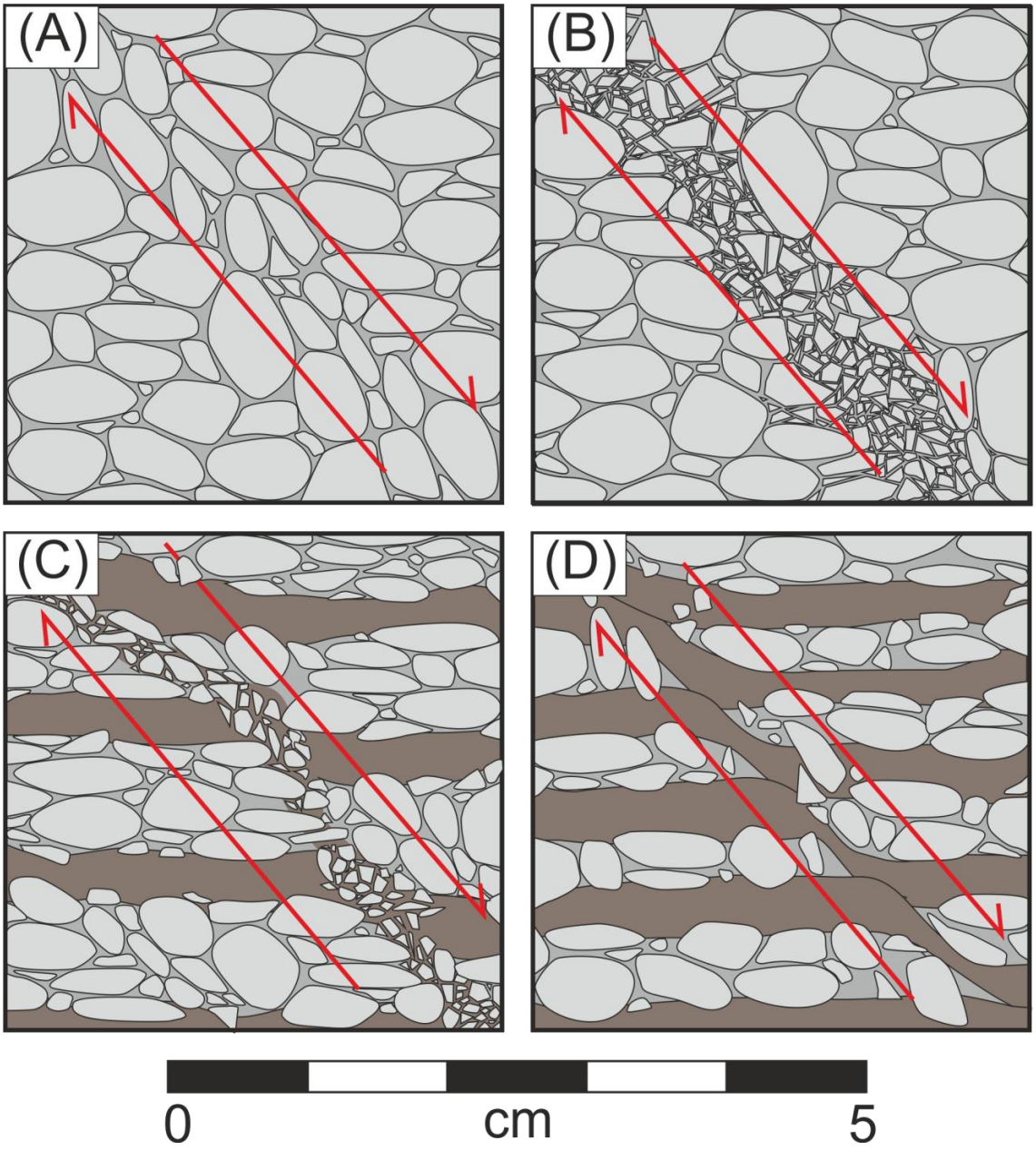

Figure 1.11. Schematic illustration of the different classifications of fault rock at the core-scale. (A) Disaggregation zone. Generally formed at low confining pressures within poorly cemented rocks with <15% clay content. Fault movement leads to grain re-orientation with the long axis of gains becoming parallel to the displacement direction. (B) Cataclasis. Deformation within well cemented, low (<15%) clay content silisiclastic sediments leads to grain fragmentation. Temperatures above 90°C may lead to the formation of a quartz cement. (C) Phyllosilicate framework fault rocks (PFFRs). Moderate clay content (15-40%). Dominated by the mixing of clay and quartz grains within the fault zone. (D) Clay smears, >40% clay content. Ductile smearing of clay rich shale layers along the fault zone.

As the clay content of the host sediment increases then the process of grain mixing during deformation becomes more dominant, with the entrainment of clay inversely correlating with permeability. These types of fault rock are often referred to as phyllosilicate-framework fault rocks (PFFRs-Fisher and Knipe, 1998), and have clay contents of between 15 and 40%. The proportion of shale within a fault rock can be estimated using algorithms such as the Shale Gouge Ratio (SGR, Yielding et al., 1997), which predicts the amount of shale in the fault rock at certain point based on the proportion of shale which has passed that point (Figure 1.12).

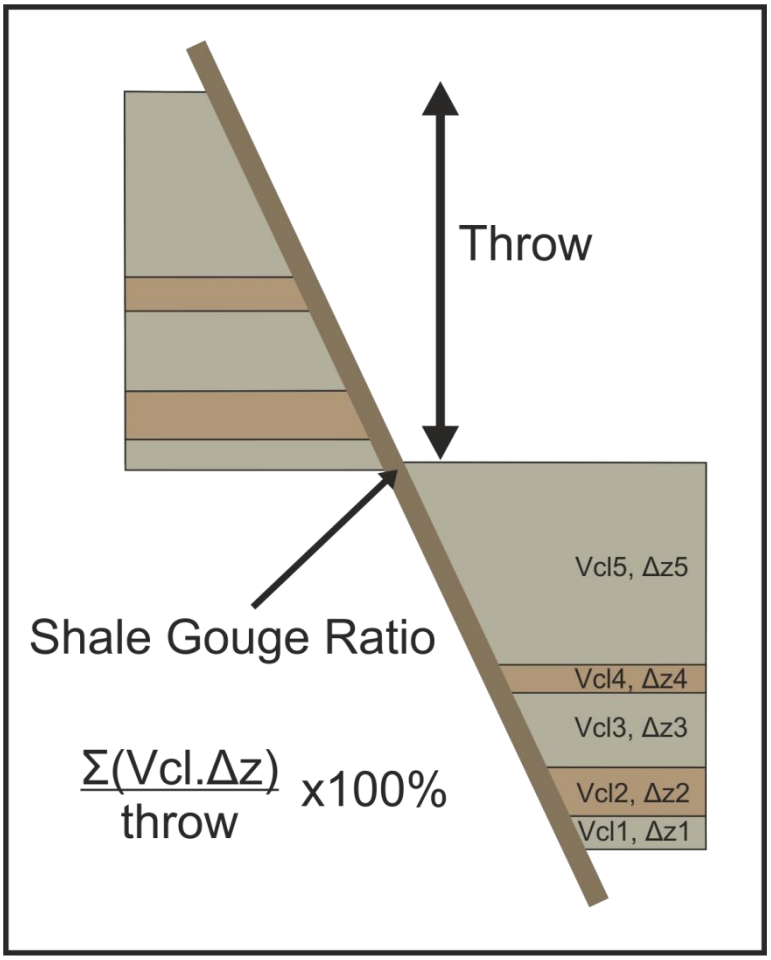

Figure 1.12. Schematic illustrating the calculation of the shale gouge ratio (SGR). The SGR value is the proportion of shale within a fault rock at a specific point on a fault. It is defined by the proportion of shale that has been displaced past that point. Modified from Yielding et al (1997).

Above approximately 40% clay, fault rocks may begin to be composed of zones of continuous clay smears, formed as intervals of more ductile clay rich lithologies are sheared during deformation (Ciftci et al., 2013). The low permeability and continuous nature of the clay smears can, in certain circumstances, has been used to account for the development of very

large across-fault pressure differences (Childs et al., 2002). Algorithms such as the Clay Smear Potential (CSP, Bouvier et al., 1989; Fullijames et al., 1996) and the Shale Smear Factor (SSF, Lindsay et al., 1993) use shale layer thickness and displacement to calculate a probability of a continuous smear being present along a fault.

1.2.6 Sealing Mechanisms of Fault Rocks

The relative importance of the petrophysical mechanisms by which faults rocks influence hydrocarbon reservoirs differ between exploration and production scale settings. During exploration the ability of a fault to trap an accumulation of oil or gas is relevant, whereas during production it is the permeability-reducing effect of faults which is important (Manzocchi et al., 2002, 2010).

1.2.6.1 Exploration Scale

A fault can support a column of hydrocarbon if the capillary entry pressure of the fault rock is greater than the buoyancy force (due to the density difference between hydrocarbon and water) of the hydrocarbon column (Schowalter, 1979; Watts, 1987; Fisher et al., 2001; Brown, 2003). The capillary entry pressure, P_c (eq 1, Schowalter, 1979), is a function of the capillary radius, P_r, the interfacial tension between hydrocarbon and water, σ, and the contact angle between the wetting (usually water) and non-wetting phase (usually hydrocarbon), θ.

(1) $$P_c = 2\sigma cos\frac{\theta}{R_c}$$

The capillary radius (which generally decreases with increasing clay content), which is defined as the minimum pore-throat radius, is generally determined experimentally using mercury injection porosimetry of core plug samples. Measured laboratory values can be converted into in-situ values using eq 2 (Schowalter, 1979);

(2) $$P_c = \gamma_h cos\theta_h Pe_m / \gamma_m cos\theta_m$$

Where γ_h = the interfacial tension of hydrocarbon and water (in dynes cm^{-1}), θ_h= the contact angle of hydrocarbon and water, Pe_m = the mercury-air capillary entry pressure, γ_m= the interfacial tension of mercury and air (dynes cm^{-1}), and θ_m= the contact angle of mercury and air.

By integrating into the equation the buoyancy differential between hydrocarbon and water, the maximum column height that a fault can support can be calculated;

(3) $$H_{cp} = \gamma_h cos\theta_h Pe_m / 0.433(\rho_w - \rho_h)\gamma_m cos\theta_m$$

Where H_{cp} = theoretical maximum hydrocarbon column height, ρ_w= water density, ρ_h= hydrocarbon density, and 0.433 is a metric-imperial conversion factor.

Fault zone complexity and heterogeneity, fault rock hydrocarbon saturation and relative permeability effects are however not accounted for within this theory (Fisher et al., 2001, and explored further in Chapters 6 and 8). Compiled data of SGR values versus across fault pressure differences and column heights provide an alternative for forecasting the maximum column height that may be supported by a fault with a specific clay content (Bretan et al., 2003). This approach implicitly accounts for fault heterogeneity and does not rely on scaling up core sample measurements to entire faults (Yielding, 2012).

1.2.6.2 Production Scale

During hydrocarbon production it is the effect of fault rocks as barriers or baffles to flow over production timescales which is of primary concern, rather than their ability to form a seal over geological time. Where reservoir rock is self-juxtaposed across a fault, the ability of hydrocarbon to flow across that fault due to a production induced pressure differential is influenced by the fault rock permeability. Processes such as cataclasis, the incorporation of clay, and cementation of a fault rock lead to reduced fault rock permeability. If this permeability reduction is sufficient and continuous along and up a fault, then it may form a barrier to flow, potentially leading to reservoir compartmentalisation. The most common approach for calculating the permeability of a fault is to calculate and map SGR values onto the modelled fault planes. A number of generic clay content to permeability transforms (figure 1.13), based upon sample analysis, can be applied to convert this SGR value into a fault permeability (Manzocchi et al., 1999; Sperrevik et al., 2002; Jolley et al., 2007), although locally calibrated values which link permeability to local burial history and diagenesis are preferred. (Freeman et al., 2008). This approach assumes that sample-scale measurements are scale invariant and can be applied to an entire fault. This has the limitation that fault geometric heterogeneity is not accounted for.

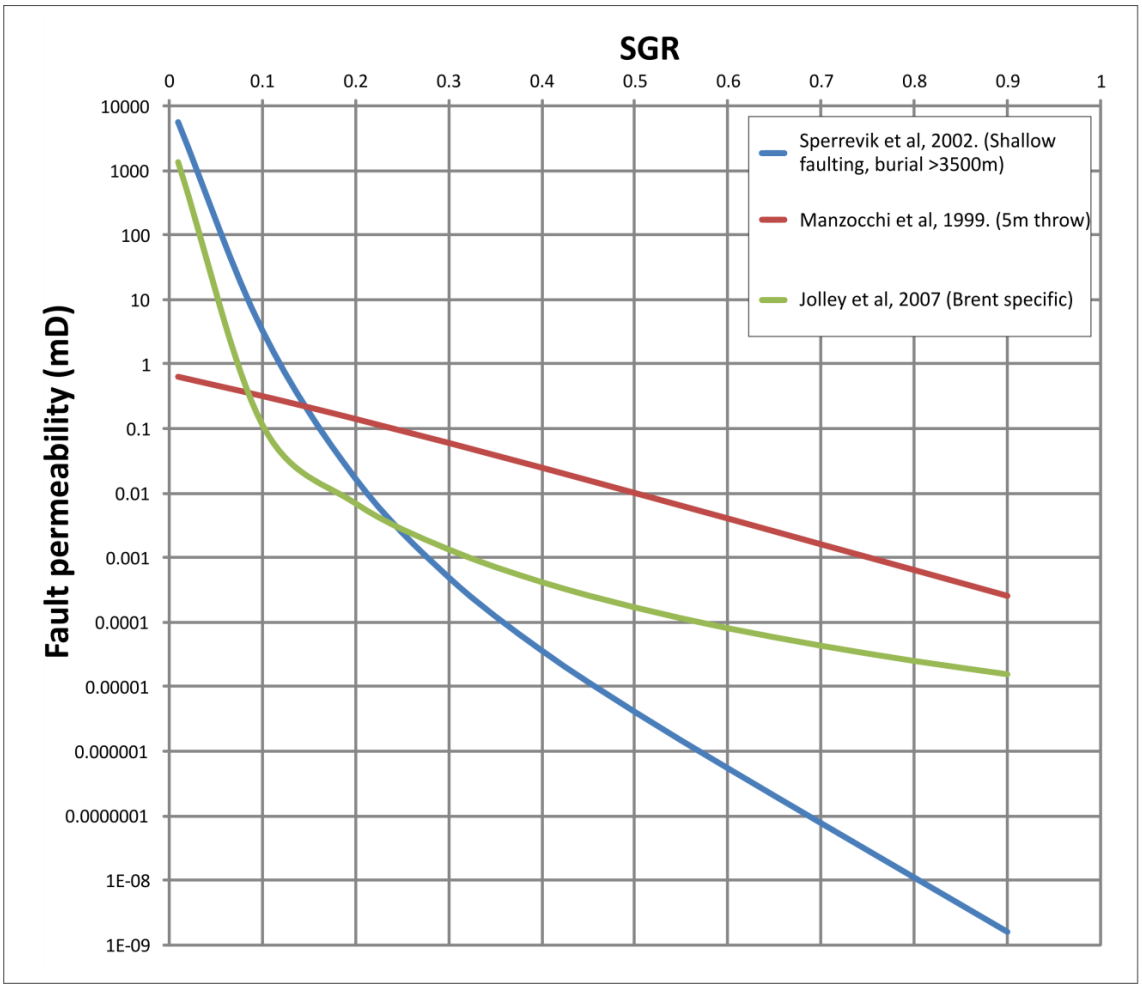

Figure 1.13. Commonly applied clay content to permeability transforms used for estimating fault rock permeability from either measured or calculated (SGR) clay content values. As mentioned, applying these calculated permeability values to the simple fault geometries within geocellular grids assumes that the fault rock properties are scale invariant and does not account for fault geometric heterogeneity (see chapter 8). Compiled from data within Manzocchi et al (1999), Sperrevik et al (2002) and Jolley et al (2007).

To incorporate the calculated values of fault rock permeability within reservoir models a degree of simplification of the faults is required. Faults are represented as 2D planes within reservoir models, rather than as the 3D grid cells with realistic dimensions containing petrophysical properties which represent the host reservoir rock. Despite this representation of faults being incorrect (since fault rock does have a discrete thickness) it is employed due to the computational difficulties of having adjacent cells of significantly different dimensions (Manzocchi et al., 2008, 2010) that modelling faults in 3D as grid cells would necessitate. Therefore, in order to incorporate fault rock permeability into reservoir simulation models fault rock is represented as a transmissibility multiplier (TM, figure 1.14) between adjacent grid

cells (Knai and Knipe., 1998; Manzocchi et al., 1999). This is a mathematical representation of the transmissibility reduction between two adjacent grid cells due to the fault rock between the cells. For example, a TM value of 0 implies a completely sealing fault, whereas a value of 1 implies a completely open fault with no permeability reduction. Values calculated using geologically derived fault-rock clay contents and clay content to permeability transforms will be within this range, with higher SGR values (and hence lower permeabilities) leading to lower TMs.

(4) $$TM = t_f \frac{\left({}^{2}/_{k_f} - {}^{1}/_{k_i} - {}^{1}/_{k_j}\right)}{\left({}^{L_i}/_{k_i} + {}^{L_j}/_{k_j}\right)}$$

As the impact of this permeability reduction is controlled by Darcy's law, the length over which it acts (i.e. the fault rock thickness) is also required, and can be estimated using relationships between displacement and thickness (e.g. Manzocchi et al., 1999; Kim and Sanderson, 2005; Childs et al., 2009). Thicker fault rocks mean that the width over which permeability is reduced is larger, hence leading to lower TM values (equation 4). The calculation of fault rock thickness generally assumes a linear relationship with fault displacement (figure 1.15). As is explored later in the thesis (chapter 8), the complex geometry of 'real' versus modelled faults may limit the validity of this assumption.

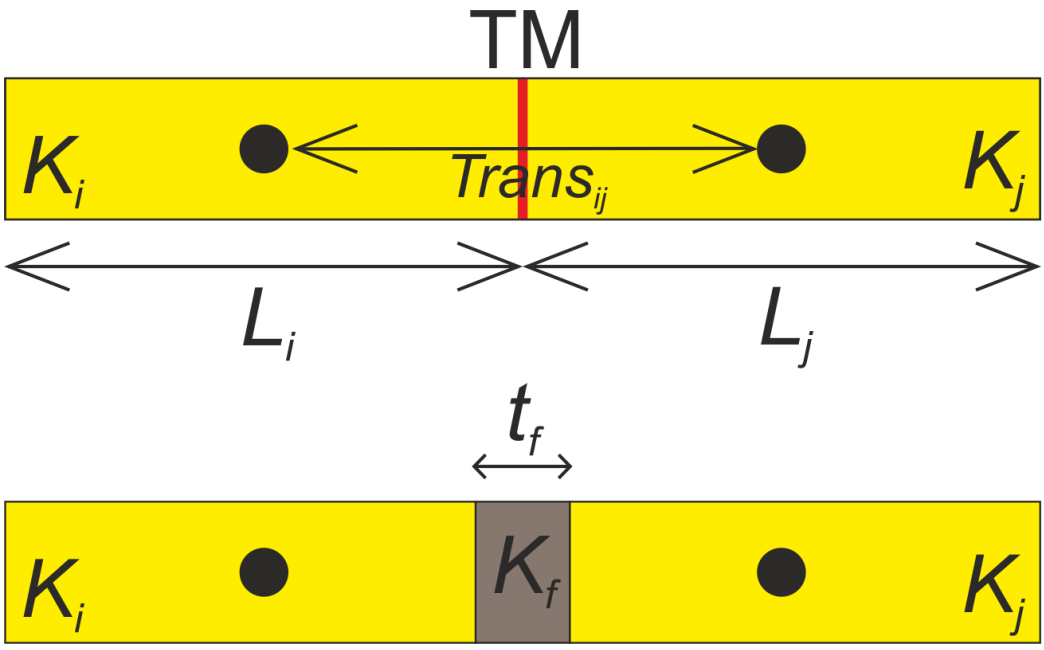

Figure 1.14 (Previous page). Schematic illustrating the calculation of transmissibility multipliers (TMs) representing a fault separating adjacent grid blocks within a geocellular model (see equation 4). Thicker fault rock (t_f) and lower permeability fault rock (k_f) lead to lower TMs for a given host permeability (K_i, K_j) and grid length (L_i, L_j). Modified from Manzocchi et al (1999).

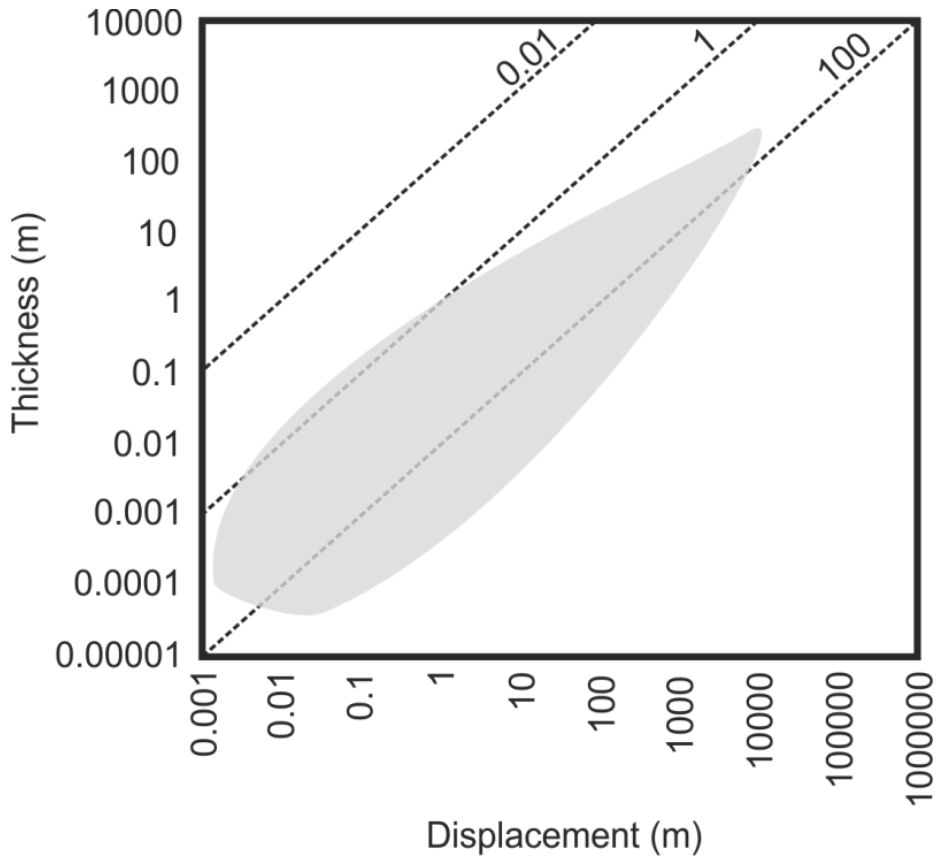

Figure 1.15. Fault rock thickness plotted against fault displacement on log:log axes. The majority of measured points plot within the transparent grey area, however the scatter is large and is influenced by the growth processes of faults (see chapter 8). A single value is hence unlikely to represent an entire fault. Modified from Childs et al (2009).

Additional, more specific, background literature is covered within the individual chapters.

Chapter 2

Methodology

2.1 Abstract

This methodology chapter serves as an overview of the broad range of techniques and methodologies which have been applied during the course of the project. As many of the aspects of the thesis can be viewed as 'stand-alone' pieces of work (linked by the common theme of fault geometric uncertainty) greater detail of the specific methodologies has been included within the individual chapters. The methodologies which have been applied can be broadly split into three main sections; Field data collection, 3D geological modelling of field data, and digital geological modelling methods.

2.2 Field Data Collection

2.2.1 Topographic Base Maps

A major aim of the thesis was to integrate a range of outcrop data within a geological modelling software environment. To accomplish this successfully a number of steps were required prior to the initiation of data collection including the generation of topographic base maps of a suitable resolution. Although detailed maps for much of mainland Greece do exist, their availability is somewhat limited. A road atlas at 1:50000 scale was used as the basis for the majority of the field locale, however more detailed hiking maps, also at 1:50000, were also employed where available. A period of reconnaissance fieldwork allowed the identification of areas where higher resolution mapping would be required. These were produced by enlarging digital versions of the available maps to the desired scale (typically 1:20000 and 1:8000). Figure 2.1 shows the location and scale of the various base maps used during data collection.

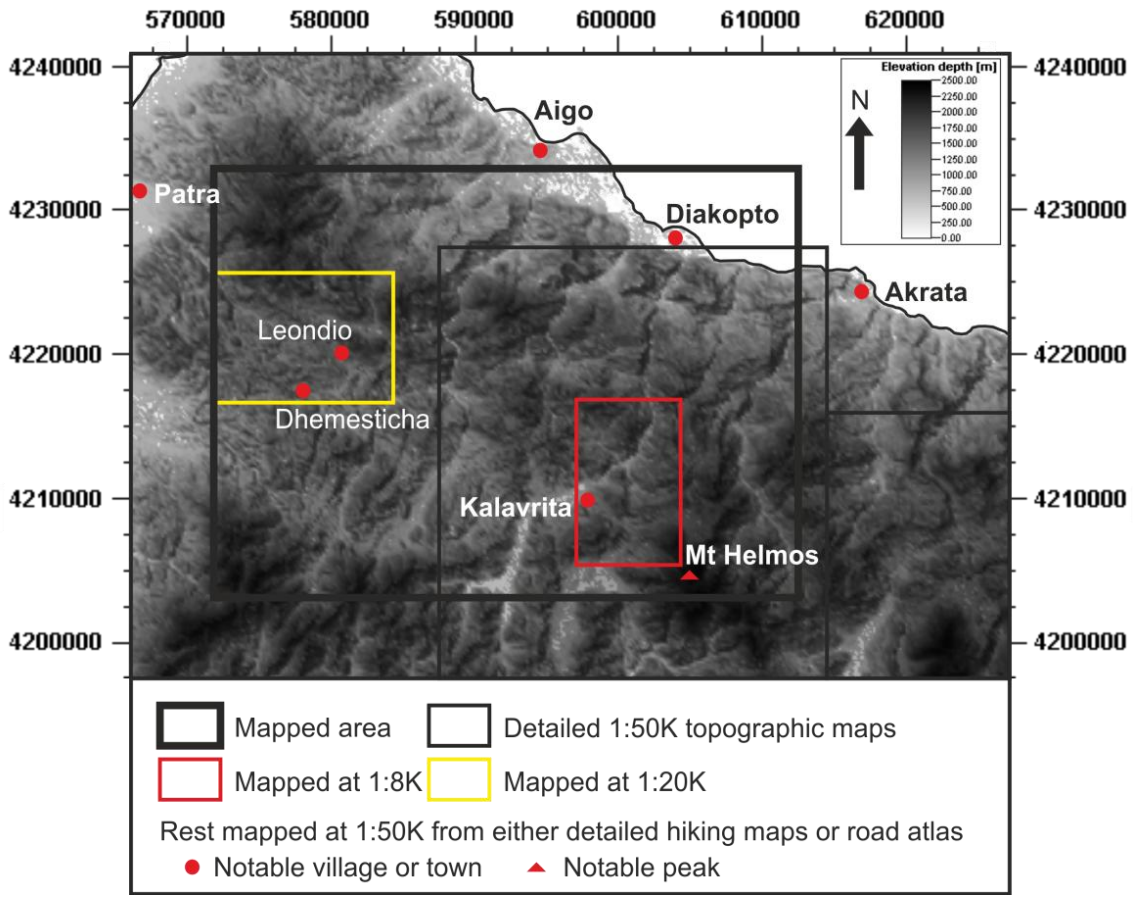

Figure 2.1. Greyscale topographic map derived from digital elevation data with insets depicting the location of detailed topographic maps (Anavasi 1:50000 walking maps) used for base maps during field data collection. The base map for the remainder consisted of a less detailed 1:50000 road atlas. The main area was mapped at 1:50000, with the insets showing the locations of higher resolution mapping.

To maintain cross-compatibility between different software programs during later modelling it was decided that field data would be geo-referenced using the international UTM coordinate system. However, the available topographic maps of the area utilised a local coordinate system not readily recognised by either handheld GPS equipment or software packages such as Petrel. To remedy this problem software including arcGIS and GeoMapper was used to overlay a UTM grid onto digital versions of the topographic maps.

2.2.2 Geological Mapping

Geological mapping provided the largest constituent of field data. As with topographic maps the availability of pre-existing geological maps was somewhat limited (Figure 2.2), restricted as it was to low resolution maps from the literature (e.g. Collier and Jones, 2004; Ford et al.,

2012; Sorel, 2000), an unpublished thesis (Flotté, 2003), and a number of maps from the Institute of Geological and Mineral Exploration (IGME). The latter of these sources focus largely on the sedimentology of the area, and to some extent neglect the structural configuration. This emphasised the requirement for a more detailed set of geological maps in order to understand the structural evolution of the area, and its influence on the stratigraphy and sedimentology.

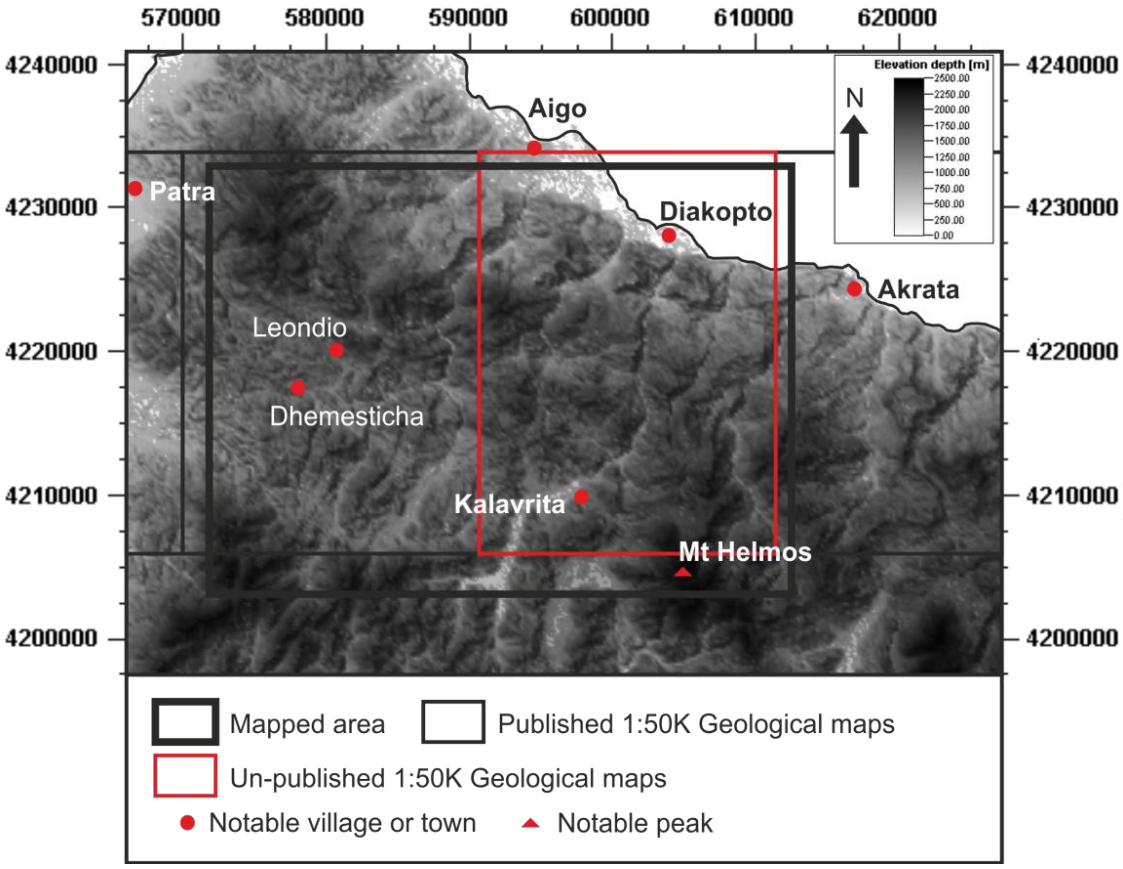

Figure 2.2. Greyscale topographic map derived from digital elevation data with insets depicting the location of pre-existing geological maps relative to the area mapped in this study. The maps indicated consist of published and unpublished maps compiled by the Greek Institute of Geology and Mineral Exploration (IGME), and exclude maps within the literature.

Reconnaissance scale geological mapping was initially conducted over a period of 2 weeks, primarily using paved and unpaved roads for access. This allowed a basic understanding of the broad scale geology to be rapidly acquired as well as permitting a strategy for more detailed data collection to be developed. More detailed mapping was conducted over two longer field seasons, each of 5 weeks, allowing an iterative mapping process (figure 2.3) where areas could

be studied in greater detail if required. Mapping consisted of locating and tracing lithological boundaries and faults, constructing transects both parallel and perpendicular to the main structural alignment, collecting structural orientation measurements for both bedding and faults, and performing sedimentological characterisation of mappable units. All data points used during construction of geological maps were geo-referenced using a GPS device and supplemented with field sketches and photographs where appropriate. Completed field maps were scanned and geo-referenced before being digitised using CorelDraw graphics software.

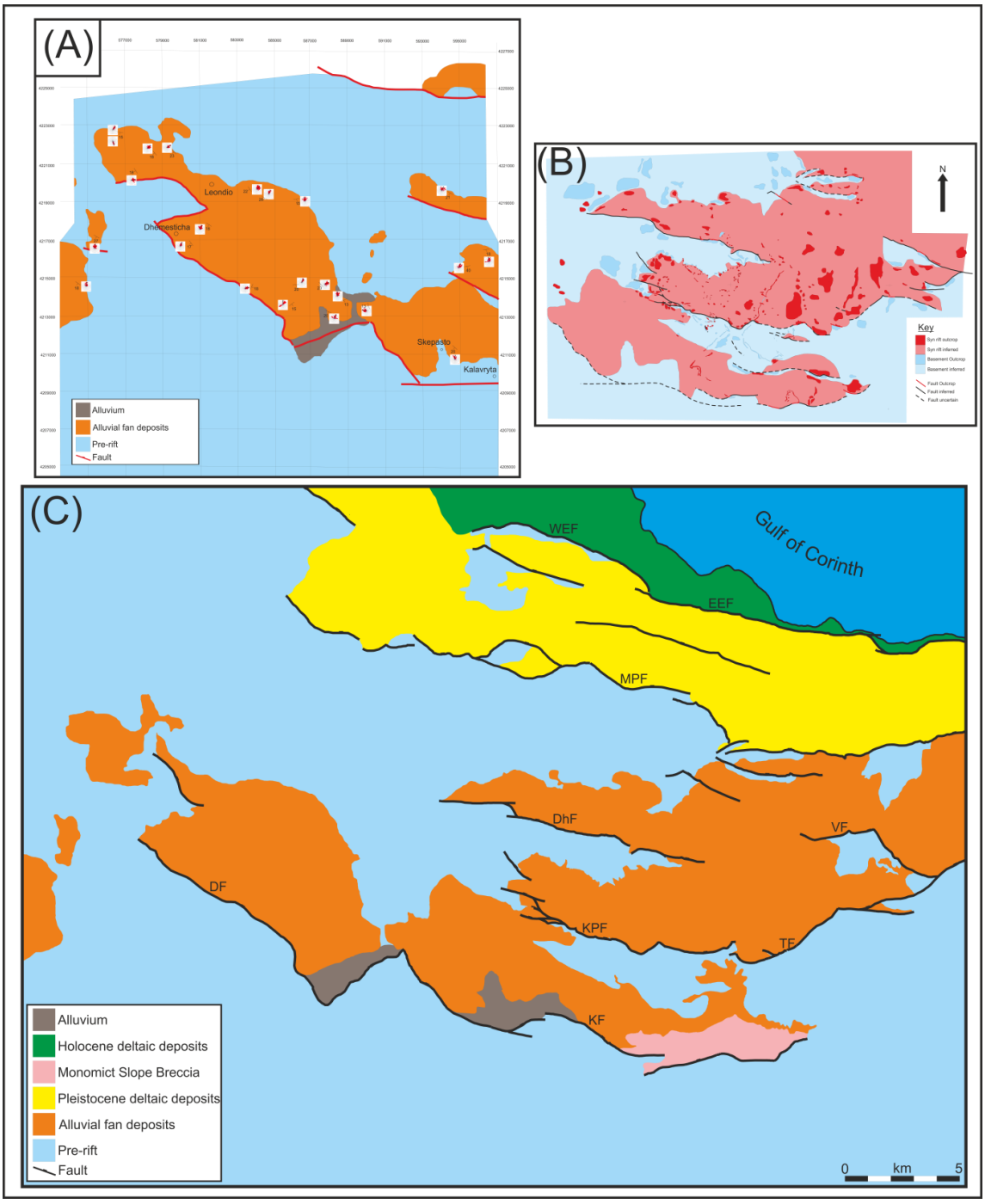

Figure 2.3 (Previous page). Iterative process of geological mapping. (A) Reconnaissance scale mapping of the western area including the Dhemesticha sub-basin. (B) Detailed mapping of eastern area illustrating the position of outcrop. (C) Lithological map compiled from data collected over multiple field seasons. For a more detailed version see chapter 3.

2.2.3 Palaeocurrent Data

The influence of faults, and in particular fault linkage zones, on sediment dispersal is relatively well understood (e.g. Chapter 1). The topographic lows resulting from relay zones can act as sediment input points into hangingwall basins, hence palaeocurrent directions within the syn-rift facies should radiate away from these point sources. Theoretically if the along strike and up section variations in palaeocurrent direction can be disentangled, then the timing of linkage of individual fault segments can be constrained (Dart et al., 1994; Gawthorpe et al., 1994).

The majority of the syn-rift facies consists of continental alluvial fans composed of channel and overbank elements, as described in chapter 3. The overbank portion is mud-dominated and contains little to no palaeocurrent information. In contrast the channel and braid-complex portions are coarse grained sands and conglomerates of pebble to boulder grade, with the conglomerates displaying clast imbrications and preferred clast alignment. The long axis of the clasts tends to align perpendicular to the flow direction due to the rolling transport mechanism. If imbrication of clasts is also present the absolute direction can be identified. To ensure statistical validity, a minimum of 50 clast orientations were recorded at each outcrop locality, along with the bedding orientation. These were later structurally restored and plotted as rose plots allowing the average flow orientation at the time of deposition to be determined (figure 2.3). To aid in the accuracy of the structural restorations the depositional dip was estimated using Palaeoslope analysis (see below).

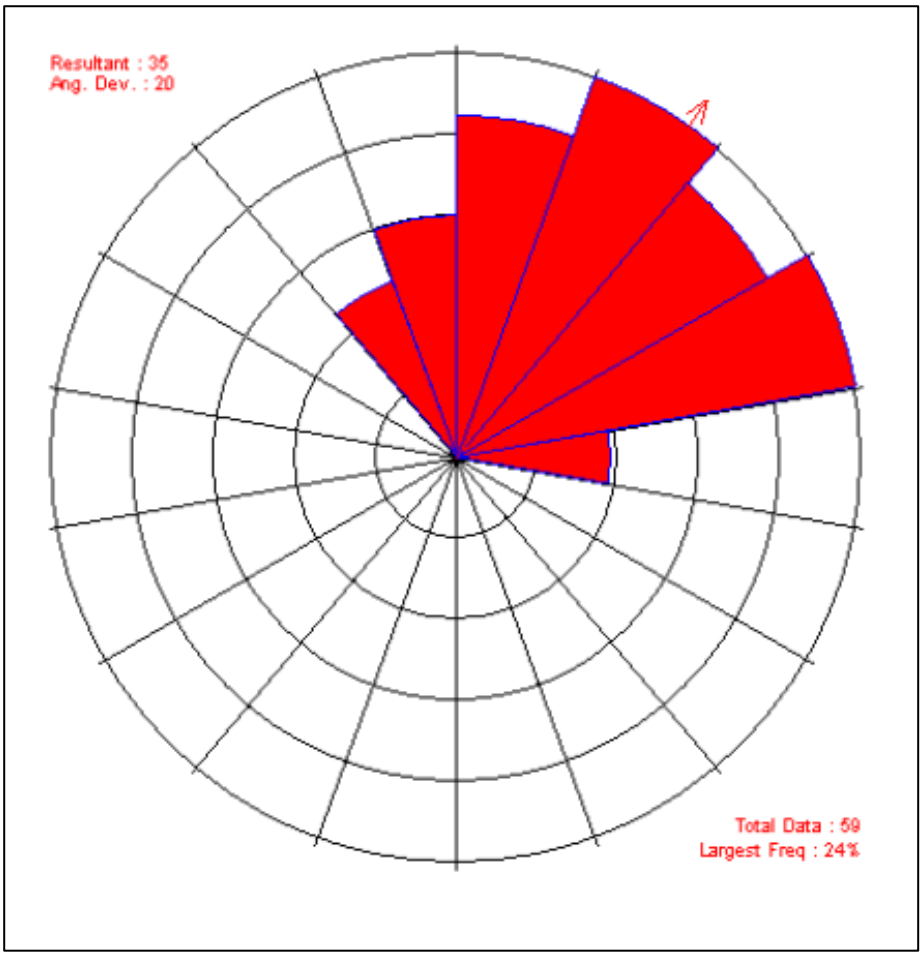

Figure 2.4. Example of a restored equal-length rose plot describing the palaeocurrent at a single outcrop location as defined by preferred clast orientation. Additional data included on the plot consist of the number of individual measurements, the resultant orientation in degrees clockwise from north, the angular deviation and the percentage of readings within the largest division.

2.2.4 Palaeoslope Data

One of the aims of the fieldwork was to establish the displacement on the faults, with one of the methods for this being the extrapolation of syn-rift, hangingwall strata towards their intersections with the faults at depth (see Chapter 3). It is recognised that alluvial fans are not necessarily deposited horizontally, with depositional dips in excess of 20° being not uncommon (e.g. Paola and Mohrig, 1996). Hence, to correctly ascertain fault displacement the depositional dip of the syn-rift strata required reconstruction. A method based on the median clast size and the flow depth was used (Paola and Mohrig, 1996). Statistically valid clast dimensions can be determined where enough measurements are collected (typically 150-200

per outcrop), although determining the channel/flow depth is often more difficult and is dependent on the quality and orientation of each individual outcrop. Where significant uncertainty was present, both minimum and maximum values for channel depth were applied to determine a possible range. Despite this the method contains too high a level of uncertainty to warrant being relied upon for statistically valid conclusions.

2.2.5 In-Situ Strength Measurements

An additional aim of data collection was to examine if any link between the mechanical properties of the stratigraphy and the fault geometries mapped in the field could be established. This undertaken by taking a series of in-situ strength measurements, with a Schmidt hammer being used for indurated outcrop, and a penetrometer used in areas of lower consolidation. Collection of data using a Schmidt hammer requires a modicum of preparation of the target outcrop. The Schmidt hammer uses a spring loaded mechanism to measure the rebound of a rock when a steel pin is fired onto its surface with a greater rebound value corresponds to a higher unconfined compressive strength (UCS). The surface used for measurement must be in-situ and must be cleared of any debris or vegetation and examined for any recent damage. If a surface is loose or damaged then the measurements will be too low. The accepted procedure for recording a representative value is to take measurements until a consistent value is returned. This ensures that any effects of weathering if the surface are negated. A minimum of 10 measurements are subsequently recorded with the mean of the highest 6 values being the characteristic value. This dimensionless measurement can then be converted into MPa using the calibration values of the individual Schmidt hammer and the lithology being tested (Katz et al., 2000). The major shortcoming when using in-situ strength measurements for analysis of geological structures is that the present day strength as measured may not represent the strength at time of deformation. Outcrops are likely to have been exhumed, as well as have been mechanically altered through, for example, cementation. This limits the extent to which present day measurements are relevant for characterising earlier properties.

2.2.6 Sample Collection

The present day position of an outcrop gives only a limited insight into its tectonic history such as its maximum burial depth. An aim of the field work was to determine the burial depth of the syn-rift sediments in order to constrain fault displacement and evolution. A number of features indicative of burial depth are present within both the syn-rift and pre-rift sequences, however the majority of these are of a scale requiring microscope identification. Hence a large number of samples were collected in order for thin sections to be prepared.

Samples were collected only from in-situ outcrop in order that orientation could be recorded along with location and present day elevation.

2.2.7 Sedimentary Logging

In order to characterise the interplay between structural evolution and sedimentation, a quantitative approach in the form of recording a series of sedimentary logs was applied to capture sedimentary facies variations (Chapter 3). Where possible, logs were recorded at intervals along transects running perpendicular to the major half-graben bounding faults. This allowed the evolution of facies from proximal to distal to be captured and correlated with the aid of photo-panels. Logs were constructed normal to bedding in order that the correct thicknesses of specific packages could be documented.

2.2.8 Sample analysis

Sample analysis in the form of optical microscopy was undertaken in order to attempt to establish the relative burial depth of syn-rift sediments, and hence the displacement on the rift faults. Since carbonates dominate the composition of the syn-rift sediments, depth estimates are dissolution-based.

Pressure dissolution in carbonates can occur at relatively shallow depths, and commonly takes two forms; interpenetration of grains or clasts leads to the formation of concavo-convex grain contacts, and can occur below approximately 200 m (Larsen and Chilingar, 1983). However, the depth range over which they occur is poorly constrained, and they hence represent only a minimum burial depth estimate. Stylolites are also depth-dependent dissolution features, which can be used to estimate the volume of removed material (Fletcher and Pollard, 1981; Peacock and Azzam, 2006). Despite this the depth at which they initiate is poorly constrained, with estimates of 90 m (Tada and Siever, 1989), 300-600 m (Ebner et al., 2009) and 800-1000 m (Railsback, 1993) being proposed.

As a result a relative, rather than an absolute, depth estimate has been pursued (see chapter 3), based upon the typical observations outlined in figure 2.5.

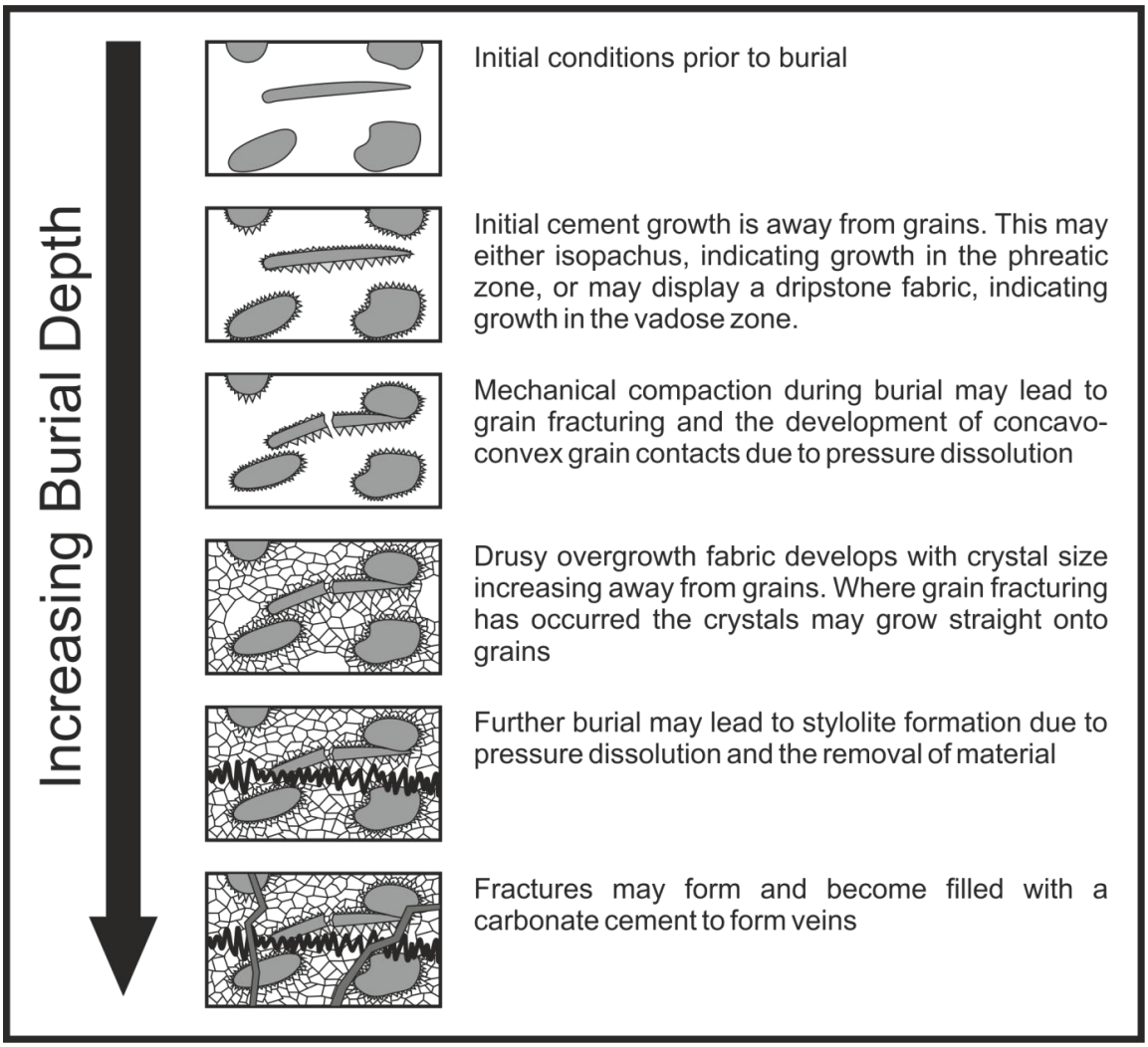

Figure 2.5. Framework for establishing a relative burial depth estimate for syn-rift sediments. Compiled from data within: Larsen and Chilingar (1983), Tucker and Bathurst (1990).

2.3 3D Geological Modelling of Field Data

The majority of geological modelling consisted of constructing and populating geocellular grids primarily using Petrel (Schlumberger 2012). It is not within the scope of this thesis to document the numerous and detailed workflows and procedures employed during geological modelling, however the key steps and non-standard approaches used to solve specific issues are outlined. Geological modelling software designed for use within the petroleum industry is primarily used for subsurface rather than outcrop data. As a result a number of novel

approaches were required to integrate field data within the 3D software environment. These are outlined in the following sections.

2.3.1 Digital Elevation Models

To digitally capture the present day topography of the field area a digital elevation model (DEM) was constructed using open-source ASTER data acquired by NASA. This is the highest quality data currently available over mainland Greece, with a resolution of 30m. The data can be downloaded as 1 degree latitude/longitude tiles in a geo-tiff format, where the elevation of each 30 x 30 m pixel is designated by its colour on a grey-scale. Prior to import into geo-modelling software this required conversion to a useable format. This was performed using 3D Move (Midland Valley 2012), with each pixel being converted to a point with its position defined by x, y, z coordinates in the UTM format. In this manner the required geo-tiff files were converted to text files and imported into Petrel as point sets where they could easily be converted into surfaces.

2.3.2 Import of Field Data

Data collected during fieldwork consisted of 2D maps and 1D points data recording the position of specific outcrops, samples or measurements such as palaeocurrent or orientation readings. By importing these data into the geo-modelling environment its full 3D architecture can be constructed and visualised in order to significantly aid analysis.

2.3.3 2D Data

Maps were imported into geo-modelling software (Petrel, Schlumberger 2012) in two formats, firstly as the scanned versions of original field maps and secondly as the digitised version. In both cases the maps were converted to jpeg format and were cropped so that the corners corresponded to a known position in UTM space. The jpeg images could then be imported, georeferenced and draped over the DEM surface to allow the 2D map to be visualised in 3D (figure 2.6).

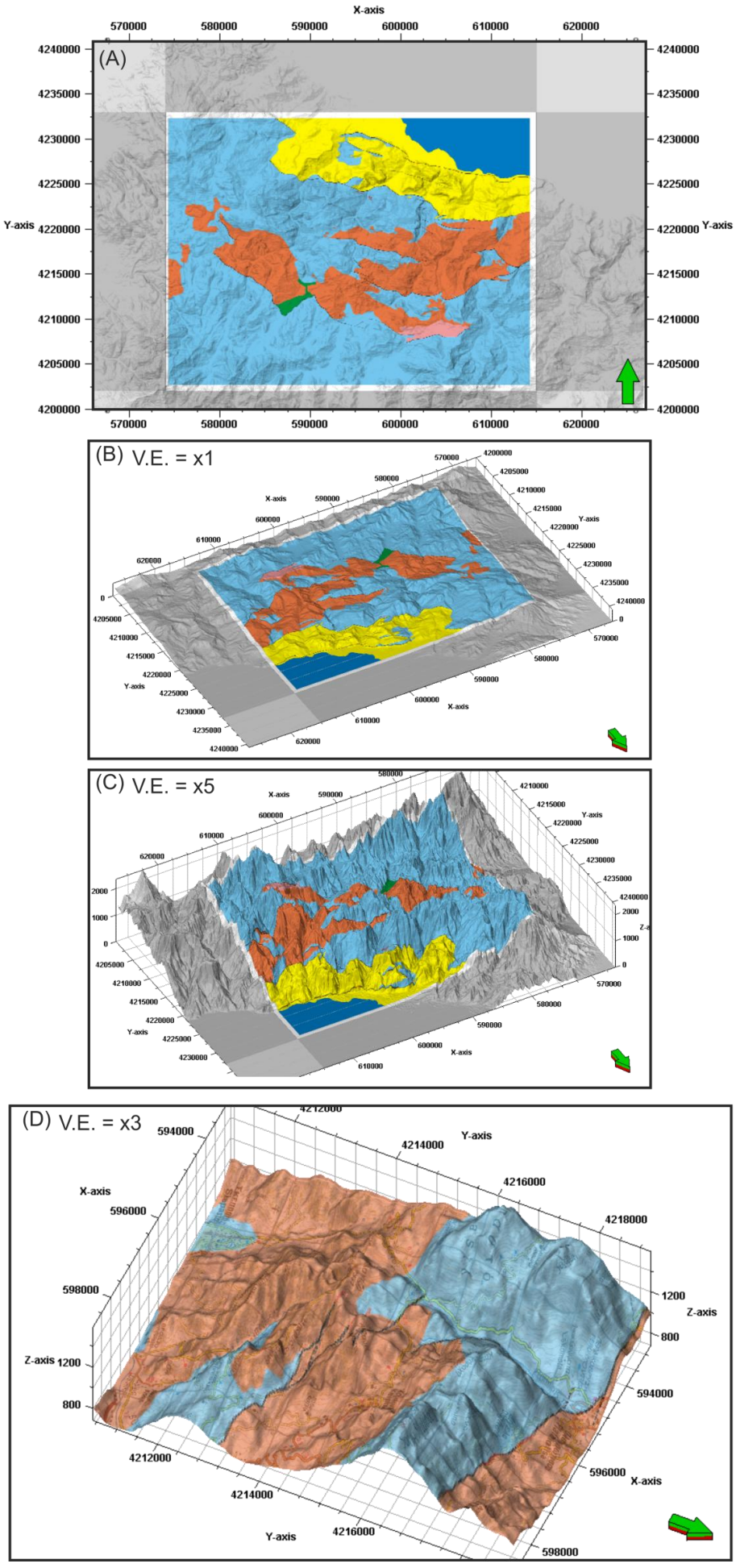
(A)
X-axis
Y-axis
570000
580000
590000
600000
610000
620000
4240000
4235000
4230000
4225000
4220000
4215000
4210000
4205000
4200000
(B) V.E. = x1
(C) V.E. = x5
(D) V.E. = x3
Z-axis
1200
800
2000
1000
0
594000
596000
598000
4212000
4214000
4216000
4218000

Figure 2.6 (Previous page). Process of combing field maps with digital elevation data. (A) Aerial view showing imported digitised geological map with corners georeferenced to allow correct positioning relative to the DEM. (B) Oblique view of DEM draped with geological map, no vertical exaggeration. (C) As (B) but 5x vertical exaggeration. (D) Oblique view of section of DEM draped with scanned and imported fair-weather fieldslip. The view is co-rendered with the detailed digital base map to allow visualisation and orientation relative to roads and other markers. V.E. = x3.

2.3.4 Point Data

Points data representing the location of specific outcrops or measurements was imported as text files in much the same way as the DEM data (figure 2.5). In addition to the x, y, z coordinates additional attributes were attached to each point to capture the measured variable. These attributes could subsequently be colour coded or represented by a symbol (e.g. dip and dip-azimuth notation) to allow easy visualisation.

2.3.5 Faults

Construction of surfaces representing faults utilises both the map and points data (figure 2.6). The outcrop locations of faults were digitised directly onto the DEM as a poly line using the imported maps as a guide. This also acted as a QC tool since the interaction of a (sub)planar surface such as a fault with a complex topography will not be expressed as a linear feature on a map. Where the fault intersects valleys and raised topography such as spurs, the position of the fault trace will be modified.

Dip and dip azimuth values for the fault surface were specified using the mean values for each specific fault, with additional control points provided by the individual orientation measurements. A surface can then be generated using the digitised polygons representing the out-cropping fault to define its intersection with the DEM.

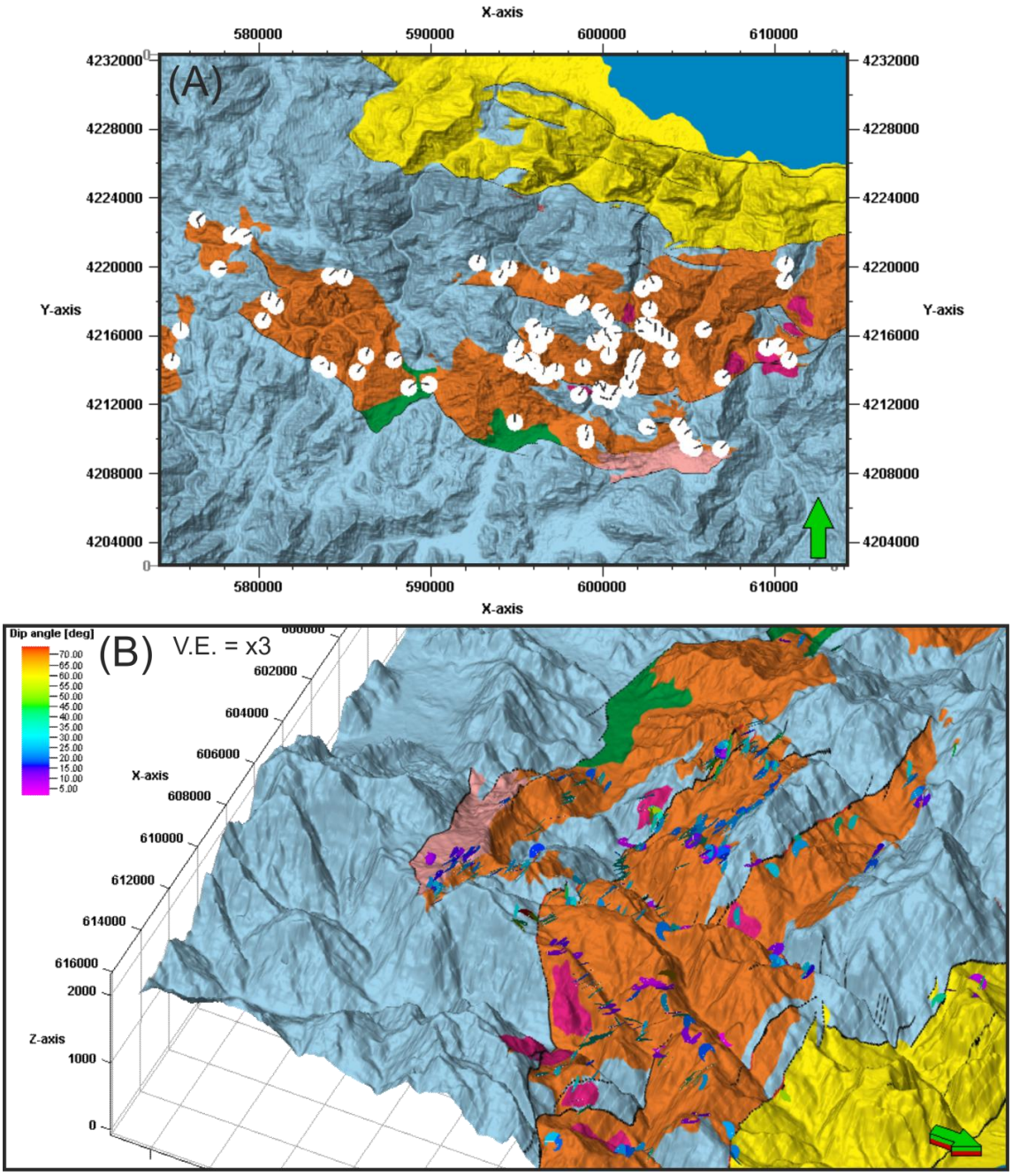

Figure 2.7. Examples of incorporating 1D field data within the geomodelling environment. (A) Aerial view showing symbols representing georeferenced and restored palaeocurrent orientations within the alluvial fan sediments. (B) Oblique view with disc symbols representing bedding orientation superimposed onto the map-draped DEM. The symbols are colour-coded for their dip magnitude. V.E. = x3.

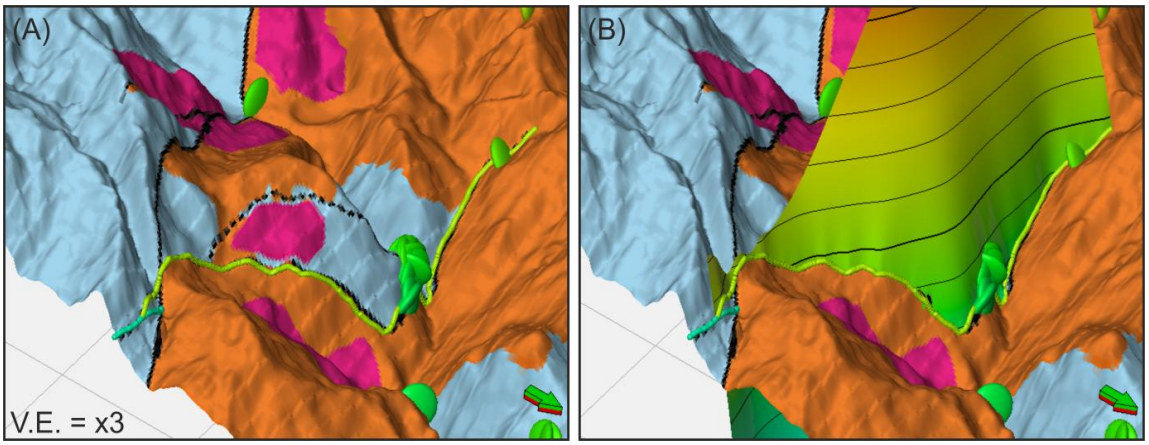

Figure 2.8. Summary of workflow for generating fault surfaces. (A) Fault trace is digitised onto the map-draped DEM (light green line). Points data representing local fault orientation measurements are also shown. (B) The mean orientation data for each individual fault is used to generate a surface constrained by the local fault orientation measurements and the outcrop fault trace.

2.3.6 Stratigraphic Surfaces

In order to define the displacement on the faults the position of the surface representing the top of the pre-rift, as well as the location of the onlap contact of the syn-rift had to be defined in each half graben (figure 2.7). Minimum values of fault displacement could then be established by projecting the dip of the syn-rift sediments at the position where they onlapped the hangingwall dip slope back towards the fault planes to define the depth of the hangingwall cut-offs. The procedure for capturing the depth of this hangingwall cut-off, and hence the 3D fault displacement, involved a number of steps for each individual hangingwall sub-basin. A series of cross-sections spaced at 1km and orientated perpendicular to the overall fault trend were constructed. The dip of the syn-rift at the exposed onlap contact was projected onto the cross-sections to define the dip of the top of the pre-rift.

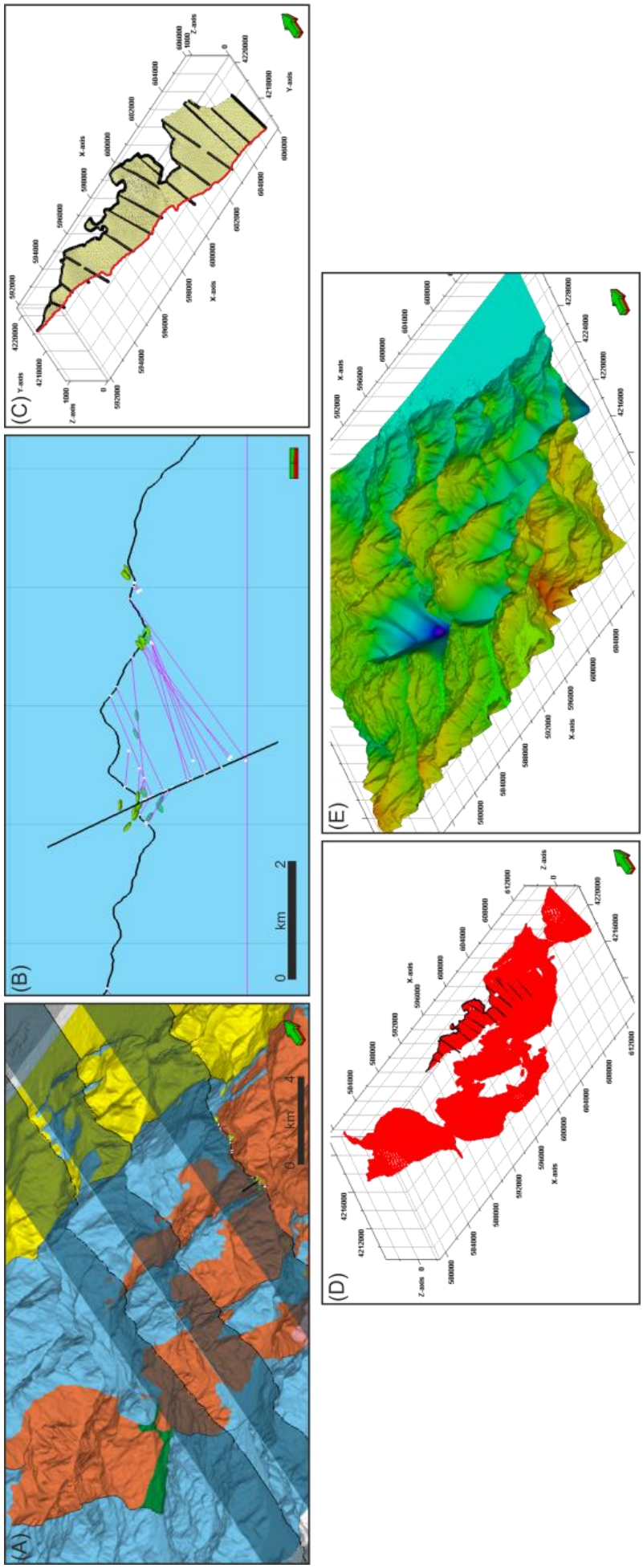
(A)
0 km 4
(B)
0 km 2
(C)
X-axis
Y-axis
Z-axis
(D)
X-axis
Z-axis
(E)
X-axis

Figure 2.9 (Previous page). Generalised workflow for generating the buried top pre-rift stratigraphic surface. (A) A series of fault-normal cross sections are generated at intervals of 1km. (B) The dip of the syn-rift strata immediately adjacent to the onlap contact for each sub-basin is projected onto each cross section and projected down-dip towards the faults. (C) The dip of the strata for each cross section is combined for each individual half graben to generate a surface. Where this surface intersects the fault defines the position of the hangingwall fault cut-off. This allows a minimum fault throw value to be estimated. (D) The surfaces for each individual sub-basin are combined, and merged with the DEM to generate an approximate top pre-rift surface (E).

For each cross-section this top-basement surface was digitised and converted into a points set. Merging the point sets for each cross section across an individual sub-basin with the digitised onlap contact allowed the generation of a surface approximating the top of the pre-rift. The top pre-rift surfaces for each basin were merged with a surface representing the present day top pre-rift outcrop in order to generate an overall top pre-rift surface.

This approach for calculating the dip of the top pre-rift within the hangingwalls yielded minimum (low-case) estimates of displacement. This is because footwall erosion and the dip of the hangingwall slope are not directly included within the calculation, both of which are likely to increase estimates of displacement (figure 2.10). Mid- and high-case estimates of displacement were also generated by incorporating these features to allow a possible range of fault displacements to be generated, albeit with a caveat: The pre-rift consists largely of carbonates uplifted and deformed during the Hellenide orogeny to form the Pindos Nappe (e.g. Skourtsos and Kranis, 2009). As a result the pre-rift was likely to have had a significant topography. Therefore caution was required when using pre-rift surfaces to infer buried geometries (figure 2.11).

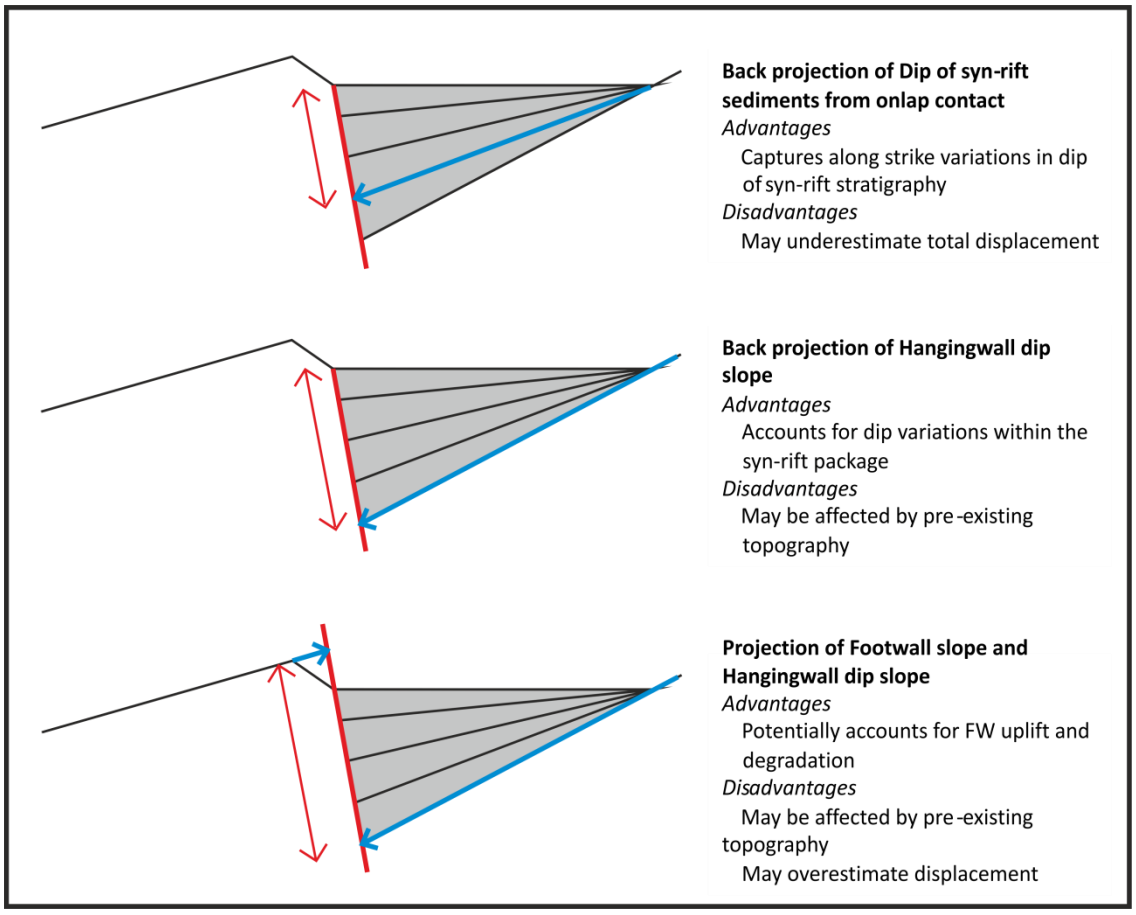

Figure 2.10. Schematic illustrating the different approaches to estimating fault displacement.

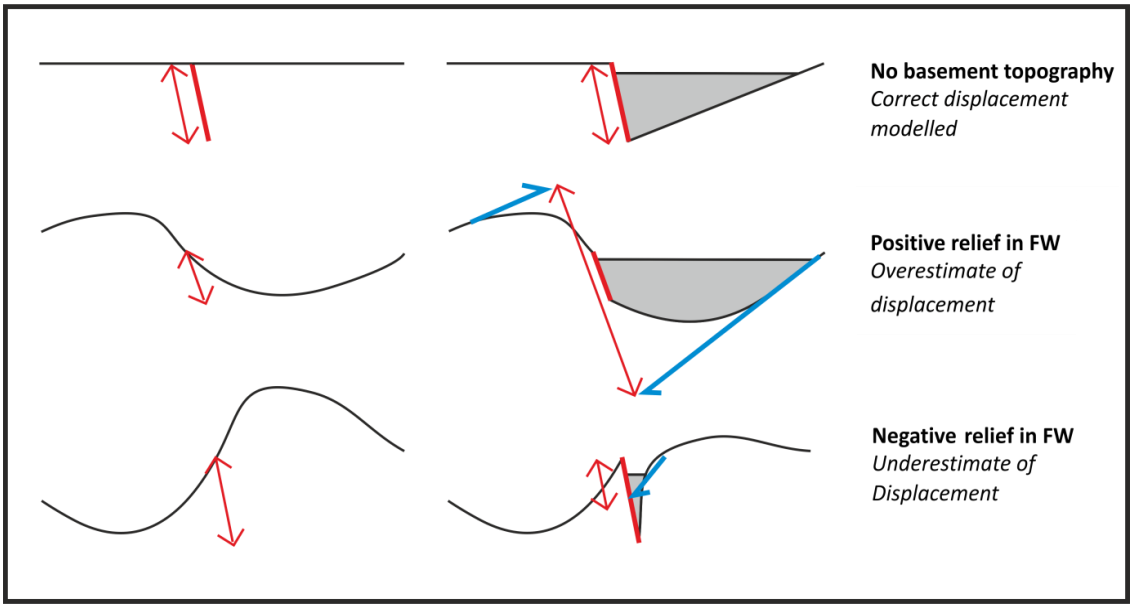

Figure 2.11. Schematic illustrating the effect of basement topography on fault displacement estimates.

2.3.7 Geo-cellular Grids

The main difficulties with modelling outcrops within geological modelling software packages is the absence of broad scale stratigraphic surface architectures as would be present when modelling from seismic data. After this problem has been resolved for the pre-rift to syn-rift boundary the workflow for generating and populating a geo-cellular grid is much the same as for when 3D seismic data is available (chapters 5, 8).

Firstly a boundary encompassing the area of interest and any faults present is constructed which defines the outer edge of the grid. Grid cell dimensions in the x and y directions are specified and the iterative process of generating a corner point grid (Schlumberger, 2012) is initiated. Within the grid faulted stratigraphic horizons are generated using the surfaces constructed from the outcrop geometries. Additional layers between the stratigraphic horizons can be generated at intervals defining the vertical (z) grid cell dimensions, with the cells subsequently populated with petrophysical properties (figure 2.12). Fault petrophysical properties such as the permeability can then be estimated using published equations, and the fault transmissibility multipliers (TMs) derived (Manzocchi et al., 1999).

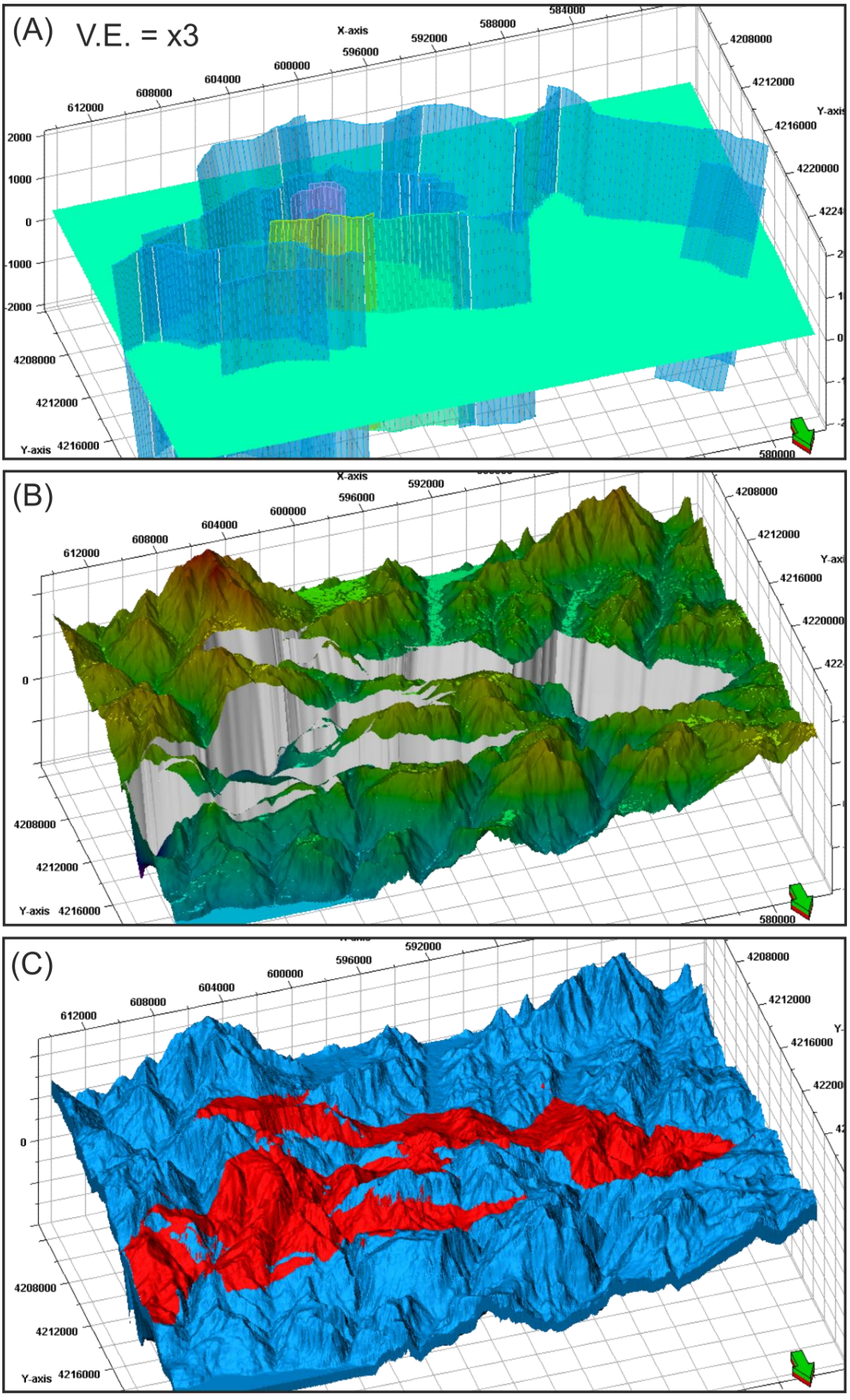
(A) V.E. = x3
X-axis
Y-axis
(B)
(C)

Figure 2.12 (Previous page). Generalised construction of a geocellular grid. (A) The grid geometry and faults are defined with the grid generated according to these limitations. (B) Input data consisting of the stratigraphic surfaces generated previously (e.g. figure 2.7) are used to define the fault displacement. (C) The grid can now be populated with petrophysical properties allowing further steps such as fluid flow modelling, seismic forward modelling and fault property modelling to be undertaken.

2.4 Digital Geological Modelling

The use of digital data, such as seismic or LIDAR DEM data, to construct a geological model is a similar process to that used for outcrop data. It is if anything perhaps slightly more straight forward since key surfaces are relatively easy to interpret or generate, rather than having to be constructed manually.

2.4.1 Seismic Interpretation

Interpretation of seismic data was performed in relation to a number of different aspects of the thesis (Chapters 4, 5, 7, 8). In all cases the seismic interpretation module of Petrel was used, with the specific details of the approaches used being covered in each individual chapter. In areas of high data quality autotracking tools were sufficient to generate high quality surfaces with fault interpretations also being relatively straight forward to produce. In areas of lower signal to noise ratio or lower resolution manipulation of the 'raw' seismic data was often required to aid interpretation of surfaces and faults. These techniques included using volume and surface attributes such as coherency, ant-tracking, variance, edge detection, dip and dip azimuth, etc. In addition geo-body interpretation tools were utilised which use approaches such as seismic facies correlation to identify channels and other features.

2.4.2 3D Geological Modelling

As with modelling of field data, 3D geological modelling was conducted primarily using Petrel (Schlumberger, 2012). The majority of the techniques and methodologies used correspond closely to those described for outcrop modelling (section 2.2).

2.4.3 Fluid Flow Simulation

Fluid flow simulation contributes a large component of the thesis. Here it is used to model the impact of differing fault geometries on reservoir performance. Despite it allowing quantification of the impact of geological factors which are often qualitatively described, its

use as a tool by geologists has remained limited, possibly because it is traditionally viewed as a reservoir engineering discipline.

Two simulators have been used within the project, the Eclipse 100 Black Oil Simulator, and FrontSim (Schlumberger 2008). The use of these different simulators corresponds to the computational time required for simulation. FrontSim requires shorter run-times, but does not capture the full range of variables to the same extent as eclipse. Hence, the different simulators have been used when their capabilities have corresponded adequately to the purposes of the simulations.

Populated geo-cellular grids constructed within Petrel form the basis for the reservoir simulation models, which are also constructed within Petrel but with the simulations themselves run externally through a command prompt dialogue. A number of steps must be completed with specific variable values assigned to allow reservoir simulations to be run. The values for the specific variables for individual simulations are shown within the relevant chapters, however an overview of the requirements is outlined here.

The first step of constructing a fluid flow simulation model is to define the position of the fluid contacts which are present within the model. The location of well heads at the surface, the well path design and the well completions, such as the casing and position of perforations, are all specified. A fluid model encompassing the physical properties of the fluids present is defined which controls the values of pressure, volume and temperature (PVT) for the fluids at the range of conditions present during simulation. Rock physics functions including the two-phase properties of the reservoir rock and its compaction behaviour are stipulated, and an aquifer model generated. A development strategy is then specified which instructs the simulator when specific wells are active, their flow rates and pressures, as well as the length of the simulation run and how often intermediary reports should be made. The final stage is to generate a simulation case, the purpose of which is to link the geological grid containing the petrophysical properties of the grid cells and the faults with the reservoir simulation model and development strategy. Each case is exported to the relevant simulator where it is run, and the results subsequently re-imported into Petrel. This allows analysis of the evolution of pressure, production rates and fluid movements through the subsurface over the course of the simulations

2.4.4 Seismic Forward Modelling

Seismic forward modelling has been used to generate synthetic 2D and 3D seismic sections and volumes from outcrop based data in order to quantify the uncertainties in fault

geometries when they are defined from seismic data (chapters 4, 8, 9). A software program called SeisRox (Norsar, 2012) has been used to generate the synthetic seismic based upon geo-cellular grids constructed within Petrel. The approaches for generating 2D and 3D seismic are quite different and have different objectives, as outlined below.

2.4.4.1 2D Synthetic Seismic

2D synthetic seismic was generated at a rift-scale in order to investigate exploration rather than production scale uncertainties pertinent to fault geometry (chapter 4). The workflow employed was subtly different in that the grids being exported from Petrel were significantly much larger than for the 3D cases. This necessitated that for each petrophysical property required within the forward modelling software an individual seg-y volume had to be created and separately exported. When all the requisite property cubes were available the forward modelling process was identical other than that a 2D rather than 3D survey design was specified.

2.4.4.2 3D Synthetic Seismic

Generation of 3D synthetic seismic cubes has been performed in order to quantify the impact of reservoir scale faults on hydrocarbon flow. The primary source data has been a high resolution (0.5 m) airborne LIDAR DEM dataset from the Afar rift (see chapters 8, 9). Forward modelling was focussed on areas of high geometric complexity around fault relay zones. The geo-cellular grids constructed from the DEM were exported from petrel using a plug-in piece of software allowing direct transfer of all the required grid properties to the forward modelling software (figure 2.9). The reflectivity and elastic properties could subsequently be calculated using Zoeppritz and Gassman's equations respectively and combined with a background model, 3D survey design and input wavelet. A ray-tracing algorithm (Gjøystdal et al., 2007) was then applied to generate the synthetic cube, which could then be exported back to Petrel for seismic interpretation.

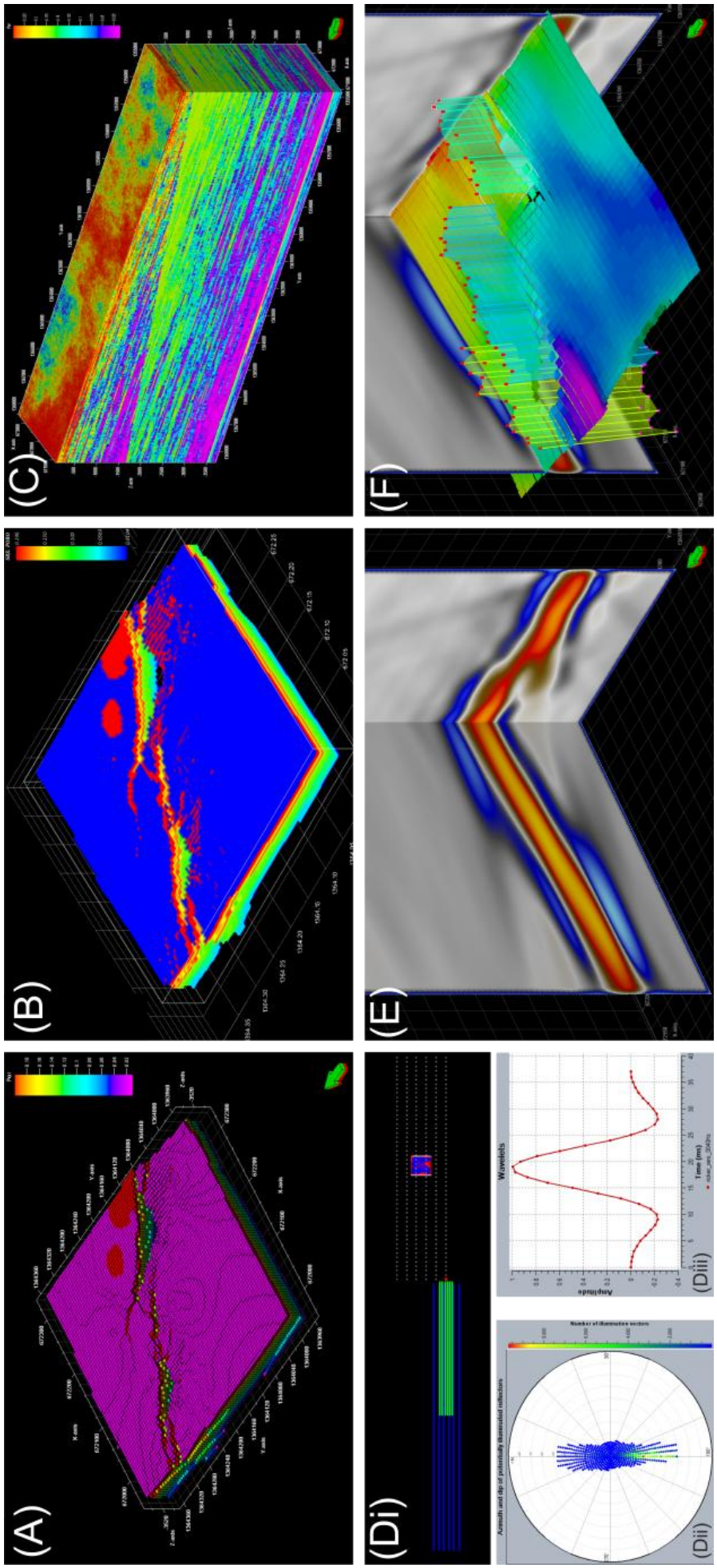
(A)
(B)
(C)
(Di)
(Dii)
(Diii)
(E)
(F)
Wavelets
Amplitude
Time (ms)

Figure 2.13 (Previous page). Generalised workflow for generating 3D synthetic forward modelled seismic cubes. (A) A geocellular grid capturing the desired architecture at a high resolution is constructed and populated with the relevant petrophysical properties. (B) The geocellular grid is exported to seismic forward modelling software where the elastic and reflectivity properties cubes are generated. These are combined with a 3D overburden model to account for wave attenuation and diffraction along the source-target-receiver travel path (C). (D) A 3D survey is designed (Di) with the specific orientations of imaged reflections calculated (Dii), and an input wavelet specified (Diii). (E) A ray-tracing algorithm is then used to generate a synthetic seismic cube of the target area. (F) This synthetic cube can then be interpreted using seismic interpretation software to generate the seismically resolvable surface and fault geometries.

2.4.5 Structural Restorations

A number of the aspects of the thesis utilise section balancing techniques to illustrate a specific argument (e.g. chapter 3). This was performed using 2D Move (Midland Valley, 2012). The approach used was to generate fault-normal cross-sections from the models generated within Petrel. These were then exported as image files to 2D move. Faults and stratigraphic horizons were then digitised and restored to their pre-rift position. Completing a series of cross-sections in this manner allowed any along-strike variation in extension to be identified (chapter 3).

Chapter 3

Structure and Evolution of the Onshore Gulf of Corinth Rift

3.1 Abstract

Within this chapter the evolution of the onshore Gulf of Corinth rift is investigated. The evolution of the rift is found to be significantly more complex than previously thought, with multiple fault segments active concurrently. Three stages of rifting are identified, with an initially dispersed rift system gradually localising onto larger fault sets which accommodate the majority of extension. A final stage of rifting sees reactivation of a number of earlier structures. Strain is portioned across multiple faults in the east, whilst further west a single, large fault accommodates extension.

Geocellular models constructed herein to aid interpretation of the rift evolution and fault distribution are used as inputs for investigating structural uncertainty at the rift scale (chapter 4).

3.2 Introduction and Aims

In order to examine the influence of fault geometries and linkages on hydrocarbon exploration uncertainty a suitable dataset encompassing rift-scale faults was required. The onshore Gulf of Corinth rift provides an excellent outcrop example. A complex and uncertain fault evolution (Collier and Jones, 2004) is superimposed upon a generalised basinward migration of fault activity, the result of which is that older faults are uplifted in the footwalls of younger faults (Ori, 1989). This leads to the preservation of a series of rotated blocks and half-grabens partially filled with a continental syn-rift stratigraphy. The topography and syn-rift stratal architecture capture along strike displacement variations which allude to the presence of structures such as relay zones. The aims of this chapter are hence twofold, and are linked to those of the following chapter. Firstly, the development of a model for the evolution and relative timing of the faults comprising the onshore portion of the southern part of the Corinth rift was required. This has been facilitated by the second aim: to construct a geological model of the onshore rift capturing the 3D fault geometry. This geological model integrates a range of field data and is used to further examine exploration scale uncertainties associated with fault geometries in Chapter 4.

3.2.1 Regional Tectonics

The eastern Mediterranean has long been recognised as an area of active tectonism (McKenzie, 1970, 1972). Various geometries of convergence and interaction of the African, Eurasian, Arabian and Anatolian plates result in a wide variety of active tectonic processes (McClusky et al., 2000). The region is dominated by the collision of the African and Arabian plates with the Eurasian plate (Figure 3.1). This results in arcuate subduction of the African plate beneath the Eurasian and Anatolian plates along the Hellenic arc and continental collision of Arabia with Eurasia leading to the fold and thrust belt of the Zagros and Caucasus mountains (McKenzie, 1970, 1972). The Arabian plate has a northwards vector of approximately 18 to 25 mm/yr compared to 10 mm/yr for the African plate (McClusky et al., 2000). This differential motion is thought to be accommodated through left lateral movement on the Dead Sea transform fault zone (McKenzie, 1972). The Eurasian plate effectively forms a buttress to the northwards movement of the Arabian plate leading to westwards extrusion of the Anatolian plate facilitated by the development of the North and East Anatolian strike-slip faults (McKenzie 1970).

Subduction of the African plate at the Hellenic arc is occurring at a faster rate than the northwards movement of the plate itself leading to slab pull and southwards migration of the arc relative to the Eurasian plate (Royden 1993). This leads to back-arc extension and continental rifting of mainland Greece to the north (Doutsos et al., 1988). It is postulated that rifting initiated at approximately 15 Ma and was distributed across the Aegean region (Armijo et al., 1996). Maximum extension occurred in the central Aegean, decreasing to the west and east resulting in the arcuate geometry of the subduction zone. Although much of mainland Greece is characterised by the continuing continental rifting the Gulf of Corinth is currently the most active rift, with extension rates averaging 5 to 15 mm/yr (Davies et al., 1997; Clarke et al., 1998; Briole et al., 2000; Bell et al., 2008). Armijo et al., (1996, 1999) suggest that westwards propagation of the north Anatolian fault has also contributed to extension in the Aegean. Dextral movement of Anatolia relative to Eurasia leads to increased extension across the gulf in addition to the extension resulting from subduction and back arc rifting. Jolivet (2001) proposes an additional control on extension in the form of gravitational collapse of the lithosphere thickened during the Hellenide orogeny. It is proposed that the Gulf of Corinth in its present form has been experiencing localised extensional deformation since at least the Pliocene (Armijo et al., 1996).

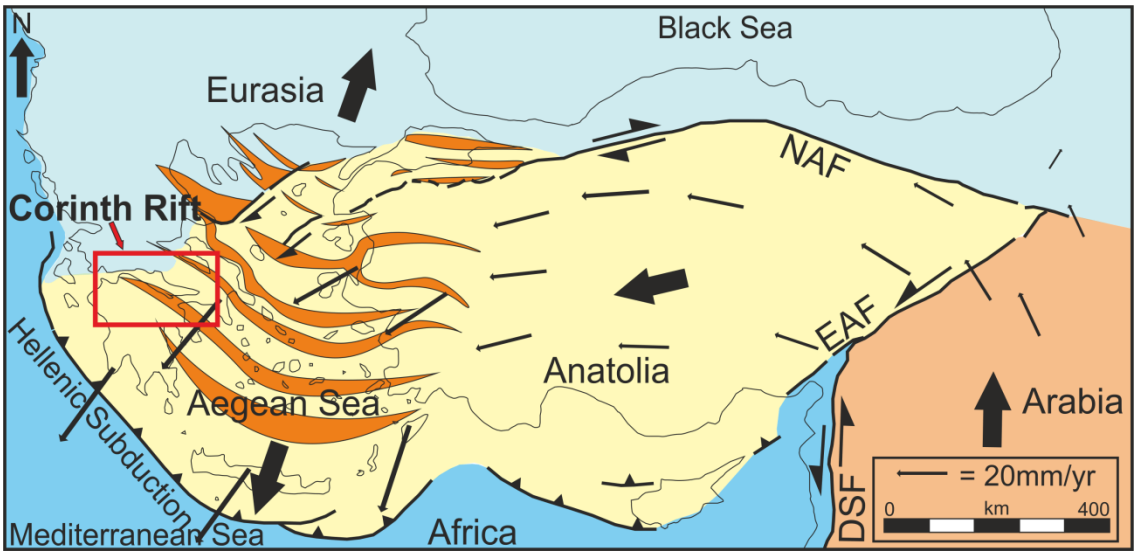

Figure 3.1. Tectonic setting of the eastern Mediterranean. The Anatolian plate is extruded westwards away from the Arabia-Eurasia collision zone and towards the Hellenic subduction zone with lateral strike-slip movement accommodated along the North Anatolian Fault (NAF) and East Anatolia Fault (EAF). Large block arrows represent mean plate motions whilst small arrows represent movement vectors. Localised rifting in the Aegean region over the last 15 Ma is indicated by the orange areas with the Corinth Rift highlighted by a red box. DSF=Dead Sea Fault. Modified from Armijo et al., (1999).

3.2.2 Structure of the Gulf of Corinth Rift

The modern day Gulf of Corinth is a large E-W orientated inlet in central Greece approximately 120 km in length with a maximum width of 27 km and maximum water depth of almost 900m (Figure 3.2). It separates the Peloponnese in the south from Central mainland Greece to the north, although the northern and southern margins are connected at the eastern termination of the Gulf by the Corinth Isthmus. The isthmus disconnects the Gulf of Corinth from the Saronic Gulf to the east, although U/Th dating suggests that a single body of water existed prior to approximately 300ka (Collier, 1990; Collier and Dart, 1991). In the west the Gulf of Corinth is separated from the Gulf of Patras and the wider Mediterranean Sea by the Straits of Rion. Water depth is as little as 60m in this area with Pleistocene eustatic sea level variations periodically resulting in the Gulf becoming cut off and existing as a lacustrine depositional setting (Perissoritas et al., 2000).

The area is actively extending and is characterised by high extension rates which are accommodated on a number of major north dipping and minor south dipping faults. These faults run east-west to NW-SE, cross cutting pre-existing NNE-SSW orientated thrusts within

the pre-rift basement (Pe-Piper and Piper, 1984). This basement consists of Mesozoic age shelf carbonates, radiolarites, flysch and ophiolite derived from the Tethys Ocean. Closure of the Tethys due to Alpine compression during the Oligocene-Miocene resulted in west to northwest vergent thrusting and formation of the Hellenide mountain chain, the remnants of which now form the pre-rift basement (Pe-Piper and Piper, 1984).

The bathymetry of the Gulf and the onshore topography to the south and north describe an asymmetric graben with the majority of extension being accommodated by both onshore and offshore north dipping faults to the south (McNeill and Collier, 2004). Younger faults develop in the hangingwalls to older faults suggesting a general trend of northwards migration of deformation over time (Ori, 1989; Sorel, 2000), however field observations suggest a more complex history (Collier and Jones, 2004). This general northwards trend results in previously subsiding sub-basins being subject to footwall uplift and consequent erosion and incision by both ancient and modern fluvial systems. The earliest observable rifting in the Gulf of Corinth is interpreted as occurring during the Mid to Late Pliocene (Ori, 1989), however due to the nature of the sediments chronostratigraphic correlation is limited. At this time sedimentation was contemporaneous with, and controlled by, movement on the southern most faults (Ori, 1989; Sorel, 2000).

King et al (1985) postulate the presence of a low angle, aseismic fault at depth beneath the eastern Gulf of Corinth to explain the surface geometries they observed. They speculate that a low angle detachment above the brittle-ductile transition would allow the formation of antithetic faults apparently prior to the main surface faults themselves. Microseismicity studies (Rietbrock et al., 1996; Rigo et al., 1996; Bernard et al., 1997) indicating the presence of a zone of earthquake foci defining a low angle surface at a depth of between 6 and 10km support this large scale geometry. These observations are in contrast to those of Sorel (2000) who suggests a low angle detachment fault at a depth of 1 to 2 km. The model of Sorel (2000) identifies the southern-most onshore fault in the region as the oldest, with progressive northwards migration of deformation resulting in a series of half grabens, with the detachment fault at their base. Although a generalised trend of northwards migration of fault activity is compatible with the overall tectonic setting, field studies by Collier and Jones (2004) suggest a more complex deformation history.

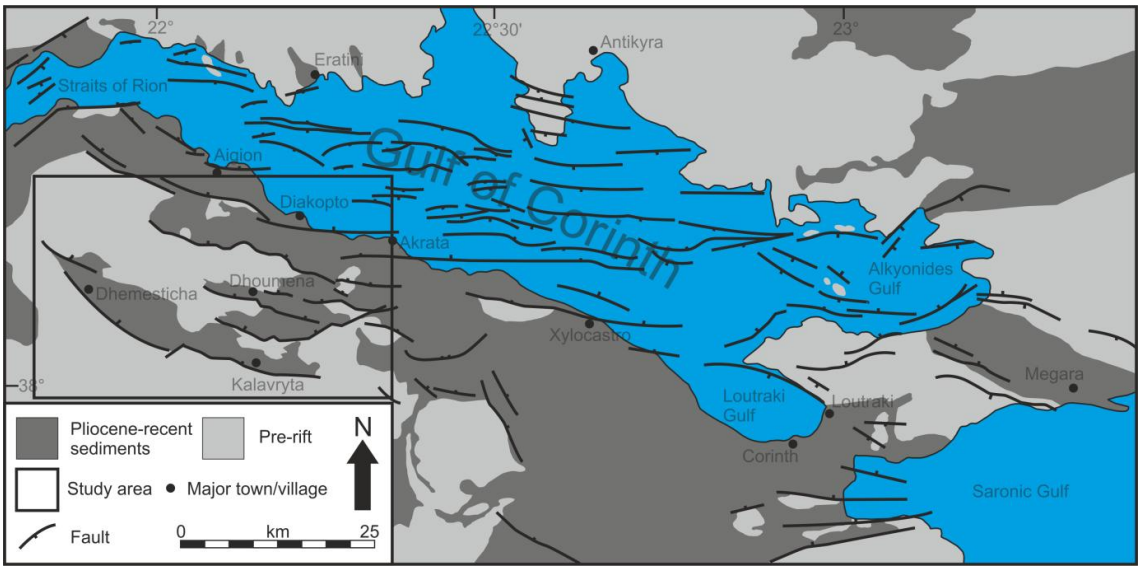

Figure 3.2. Map showing both the onshore and offshore structural configuration of the Gulf of Corinth rift. The area covered by this study is highlighted. Modified after Bell et al (2011); Taylor et al (2011); Ford et al (2013).

3.2.3 Chronostratigraphic Correlation and Fault Timing

Spatial and temporal distribution of faulting in the Gulf of Corinth area is a subject of some debate. Although it is generally agreed that dominant active faulting has broadly migrated basinward over time (Ori, 1989; Jackson, 1999; Goldsworthy and Jackson, 2001), the detail over which this pattern is superimposed is disputed. Sorel (2000) suggests a sequential northwards migration of activity, with little to no variation. This is in contrast to other authors (Collier and Jones, 2004; Rohais et al., 2007) who suggest a more distribute history of faulting, at least in the early stage of rifting. For example, Causse et al (2004) use U/Th dating to suggest that the Dhoumena fault, was active at approximately 0.125 Ma, an age significantly out of sequence with the northwards progression model, and potentially indicating that multiple faults may have been active concurrently. Nevertheless, absolute age markers are rare and hence the timing of fault activity is, in detail, relatively poorly constrained.

The onshore portion of the Gulf of Corinth Rift consists of a series of approximately ESE-WNW trending, north dipping fault sets forming a succession of hangingwall half graben depocentres. These depocentres were in-filled with continental lacustrine to fluvial-alluvial syn-rift sediments, passing northwards into Gilbert style fan deltas (Poulimenos et al., 1989; Ori, 1989; Doutsos and Poulimenos, 1992; Dart et al., 1994). Due to their depositional nature the age of

these sediments, and hence also the timing of fault initiation, is poorly constrained. Early stage syn-rift intermontane lacustrine sediments within boreholes in the vicinity of Kalavryta have been observed to contain various lignite facies dated as Lower Pliocene (5.32-3.58 Ma, Papanicolaou et al., 2000). These likely correspond to the observations of this study at the base of the syn-rift sequence approximately 5km to the northwest of Kalavryta. Although paleontological evidence is scarce throughout the continental syn-rift sequence as a whole, mammalian fossils to the east date early conglomerates in this region as Lower Pleistocene (1.8-0.78 Ma, Symeonidis et al., 1987). Further constraint can be derived from the age of the Gilbert deltas in the uplifted footwalls to the active faults located along the present coastline. These deltas are located in the hangingwall to the Mamoussia-Pirgahki fault set which marks the boundary between continental and marine sedimentation. The activity of the faults to the south of the Mamoussia-Pirghaki fault is a subject of debate and this leads to uncertainty in the age of their related hangingwall sediments.

Biostratigraphic analysis by Malartre et al (2004) indicate that deposition of the Vouraikos fan delta occurred during the early Pleistocene (Figure 3.3). Ford et al. (2007, 2012) refine this further using palynology to suggest delta formation initiated at 1.1-1.5 Ma, terminating at approximately 0.7 Ma. They describe a coarse grained braided fluvial to overbank formation ('Ladapotamus formation') which unconformably overlies the basement Mesozoic carbonates at the base of the Vouraikos delta, separated from the overlying transitional to deltaic sediments by an unconformity. This formation is tentatively correlated to the distal portion of the alluvial fan facies observed to the south in the footwall to the Mamoussia-Pirgahki fault. This correlation is reinforced by pollen samples from of the alluvial sediments in the footwall being dated as approximately 1.1 Ma (Ford et al., 2007). This provides a constraint not only on the timing of activity of the Mamoussia-Pirgahki fault, but also on the minimum age of continental sedimentation in the immediate area. Further to the west, also in the hangingwall to Mamoussia-Pirgahki fault, the Kerinitis delta records a similar history. Dart et al, 1994 suggest a Mid-Pleistocene age for the oldest deltaic sediments; this estimate is constrained by correlation with neighbouring deltas to approximately 0.8 Ma for the age of initiation (Backert et al., 2010). Further to the east, in the area around the Corinth Isthmus, andesite volcanics near the base of the syn-rift sequence have been dated at 4Ma (Collier and Dart, 1991). Flotte et al (2001) used U/Th dating of fault related calcites to suggest an age of 0.38 Ma for the Valimi fault. Those authors did however concede that since these were syn-rift samples they were unlikely to record the time of initiation of faulting. Although the data is relatively sparse it does constrain continental sedimentation within the rift as occurring between 5.32-3.58 to

1.5-0.8 Ma. The age of breccia deposits at the eastern end of the Kalavryta fault is not constrained but is estimated to be less than 0.2 Ma (Ford et al., 2013).

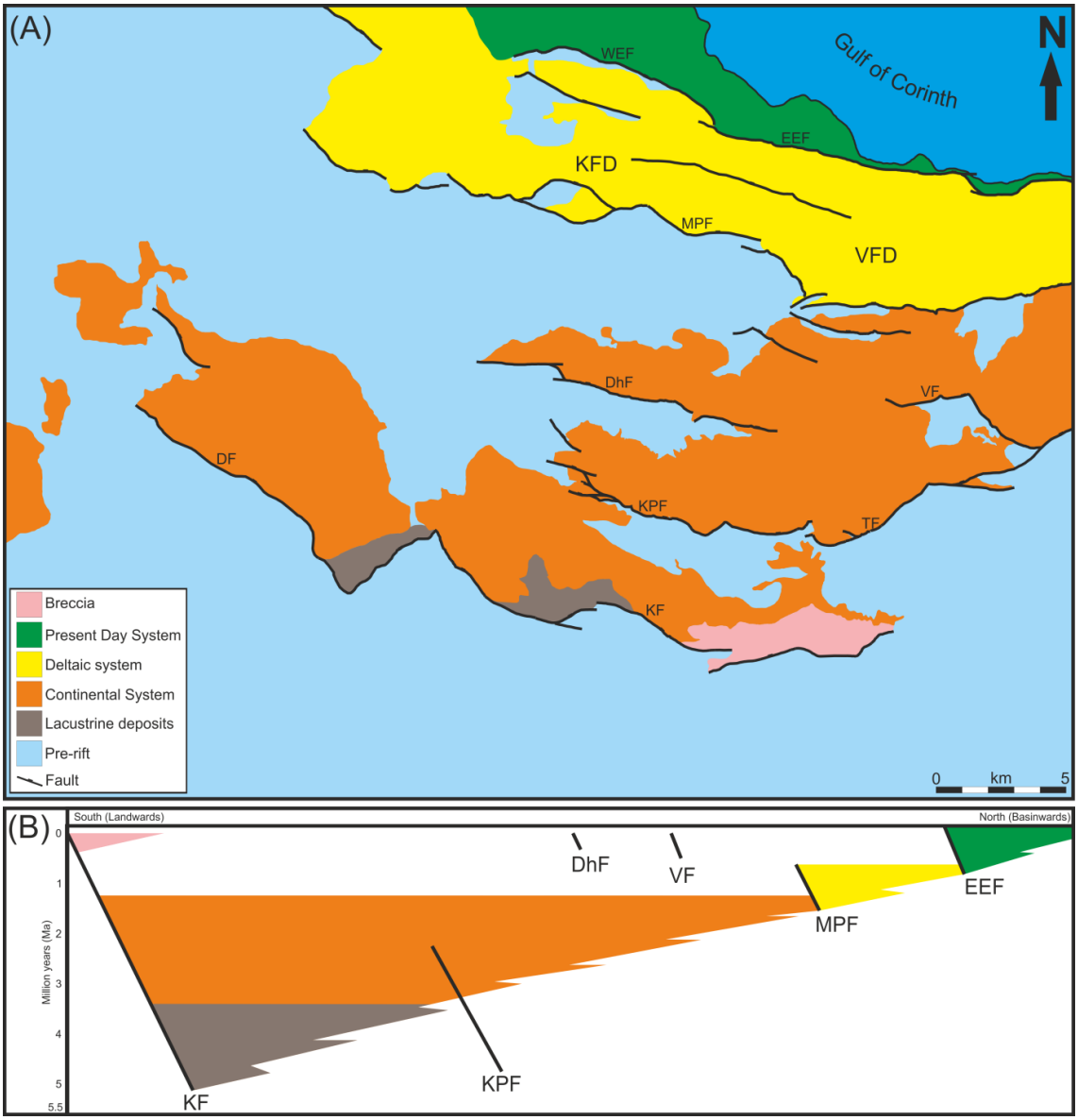

Figure 3.3. Map (A), and conceptual north-south orientated chronostratigraphic diagram (B) illustrating published timings of faulting and deposition. KF = Kalavryta fault, KPF = Kerpini fault, TF = Tsivlos fault, DF = Dhemesticha fault, DhF = Dhoumena fault, VF = Valimi fault, MPF = Mamoussia-Pirgahki fault, EEF = eastern Eliki fault, WEF = western Eliki fault, KFD = Kerinitis fan delta, VFD = Vouraikos fan delta. Compiled from data within; Symeonidis et al (1987); Collier and Dart (1991); Papanicolaou et al (2000); Flotte et al (2001); Causse et al (2004); Malartre et al (2004); Ford et al (2007, 2012); Backert et al (2010).

3.3 Mapping and Modelling methodology

In order to better constrain the structural evolution of the area a variety of methodologies have been employed. Geo-referenced field data such as fault and bedding orientations have been integrated with detailed outcrop mapping and a Digital Elevation Model (DEM) within the 3D geomodelling environment of Petrel (See methodology in chapter 2). Geological information is draped onto a DEM surface to allow 3D visualisation of outcrop patterns and rapid identification of spatial variation of data, both in terms of its distribution and properties. A confidence attribute can also be attached to each data point to aid in reconciling anomalous values or interpretations. 3D geomodelling software is primarily used in conjunction with 2D and 3D seismic data to constrain subsurface geometries. When using this software to model outcrops where no subsurface constraint is available, it is important to fully exploit all surface data. Since the topographic surface described by the DEM is highly incised and eroded, there are numerous areas, such as valleys, where vertical sections effectively capture the equivalent of the local subsurface geometry and any variation in the orientation of the syn-rift stratigraphy. Given that the majority of the syn-rift sediments are back rotated, the outcrop tends to increase in age with distance from the faults. Horizontal transects are hence an effective tool when identifying any up sequence variation in orientation, for example fanning dips, associated with syn-rift strata. When coupled with surface data these transects significantly improve the constraint of subsurface geometries (Figure 3.4).

Figure 3.4 (next page). Horizontal transects provide additional constraint on rift evolution. (A) Photo-panorama of dip fan within south dipping alluvial sediments along the Ladapotamus river valley to the north of the Tsivlos fault (located right of the image). (B) Plot of stratigraphic dip against distance from the fault. As a result of the dip, the age of the strata increases with distance from the fault. Increasing dip with distance alludes to the syn-rift nature of these deposits. (C) Elevation against dip along the same transect. Dip increases as elevation decreases, since the higher, younger sediments have been subject to less fault rotation.

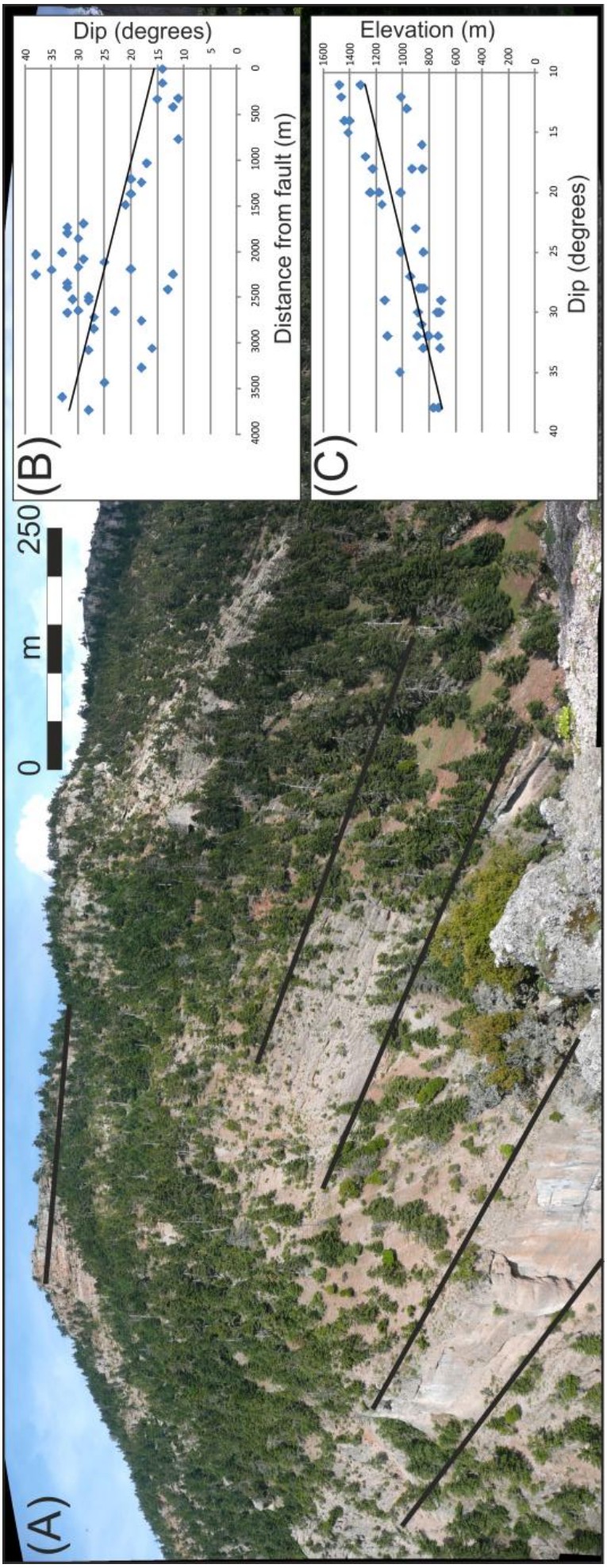
(A)
0
m
250
(B)
Dip (degrees)
Distance from fault (m)
(C)
Elevation (m)
Dip (degrees)

A key aim of building a 3D model of the study area was to capture along strike variations in fault displacement. The displacement fields of the faults can reveal information about their interaction and growth history, as well as aiding in the identification of displacement minima often associated with relay zones (Peacock and Sanderson, 1994). To this end it was important to accurately model the surface describing the top of the pre-rift carbonate basement as this provided a marker for characterising the displacement distribution of the rift faults. A number of obstacles needed to be overcome to allow reasonable estimates to be made. The primary difficulty relates to estimating the subsurface depth of the hangingwall cut off along the length of a fault, since it is buried beneath the overlying syn-rift sequence. To estimate the depth of this intersection between the fault plane and the top carbonate surface in the hangingwall, and hence the amount of hangingwall displacement across the fault, three methods have been employed (figure 2.10). The first method involves projecting the dip of the syn-rift sediments at the position where they onlap the hangingwall dip slope back towards the faults along a series of equally spaced transects orientated normal to the strike of the fault. The second method is similar, however rather than back-projecting the dip of the syn-rift sediments, the dip of the underlying basement onto which the sediments onlap is used. Both methods result in a series of cross sections describing the projected subsurface geometry. The cross sections are then used to constrain the geometry of a surface corresponding to the top of the basement, from which displacement:length data can be extracted. These methods assume that the surface position of the fault corresponds to the footwall cut off and are hence minimum displacement estimates. To further constrain the estimates of along strike displacement distribution a third method was employed to account for footwall degradation. This involved projecting the footwall topography towards the fault plane with their intersection corresponding to the position of the footwall cut off. The three methods provide the equivalent of low, base and high case estimates of displacement. It must be stressed that although these methodologies produce reasonable results, there is a large degree of uncertainty, mainly due to uncertainties associated with the effects of any pre-existing basement topography on displacement estimates (figures 2.10, 2.11). In addition, since the calculation of displacement is based upon back-projected strata, the hangingwall cut-off geometries which are predicted will capture only strain accommodated through discrete offsets. As a result the presence of any ductile bed rotations at depth is uncertain. This potentially has implications for the interpretation of fault evolution as continuous deformation, such as rotation of strata, often accounts for the displacement minima frequently observed at relay zones (Walsh et al., 2003).

Following construction of the top pre-rift surface, isochore maps can be constructed for the syn-rift stratigraphy (Figure 3.5). In addition displacement-length plots can be constructed for each individual fault, and for the fault system as a whole. This is done in two ways, either for the true fault lengths, or for the fault length as projected onto a plane parallel to the overall fault strike. Since faults are not linear features their true length is greater than the straight-line distance between their two tips. As a result true-length plots often do not capture distortions in displacement as a result of fault overlap. By projecting displacements onto a fault-parallel plane the displacement variations caused by strain partitioning across overlapping faults is more easily discernible. The difference in d:L ratios between the two approaches can be significant, and it is often unclear within the literature which approach has been used.

The spatial variations in displacement can be used to identify areas of high subsidence associated with prolonged or rapid fault activity, and help to constrain the relative timing of fault activity and deposition of the associated syn-rift sediments in the area.

Figure 3.5 (Next page). (A) Oblique view looking south onto modelled top-basement surface (V.E. = x2). Fault planes are shown in blue. (B) Isochore map of syn-rift strata, with a maximum thickness of 2000m.

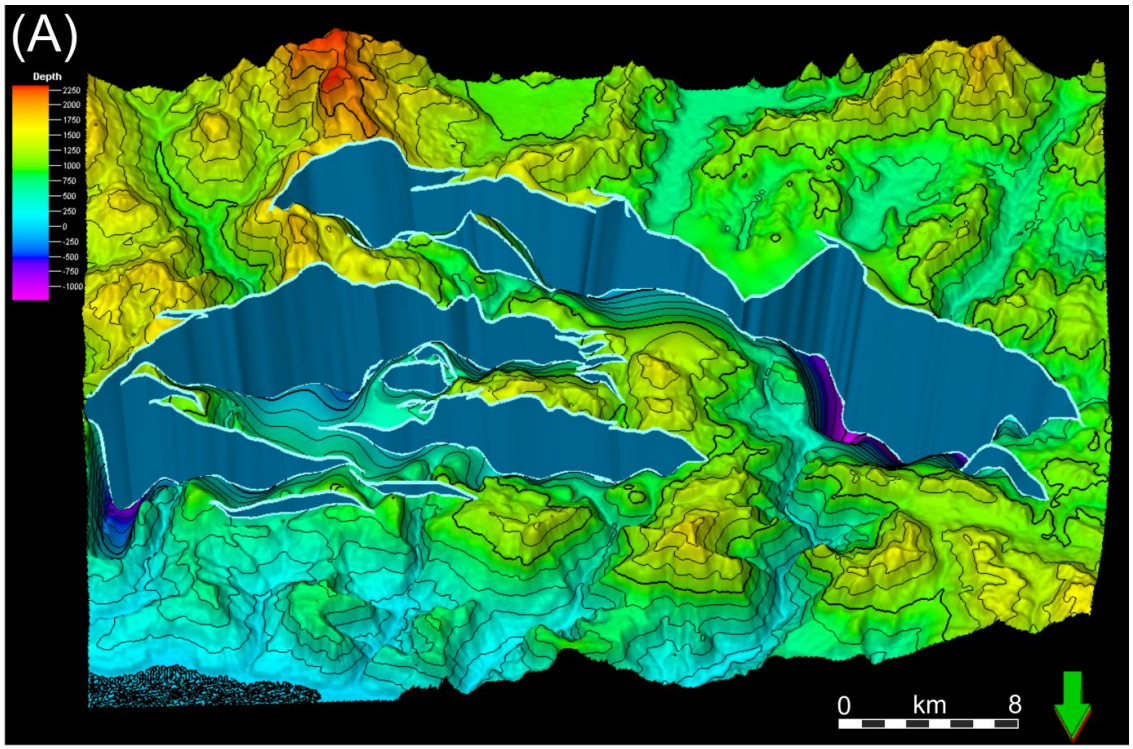
(A)
Depth
2250
2000
1750
1500
1250
1000
750
500
250
0
-250
-500
-750
-1000
0
km
8

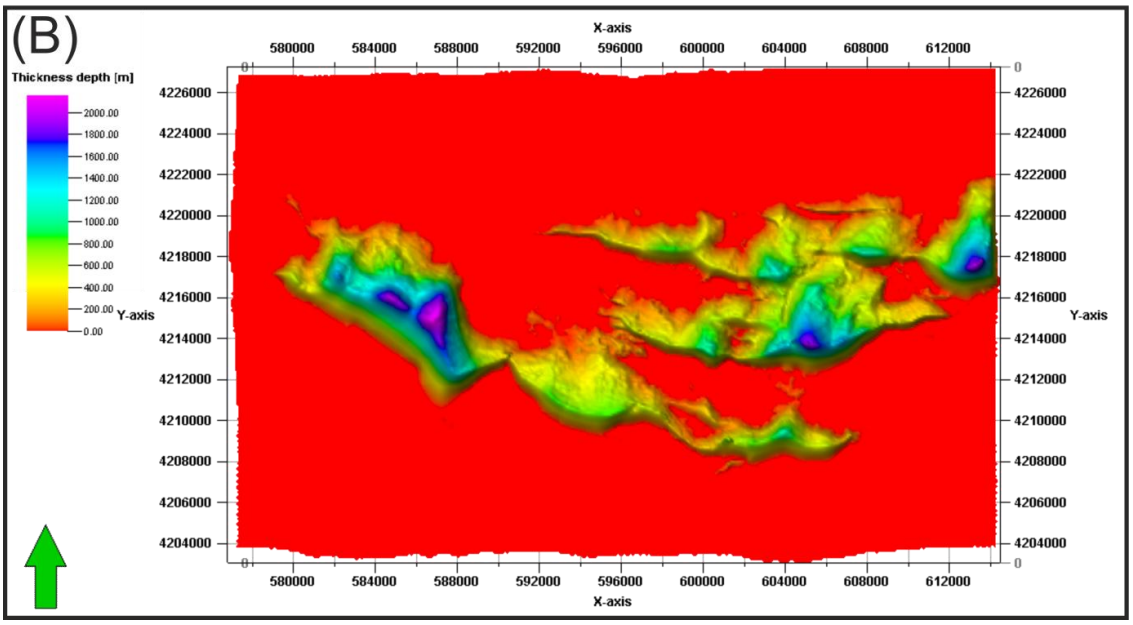
(B)
Thickness depth [m]
2000.00
1800.00
1600.00
1400.00
1200.00
1000.00
800.00
600.00
400.00
200.00
0.00
Y-axis
X-axis
580000
584000
588000
592000
596000
600000
604000
608000
612000
4226000
4224000
4222000
4220000
4218000
4216000
4214000
4212000
4210000
4208000
4206000
4204000

3.4 Onshore Structural Evolution and Lithostratigraphic Framework

As previously mentioned, this study focuses on the structural evolution of the continental rift system and the associated fluvial-alluvial sedimentation. Given the absence of absolute age data, relative timing of fault activity has been discerned using fault and stratal architecture relationships. Constraining the timing of faulting using stratal geometries required that a lithostratigraphic framework be established to aid correlation of sedimentary deposits across faults and between basins.

The scarcity of datable markers within the onshore continental sediments limits the ability to confidently use chronostratigraphy to correlate between adjacent half grabens. As a result a lithostratigraphic framework provides an alternative, if more uncertain, means of establishing a coupled sedimentation-structural evolution model.

Previous work has illustrated the extent to which sedimentation is controlled by rift evolution (Gawthorpe et al., 1994; Collier and Dart, 2004), hence a lithostratigraphic framework has been established in terms of the structural configuration and timing. In the broadest sense the stratigraphy is classified as being either pre-, or syn-rift in origin. Given that rifting is still occurring there is, as yet, no post-rift stratigraphy.

3.4.1 Pre-rift

The pre-rift 'basement' on which the present day rift is superimposed was highly deformed during the formation of the Hellenide mountain range during the Cretaceous to Mid-Cenozoic (Roberts and Jackson, 1991) with thrust sheet emplacement towards the W-WSW (Pe-Piper and Piper, 1991). It is predominantly composed of Tethyan pelagic shelf carbonates deposited during the Mesozoic (Degnan and Robertson, 1998) with subsidiary radiolarite, chert and ophiolite as well as flysch sandstone turbidites deposited during the Palaeocene-Eocene (Piper, 2006; Faupl et al., 2007). The pre-rift in the study area (figure 3.6) is part of the Pindos nappe which in turn overlies the Gavrovo-Tripolitza thrust sheet and Zarouchla complex (Skourtsos and Kranis, 2009). Despite a 15-20 Myr unconformity between the main phase of compressional Hellenide deformation of the pre-rift, and the onset of rifting and deposition of the syn-rift, there is evidence to suggest that a significant inherited palaeo-topography with relief of up to 1000m (Ford et al., 2013) was present at the onset of rifting in the Pliocene-Pleistocene.

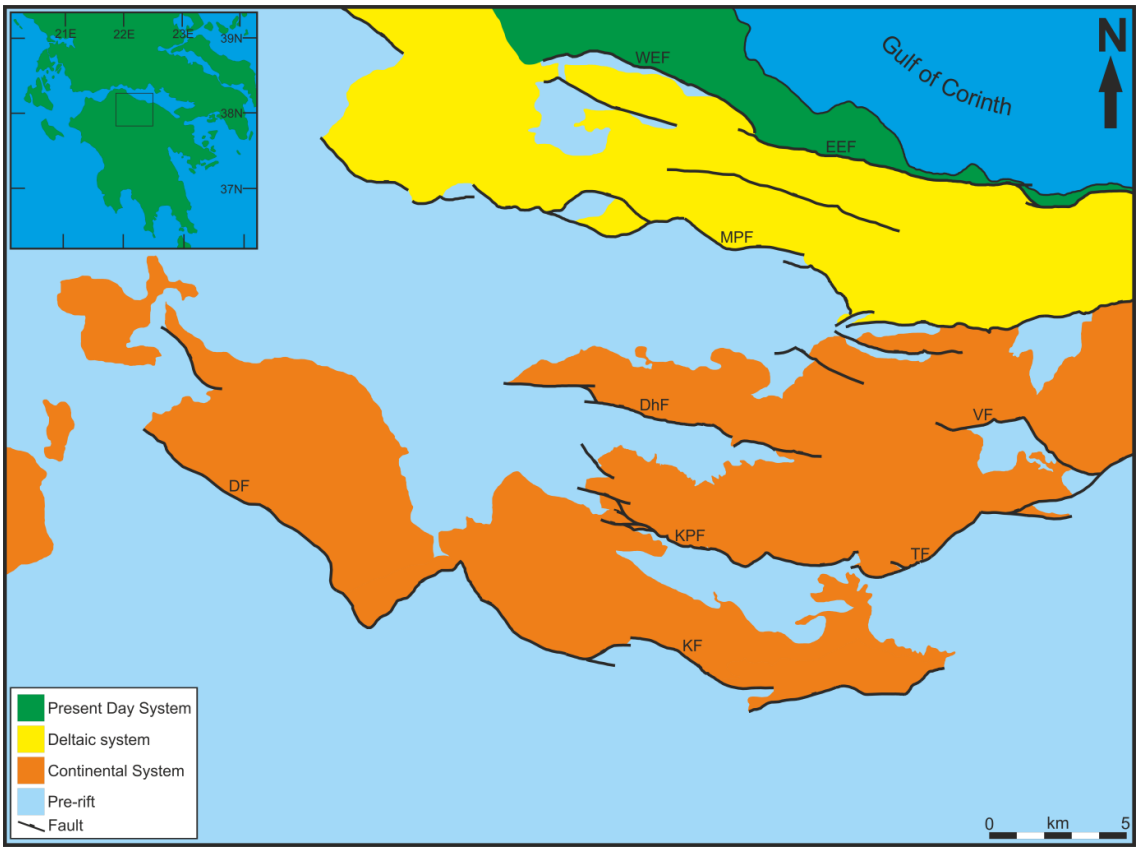

Figure 3.6. Map showing distribution of main depositional units and faults. Inset shows field area location on the Peloponnese peninsula. DF = Dhemesticha fault, DhF = Dhoumena fault, VF = Valimi fault, MPF = Mamoussia-Pirgahki fault, EEF = eastern Eliki fault, WEF = western Eliki fault. Also see more detailed map in the appendix.

3.4.2 Syn-rift

The syn-rift stratigraphy can be sub-divided into three distinct elements (Figure 3.7) based largely upon their age, depositional environment and geographic location. The overall timing of fault activity has migrated northwards other time (albeit with additional complexity superimposed), with progressive back rotation of syn-rift sediments within the hangingwall depo-centres (Poulimenos et al., 1989; Ori, 1989; Doutsos and Poulimenos, 1992). This migration, with concomitant uplift of fault footwall blocks and subsidence of hangingwall blocks, has lead to the present day outcrop pattern, describing a general trend of younger sediments from south to north. In addition the depositional environment shows a general trend of increasing water depth towards the north (Poulimenos et al, 1989; Ford et al., 2007; 2012. The three elements of the syn-rift stratigraphy consist of an early (circa <5 Ma, Papanicolaou et al, 2000; Ford et al., 2007), predominantly continentally deposited system ('continental system'), a 'deltaic system' (circa <1.1-1.5 Ma, Ford et al., 2007, 2012) and the

recent to present day (circa <0.7 Ma, McNeill and Collier, 2004; Ford et al., 2007) deltaic to slope system ('present day system'). The focus of this work is predominantly on the continental sediments, although the younger sediments are also described here for clarity. Previous authors (Rohais et al., 2007; Backert et al., 2010; Ford et al., 2012) have often opted to sub-divide the stratigraphy of the area into detailed lithofacies units, however since this study is primarily focussed on the structural evolution rather than the detailed sedimentology, the simple framework outlined here has sufficed.

3.4.2.1 Continental System (<5 Ma)

The fanning dips of the continental system attest to its syn-rift nature (Figure 3.4), with the sediment input from the south being largely controlled by the Kalavryta-Dhemesticha fault set (Collier and Jones, 2004; Ford et al., 2012). Within the syn-rift sequence are a number of internal angular unconformities across which there are subtle facies changes. These facies changes, along with the differing dip magnitudes, allow the continental system to be sub-divided into three depositional phases consisting of early, middle and late.

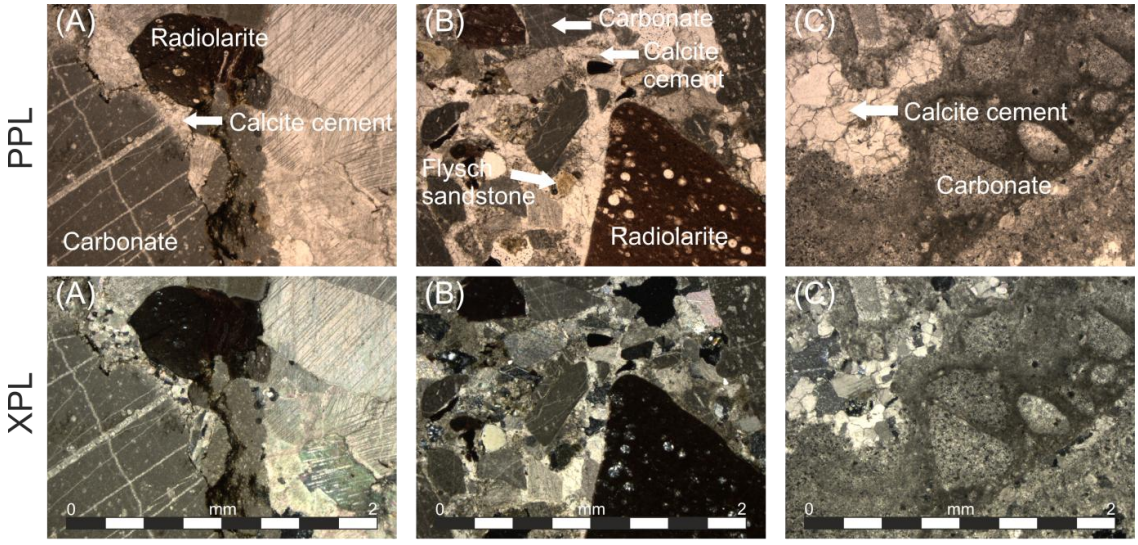

Figure 3.7. Plane and cross polarised light photographs illustrating the variation in composition of different stages of basin fill. (A, Oldest) Initial dispersed rifting resulted in depocentres filled with both hinterland and locally derived material. (B) The main progradational alluvial fan is compositionally varied, dominated by sediments with a hinterland provenance. This includes sandstone, chert, radiolarite and carbonate lithologies. (C, Youngest) The breccia stratigraphically above the main alluvial fan in the hangingwall to the Kalavryta fault is composed entirely of carbonate material derived from the local footwall. All stages display carbonate cementation to varying degrees, with both vadose and phreatic cements observed.

3.4.2.1.1 Early Stage Continental System (Phase 1)

The base of the syn-rift succession is exposed at a limited number of localities where it onlaps the pre-rift 'basement' (Figures 3.8, 3.9). To the south, the earliest exposed continental sediments consists of fine grained lacustrine marls containing occasional lignite (also observed by Papanicolaou et al, 2000) which coarsen upwards into fluvial-alluvial conglomerates constituting the middle phase of continental sedimentation (Figure 3.9). These sediments are interpreted as being deposited passively within inter-montane lows present within the pre-rift topography. Further north, the earliest syn-rift is distinctly different, consisting of well indurated breccias and conglomerates. Although a range of clast compositions is present it is dominated by carbonate with clasts often supported by a calcite cement (figure 3.7, 3.10). The pervasive cementation, possibly combined with a greater burial depth, leads to a higher compressive strength relative to the younger conglomerates (Figure 3.11). This is however a generalised trend, since the measurement of present day in-situ strength does not necessarily correspond to the strength at the time of deposition.

Cementation consists of an isopachus calcite spar overgrown by a drusy fabric (Figure 3.7, 3.10), indicating that cementation occurred below the palaeo water table, within the phreatic zone. The relative lack of grain contact dissolution suggests that cement growth, and hence support of the clasts, was rapid and occurred at a comparatively shallow depth. Stylolite formation at contacts between grains and cement suggests that further post-cementation burial occurred, possibly as a result of loading by younger sediments.

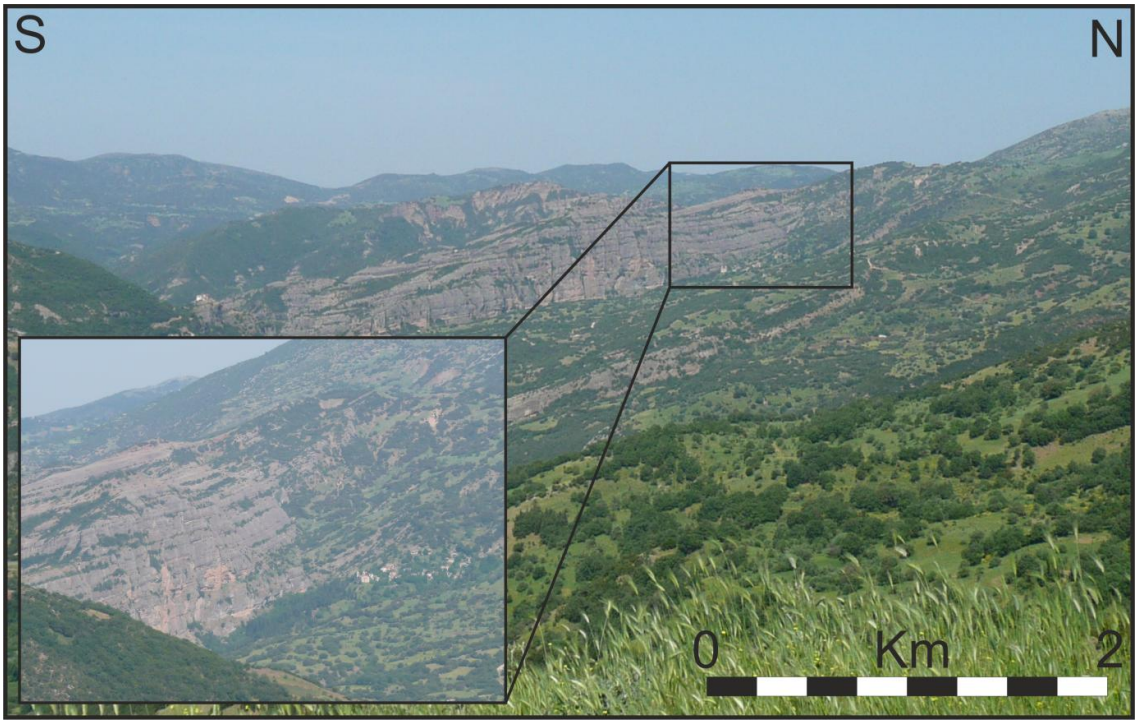

Figure 3.8 (Previous page). Onlap of alluvial fan syn-rift stratigraphy onto the hangingwall dip-slope of the Dhemesticha basin. The inset shows a close up of the onlap contact.

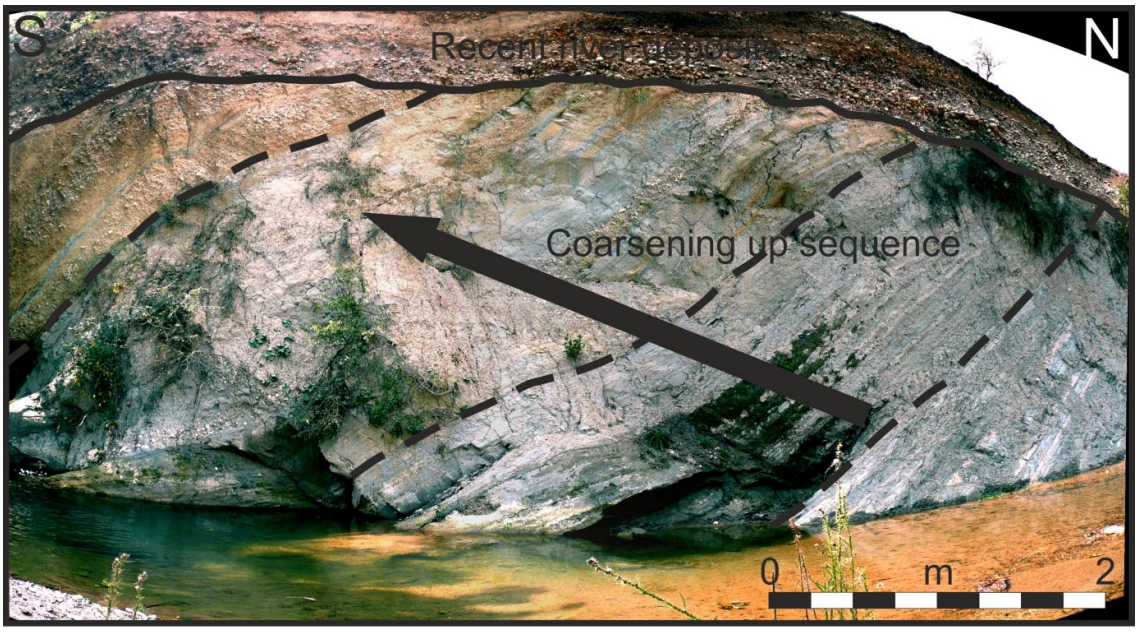

Figure 3.9. Field photograph illustrating the coarsening up sequence at the base of the continental syn-rift. A transition from inter-montane lacustrine to alluvial conglomerate deposits is observed.


(A)
0
mm
5
(B)
Stylolite
0
mm
2
(C)
Isopachus cement
Drusy overgrowth
0
mm
3

Figure 3.10 (Previous page). Thin section images of phase 1, early continental conglomerate. (A) PPL image showing stylolite occurrence at grain-cement boundary, and within cement indicating post cementation burial. (B) Close up image of the boxed area within (A). The stylolite is annotated for clarity. (C) XPL image showing the isopachus fibrous cement forming a halo to a bioclastic grain. A drusy spar cement overgrowth is also labelled. The composition of this early conglomerate is dominated by carbonate clasts likely derived from the local footwall, although a small fraction of non-carbonate grains are also present.

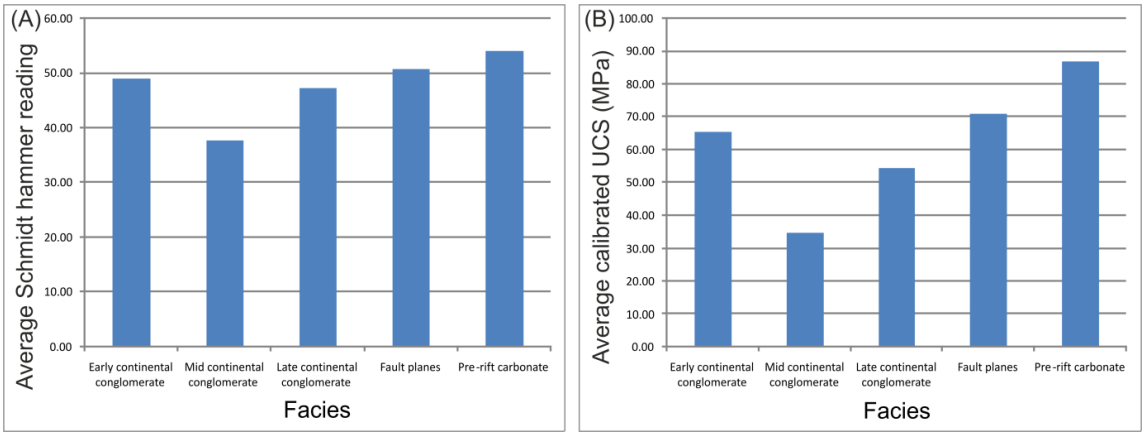

Figure 3.11. In-situ rock strength by facies. (A) Un-calibrated Schmidt hammer readings. (B) Calibrated Schmidt hammer readings as unconfined compressive strength (UCS). The differences in strength are likely to result from a combination of facies, local cementation and potentially the depth of burial Nevertheless, although these measurements give a reasonable estimate of the present day strength, they do not necessarily relate to the strength at the time of deformation.

3.4.2.1.2 Middle Stage Continental System (Phase 2)

The second phase of continental sedimentation is the most widespread and contributes the vast majority of sediments to the syn-rift stratigraphy of the area. Fluvial-alluvial conglomerates, sandstones and silt to mud overbank sediments describe a gradual reduction in the net:gross (Figures 3.12, 3.13, 3.14), from the hangingwall basin of the Kalavryta-Dhemesticha fault set in the south to the Mamoussia-Pirgahki fault set in the north. The outcrop pattern describes a broad amalgamated alluvial fan fed by a distributive river system with multiple entry points along the Kalavryta-Dhemesticha fault set, the largest of these entry points being the Vouraikos river. This fan system extends over, and is offset by multiple faults and their associated half-grabens to the north, indicating that its deposition, at least partially,

pre-dates activity on these fault systems. To the north the fan is observed to onlap earlier deposits (Figure 3.8). Palaeoslope analysis, although highly uncertain, indicates that depositional dips were negligible, at least for the areas currently exposed (Figure 3.15). Qualitative observations adjacent to the Kalavryta fault indicate that clasts decrease in size (Figure 3.16) and increase in roundness northwards away from the fault suggesting sediment entered the hangingwall basin from the uplifted footwall block. This general fining northwards trend is to a lesser degree mirrored across the depocentre as a whole illustrating the transition from proximal, through medial to distal sedimentation. Clast analysis of the conglomerate facies within the Dhemesticha sub-basin suggest a hinterland provenance, with mixed clast compositions (Figure 3.17) reflecting that of the pre-rift stratigraphy to the south. This analysis correlates well with previous analyses across the fan system as a whole (Doutsos and Poulimenos, 1992; Ford et al., 2013).

Conglomerates range between being clast and matrix supported depending on the net:gross, itself generally controlled by proximity to sediment entry points. The matrix itself is predominantly composed of silt and mud, with variable degrees of calcite cementation. Although many depth dependent features (Figure 18, 19) are preserved within the conglomerates, their occurrence is sporadic. Localised process, such as meteoric water drainage coupled with cement dissolution and re-crystallisation, often lead to potentially diagnostic features being over-printed. This limits thin section analysis to being qualitative rather than quantitative in respect to estimating burial depths. Similarly porosity values correlate poorly with depth estimates based upon individual sub-basin structure (Figure 20). Again, this is due to localised cement dissolution and re-crystallisation, as well as the uncertainties with estimating the palaeo-depth based upon the present day, uplifted topography.

Figure 3.12 (next page). A gradual northwards (more distal) decrease in net:gross of the continental alluvial fan can be observed along the Vouraikos river valley north of the Dhoumena fault.


S
0 km 0.5
N

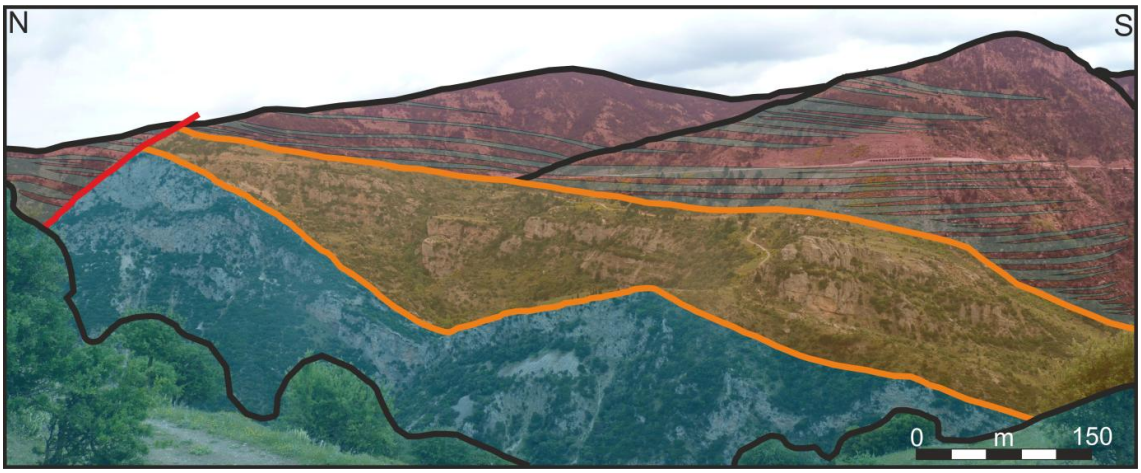

Figure 3.13. Distal continental alluvial fan sediments onlapping early phase graben fill to the north of the Dhoumena fault block.

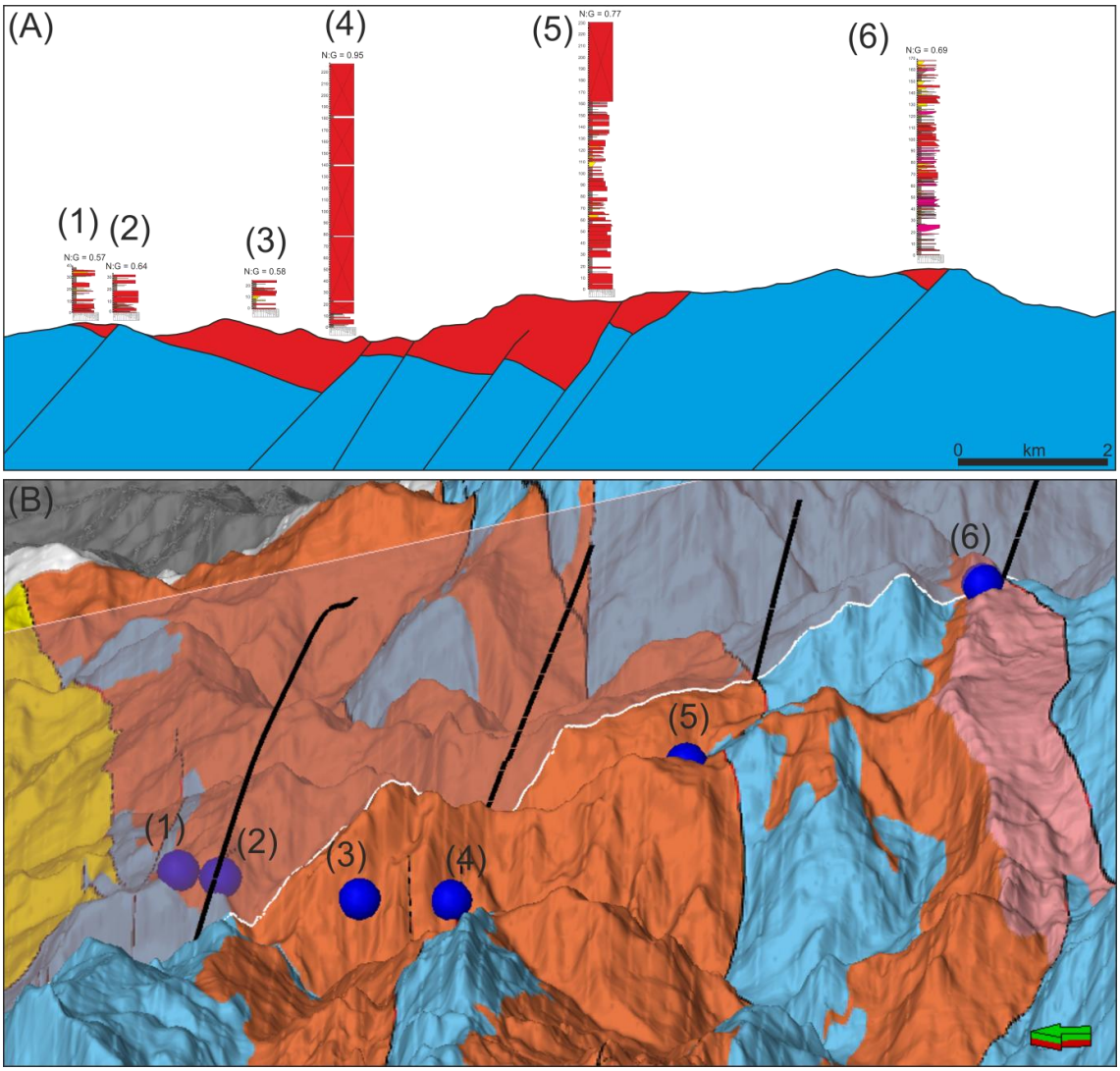

Figure 3.14 (Previous page). The middle phase of continental sedimentation describes a general decrease in net:gross to the north reflecting an increase in distance from the sediment entry point. (A) Sedimentary logs and cross section illustrating the decrease in net:gross. The vertical exaggeration on the logs is x15. (B) Oblique view of map-draped DEM showing the position of the logs and cross-section in (A). You need to say that the brown colour represents the syn-rift areal extent.

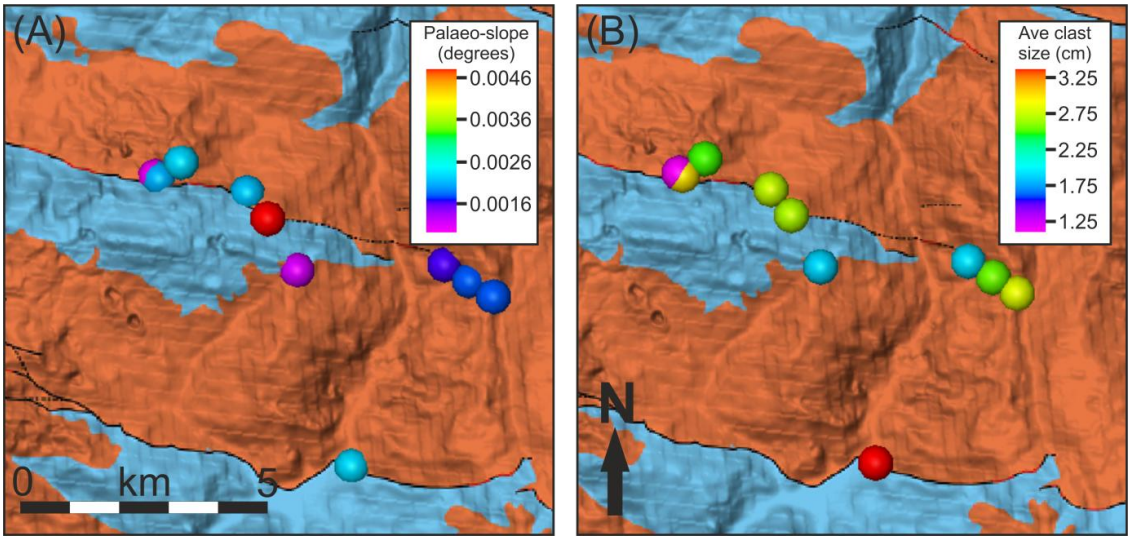

Figure 3.15. Maps showing integration of field data within the geo-modelling environment. (A) Palaeoslope data for syn-rift deposits in the Kerpini and Dhoumena sub-basins. Depositional dips are negligible and hence do not effect fault displacement estimates. (B) Average clast sizes from same sample locations as (A). Clast size generally decreases towards the north, with distance from the main sediment entry point in the south. Ref in text missing?

Figure 3.16. Outcrop of Kalavryta fault plane to the east of Kalavryta village. Hangingwall sediments adjacent to the fault are dominated by angular blocks which decrease in size and become more rounded with increasing distance.

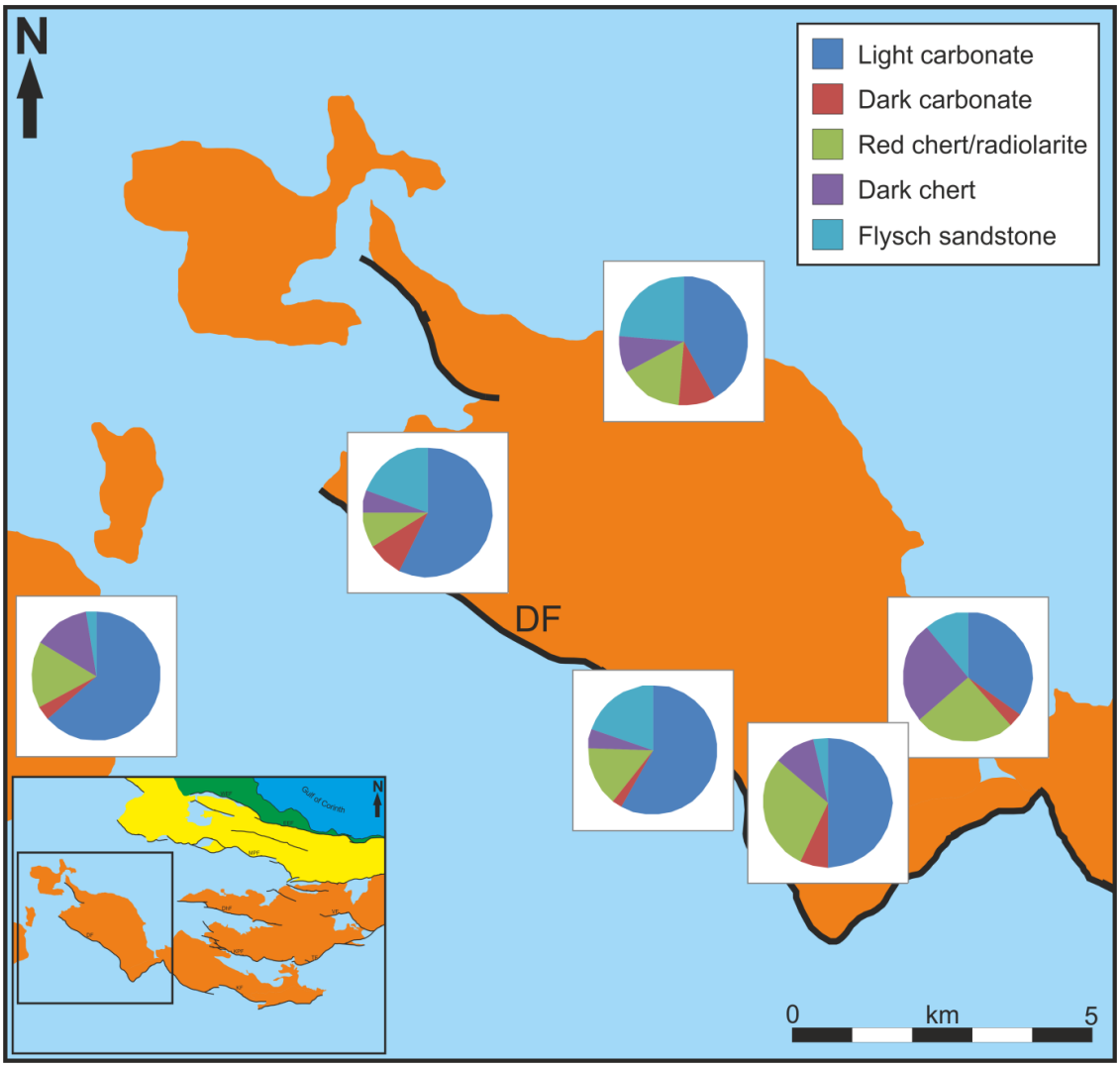

Figure 3.17. Map of Dhemesticha sub-basin with pie charts illustrating the clast composition at various outcrops. See inset map for location.

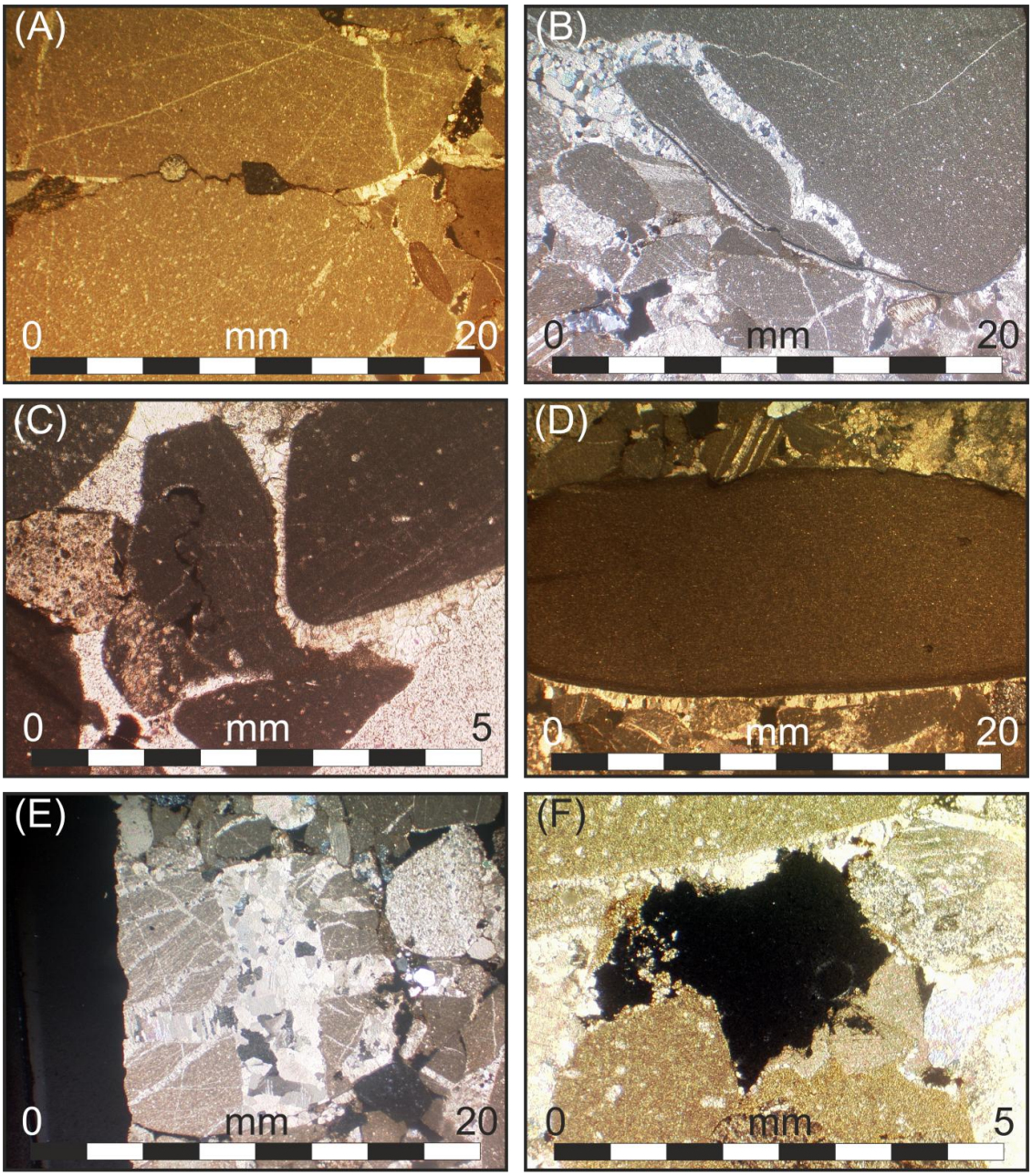

Figure 3.18. Thin section images illustrating the range of depth-dependent features present within the middle stage continental conglomerate facies. All images are from a single sample. (A) Sutured contact between carbonate clasts indicative of compaction induced dissolution. (B) Clast fractured during burial with fracture in-filled by later calcite cementation. (C) Concavo-convex contact indicating clast dissolution during burial, with later stage infill cementation. (D) Dripstone cement present only on the underside of clast indicating cementation within the vadose zone above the water table. (E) Clast with multiple sets of cross-cutting cemented fractures illustrating at least two phases of deformation. As the cementation does not extend beyond the edge of the clast it is likely that the fractures originated during Hellenide deformation of the carbonate hinterland, i.e. prior to erosion and subsequent re-deposition as a component of an alluvial fan system. (F) Possible primary porosity with cement dissolution and grain etching leading to the creation of secondary porosity.

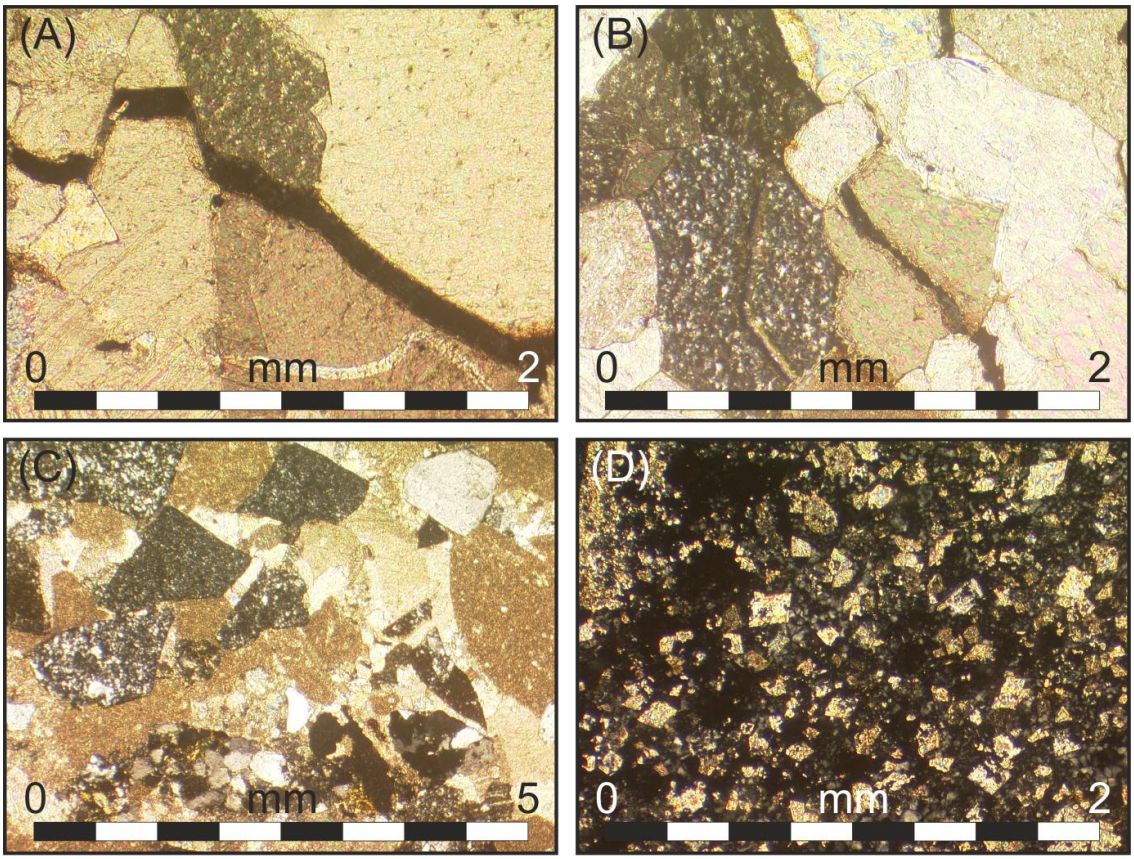

Figure 3.19. Thin section images showing additional features present within continental alluvial fan sediments. (A, B) Open fractures along clast, grain and crystal boundaries possibly indicating reduction in confining pressure during exhumation and un-roofing. (C) Angular grains within finer fluvial facies. Grains are matrix supported, with very little primary porosity visible. The matrix consists primarily of silt grade material. As a result of the support provided by the matrix, limited compaction features are observed compared to the coarser grained, clast supported conglomerates. (D) Localised, rather than widespread, dolomitization of carbonate bioclasts.

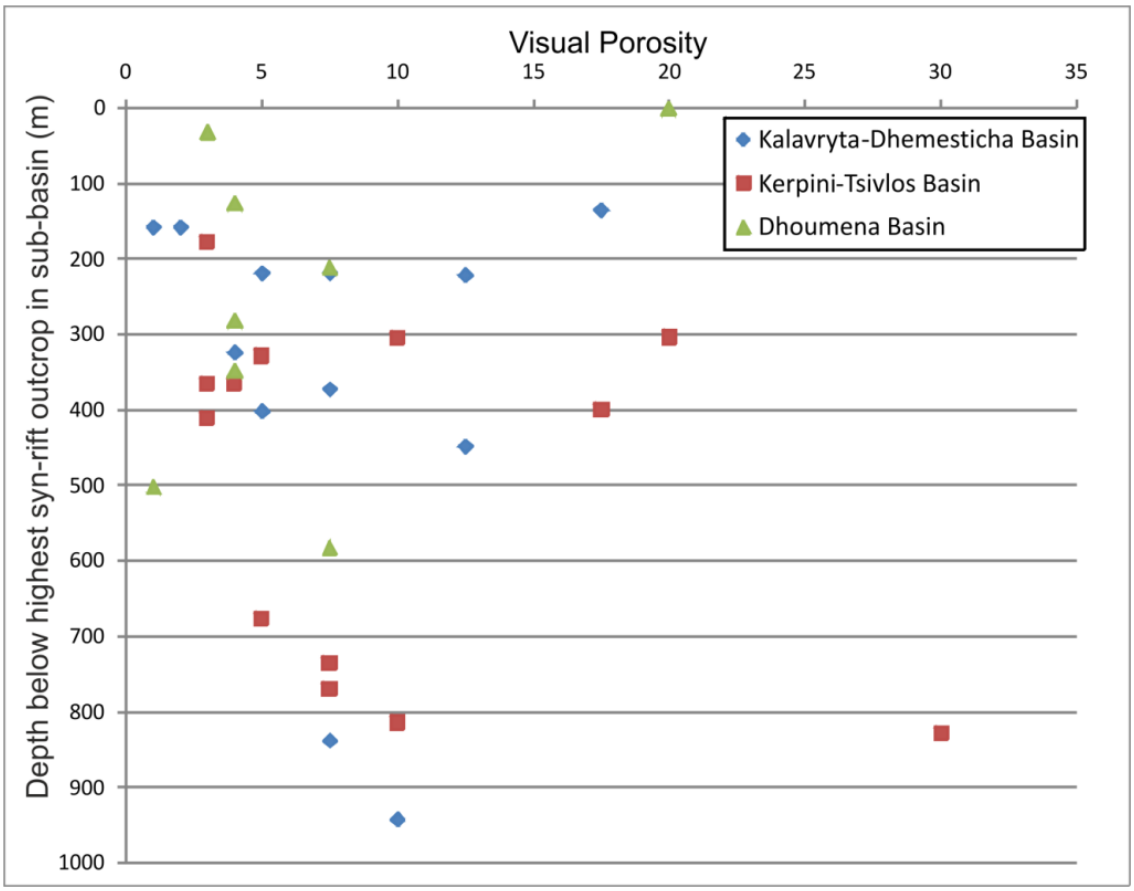

Figure 3.20. Visual porosity from thin section observations. Porosity values are sub-divided by sub-basin and are plotted against sample depth relative to the highest syn-rift within that sub-basin. Theoretically porosity should decrease with depth, however no correlation can be observed, suggesting that in this instance porosity is not a good proxy for paleao-depth. This may be due to dissolution and cementation effects during burial and subsequent uplift.

3.4.2.1.3 Late Stage Continental System (Phase 3)

The last stage of syn-rift continental sedimentation is localised to the eastern end of the Kalavryta fault set (Figure 3.3), overlying the phase 2 alluvial sediments. A significant angular discordance of 8° exists between the two phases of deposition, with phase 2 sediments dipping at 25° S, and phase 3 dipping at 17° S (Figure 3.21). Compositionally this phase is essentially a monomict, dominated by carbonate and carbonate cement, with very few, if any, additional components (Figure 3.22). Clasts are generally sub-angular indicating a local provenance, with previous work describing the facies as slope breccias (Ford et al., 2013). Dissolution is common with significant vuggy porosity being present. Localised, interfingered occurrences of compositionally varied deposits do occur at the fringes of the slope breccia outcrop, potentially indicating the concurrent presence of minor fluvial input routes.

Figure 3.21. Images of 'phase 3' monomict breccias. (A) Dissolution of the carbonate dominated lithology leads to the development of vuggy porosity. (B) View of onlap contact between phase 2 and 3 facies. (C) An angular unconformity of 8° exists between the two phases of deposition. (D) View of onlap contact illustrating the difference in texture.

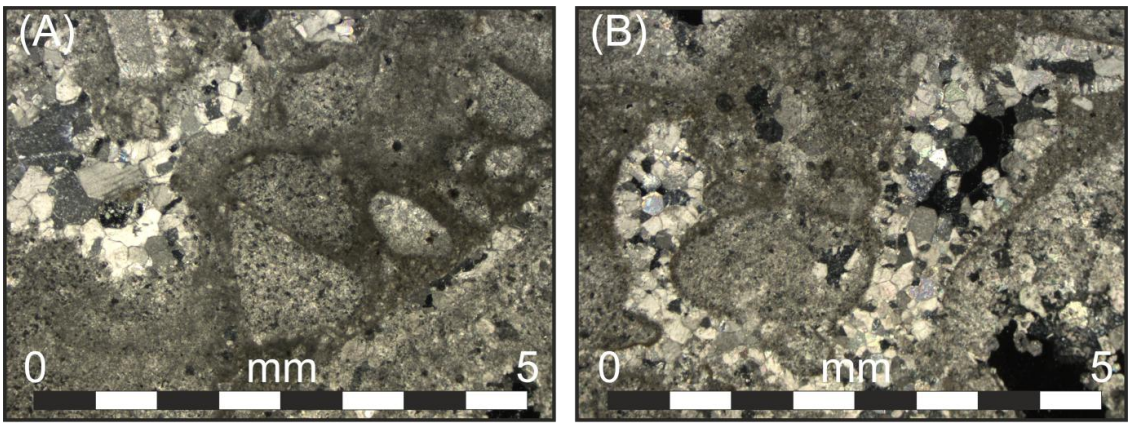

Figure 3.22. XPL thin section images of phase 3, slope breccia facies. (A) Carbonate dominated composition with very few additional components. (B) Cementation is primarily in the form of drusy fabric calcite. Primary porosity is limited, although dissolution has resulted in occurrences of secondary porosity.

3.4.2.2 Deltaic System (<1.5 Ma)

The deltaic system is restricted to the hangingwall of the Mamoussia-Pirgahki fault set (Figure 3.3) and predominantly consists of a number of large, and often overlapping, Gilbert-type fan deltas. The sedimentology and stratigraphy of these deltas has been comprehensively described (Ori et al., 1991; Dart et al., 1994; Malarte et al., 2004; Ford et al., 2007; Rohais et al., 2007; Backert et al., 2010), and is dominated by clast supported, high porosity pebble-grade conglomerates with a similar composition to the hinterland from which they are sourced. Accommodation space created largely by subsidence of the hangingwall of the Mamoussia-Pirgahki fault set lead to deltaic sedimentation initiating at approximately 1.5 Ma (Ford et al., 2007, 2013), with the sediment being supplied from a series of antecedent rivers, the position of which appears to have remained relatively constant since at least the initiation of rifting, their position possibly controlled by the pre-existing palaeo-relief (Collier and Gawthorpe, 1995; Jackson et al., 2006; Ford et al., 2013). Relative sea-level variations (Gawthorpe et al., 1994) are recorded by the sedimentary architecture of the deltas, with distinct phases of progradation and aggradation, as well as periods of sea-level highstand being observed (Dart et al., 1994).

3.4.2.3 Present Day System (<0.7 Ma)

Initiation of displacement accumulation on the eastern and western Elike faults during the late Pleistocene (McNeil and Collier., 2004; McNeil et al., 2005) resulted in footwall uplift and incision by the major fluvial systems into the Gilbert deltas which they had previously fed. Onshore sedimentation is again dominated by a series of small scale Gilbert fan deltas with sand to conglomeratic facies being present. Delta tops form distinct, low relief, arcs building out into the Gulf (Figure 3.23). The onshore sediments have offshore time-equivalent deposits consisting of density currents and turbidites as well as deeper water pelagic sediments closer to the axis of the Gulf (Bell et al., 2008, 2009; Taylor et al., 2011).

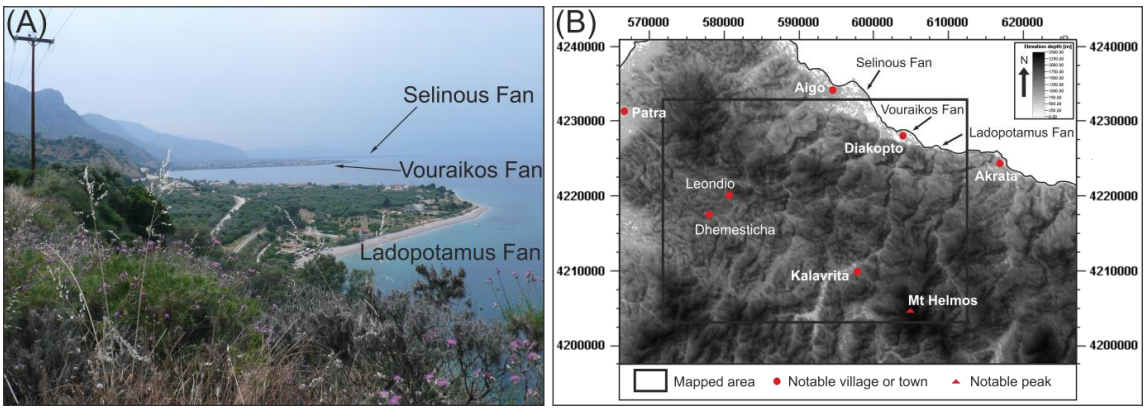

Figure 3.23 (Previous page). (A) View west along Gulf of Corinth coastline showing present day fan deltas. (B) Map showing the location of the fans in (A).

3.5 Structural analysis

Obtaining fault geometry information from the 3D geocellular model of the area allows us to quickly identify displacement minima associated with linkage zones, and hence aid assessment of the evolution of the fault system. This has been performed for all three displacement cases. Figure 3.24 shows the strike parallel distance along each fault plotted against its down-dip displacement for the high, base and low throw cases. The starting position of each fault on the graph is the equivalent to its lateral position so that the distribution of strain across the area can be observed. Hence, the left of the graphs approximates west whilst the right approximates east. The cumulative displacement is also plotted. As is observable in the model (Figure 3.25) strain is localised onto large single faults in the western and eastern areas with extension partitioned over multiple faults across the centre. Displacement minima are identifiable along strike on many of the faults suggesting the presence or relay zones where either hard linkage did not occur, or where post linkage profile re-adjustment has not been sufficient to remove the displacement minimum. The presence of these significant relay zone displacement minima would imply that either fault linkage has occurred relatively late (Walsh et al., 2003), or that a significant component of displacement, probably in the form of continuous ductile deformation, is missing from the models constructed as part of this study (e.g. Walsh et al., 2001, 2002; Long and Imber 2010).

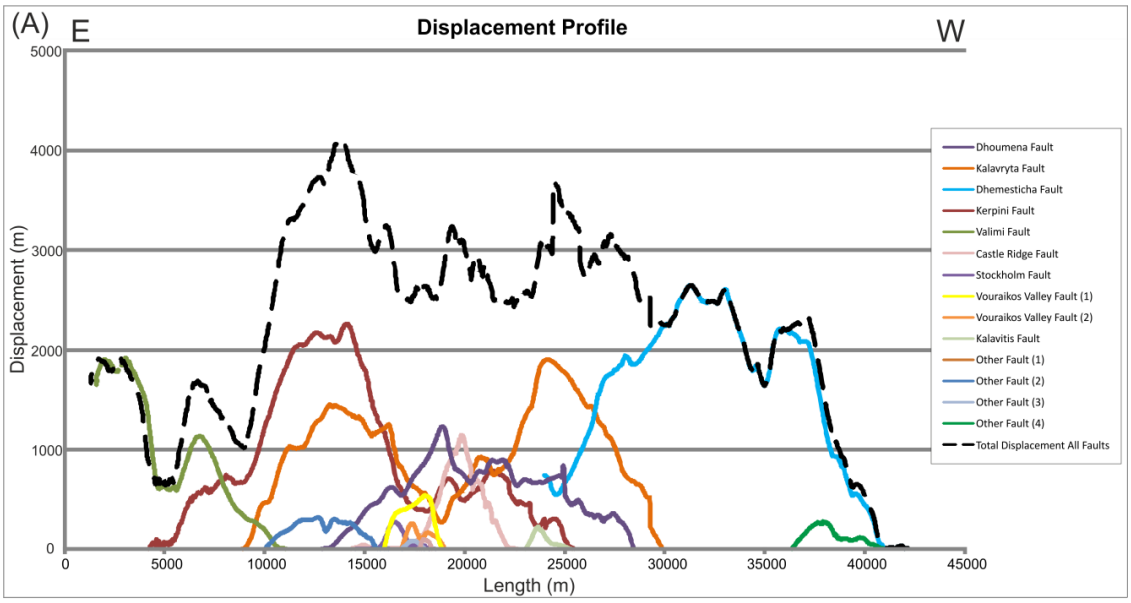
(A)
E
Displacement Profile
W
Displacement (m)
Length (m)
Dhoumena Fault
Kalavryta Fault
Dhemesticha Fault
Kerpini Fault
Valimi Fault
Castle Ridge Fault
Stockholm Fault
Vouraikos Valley Fault (1)
Vouraikos Valley Fault (2)
Kalavitis Fault
Other Fault (1)
Other Fault (2)
Other Fault (3)
Other Fault (4)
Total Displacement All Faults

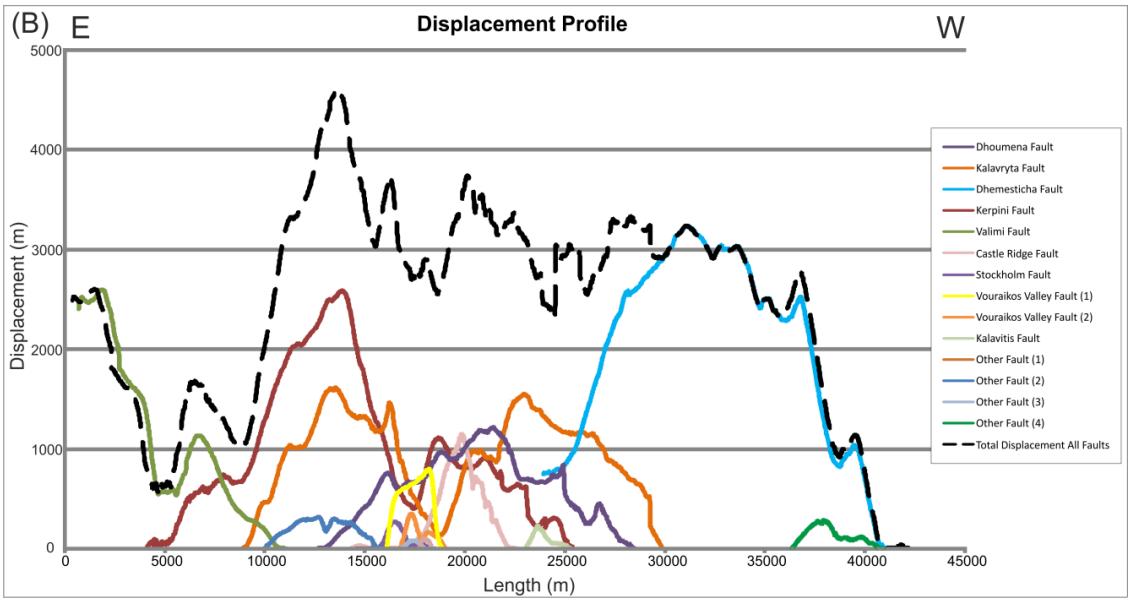
(B)
E
Displacement Profile
W
Displacement (m)
Length (m)
Dhoumena Fault
Kalavryta Fault
Dhemesticha Fault
Kerpini Fault
Valimi Fault
Castle Ridge Fault
Stockholm Fault
Vouraikos Valley Fault (1)
Vouraikos Valley Fault (2)
Kalavitis Fault
Other Fault (1)
Other Fault (2)
Other Fault (3)
Other Fault (4)
Total Displacement All Faults

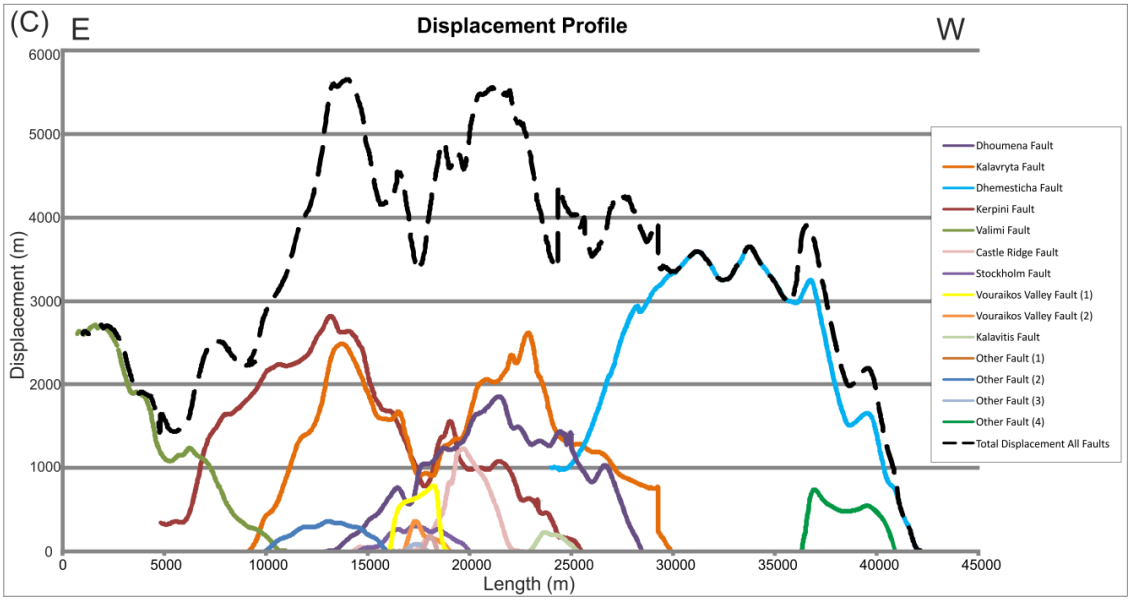
(C)
E
Displacement Profile
W
Displacement (m)
Length (m)
Dhoumena Fault
Kalavryta Fault
Dhemesticha Fault
Kerpini Fault
Valimi Fault
Castle Ridge Fault
Stockholm Fault
Vouraikos Valley Fault (1)
Vouraikos Valley Fault (2)
Kalavitis Fault
Other Fault (1)
Other Fault (2)
Other Fault (3)
Other Fault (4)
Total Displacement All Faults

Figure 3.24 (Previous page). Low (A), Mid (B) and High (C) displacement length-plots generated using true fault length as measured along the map trace of the fault. This leads to greater lengths than when displacement is projected onto a planar, strike-parallel plane (Figure 3.25). Displacements are based upon the different approaches outlined in Chapter 2 (Figure 2.10).

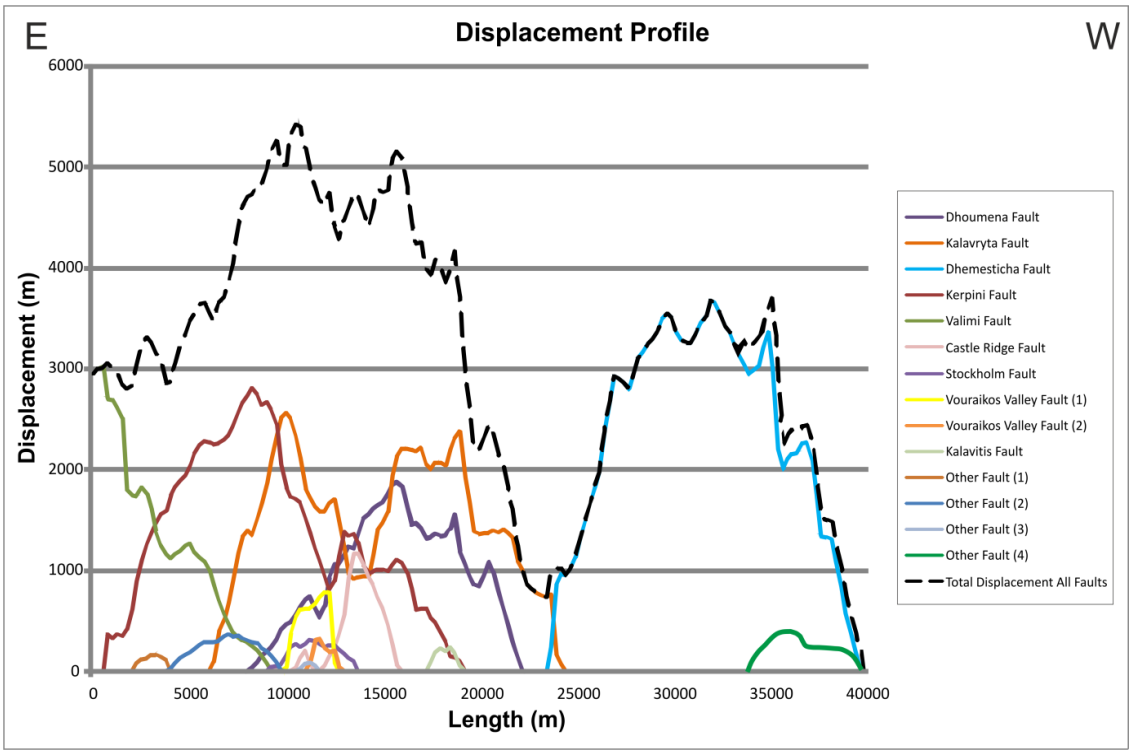

Figure 3.25. Mid-case displacement-length plots for faults with displacement projected onto a strike-parallel plane (approximately E-W). The disparity in cumulative displacement between the east and west areas is clearly seen, with a significant displacement minima observed between the two areas. In the eastern area to the north of the Kalavryta fault strain is partitioned across multiple faults, whereas further west a single fault, the Dhemesticha fault, accommodates almost all of the strain.

The d:L ratios for the faults are slightly higher (Figure 3.26) than the generally accepted range 0.1-0.001 (Kim and Sanderson, 2005), indicating that the faults have accumulated a large amount of displacement for their lengths. There are a number of possible explanations for this anomaly. The lengths have been calculated for each individual fault segment, rather than for the fault sets as a whole. If a fault set is linked, either kinematically or physically, then the individual segments will become 'over-displaced' as displacement accrues on the fault set as a whole (Cartwright et al., 1995; Cowie et al., 2000). Alternatively the high d:L ratios may be explained by the pre-existing basement topography influencing estimates of displacement. If positive relief is present in the footwall prior to faulting then displacement will tend to be overestimated (figures 2.10, 2.11).

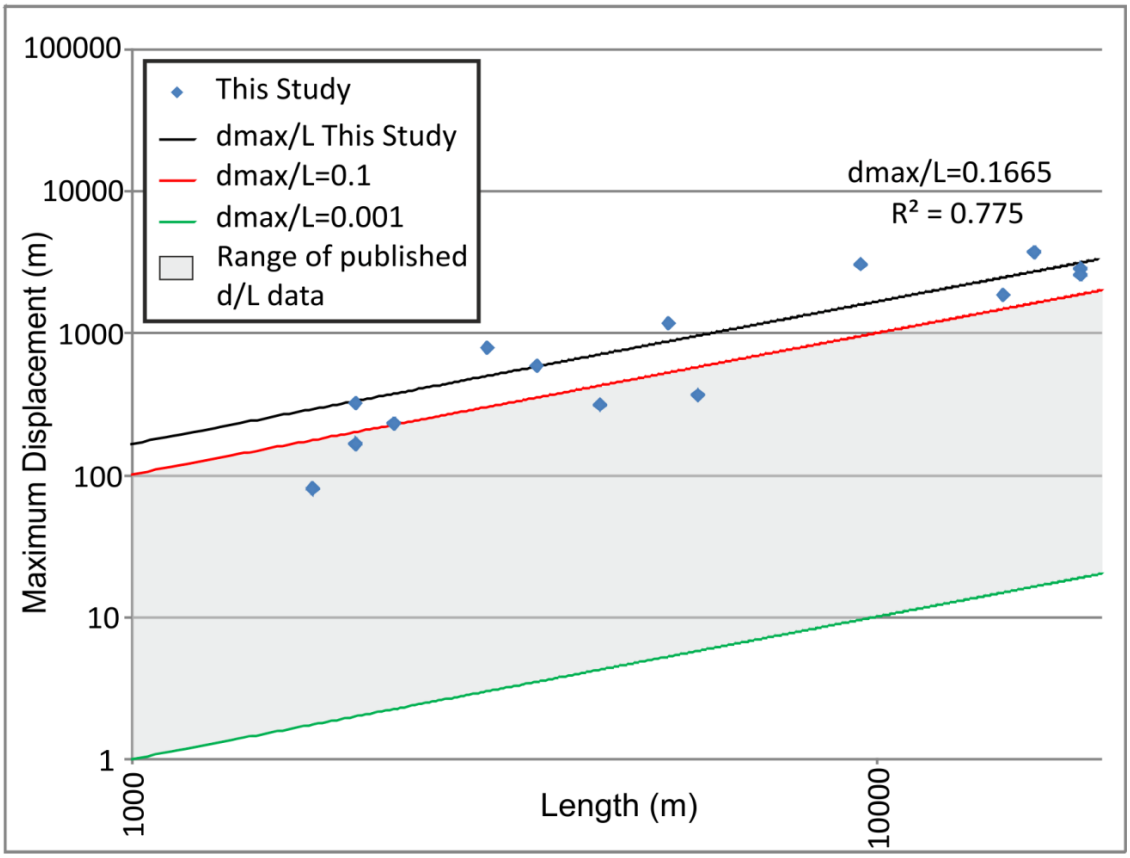

Figure 3.26. Displacement:Length (d:L) plot of onshore Gulf of Corinth faults for the mid-case displacement scenario. The red and green lines represent the upper and lower bounds of published d:L data (Kim and Sanderson, 2005). The majority of the modelled faults fall above this range indicating a high d:L ratio.

3.5.1 Structural Restoration

The disparity in cumulative displacement between the east and west of the field area (figure 3.25) is problematic. There is no evidence of strain partitioning or temporal overlap between the Dhemesticha fault and the later Mamoussia-Pirgahki and Eliki fault sets to the north, hence an additional mechanism must be responsible for the discrepancy in displacement. In addition the strike of the mapped faults changes from approximately WNW-ESE in the east to NW-SE in the west. Figure 3.27 shows restored cross-sections to illustrate the discrepancy in extension from east to west, and the influence of the variation in fault strike. Where restored sections are aligned N-S, parallel to the overall extension direction, a significant discrepancy in restored length is present between the eastern and western areas, suggestive of an extension deficit. Conversely, if the restorations are performed normal to fault strike, rather than parallel to the overall extension direction, the disparity in extension is minimal due to no extension being unaccounted for through out of plane movement. This suggests that deformation on the fault was of a predominantly dip-slip motion, a conclusion supported by fault plane kinematic indicators (Roberts, 1996; Skourtsos and Kranis, 2009). The extension direction therefore rotates from NNE-SSW to approximately NE-SW from east to west, a pattern which is also broadly observed both onshore and offshore for the Corinth rift as a whole (figure 3.2).

Present day geodetic data suggest that extension rates increase westwards from 5 to 15 mm/yr (Davies et al., 1997; Clarke et al., 1998; Briole et al., 2000). The amount of extension across the area is however greater in the central portion of the rift than the western portion, suggesting that the present day westwards increase in extension rate has not always been the case (Bell et al., 2008, 2011). The current extension rate pattern is a response to a-symmetrical fault growth and linkage processes which resulted in a strain deficit towards the west of the Gulf (Bell et al., 2011), which would therefore have had a palaeo-extension rate less than that of the central and eastern areas. It is this along strike variation in extension rate, which is speculated to be the reason for both the discrepancy in cumulative displacement across the onshore faults, and the clockwise rotation further west.

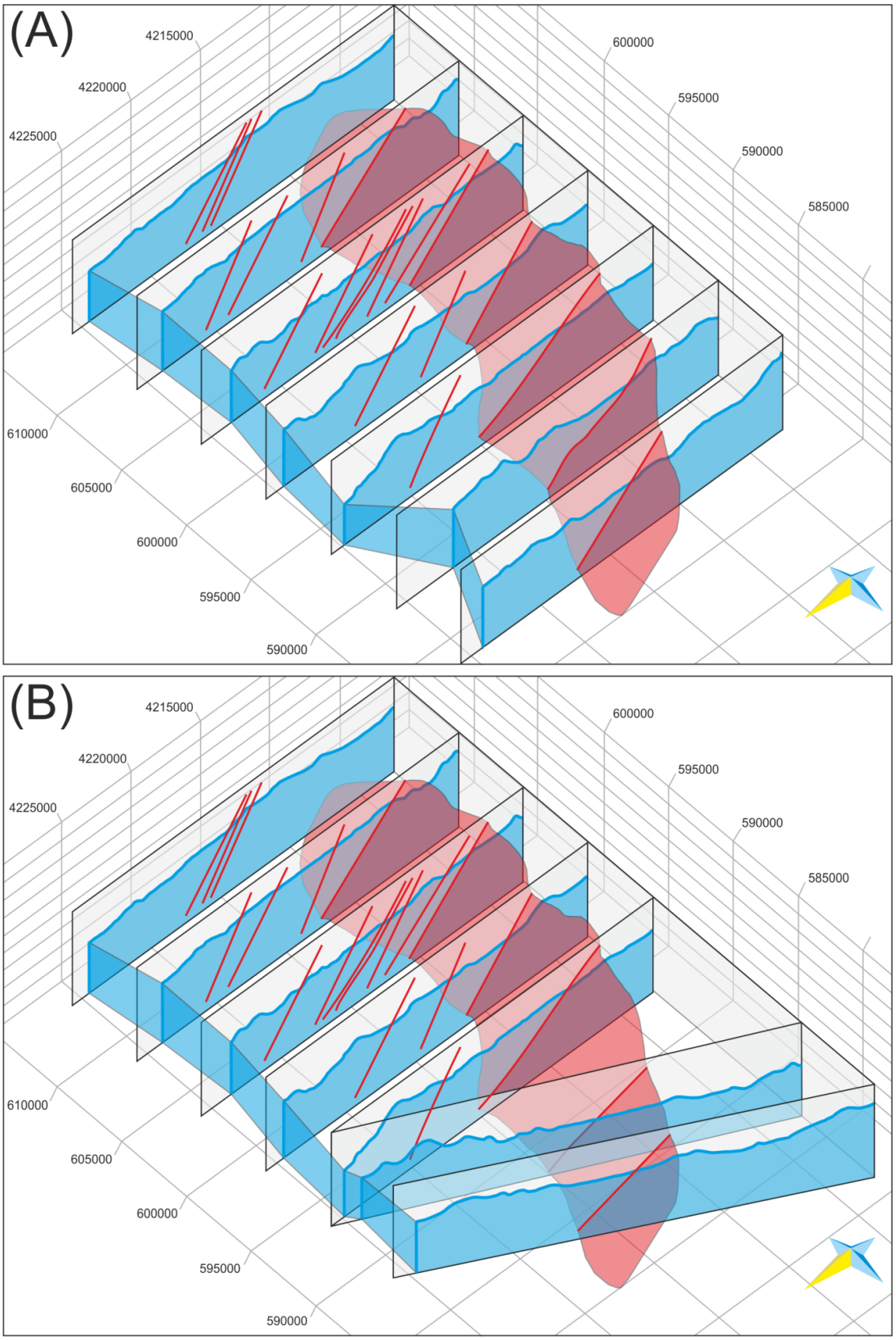
(A)
4215000
4220000
4225000
600000
595000
590000
585000
610000
605000
600000
595000
590000
(B)
4215000
4220000
4225000
600000
595000
590000
585000
610000
605000
600000
595000
590000

Figure 3.27 (Previous page). Oblique views of restored sections across field area as derived from 3D geocellular models. Start and end points of the sections are located at the same arbitrary latitude, with the southern end of the sections pinned. Faults are shown in red with the Kalavryta-Dhemesticha fault plane shown in semi-transparency. (A) Extension parallel cross sections with a N-S orientation. The orientation change between the Kalavryta and Dhemesticha faults leads to a poorly balanced section. (B) Re-orientating the sections to be strike-normal leads to significantly more balanced restoration across the area.

3.6 Conceptual Model for Onshore Rift System Evolution

The field data, maps and 3D geological models capturing along strike displacement variations have been synthesised to construct a model of the evolution of the early onshore rift and the deposition of the continental syn-rift sediments. A copy is also shown in the appendix. This model is based upon the assumption that the rift faults grew according to the theory of fault growth illustrated by Cowie et al (2000). Although this model works to describe the observed fault geometries, it does not necessarily account for the long rupture repeat times that would be required to develop the large displacements observed if the faults can grown through 'coincidental' linkage (Walsh et al., 2003).

(A) It is proposed that initial extensional stress across the area was accommodated through dispersed rifting on a number of isolated faults, comparable in geometry to numerical models of rift evolution proposed by Cowie et al (2000). Small sub-basins develop in the hangingwalls to these faults with fine grained lacustrine conditions evident west of Kalavryta along with occasional occurrences of lignite (Papanicolaou et al, 2000). Other sub-basins are filled with coarser sediments composed of a mixture of local footwall-derived material and a subordinate component of compositionally varied river transported sediment with a hinterland provenance (figure 3.10). This is best observed north of the Kerpini fault where early rift sediments are onlapped by later alluvial fan deposits (Figure 3.12, 3.13). It is likely that established fluvial systems existed with their positions controlled by the pre-existing, approximately NNE=SSW orientated, structural fabric of the Hellenide Mountain range. The extent to which the courses of these river systems were influenced by early fault growth is unclear and is largely dependent on the relative rates of deformation and incision.

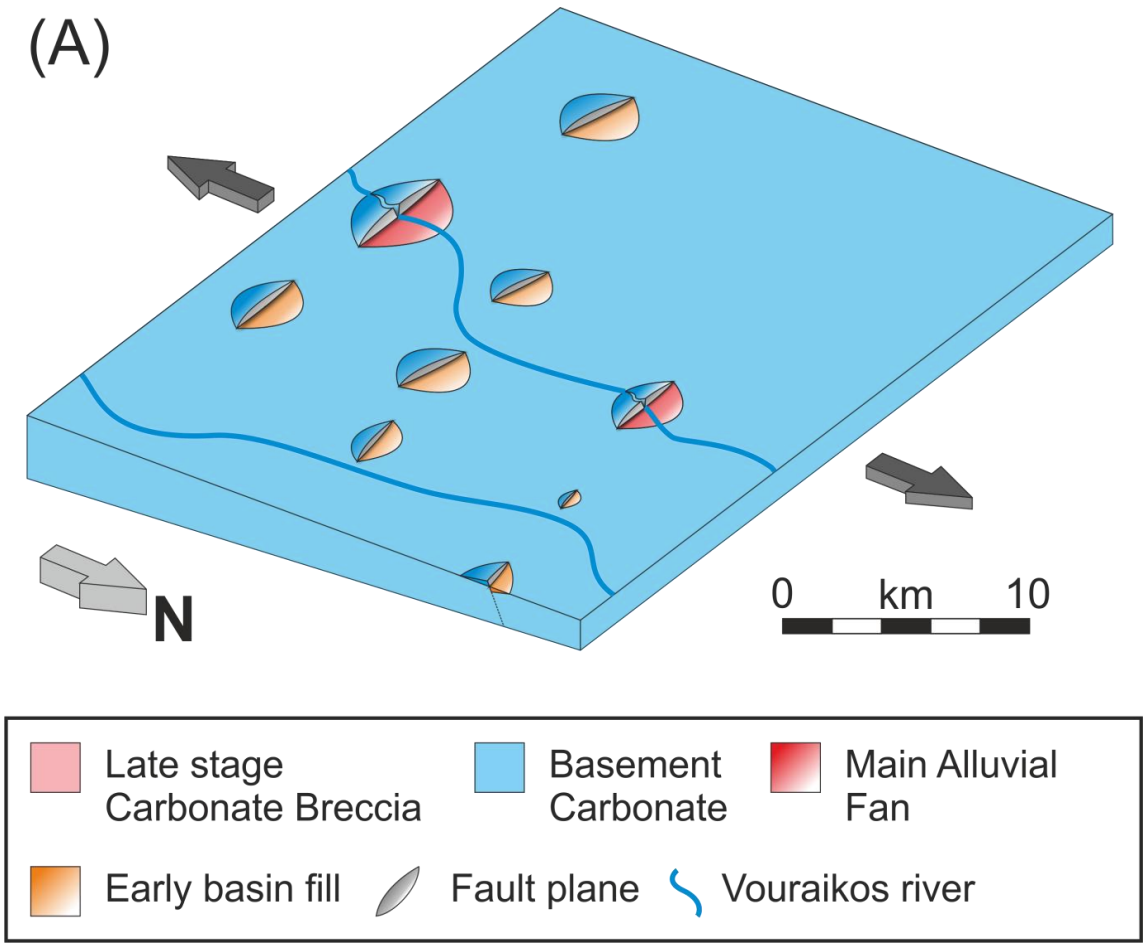

(B) As extension continues deformation begins to localise in the south of the area onto what later becomes the Kalavryta fault set. It is likely that at this early stage sediment supply would have outpaced accommodation space creation since the individual fault segments would not yet have been linked. However, as early sub-basins in the hangingwalls to the faults begin to be in-filled by footwall-derived fluvial sediments, the individual hangingwall fans begin to coalesce. This results in the formation of a distributive alluvial system which starts to prograde across the hangingwall area, with onlap onto the topographic highs of the footwall crests of the proto-Kerpini fault set, hence revealing their presence due to dispersed rifting in the initial stage of evolution. The compositionally variable nature of the sediment suggests a hinterland provenance combined with a proportion of locally derived material (Figure 3.7, 3.17). Palaeocurrent data indicates that the main sediment input point was the palaeo-Vouraikos river to the southwest of Kalavryta, with the majority of sediments fanning out radially from this point (Figure 3.28). The incision rate exceeded the rate of footwall uplift, and hence allowed the river to maintain its antecedent course, despite

lower footwall uplift further to the east. There is however also palaeocurrent evidence that multiple secondary input systems were located along strike to the east and west, albeit supplying a lower proportion of the sediment to the basin. The position of these systems was likely controlled by a combination of the pre-existing topography and local perturbations in this topography caused by footwall uplift of the developing faults, with displacement minima between fault segments acting as supply conduits to the hangingwall basin. Isochore mapping, along strike displacement distribution and increasing rotation of bedding with age (figure 3.4) suggest that eastern segments of the Kerpini-Tsivlos fault set may also have been active at this early stage, with its hangingwall basin possibly supplied with sediment from the Krathis river. The relative timing of the initiation of the Dhemesticha fault set to the west is unclear. Although its large displacement suggests a sustained period of activity, the significant displacement minima between the Kalavaryta and Dhemesticha faults suggests a relatively late interaction.

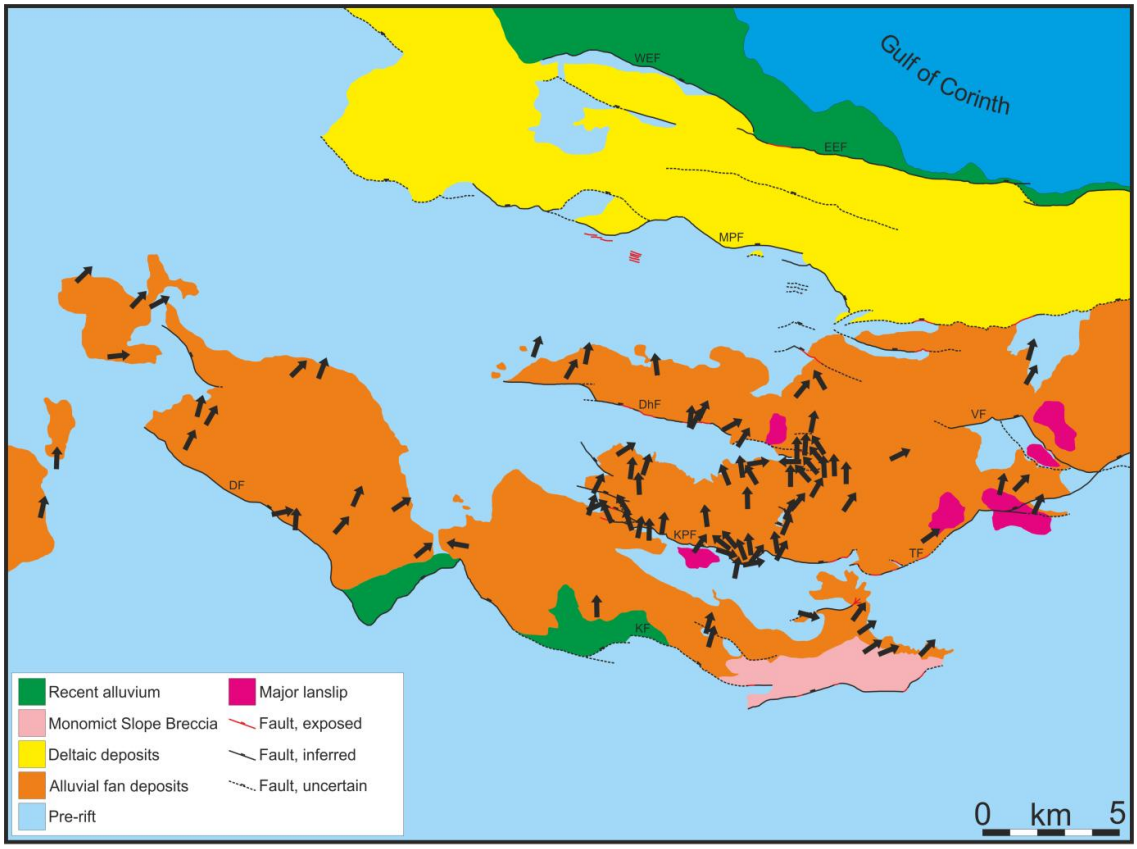

Figure 3.28. Palaeocurrent data from the 'phase 2' syn-rift alluvial fan, showing a north to NNE average orientation. Orientations are broadly radiate away from the sediment entry point of the Vouraikos river indicating its continuous presence during deposition. Superimposed on this radial distribution are internal variations due to the distributive nature of the fan system.

(B)

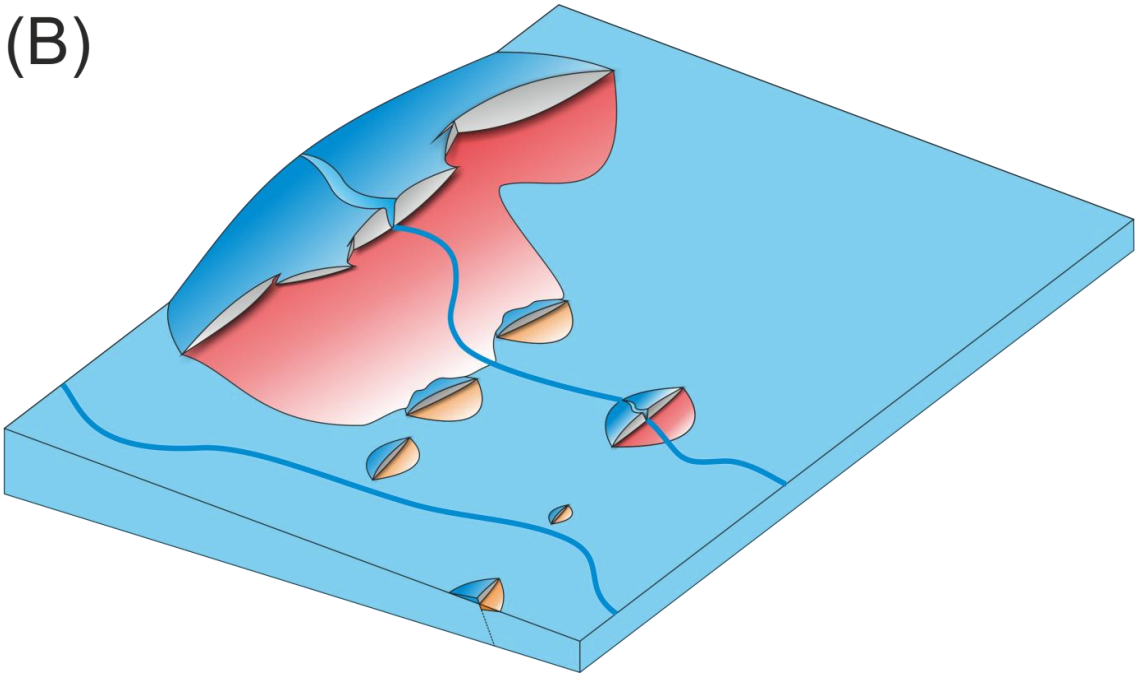

(C) With continuing extension the individual segments of the Kalavryta fault set begin to interact, with profile re-adjustment resulting in a rapid increase in the deformation rate around displacement minima associated with relay zones. This increasing displacement results in high strain and breaching of relays with the fault set becoming hard linked. The rate of accommodation creation in the hangingwall increases as does footwall uplift, potentially re-directing secondary rivers and hence limiting sediment input into the basin. An additional possibility is that these secondary rivers are diverted into the Vouraikos as tributaries, hence increasing its erosive potential. Sub-basins in the hangingwall to the proto-Kerpini fault set preserved from the initial stage of dispersed rifting may become filled with distal alluvial fan deposits.

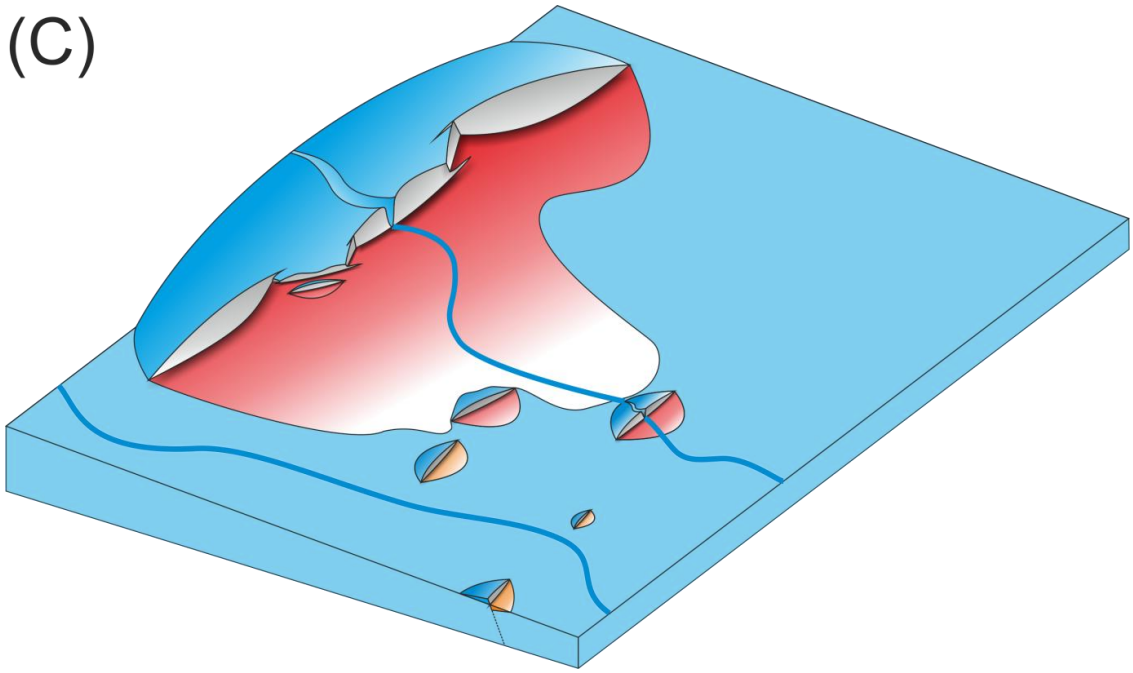

(D) To the east regional extension begins to be accommodated by activity on the Tsivlos fault. This results in a reduction in stress normal to the fault (Ackermann and Schilsche, 1997; Gupta and Scholz, 2000) which in turn limits the eastwards propagation of the Kalavryta fault set to the south. Further west where no overlap occurs displacement continues unimpeded on the Dhemesticha fault. This is reflected in the displacement disparity between the Dhemesticha and Kalavryta faults (figures 3.24, 3.25). It is possible that continued deposition in the Dhemesticha sub-basin lead to progradation and coalescence with the Kalavryta fan. The decrease in extension, and hence in accommodation creation on the eastern segment of the Kalavyta fault set does not lead to renewed progradation, rather the majority of the sediment flux is captured by the newly forming basin in the hangingwall to the Tsivlos fault. Entry into the Tsivlos basin was likely to be at the western end of the Tsivlos fault set, in a topographic low formed by the relay zone between the Tsivlos fault to the east and the proto-Kerpini fault to the west (figure 3.29).

(D)

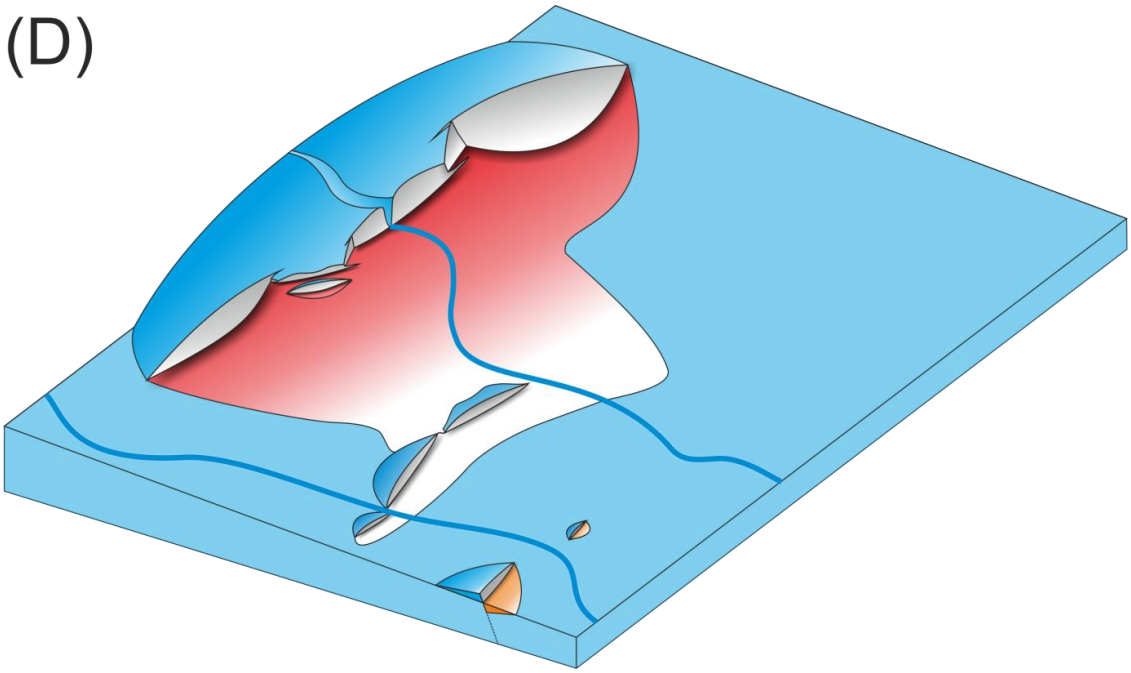

(E) Linkage of the individual segments of the Tsivlos fault results in a rapid increase in both displacement rate and the available accommodation space in its hangingwall. The fans in the hangingwalls to the Tsivlos and Kalavryta fault begin to coalesce leading to northward progradation. Initially aggradation is dominant with sediment stored up dip in the immediate hangingwall to the fault set. Gradually however the sediment supply rate begins to outpace creation of accommodation space resulting in progradation of a broad alluvial fan across a wide area. This distributive system extends at least 10km north into the hangingwall, first onlapping and then burying the footwall crest of the proto-Dhoumena fault. Field observations, data collected along transects perpendicular to the fault system, and high sediment thickness in the hangingwall of the Tsivlos fault compared to the Kalavryta fault (figure 3.5) indicate that this may have been the main depocentre at this stage, with sediment input possibly from both the Krathis and Vouraikos rivers. To the west, displacement continues on the Dhemesticha fault, with local stresses leading to the formation of a subsidiary fault to the north west of the main fault.

An angular unconformity between phase 2 and phase 3 facies at the eastern end of the Kalavryta fault (figure 3.21) indicates continuing displacement, albeit with a lack of deposition. This reason for this reactivation of the Kalavryta fault set is unclear, however a corresponding reduction in slip rates on other concurrently active faults would be expected given a constant regional rate of extension. Although reactivation would result in creation of accommodation space in the Kalavryta depocentre, earlier

incision by the Vouraikos river as a response to subsidence in the hangingwall of the Kerpini-Tsivlos fault to the north would have resulted in the majority of sediment by-passing the Kalavryta depocentre, despite the available accommodation space. This may also have been facilitated by uplift of the footwall to the Kerpini-Tsivlos fault set. Footwall uplift in the Gulf of Corinth region is common as illustrated by the present altitude of deltaic deposits in the footwalls to the active coastal faults (De Martini et al 2004; McNeill and Collier, 2004), with uplift to subsidence ratios of 1:1.3-3.5 (Armijo et al 1996; McNeill and Collier 2004). As the footwall to an active fault is uplifted it may experience increased erosion and instability, as well as leading to an increase in the catchment area of rivers supplying sediment to its hangingwall. This process may have also contributed to the relative increase in the sediment supply to the Kerpini-Tsivlos basin. Another potential explanation may relate to extensional strain becoming partitioned across a number of faults rather than being localised onto the Kerpini-Tsivlos fault set, hence resulting in a lower rate of accommodation space generation. As mentioned, field relationships indicate that at least a localised portion of the eastern end of the Kalavryta fault was active subsequent to the cessation of deposition in its hangingwall.

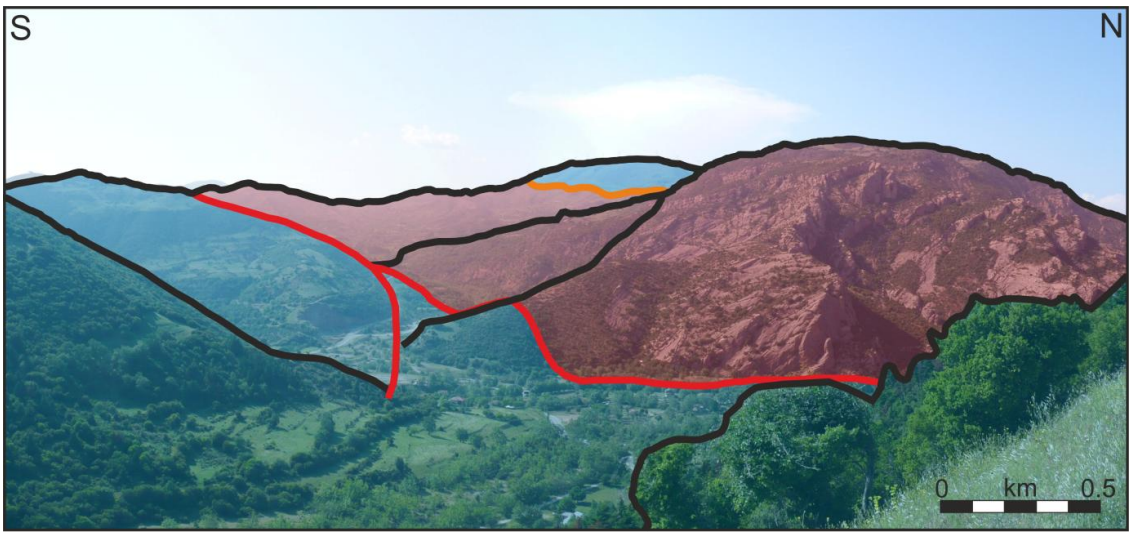

Figure 3.29. Obliquely orientated photograph of hard linked relay zone at the eastern end of the Kerpini fault where it links to the Tsivlos fault (see Red line). There is a marked orientation change of the fault corresponding to the position of the Vouraikos river. Where is that? Note that the Tsivlos fault is obscured in this view.

(E)

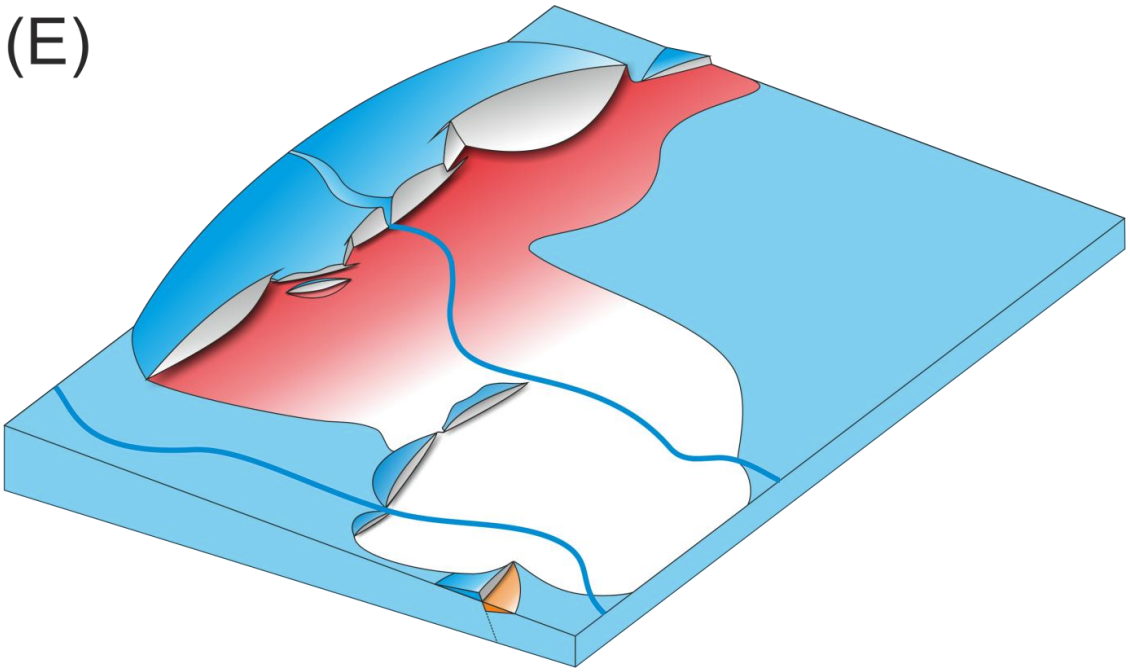

(F) The hard linkage of the Kerpini-Tsivlos fault set leads to profile re-adjustment and rapidly increasing displacement at former relay zones. Back rotated aggradational conglomerates in the immediate hangingwall to the Tsivlos fault show fanning dips, attesting to their syn-rift nature (Figure 3.4). This is in contrast to the Kerpini fault where only normal drag is recorded by the dips of the syn-rift stratigraphy (figure 3.30). This indicates that the Kerpini fault was active subsequent to the deposition of the main alluvial fan. Increasing displacement on the Kerpini fault leads to its westwards propagation and the formation of a number of splays, some of which displace the upper portions of sediments in the Kalavryta hangingwall basin (Figure 3.31). Its eastern tip also propagates, overlapping, interacting and finally linking with the western tip of the Tsivlos fault (Figure 3.29). The geometry of this relay area suggests a linking fault propagating across a west dipping relay ramp, its orientation and location closely matched by the course of the present day Vouraikos river. The large amount of displacement accrued subsequent to linkage occurring suggests that this fault grew by first establishing its length through a combination of lateral propagation and linkage of individual segments followed by accumulation of displacement. This is consistent with observations from the Mamoussia-Pirgahki fault set and with observations of the Aigion fault by McNeil et al (2007).

Eastwards propagation of the Kerpini-Tsivlos fault set is limited by strain being accommodated instead on the Valimi fault set to the North. Westwards propagation is also limited, with additional strain being accommodated by a number of splays. The reason for this stalling in westwards propagation of the Kerpini fault set is as yet unclear, however it is speculated that a mechanical barrier, or pre-existing structure may be the cause. The presence of a large, un-faulted ridge of basement carbonate with significantly greater relief than the surrounding area (Skepasto mountain, 1573 m) forms the basis for this speculation. To the west displacement accumulation continues on the Dhemesticha fault.

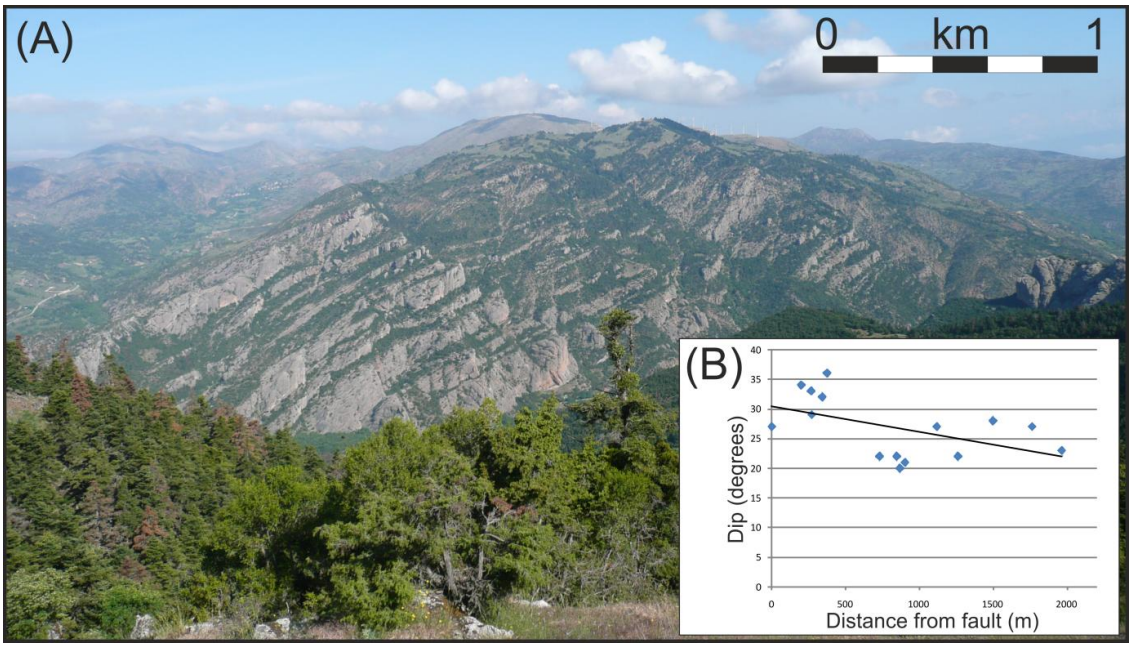

Figure 3.30. (A) Photograph looking west at the hangingwall fill of the Kerpini fault. Limit dip variation is observed indicating that deposition pre-dated deformation on the Kerpini fault. (B) Dip plotted against distance from the fault. Dip does not increase with distance unlike for the Tsivlos depocentre (figure 3.4). Dips are steepest close to the fault, indicative of reverse drag.

Figure 3.31. Field photograph of faulted alluvial fan deposits adjacent to the western tip of the Kerpini fault. The inset shows a close up view of the fault plane and a zone of fault gouge in the immediate footwall. This outcrop confirms that the Kerpini fault was active subsequent to deposition and progradation of the alluvial in the hangingwall to the Kalavryta fault.

(F)

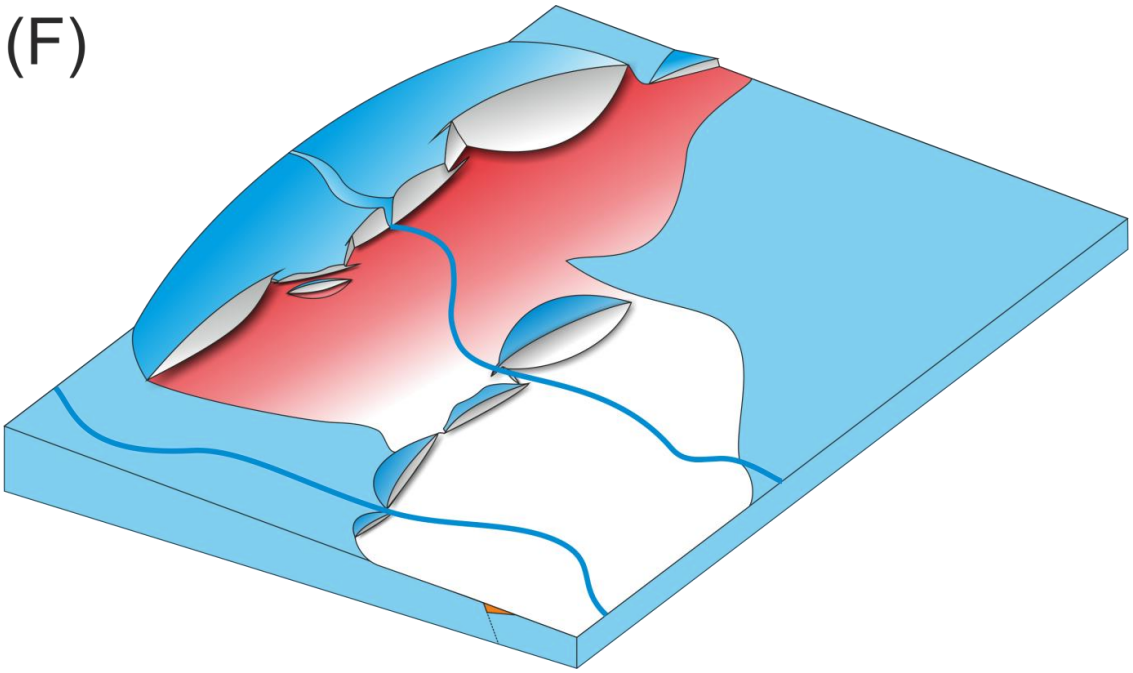

(G) The deformation front moves northwards with strain accommodation switching to the Valimi fault set, which offsets the distal facies of the Kerpini-Tsivlos sub-basin deposits. Along strike displacement variations suggest that the fault can be divided into two segments; an eastern segment active concurrently with the Kerpini-Tsivlos fault set, and a western segment active after the majority of deposition in the Kerpini-Tsivlos basin had occurred. To the west strain is accommodated through reactivation of the now buried Dhoumena fault. A monocline forms over the fault as it propagates upwards through the syn-rift strata in the hangingwall to the Kerpini-Tsivlos fault set.

An increase in the dip from the Kerpini-Tsivlos basin to the western margin of the Valimi basin suggests that deformation on this part of the Valimi fault occurred after the deposition of the alluvial fan. The Valimi fault has very high displacement gradients (figures 3.24, 3.25) where it overlaps with the eastern segment of the Kerpini-Tsivlos fault set suggesting that the two may have been active concurrently with lateral propagation potentially being limited by stress shadow effects (Ackermann and Schilsche, 1997; Gupta and Scholz, 2000). It also has a large accumulated throw, with the lateral extent of its hangingwall extending beyond the margins of the studied area, indicating that it accommodated regional extension to the east. Sediments in the hangingwall to the fault are correlatable with the medial to distal facies observed in the Kerpini-Tsivlos basin, but become dominated by distal facies further to the east,

consistent with the model of a broad, arcuate alluvial fan. A significant displacement minima between the segments suggest a relatively late linkage, likely following removal of the 'displacement shadow' caused by the Kerpini-Tsivlos fault set, which would have subsequently allowed westward propagation and hard linkage of the Valimi fault set.

(G)

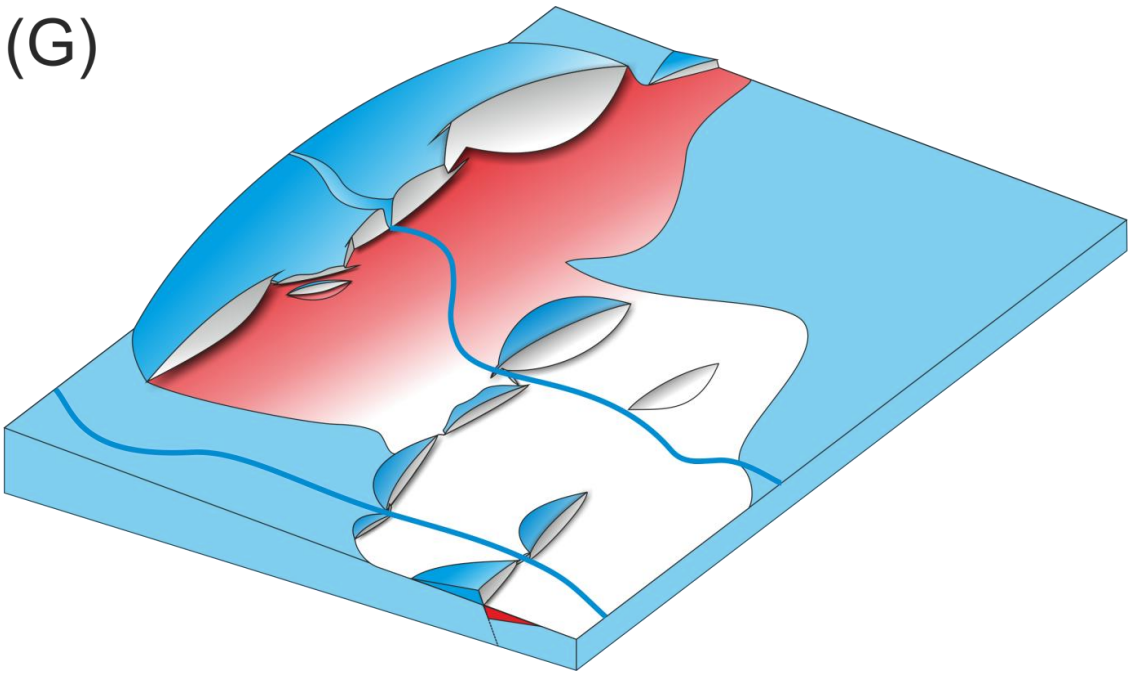

(H) Continued deformation on the Dhoumena fault demonstrably postdates alluvial fan deposition by offsetting sediments in the form of a breached fault propagation fold (figure 3.32). A significant hangingwall syncline is observable close to the village of Dhoumena, and adjacent to the exposed fault plane (figure 3.33). Northwards dipping packages of alluvial fan sediment are also preserved in the vicinity of the Megaspillion monastery to the east, where deformation is expressed as a monocline above the buried upper tip of the ellipse of the fault. The occurrence of northwards dips related to folding is restricted to the local hangingwall of the Dhoumena fault. Sediments further away from the fault, beyond the wavelength of the monoclinal folding are unaffected and are back-rotated in a similar manner to sediments in the hangingwalls of the other faults in the area. The exposure of the fault plane adjacent to the hangingwall syncline (figures 3.32, 3.33), as well as exposure of the basement carbonates along the footwall crest implies that the fault continued to propagate through, and offset, its own monocline. The broad monocline preserved at the present

day erosion surface to the east of the Megaspillion monastery, marks the lateral extent of the approximate expression of the Dhoumena fault beneath the surface. The Valimi fault set is also propagating westwards potentially beginning to link at depth with the Dhoumena fault.

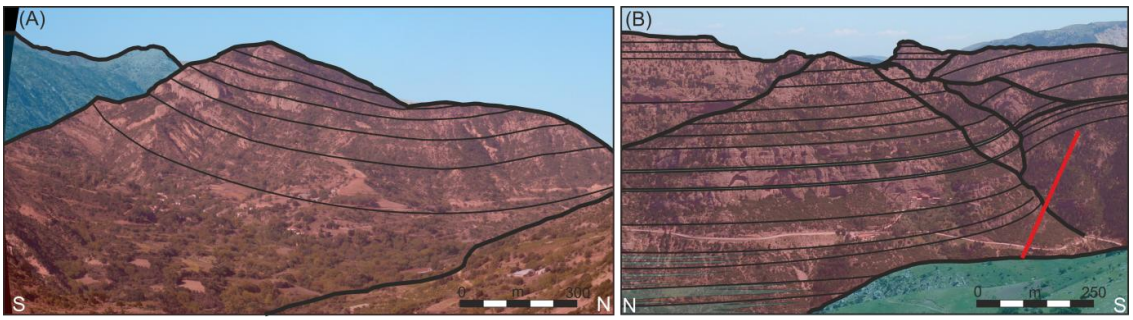

Figure 3.32. Monocline developed above the upwards propagating tip of the Dhoumena fault. (A) Annotated photograph illustrating the hangingwall syncline adjacent to Dhoumena village. (B) View across Vouraikos valley showing fault-tip monocline adjacent to the Megaspillion monastery. The position of the Dhoumena fault is indicated.

Figure 3.33. View of outcrop of the Dhoumena fault plane.

The monomict ‘phase 3’ breccias and conglomerates are deposited at the eastern end of the Kalavryta fault set, forming an angular unconformity where they onlap the underlying alluvial fan deposits. Movement on the Kalavryta fault continues after this deposition, evidenced by a back rotated dip of approximately 6°.

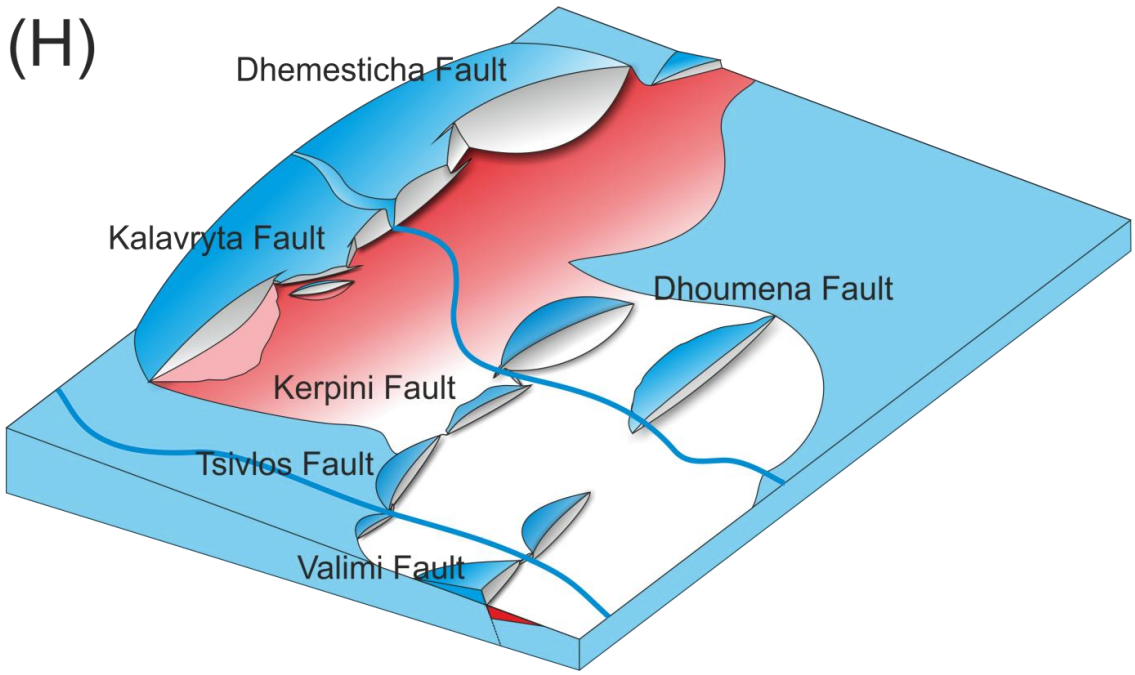

It is unclear whether deformation on the Dhoumena and Valimi faults pre- or post-dates activity on the Mamoussia-Pirgahki fault set to the north. Dating by Flotte et al (2001) and Causse et al (2004) place activity on the Valimi and Dhoumena faults as 0.38 and 0.125 Ma respectively. The temporal relationship between continental faulting and sedimentation, and deltaic sedimentation in the hangingwall to the Mamoussia-Pirgahki fault set can however be partially constrained. Distal continental alluvial fan sediments at the base of the Vouraikos fan delta implies that the Mamoussia-Pirgahki fault initiated after deposition of the continental sediments. Previously it has been thought that this coincided with cessation of activity on faults further to the south (Sorel, 2000). However this study suggests that the degree of post depositional rotation of the continental sediments in the hangingwalls of the southern faults (Kalavryta, Kerpini-Tsivlos) is indicative of their continued activity, concurrent with deformation on the Mamoussia-Pirgahki fault set. Long term eustatic sea level fall during the Plio-Pleistocene (Miller et al, 2005) combined with local relative sea level fall due to footwall

uplift along the Mamoussia-Pirgahki fault set would have resulted in sediment supply bypassing the continental depo-centres. The Vouraikos and Krathis rivers switch from being distributive systems to erosive valleys which rapidly become laterally confined resulting in up to 800m of incision through the alluvial fans they previously supplied sediment to. Continuing activity of the onshore faults back rotates the alluvial fan sediments to their present dip of an average of approximately 25°. Ford et al (2007, 2013) date the initiation of the Mamoussia-Pirgahki fault set in the region of the Vouraikos fan delta at 1.5-0.7Ma. Our observations would therefore broadly agree with those of Flotte et al (2001) and Causse et al (2004), who date both the Valimi and Dhoumena faults as being active subsequent to this time. The process of footwall uplift and incision is repeated for the Voraikos and Kerinitis fan deltas following initiation of the Eliki fault set, with the same river systems now supplying sediment to modern deltas on the margins of the Gulf.

An area of uncertainty with the model constructed for this study stems from the continued movement of the Kalavryta fault set. A secondary fan composed solely of local footwall derived carbonate outcrops in the hangingwall to the eastern portion of the Kalavryta fault set. This onlaps the main alluvial fan with the respective dips indicating that at the time of the secondary fans deposition the main alluvial fan dipped at approximately 8 degrees towards the fault. The entire area was subsequently rotated by a further 17 degrees (Figure 3.21). This implies two things; 1) A significant amount of displacement (equivalent to 8 degrees of rotation) occurred on the Kalavryta fault following cessation of deposition of alluvial deposits in the immediate hangingwall. 2) An additional 17 degrees of rotation, almost 70% of the total observable at the present day land surface, occurs subsequent to deposition of the secondary fan. Although this secondary fan is only preserved at the eastern end of the Kalavryta fault set the dips of the underlying alluvial fan are consistent along the entire strike of the fault, indicating that this late movement was not simply restricted to the eastern segment. This has major implications for the evolution of the rift system. Continuous and/or late activity on the Kalavryta fault set necessitates a more complex model than the simple northwards progression previously proposed. In analogous settings late stage fault movement and associated deposition may significantly modify fairway distribution, as well as compromising seal integrity.

3.7 Relay Zones, Structural Inheritance and Fluvial Incision

One of the subsidiary aims of field data collection, mapping and structural modelling was to evaluate the role of relay zones in determining the position of fluvial sediment transport pathways. Conventional models of fluvial-fault interaction suggest that topographic distortion

as a result of footwall uplift, hangingwall subsidence and fault linkage will lead to fluvial pathways migrating towards the topographic lows produced by fault relay zones (Lambiase and Bosworth, 1995; Gupta et al., 1999; Cowie et al., 2000). Although this is likely to be the case for situations where the pre-rift strata is horizontal, it is less likely where a pre-existing topography is present at rift initiation (Collier and Gawthorpe, 1995; Jackson et al., 2006; Ford et al., 2013), as is the case for the Gulf of Corinth, with fluvial systems likely to be well established prior to rifting. Whether rift-related topography influences the position of river courses will depend on the relative rates of topographic variation (controlled by slip rate on faults) and fluvial incision. Where footwall uplift exceeds incision rate, rivers are likely to be diverted through relay zones, whilst if the incision rate exceeds uplift, then it is likely that the pre-existing course of rivers will be maintained.

3.7.1 Structural Inheritance

Inheritance of pre-existing basement structures has often been cited as a factor influencing the geometry and behaviour of later fault systems (Paton, 2004, 2006; Molliex et al, 2011; Wilson et al, 2010). The majority of observations have described reactivation or inversion of earlier structures in similar orientations, with low angular differences between the assumed stress fields sometimes accompanied by vertical linkage of different generations of faults (Dore et al, 1997; Bailey et al, 2005). Reactivation or inversion of less favourably orientated structures is possible given low friction coefficients along fault planes or anomalously high fluid overpressures (Sibson, 1995). De Paola et al (2005) noted that oblique reactivation is also possible under trans-tentional or trans-compressional stress regimes, with the style of deformation in wrench zones influenced by the compressibility of the deforming lithology. Structures at high angles to rift systems have been suggested as influencing rift segmentation, and the location and development of relay and transfer zones (Morley et al, 2004, Nelson et al, 1992; Tsikalas et al, 2001).

Within the Gulf of Corinth the topic of structural inheritance has been raised in a number of different contexts. Although the general orientation of the pre-rift compressional fabric is NNW to SSE, Taylor et al (2011) identify a region along the north coast of the central and eastern Gulf where the pre-rift fabric is orientated sub-parallel to the rift faults (WNW-ESE). They observe that this localised alignment of the pre-rift fabric normal to the extension direction occurs where the Gulf is widest and horizontal extension is large, suggesting that it plays an important role in the large scale architecture of the rift. Ghisetti and Vezzani (2005) suggest the NNW-SSE trending culmination of the Zarouchla thrust acts as a geomechanical barrier to lateral propagation of the later extensional fault system. They propose that this

leads to segmentation of the onshore rift into two discrete basins, the Derveni-Corinth to the east and the Aigion to the west with the separate basins showing distinct fault geometries. The observations of this study partially agree with this interpretation in that the eastern tip of the Kalavryta fault is located adjacent to the assumed position of the culmination, however mapping during this study traces both the Tsivlos and Valimi faults across its assumed position.

As previously mentioned the rift faults are highly segmented, being kinematically or physically linked by a range of different relay zone geometries. It is tempting to suggest that the positions and orientations of the relay zones are controlled by heterogeneities and the pre-existing structural fabric within the basement carbonate of the Pindos nappe, since their orientations correlate reasonably well. Reactivation of a Hellenide thrust was suggested by Lyon-Caen et al, (2004) as a possible explanation for the 2000-2001 Agios Ioanis earthquake swarm, with fault plane solutions suggesting a fault orientated NE-SW, dipping to the NW, and with oblique slip vectors. The vergence direction of the thrusting within the carbonate basement however is to the west to northwest, hence with dips to the east to southeast, ruling out their reactivation as a northwest dipping transverse faults linking left stepping segments of the extensional fault sets. Geometrically and geomechanically the reactivation of low angle compressional structures within the carbonate basement as normal linking faults appears to be unrealistic (Jackson, 1987), and is not supported by the field data collected as part of this study.

3.8 Discussion and Conclusions

The initial aims of this chapter were two-fold: the primary aim being to use a range of field data to condition a 3D geological model of the field area to use for examining exploration scale structural uncertainty (Explored further in Chapter 4). A secondary aim was to establish a model for the evolution of the rift, constrained by field data as well as stratal relationships and fault geometries defined during the modelling process.

Three separate 3D models encompassing low-, mid-, and high displacement estimates have been constructed using three approaches (Figure 2.10). Although these models have aided the development of a conceptual model for the evolution of the rift there still exists a number of uncertainties, with the lack of age data also resulting in timings being relative, rather than absolute. One of the key lines of evidence utilised for the model of rift evolution is the along strike displacement variations associated with the linkage history of the fault system. Although distinct displacement minima are observed, they do not necessarily have to correspond to the location of relay- or palaeo-relay zones. The uncertainty associated with calculating the sub-surface position of hangingwall cut-offs, and hence fault displacement is significant, and may lead to artefacts being produced. Rifting occurred across a high relief basement, and it is highly

likely that this basement relief has lead to anomalies in along-strike displacement magnitudes being present. Nevertheless, and despite the uncertainties, the three approaches used to calculate displacement do not result in estimates which are at least, consistent. High estimated displacement:length ratios can be explained by the individual fault segments being over-displaced due to kinematic or physical interaction, via relay zones, with other faults. This then supports the hypothesis that the observed displacement minima do in fact correspond to relay zones, and hence that they can be used to constrain the evolution of the rift.

A number of points remain un-resolved. Firstly, it is clear from the models and from restoration data that there is a significant difference in the way that displacement is accommodated between the eastern and western parts of the field area. In the east, multiple faults accommodate extensional strain whilst to the west a single larger fault is present. Although the evolution model presented accounts for this difference, it does not explain the reasons for it. Secondly, the 'phase 3' monomict breccias deposits are enigmatic. On one hand the angular unconformity where they onlap the underlying alluvial fan deposits proves that out of sequence faulting has occurred. Again, however, the reasons for this are unclear.

Despite these uncertainties a number of conclusions can be drawn;

● Initial rifting was relatively distributed across the area, evidenced by distal portions of the main alluvial fan onlapping early graben fill.

● Localisation of strain onto the Kalavryta fault set resulted in progradation of an alluvial fan across a broad area. Sediment was later diverted into accommodation space created by the Tsivlos fault set.

● Fanning dips within the hangingwall of the Tsivlos fault are not reflected in the adjacent Kerpini fault which displays parallel dipping strata. This indicates that the Kerpini fault became active after the Tsivlos fault (which it later linked to) and after deposition of the main fan.

● Displacement on the Dhoumena fault also occurred subsequent to fan deposition resulting in the formation of a monocline above its upwards propagating tip. It remains unclear how this relates to timing of faulting on the Mamoussia-Pirgahki fault to the north.

● The Dhemesticha fault accommodates almost the equivalent displacement as all of the faults to the east combined. The reason for this is unclear, although may be a combination of lateral variability in stratigraphic mechanical properties and a rotation of the regional extension direction from east to west.

● Fault linkage and strain partitioning across multiple faults (at least in the east) resulted in significant sediment bypass occurring.

● The evolution of the rift was not a simple northwards progression of faulting with deposition in successive hangingwall sub-basins. Instead, out of sequence faulting is superimposed on a general northwards migration trend, albeit with significant interaction of sub-basins.

Chapter 4

The Onshore Gulf of Corinth Rift as a Hydrocarbon Exploration Analogue

4.1 Abstract

The Onshore Gulf of Corinth Rift provides an excellent analogue for rift-scale structural uncertainty in the context of hydrocarbon exploration. Synthetic seismic sections have been generated across the rift based upon fault geometries illustrated in Chapter 2. Comparison of these sections with the known geometry allows quantification of uncertainties encountered when extrapolating 2D data into three dimensions. Syn-rift reservoir facies distribution, trap integrity, volumetrics and pore pressure predictions are all influenced by how along strike displacement variations on faults are interpreted.

4.2 Introduction and Aims

In a hydrocarbon exploration setting relay zones often define structural spill points, and can hence control the potential volume of hydrocarbon within a trap. Typically only sparse 2D seismic data is available during the exploration phase, leading to significant uncertainty in along strike displacement variations and the locations of relay zones. Fault geometric uncertainty therefore potentially has significant implications for the volumetrics, and ultimately the economic viability, of a prospect.

The aim of this chapter is to use the fault and syn-rift stratigraphic geometries identified from the Gulf of Corinth field data presented in chapter 3 (Figure 4.1) as a case study to explore some of the fault related geometric uncertainties which may be encountered during hydrocarbon exploration where only limited data may be available. A number of the potential implications of this geometric uncertainty are also examined. A series of 2D synthetic seismic sections have been generated across the 3D geological model constructed from the field data. Comparison of the relatively well constrained mapped geometries with those identifiable from the synthetic seismic sections allows the influence of uncertainty in along strike displacement continuity to be explored.

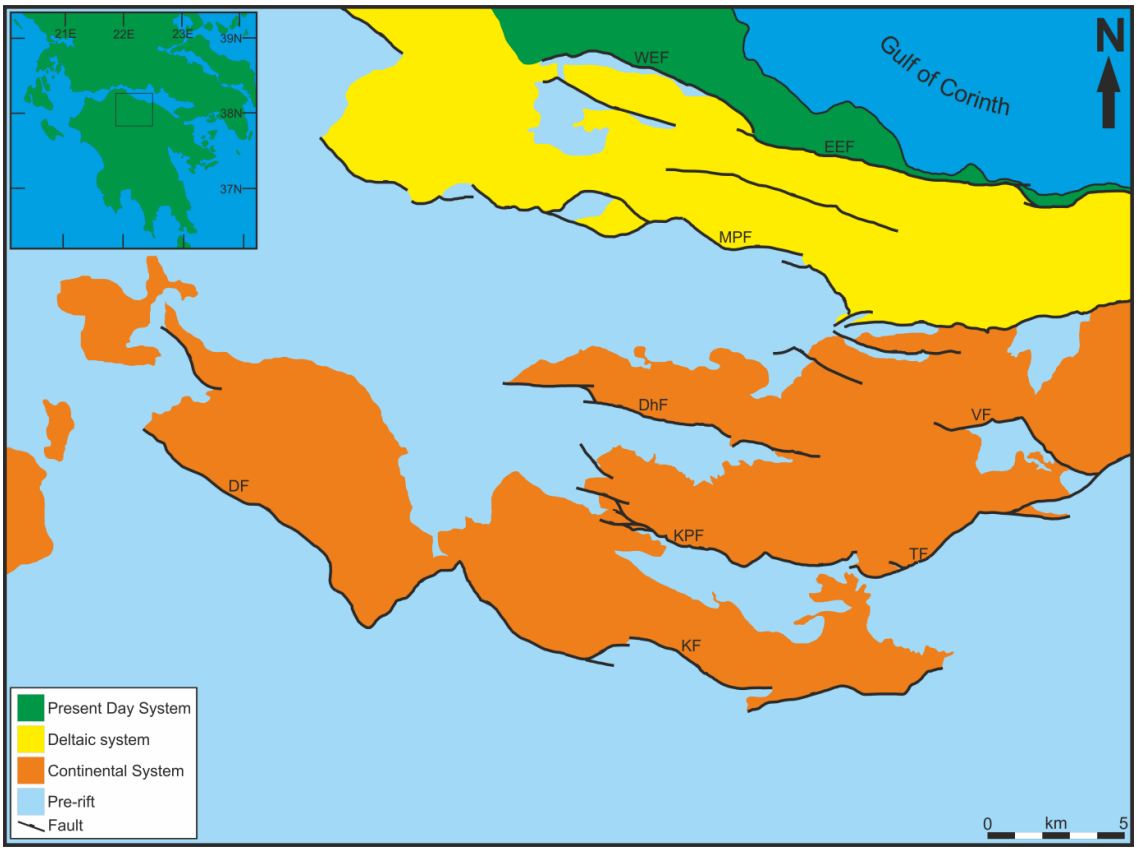

Figure 4.1. Map showing distribution of main depositional units and faults used to construct geocellular grid and subsequent synthetic seismic sections. Inset shows field area location on the Peloponnese peninsula. DF = Dhemesticha fault, DhF = Dhoumena fault, VF = Valimi fault, MPF = Mamoussia-Pirgahki fault, EEF = eastern Eliki fault, WEF = western Eliki fault.

4.2.1 Fault Geometric Uncertainty During Hydrocarbon Exploration

Faults influence hydrocarbon exploration in a number of ways including through the formation of traps, influencing trap and seal integrity, controlling subsidence and hence maturation history, as well as controlling and modifying syn-rift sediment distribution and stratigraphic architecture. During the exploration phase of hydrocarbon development, data are typically sparse, hence the magnitude of the influence of faults is often uncertain. Here, the Gulf of Corinth rift is used as an analogue for investigating reservoir volumetric uncertainties, firstly through trap geometry in the form of tilted footwall fault blocks and secondly through the distribution of syn-rift reservoir facies within hangingwall basins. In both instances the extrapolation of 2D data into the third dimension is critical when evaluating potential volumes, connectivity and prospectivity.

4.2.1.1 Tilted Fault Blocks and Volumetrics

A common trap geometry in extensional provinces is that of the tilted fault block (Struijk and Green, 1991; Yielding et al., 1992; Dominguez, 2007). During extensional faulting a combination of elastic (McKensie, 1978; Barr, 1987; Jackson et al., 1988) and flexural (Kuznir et al., 1991, 1995) processes lead to reverse drag adjacent to normal faults. This drag takes the form of basin-forming subsidence in the hangingwall and uplift of the footwall (Yielding and Roberts, 1992). The wavelength of the reverse drag is proportional to the elastic thickness of the crust with the relative amplitudes of footwall uplift and hangingwall subsidence controlled by loading of the hangingwall (Jackson and McKensie, 1983). A low density load, such as water, will allow greater footwall uplift, whilst a denser load, such as a syn-rift stratigraphy will increase subsidence of the entire local lithosphere including both the hangingwall and footwall. The relief generated by footwall uplift provides a trapping structure for buoyant hydrocarbons. Aside from the petrophysical properties of the reservoir (porosity, fluid saturation etc), the volume of hydrocarbon which can be trapped depends on the interplay between along strike displacement continuity and the thickness of the reservoir interval. This is often visualised using Allan diagrams and juxtaposition/triangle diagrams (Allan, 1989; Knipe, 1997). Where displacement is less than reservoir thickness, fluid can potentially flow across the fault into the adjacent fault block. Hydrocarbon column heights which can be supported by the fault are therefore dependent on both the fault geometry and the fault rock petrophysical properties (Yielding et al., 1997, 2010; Fisher and Knipe, 1998; Sperrevik et al., 2002) Conversely where displacement is greater than reservoir thickness a juxtaposition seal is formed between the adjacent fault blocks. In this instance the hydrocarbon column height is controlled by the structural spill point. The location of the structural spill point will generally be at displacement minima, such as relay zones, however the likelihood that a 2D seismic section will intersected a displacement minima is low. Therefore being able to predict and account for along strike displacement minima is critical in order to prevent trap volumetrics from being overestimated.

4.2.1.2 Syn-Rift Reservoir Facies Distribution

Faults can also control the distribution of reservoir facies within their hangingwalls, both through sediment dispersal and basin entry points (Gupta et al., 1999), general sub-basin geometry (Dawers and Underhill, 2000; Cowie et al., 2000; McLeod et al., 2002) as well as influencing reservoir quality and facies (Brehm, 2003; Fletcher, 2003). Where only 2D seismic data is available, correlating the extent of syn-rift deposits between sections is highly uncertain and can depend upon the evolution of the fault system. Models of early versus late linkage

(Cowie et al., 2000; Figure 4.2) describe how sub-basin geometry is related to fault growth history, assuming that faults are initially isolated rather than growing coherently (Walsh et al., 2003). In early linked systems there is limited kinematic interaction prior to physical linkage occurring (Cartwright et al., 1995), leading to the rapid formation of a broad, shallow depocentre in the hangingwall to the linked faults. As profile re-adjustment progresses, the basin becomes deeper. In contrast, with late linkage, kinematic interaction allows fault profile re-adjustment to occur prior to physical linkage (Peacock and Sanderson, 1991; Gupta and Scholz, 2000). This leads to the sub-basins of the individual faults remaining distinct, albeit with areas towards the centre of fault sets experiencing greater subsidence. When physical linkage occurs, a broad depocentre forms above the coalescing sub-basins. The stage of evolution of a rift system, and the way that linkage has occurred can therefore significantly influence syn-rift sediment distributions and connectivity of reservoir facies between sub-basins. Whether linkage occurs early or late will depend on the three-dimensional fault geometry (Walsh et al., 2003), the nature of which is often elusive with 2D data.

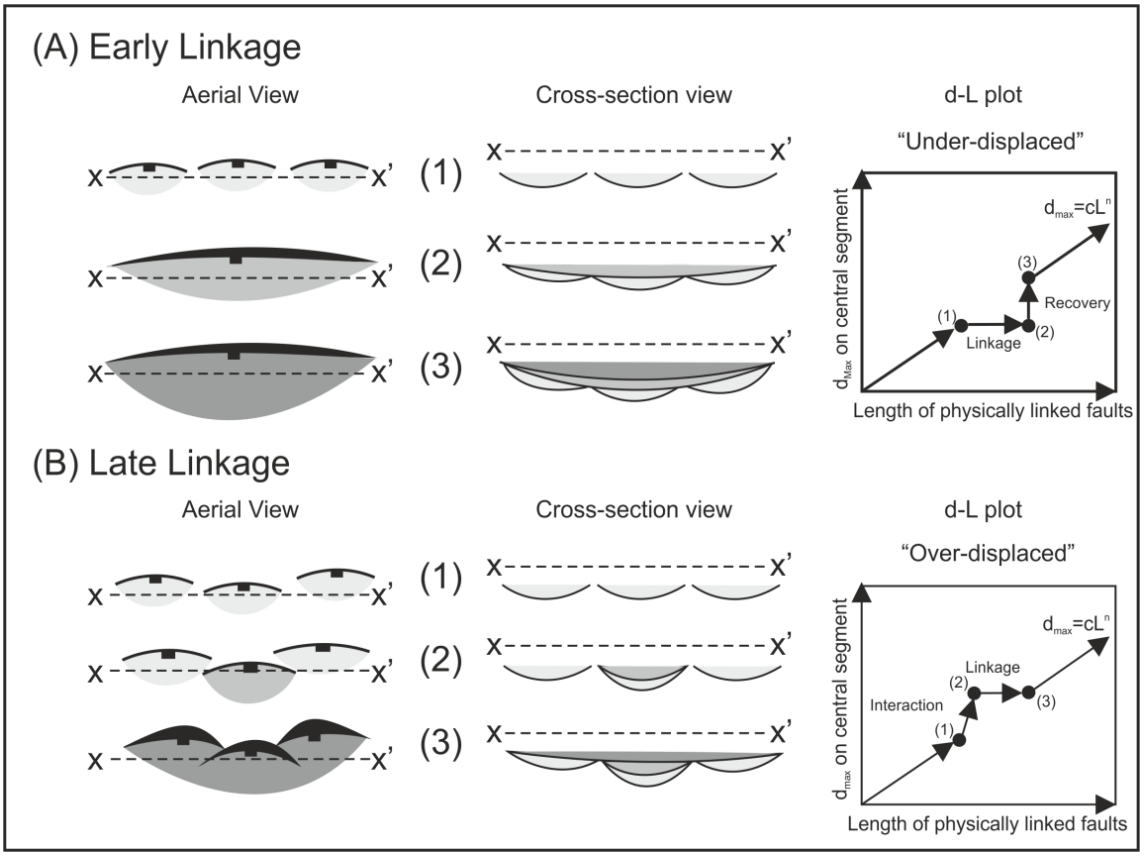

Figure 4.2. Schematic figure of early and late linkage models, modified from Cowie et al., (2000). It should be noted that although these models may describe the observed geometries, they do not necessarily capture the growth mechanisms of linked faults (e.g. Walsh et al., 2003).

4.2.1.3 Pressure

In addition to indefinite volumetric estimates, the uncertainty in hydrocarbon column heights leads to inexact predictions of pressure due to buoyancy within reservoir intervals. Estimating the maximum column height within a fault controlled trap depends on correctly identifying the crest of the trapping structure, as well as its spill points. If the geometry allows for a greater column height than is predicted from 2D seismic data, then the buoyancy pressure at the crest of the structure will be greater than anticipated. This may have major implications for trap integrity. A top seal can be breached in two main ways, firstly due to membrane leakage where the buoyancy pressure at the crest of the trap exceeds the capillary entry pressure of the top seal (Schwolater, 1979; Watts, 1987; Ingram and Urai., 1999). Where a top seal has a very high capillary entry pressure, such as for low permeability shales, the second mechanism of breaching through the formation of hydraulic fractures may occur (Swarbrick et al., 2010; Zhang and Ghassemi 2011).

4.2.1.4 Membrane Leakage

Membrane leakage of a top seal occurs when its capillary entry pressure is exceeded by the pressure due to buoyancy of the hydrocarbon column beneath it. The capillary entry pressure depends upon the pore throat radius, the interfacial tension and the contact angle between the wetting and non-wetting fluid phases present;

$$P_e = \frac{2\gamma \cos\theta}{r}$$

Where, P_e = Capillary entry pressure, γ = Interfacial tension, θ = Contact angle, and r = pore throat radius (Schwolater, 1979; Watts, 1987). See the introduction chapter, and references for more details. The buoyancy pressure of the hydrocarbon column depends upon the density differential between the hydrocarbon and water within the reservoir. The less dense hydrocarbon is buoyant and hence exerts an upwards pressure on the base of the top seal. For a horizontal oil-water contact (i.e. no hydrodynamic tilting of contacts-Dennis et al., 2005) this pressure is greatest at the crest of a trapping structure, where the hydrocarbon column is greatest. For a top seal with a known capillary entry pressure, the maximum hydrocarbon column which can be supported can be calculated from the hydrocarbon density;

$$h = \frac{P_e}{g\Delta P}$$

If the column height exceeds this value, then membrane leakage through the top seal will occur. This approach is similar, although not identical, to the approach used to estimate column heights trapped against faults (Fisher et al., 2001; Brown, 2003).

A top seal lithology such as shale or chalk (Swarbrick et al., 2010) will have a high capillary entry pressure, and will be unlikely to experience significant membrane leakage over short timescales (10s Ma). This does however assume that membrane sealing capacity is uniform and homogenous, an unlikely prospect given the heterogeneity inherent in geological systems (Aplin and Macquaker, 2011; Armitage et al., 2011). Nevertheless, membrane seals are generally expected to support column heights in excess of 2000m for very low permeability shale cap rocks (Ingram and Urai, 1999) based upon mercury injection porosimetry of individual samples. As column heights approach this value, the second mechanism of leakage, via mechanical fracturing of the seal lithology, becomes important.

4.2.1.5 Mechanical Leakage

Hydraulic fracturing may occur when the pore fluid pressure exceeds the fracture strength of the top seal. For tensile fracture formation the value of pore pressure at which fracturing occurs depends on the local stress conditions and the tensile strength of the top seal, and occurs when;

$$P_f = \sigma_3 + T$$

Where P_f = the pore fluid pressure, σ_3 = the minimum horizontal stress and T = the tensile strength of the top seal. For a given tensile rock strength an increased pore fluid pressure therefore increases the likelihood of fracture formation. Whether tensile or shear fractures form depends on the in situ minimum and maximum normal stresses. A high differential stress (σ_1-σ_3) is more likely to lead to the formation of shear fractures, albeit at a lower increase of pore fluid pressure (Figure 4.3). Whether or not shear fracture formation leads to leakage depends on if the fractures become dilated or not. Stronger, more brittle rocks being more likely to become dilated than weaker, less consolidated and more ductile ones such as shale (Ingram and Urai, 1999).

In the case where pre-existing fractures are present, a lower pore pressure is required to cause reactivation and frictional sliding (figure 4.3), potentially leading to fracture dilation and hence the formation of leak pathways (Clayton and Hay, 1994; Ingram and Urai, 1999). Asperities along fractures and fracture curvature will lead to fractures opening within brittle lithologies, whereas they will tend to remain tight when hosted in more ductile rocks (Ingram and Urai, 1999).

The pore fluid pressure is a function of the local overpressure and the buoyancy of the hydrocarbon immediately below the top seal (Clayton and Hay, 1994). A larger hydrocarbon column height will have a higher buoyancy pressure and will hence increase the pore fluid pressure, therefore reducing the effective stress and increasing the likelihood of either formation of new fractures or of frictional sliding on pre-existing fractures.

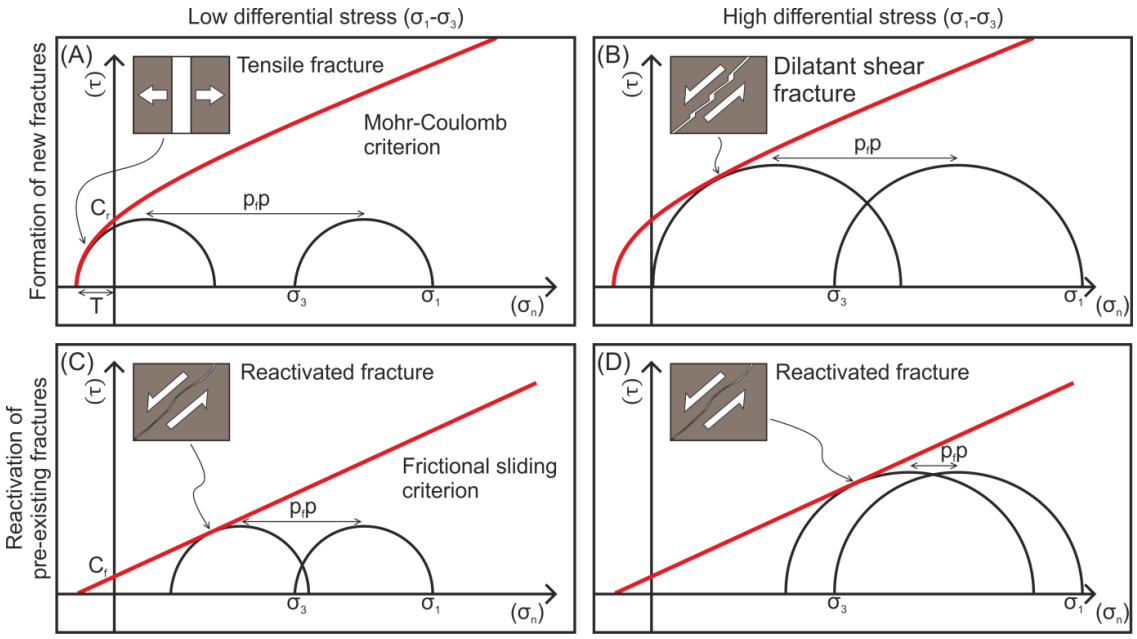

Figure 4.3. Schematic Mohr diagrams illustrating the effect on fracture formation and reactivation of increased pore fluid pressure (p_fp) under different conditions. $\boldsymbol{\tau}$ = Shear stress, σ_n = normal stress, C_r = Intact rock cohesion, C_f = Fracture cohesion, σ_1 = Maximum principal stress, σ_3 = Minimum principal stress, T = Rock tensile strength. Note that the initial value of σ_3 is the same for all cases. (A) A low differential stress ($\sigma_1 - \sigma_3$). No pre-existing fractures are present therefore the Mohr-Coulomb failure criterion is applicable. Increasing the pore pressure reduces the effective stress, shifting the Mohr circle to the left into the tensile failure region. If the minimum stress (σ_3) is negative, tensile fractures will form perpendicular to σ_3. (B) As (A) but with a higher differential stress. Increasing the pore pressure leads to the Mohr circle intersecting the failure envelope whilst σ_3 is still positive, leading to the formation of shear fractures, although a smaller p_fp increase is required for fracture formation than for low differential stress. (C) Low differential stress. The presence of pre-existing fractures means that the friction sliding criterion is applicable, and a lower p_fp increase is required in order to reactivate the fractures. (D) A higher differential stress requires a smaller p_fp increase for fracture reactivation. It should be noted that the diagrams above assume that no pore pressure coupling occurs (see chapter 9 for more details, and e.g. Zoback, 2007), and hence that the differential stress remains constant during depletion or injection.

4.3 Methodology

The fault geometries and syn-rift stratigraphic architecture from the onshore Gulf of Corinth rift field area are relatively well constrained, with the three dimensional geometry captured within a geocellular grid (see chapter 2, 3 and figure 4.4). The generation of synthetic seismic sections across this grid allows the geometries to be observed in the context of a hydrocarbon exploration scenario, where the limitations of sparse 2D data lead to significant geometric uncertainty. The procedure for generating the synthetic seismic sections is a four-step process.

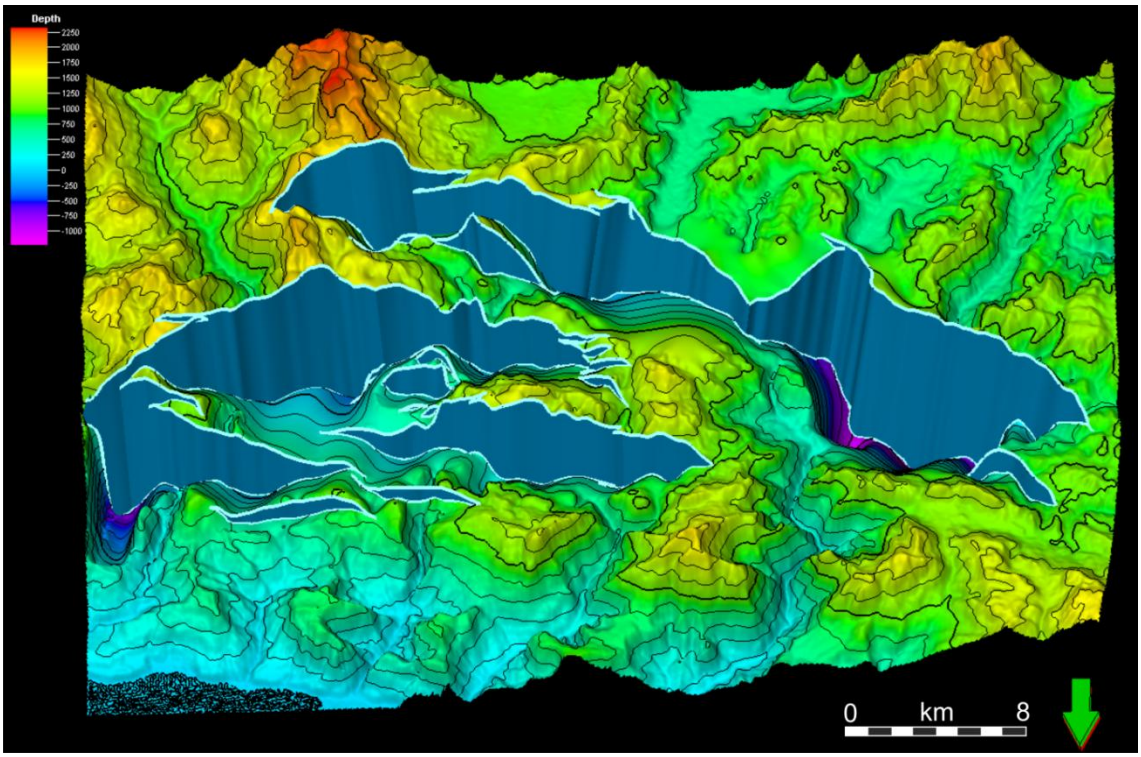

Figure 4.4. Oblique view of top pre-rift surface and faults within geocellular grid. V.E. = x3. The grid can subsequently be populated with the petrophysical properties appropriate to the pre-, syn-, and post-rift facies as outlined in table 4.1.

The geocellular grid capturing the 3D fault geometries is translated from its physical elevation to a sub-surface depth of 4000 m. Pre-rift and syn-rift zones are designated, as well as an overlying zone of post-rift shale designed to represent a regional top seal. These zones are stochastically populated with mineralogical fractions using a sequential Gaussian distribution function. Upper and lower bounds broadly correspond to those observed in the field area (table 4.1). A porosity property based on published generalised depth trends for carbonate, conglomerate and shale, is also defined (figure 4.5), with the upper and lower bounds based upon observation of thin sections from the field area (figure 3.20). Examples of the populated grids are shown in figure 4.6.

	Calcite fraction	Quartz fraction	Sand fraction	Shale fraction	Porosity
Post-rift	0-0.17	0-0.02	0-0.34	0.4414-1	0.0013-0.2
Syn-rift	0.3-0.81	0.09-0.35	0.04-0.14	0.0558-0.21	0.0044-0.15
Pre-rift	0.8-1	0-0.02	0-0.14	0-0.04	0.0053-0.18

Table 4.1. Mineralogical fractions used to populate pre-, syn-, and post-rift sequences. The values for the pre-rift assumes an almost entirely carbonate composition, whilst the syn-rift composition is constrained by values observed in the field (Figure 3.17). Composition for the post-rift stratigraphy is synthetic, but is nevertheless dominated by shale. Where possible porosity is also constrained using visual estimates from optical thin section analysis (Chapter 3, figure 3.20).

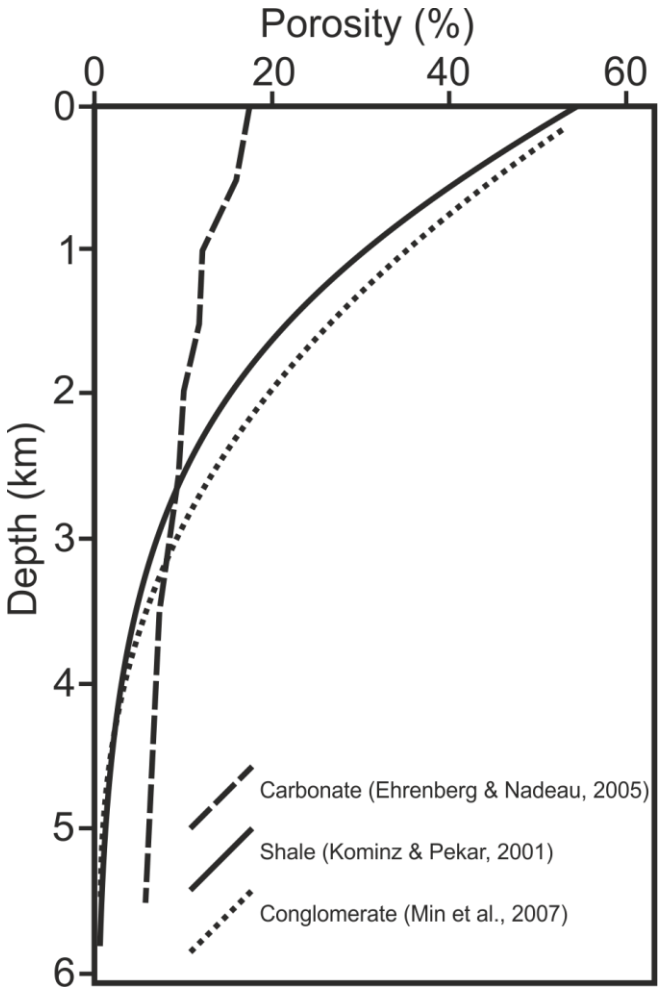

Figure 4.5. Published depth trends used to condition population of porosity property within the geocellular grid. After Kominz and Pekar, 2001; Ehrenberg and Nadeau, 2005; Min et al., 2007.

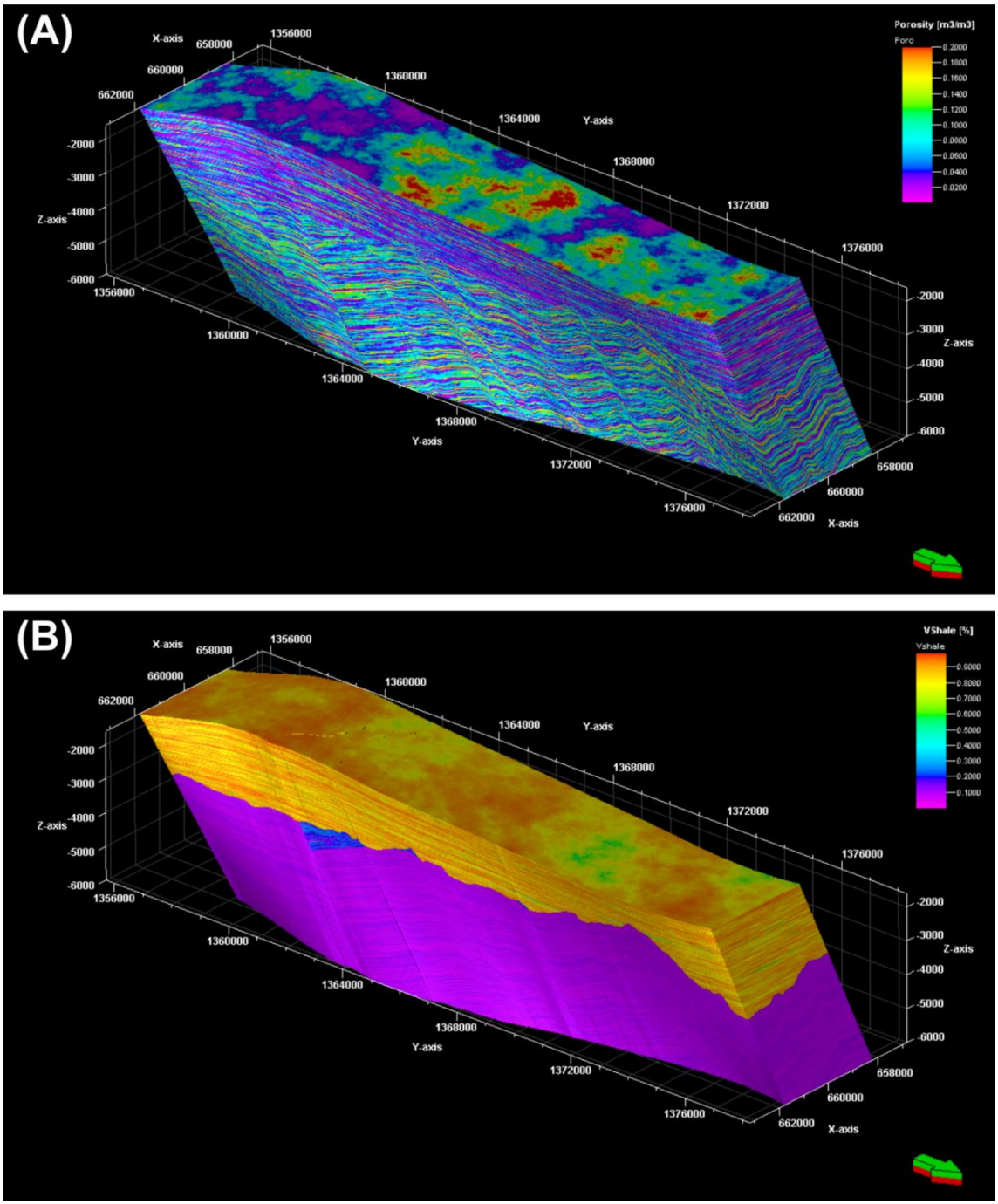

Figure 4.6. Oblique view of examples of populated geocellular grids used during forward modelling process. (A) Porosity, (B) VShale.

An oil-water contact is assigned at a constant depth of 3500 m, with hydrocarbon saturations of 0.7 within the oil leg and zero elsewhere. These values represent those typically expected in a water-wet reservoir (Ahmed, 2010). Pore pressures are assigned separately for the pre-, syn, and post rift stratigraphies (figure 4.7). The post-rift has a hydrostatic gradient of 9.792 MPa/km (0.433 psi/ft), with the underlying pre- and syn-rift strata being overpressured by 5 MPa (725 psi). The oil column within the syn-rift has a pressure gradient of 6.785 MPa/m (0.3

psi/ft). The petrophysical, mineralogical and pressure properties are converted into individual high resolution seg-y volumes covering the positions where seven synthetic seismic sections will be generated (figures 4.8, 4.9). These seg-y property cubes are subsequently exported to seismic forward modelling software.

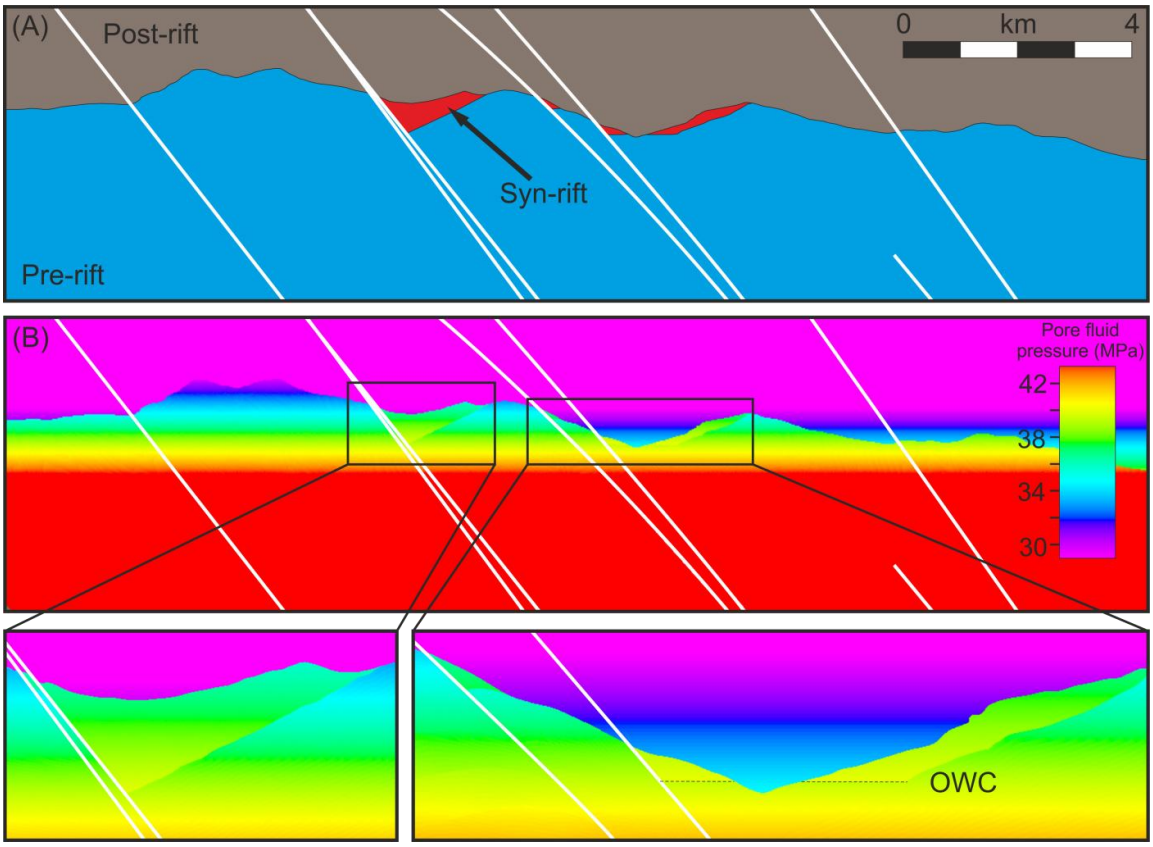

Figure 4.7. Cross-sections through model illustrating pore fluid pressure distribution. (A) Distribution of pre-, syn-, and post rift intervals. The syn-rift is defined as the reservoir interval. (B) Pore fluid pressure. The colour scale is adjusted to highlight pressure differences within the syn-rift interval due to the fluid density contrasts between oil and water. This is highlighted in the expanded insets.

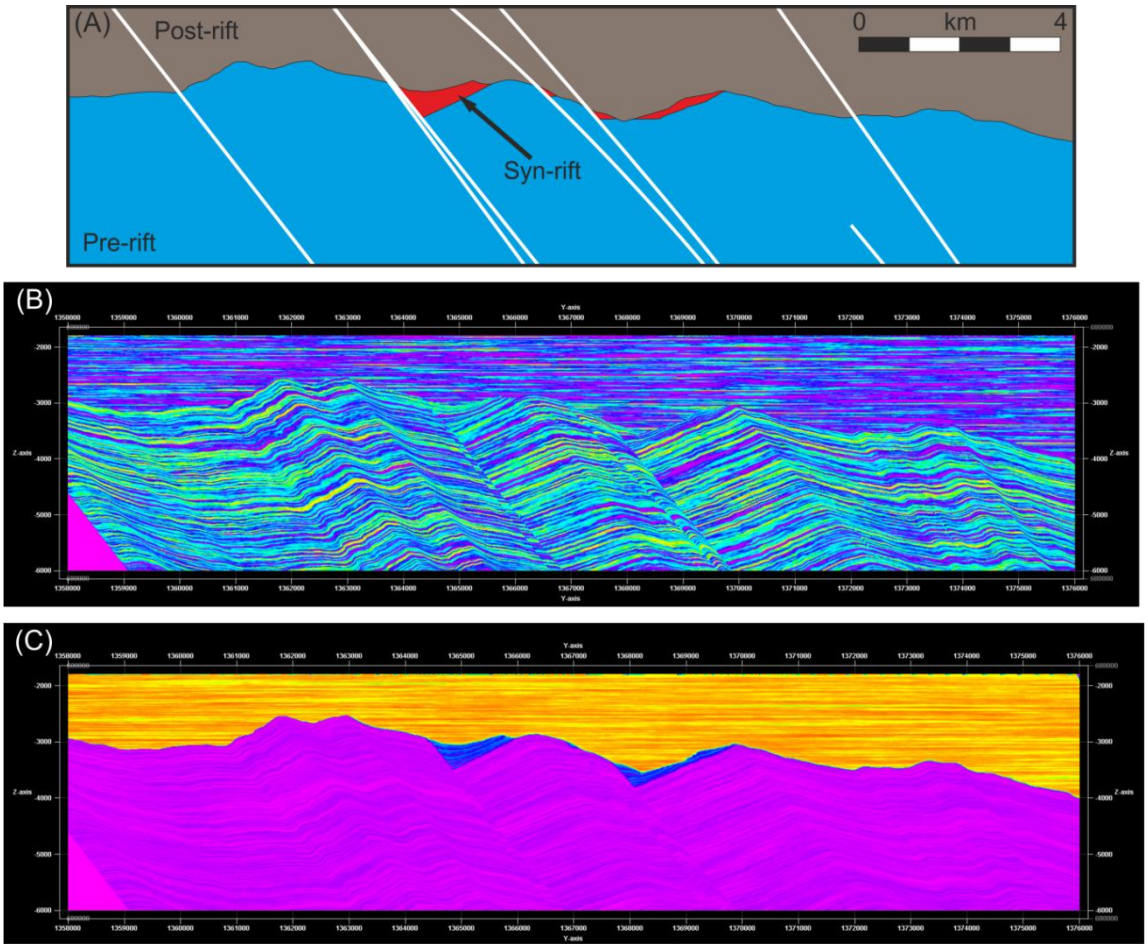

Figure 4.8. Examples of property cubes converted into seg-y volumes to allow export to seismic forward modelling software. (A) Distribution of pre-, syn-, and post rift intervals. (B) Porosity, (C) VShale.

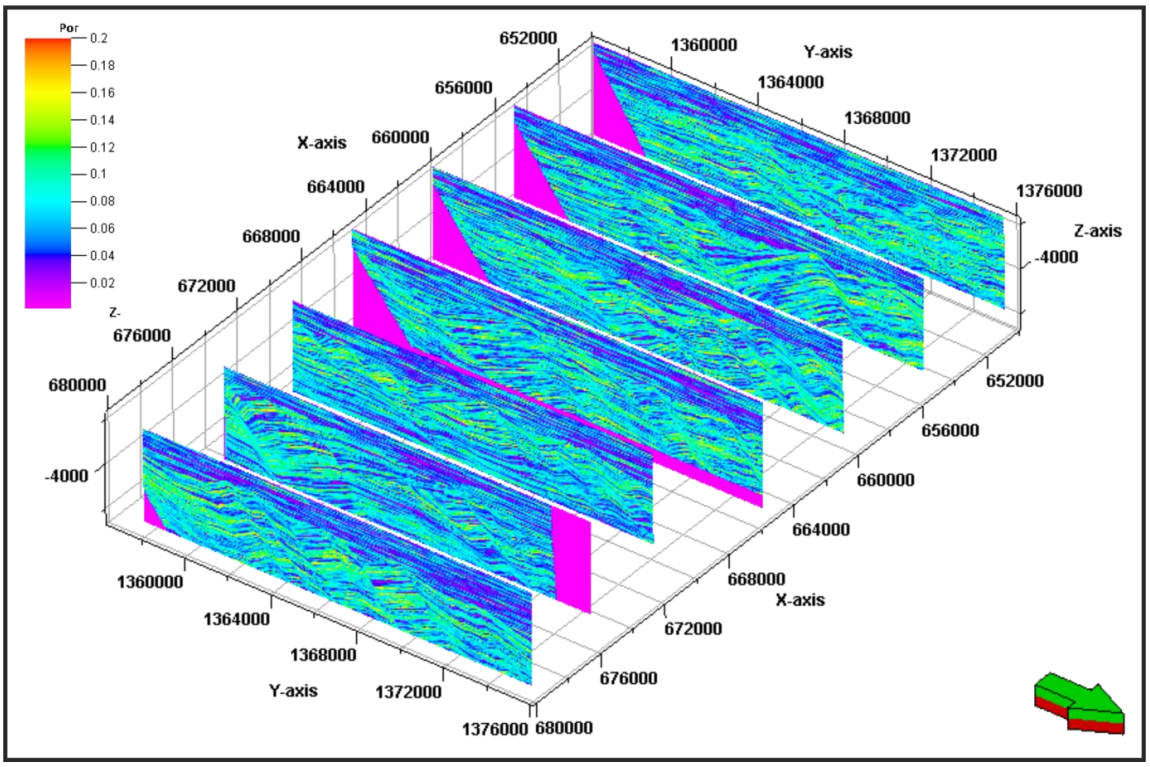

Figure 4.9. Oblique view of sections through geocellular grid populated with a porosity property. These sections correspond to the position at which 2D synthetic sections are generated. Sections have a spacing of 5 km.

To account for seismic wave propagation, attenuation and diffraction along the travel path between the seismic sources and the receivers, a coarse scale grid (250 x 250 x 33 m cell dimensions) capturing the properties of the overburden was constructed (figure 4.10). The overburden is representative of a regional shale, and is hence populated using the same methodology (sequential Gaussian simulation) and property bounds used to generate the post-rift interval. These properties are also exported to the seismic forward modelling software to be used in conjunction with a ray-tracing algorithm (Gjøystdal et al., 2007)

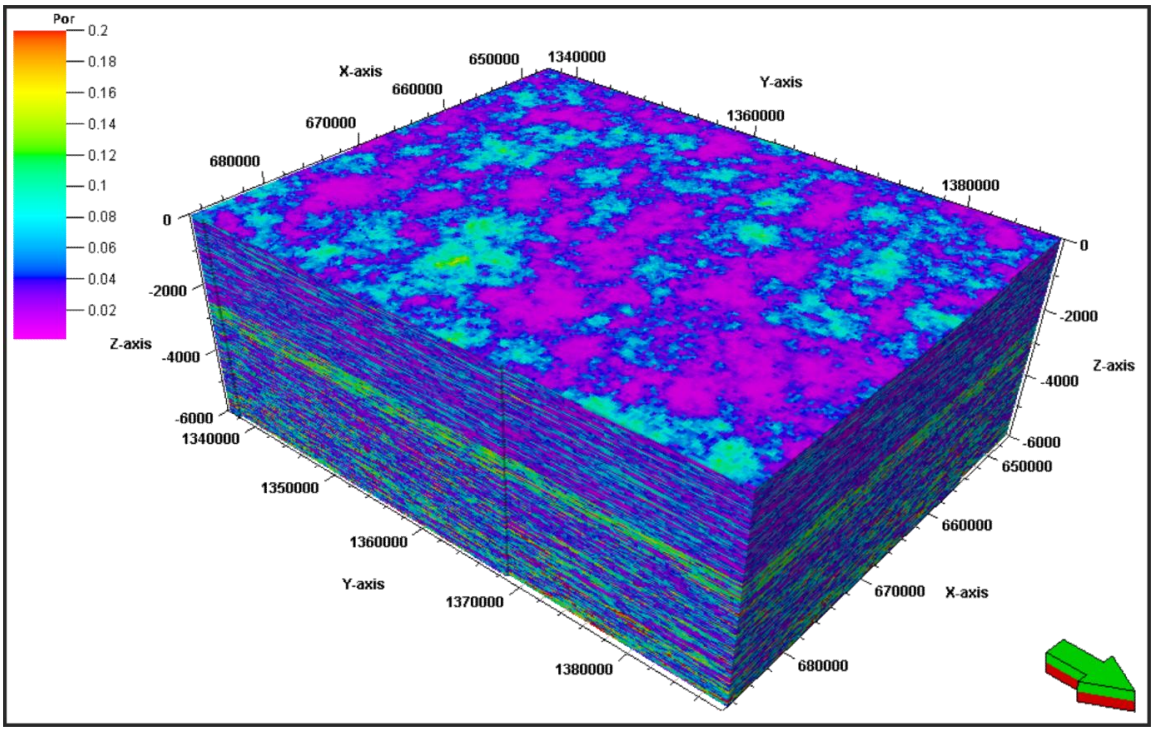

Figure 4.10. Coarse scale background model generated using sequential Gaussian simulation. The model is used to account for wave propagation effects between survey-source, target and receiver. Porosity is shown although cubes for pressure, fluid saturation, Shale, Sand, Calcite, and Quartz were also generated.

The seg-y property cubes are imported into the seismic forward modelling software, where density values for the individual mineralogical and fluid components are assigned (Table 4.2) and used to calculate the overall density assuming a Reuss mixing model. The pore fluid pressure property is used to estimate the confining pressure and the effective pressure based upon a lithostatic gradient of 22.5 MPa/km. Gassmann's theory is then applied along with the fluid properties (Table 4.2) and saturation distribution to determine the elastic properties of the model, with reflectivity subsequently calculated using the Zoeppritz equations (Gjøystdal et al., 2007).

PROPERTY	VALUE
Shale density	2.6 g/cm^3
Sand density	2.65 g/cm^3
Calcite density	2.71 g/cm^3
Quartz density	2.65 g/cm^3
Shale bulk modulus	21 GPa
Sand bulk modulus	37 GPa
Calcite bulk modulus	76.8 GPa
Quartz bulk modulus	36 GPa
Shale shear modulus	7 GPa
Sand shear modulus	44 GPa
Calcite shear modulus	32 GPa
Quartz shear modulus	31 GPa
Water density	1.02 g/cm^3
Water bulk modulus	2.78 GPa
Oil density	0.65 g/cm^3
Oil bulk modulus	1.45 GPa

Table 4.2. Physical properties used for generation of elastic and reflectivity cubes used in the seismic forward modelling process.

A 2D seismic survey with a design typical for exploration purposes (O'Dowd, pers. comm.) was constructed (Table 4.3), with this geometry repeated to correspond to the position of each target section (figure 4.11).

Property	Value
Depth	100 m
Offset	100 m
Streamer Length	10000 m
Receiver spacing	25 m
Shot line length	30000 m
Shot spacing	50 m
Input wavelet	40 Hz Ricker

Table 4.3. Geometries used for 2D survey design (O'Dowd, pers. comm.).

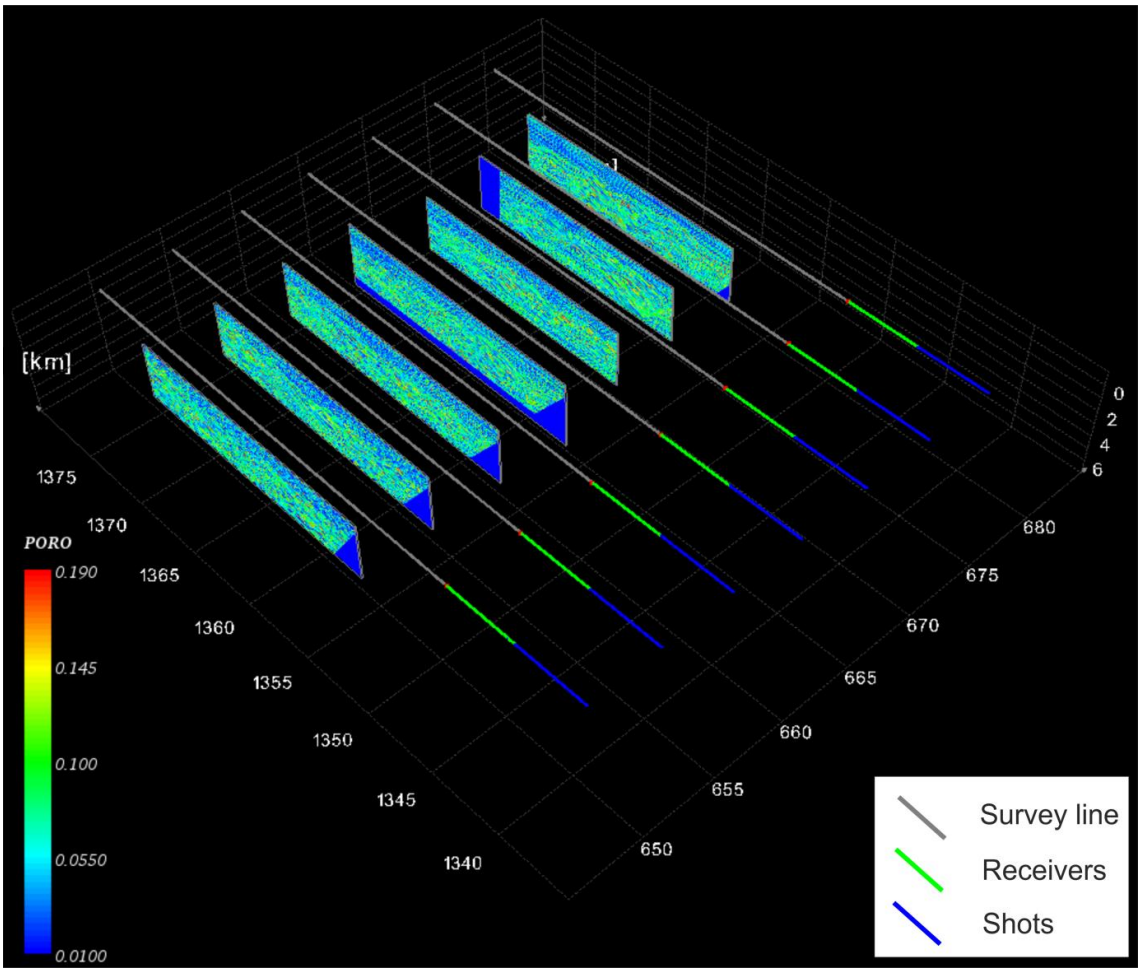

Figure 4.11. Oblique view of 2D survey geometries with porosity sections for reference.

The derived elastic and reflectivity properties are combined with the survey design, input wavelet and background model (figure 4.10) to generate a series of synthetic 2D seismic sections (figure 4.12) using a ray-tracing algorithm (Gjøystdal et al., 2007). These sections were then interpreted using standard seismic interpretation software, with faults, top pre-rift and top syn-rift surfaces being interpreted. The interpretation was carried out independently by a third party so as to minimise interpretation bias. The third party is an experienced structural geologist with experience in interpreting exploration scale 2D seismic datasets. Their seismic interpretations for the seven 2D sections (figure 4.13) were extrapolated using a convergent interpolation algorithm in order to generate 3D surfaces for the faults, and the top pre-rift and syn-rift stratigraphic surfaces (figure 4.14). These surfaces allow the construction of a fault-horizon model analogous to those used during in hydrocarbon exploration and prospect identification, risking and ranking. Comparison of the models constrained using 3D outcrop data, and the model derived from synthetic seismic data allows exploration scale geometric uncertainty to be quantified in a number of ways, for example by comparing fault-

displacement profiles (figure 4.15). Despite this it is stressed that the geometric uncertainties examined here are specific to the Gulf of Corinth, and as such should not be viewed as general cases.

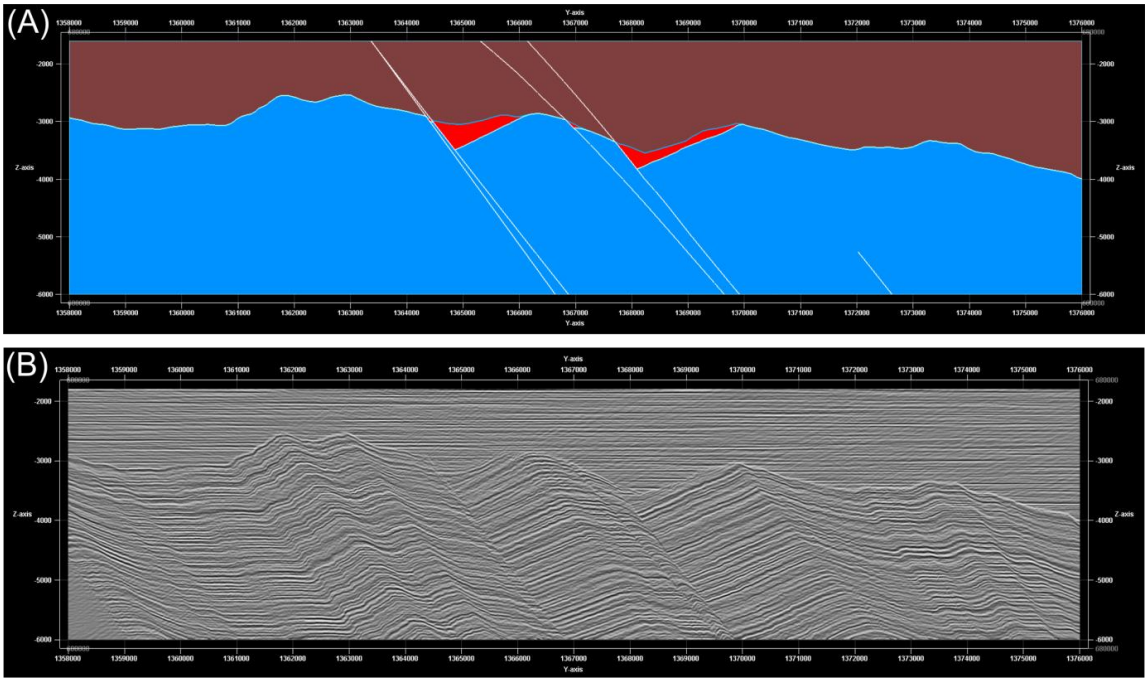

Figure 4.12. Comparison of known pre-, syn- and post-rift geometry (A) and the resulting synthetic seismic section (B).

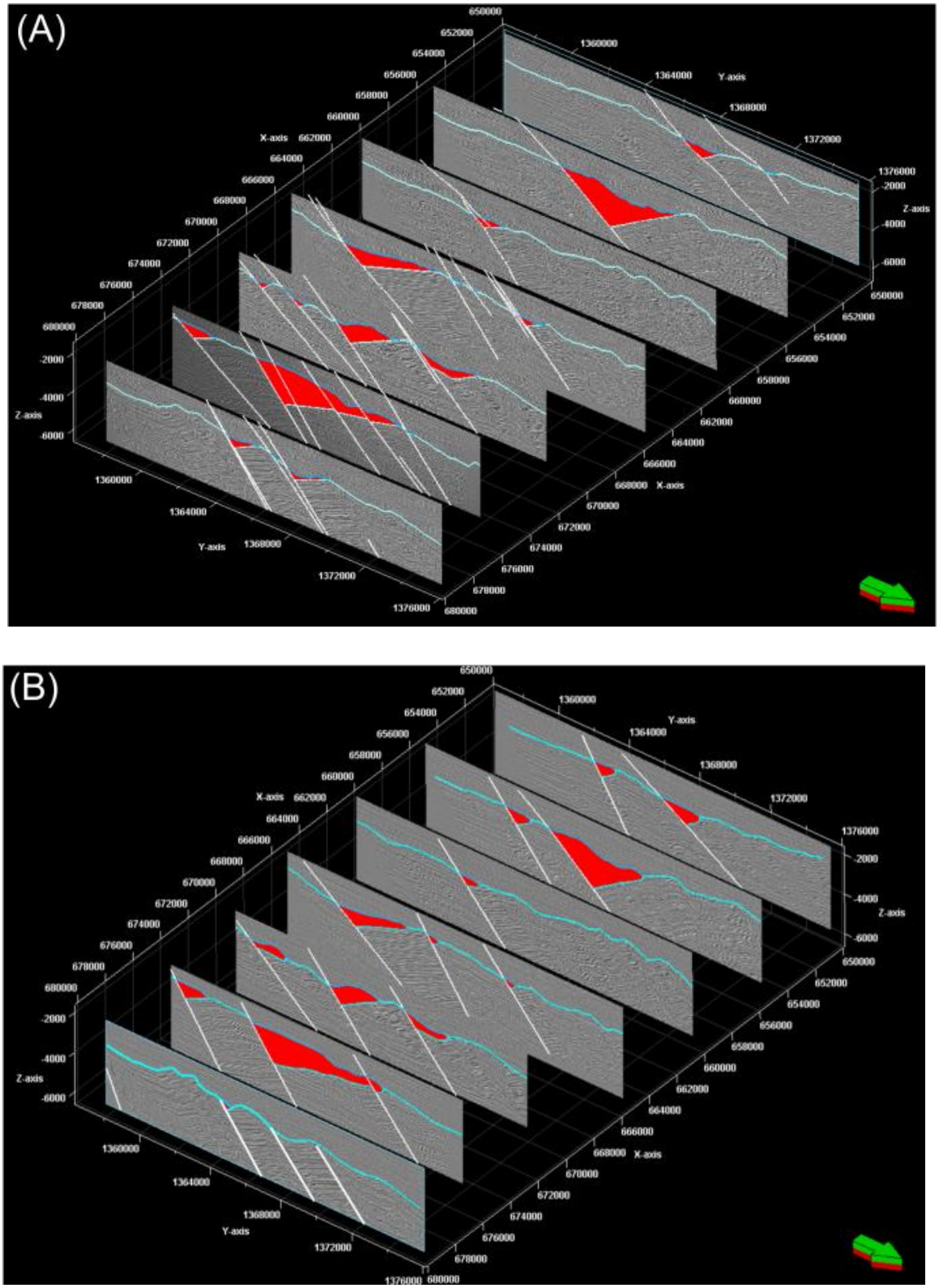

Figure 4.13. Synthetic seismic sections through the Gulf of Corinth rift geometry defined from field data in chapter 3. (A) The syn-rift distribution, top pre-rift surface and fault geometries defined from field data are superimposed onto the seismic sections. (B) The syn-rift distribution as defined by the interpreted surface and fault geometries. 2D sections have a spacing of 5 km.

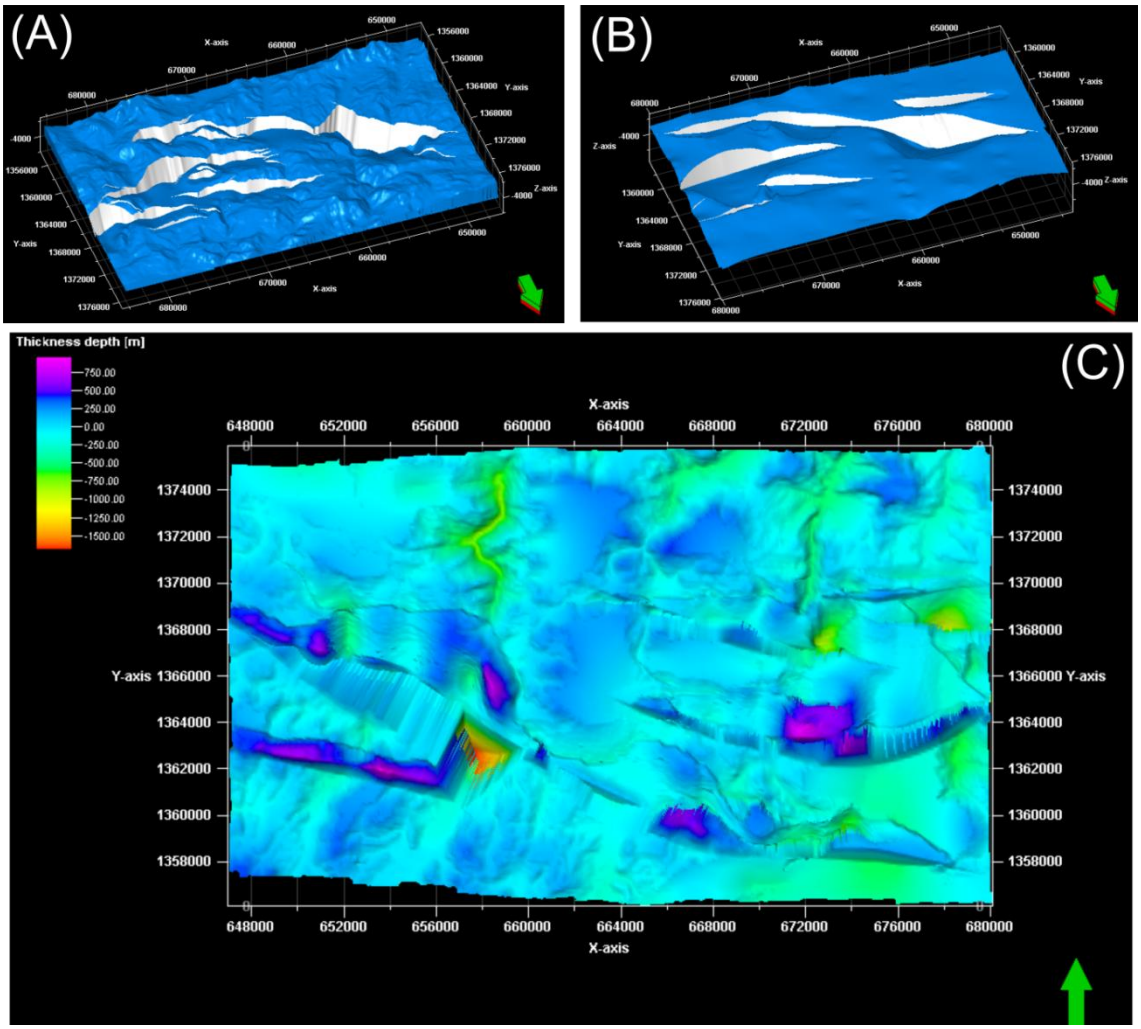

Figure 4.14. Comparison of outcrop-derived top pre-rift surface and faults (A), and top pre-rift surface and faults generated from extrapolation of 2D seismic interpretation (B). Although the broad scale geometries are similar, the seismically resolvable model (B) is significantly simplified relative to the outcrop-derived one (A). (C) Aerial view of an isochore map highlighting the differences between the outcrop-derived (A) and seismically interpreted (B) top pre-rift surfaces. Positive differences are shown in purple, negative in red.

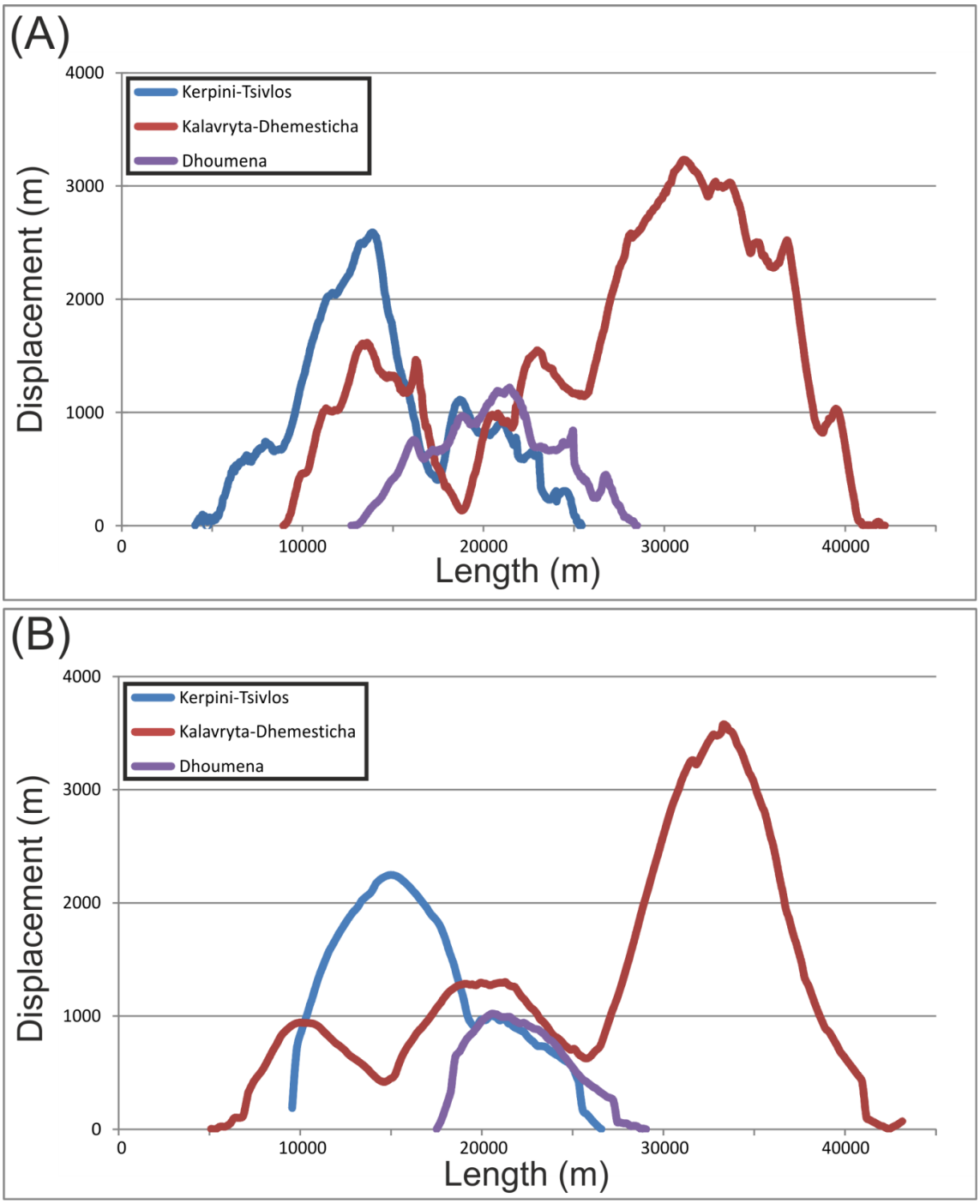

Figure 4.15. Comparison of displacement: Length plots for selected faults from (A) Outcrop-defined geometry, and (B) Seismically resolvable geometry. Overall the profiles are relatively similar, although much of the detail observed at outcrop is missing at the scale of seismic resolution.

4.4 Results

4.4.1 Syn-Rift Reservoir

To a large extent, fault geometries control the distribution, thickness and volume of syn-rift sediments within hangingwall basins. In the Gulf of Corinth rift, from which the synthetic seismic sections are generated, the volumetric majority of continental syn-rift deposits do not form a viable reservoir due to the high proportion of low net:gross overbank shale facies. Despite the basin-fill not being of a reservoir facies, geometrically the basins are very similar to many exploration provinces. In such situations mapping the extent of the syn-rift facies would be crucial when generating volumetric estimates. Where only 2D seismic data exists the 3D extent of a facies is significantly uncertain, with limited constraint on the fault displacement minima which often control facies distribution (Athmer and Luthi, 2011).

4.4.2 Connected Volume

Connectivity of reservoir facies in the hangingwall block of a fault set depends upon a balance between the evolutionary maturity of the fault set and the sediment input rate into the depocentre (Gawthorpe et al., 1994). This balance is known as the accommodation to supply ratio (A:S), and controls whether a basin is underfilled, or overfilled (Jervey, 1988). Accommodation is controlled by subsidence on faults and sea level variations, whilst sediment supply is predominantly a function of climate and hinterland uplift. Fault growth processes (i.e. linkage of fault segments) lead to along-strike variations in displacement and displacement rates, and hence on generation of accommodation space, in turn influencing connectivity of hangingwall sediments (figure 4.2). We can observe this influence in the isochore data for the models (figure 4.16). Where linkage of fault segments has occurred relatively early during fault set growth, profile readjustment (Cowie et al., 2000) leads to sediment thicknesses which vary consistently along strike (e.g. Tsivlos fault, see figure 4.1). Where segments have not linked, or have linked late, topographic highs (‘Intra Basinal Highs’, Cowie et al., 2000; figure 4.2) at relay zones may act as barriers to the amalgamation of sub-basin sediments (e.g. Dhemesticha-Kalavryta fault set, figures 4.1, 4.16). In turn this effects the connectivity of the syn-rift reservoir facies (figure 4.17).

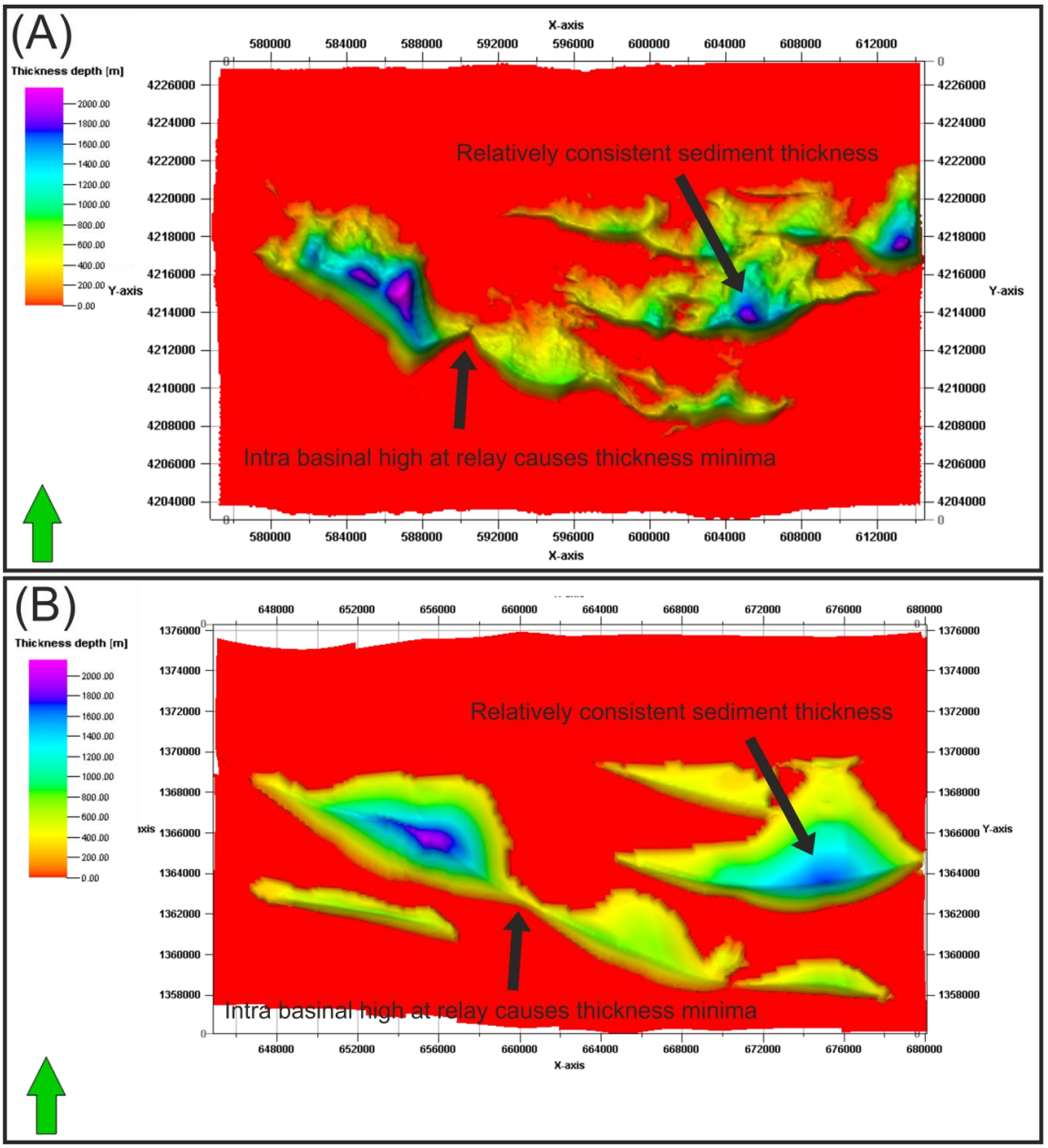

Figure 4.16. Isochore maps for syn-rift of the field based (A), and synthetic 2D seismic based (B), Gulf of Corinth rift geomodels. Low syn-rift sediment thicknesses along fault strike are indicative of intra basinal highs potentially due to the presence of late-forming fault overlaps. More consistent along strike thicknesses are suggestive of earlier fault linkage (Cowie et al., 2000).

For the outcrop based model, where syn-rift sediment distribution has been mapped in the field, connectivity is high between sub-basins, with a connected pore volume of 1.1×10^{11} m^3 (assuming 10% porosity). In an exploration scenario where the syn-rift represented the target reservoir facies this would be advantages. Interpretation of the sparse 2D synthetic seismic sections (which are generated using the outcrop-based geometry) leads to significant uncertainty in the distribution of the syn-rift facies, in this case leading to lower connectivity

between sub-basins. Based on this interpretation three distinctly separate prospects exist with pore volumes of $4.7x10^9$ m^3, $4.6x10^{10}$ m^3 and $5.4x10^{10}$ m^3.

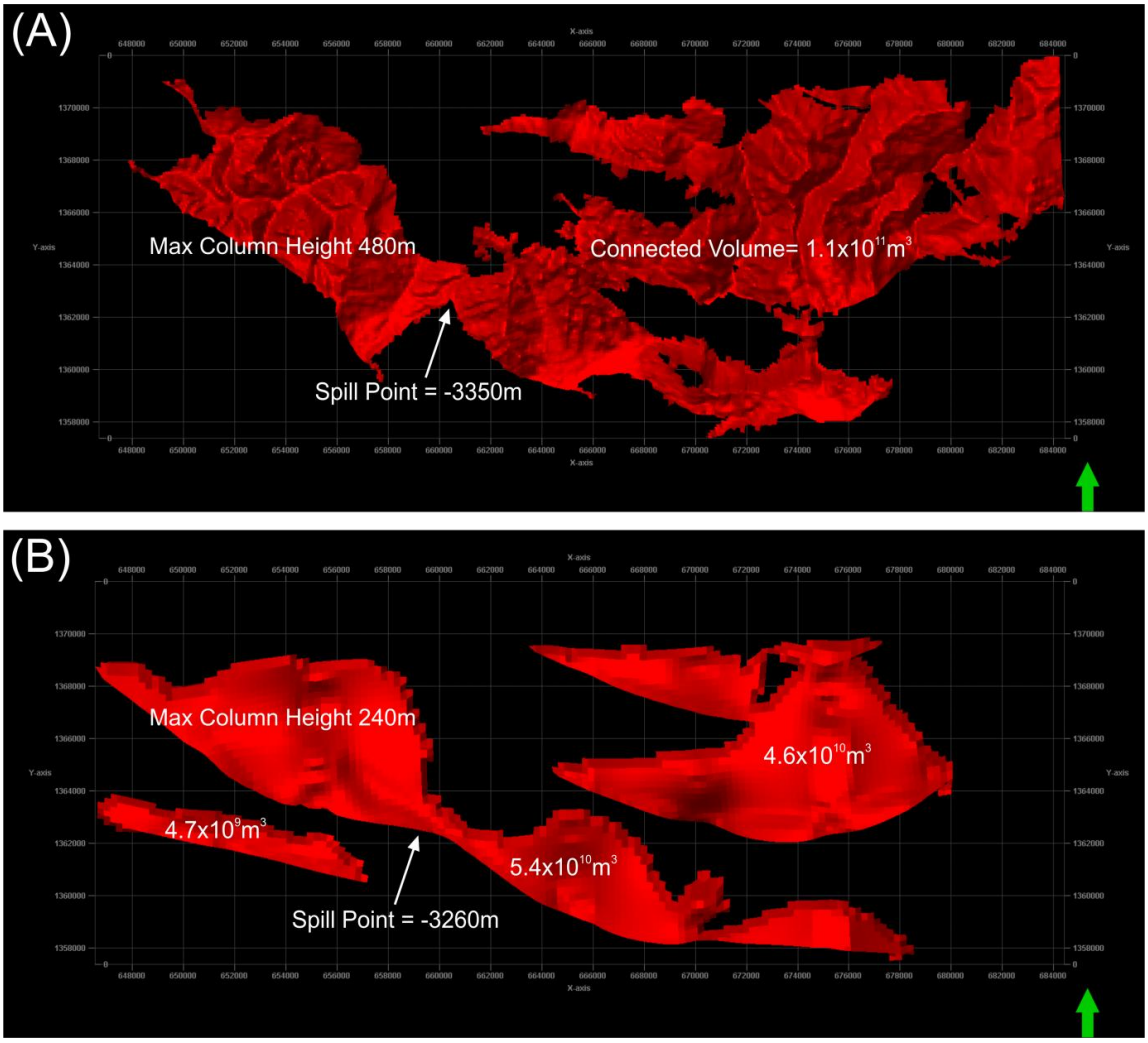

Figure 4.17. Aerial views of syn-rift distribution for field data based model (A) and model derived from 2D synthetic seismic data (B).

4.4.3 Spill Point and Column Height

Uncertainty in syn-rift distribution where only sparse data is available also effects estimates of the depth of structural spill points, and hence of potential hydrocarbon column heights. The spacing of 2D data (in this case 5 km) means that is unlikely that the structurally shallowest position will be intersected and directly identified, but that it will be based upon lateral projection of the available data. Similarly, the depth of the crest of a structure will remain uncertain. Figures 4.18 and 4.19 show an example of this for the Dhemesticha sub-basin (see figure 4.1). For the field data based model 3D constraint on the geometry exists and permits

the true crest and spill point to be identified. In contrast the spacing of the exploration geometry 2D seismic data prevents the exact depths from being identified. For this example the result of this geometric uncertainty is a column height of 50% of the true value.

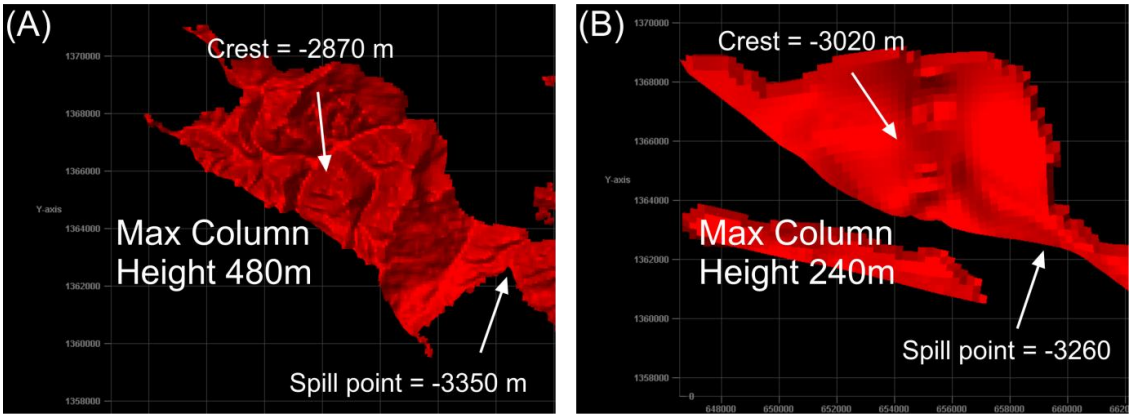

Figure 4.18. Aerial views showing comparison of estimated potential column heights for the Dhemesticha sub-basin based upon the outcrop-derived fault and syn-rift geometry (A) and that based on the synthetic 2D seismic data (B). The shallower crest and deeper structural spill point of the outcrop derived geometry lead to a significantly larger potential column height than that of the 2D seismic based model.

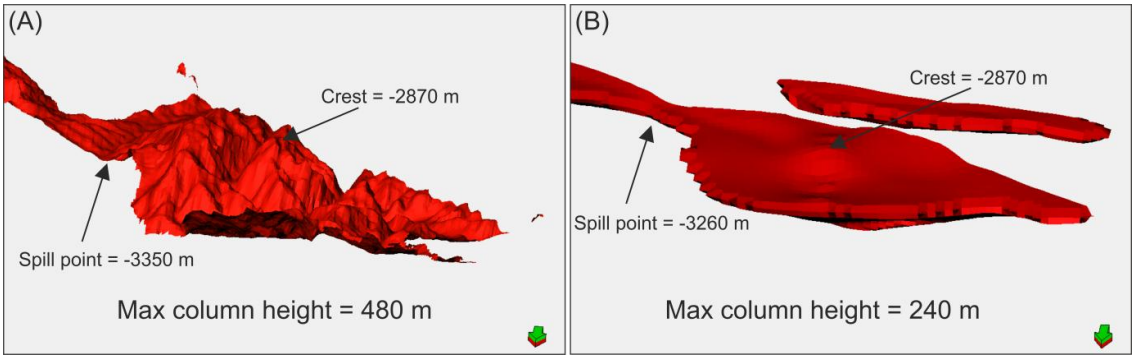

Figure 4.19. Oblique views of the modelled syn-rift fill in the Dhemesticha sub-basin shown in figure 4.18. The figure illustrates the difference in the depth of the structural crest, the spill point and the corresponding difference in predicted maximum column height for the outcrop-derived (A), and seismically resolvable (B) geometries.

4.4.4 Pore Fluid Pressure

Uncertainty in the column height leads to uncertainty in the pore fluid pressure within a prospect, with implications for trap integrity and well balancing during drilling. For the example of the Dhemesticha sub-basin (figure 4.18, 4,19), the difference in predicted column height leads to different estimates in pore fluid pressure due to buoyancy (figure 4.20). The smaller hydrocarbon column height predicted by the seismically resolvable geometry results in a lower pore fluid pressure than would actually be present (105 psi versus 210 psi). This is important for two reasons. Firstly, the pore fluid pressure within the prospect will be closer to the top seal fracture pressure, and its capillary entry pressure, than anticipated. Depending on how overpressured the reservoir stratigraphy has become during burial, the top seal may have failed, either through mechanical or capillary failure. Secondly, a greater pressure than anticipated would be encountered at a shallower depth during drilling. This may result in the well being underbalanced, allowing an influx of fluids into the well and a pressure 'kick'. For this example however the differences in pressure between the seismically resolvable geometry and the actual geometry are relatively small, and may well be within drilling tolerances (Redmann, 1991).

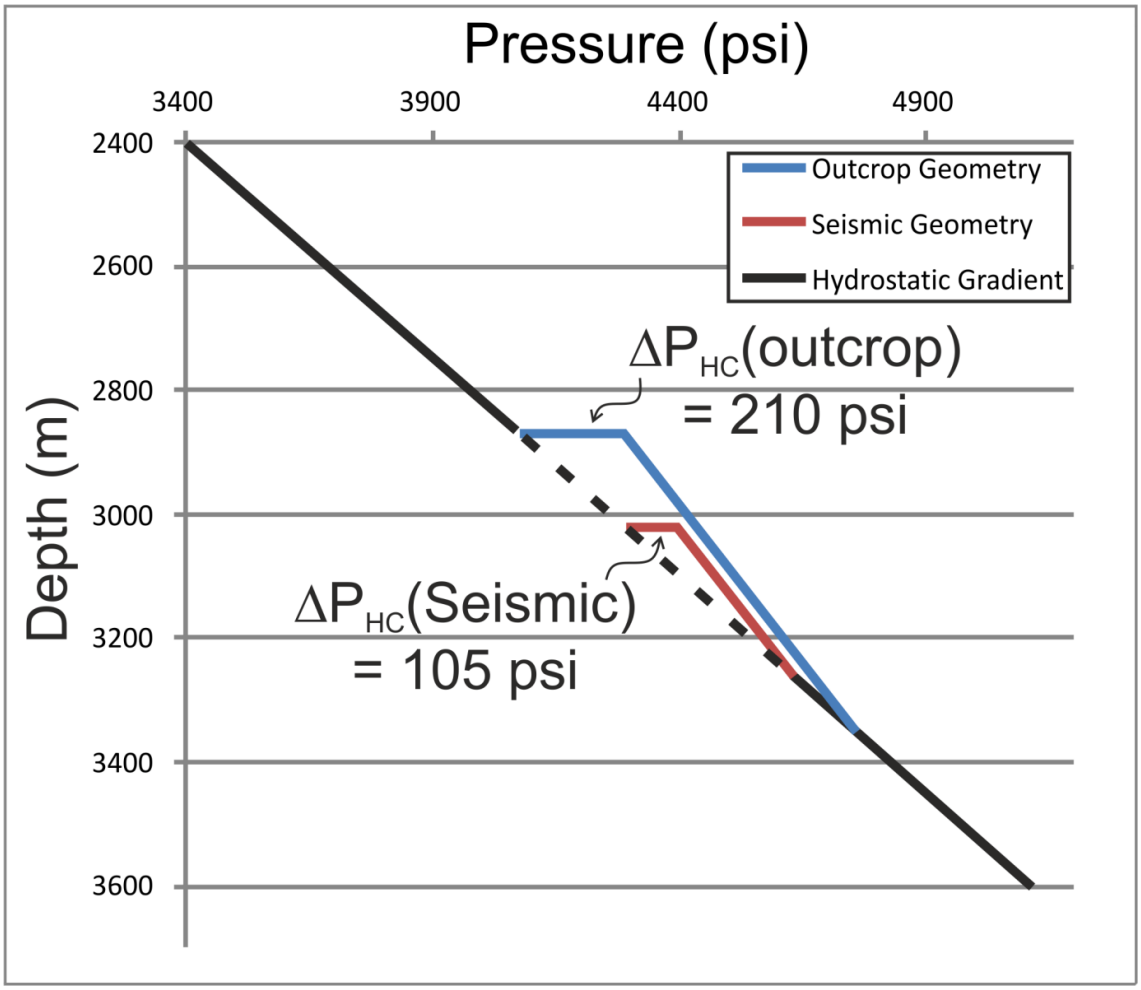

Figure 4.20 (Previous page). Plot of pressure versus depth for the outcrop derived and seismically resolvable prospect geometries shown in figure 4.17. The difference in predicted column height leads to an underestimate in pore fluid pressure for the seismically resolvable geometry relative to the outcrop derived geometry.

4.4.5 Tilted Fault Block Reservoir

Many prospects are formed in the tilted footwall blocks of large faults due to the process of footwall uplift. The along strike decrease in displacement and uplift allows 3-way closure against the fault (figure 4.21). If displacement on the fault is greater that the thickness of the reservoir interval, and the reservoir interval is juxtaposed against an impermeable lithology, then a suitable hydrocarbon trap may exist. In the Gulf of Corinth rift the footwall block to the Dhoumena fault is an excellent example of along strike displacement variation, and hence an analogue to a tilted fault block hydrocarbon trap (figure 4.22).

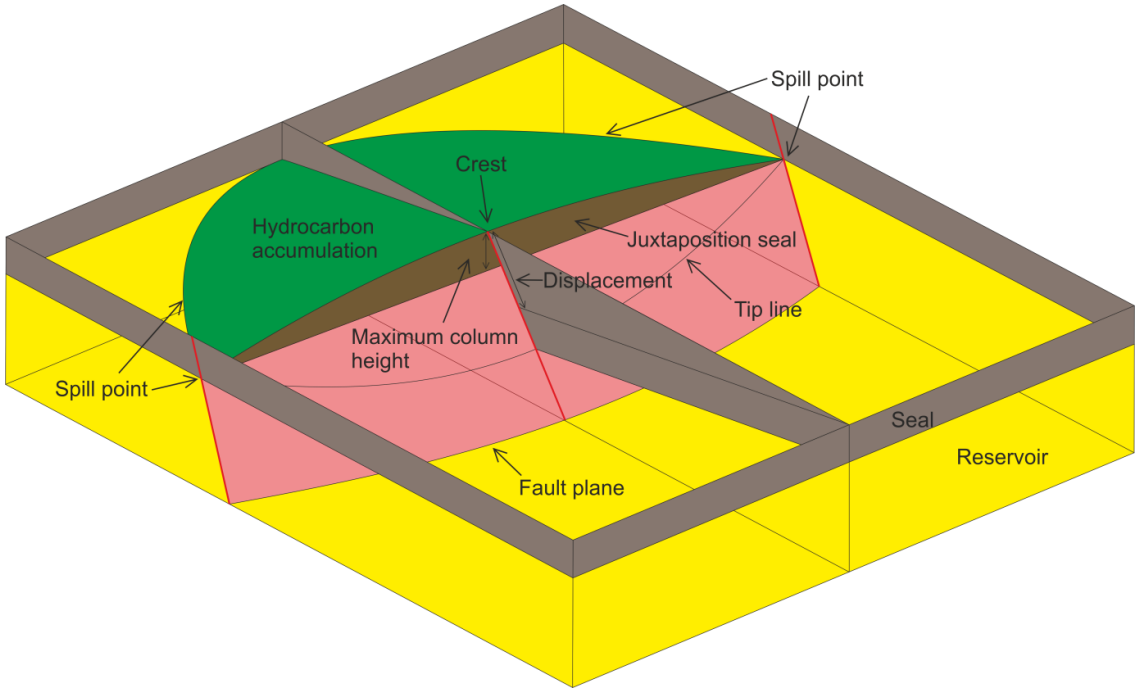

Figure 4.21. Idealised schematic of a tilted fault block trap. Footwall uplift generates relief in the form of a half-dome which abuts the fault plane. Hydrocarbons can fill this dome down to the spill points, which are located at the fault tips where displacement is zero, and in the footwall where uplift is zero.

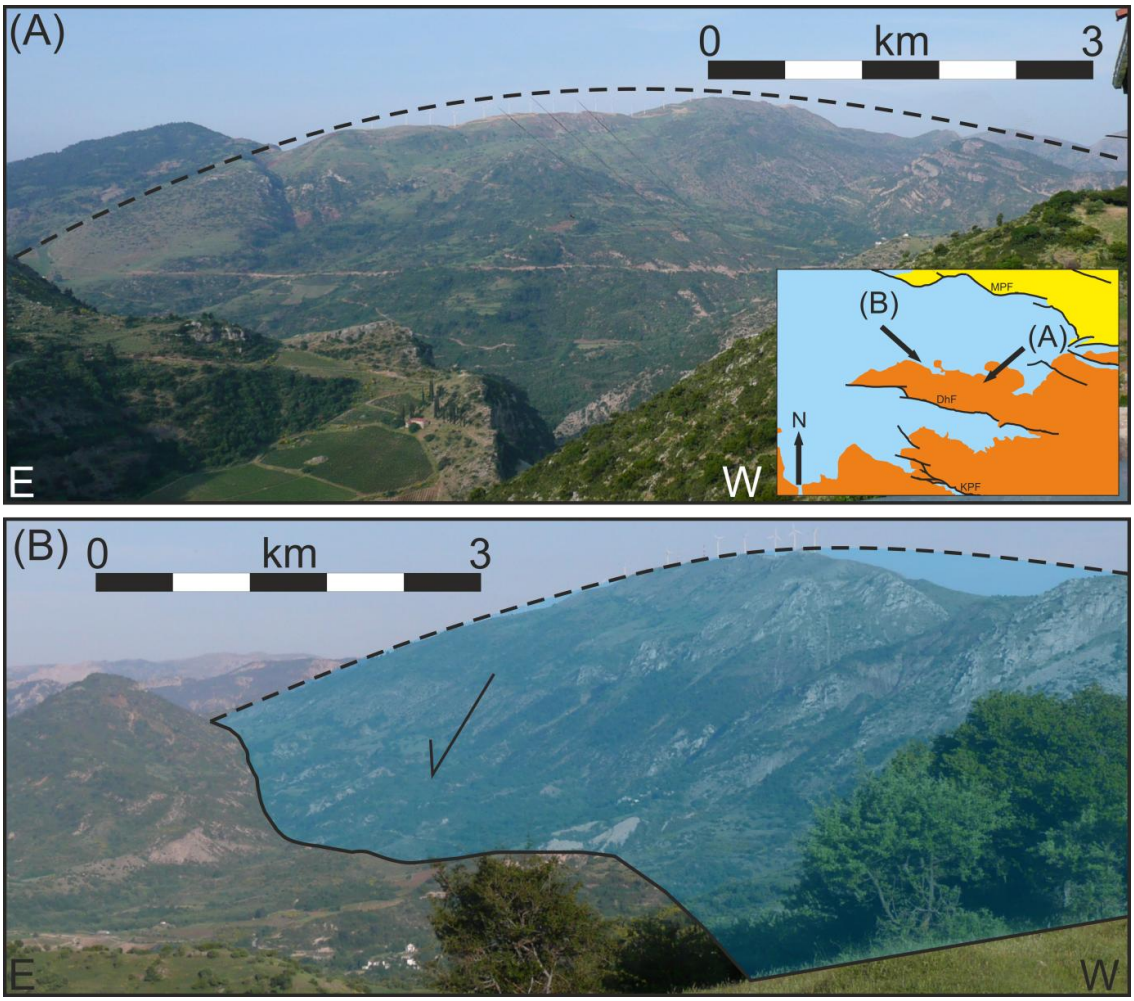

Figure 4.22. The Dhoumena fault block provides an excellent analogue for tilted fault block type traps. The footwall crest describes the typical displacement pattern of footwall uplift, with the maximum in the centre, decreasing to zero at the fault tips (A, B). Inset shows the location and direction of the two viewpoints. Approximate orientations of photographs are indicated, with faults dipping at approximately 50 degrees to the North.

Using the DEM and fault displacement data it is possible to calculate the theoretical spill points and crest for the Dhoumena fault block for both the field-based and seismically forward modelled geometries. The spill points are defined as the maximum depth at which the fault block is isolated from adjacent structures (figure 4.23). The volumetrics, maximum potential column heights (figure 4.23) and pore fluid pressures (figure 4.24), can hence be calculated for both geometries. As with the syn-rift reservoir, complexity of the surface representing the top of the reservoir unit leads to a significant disparity in the maximum column height for the two geometries. A greater column than predicted would be present, leading to pore fluid pressure being under estimated (figure 4.24).

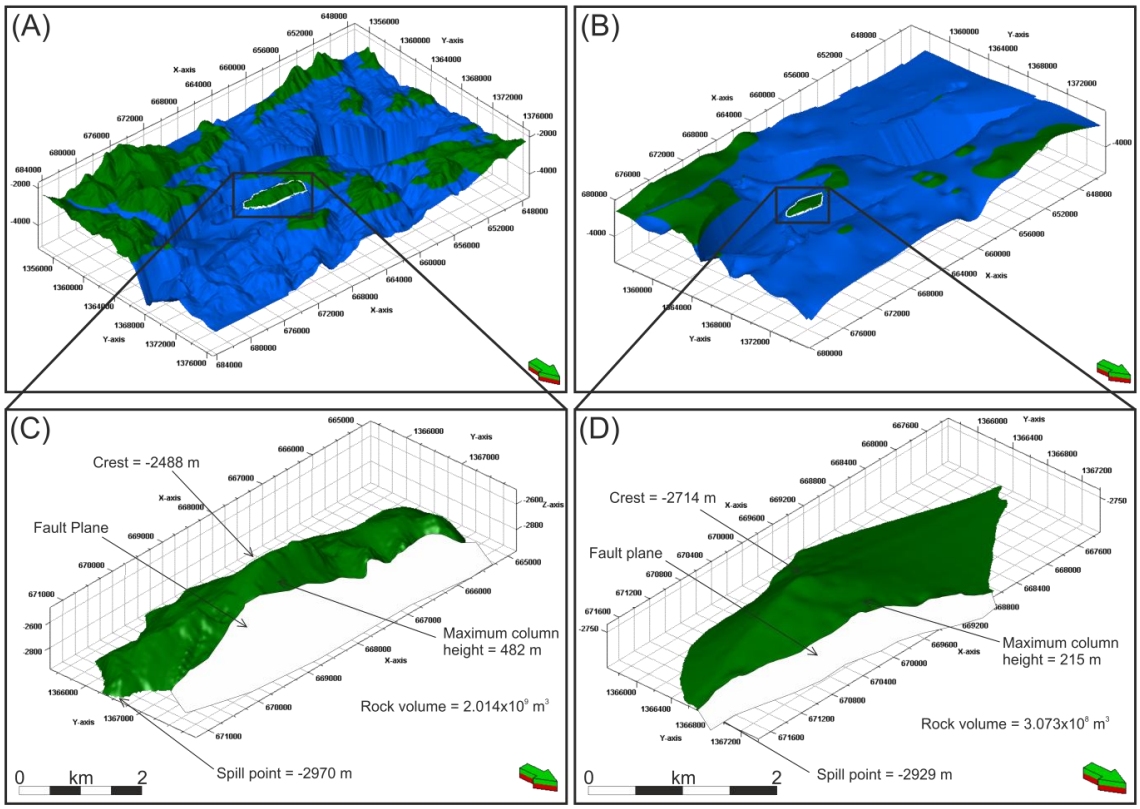

Figure 4.23. Oblique view of top pre-rift surfaces for the outcrop-derived (A) and seismically-derived (B) geometries. The location of the Dhoumena fault footwall tilted fault block trap is indicated, with the structural spill point highlighted. Above the spill point is green, below is blue. (C) and (D) show close up views of the trap for the outcrop-, and seismically-derived geometries respectively. The depth of the predicted spill points, crests and resulting maximum column heights are indicated, along with the rock volume of the trap.

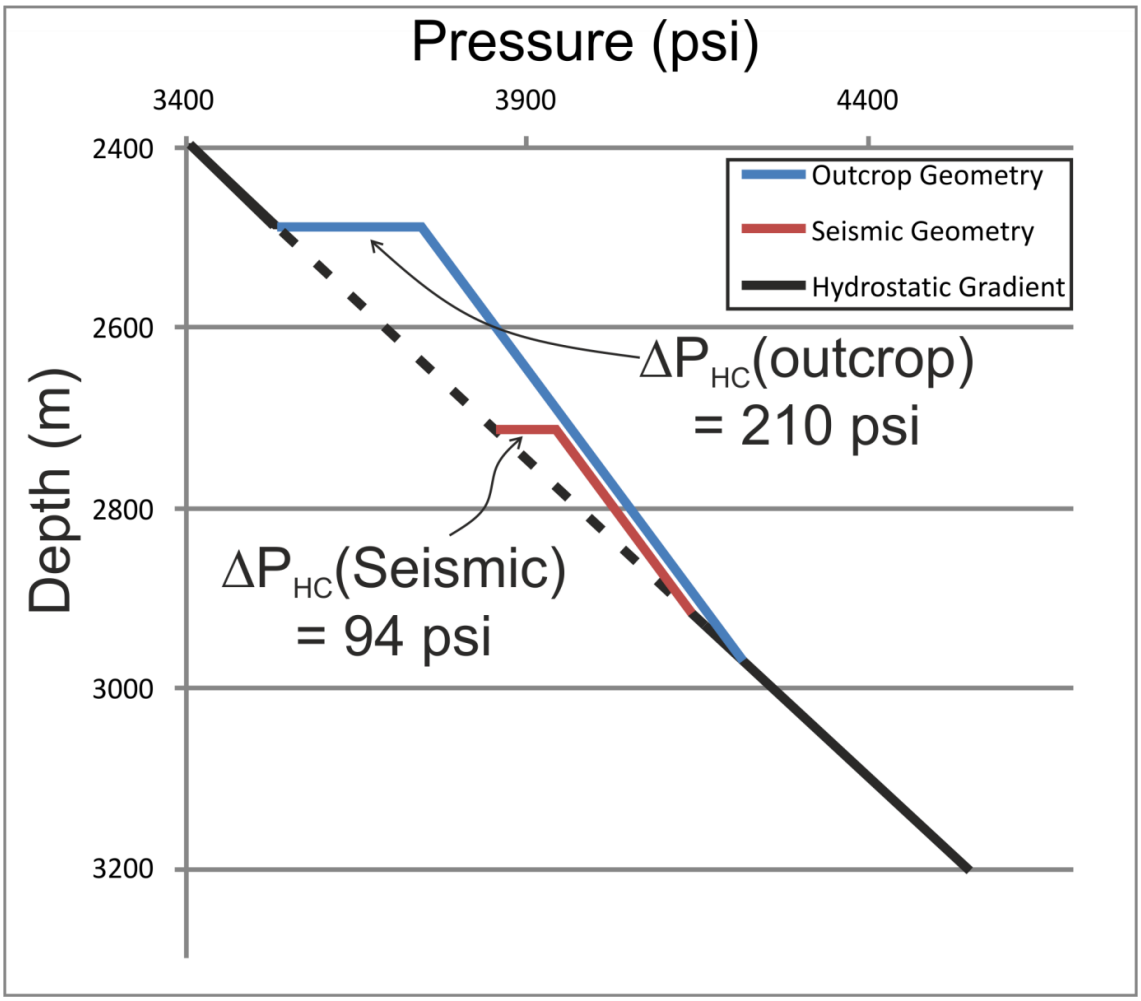

Figure 4.24. Pressure versus depth for seismically resolvable and outcrop-derived tilted fault block trap geometries shown in figure 4.19, assuming that traps are filled to their spill points, and that no there is no additional overpressure.

4.4.6 Fault Rock Supported Column Height

For a tilted fault block trap the fault provides the fourth direction of closure, typically by juxtaposing the permeable reservoir facies against an impermeable lithology such as shale in the hangingwall. The column height which can be supported is controlled by the structural spill point and the top seal integrity. In the situation where the juxtaposed lithology is not impermeable then the column height which can be supported depends on the sealing capacity of the fault rocks (Yielding et al., 1997; Fisher & Knipe, 1998; Sperrevik et al., 2002; Bretan et al., 2003; Yielding, 2012). This is a function of the fault rock capillary entry pressure and the buoyancy of the hydrocarbon column (Schowalter, 1979; Watts 1987; Fisher et al., 2001; Brown, 2003). Where the buoyancy pressure is greater than the capillary entry pressure

('threshold pressure') hydrocarbon will be imbibed into the fault rock, and can migrate across the fault.

Column height estimation is often conducted by relating threshold pressure, and hence column height, to fault rock clay content, either through direct sample measurements (Sperrevik et al., 2002) or using the SGR algorithm as a proxy (Bretan et al., 2003). Neither approach is ideal (see chapter 1) given the inherent heterogeneity of geological systems, with a less deterministic, semi-probabilistic approach being preferred (Childs et al., 2007; Yielding, 2012). Nevertheless, these approaches provide a good mechanism for illustrating the impact of seismic resolution related geometric uncertainty on fault seal prediction.

SGR values are determined by the stratigraphy and fault displacement, hence uncertainty in fault displacement distributions will lead to uncertainty in SGR calculations and hence in predicted column heights. This is illustrated by comparing the predicted column heights for the Gulf of Corinth outcrop derived geometry and the seismically resolvable geometry. This is again conducted using the Dhoumena fault block as an example. A simple layercake synthetic stratigraphy (as may be available during hydrocarbon exploration) composed of inter-bedded shales and sands (figure 4.25) is used to populate the outcrop-defined, and seismically resolvable geometries. SGR values are then calculated for the fault plane where the footwall block is juxtaposed against the hangingwall block (figure 4.26). The along-strike structural spill point (assuming no additional spill points within the footwall, e.g. figure 4.23,) is also shown. A juxtaposition diagram approach (Allan, 1989; Knipe, 1997) is used to generate a fault plane map of the position of juxtaposition seals and potential leak points. The approach of Bretan et al (2003) is used to derive fault threshold pressure from the calculated SGR values, with these values superimposed upon the sand:sand juxtaposition windows (figure 4.26). A hydrocarbon density of 0.6 g/cm^3 is used to generate the column height that can be supported at every point along the fault, and is hence used in conjunction with the juxtaposition map to estimate the fault rock controlled column height.

The structural spill point for the outcrop-derived fault geometry is controlled by an area of decreased displacement corresponding to the position of a relay zone. Unusually, the fault tip is at a higher elevation than the relay zone (figure 4.26), hence the relay zone actually increases the depth of the structural spill point in this instance. This leads to the outcrop-derived geometry having a greater column height than the seismically resolvable geometry (543 m versus 487 m), in the situation when the spill point is structurally controlled. However, when the fault rock properties are taken into account the column height is significantly reduced for both geometries. The fault geometry influences the distribution of the stratigraphy

against the fault, resulting in a juxtaposition seal being present at the crest of the structure for the seismically resolvable geometry. This increases the potential column height relative to the outcrop-derived geometry where no crestal juxtaposition seal is present. In this situation the outcrop-derived geometry can support a smaller hydrocarbon column than the seismically resolvable geometry (113 m versus 187 m).

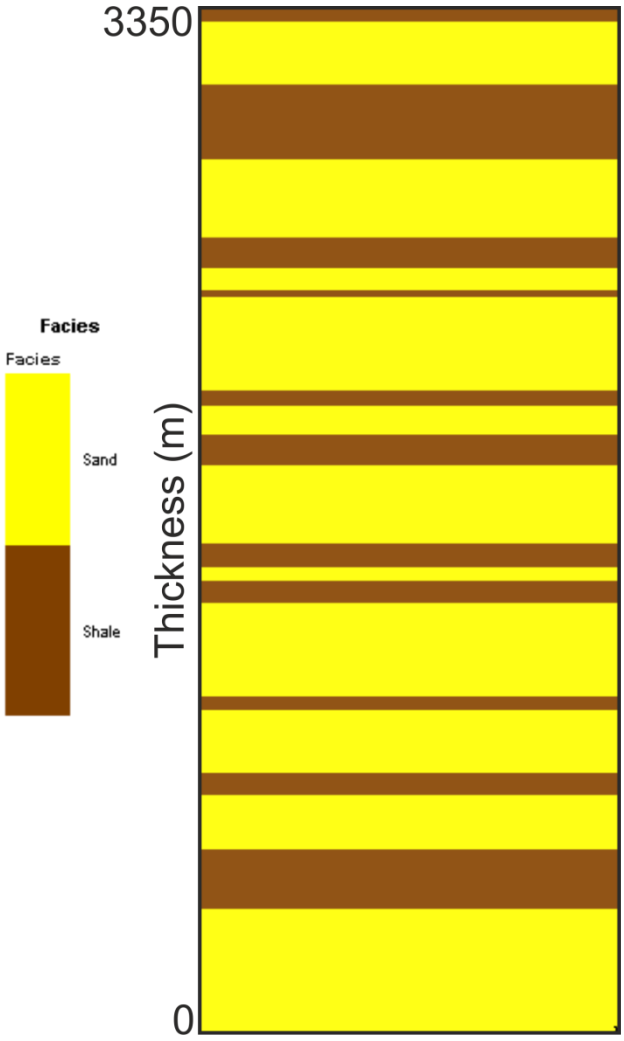

Figure 4.25. High net:gross (0.63) synthetic stratigraphy used to populate outcrop and seismically resolvable models. For the purposes of SGR calculation sand is defined as having 10% clay content whilst shale has 70% clay content (Shaw and Weaver, 1965).

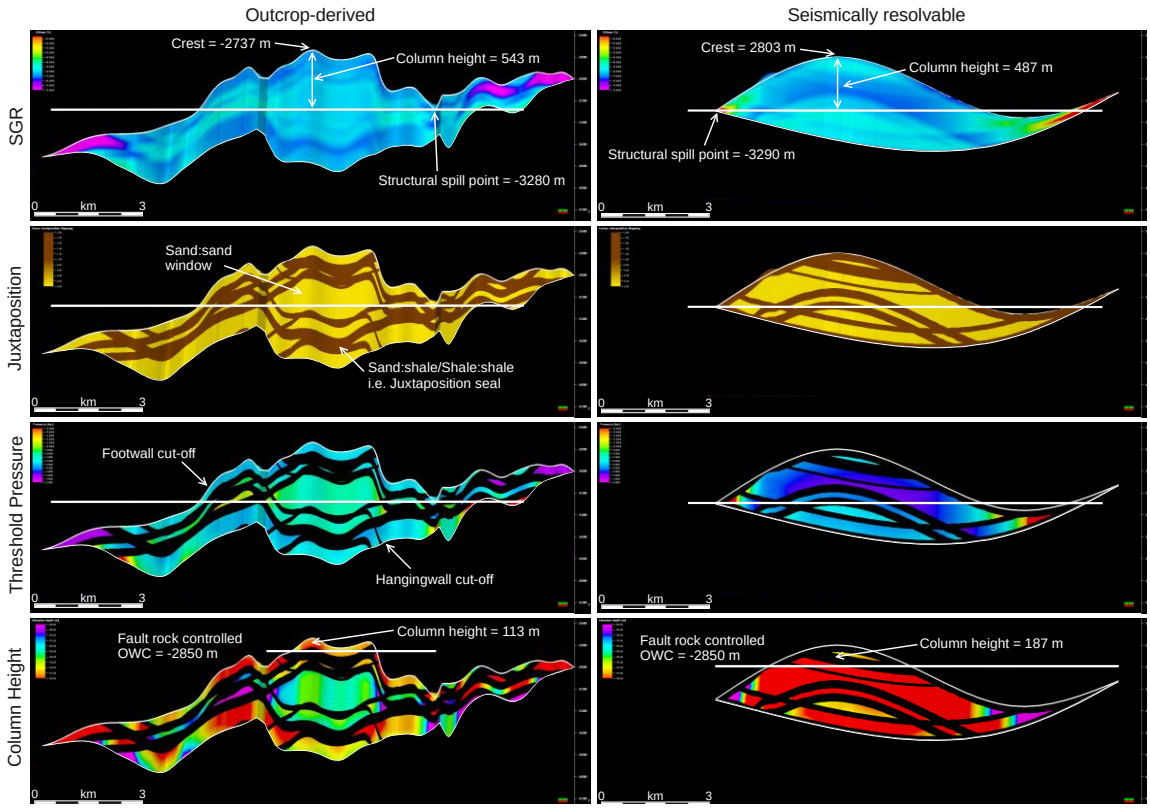

Figure 4.26. Fault-normal views of the Dhoumena fault plane displaying fault properties for both the outcrop-derived and seismically resolvable fault geometries. Properties shown, from top to bottom are; SGR, Juxtaposition, Threshold pressure and predicted column height.

4.5 Discussion

The aims of this chapter were to use the geometries defined through field data collection, (and presented in chapter 3), to illustrate some of consequences of fault geometric uncertainty at the scale of hydrocarbon exploration. This has been achieved by using seismic forward modelling to generate a series of synthetic 2D seismic sections across the Gulf of Corinth field area. The uncertainty in the 3D fault geometry when only sparse 2D data is available is evident from the differences in the outcrop-defined, and seismically resolvable models (Figures 4.13, 4.14, 4.16, 4.17). The uncertainty in fault, and associated syn-rift stratigraphic geometries, leads to uncertainty in volumetric estimates, structural spill points, pore fluid pressure and fault rock supported column heights.

The uncertainties presented are specific to the Gulf of Corinth geometry, and the petrophysical properties modelled within that geometrical framework. Although geometrical uncertainty exists in all situations where only a restricted amount of data is available, the consequences of that uncertainty are not necessarily consistent. For example, the seismically resolvable

geometry shown here suggests that the syn-rift facies is relatively isolated between individual sub-basins, contrasting with the 'real' syn-rift geometry which shows high connectivity. However, there is nothing suggesting that syn-rift stratigraphy will always have higher connectivity than can be identified in seismic data, rather that it will depend on the specific geometry in question. Hence, the examples portrayed here are simply an example of the potential implications that may arise from exploration-scale structural uncertainty. These uncertainties are relatively self-evident, with numerous published examples of how they relate to the sparse nature of 2D seismic data (e.g. Needham et al., 1996; Childs et al., 1997; Jolley et al., 2007). A number of studies have utilised 2D seismic forward modelling to generate synthetic seismic across known geometries and facies distributions (Johansen et al., 1994; Hodgetts and Howell, 2000; Alaei and Petersen, 2007), however few if any use the technique to illustrate the potential uncertainties pertinent to hydrocarbon exploration as described here.

Using the technique of seismic forward modelling to illustrate structural uncertainty is not without its own methodological uncertainties, for example the observation that faults formed at the topographic surface (as in Greece), and subsequently buried would reduce in dip due to compaction of the surrounding stratigraphy. This is not reflected in the model since the outcrop geometries have simply been translated to depth, and hence neither do they say anything about the fault growth history. This is however largely irrelevant in respect of the illustrative (rather than quantitative) aims of this chapter. It is the difference between the synthetic seismic data and the original model used to generate that seismic data that is important.

Other than the generalised uncertainties which have been discussed a number of additional observations can be made that can be applied more broadly. Displacement profiles are broadly similar for the outcrop-derived and seismically-resolvable fault geometries (Figure 4.15), although the detail observed at outcrop is significantly greater than can be observed with 2D data. The extrapolation of faults between 2D sections inevitably leads to uncertainty, with structures such as relay zones often being unobserved. The location of fault tips and displacement maxima are also uncertain, resulting in inaccurate estimates of fault displacement length ratios. In turn this can impact on the understanding of how a basin evolved (e.g. Figure 4.2). The non-identification of displacement minima tends to lead to the smoothing of fault profiles, and the treatment of fault sets as individual faults, rather than as being composed of multiple segments. This may have the effect of displacement:length ratios being underestimated in 2D seismic data.

4.6 Conclusions

Synthetic seismic sections across known outcrop geometries highlight the uncertainties when basing a 3D geometric model on 2D data. The synthetic sections can provide a useful tool for understanding the potential impact of structural uncertainty in rift settings.

• Widely spaced 2D sections are unlikely to correspond spatially to features such as displacement minima associated with relay zones. This leads to uncertainty when predicting spill points, structural crests and column heights, as well as identifying the location of sediment entry points in to basins.

• The uncertainty in column height as a result of poorly constrained structural geometry leads to variations in pore pressure prediction, with implications for drilling strategies.

• The disparities between fault geometries constrained in 3D and those in 2D can lead to significant variation in how stratigraphy is modelled to intersect with, and is mapped onto faults. In turn fault rock properties, and hence potential supported column heights, may vary considerably.

Chapter 5

Sub-Seismic Fault Tips and Breached Relay Zones: Their Prediction and Effect on Fault Network Connectivity in Reservoir Models

5.1 Abstract

The effect of sub-seismic scale fault tips and relay-zone breaching faults on the connectivity of reservoir faults has been examined by using the currently-producing Penguins C oilfield in the North Sea as a case study. A subset of a 3D seismic volume covering the oilfield has been interpreted and high-resolution geological models constructed to allow evaluation of the different approaches to incorporating sub-seismic fault geometries. Two methods for incorporating sub-seismic fault tips are reviewed, modified and compared. In addition a simple relationship has been developed for predicting the presence or absence of sub-seismic scale breaching faults at relay zones. Incorporating these features leads to significantly increased fault network connectivity and hence reservoir segmentation.

5.2 Introduction and Aims

The aim of this chapter is to assess the impact of incorporating sub-seismic fault tips and small scale relay zone breaching faults on reservoir segmentation. This has been accomplished by developing a number of predictive tools and subsequently applying these tools to a sub-surface dataset.

Faults influence hydrocarbon exploration and production across a range of scales, from trap definition and integrity, to borehole stability. At the reservoir scale faults can cause static and/or dynamic compartmentalisation, potentially leading to modification of drilling and development strategies (Manzocchi et al*.,* 2007; Freeman et al., 2010; Jolley et al., 2010; McKie et al., 2010). Conversely faults may enhance connectivity of reservoir facies (Bailey et al., 2002) as well as increasing sweep efficiency during production (Manzocchi et al., 2008a, b; Rotevatn et al., 2009a, b). The magnitude of the effect of faults upon hydrocarbon production is dependent on both their geometry and the petrophysical properties of any fault rock which may be developed.

Fault geometry controls throw distribution and hence the across-fault juxtaposition of reservoir units, whilst the petrophysical properties of the fault rock determine how a fault may impede fluid flow under the specific reservoir conditions (e.g. Pressure, saturation, fluid properties). Fault geometry is controlled by tectonic history (Paton, 2006), interaction with other structures (Peacock and Sanderson, 1991; Trudgill and Cartwright, 1994) and the

mechanical properties of the faulted medium (Martel, 1999; Soliva et al., 2006; Morris et al., 2009). The petrophysical properties of the fault rock (Yielding et al., 1997; Knipe et al., 1998; Fisher and Knipe, 1998; Fisher et al., 2001; Sperrevik et al., 2002) are determined by the petrophysical properties of the stratigraphy, the burial history, the timing and depth of faulting, and the fault geometry and displacement. Accurately modelling both the geometry and petrophysical properties of faults, and capturing the associated uncertainty, is therefore critical for successfully evaluating their effect upon hydrocarbon production.

Previous work has indicated that manipulating modelled faults to include sub-seismic geometries can have a non-trivial impact on compartmentalisation for faulted reservoirs (Pickering et al., 1997; Manzocchi et al., 2008a, b; Rotevatn and Fossen, 2011). Incorporation of sub-seismic fault tips may lead to increased fault connectivity and reservoir segmentation and potentially to increased reservoir compartmentalisation (Pickering et al, 1997; Rotevatn and Fossen, 2011). Intact sub-seismic scale fault relay zones may enhance across-fault communication (Manzocchi et al., 2008a, b), whereas sub-seismic faults breaching identifiable relay zones may inhibit across-fault flow.

5.2.1 Sub-Seismic Fault Geometries

Fault controlled reservoir compartmentalisation occurs when fault geometries and petrophysical properties combine to prevent fluid flow between fault bound compartments on either a geological or hydrocarbon production timescale (Jolley et al., 2010). From a geometric perspective the key uncertainty when interpreting faults from reflection seismic data relates to the spatial resolution of the seismic data. A value of ¼λ is often quoted as the theoretical minimum fault offset that can be detected based upon the Fresnel zone phenomenon (Townsend et al., 1998; Gadallah and Fisher, 2004). However, other factors such as the acoustic impedance contrast in the vicinity of faults and the bandwidth of the seismic pulse also contribute to the minimum observable fault offset, with throws of 1/8λ or less potentially being imaged (Jolley et al., 2007). Any fault, or part of a fault, that has a throw value less than the vertical resolution of the seismic data will not be resolved, and can be described as being ‘sub-seismic’ (figure 5.1). The throw of an idealised isolated fault decreases from a maximum at its centre to zero at the fault tips (Barnett et al., 1987). Hence, fault tips are un-resolvable in seismic data, with the result being that the length of faults is often underestimated. Extending the lengths of faults to include the sub-seismic fault tips may lead to a greater degree of fault connectivity and reservoir segmentation than initially identified and, depending on the resulting juxtapositions and petrophysical properties of the faults, may lead to increased reservoir compartmentalisation. Even in cases where incorporation of sub-seismic fault tips

does not lead to increased reservoir segmentation the production response may still be influenced. Longer fault tips may result in increased flow tortuosity, potentially effecting production rates and sweep efficiency (Manzocchi et al., 2008a). The amount of additional sub-seismic length which is added to faults therefore strongly influences the connectivity of the fault network and hence its effect on hydrocarbon production.

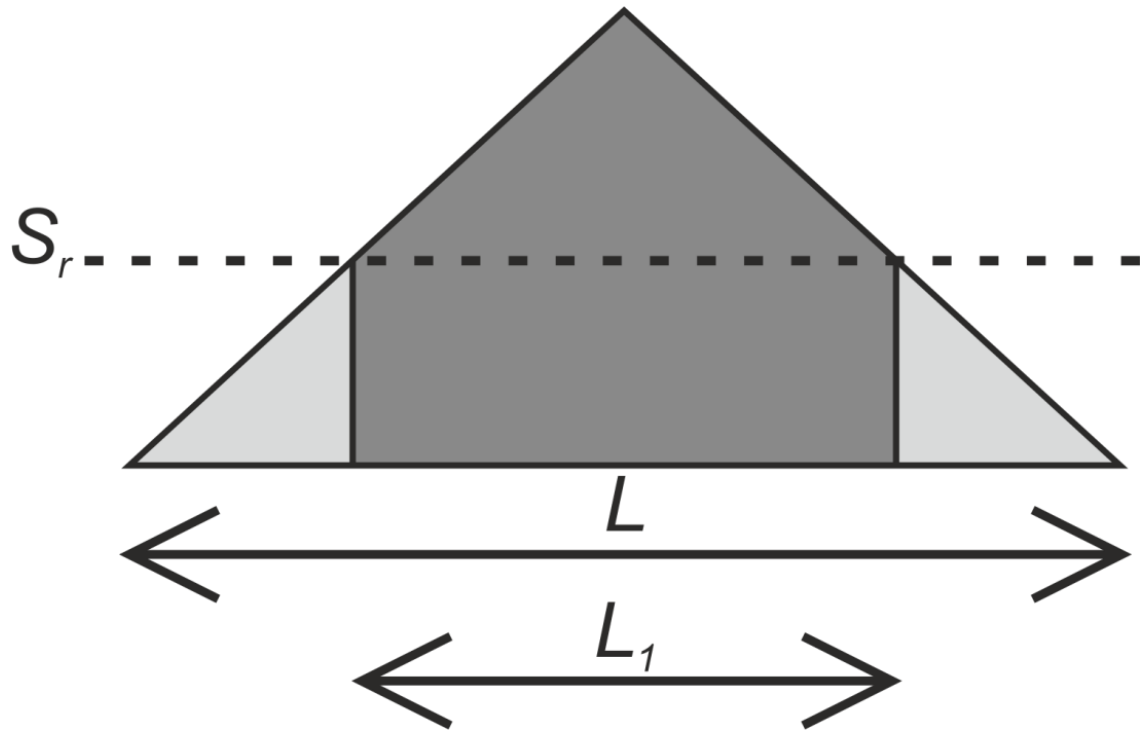

Figure 5.1. Schematic illustrating how sub-seismic fault tips lead to underestimates in fault length. Where displacement is less than seismic resolution (S_r) fault tips are not imaged. This leads to the resolvable length (L_1) being less than the actual length (L).

Fault linkage geometry is another factor which influences hydrocarbon production in faulted reservoirs. Numerous studies over the previous two decades have highlighted the evolution of extensional faults, from the initiation of individual discontinuities as a response to local or regional extension, through stages of growth, interaction, linkage and continued growth (Peacock and Sanderson, 1991; Childs et al., 1995; Cowie et al., 2000). Relay zones are ubiquitous at all stages of this process, and their potential influence on hydrocarbon exploration and production is well documented (Peacock and Sanderson, 1994; Rotevatn et al., 2007; Athmer and Luhti, 2011). At the exploration scale relay zones are often cited as influencing sediment distribution both onshore (Gawthorpe and Hurst, 1993; Collier and Gawthorpe, 1995) and offshore (Athmer et al., 2010), and of being preferential pathways for

hydrocarbon migration (Morley et al., 1990). They can also both form, and be a risk to, structural traps (Gras and Thusu, 1998; Bense and Van Balen, 2004; Fossen et al., 2010). At the production scale a well-connected intra reservoir fault network may lead to static and/or dynamic compartmentalisation where the across-fault juxtapositions and fault rock properties are such that capillary entry pressures are high enough (and/or permeabilities low enough) to support across-fault pressure differences on geological and/or production timescales (Schowalter, 1979; Watts, 1987; Fisher et al., 2001; Brown, 2003; Jolley et al., 2010). In fault compartmentalised reservoirs determining the presence or absence of relays zones is therefore critical since they may provide flow pathways between compartments across otherwise sealing faults (Manzocchi et al., 2008a, b). For open relay zones the flow characteristics across individual ramps have been shown to be dependent on both the petrophysical properties of the stratigraphy and the internal deformation of the relay ramp (Rotevatn et al., 2009a, 2009b, Rotevatn and Fossen, 2011) whilst for breached relay zones the geometry and position of the breaching fault(s) has a significant influence under certain conditions (See chapter 7).

As is the case for fault tips, relay zones close to or below the limit of resolution may not be fully resolvable in seismic data. This is potentially important in two ways. Firstly, open relays may be present where only a single fault plane can be resolved, leading to enhanced across-fault flow. Secondly sub-seismic breaching faults may be present where an open relay is observed. The discrete offsets associated with breached, as opposed to intact, relay zones may result in unfavourable juxtapositions for across-fault flow and the development of baffling or sealing fault rocks such as clay smears. Predicting the presence or absence of small scale, sub-seismic faults which breach relay zones is therefore a powerful tool when assessing the segmentation and compartmentalisation of a reservoir.

An assessment of the impact on reservoir segmentation of incorporating sub-seismic scale structural features has been conducted using the Penguins oilfield as a case study. This dataset, in conjunction with other data sources, has allowed the development of a number of predictive tools for incorporating these sub-seismic scale structures.

5.3 Case Study: Penguins Oilfield

The Penguins Cluster consists of four oil and gas fields located in the east Shetland basin to the northwest of the Viking Graben in the northern North Sea (Figure 5.2). The fields lie on the flanks of a north-south trending horst with reservoirs in both Triassic and Jurassic sediments (Dominguez, 2007). Reservoir scale faulting is pervasive throughout the area making it an ideal location to study the influence of sub-seismic fault geometries upon reservoir segmentation. A

sub-area of the Penguin C field has been used as the basis for constructing a number of structural models to test the impact of incorporating sub-seismic fault tips and breached relays upon reservoir segmentation (figures 5.3, 5.4). A 3D pre-stack depth migrated seismic volume was interpreted on every trace for both horizons and faults, with the traces aligned perpendicular to the average strike of the fault system resulting in a line spacing of approximately 25m (figure 5.5). Dip magnitude, coherency and amplitude attributes were used to aid the interpretation and to ensure that the minimum resolvable throw has been consistently identified (figure 5.5). For the majority of interpreted faults the minimum throw observable towards the tips is approximately 5 m, significantly less than the throw which would be implied if assuming a value of 1/4λ (approximately 25 m).

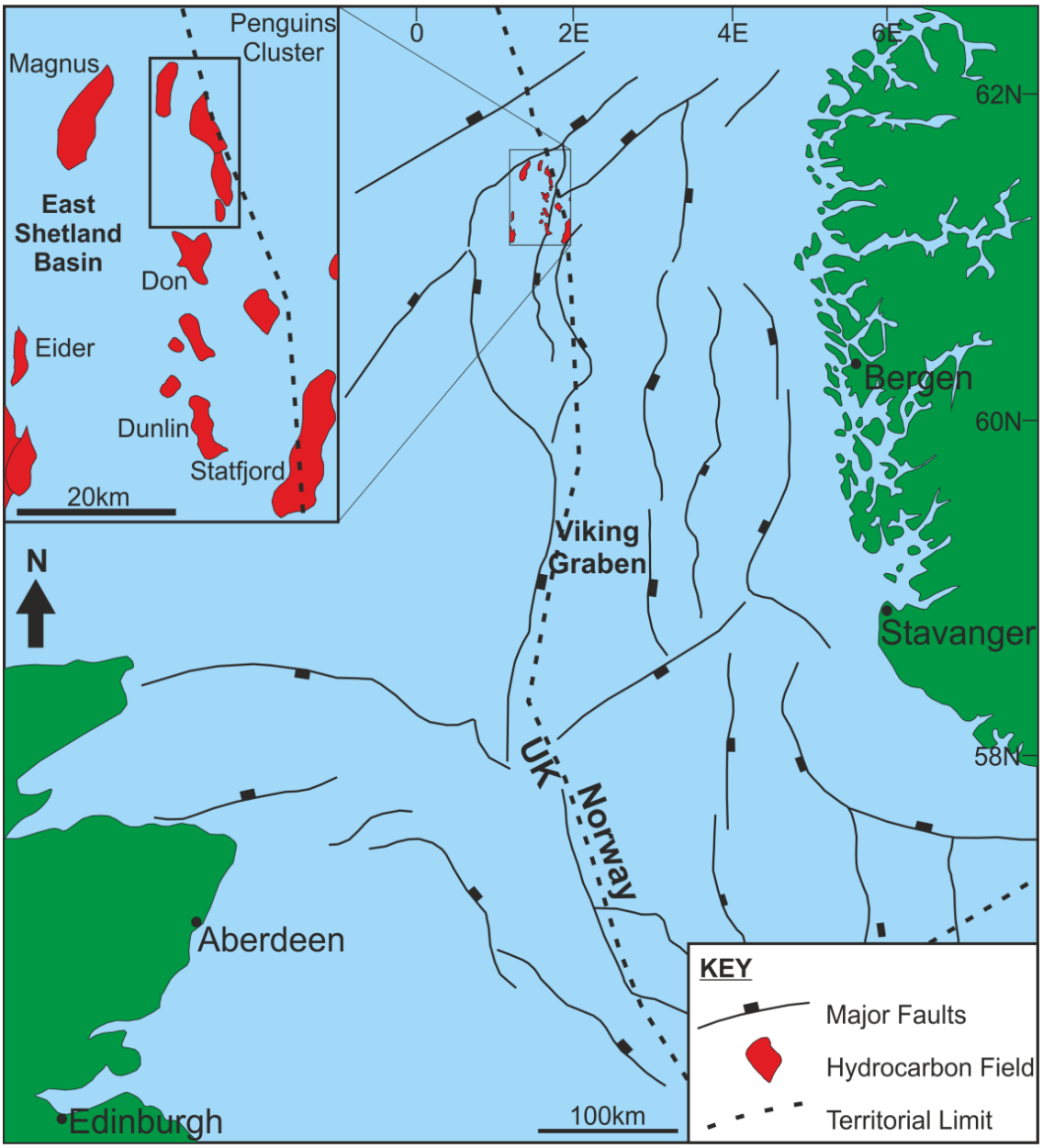

Figure 5.2. Map of the northern North Sea highlighting the location of the Penguins cluster in relation to key structural elements and adjacent oilfields. Modified after Roberts et al., 1995.

Seismic amplitudes decrease with proximity to faults (figure 5.5) due to diffractions off the relatively steeply dipping fault plains (Townsend et al., 1998). This also leads to 'seismic drag', the effect of which is to obscure the position of hangingwall and footwall cut-offs (e.g. Freeman et al., 2010). Uncertainty therefore exists as to the exact across-fault juxtapositions. The general approach is to assume that all 'seismic drag' is an artefact, i.e. that no physical normal drag of the strata is present. Although it is likely that for some faults and stratigraphies physical drag may well occur (Jackson et al., 2006; Long and Imber, 2010) it is not easily quantified in sub-surface data. We have therefore made the supposition that all the 'seismic drag' in our dataset is an artefact, and have hence modelled cut-offs by using a parallel projection of input surfaces towards faults from the position at which amplitudes begin to decay. This approach has allowed consistency in the positioning of fault-horizon intersections.

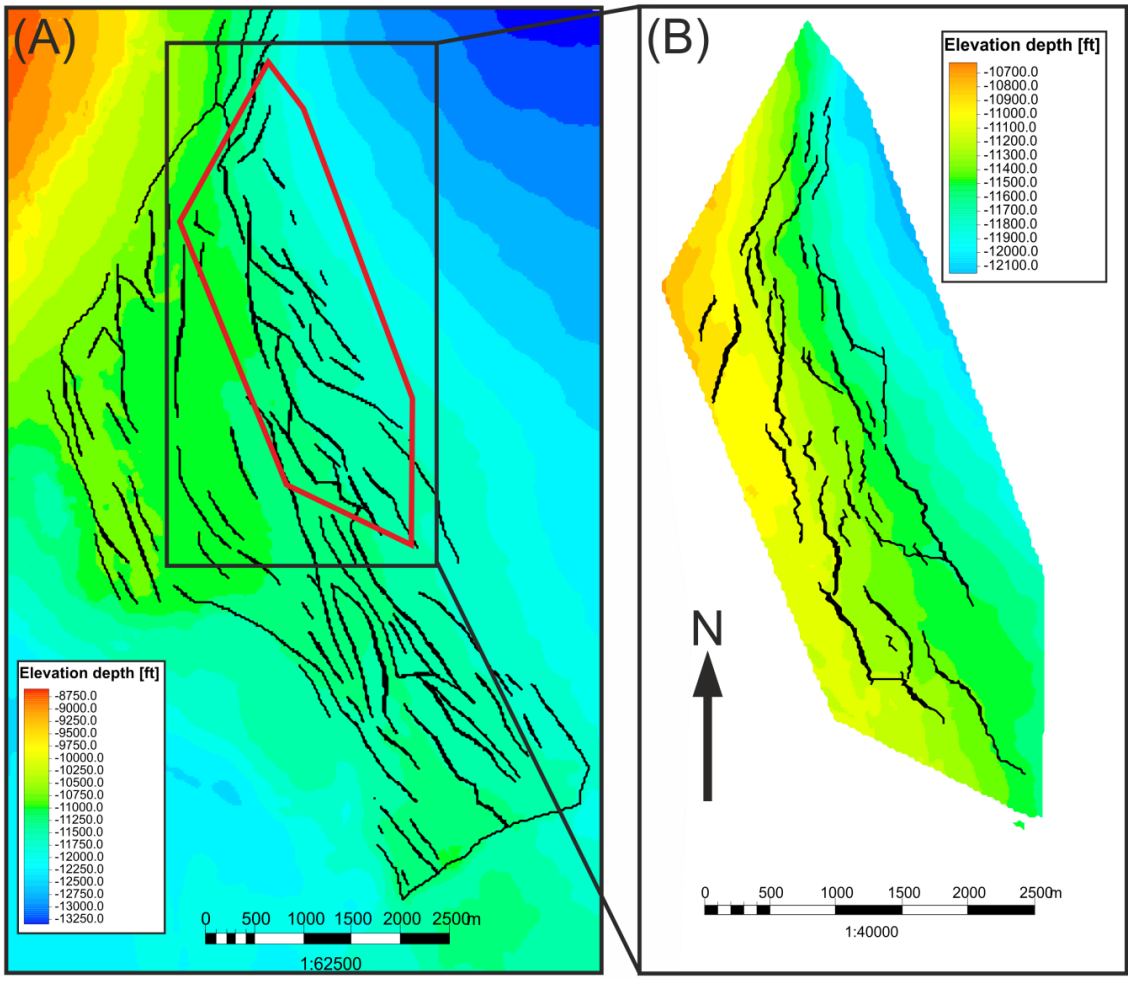

Figure 5.3. Maps showing structure of the Penguin C oilfield used within this study. (A) Broad scale structure with top reservoir horizon coloured by depth and coarsely interpreted fault network. (B) Inset shows location of sub-area used for detailed analysis. In this area fault and horizon interpretation was conducted on every seismic trace so as to maximise the precision of the modelled geometries.

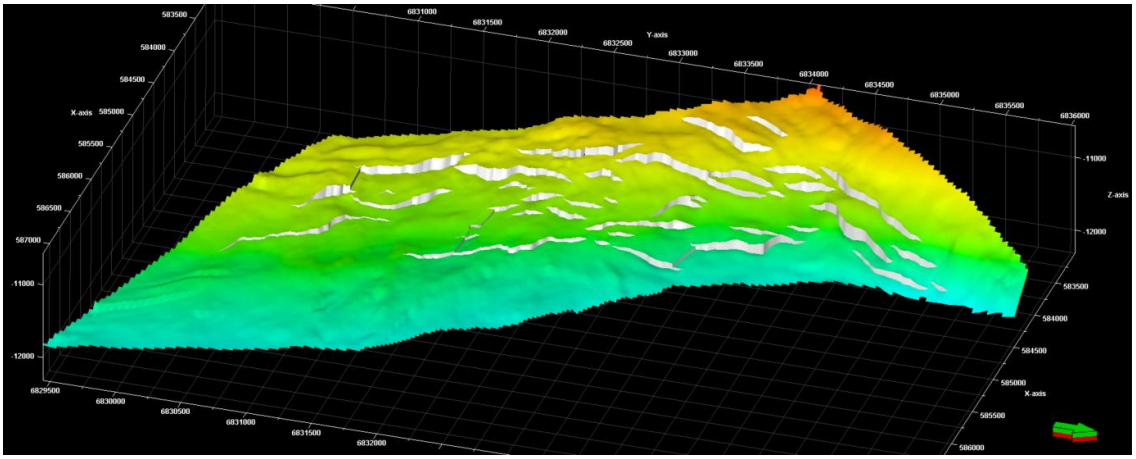

Figure 5.4. Oblique view of top reservoir horizon and fault planes for the subset of the Penguins oilfield dataset. V.E. = x2.

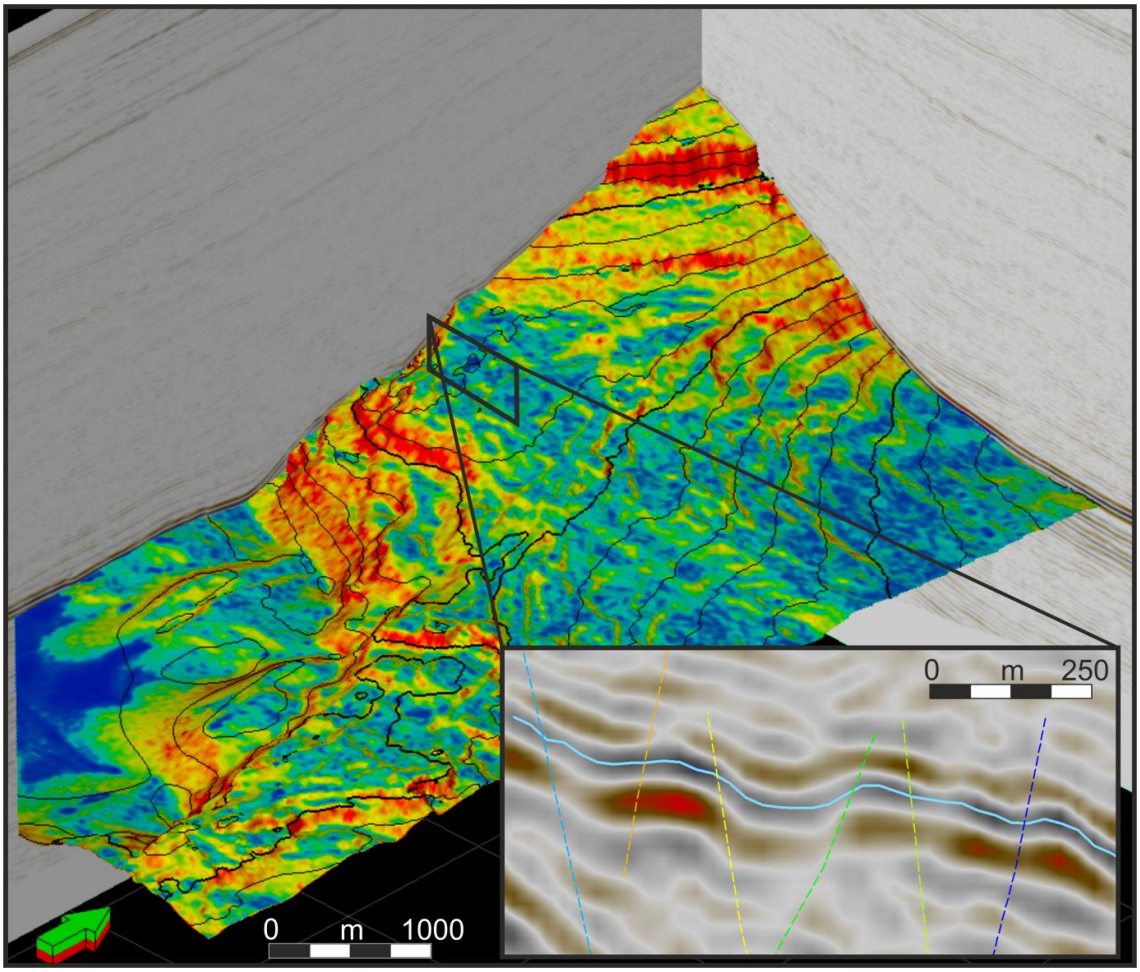

Figure 5.5. Oblique view showing pre-stack depth migrated (PSDM) seismic dataset used within this study. Surface is coloured by an 'edge detection' attribute highlighting the position of faults, with 'hot' colours indicating a high probability of a fault. V.E. = 2. Inset shows a cross-line (no vertical exaggeration) showing the top reservoir horizon and a series of small-scale antithetic faults.

5.4 Sub-Seismic Fault Geometries

In this section a number of both existing and newly developed approaches for predicting and incorporating sub-seismic fault geometries are examined and subsequently applied in the context of the Penguins C dataset.

5.4.1 Fault Tips

Two principle methods for estimating sub-seismic fault tip length can be applied. (1) A statistical approach based upon analysis of the dimensions of the identifiable fault population, and (2) projecting fault tips based upon the adjacent throw gradient of the fault. Here each approach is reviewed, its validity examined, and a number of modifications suggested based upon observations from both the Penguins dataset and the existing literature.

5.4.1.1 Statistical Approach

The statistical approach to estimating the length of sub-seismic fault tips is based upon analysis of the relationship between length and maximum throw of a population of faults (see Kim and Sanderson, 2005), summarised by a power law relationship of the form;

$$t_{max}=cL^{n}$$

where t_{max} is the maximum throw, L is the length, n is the exponent value and c relates to the throw at a unit length. The value of the exponent is critical as it indicates whether a linear scaling law can be applied to a fault population or not. For exponents of 1 a linear relationship applies, where c is the ratio t_{max}:L. For exponents that are not equal to 1, a scale dependent relationship is implied. For values where $n<1$ the length dimension of a fault increases faster than the throw dimension, whilst the converse is true for values where $n>1$. Published datasets suggest a range of values for n based on different datasets. Fossen and Hesthammer (1997) suggest a value of 0.5 based on analysis of deformation bands, whilst a figure of 1 has been put forward based upon mechanical models (e.g. Cowie and Scholz, 1992a) and empirical relationships (e.g. Schlische et al., 1996). Marrett and Allmendinger (1991) propose a value of 1.5 and Walsh and Watterson (1988) a value of 2 based upon both seismic and outcrop data. Despite this, when multiple datasets are combined it is generally shown that a linear relationship (i.e. n=1) can be applied (Kim and Sanderson, 2005).

In seismic data smaller faults will have a greater proportion of their length below seismic resolution than larger faults (Figure 5.6). Data derived from fault populations identified in seismic datasets will therefore tend to display a power law relationship between length and throw where $n<1$. To correct for this effect a constant value representing the sub-seismic

portion of fault length can be incrementally added to the length dimension of every fault in a population until a power law trend line reaches the stage where it has an exponent of 1 (Pickering et al., 1997). Half of this value represents the sub-seismic length expected at each fault tip.

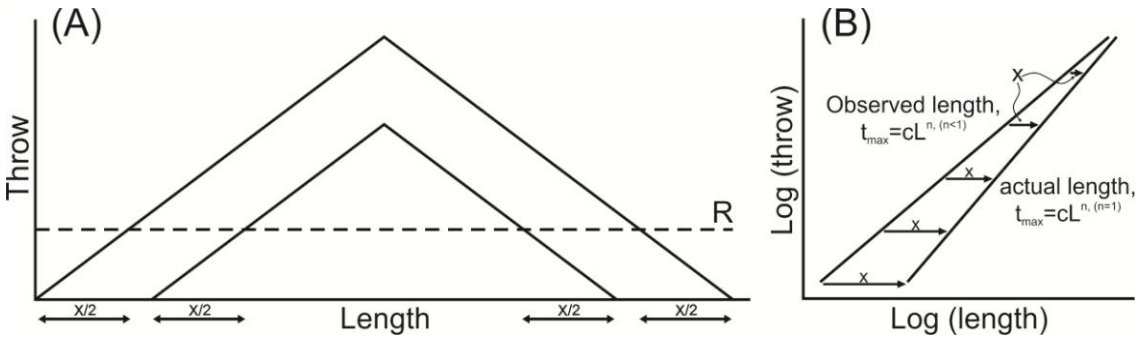

Figure 5.6. (A) Plot of fault throw against fault length. R=limit of seismic resolution. If a constant throw gradient is assumed then the sub-seismic tip length will be consistent for sizes of fault, hence small faults have a greater proportion of their length below seismic resolution than larger faults. This results in an exponent value <1 on a log:log plot of throw against length (B). By incrementally adding a constant length to all faults within a dataset until a linear relationship is achieved (n=1) the sub-seismic tip length can be determined.

The detailed sub-area of the Penguin C seismic dataset used includes thirty five faults (figures 5.3, 5.4). Although this is a relatively small population size for statistical analysis, the high resolution of the picks results in a relatively low standard deviation. In addition, a coarse interpretation over a broader area (using every tenth seismic trace) has been performed (figures 5.3, 5.5). This includes a larger population size of 108 faults, which, although displaying a significantly higher standard deviation, does show a good correspondence between the exponents of the trendlines with the high resolution interpretation (figure 5.7). This suggests that the high resolution, relatively small population dataset is valid for statistical analysis.

Using a reduced major axis regression (RMA) best fit suggests that an additional 200m of length is required to account for the sub-seismic fault tips and to produce a linear relationship between length and maximum throw (Figure 5.7). This additional sub-seismic length would be incorporated as 100m at each tip.

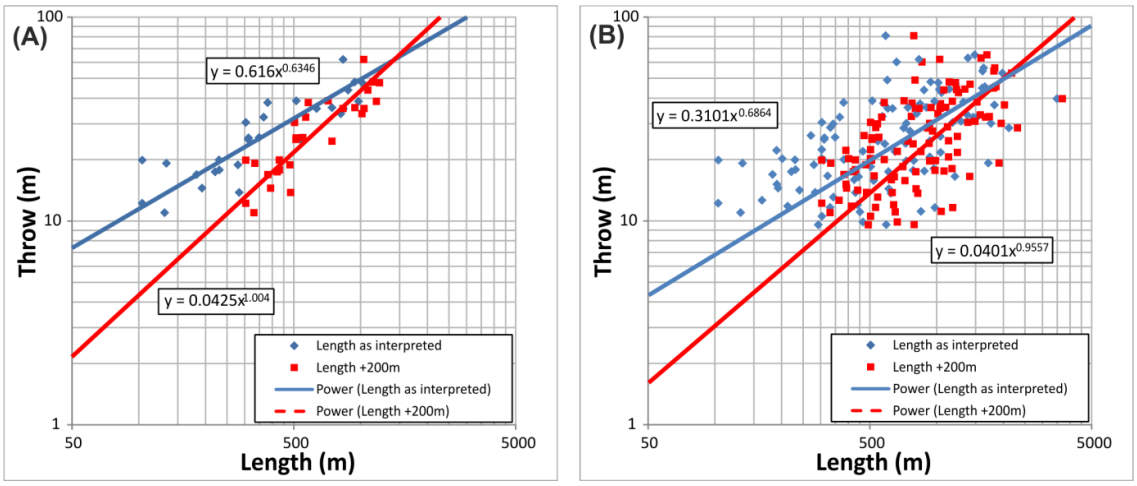

Figure 5.7. Log:log plot of maximum throw against length for the faults as interpreted (diamonds) and with an additional 200m of length (squares). Trendlines are reduced major axis regression (RMA). (A) Detailed fault picks within sub area of field. (B) Lower resolution fault picks for entire field, picked on every 5th trace. The good correlation between the exponents of the two scales of interpretation suggest that although the detailed fault picks represent a relatively small dataset a statistical analysis is still valid.

5.4.1.2 Throw Gradient Approach

Pickering et al (1997) used the average linear throw gradient for a fault network to project fault tips below the limit of seismic resolution, citing significant variation of the throw gradient as the reason for using an average value. Cowie and Shipton (1998) showed that for an individual fault the tip gradient tended towards being linear, but varied as the fault grew. The effect of fault interaction has also been shown to significantly distort throw profiles and throw gradients due to stress field perturbations (Burgmann et al., 1994). Observed throw profiles for interacting faults are hence considerably different to observations for isolated faults (Peacock and Sanderson, 1996, Nicol et al., 1996).

Tip restriction caused by fault interaction results in an increase in the throw gradient where faults are overlapping (Figure 5.8). The implication is that the sub-seismic portion of length will be lower for tip-restricted faults than for unrestricted faults, a hypothesis corroborated by observations from the Penguins dataset interrogated within this chapter (figure 5.9). It is therefore suggested herein that using a single throw gradient to calculate tip length for an entire fault population is geologically unrealistic. Instead a modification is proposed where the average throw is gradient is calculated over a finite length at the seismically resolvable fault tip. This also has the effect of minimising the large fluctuations in throw gradient that have been observed elsewhere (Pickering et al., 1997, Cowie and Shipton, 1998). Using this

approach the sub-seismic length can be calculated for each fault tip individually, so as to account for the effects of tip restriction and throw gradient variability. The length over which the throw gradient is calculated has been defined as 200 m, based upon observations from the Penguins dataset (figure 5.9). This length produces a good balance between smoothing out fluctuations, and accounting for the seismic line spacing (25 m). This value is hence specific to this dataset, and would require adjustment with other dataset dependent on their resolution. The major uncertainty with this approach is defining the vertical resolution of the seismic data. The sub-seismic fault length at each tip is calculated by dividing the vertical resolution by the throw gradient, hence a lower resolution will result in a larger prediction of the sub-seismic length (Figure 5.8).

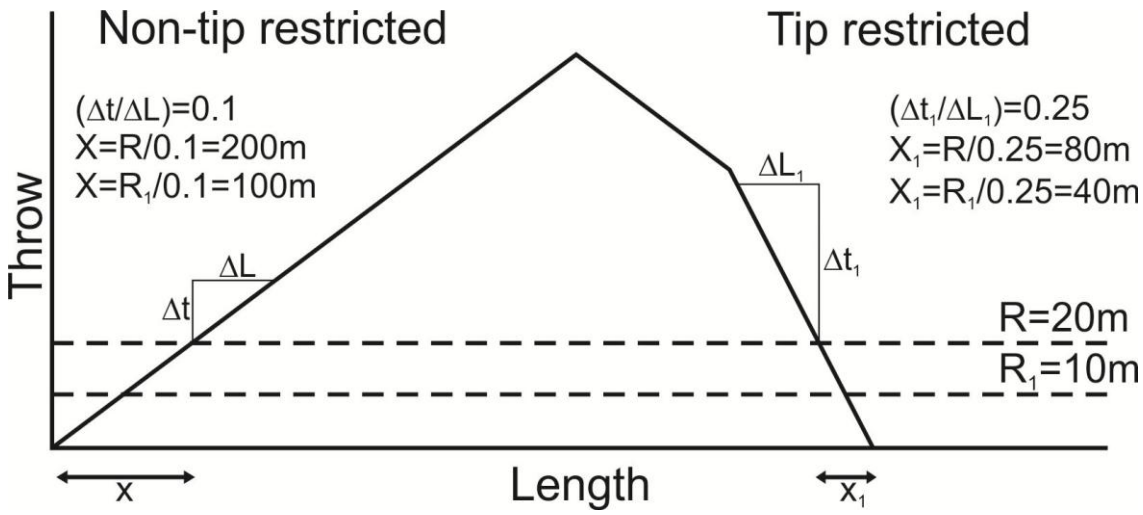

Figure 5.8. Schematic illustrating the influence of throw gradient (Δt/ΔL) and estimated seismic resolution (R) on predicted sub-seismic tip length. The high throw gradients associated with tip restricted faults result in shorter sub-seismic fault tips compared to non-tip restricted faults. Lower estimates of seismic resolution result in longer predicted sub-seismic tip lengths for a given throw gradient. Adapted from concepts illustrated within Rotevatn and Fossen (2011).

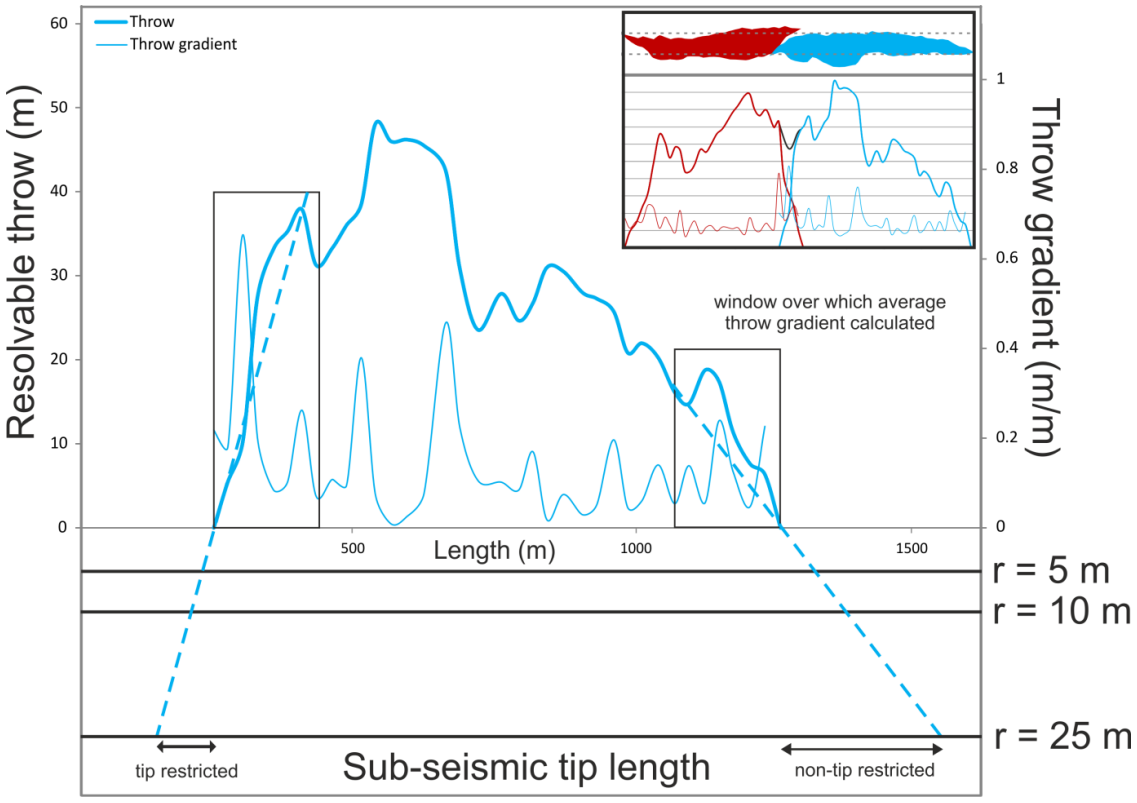

Figure 5.9. Example from Penguins dataset of how the estimate used for the resolution of seismic data influences predictions of sub-seismic fault tip length for both a tip-restricted (left) and non-tip restricted (right) fault tip. Note that throw and length do not use the same scale. Inset shows the location of the fault relative to the adjacent relay zone. Tip restriction at the relay leads to an increased throw gradient, and hence shorter sub-seismic fault tips. Where the fault tip is unrestricted the sub-seismic fault tips are longer. A lower resolution dataset will lead to a larger sub-seismic tip length.

5.4.2 Sub-Seismic Relay Zones

A number of recent studies have used outcrop examples as the basis for studying fluid flow across individual relay zones (Rotevatn et al., 2009a,b; Rotevatn and Fossen, 2011; chapter 7, 8). These contributions refer to single isolated relay zones where the simulation grid has been specifically designed to force fluids to flow across the relays. In hydrocarbon reservoirs the grid boundaries will be controlled by the lateral extent of the reservoir, the location of bounding faults, and the oil water contact. As a result the influence on the fluid flow properties of relay zones is a function of the connectivity of the intra reservoir fault network. Hesthammer and Fossen (2000) recognised that sub-seismic relays can have a major influence on fault seal potential, given that they may allow hydraulic continuity across faults otherwise predicted to be sealing. Abrupt changes in fault strike as well as displacement minima are often indicators

of the presence of relay zones (Hesthammer and Fossen, 2000), which may allow their deterministic inclusion in simulation models. Manzocchi et al (2008a) used the approach of stochastic population of sub-seismic relays to investigate their effect on flow simulation. They found that the relative importance of sub-seismic relays compared to other structural uncertainties increased with the degree of compartmentalisation of a reservoir. Since seismic data is limited in its horizontal resolution due to Fresnel zone effects, it is often not possible to distinguish faults which have a lateral spacing lower than the horizontal resolution of the data. It is therefore plausible that a fault interpreted as a continuous structure may in fact be composed of a number of segments, connected by breached or open relays.

An alternative explored here is to look at the importance of incorporating sub-seismic breaching faults across relay zones that are otherwise interpreted from seismic data as open structures. Depending on the associated fault plane properties and across-fault juxtapositions these structures may significantly influence reservoir compartmentalisation, and as a result represent a non-trivial uncertainty. Although extending the tips of faults may lead to increased fault connectivity where fault strikes are oblique to one another, the same cannot be said for situations where faults overlap but are relatively parallel, hence forming a relay zone. Extending faults in this case simply increases the degree of overlap, resulting in increased flow tortuosity, but not introducing a physical, and potentially sealing or baffling, connection between the faults. An empirical relationship linking seismically observable geometries to relay zone integrity may therefore be a powerful tool. A number of authors (Aydin and Schultz, 1990; Huggins et al., 1995; Long and Imber, 2011) have proposed geometric relationships between the separation and overlap dimensions of relay zones, however no clear relationship exists between overlap:separation ratios and the degree to which a relay zone is soft or hard linked (Gupta and Scholz, 2000; Soliva and Benedicto, 2004).

To attempt to address this, and to develop a predictive tool for assessing sub-seismic relay zone integrity, a dataset has been compiled from sources within the existing literature, including outcrop, LIDAR and seismic data. In addition, data from this study is also included (figure 5.4).

The data compiled includes displacement profiles of relay zones with dimensions such as separation, overlap, and relay throw. From this data variables such as the throw gradient can be derived. These measurements have been used identify a relationship between throw gradient and relay zone integrity. Figure 5.10 shows a cross plot of fault relay zone overlap versus relay throw for 88 open and partially breached relay zones across a range of scales. Relay throw is defined as the cumulative throw of the two overlapping faults defining a relay

zone, measured at the centre of the relay zone (Figure 5.11). It includes only the throw of the overlapping faults, not any component of ductile deformation associated with rotation of the relay zone. Relay zones which are fully breached, i.e. have undergone throw profile re-adjustment, are not included. In seismic data these would be observable as continuous faults, possibly identified by 'jogs' in the fault trace. Whilst potentially being sites of reduced throw, they would not be below the seismic resolution and hence do not contribute to the prediction of sub-seismic linking faults.

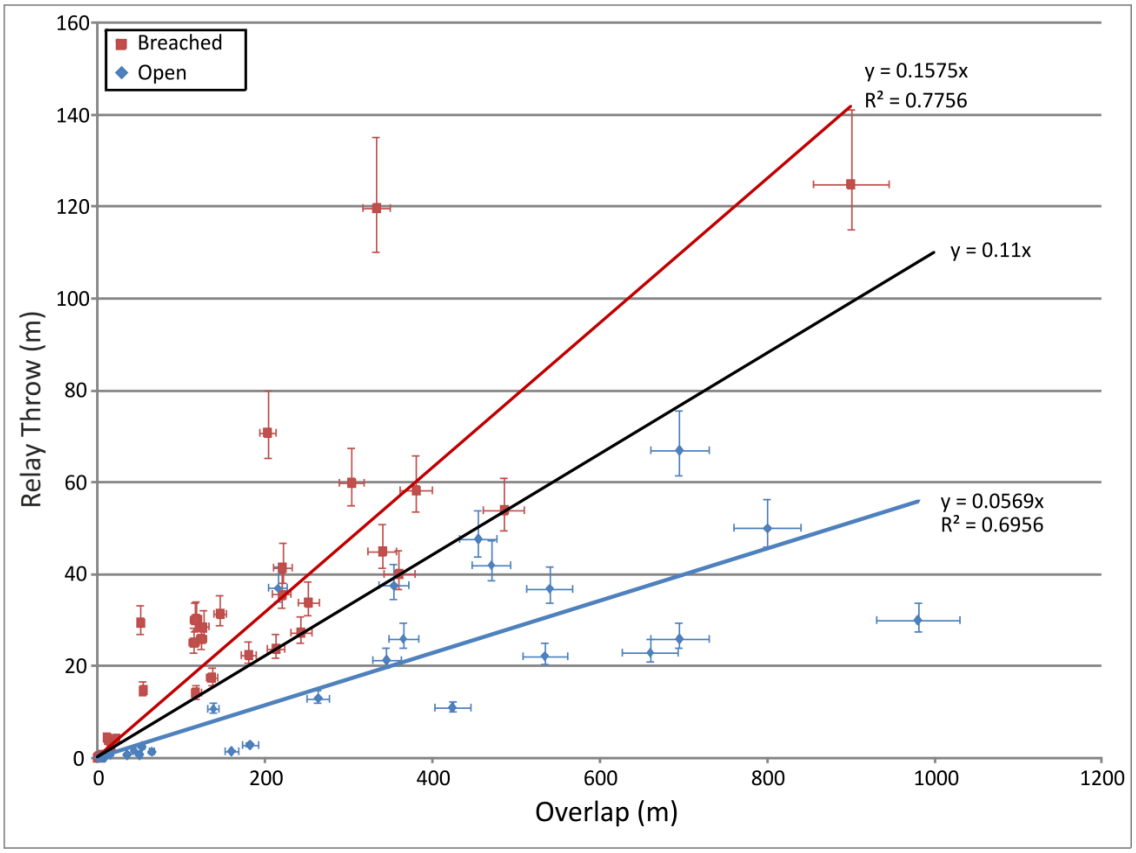

Figure 5.10. Cross plot of cumulative relay throw against overlap for 88 relay zones. Breached and open relays are clearly clustered in separate fields, with low relay throw:overlap ratios indicating intact relays, and high ratios indicating breached relays. 5% error bars are included for fault length measurements, and vertical error bars representing 10° to account for variation in fault dip are also included. Data compiled from; Walsh and Watterson, 1990; Peacock and Sanderson, 1991, 1994; Cowie et al, 1994; Childs et al, 1995; Huggins et al, 1995; Cartwright et al, 1996; Schlische et al, 1996; Willemse et al, 1996; Davies et al, 1997; Bohnenstiehl and Kleinrock, 1999, 2000; Mansfield and Cartwright, 2001; Imber et al, 2004; Soliva and Benedicto, 2004; Taylor et al, 2004; Mirabella et al, 2005; Hus et al, 2006; Rotevatn et al, 2007; Polit et al, 2009; Long, 2011. See figures 5.12, 5.13, 5.14 for examples from this study.

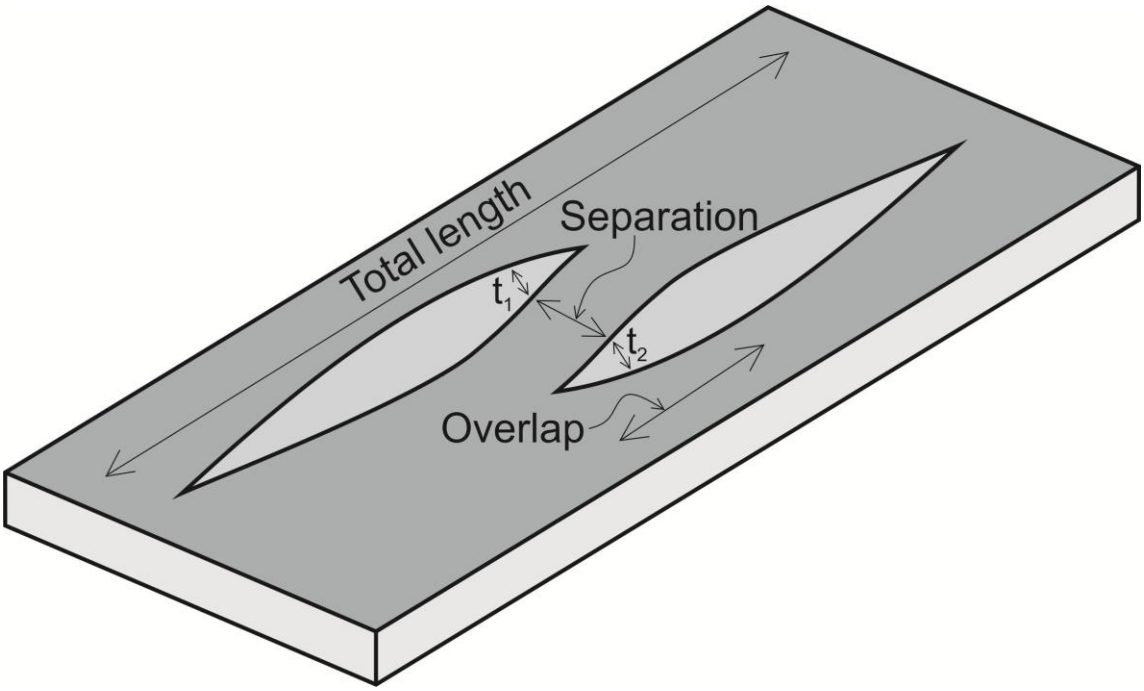

Figure 5.11. Schematic defining the measurements used in the analysis of relay geometry. Interacting relays are defined as having a separation of less than 15% the total length (Gupta and Scholz, 2000). Cumulative relay throw is t1 + t2, and, like separation, is measured at the centre of the relay zone.

Overlap plotted against relay throw is equivalent to the throw gradient where faults are overlapping. Lower throws for a given overlap equate to low throw gradients and a lower likelihood that a relay zone is breached. Using this criteria open and breached relays plot in two distinct fields, although a degree of encroachment is observed. The data used have been selected to minimise the potential for scatter introduced by different methodologies of acquisition, nevertheless some variation is inevitable. We have chosen to use throw rather than displacement since this is representative of the majority of the available data, although dip variations between different faults may introduce some error. Where fault dip data are not available a dip of 60° has been assumed, however error bars accounting for values 10° either side of this are also included. Similarly 5% error bars are included for the measurement of overlap (Figure 5.11). We have defined interacting faults as those whose separation is less than 15% of their combined total length. Overlapping faults separated by greater than 15% of their total length are unlikely to have kinematically interacting stress fields (See discussion section) and will hence have a low probability of being linked by sub-seismic scale breaching faults (Willemse, 1997; Gupta and Scholz, 2000). The overlap dimensions used in figure 5.10 also include fault tips calculated using the local throw gradient (section 5.4.1.2).

A dividing line can be placed at the apex of the fields representing breached and open relay zones on figure 5.10. The confidence of the prediction as to the existence or absence of a breaching fault increases away from this line. This suggests that high ratios of relay throw:Overlap are indicative of breaching faults, whilst low ratios indicate intact relays. The maximum throw of any sub-seismic breaching faults will be by definition equivalent to the resolution of the seismic data, with throw values likely to decrease with proximity to the intact relay field of the plot. Figures 5.12, 5.13, 5.14 show examples of both interacting and non-interacting faults from the Penguin C dataset.

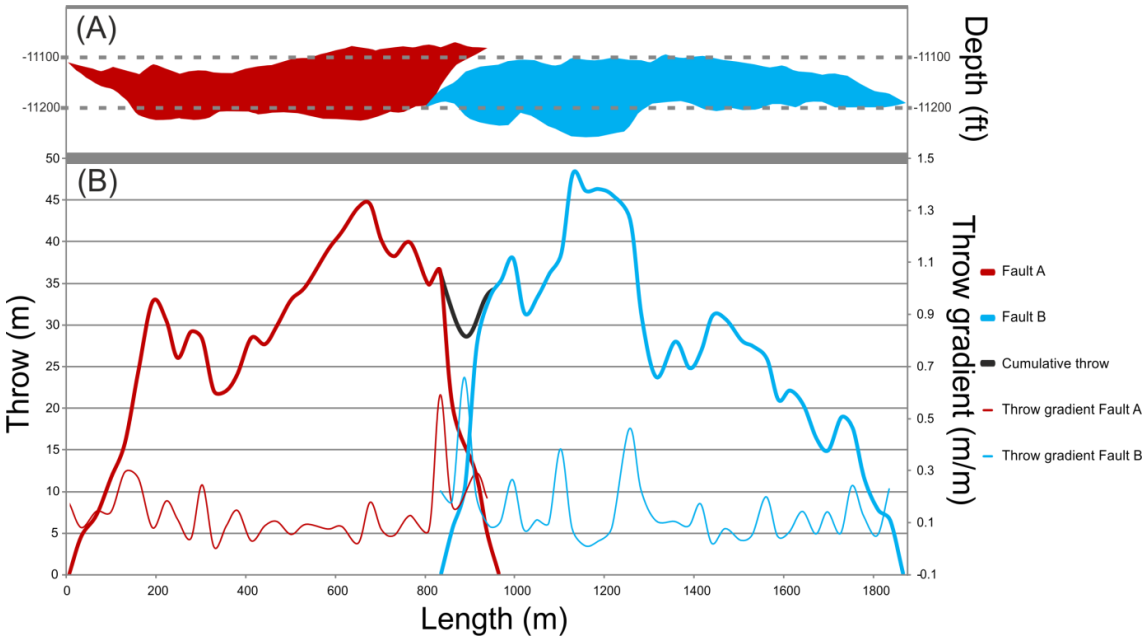

Figure 5.12. (A) Perpendicular view of two interacting faults from our dataset as defined by top reservoir footwall and hangingwall cut-offs. Vertical exaggeration is x3. (B) Throw and throw gradient profiles of the shown faults in (A). An increase in the throw gradient is observed where the faults overlap and are interacting. Fault interaction and tip restriction has resulted in migration of the position of maximum throw on the two fault segments towards the relay zone. The breaching criteria (figure 5.10) suggests that a sub-seismic breaching fault should link the two fault segments.

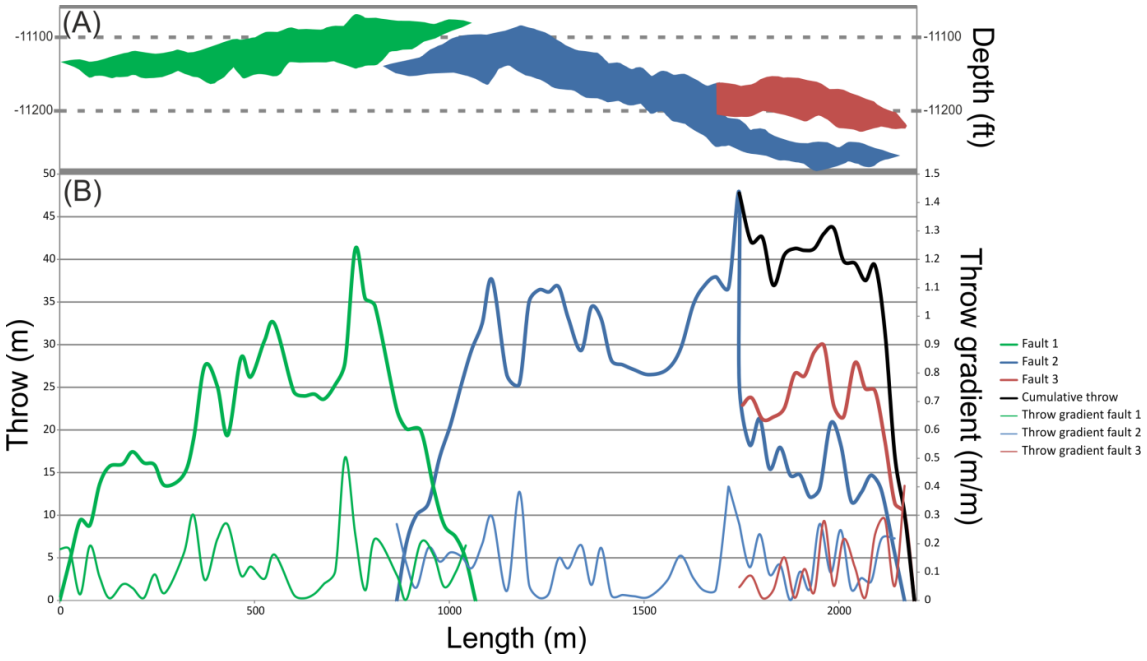

Figure 5.13. Example of interacting fault geometry from the Penguin C dataset. (A) Fault-normal view of fault planes as defined by the top reservoir footwall and hangingwall cut-offs. V.E. = x 3. (B) Throw and throw gradient profiles of the faults in (A). The displacement maxima of faults 1 (green) and 2 (blue) have migrated from the fault centres towards the relay zone where they overlap.

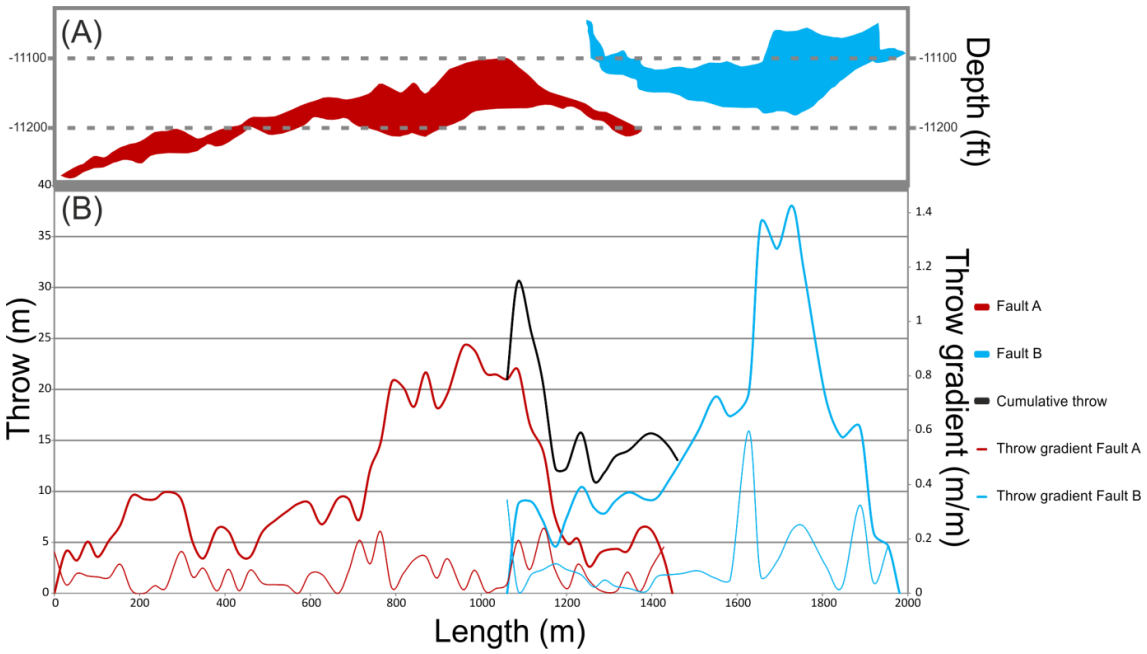

Figure 5.14 (Previous page). An example of a pair of overlapping faults from the Penguins dataset which display limited kinematic interaction. (A) Perpendicular view of fault planes illustrating displacement distribution as defined by top reservoir footwall and hangingwall cut-offs. V.E. = x 3. (B) Throw, and throw gradient profiles. Little to no increase in the throw gradient where the faults overlap suggests limited interaction. The likelihood of a sub-seismic breaching fault being present is hence low. High displacement gradients elsewhere on the faults may however indicate the position of sub-seismic scale splays.

5.5 Effect of Sub-Seismic Structure on Reservoir Segmentation

To assess the impact on reservoir segmentation of incorporating sub-seismic fault tips and breached relay zones, the predictive tools described and developed herein have been applied to the Penguin C dataset. This has been achieved by constructing a series of 3D structural models based upon the original detailed interpretation (figure 5.3). These models have subsequently been modified using the approaches previously described.

Tips have been extended by including the additional length parallel to the average strike of the last observable 200m of the fault, with extended tips being truncated should they intersect other faults. This approach has been used to include sub-seismic tip length based upon statistical analysis (figure 5.15B), and the local throw gradient and seismic resolution (Figure 5.15C, D, E). The resolution of the Penguins dataset is approximately 5m, since this is the minimum throw which can be detected using a range of seismic attributes. However, to illustrate the effect that varying the estimate of seismic resolution (figure 5.6) can have on the predicted sub-seismic fault length we have constructed separate models with assumed resolutions of 5, 10 and 25m respectively. The fault geometries described in figure 5.15B, C and D show realistic throw profiles suggesting all are reasonable estimates for sub-seismic tip length. However, figure 5.15E, based upon a seismic resolution of 25m, displays an unrealistically long fault tip illustrating the errors which can be introduced by utilising too low an estimate for the seismic resolution.

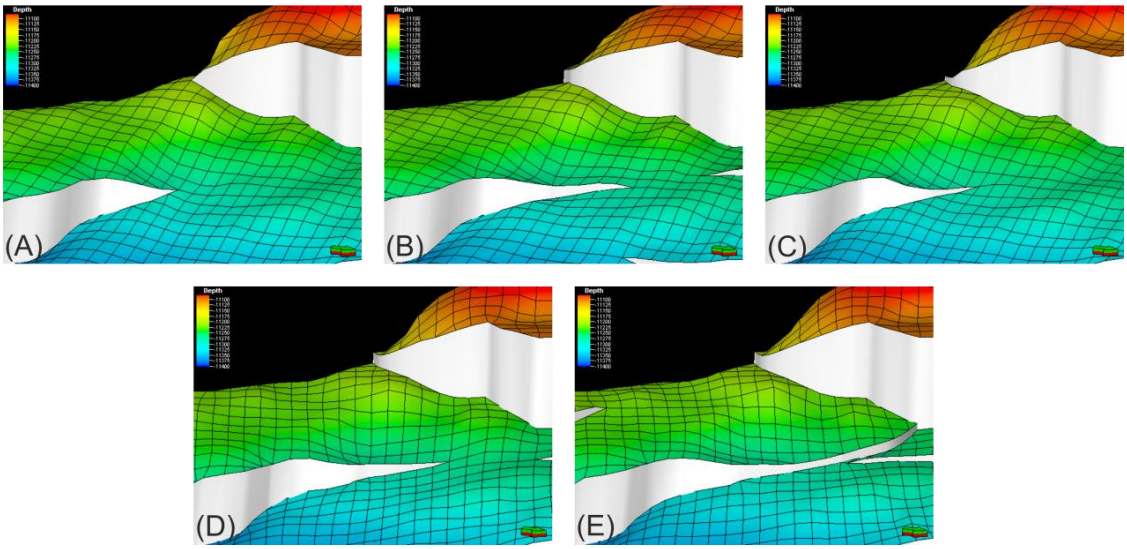

Figure 5.15. 3D oblique views (x5 vertical exaggeration) of the effect of extending fault tip length using the different methodologies described in the text. Fault surfaces are shown in white, whilst the horizon surface is coloured by depth. Grid lines on the surfaces correspond to the cell geometry and have sides of approximately 25m. (A) Interpreted fault tip length based upon seismic interpretation using attribute analysis. B) Fault tips extended using the statistical approach. (C), (D) and (E) Fault tips extended using the displacement gradient in the final 100m of the fault assuming a seismic resolution of 5, 10 and 25m respectively. Over extending the fault tips, as is the case in (E), may lead to unrealistic fault geometries.

A similar approach has been used to incorporate relay-zone breaching faults. Using the predictive criterion developed through this research (figure 5.10) suggests that 17 out of 20 of the interacting relay zones identified in our data are likely to be breached.

Fault connectivity and reservoir segmentation increase significantly when sub-seismic fault tips and breached relay zones are incorporated into the structural model (Figure 5.16). The increase in fault network connectivity and reservoir segmentation due to additional fault tip length alone is relatively limited until very large amounts of additional length are included (e.g. Figure 5.16I). This is a result of the narrow range of strike orientations for this particular fault network. A wider range of strikes would lead to faults being more obliquely orientated relative to one another, with subsequent elongation more likely to result in increased fault connectivity and hence reservoir segmentation. Since the fault network in this case is largely sub-parallel, the inclusion of sub-seismic faults which breach relay zones becomes more significant. When combined with breached relay zones even relatively low amounts of fault tip

extension can lead to a significant increase in the degree of reservoir segmentation (e.g. Figure 5.16E, F).

It must be noted that although the degree of fault network connectivity increases with inclusion of fault tips and breached relays, this does not necessarily imply a greater degree of reservoir compartmentalisation. The sealing or baffling nature of the faults is dependent upon the petrophysical properties of the stratigraphy which has been faulted as well as the burial history. In situations where fault connectivity is not significantly increased the modification of fault geometries may still have an impact on oil production and sweep efficiency due to alteration of reservoir juxtapositions and fluid flow pathways.

Figure 5.16 (Next page). Maps showing the effect of incorporating sub-seismic fault tips and relays on the connectivity of the fault network. Breached relays have been incorporated according to the criteria determined in figure 4. Colours represent isolated fault bound compartments. (A) As interpreted. (B) As interpreted, with the addition of breached relays according to the breaching criteria in figure 4. (C) Statistically elongated fault tips, open relays. (D) Statistically elongated fault tips, breached relays. (E) Elongated fault tips based on throw gradient and seismic resolution of 5m, open relays. (F) As (E), but with breached relays. (G) Elongated fault tips based on throw gradient and seismic resolution of 10m, open relays. (H) As (G), but with breached relays. (I) Elongated fault tips based on throw gradient and seismic resolution of 25m, open relays. (J) As (I), but with breached relays.

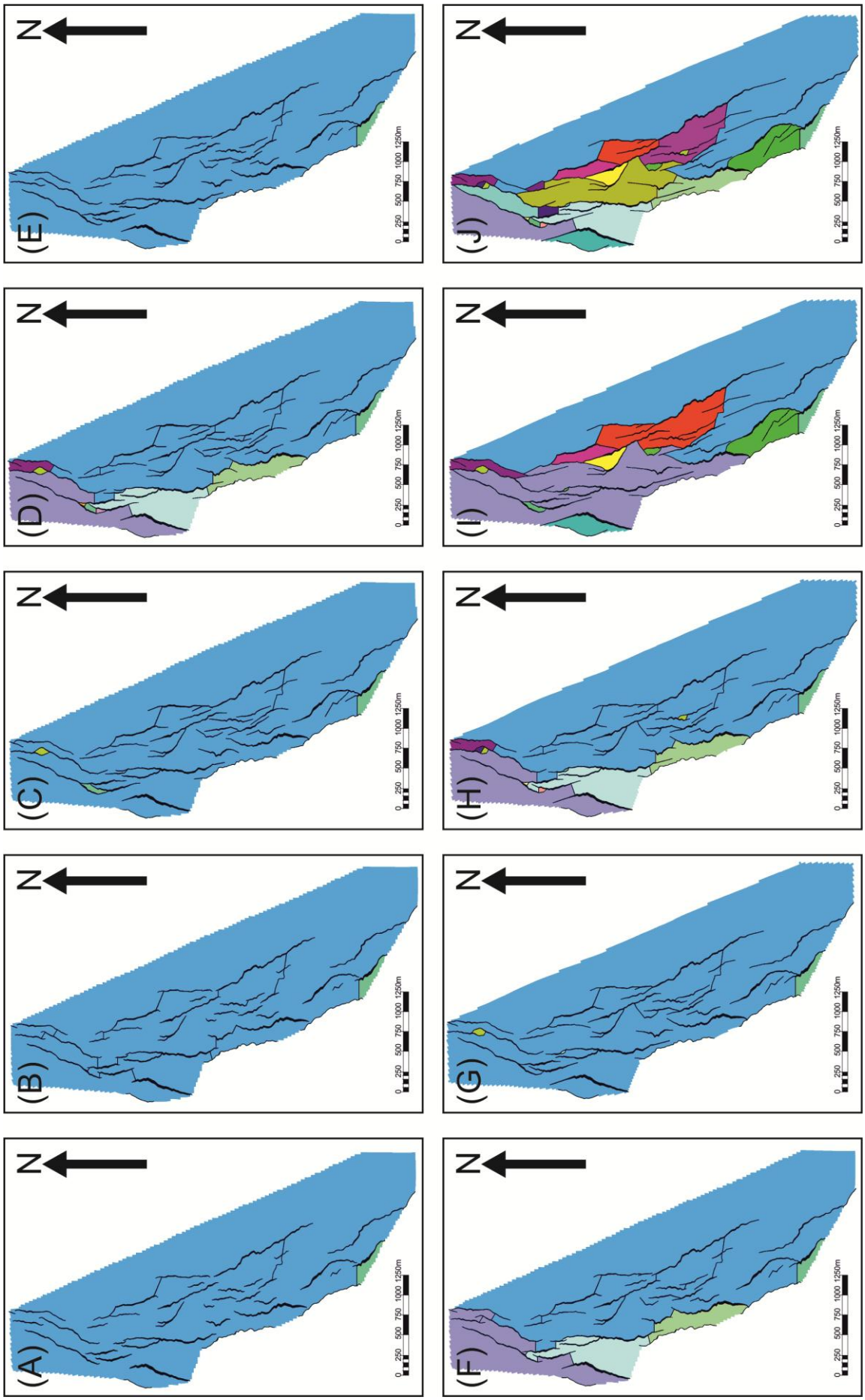
(A)
(B)
(C)
(D)
(E)
(F)
(G)
(H)
(I)
(J)
N
0 250 500 750 1000 1250m

5.6 Discussion

5.6.1 Uncertainty with Statistical Fault Tip Length Prediction

Although using the statistical approach to estimate sub-seismic tip lengths is relatively simple, it has numerous associated uncertainties. Even within a single dataset there tends to be a relatively large scatter when fault length and maximum throw are cross-plotted. This leads to low correlation trend lines and hence a high degree of uncertainty in fault tip length predictions. This scatter arises from a number of sources. As with all interpretations a large degree of uncertainty is associated with the fault picks made by the interpreter, as well as the method of interpretation. Seismic surface and volume attributes such as dip, coherency and amplitude allow smaller fault offsets to be detected than are identifiable in the section view alone (Townsend et al., 1998; Jolley et al., 2007). If not all faults in a dataset are interpreted using the same or similar methodologies then unnecessary spread will be introduced into fault length measurements, with the effect magnified where multiple interpreters have worked on a dataset. In general it is not standard practise to interpret every fault on every available inline, crossline or arbitrary line. Line spacing in modern 3D seismic datasets may be 12.5 to 25m. The potential uncertainty in the position of the imaged fault tip will therefore be the line spacing multiplied by the number of lines between picks.

The vertical position of a faulted horizon relative to a fault can strongly influence the proportion of a fault tip which is below seismic resolution, and hence the observed t_{max}:L ratio (Walsh and Watterson, 1988). The sub-seismic tip length increases as the angle between a faulted horizon and the displacement contours decreases (Figure 5.17). This effect is especially prominent for high aspect ratio faults (fault length>fault height, Willemse et al., 1996). As a result horizons located away from the vertical centre of a fault will have a larger sub-seismic length than those located at the centre of a fault. The aspect ratio of a fault is to some extent controlled by vertical variations in the mechanical properties of the stratigraphy (Schultz and Fossen, 2002; Long and Imber, 2011). A fault whose vertical extent is mechanically constrained will tend to have a high aspect ratio compared to a non-constrained fault, leading to a greater increase of the sub-seismic tip length with distance from the fault centre. Since it is unlikely that any given seismic horizon will be located at the same vertical position relative to all faults within a population, the resulting variation in observed t_{max}:L ratio will introduce additional scatter into a dataset.

The most important factor to introduce scatter to plots of length versus maximum throw is the process of fault growth through segment linkage (Cartwright et al., 1995; Pickering et al., 1997). The transfer of displacement between fault segments via relay ramps and connecting

faults (Larsen, 1988) is observed to distort both the t_{max}:L ratio of the resulting linked fault, and its individual components (Peacock and Sanderson, 1991, 1994; Cowie et al., 2000). A linked fault may have a lesser or greater throw relative to the mean for a particular dataset depending on whether a physical linkage develops early (Cartwright et al., 1995) or late (Peacock and Sanderson, 1994; Gupta and Scholz, 2000). In the case of early linkage faults experience limited kinematic interaction and associated profile re-adjustment prior to physical linkage occurring. Immediately following linkage of two or more individual fault segments the resulting fault will have a low throw relative to its length. Post linkage accumulation of throw results in readjustment of the throw profile. In contrast, late linking faults (Peacock and Sanderson, 1994; Gupta and Scholz, 2000) experience kinematic interaction prior to physical linkage occurring (Figure 5.18). As two or more segments propagate and overlap to form a relay zone their respective stress fields begin to interact (Gupta et al., 1998; Gupta and Scholz, 2000). This interaction results in modification of the throw profiles of the individual segments, with migration of the position of maximum throw towards relay zones (Figures 5.18, 5.12). Throw gradients at interacting fault tips increase and the t_{max}:L ratio for the individual segments also increases. Stress becomes concentrated in relay zones with physical linkage eventually ensuing followed by re-adjustment of the profile of the resultant single fault.

In seismic data resolution issues complicate the situation somewhat. Lateral resolution may lead to difficulties in distinguishing closely spaced, yet separate, structures (Figure 5.18). As a result faults picked as a single structure may in fact be composed of two or more faults, leading to the t_{max}:L ratio being underestimated. Conversely displacement minima along strike of linked faults may incorrectly be interpreted as open relays between separate fault segments. If this occurs measured t_{max}:L ratios will tend to be overestimated.

The model for rift evolution proposed by Cowie et al (2000) suggests that fault activity is to some extent relatively transient, with localisation of deformation onto larger faults leading to abandonment of smaller faults (Ackermann and Schlische, 1997; Willemse, 1997). These abandoned faults will display a range of stages of linkage. Any natural dataset (e.g. outcrop, seismic) represents an effectively instantaneous snapshot of a dynamic system. When this is considered with models for fault and rift evolution it is inevitable that datasets will display a range of t_{max}:L ratios, with statistical methods for estimating fault dimensions containing much uncertainty. As a consequence assigning a single ‘n’ value to a dataset to estimate sub-seismic fault tip length is geologically non-ideal.

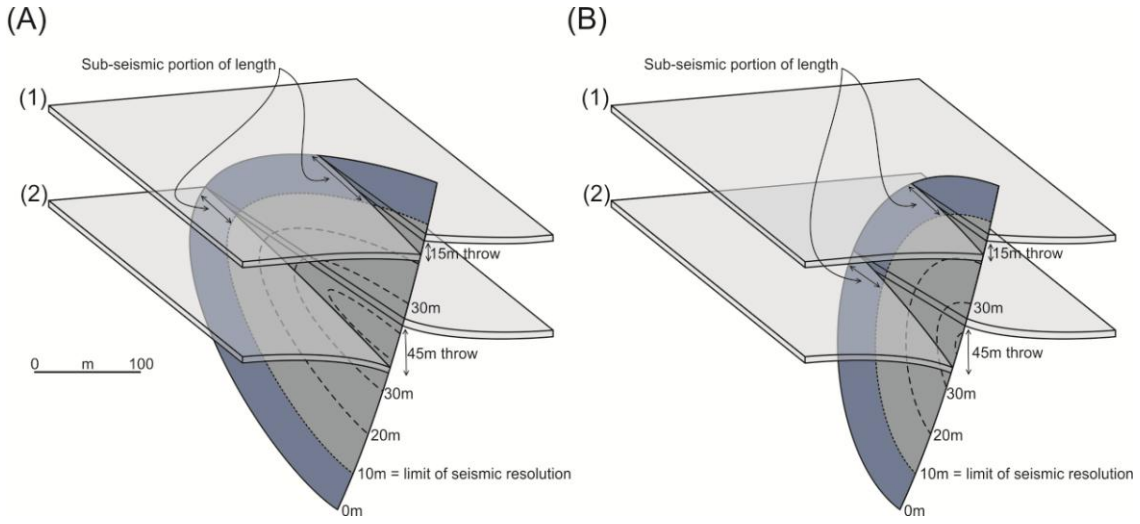

Figure 5.17. Schematic diagram of half fault plains for high (A) and low (B) aspect ratio faults illustrating the difference that the position of a horizon relative to a fault has on measured tmax:L values. Horizon (1) is located towards the top of the fault, intersecting the throw contours at an oblique angle, whilst horizon (2) is located at the fault centre and is perpendicular to the throw contours. The sub-seismic tip length is greater for horizon (1) for both faults, however this effect is larger for the high aspect ratio fault (A). Modified after (Gauthier and Lake, 1993).

The throw gradient may to some extent control the stress concentration within a relay zone, however the yield strength of the medium influences at what stress brittle strain occurs. It is likely therefore that there is a strong bulk mechanical control on when a relay zone becomes breached, itself influenced by factors such as lithology, porosity, cementation, confining pressure at time of faulting, etc. We do not however have sufficient data here to produce meaningful correlations of these variables. Other factors leading to scatter may include the regional extension rate, local strain rate, and the presence of any pre-existing fabrics or discontinuities within the rock mass.

Using the local displacement gradients of individual faults to calculate sub-seismic tip lengths accounts for many of the uncertainties introduced by using a statistical analysis of an entire fault network, and is our preferred methodology. The displacement gradient approach is not however without its own uncertainties, primarily in the form of applying the correct seismic resolution. A lower resolution will result in the calculation of longer tip lengths for a given displacement gradient (Figure 5.15). Jolley et al (2007) showed that the minimum throw which can be detected is often lower than the 1/4λ resolution which is often been invoked. The value for the minimum detectable throw will depend not only on the geophysical properties of the

data, but also on the attributes used for fault detection and interpretation. It is therefore logical that the minimum detectable throw, as defined by careful analysis of a range of seismic attributes, rather than a 'rule of thumb' value is used when determining the length of sub-seismic fault tips.

Depending on the associated fault plane properties and cross fault juxtapositions, breached relay zones may significantly influence reservoir compartmentalisation, and as a result represent a non-trivial uncertainty. Although extending the tips of faults may lead to increased fault connectivity where fault strikes are oblique to one another, the same cannot be said for situations where faults overlap but are relatively parallel, forming a relay zone. Extending faults in this case simply increases the degree of overlap, resulting in increased flow tortuosity, but not introducing a physical, and potentially sealing or baffling, connection between the faults. Empirical prediction of the occurrence of sub-seismic scale faults which breach relay zones used in combination with fault tip length calculations provides a clearer prediction of reservoir segmentation.

5.6.2 Fault Growth Kinematics

Here the methods developed herein of using the throw gradient to predict sub-seismic fault tips and relay-breaching faults are reconciled with theoretical processes of fault growth kinematics. Normal fault rupturing is a plastic strain response to extensional stress, with lateral propagation of a fault occurring when the stress concentration at its tips exceeds the yield strength of the rock (Cowie and Scholz, 1992b). Following rupture the stress in the footwall and hangingwall of a fault is relaxed, whilst stress remains concentrated at the fault tips. The magnitude of the stress relaxation decreases away from the fault (Figure 5.18). For an overlapping fault to laterally propagate into an area of stress relaxation, the stress concentration at its tip must exceed the yield strength of the rock plus the value of the stress relaxation (Gupta and Scholz, 2000). If the yield strength is constant, the magnitude of the stress relaxation is the controlling factor upon how far an overlapping fault can propagate. The position at which propagation can no longer take place occurs at the value of stress relaxation termed the critical stress drop contour, with fault tips becoming 'pinned' to this contour. Increasing overlap and decreasing separation lead to increased interaction of the elastic stress fields, limiting lateral fault propagation within those stress fields to the position of the critical stress drop contour. To some extent therefore, the dimensions of fault overlap and separation are controlled by the location of the critical stress drop contour (Gupta and Scholz, 2000), although additional factors such as fault aspect ratio (Willemse, 1997) and the mechanical properties of the stratigraphy (Long and Imber, 2011) also have an influence.

If extension continues following overlapping fault tips becoming ‘pinned’ to the critical stress drop contour, positive throw anomalies arise in the overlap zone (Figure 5.18) (Gupta and Scholz, 2000). This localised increase in throw results in increased throw gradients, hence overlapping faults tend to have shorter sub-seismic tip lengths than isolated faults. The increased throw gradients lead to concentration of stress at the fault tips and within the relay zone. As extension continues, and throw gradients continue to steepen, the stress concentration within the relay zone will begin to exceed the yield strength of the rock, at which point a physical linkage will begin to form. This will tend to be at the position of maximum curvature of the relay ramp, usually at its base, top, or both. We can hence infer that the throw gradient is indicative as to the degree of physical linkage within a relay zone. In the case where linking faults are below the limit of seismic resolution this knowledge can be used to predict their presence (Figure 5.10).

A deficiency with this model of fault growth is that it assumes that faults have grown as separate structures (e.g. Cartwright et al., 2005) rather than as a coherent system interacting from initiation (Walsh et al., 2003).

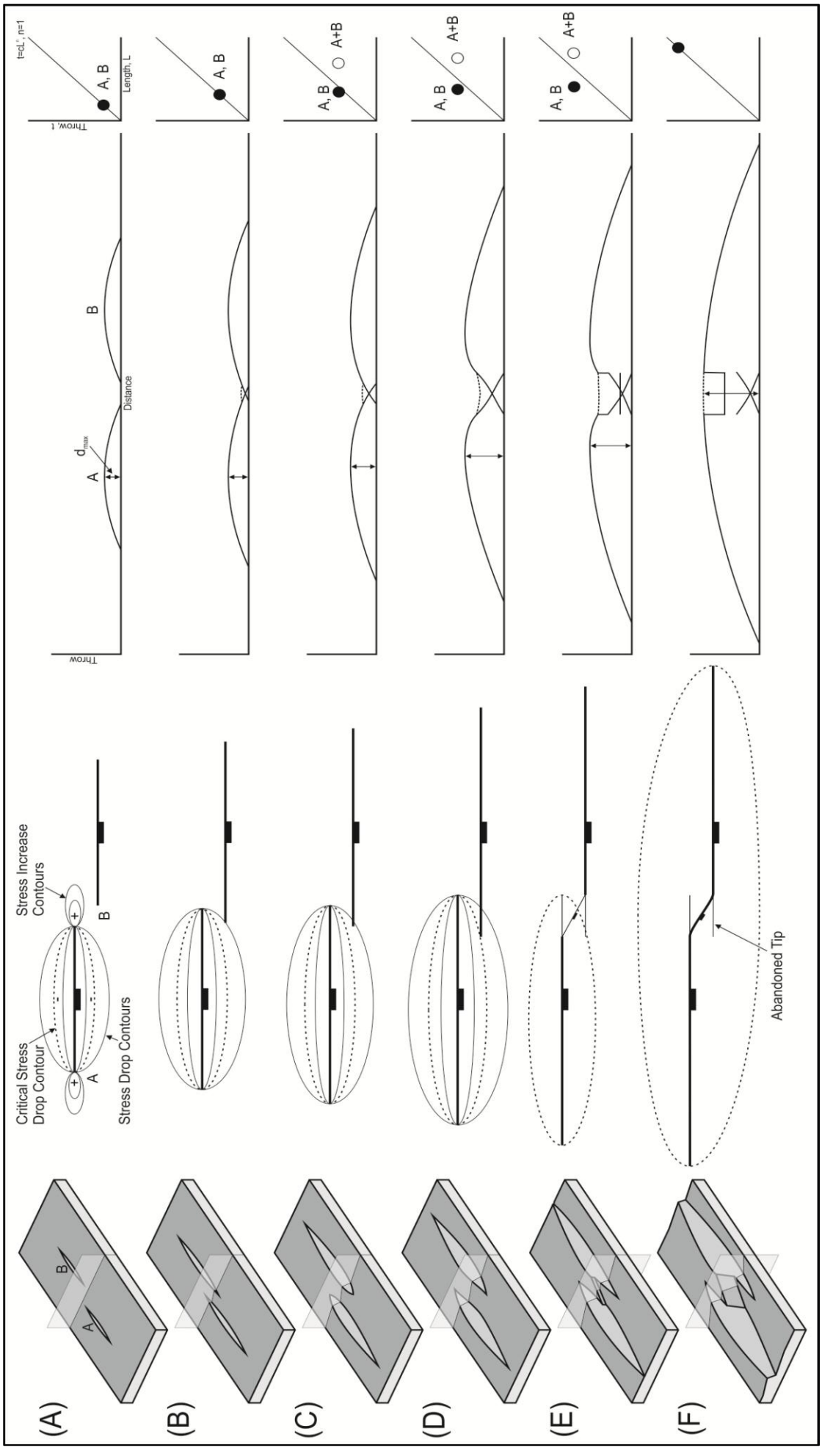
(A)
(B)
(C)
(D)
(E)
(F)
A
B
Stress Increase Contours
Critical Stress Drop Contour
Stress Drop Contours
Abandoned Tip
Throw
Distance
Throw, t
Length, L
t=dmax, n=1
A, B
A+B

Figure 5.18 (Previous page). Schematic diagrams describing the evolution of a relay zone in terms of stress field interaction, throw profile and throw:length plots. (A) Underlapping faults have little to no stress field interaction. They have symmetrical throw profiles, and plot in the same position on a throw:length plot. (B) At the initial stages of overlap the stress fields do not interact sufficiently to effect the fault growth. (C) Increasing overlap leads to interaction with the critical stress drop contour (Gupta and Scholz, 2000). This leads to tip restriction and migration of the position of maximum throw. Depending on whether the faults are defined as separate structures or as a single interacting structure determines where they plot on a throw:length plot. (D) Extension continues as does throw accumulation, however stress field interaction prevents lateral tip propagation, hence the throw gradient within the relay zone increases and the throw profiles become progressively more asymmetrical. (E) Above a critical throw gradient the yield strength of the rock is overcome, and a breaching fault initiates. The position of maximum throw continues to migrate towards the centre of the linked fault pair. If the faults are defined as being separate, they will appear as short, high throw structures on a throw:length plot. Conversely if they are defined as a single structure they will appear to be a longer, low throw structure. Defining interacting faults as single or separate structures is a major cause of introducing scatter into fault populations. (F) Post linkage profile re-adjustment occurs, with the fault now behaving as a single structure. The throw profile is equivalent to the initially isolated faults in (A), with the throw:length plotting along the same relationship.

Figure 5.19 schematically illustrates the progression of a relay from its initial underlapping stage, through early interaction and breaching to a final, fully breached, stage in terms of relay throw:overlap ratios. The position of an individual relay zone on this plot is determined by its initial overlap and separation dimensions, which are controlled by the spacing of the individual, pre-linkage fault segments. Closely spaced fault segments lead to low separations and will hence begin to interact at low overlaps. In this situation a relatively low relay throw can therefore result in a steep enough throw gradient to stimulate the propagation of a breaching fault. Conversely more widely separated fault segments will begin to interact at larger overlap dimensions leading to a greater amount of relay throw being required to achieve a throw gradient sufficient to induce breaching. The variation seen in the dimensions of the relay zones in figure 5.10 can therefore be interpreted as being a function of the initial separation of the pre-linkage fault segments.

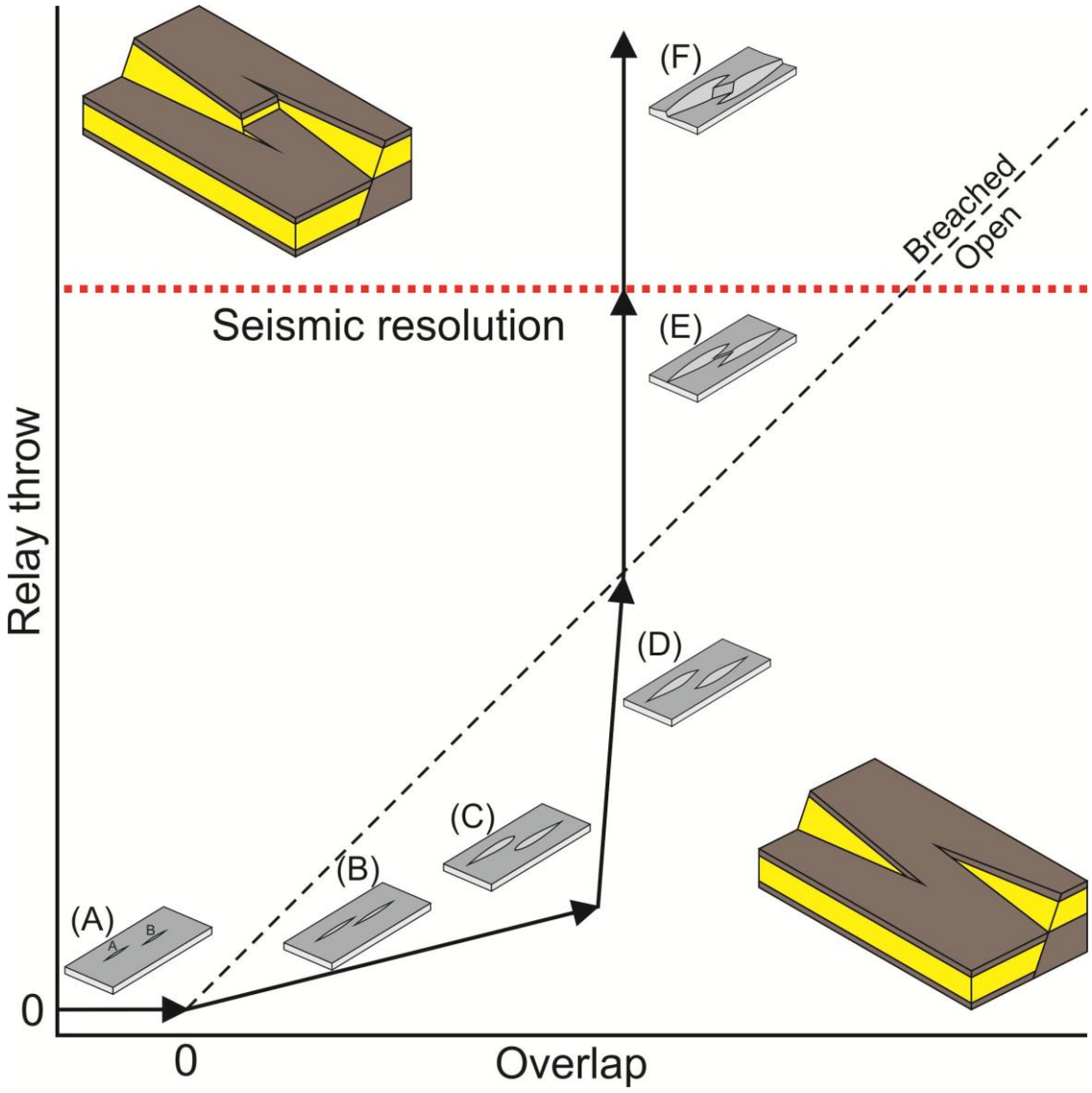

Figure 5.19. Schematic plot of relay zone evolution relative to relay throw and overlap. Labelling is equivalent to that in figure 6. (A) Initially underlapping faults have zero overlap and zero cumulative relay throw. (B) As faults overlap, the relay throw begins to increase. (C) As the critical stress drop contours are intersected the amount of overlap can no longer significantly increase. (D) A small increase in overlap is accompanied by a large increase in relay throw as throw gradients steepen due to the interaction of stress fields. (E) The relay zone becomes breached, with relay throw:overlap ratios increasing into the breached field. (F) Profile re-adjustment leads to throw accumulation on the breaching fault which eventually results in it becoming visible in seismic data.

If our criterion is applied to a seismic dataset where sub-seismic tip length has not been accounted for then the overlap length will be lower. Enhanced tip restriction and higher throw

gradients at breached relays will lead to a lower proportion of their length being below seismic resolution compared to open relays. This results in an increase in the gradient of the line separating the breached and open fields (Figure 5.20), as well as the two fields becoming less distinguishable at low overlaps. Sub-seismic tips should therefore be included in the overlap dimension used to maximise the accuracy of the criterion.

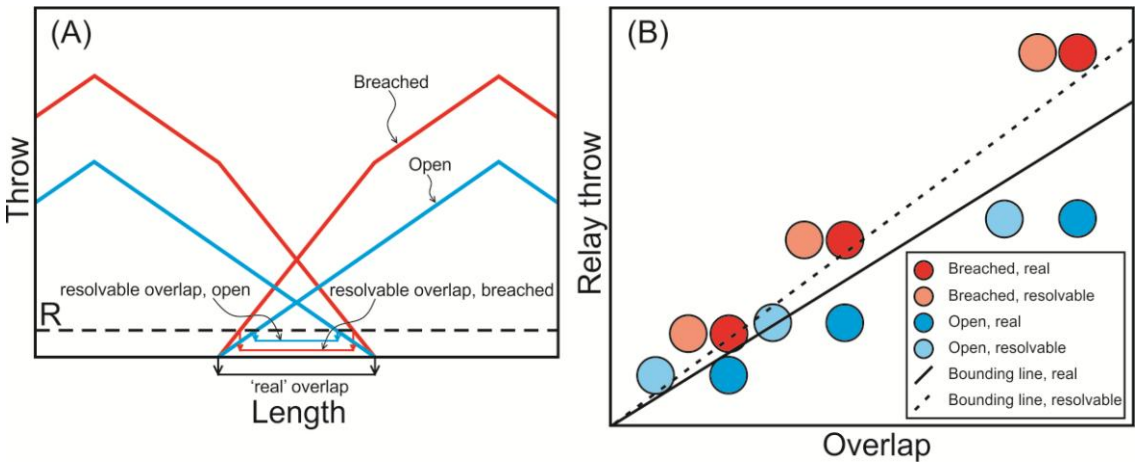

Figure 5.20. (A) Throw against length for open and breached relay zones of equal overlap dimensions. R=limit of seismic resolution. The increase in displacement gradient as a result of tip restriction leads to larger seismically resolvable overlap for the breached relay compared to the open relay. (B) The disparity between the 'real' and resolvable overlap dimensions for open and breached relay zones leads to an increase in the gradient of the line separating breached and open relays on a plot of relay throw against overlap.

5.7 Conclusions

A detailed horizon and fault interpretation of a subset of a 3D seismic dataset from the northern North Sea has been performed. The length of sub-seismic fault tips has been estimated using both a statistical analysis of the fault network as a whole, and by using the geometric characteristics of each fault individually.

A criterion for determining the integrity of relay zones where breaching faults are below seismic resolution has been developed. The criterion is based upon work from this study and from numerous published datasets and uses measurements easily obtainable from 3D seismic data. It is reconcilable with accepted theories for fault growth and linkage. The breaching criterion has been combined with estimates for sub-seismic tip length to estimate the impact

on fault network connectivity and resulting segmentation of the reservoir. The following conclusions can be drawn from this work;

• Using a statistical approach for estimating sub-seismic fault tip length does not account for numerous geological and data-related uncertainties, and may introduce additional statistical uncertainty.

• The local displacement gradient adjacent to a fault tip, combined with an accurate assessment of the seismic resolution, provides more geologically realistic estimates of sub-seismic fault tip length as well as accounting for tip restriction caused by fault interaction.

• The displacement gradient at fault tips can be used to estimate the integrity of relay ramps separating overlapping faults where the throw of a breaching fault (if present) is below the scale of seismic resolution. This can be expressed as a plot of overlap versus cumulative relay throw. Low relay throw to overlap ratios are indicative of a higher likelihood of relays being intact, whilst higher ratios suggest the presence of breaching faults.

•Where faults have sub-parallel strikes, small increases in length alone do not lead to significant increases in connectivity and reservoir segmentation. If a lower seismic resolution is inferred, sub-seismic fault tip lengths will increase for a given displacement gradient leading to a greater degree of fault network connectivity and hence reservoir segmentation. It is therefore critical that seismic resolution is defined correctly.

•Small scale faults which breach relay ramps pose a comparatively greater risk for reservoir segmentation than sub-seismic fault tips in situations where the range in fault strikes is relatively restricted.

Chapter 6

The Influence of Sub-Seismic Fault Tips and Breached Relay Zones on Simulated Oil Production

6.1 Abstract

The previous chapter examined different approaches for predicting and incorporating sub-seismic fault tips and breached relay zones within reservoir models. Here, the effect of this sub-seismic structure on oil production is tested by running a series of reservoir simulations. The results of these simulations suggests that although incorporating sub-seismic structure may lead to additional reservoir segmentation, this does not necessarily equate to reservoir compartmentalisation in the form of non-permeable faults. Indeed, increasing fault tip length may enhance the oil sweep pattern of a reservoir and hence aid recovery. Including sub-seismic structure seems to have a greater impact on water production rates and volumes than on oil production, an observation which is economically beneficial.

6.2 Introduction and Aims

Characterising how faults influence fluid flow in the sub-surface is a major uncertainty during hydrocarbon exploration and production. Correctly incorporating their geometric and petrophysical properties within reservoir and simulation models is therefore highly important (Jolley et al., 2007; Manzocchi et al., 2008). Fault-normal hydrocarbon flow is influenced by juxtaposition across faults of stratigraphic units with dissimilar petrophysical properties, and by the petrophysical properties of any fault rocks which may be developed (Yielding et al., 1997; Knipe et al., 1998; Sperrevik et al., 2002). Both the distribution of cross-fault juxtapositions and of fault rock petrophysical properties are, to varying extents, controlled by fault geometry. Limitations on the resolution of seismic data prevent fault geometries from being fully imaged in the subsurface. The faults, and parts of faults, which cannot be imaged are termed sub-seismic. The aims of this chapter are to investigate the effects on simulated fluid flow in the subsurface of two key aspects of sub-seismic fault geometry, namely sub-seismic fault tips and faults which breach relay ramps. The dataset used in chapter 5, for a subset of the Penguins oilfield, is employed as a basis for a series of geological and simulation models.

6.2.1 Fault growth and linkage

Over the last 20 years significant advances have been made in understanding the evolution of faults in rift systems. It is widely recognised that extensional faults evolve through a process of

initiation, growth, interaction, linkage and continued growth (Peacock & Sanderson 1994; Trudgill & Cartwright, 1994; Cartwright et al., 1995, 1996; Childs et al., 1995; Cowie et al., 2000; Gupta & Scholz, 2000; Walsh et al., 2003). Linkage of overlapping fault segments occurs at relay zones (Peacock & Sanderson, 1991). Initially, overlapping faults will be separated by a volume of intact rock termed a relay ramp (Larsen, 1988). As extension and hence displacement continues, the relay ramp becomes progressively rotated. This increasing rotation may be accompanied by minor brittle strain within the ramp in the form of deformation bands, fractures and small scale faults (Ferrill & Morris 2001; Rotevatn et al., 2007). Eventually the relay ramp becomes breached, with strain being accommodated in the form of a discrete fault (or faults) which propagates to link the two initially separate fault segments (peacock & Sanderson, 1991; Cartwright et al., 1995, 1996). Following linkage the overlapping tips may become abandoned with the now connected fault segments behaving as a continuous single structure. The maturity of linkage of a fault set depends upon the position of observation (Walsh et al., 2003). For example a soft linked relay may be observed at one horizon, although may be hard linked at depth, indicating that the growth of the fault set was coherent rather than coincidental (Walsh et al., 2002, 2003).

6.2.2 Faults in Seismic Data

The steep dip of faults generally precludes their direct imaging using seismic reflection surveys, therefore the primary methodology for identifying seismic scale faults is the observation of offset reflectors. Seismic reflection theory predicts that the minimum resolvable vertical separation of two reflectors is approximately one quarter of the wavelength. This value is also often used as an approximation as to the minimum fault offset which can be resolved, however the use of seismic attributes such as amplitude, dip and coherency can greatly improve upon this (Townsend et al., 1998; Jolley et al., 2007). For example, Jolley et al (2007) found that amplitude reduction in the vicinity of faults, caused by loss of reflected seismic energy due to diffractions, allowed fault detection down to 1/8 λ. Despite the use of increasingly sophisticated seismic attribute analysis the minimum resolvable fault offsets are still limited by the resolution of the seismic data, and specifically its wavelength at the faulted horizon. The wavelength is the quotient of the velocity by the frequency. Velocity will tend to increase with density (and hence depth), whilst preferential attenuation of higher frequencies will reduce the dominant frequency of a seismic wavelet with increasing path length. As a result the wavelength increases and the resolution decreases with depth. If the depth of the area of interest is known, a seismic survey can be tailored to maximise the resolution at that depth by altering the survey design and bandwidth of the input wavelet, however many faults will still remain undetectable, and are hence termed as being of sub-seismic scale.

Notwithstanding the increased use of seismic attributes in fault detection, the process of seismic interpretation remains largely subjective (e.g. Bond et al., 2012). Caution must therefore be exercised when comparing the resolution of a dataset and the resolution of an interpretation of that dataset. Different seismic interpreters will interpret the same fault geometries in different ways, with corresponding variations in the minimum offsets which are identified. As a result, the maximum resolution of a seismic dataset may not coincide with the resolution which is interpreted and modelled.

The fault geometries established in chapter 5 using the pre-stack depth migrated (PSDM) 3D seismic survey covering the Penguins oilfield are used within this chapter to generate a series of geological models populated with petrophysical properties derived from local well data. Fluid flow simulations are then performed to investigate the effect of sub-seismic fault tips and breached relay zones on hydrocarbon recovery.

6.2.3 Sub-Seismic Fault Tips

The displacement across a fault decreases from a maximum close to the fault centre to zero at the fault tips (Barnett et al., 1987). In seismic datasets displacements below the limit of resolution will not be imaged, leading to the fault tips not being identifiable. As a consequence the interpreted length of faults is often significantly less than their actual length (Figure 6.1). This may have significant implications for the validity of geological and simulation models built directly from seismic interpretations. Incorporating sub-seismic fault tips in reservoir models may lead to an increase in modelled fault connectivity. Conversely, not accounting for their presence may lead to an underestimate in reservoir segmentation (Pickering et al., 1997; Rotevatn et al., 2011). Depending on the cross-fault fluid flow properties, a more connected fault network may result in increased reservoir compartmentalisation, a considerable consideration when planning well locations.

Two methodologies for predicting and incorporating sub-seismic fault tips into reservoir models are herein compared. The first is a statistical approach based upon the properties of a fault population as a whole, whilst the second method uses a geometric approach based upon the dimensions of individual faults. For a full description of the methodologies and their limitations see chapter 5.

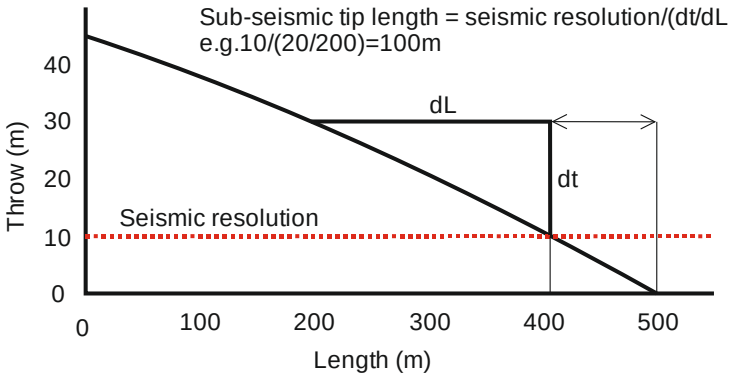

Figure 6.1 (Previous page). Length-throw plot illustrating how the displacement gradient and seismic resolution can be used to estimate sub-seismic fault tip length.

6.2.4 Relay Ramps

The likelihood of a sub-seismic breaching fault being present across a relay zone observable in a seismic dataset can be constrained by the throw gradient of the two overlapping faults (chapter 5). High throw gradients tend to indicate high stress and an increased likelihood of a breaching fault being present, with fault overlap and cumulative relay throw as a proxy for the displacement gradient (figure 6.2). High ratios of relay throw:overlap are indicative of the presence of a breaching fault, whilst low ratios suggest that the relay zone is open.

Figure 6.2 (Next page). Schematic plot of relay zone evolution relative to relay throw and overlap developed from data presented in chapter 5. (A) Initially underlapping faults have zero overlap and zero cumulative relay throw. (B) As faults overlap, the relay throw begins to increase. (C) As the critical stress drop contours are intersected the amount of overlap can no longer significantly increase. (D) A small increase in overlap is accompanied by a large increase in relay throw as throw gradients steepen due to the interaction of stress fields. (E) The relay zone becomes breached, with relay throw:overlap ratios increasing into the breached field. (F) Profile re-adjustment leads to throw accumulation on the breaching fault which eventually results in it becoming visible in seismic data. It should be noted that this evolutionary model only accounts for fault growth and linkage at the plane of observation. It does not account for out of plane growth and linkage (Walsh et al., 2003).

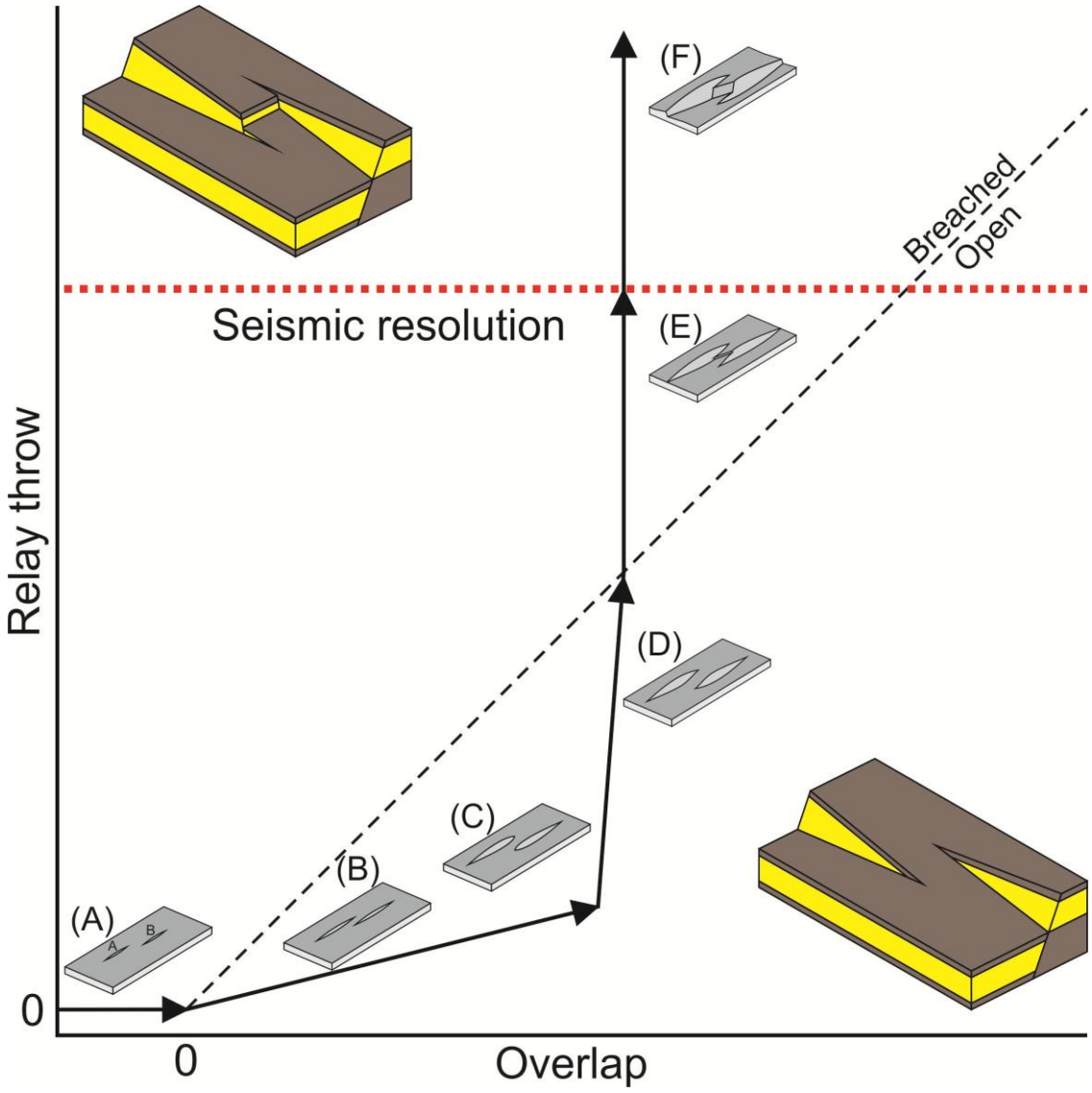
(F)
Breached
Open
Seismic resolution
(E)
Relay throw
(D)
(C)
(B)
(A)
A
B
0
0
Overlap

6.3 Geological and Simulation models

To assess the impact of sub-seismic fault tips and breached relay zones on hydrocarbon production a series of reservoir simulations have been performed using the fault geometries defined in chapter 5. The different approaches for incorporating sub-seismic fault tips are used to estimate sub-seismic tip length, with the results applied to the original seismic interpretation to generate a series of models of varying sub-seismic tip length. Each geological model is sub-divided to include scenarios excluding and including breached relays (figure 6.3) as defined by the breaching criteria defined in chapter 5 (and illustrated in figure 6.2). As sub-seismic fault tip length is increased the fault network becomes increasingly connected, and the reservoir segmented (figure 6.3).

Figure 6.3 (next page). Maps showing the effect of incorporating sub-seismic fault tips and relays on the connectivity of the fault network. Breached relays have been incorporated according to the criteria determined in figure 6. Colours represent isolated fault bound compartments. (A) As interpreted. (B) As interpreted, with the addition of breached relays according to the breaching criteria in figure 6.2 (C) Statistically elongated fault tips, open relays. (D) Statistically elongated fault tips, breached relays. (E) Elongated fault tips based on displacement gradient and seismic resolution of 5m, open relays. (F) As (E), but with breached relays. (G) Elongated fault tips based on displacement gradient and seismic resolution of 10 m, open relays. (H) As (G), but with breached relays. (I) Elongated fault tips based on displacement gradient and seismic resolution of 25 m, open relays. (J) As (I), but with breached relays.

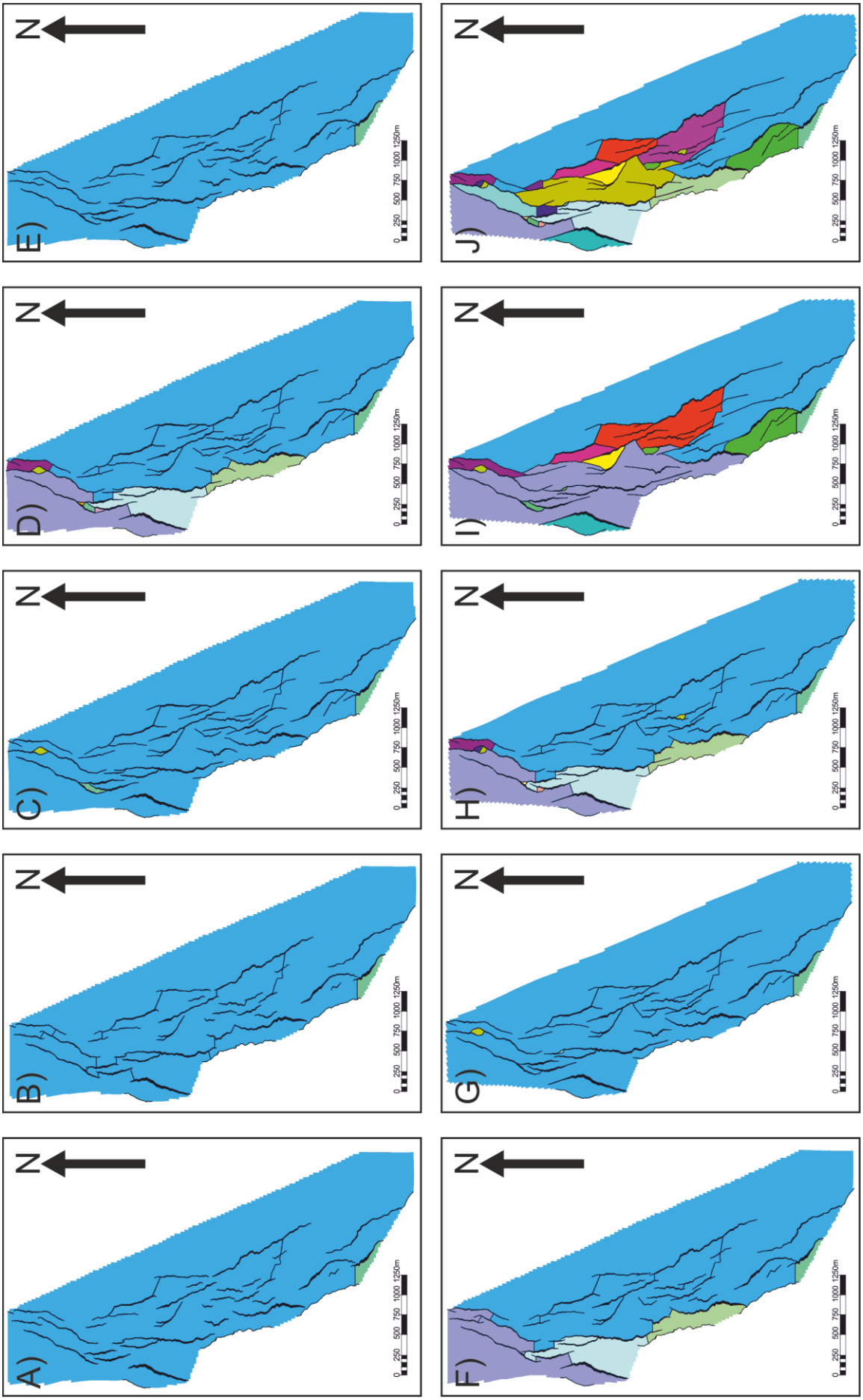
A)
B)
C)
D)
E)
F)
G)
H)
I)
J)
N
0 250 500 750 1000 1250m

The geometry of the grid boundary for the geological model has a major influence on the outcomes of the subsequent simulations. Where all faults are isolated from the edges of the grid, their influence on production is difficult to determine since fluids tend to flow around rather than across them. This may result in increased flow tortuosity, however compartmentalisation is unlikely to occur. The grid boundary has therefore been designed to ensure that for the fault model built directly from the seismic interpretation (Figure 6.3a), a limited number of open pathways exist between the injection and production wells (Figure 6.4). This mimics the geometry of the full field model, where the grid boundary is formed from bounding faults on three sides and the oil water contact down dip. This geometry therefore provides a realistic case for studying the effects of extending fault tips and incorporating breached relay zones in a relatively open system. Interpretation of the fault network was conducted on every seismic trace, with a resulting spacing for fault picks of 25 m. To capture this same detailed variation in throw a grid cell geometry of 25 m has also been used, with the fault picks converted directly to fault pillars with no loss of spatial positioning or resolution. In this manner the maximum resolution available has been included within the model, without the introduction of spurious data that may result if a finer grid dimension is used.

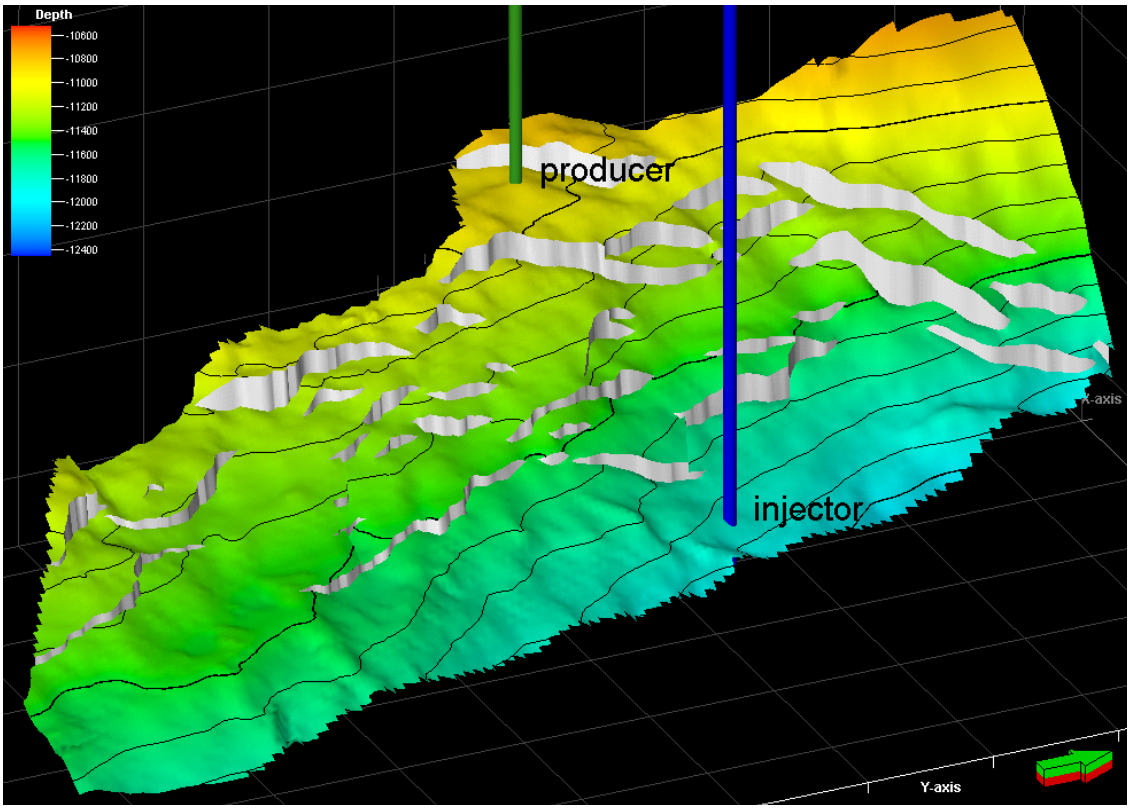

Figure 6.4. 3D oblique view of the top reservoir horizon and un-modified fault network (as shown in map view in figure 6.3a), along with the positions of the production and injection wells. Vertical exaggeration is x5, with faults coloured white and the top reservoir surface coloured by depth. Each axis square has sides of 500m.

To allow reservoir simulation of the different fault geometries a number of stratigraphic and petrophysical properties are required to be populated within each geo-cellular grid. These properties, and the range of values used, are shown in table 6.1. The values were derived by extracting the relevant properties (Vshale, porosity, permeability) from the local well stratigraphy and arithmetically up-scaling them to 20 zones of equal thickness within the reservoir interval (figure 6.5). The reservoir stratigraphy is that of the Brent group, a vertically heterogeneous shaly sand. Properties within each of the 20 layers were treated as isotropic. Extrapolation across the model has purposely been done in a layercake fashion with a constant thickness so as to exclude the effects of stratigraphic variation on fault plane property calculations.

Reservoir Interval		
Permeability	15.01-50.13	mD
Porosity	0.05-0.2067	
Vclay	6.43-56.75	%
Overburden/underburden		
Permeability	0.0001	mD
Porosity	0.0001	
Vclay	65	%
Initial oil in Place	$195x10^6$	STB

Table 6.1. Petrophysical properties used to populate geological models. Properties are derived from local well data (figure 6.5), and have been upscaled into 20 discrete layers of equal thickness. The models have been populated in a 'layercake' fashion so as to eliminate the influence of stratigraphic variation on the simulation results.

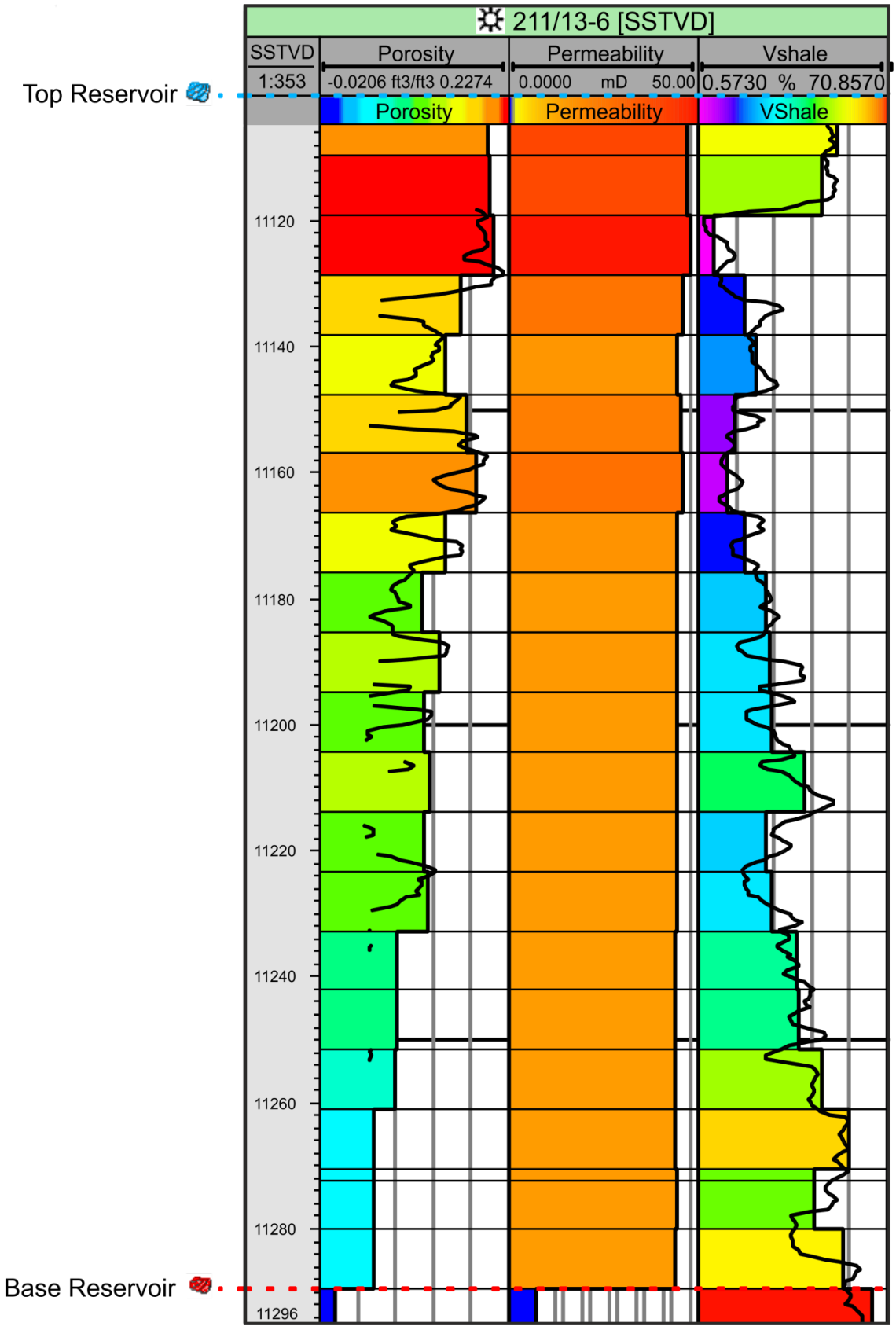

Figure 6.5. Well section illustrating upscaled porosity, permeability and Vshale values used during population of the models. The original well-log curves are superimposed where available.

6.3.1 Fault Rock Properties

Transmissibility multipliers (Manzocchi et al., 1999) are used in reservoir simulators for numerically representing faults. They allow the reduction in permeability between grid cells separated by faults to be captured within the simulation model. The scope of this chapter does not cover the uncertainties associated with calculating fault rock properties and transmissibility multipliers (see e.g. Freeman et al., 2008), however it has been important to use meaningful and geologically reasonable values. A proprietary fault seal study of core from the Penguin oil field found little evidence of cataclasis or subsequent quartz cementation suggesting that faulting occurred at relatively low confining pressures (Fisher & Knipe, 1998). Hence, the primary mechanism for cross fault permeability reduction in this case is identified as incorporation of clay into the fault rock. The distribution of clay within the fault rocks can be calculated using the Shale Gouge Ratio (SGR) algorithm (Yielding et al., 1997), based upon fault throw and the clay content of the faulted stratigraphy. Since the clay distribution (Vclay) within the stratigraphy cannot be easily calculated from well logs it is common practice to instead use the shale distribution (Vshale). This may lead to an overestimate in the sealing capacity of faults since the average clay content of shales is approximately 65 % (Shaw & Weaver, 1965). To account for this we have multiplied the log-derived Vshale values by 0.65 in order to arrive at an approximation of the Vclay value prior to calculating the SGR. SGR values are converted to fault rock permeability by means of a clay content to permeability transform, an empirical relationship derived from petrophysical measurements of core plug samples (Manzocchi et al., 1999; Sperrevik et al., 2002; Jolley et al., 2007). In this case we have used the relationship proposed by Jolley et al (2007), since it is the most relevant for the burial history, depth, sedimentology and tectonic province of the studied area. A fault throw to fault rock thickness ratio of 100:1 has been used, with an upper limit of 1m. Fault rock permeability is combined with fault rock thickness, host rock permeability and grid cell dimensions to calculate the fault transmissibility multipliers used in simulation (Manzocchi et al., 1999). Single vertical production and injection wells have been placed perpendicular to the average orientation of the faults, with the production well in an up-dip location (figure 6.4). Reservoir simulation was conducted using Schumberger's Eclipse 100 black oil simulator. Simulations were run over a period of 40 years, with a constant injection rate of 5000 STB/day and an initial target oil production rate also of 5000 STB/day. Additional simulation parameters are included in table 6.2. In addition to the ten different fault geometries (figure 6.3), an un-faulted grid has also been simulated for comparison.

Reservoir Conditions		
Min Pressure	2100	psi
Max Pressure	8400	psi
Temperature	212	°F
Reference Pressure	8076	psi
Datum depth	-3596.64	m
Fluid Properties		
Oil density	40.6	lbm/ft3
Bubble point pressure	2065	psi
Water Salinity	30000	ppm
Rock physics functions		
Residual oil saturation to water	0.25	
Critical water saturation (Swcr)	0.35	
Corey correlation (water)	4	
Corey correlation (oil-water)	3	
Min water saturation	0.3	
Max water saturation	1	
Max relative permeability of water	1	
Max relative permeability of oil	0.8	
Rock compaction functions		
Compressibility	0.00000599	1/psi
Rock reference pressure	5801	psi
Aquifer properties		
Aquifer type	Carter Tracy	
Drive direction	Bottom up, Grid edges	
Initial pressure	8076	psi
Permeability	50	mD
Porosity	0.25	
External radius	500	ft
Thickness	200	ft
Development strategy		
Simulation run time	40	years
Reporting frequency	6	months
Target oil production rate	5000	STB/day
Injection replacement fraction target	1	
Min bottom hole pressure (producer)	2200	psi
Water injection rate	5000	STB/day

Table 6.2 (Previous page). Parameters used during reservoir simulation. Many of these properties are derived from similar studies (e.g. Manzocchi et al., 2008; Rotevatn et al., 2009; Rotevatn and Fossen 2011).

6.3.2 Fault Threshold Pressures

Assuming a hydrocarbon-water-rock system, hydrocarbon flow across faults cannot occur until the capillary threshold pressure of the fault has been exceeded (Schowalter, 1979). Due to buoyancy effects, threshold pressures are most likely to be exceeded at the shallowest point where a hydrocarbon bearing bed intersects a fault (Schowalter, 1979). When this occurs oil will be imbibed into the fault zone and the relative permeability of oil will therefore increase, along with its saturation.

In typical simulation software individual faults are assigned single threshold pressures representing the entire fault. Once this value is exceeded at any point on the fault, the entire fault becomes transmissive to hydrocarbons, albeit with flow at any single point on the fault controlled by the assigned local transmissibility multipliers. This treatment of faults within simulation software packages does not account for two important factors. Firstly, that a single threshold pressure value is unlikely to be applicable to an entire fault, and secondly that transmissibility multipliers do not discriminate between different fluid phases. These issues are addressed further in the discussion section.

Threshold pressure tends to increase with decreasing permeability due to a reduction in pore throat diameter (Manzocchi et al., 2002; Sperrevik et al., 2002). Fault permeability is controlled by the composition, structure and petrophysical properties of the fault rocks which are in turn functions of the petrophysical properties of the stratigraphy, the throw distribution along and across the fault and the burial history. Since these parameters are often highly spatially variable it seems extremely unlikely that a single threshold pressure value is applicable to a whole fault, with the minimum rather than the mean threshold pressure value being critical (e.g. Tueckmantel et al., 2010), since this is the most likely to leak. We postulate that a more geologically realistic scenario would be that the threshold pressures on a fault vary depending on fluid saturation of the fault rock and on the fault rock properties. In this situation threshold pressures would be exceeded at discrete locations along the fault, with cross fault flow focussed at these localities. This may have important consequences for correctly predicting flow pathways relevant for efficient well placement.

An additional uncertainty when quantifying the threshold pressure to be used during simulation is the conversion between the measured Hg-air values and the in situ Hydrocarbon-water values. Although this is possible using the equations defined by Purcell (1949), variables such as interfacial tension and contact angle are often unknown for the reservoir P-T conditions. Interfacial tension has been shown to vary with temperature and pressure (i.e. depth) for a specific hydrocarbon composition (see e.g. Yielding et al., 2010, figure 9). Similarly the contact angle varies with the wetting phase of the fault rock, with angles below 90° usually implying water-wet and above 90° implying oil-wet (Schowalter, 1979). It is generally assumed that sedimentary rocks in the subsurface will be water-wet due to exposure of grain surfaces to water during deposition and early burial. Migration of hydrocarbons over geological timescales may however lead to rocks becoming partially oil-wet. In the case of fault rocks this will have the effect of reducing their threshold pressures (Schowalter, 1979).

Since only single values of threshold pressure can be assigned to each fault using traditional simulation software we have assessed the influence of varying the threshold pressure by running simulations for low, base and high case scenarios. For each scenario every fault has been assigned the same threshold pressure value. Low case scenarios use an in-situ threshold pressure of 30 psi. This value is based upon two assumptions. Firstly that minimum threshold pressures control cross fault flow (Tueckmantel et al., 2010). The second assumption is that threshold pressure is being controlled by the clay content of the fault rocks as defined by the SGR algorithm. Since core from the reservoir presents little to no evidence of cataclasis or cementation we believe that this assumption is reasonable. This being the case, the minimum SGR value consistently present at self juxtaposed reservoir on every fault (15.5%, as calculated using the SGR algorithm) has been used to calculate the corresponding threshold pressure (30 psi). To do this an empirical equation has been used (1), defined in Bretan et al (2003) which utilises a global dataset;

$$(1)\quad y = 10^{(SGR/27-C)},$$

Where y = In-situ threshold pressure (bar), C = Depth dependent constant, in this case 0.25.

A mid-case threshold pressure value of 142psi has been derived using equation (1) utilising the mean SGR value found where the reservoir is self juxtaposed (33.5%). High-case threshold pressures (300 psi), based on the highest consistently present SGR value at areas of self juxtaposition (42.5%) have also been simulated.

6.4 Simulation Results

The simulation models capture both geometric (sub-seismic fault tips and breached relay zones) and petrophysical (fault threshold pressures) uncertainties. To more easily assess their relative contributions we first examine the geometric uncertainties based upon the mid-case fault threshold pressures. This is followed by examination of the effect of varying the fault threshold pressure.

6.4.1 Sub-Seismic Fault Tips and Breached Relay Zones

Comparison of the simulation results for the different structural geometries reveals a number of significant differences. Since the models use stratigraphies populated with identical petrophysical properties we can conclude that the differences observed are solely a consequence of the different structural geometries modelled. Figure 6.6 shows oil and water production rates, and cumulative oil and water production plotted against time for the different simulation models. Cumulative oil production is similar for all models over the full simulation run time, with less than 5% difference between the best and worst performing cases (Figure 6.7). Recovery factors are between 23.8% and 25% after 40 years of production. Oil production rates initially appear to have similar trends for all the models, with production rates declining following water breakthrough after approximately 16 years. In contrast, water production rates and cumulative water production show considerable variations between the different geometries. Models where breaching faults are included consistently have lower water production rates and lower cumulative water production than their un-breached counterparts. Similarly water production (rate and cumulative) decreases with increasing fault tip length (Figure 6.7), a trend which is not mirrored for cumulative oil production.

Figure 6.6 (Next page). Production simulation results for mid-case fault threshold pressures (142 psi). (A) Oil (solid lines), and water (dashed lines) production rates for the different structural models. (B) Cumulative produced volume of oil (Solid lines) and water (dashed lines). For both production rate and produced volume, varying the fault tip length and connectivity of the fault network influences water flow to a greater extent than oil flow.

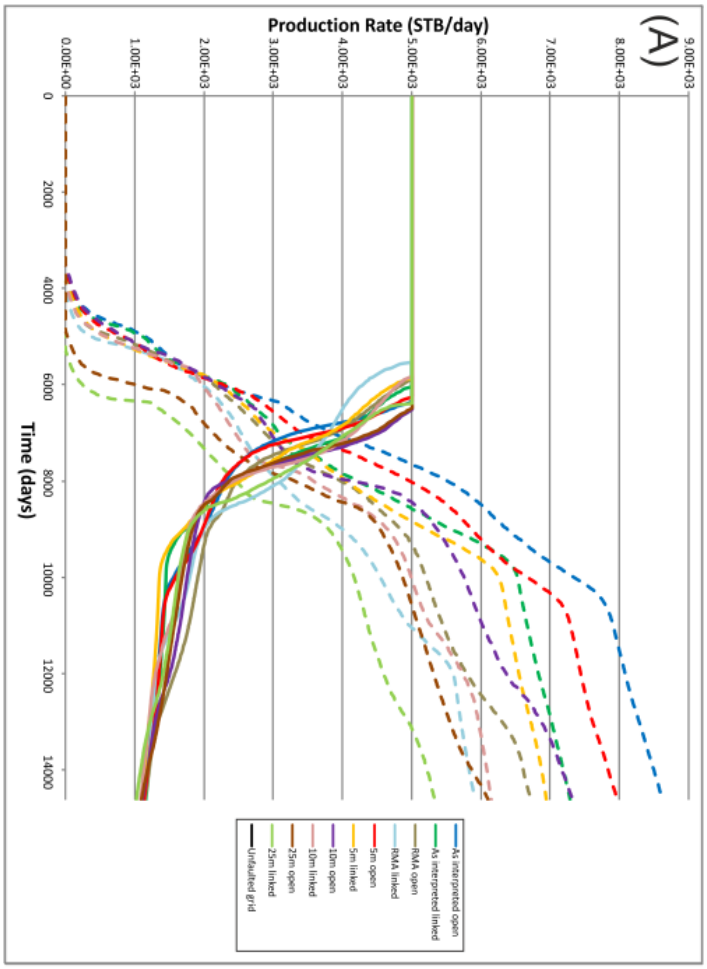
(A)
Production Rate (STB/day)
9.00E+03
8.00E+03
7.00E+03
6.00E+03
5.00E+03
4.00E+03
3.00E+03
2.00E+03
1.00E+03
0.00E+00
0
2000
4000
6000
8000
10000
12000
14000
Time (days)
As interpreted open
As interpreted linked
RMA open
RMA linked
5m open
5m linked
10m open
10m linked
25m open
25m linked
Unfaulted grid

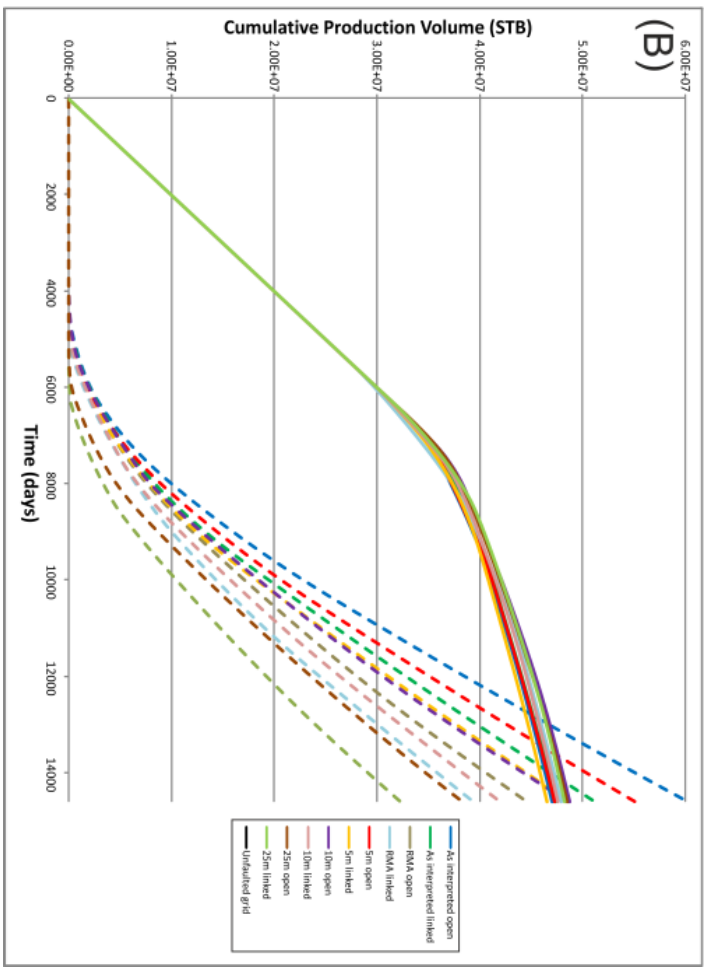
(B)
Cumulative Production Volume (STB)
6.00E+07
5.00E+07
4.00E+07
3.00E+07
2.00E+07
1.00E+07
0.00E+00
0
2000
4000
6000
8000
10000
12000
14000
Time (days)
As interpreted open
As interpreted linked
RMA open
RMA linked
5m open
5m linked
10m open
10m linked
25m open
25m linked
Unfaulted grid

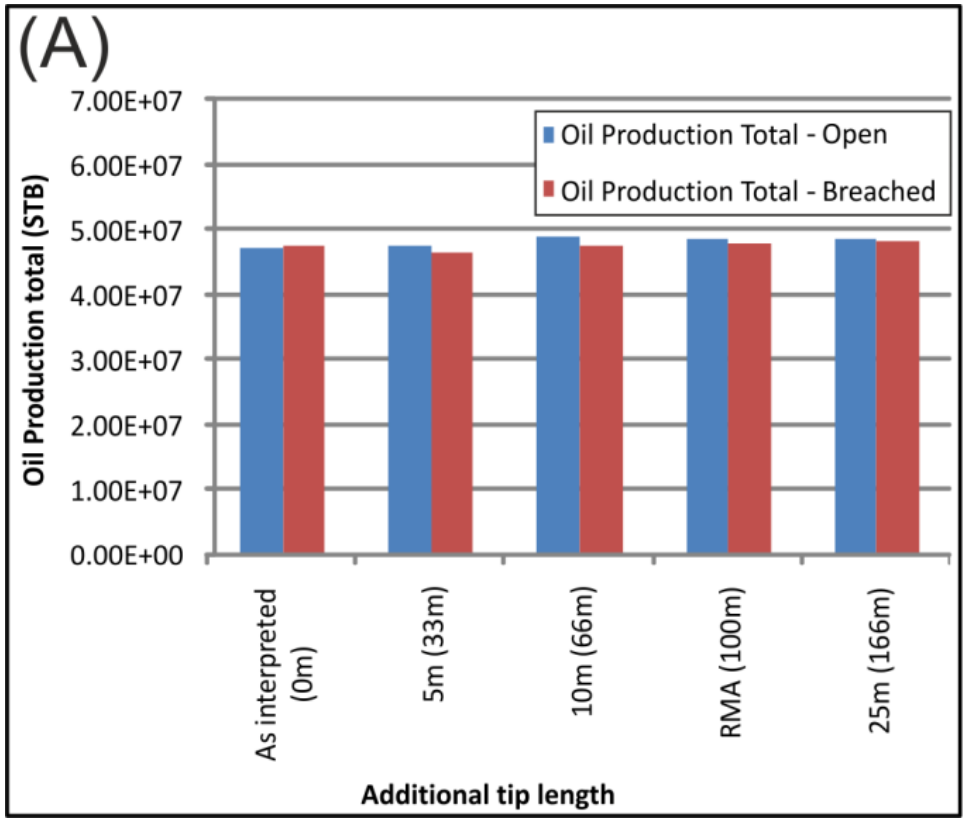
(A)
7.00E+07
6.00E+07
5.00E+07
4.00E+07
3.00E+07
2.00E+07
1.00E+07
0.00E+00
Oil Production total (STB)
Oil Production Total - Open
Oil Production Total - Breached
As interpreted (0m)
5m (33m)
10m (66m)
RMA (100m)
25m (166m)
Additional tip length

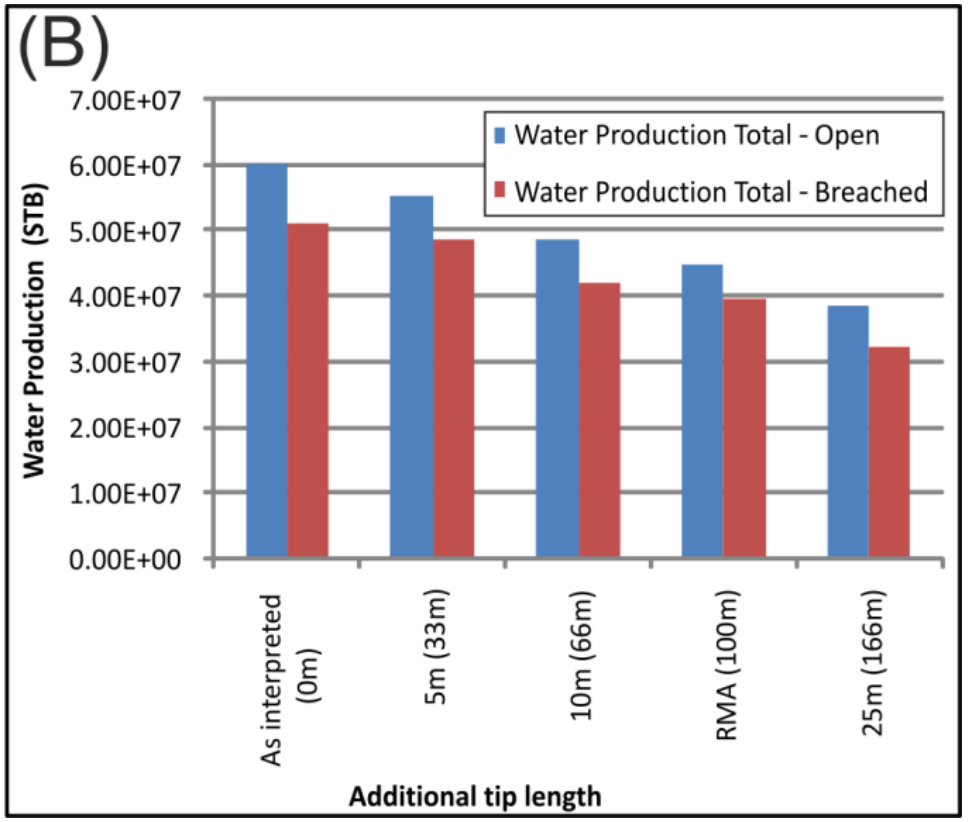
(B)
7.00E+07
6.00E+07
5.00E+07
4.00E+07
3.00E+07
2.00E+07
1.00E+07
0.00E+00
Water Production (STB)
Water Production Total - Open
Water Production Total - Breached
As interpreted (0m)
5m (33m)
10m (66m)
RMA (100m)
25m (166m)
Additional tip length

Figure 6.7 (Previous page). Comparison of total produced oil (A) and water (B) volumes, for both open (blue) and breached (red) configurations for the mid-case fault threshold pressure (142 psi). The charts are arranged so that the modelled fault tip, and hence fault network connectivity, length increases to the right. Whereas including breaching faults and additional tip length has only limited influence on produced oil volumes (A), the impact on produced water (B) is significant. Increasing the tip length decreases the volume of produced water, with models including relay zone-breaching faults also consistently leading to lower water production.

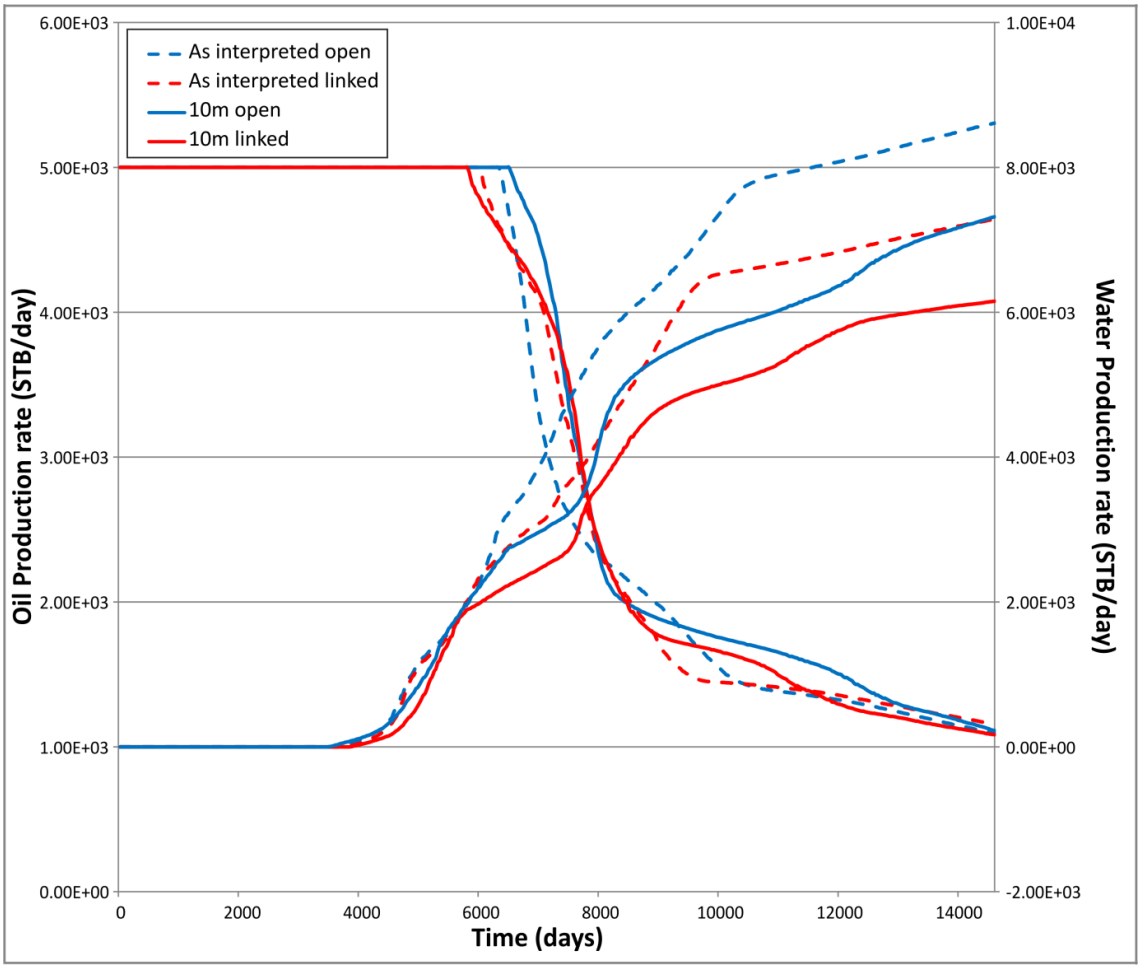

Figure 6.8. Summary of production oil and water rate results illustrating the general trends which can be observed for the mid-case fault threshold pressure (142 psi). Breached and unbreached cases for the model based on the unaltered interpretation and the model with extended fault tips assuming a seismic resolution of 10m are shown. Altering the fault geometry has a limited impact on the oil production rate, however increasing the fault tip length and including breaching faults across relays both lead to a reduction in the water production rate.

Although cumulative oil production does not vary drastically, and production rates appear to follow a similar trend for the different models, a number of noteworthy tendencies can be identified from the production data. The general pattern for oil production rates is one of rapid decline shortly following water breakthrough with a subsequent stabilisation to a more gradual production rate decline. Within this pattern however variations in the fault tip length and the relay integrity lead to a number of behaviours that may be significant in terms of their predictability. Figure 6.8 compares four, rather than the full ten, geometries to allow these behaviours to be more easily observed, with these observations summarised schematically in figure 6.9. As previously described water production rates are lower for models with longer fault tips, with the inclusion of breached relays leading to lower water production rates compared to un-breached relays. Water breakthrough times are broadly similar. In terms of oil production rates, increasing the length of fault tips tends to lead to an earlier onset of production decline. The rate of decline however is slower than for shorter fault tips, leading to overall similar cumulative production over the full course of the simulations. Inclusion of breached relays has a comparable effect, with an earlier onset but more gradual decline in production rate when compared to open relays. The difference between the onset of production decline between open and breached cases decreases with decreasing fault tip length. These behaviours are applicable to all the models with the exception of those where the fault tips have been extended based upon a seismic resolution of 25m. This is likely due to the increased number of fault intersections created in this scenario (figure 6.2) leading to less predictable flow pathways.

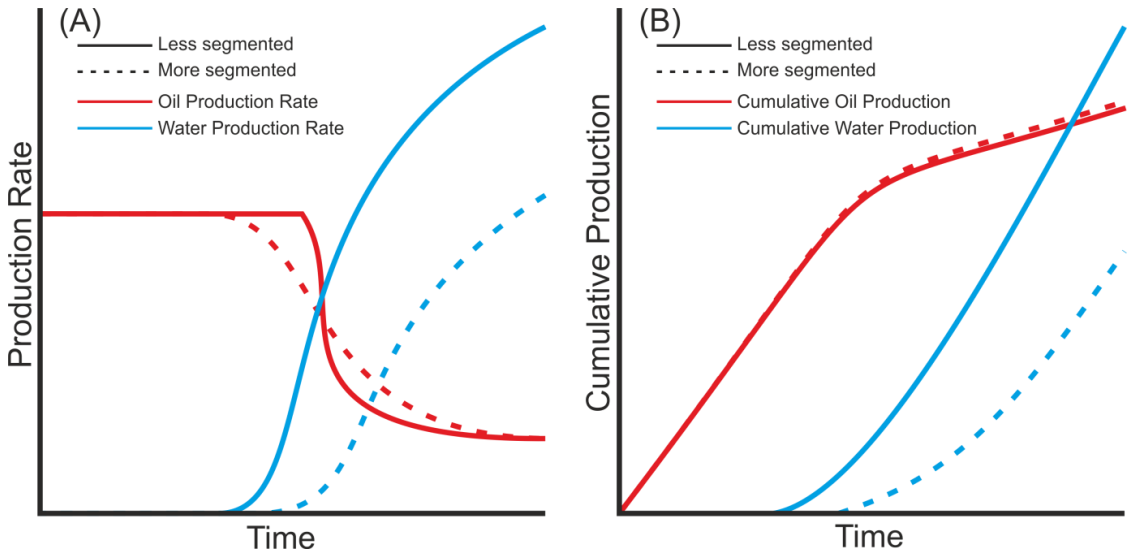

Figure 6.9. Schematic summary of the influence of including relay zone breaching faults and sub-seismic fault tips on production rates (A) and production volumes (B).

6.4.2 Fault Threshold Pressures

Varying the fault threshold pressures has a significant impact on both oil and water production rates, as well as cumulative production volumes (figures 6.10, 6.11). Figures 6.12 and 6.13 summarise the generalised trends that can be observed. Similar trends are observed for models where the fault threshold pressure has been assigned as 30 psi, although the relative effect is less pronounced (figures 6.10, 6.11, 6.12). In contrast the models where faults have been assigned high threshold pressure values of 300psi show significant differences between the different fault geometries. A noticeable trend seems to be that for each specific geometry the onset of production decline tends to be earlier for higher threshold pressures, whilst the cumulative oil and water production volumes and the bottom hole pressure at the production well tend to be lower with increasing threshold pressures. The timing of water breakthrough is however more complex, with higher threshold pressures leading to earlier breakthrough for more open fault networks and later breakthrough for more connected fault networks. This complexity is reflected in the variability in production rates and cumulative volumes between the different geometric models, with variability increasing significantly with the fault threshold pressure. This suggests that assigning the correct fault threshold pressure becomes more important when the fault network is highly segmented. Conversely, incorporating sub-seismic fault tips and relay zone breaching faults becomes increasing important if fault threshold pressures are assumed to be high (e.g. for a high clay content stratigraphy).

An important assumption to note is that of the validity of the representation of threshold pressures within conventional reservoir simulators. Recent work (Manzocchi et al., 2010, 2012) has shown that across fault flow is often initialised prior to the threshold pressure of a fault being exceeded, hence leading to overestimates in across-fault flow.

Figure 6.10 (Next page). Simulation results for the different structural configurations and fault threshold pressures. The upper row shows variation in production rates, whilst the bottom row shows variation in produced volumes for oil (solid lines) and water (dashed lines). As fault threshold is increased the variation in simulation results between the different structural configurations also increases. This is especially the case for the water production rate and produced volume. See text for discussion.

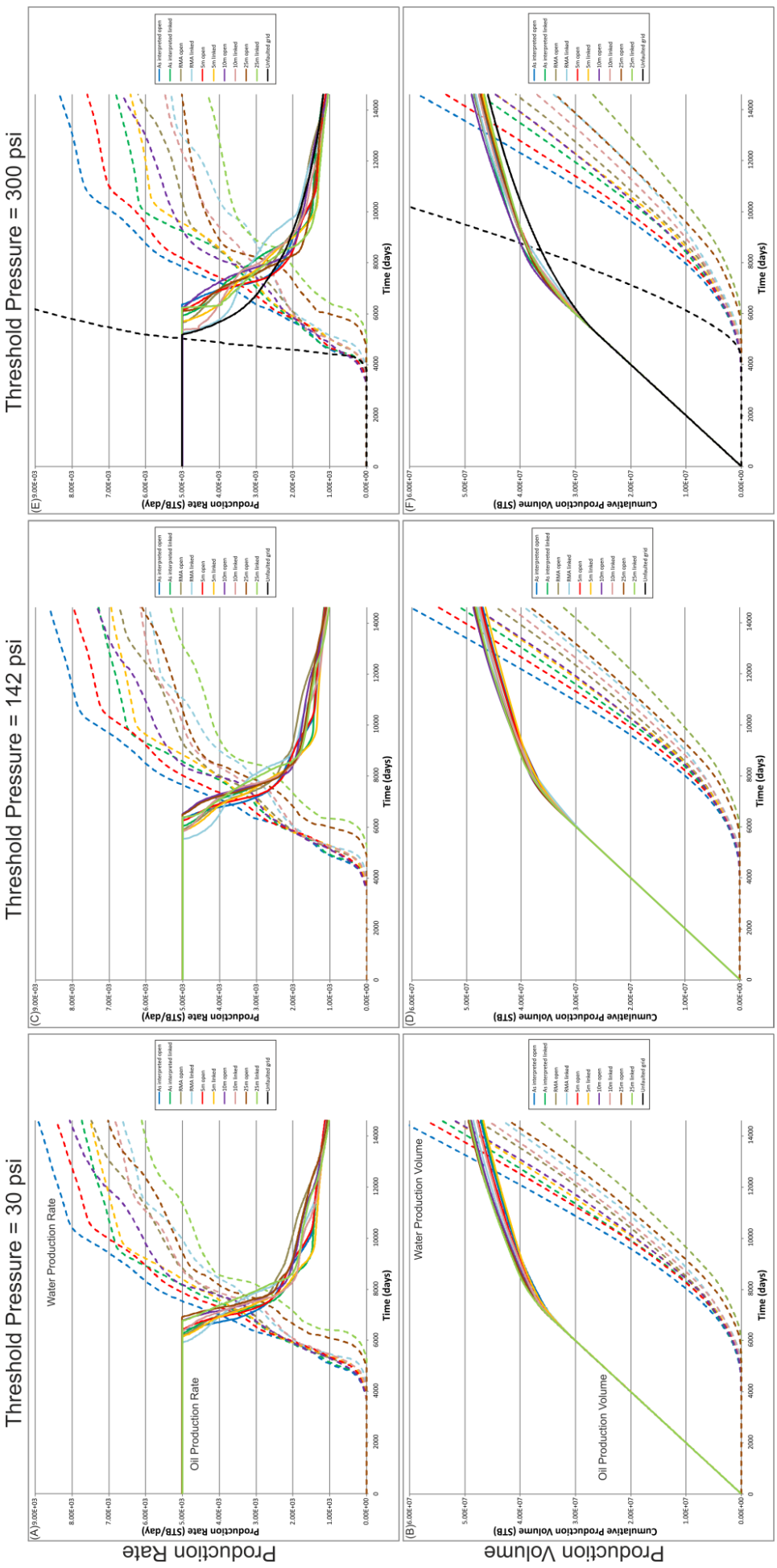
Threshold Pressure = 30 psi
Threshold Pressure = 142 psi
Threshold Pressure = 300 psi
Production Rate
Production Volume
Water Production Rate
Oil Production Rate
Water Production Volume
Oil Production Volume
Production Rate (STB/day)
Cumulative Production Volume (STB)
Time (days)
(A)
(B)
(C)
(D)
(E)
(F)

Threshold Pressure = 30psi

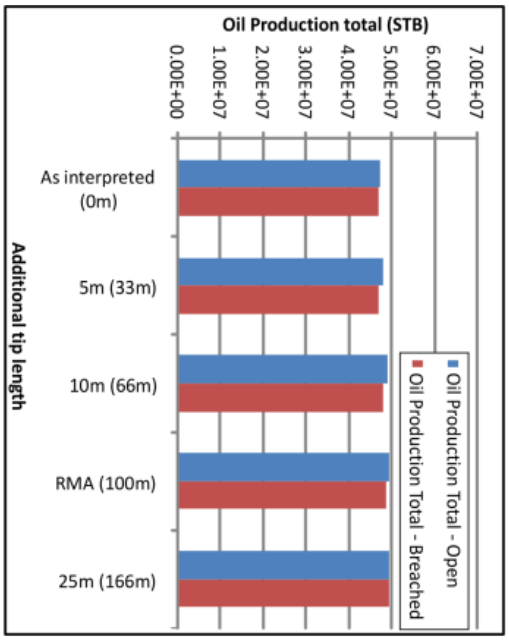

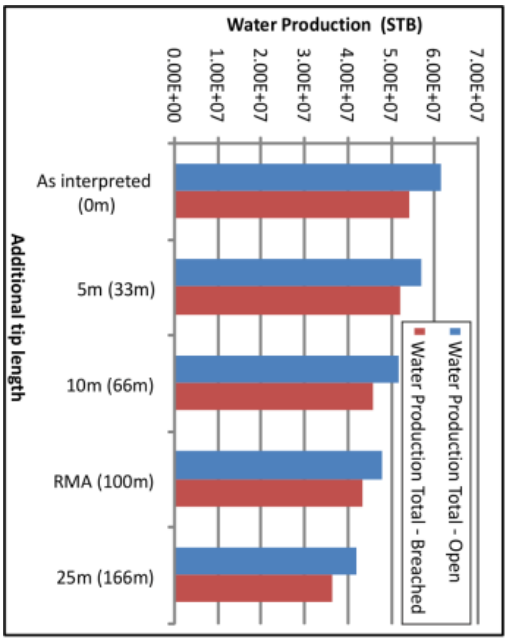

Threshold Pressure = 142psi

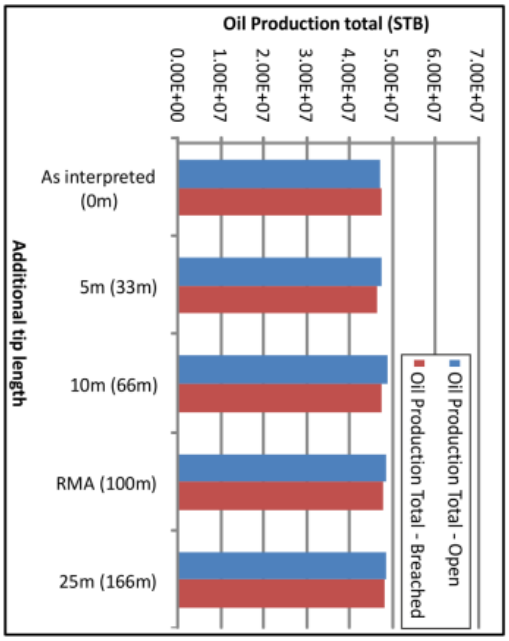

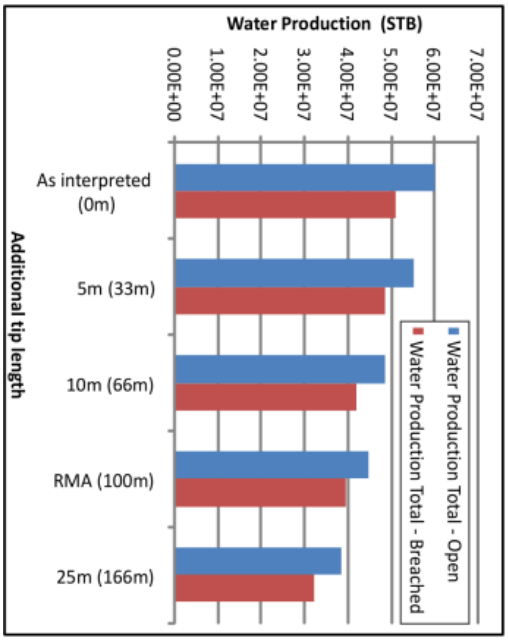

Threshold Pressure = 300psi

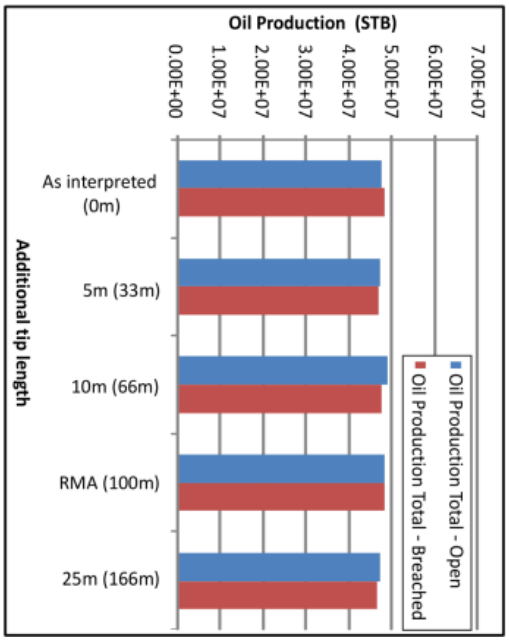

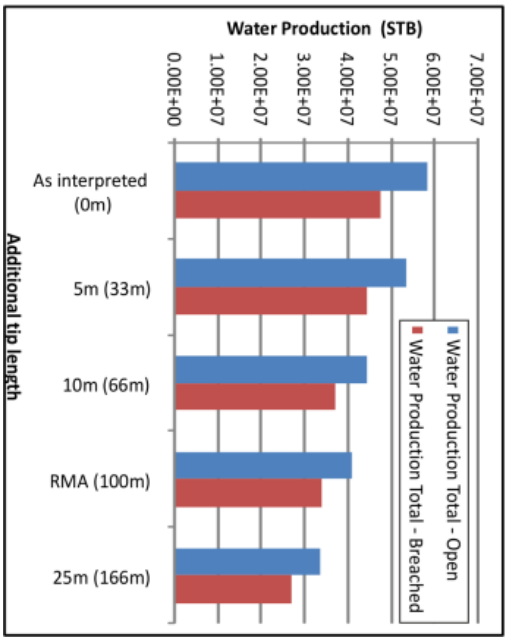

Figure 6.11 (Previous page). Graphs showing total oil and water production volumes at the final simulation timestep for each structural configuration and threshold pressure. Varying threshold pressure does not significantly influence the oil production volumes, although the produced water volumes are significantly reduced when higher fault threshold pressures are employed.

Figure 6.12 (Next page). Summary graphs illustrating the effect of increasing fault tip length, including breaching faults across relay zones and varying the fault threshold pressure on oil and water production rates over the course of the simulations. For clarity only results for the original interpretation and the model with tips extended assuming a seismic resolution of 10m are included. Fault threshold pressures are 30 psi (A), 142 psi (B), and 300 psi (C). The impact on production of increasing fault network connectivity increases with fault threshold pressure.

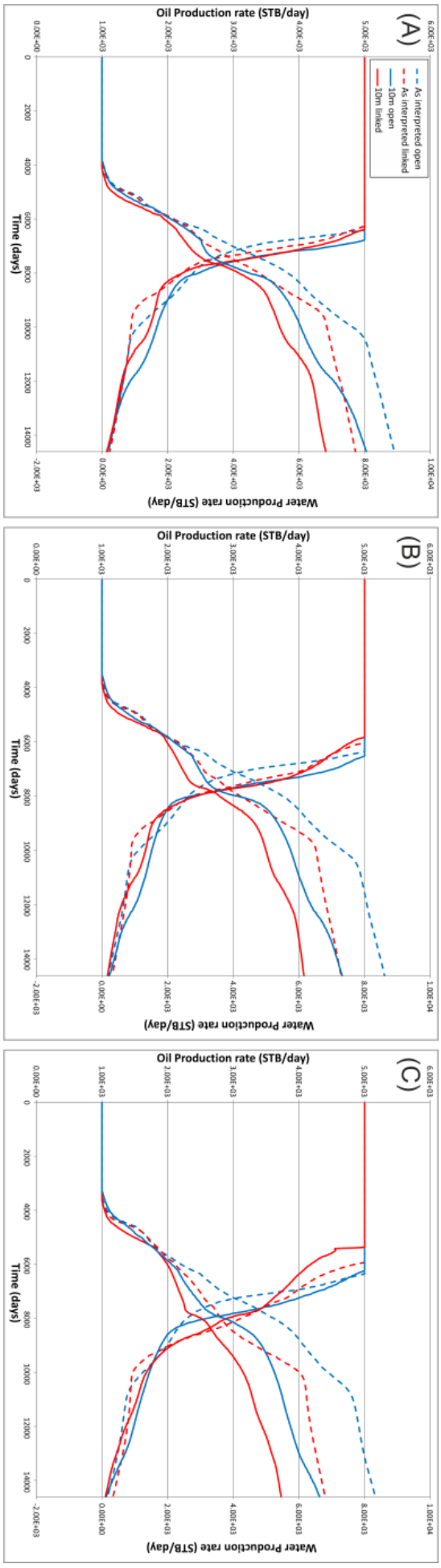
(A)
Oil Production rate (STB/day)
Water Production rate (STB/day)
Time (days)
As interpreted open
As interpreted linked
10m open
10m linked
(B)
Oil Production rate (STB/day)
Water Production rate (STB/day)
Time (days)
(C)
Oil Production rate (STB/day)
Water Production rate (STB/day)
Time (days)

(A)
Cumulative Volume/Pressure/Rate
OPT, WPT, BHP
Onset of production decline
Timing of water breakthrough
(B)
Cumulative Volume/Pressure/Rate
Variability in OPR, OPT, WPR, WPT, BHP
Variability in onset of production decline
Variability in timing of water breakthrough
Threshold Pressure/Time
Threshold Pressure/Time
Oil Production Rate
Cumulative Oil Production
Bottom Hole Pressure
Water Production Rate
Cumulative Water Production

Figure 6.13 (Previous page). Schematic graphs summarising the impact of varying the fault threshold pressure during simulation. (A) General trends. The onset of production decline occurs earlier for higher threshold pressures, leading to a lower cumulative produced volume. The water production rate, cumulative volume of produced water and bottom hole pressure at the production well are all lower for higher fault threshold pressures. (B) Variability of simulation results between different structural configurations for increased fault threshold pressure. At low threshold pressures the simulation results for the ten different fault network configurations (figure 6.3) are relatively similar. However, as threshold pressure is increased the variability of the simulation results also increases. This indicates that fault network connectivity becomes more important when attempting to achieve a realistic forward prediction or accurate history match when fault threshold pressures are expected to be high. OPT = Oil Production Total, OPR = Oil Production Rate, WPT = Water Production Total, WPR = Water Production Rate, BHP = Bottom Hole

6.4.3 Pressure and Saturation Distribution

Pressure distribution within the reservoir following 40 years of simulated production is influenced by a combination of the fault connectivity and the fault threshold pressure (figure 6.14). For a given degree of fault connectivity, the pressure distribution begins to become discretised (rather than varying continuously) across faults only when connectivity of the fault network is such that hydraulic continuity between fault bound segments is lost. Hence open fault networks where relay ramps remain intact tend to have similar pressure distributions regardless of fault tip length. The exception to this is the case where fault tips have been significantly extended (e.g. figure 6.3i), such that fault connectivity is increased irrespective of relay zone integrity. Similarly pressure discretisation varies significantly with threshold pressure only for geometrically connected fault networks. An open, low connectivity fault network does not result in substantial increases in pressure compartmentalisation with increased fault threshold pressure.

The oil saturation distribution within the reservoir also displays non-trivial variability dependent on fault network connectivity and fault threshold pressures (figure 6.15). As with pressure distribution, saturation is most significantly influenced by a combination of both fault connectivity and threshold pressure. Dissimilarly however, increasing the fault threshold pressure for a given geometric configuration, even for open fault networks, leads to a noteworthy increase in the complexity of the oil saturation distribution at the end of the simulations run times. The effect of increasing fault connectivity for a given threshold pressure

value also increases saturation distribution complexity, with the effect being more pronounced for higher fault threshold pressure values. The higher threshold pressures mean that fluid has to flow around, rather than across faults. This simultaneously increases the effectiveness of the sweep of the reservoir, whilst also trapping some oil down-dip of faults which would otherwise be permeable to flow (figure 6.15).

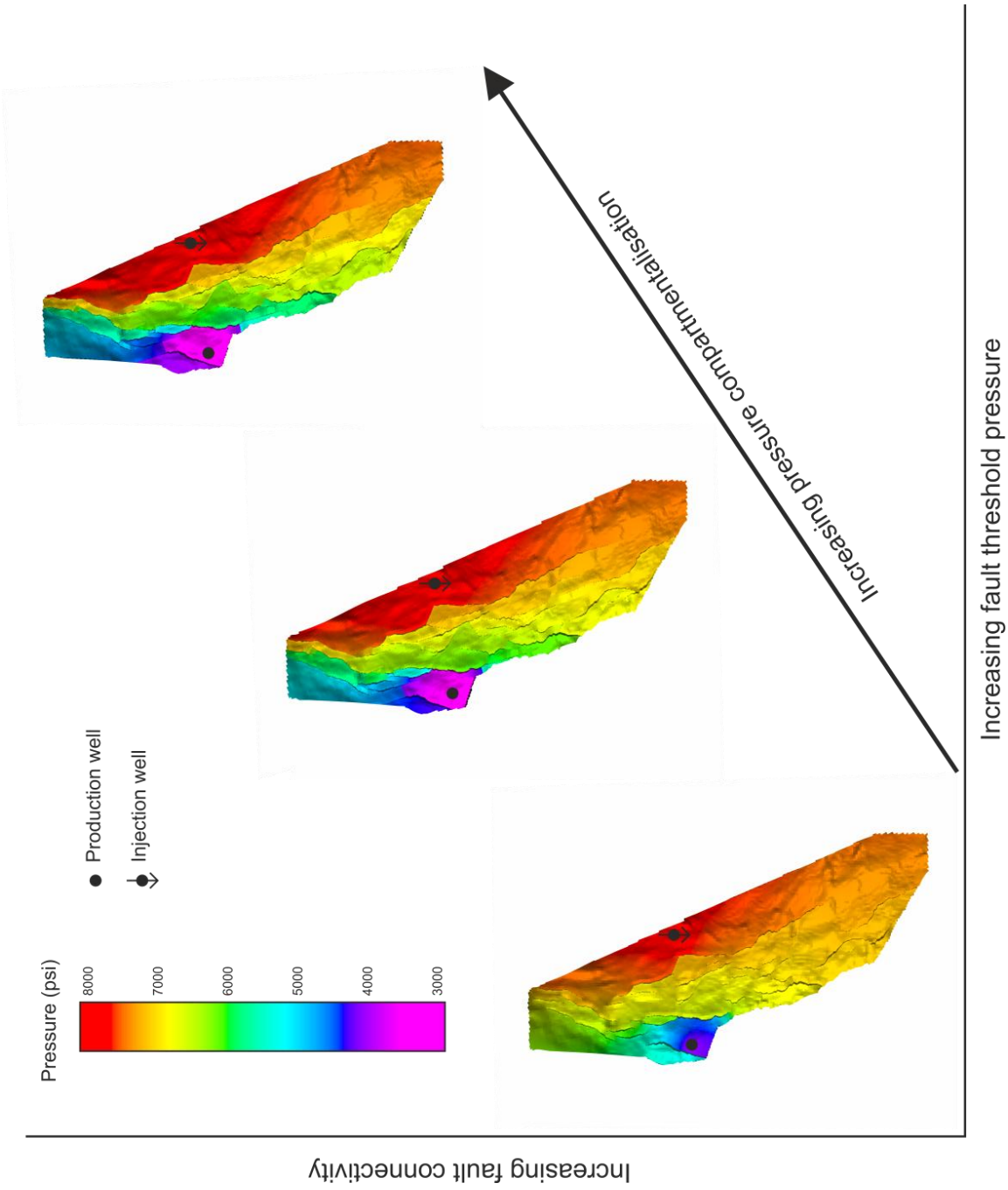

Figure 6.14. Map views of reservoir pressure at the final simulation timestep. Pressure compartmentalisation increases with increasing fault network connectivity and fault threshold pressure.

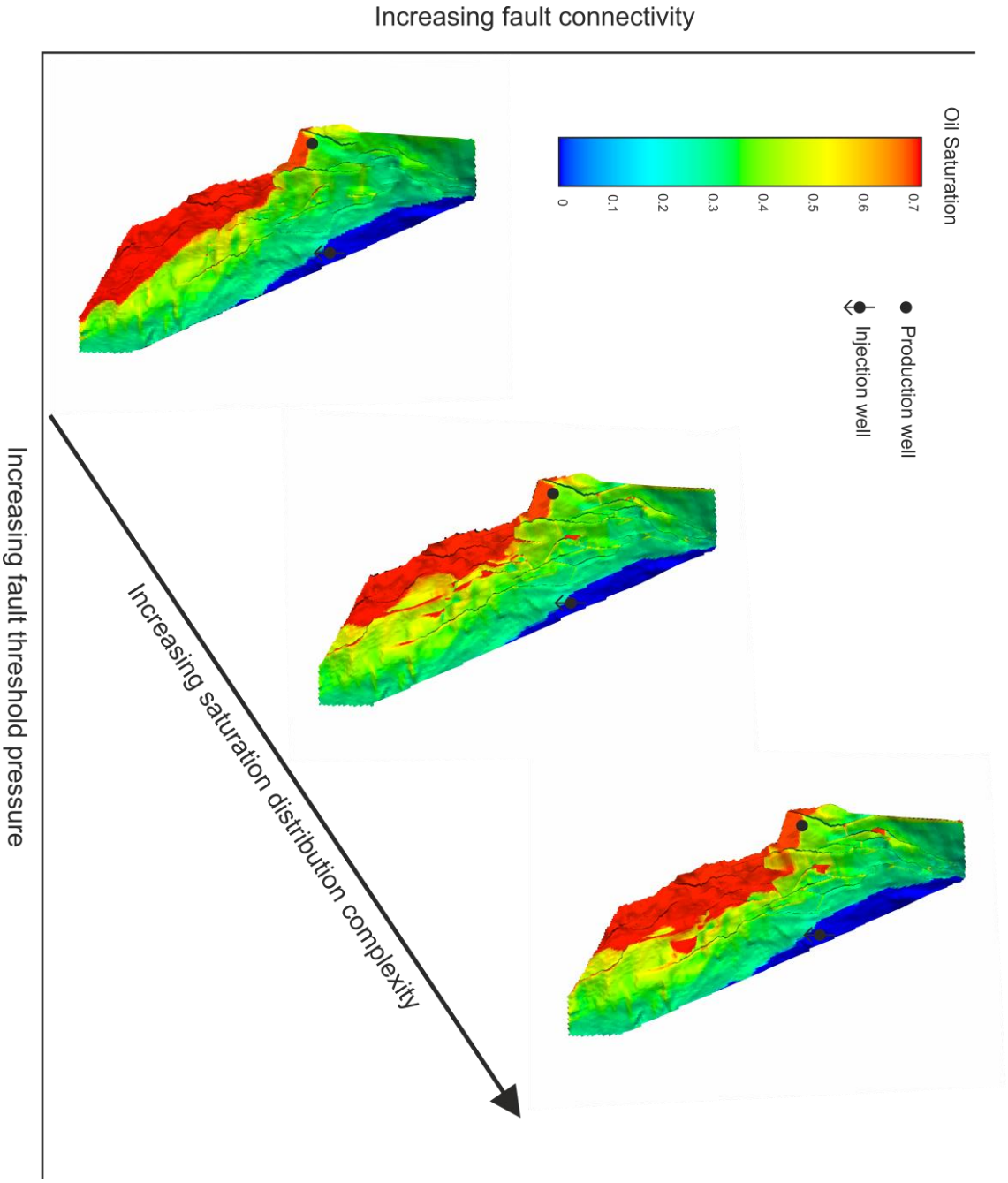

Figure 6.15. Map views of fluid saturation of reservoir interval at final simulation timestep. The complexity of the distribution of remaining oil increases as fault threshold pressure and fault network connectivity increase.

6.5 Discussion

6.5.1 Sub-Seismic Fault Tips, Relay Zones and Threshold Pressures

Fault tips and low throw relay zone breaching faults may be unresolvable in seismic data (e.g. Rotevatn and Fossen, 2011), and are hence described as being of sub-seismic proportions. Incorporating these sub-seismic features into reservoir models can potentially lead to significant increases in fault network connectivity and reservoir segmentation (Pickering et al., 1997). The influence of increased fault connectivity on simulated hydrocarbon production and recovery will be dependent upon the cross fault stratigraphic juxtapositions and fault rocks which are developed. The North Sea example considered here has a relatively open fault network when viewed at the resolution of seismic data. Low to moderate increases in fault tip length have little impact on reservoir segmentation unless combined with breached relay zones. High fault tip lengths lead to increased fault connectivity and reservoir segmentation due to extended faults truncating against existing structures. Including breaching faults across otherwise open relay zones further increases reservoir segmentation.

The increase in reservoir segmentation for a given increase in fault tip length is somewhat influenced by the range in strikes of a fault population (Pickering et al., 1997). In the dataset used here the range in strikes is relatively limited, leading to increased fault connectivity and reservoir segmentation only where large additional tip lengths are included. A larger range in strike values would lead to increased fault connectivity and reservoir segmentation at lower tip lengths. Conversely, including breaching faults across relay zones leads to significant increases in connectivity and reservoir segmentation, even where the range in fault strike orientation is relatively restricted.

Since even the most segmented of our models display relatively similar production results to the less segmented models it is apparent that a distinction is required between the terms reservoir segmentation and compartmentalisation. Our results show that a reservoir which is segmented by connected faults may not necessarily be compartmentalised. Compartmentalisation implies that different compartments do not experience pressure communication (Jolley et al., 2010), and hence that across-fault flow does not occur. To achieve compartmentalisation depends on both the geometric segmentation of a reservoir interval via a highly connected fault network, and either the fault displacements being consistently larger than the reservoir thickness (i.e. a juxtaposition seal), or very low permeability fault rocks.

6.5.2 Implications for Reservoir Development

Although cumulative oil production volumes tend to be broadly similar over the course of the simulations for the base case threshold pressure values (142psi), the economics of an oil field are often influenced to a greater extent by the production rates that can be achieved rather than the total volume of oil which can be produced (e.g. Manzocchi et al., 2008). The difference in the onset of production decline between the different fault geometries modelled is a maximum of approximately three years. The model which experiences the latest onset of production decline is that which utilises the original, un-modified fault interpretation. This is significant for a number of reasons. Although it is generally routine for multiple realisations of stratigraphic, facies, petrophysical, and increasingly fault plane property models to be incorporated into uncertainty analysis during reservoir development it is less common for structural geometric uncertainty to be assessed (Freeman et al. 2010). The initial fault interpretation is therefore likely to be incorporated into base-case models. According to these simulations this will result in the time to the onset of production decline being overestimated relative to cases where sub-seismic fault tips and breaching faults are included. In addition a non-trivial cost of oil production relates to the treatment and disposal of produced water. Our model based upon the un-modified fault interpretation leads to the largest volumes of produced water. Predictive simulations where sub-seismic fault tips are included may therefore lead to greater accuracy when forecasting a fields economic potential.

It must be remembered that the models simulated here eliminate uncertainty associated with petrophysical property distribution within the subsurface by using identically populated geocellular grids. The variations in simulation results are therefore exclusively influenced by the inclusion or otherwise of sub-seismic fault tips and breached relay zones. The non-uniqueness of petrophysical property distribution in the subsurface may lead to the predictability of the trends observed in our results being diminished. Similarly the influence of incorporating sub-seismic scale structural features may be dependent on the degree of observable fault compartmentalisation within a field. Our un-modified interpretation resulted in a relatively open fault network, with a low number of fault-bound compartments. As a result increasing the fault lengths and including sub-seismic breached relay zones leads to a significant increase in fault connectivity. For situations where a field is significantly compartmentalised at the scale of interpretation, the effects of increasing fault connectivity may be relatively lower.

Approaches such as drilling horizontal wells across multiple compartments are designed to minimise the effects of fault related compartmentalisation. Our models purposely used a

single vertical well to fully capture the effects of altering the fault geometries. It is unclear as to the simulated response that would be generated if a development strategy employing horizontal and/or multiple wells were to be adopted.

6.5.3 Two Phase Properties of Fault Rocks

Within a grid cell in a simulation model the relative permeability of each phase present can be dynamically calculated by referencing the saturation of the grid cell at each stage of a simulation to relative permeability curves based upon the fluid properties and absolute permeability. Hence as the oil saturation of a grid cell decreases, so does the relative permeability of oil within that cell. Below a critical saturation the relative permeability decreases such that oil flow can no longer occur. This is the primary reason for limitations on recovery factors from hydrocarbon reservoirs. Unlike grid cells, faults within standard simulation models are represented as two-dimensional discontinuities with no associated volume. As a result the saturation of the fault rock is not incorporated within the simulation parameters, and the faults are treated as single phase transmissibility multipliers based upon the absolute fault rock permeability (Manzocchi et al. 1999). Manzocchi et al (2002) outlined two methodologies for incorporating two-phase flow properties of fault rocks into simulation models. The first method incorporates faults as discrete grid cells rather than as numerical representations. As they pointed out however, although this method allows the inclusion of a large range of fault parameters it is restricted by computational difficulties. The second methodology involves using pseudo relative transmissibility multipliers associated with the upstream grid block adjacent to a fault. In both cases significant differences in simulated production were observed relative to the use of absolute, single phase transmissibility multipliers. Manzocchi et al, (2008b) compared the influence of two-phase fault rock properties on simulated oil production from a synthetic reservoir model with other fault-related uncertainties. Their results suggested that the two-phase properties of fault rocks present a significant uncertainty, however that this uncertainty would likely be reduced with increasing availability of experimental two-phase fault rock data. In recent years this data has begun to become available (Al-Hinai et al., 2007; Tueckmantel et al., 2012a), and can be incorporated into specialist simulation software (e.g. TransGen, Badley Geoscience) using the upscaled pseudo relative permeability approach outlined by Manzocchi et al (2002, 2008b). Tueckmantel et al, (2012b) used this methodology to demonstrate the difference between using single-phase transmissibility multipliers and laboratory-derived two-phase properties in the case of CO_2 sequestration in faulted saline aquifers. They concluded that ignoring the two-phase properties of fault rocks may pose a significant risk to pressure prediction and trap integrity during injection of CO_2 into the subsurface.

It is our suspicion that two-phase fault rock properties (or lack thereof) may be influencing the simulation results presented here, in particular the water production. The more segmented of our models display a lower cumulative produced volume of water over the course of the simulation runs. One explanation for this may be that since two-phase fault rock properties are not employed, and single values of fault permeability are used within the simulator, then the relative permeability of water is being underestimated for the fault rock. This results in reduced across fault flow of water and hence lower water production than may be the case in reality. This effect seems to be magnified for higher fault threshold pressures.

Alternatively (and perhaps the more likely explanation) is that the disparity between produced oil and produced water could be a result of relative permeability effects within the grid cells themselves. Within the reservoir interval oil saturation is high compared to water saturation, and hence oil is more mobile due to its higher relative permeability. It is therefore easier for oil to flow around faults than water, with the result being that increasing fault tip length does not significantly impact oil flow. Conversely, since water has a low relative permeability any increase in fault length significantly increases the time which it takes for water to flow around the faults. It would be expected that as a reservoir became depleted and the relative permeability of water increased, then fault length and connectivity would begin to impede oil flow to a greater extent, and water flow to a lesser extent.

6.5.4 Fault Threshold Pressures

Fisher et al, (2001, figure 3) conceptually illustrated that for positions lower down a fault the buoyancy force is reduced and there will hence be a lower likelihood of the threshold pressure being exceeded. They suggest that this leads to lower across-fault flow rates with proximity to the free water level due to reduced oil saturation of the fault and hence reduced relative permeability for oil. This concept is not however integrated into the functionality of conventional fluid flow simulators, where only a single threshold pressure value for the entirety of a fault can be assigned. Once this value has been exceeded then the whole fault becomes active for across-fault flow at the same instant, albeit with fault permeability controlled by the transmissibility multipliers. It is however geologically unrealistic to assign single fault threshold pressures values. Fault threshold pressure is dependent on the pore throat diameter, and hence indirectly on the proportion of shale (or other mechanisms, e.g. cementation) incorporated along the fault (Bretan et al., 2003; Yielding et al., 2010). As a result different parts of a fault with inevitably have different threshold pressures, depending on the local stratigraphic properties. The model of Fisher et al, (2001) represents a composite scenario, where faults have uniform threshold pressures, but where across-fault flow rates are

influenced by relative permeability effects. We would suggest a modification, wherein different parts of a fault have different threshold pressures as controlled by fault zone architecture and distribution of fault petrophysical properties. In this case the point on a fault where threshold pressure is initially exceeded is dependent on both the distribution of threshold pressures on a fault, and the buoyancy force at a specific threshold pressure value. The leak point may therefore not necessarily be located at the crest of a bed-fault intersection. For simplicities sake however let us assume that the position on a hypothetical fault where the threshold pressure of the fault rock is initially exceeded is located at the shallowest position on the fault. Oil enters the fault rock at this position, displaces water and increases the oil saturation and hence its relative permeability. Any cross fault pressure differential can now drive oil across the fault, with oil relative permeability increasing to a maximum. The position of across-fault flow is however localised to where the threshold pressure was initially exceeded. Away from this position the threshold pressure is still higher than the buoyancy forces, hence preventing oil from entering the fault. Since pressure is now equalising across the fault this is likely to remain the case, assuming that there is no occurrence of along-fault flow, which may lead to increased oil saturation and decreased threshold pressures elsewhere on the fault. Across-fault flow of hydrocarbons will therefore likely be restricted to localised 'windows' where the threshold pressure has initially been exceeded, in contrast to within simulators where an entire fault becomes active at the same threshold pressure value, and subsequent across-fault flow is determined by the fault TMs and hence Darcy's law. This may in fact however be a moot argument, since areas of low threshold pressure values (assuming threshold pressure is controlled by shale/clay content) will also correspond to less flow-restrictive TMs.

6.6 Conclusions

The simulation results presented within this chapter lead to a number of conclusions regarding the effects of incorporating fault tips, breaching faults across relay zones and varying the fault threshold pressure during simulations.

• A segmented reservoir does not necessarily imply that the reservoir is compartmentalised.

• Cumulative produced water volume and water production rate decreases as fault tip length is increased, and/or the reservoir becomes more segmented.

• Increased reservoir segmentation/fault tip length leads to an earlier onset of oil production decline, but the rate of production decline is slower than for less segmented cases.

• Cumulative produced oil volumes are marginally higher for the more segmented cases, likely due to an enhanced sweep pattern.

• The influence of including sub-seismic fault tips and relay zone breaching faults increases with increasing fault threshold pressures.

• Variability in simulation results for different degrees of reservoir segmentation increases with increasing fault threshold pressure.

• Higher fault threshold pressures tend to limit water production for a given structural configuration, although have limited impact on oil production.

• Relative permeability effects (both within grid cells and for faults) may control the magnitude of the influence of fault length and connectivity on oil and water flow within a reservoir. This will alter dynamically during production as saturations, and hence relative permeabilities, change.

Chapter 7

The Influence of Relay Zone Geometry and Distributed Deformation on Across-Fault Hydrocarbon Flow

7.1 Abstract

The influence of fault relay-zone architecture on across-fault fluid flow is investigated using example geometries observed in the Gulf of Corinth rift. These outcrop analogues are used as a guide to generate geocellular models encompassing a range of different relay zone geometries. Simulations of oil production across these relay zones illustrates the local impact of varying the geometric configuration. In addition the impact of including varying degrees of distributed deformation in the form of normal drag is assessed. For all cases of relay zone architecture including distributed deformation increases the juxtaposition area and enhances across fault flow.

7.2 Introduction and Aims

Chapter 6 illustrated how the incorporation of intact versus breached relay zones can effect hydrocarbon production at the field scale. This chapter focuses on the scale of individual fault-sets, and how varying their geometry may locally influence fluid flow.

Relay zones play a critical role in the process of fault evolution and growth (Peacock and Sanderson 1994; Cartwright et al., 1996; Childs et al., 1995, 2009). Depending upon their linkage history they may (or may not) be the location of displacement minima (Peacock and Sanderson, 1991; Cartwright et al., 1995; Walsh et al., 2002, 2003), and hence influence the depth of structural spill points within fault-controlled hydrocarbon traps (chapter 4). Relay zones are also important during hydrocarbon field appraisal and development, with their geometry allowing across-fault connectivity of otherwise separated stratigraphy. In turn this allows hydraulic continuity across faults which may otherwise form juxtaposition seals and be pressure compartmentalising (Manzocchi et al., 2008a, b, 2010). The precise geometry of a relay zone may influence how fluids can flow across it. This chapter explores how different relay zone geometries influence across-relay fluid flow during hydrocarbon production, using example geometries from both the Gulf of Corinth rift, and sub-surface data.

Seismic resolution often does not allow imaging and full constraint of fault and fault linkage geometries, hence leading to uncertainty in cross-fault juxtapositions and fault rock properties. Limitations of seismic resolution often permit multiple, equally valid, interpretations of fault and fault relay geometries to be constructed, however it is common that only a single

geometry is modelled and taken forward as the base case for simulation. In addition, geometries observed in the field show (figures 3.32, 7.2) that normal drag occurs at multiple scales and can have significant implications for cross-fault juxtapositions (Freeman et al., 2008; Wibberley et al., 2008; Povey, 2010), and hence cross-fault flow and reservoir compartmentalisation (figure 7.1). Towards fault tips where displacement is relatively low, strain may be accommodated entirely through ductile deformation in the form of fault tip monoclines (figure 7.2). This effectively reduces the length of the discrete offset on a fault. During geological modelling it is standard practise to project key stratigraphic horizons towards faults from a set distance. This removes all drag, whether a processing artefact or a genuine geometry. Here we apply geometries observed in the field to an analogous North Sea seismic dataset to show the effect that geometric uncertainty, including normal drag, can have on simulated reservoir performance.

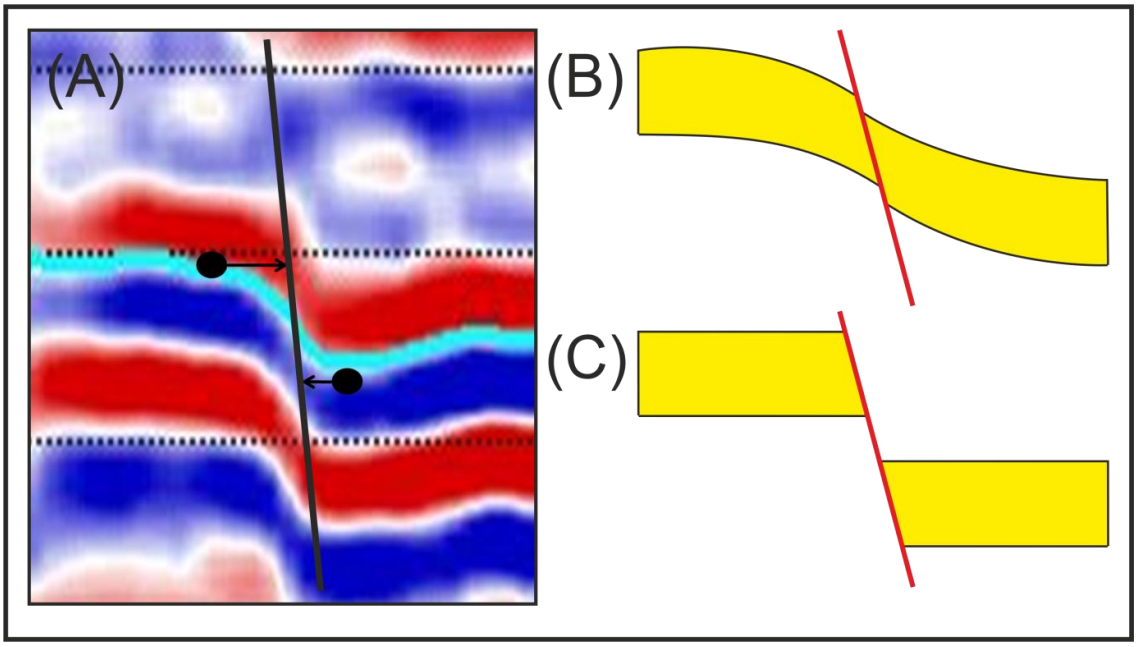

Figure 7.1. Images illustrating the effect of normal drag on across-fault juxtaposition. (A) Amplitude deterioration at normal faults leads to 'seismic drag' which obscures the position of footwall and hangingwall cut-offs. Common industry practice is to assume that no normal drag is present, with cut-off positions modelled by using a parallel projection of horizons to determine their intersection with faults. (B) If normal drag is incorporated the throw on a fault is effectively reduced leading to enhanced across-fault juxtaposition relative to the case where all drag is excluded (C).

7.3 Relay Zone Geometries

7.3.1 Gulf of Corinth Relay Zone Geometries

The onshore Gulf of Corinth rift (chapter 3) presents a number of examples of normal drag at faults (figure 7.2) as well as a range of relay zone geometries at outcrop scale (figures 7.3, 7.4). These geometries consist of hard linked relay zones where either one fault has propagated to link to another, or where a separate linking fault has nucleated across a relay ramp.

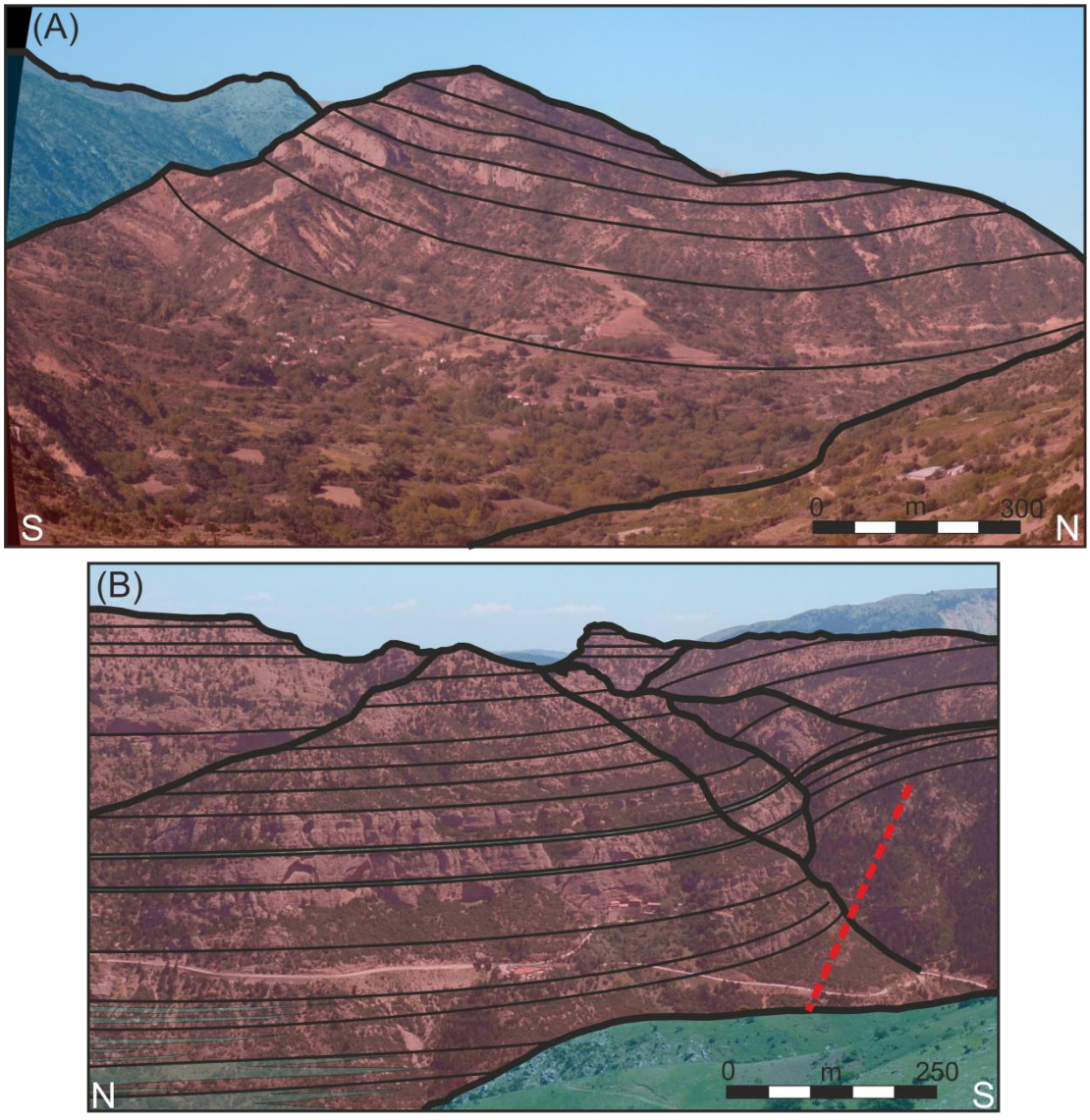

Figure 7.2. Propagation of the Dhoumena fault through the overlying sediments has resulted in the formation of a hangingwall syncline (A) analogous to large scale normal drag. Towards the tip of the fault there is a limited amount of discrete displacement, with deformation instead accommodated through the formation of a fault tip monocline (B).

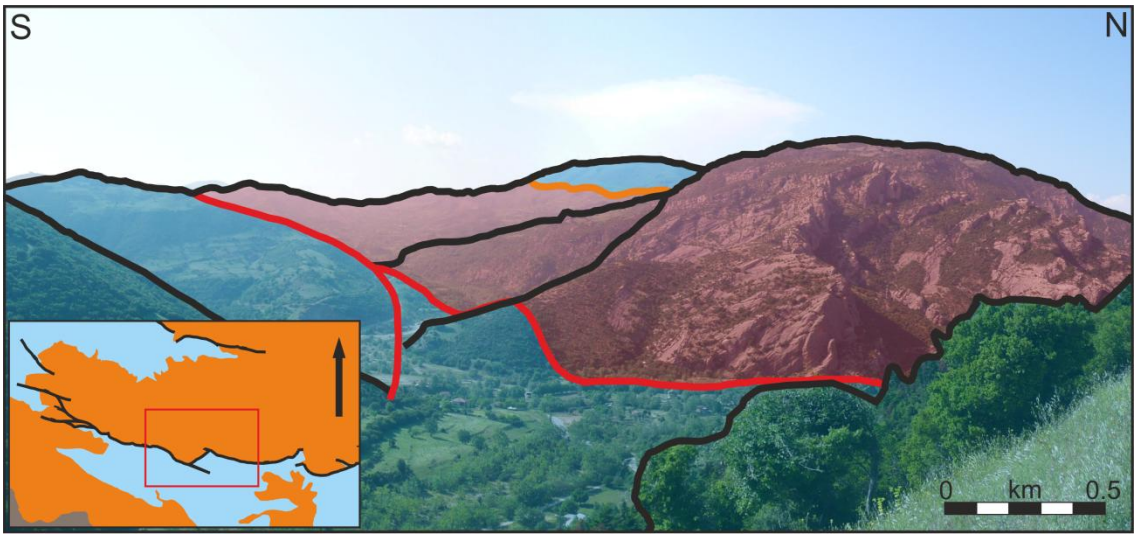

Figure 7.3. Obliquely orientated annotated photograph of the Kerpini fault relay zone. The inset map illustrates the location of the relay zone (see chapter 3 for detailed map). The outcrop suggests that the relay geometry is similar to that of the 'singly breached relay' shown in figure 7.6.

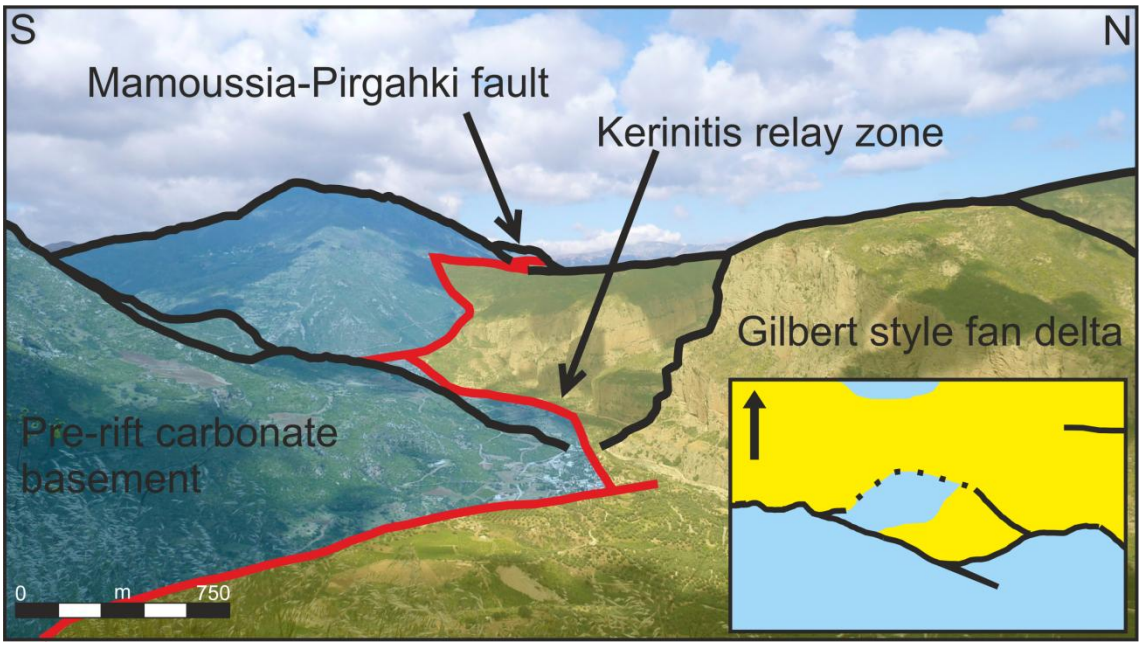

Figure 7.4. Annotated photograph of the Kerinitis relay zone on the Mamoussia-Pirgahki fault. The relay geometry is analogous to that of a single linking fault (figure 7.6). The inset is taken from the main geological maps presented in chapter 3.

Although the geometries identified in the field provide a basis for modelling the influence of relay zones on fluid flow, they do not capture the full range of relay zone geometries. A number of geometries derived from published literature have also been incorporated (e.g. Rotevatn et al., 2009; Soliva and Benedicto., 2004), assuming that the observed geometries are applicable across a range of scales.

7.3.2 Subsurface Data

The geometries observed at outcrop provide an insight into the potential architecture of relay zones in the subsurface where limitations of seismic resolution prevent a unique interpretation. This is especially the case for intra-reservoir scale faults, where displacements approach the resolution of the data, and are hence difficult to discern. These uncertainties in fault geometry can have significant impacts on the performance of a field due to variations in how fault displacement, and hence across-fault reservoir juxtapositions and fault rock properties, are modelled. To illustrate the impact of uncertainty in relay zone architecture and normal drag a 3D seismic dataset from the North Sea has been utilised. The resolution of the dataset means that multiple interpretations of fault architecture can be made and are all equally valid (figure 7.5). The relay zone geometries observed in the field provide a basis for the interpretation of a reservoir scale fault within the dataset.

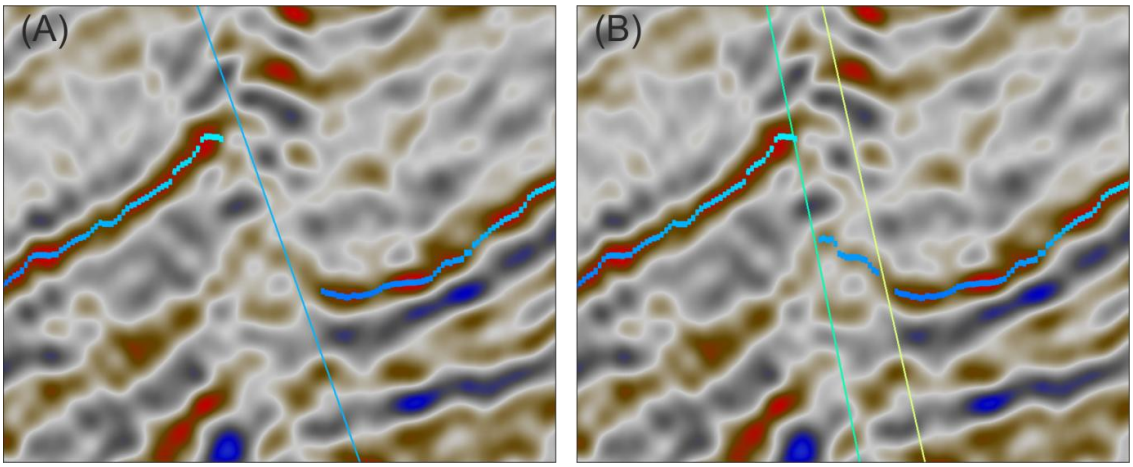

Figure 7.5. Cross-section through 3D seismic dataset from the North sea showing different, but equally valid, fault interpretations. (A) Single fault plane. (B) Overlapping faults consistent with a relay zone geometry. Deterioration of seismic amplitudes close to the fault(s) prevent a unique interpretation from being made.

7.4 Methodology

Six separate fault geometry interpretations based on seismic data from the North Sea have been modelled (Figure 7.6). Each fault model has been populated with three distinct horizon geometries (Figure 7.6, 7.7, 7.8). The fault intersections of the horizons have been modified to incorporate varying degrees of normal drag, consistent with geometries observed in the field. This results in each fault model having horizons showing no drag (100% throw), moderate drag (80% throw) and significant drag (50% throw) at the level of the uppermost stratigraphic layer (figure 7.8). These values correspond well with previously observed estimates of main slip planes accommodating 50% to 80% of total fault displacement (Freeman et al., 2008; Povey, 2010; Figure 7.7). All other parameters are constant between the models with a simple, homogenous reservoir stratigraphy uniformly populated with reservoir properties (Table 7.1). Effectively impermeable layers have been modelled above and below the reservoir interval with a standard SGR algorithm used to calculate fault rock properties (Yielding et al., 1997; Manzocchi et al., 1999; Jolley et al., 2007).

Figure 7.6 (Next page). Oblique views of relay geometries used during reservoir simulation. Fault planes are shown in white and illustrate the varied amounts of normal drag which have been incorporated. The reservoir interval is shown in yellow, whilst non reservoir top and base seals are in brown.

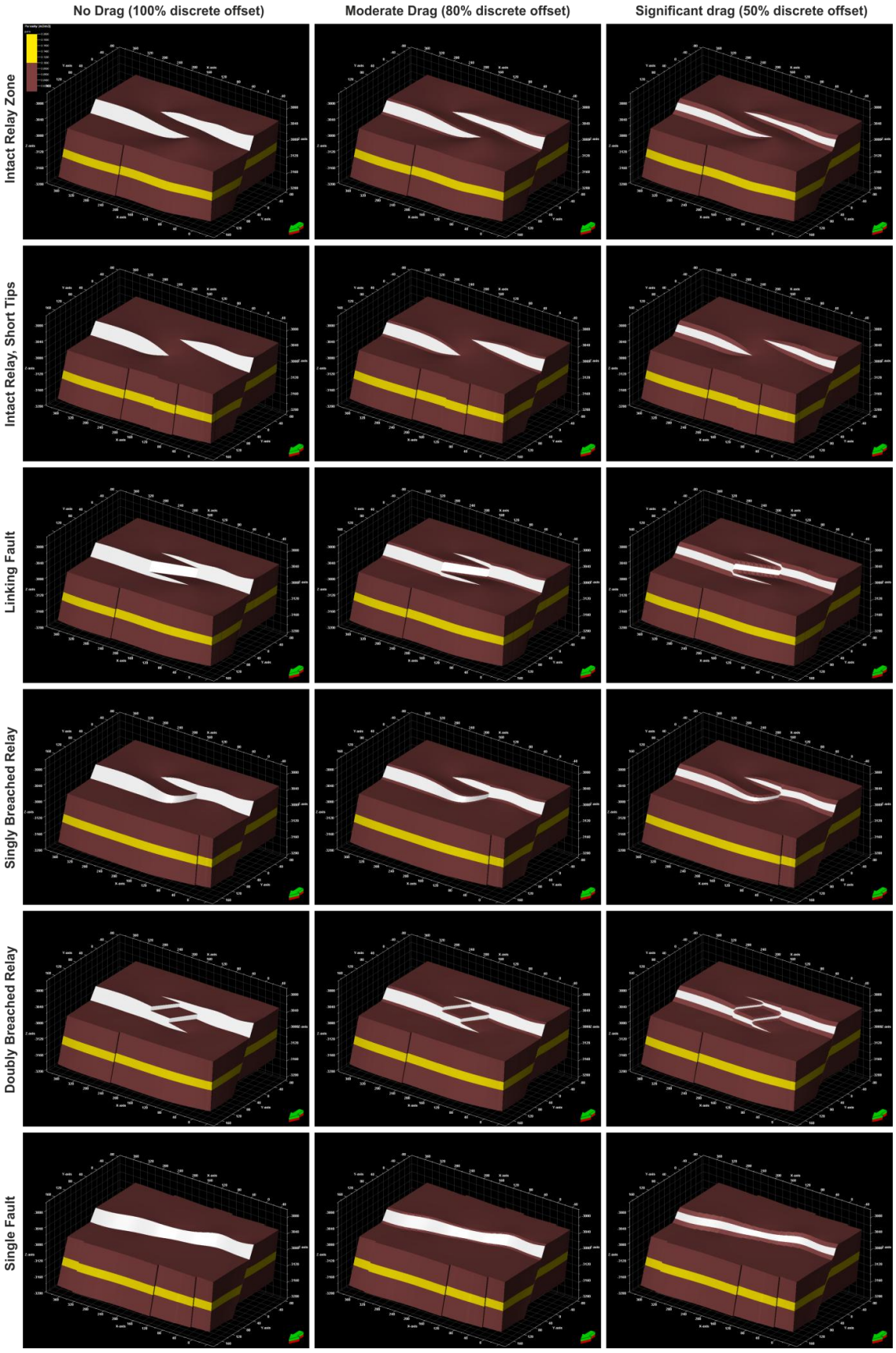
No Drag (100% discrete offset)
Moderate Drag (80% discrete offset)
Significant drag (50% discrete offset)
Intact Relay Zone
Intact Relay, Short Tips
Linking Fault
Singly Breached Relay
Doubly Breached Relay
Single Fault

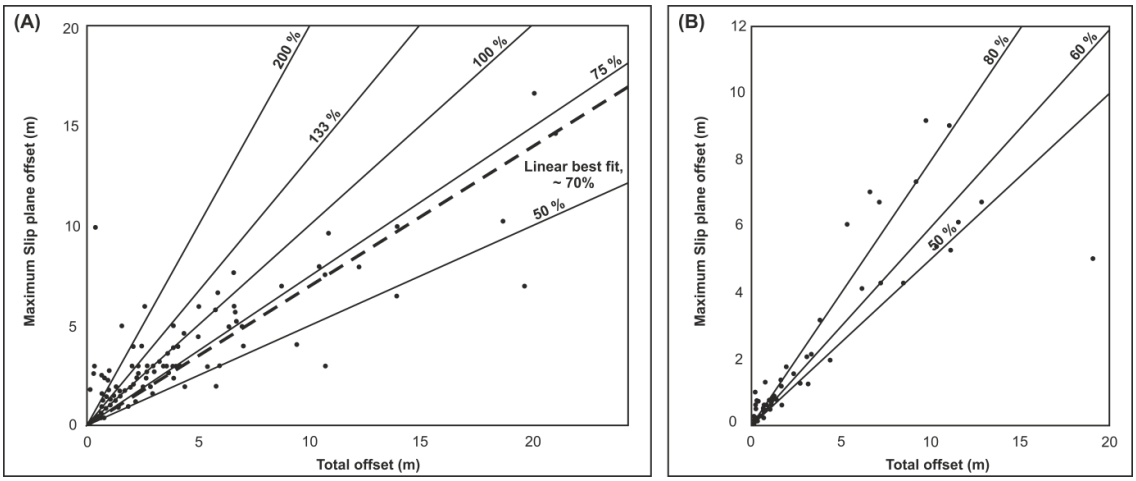

Figure 7.7. Plots of total offset versus maximum offset on a single slip surface for outcrop examples suggest that between 50 % and 80 % of fault displacement is accommodated on a single slip surface with the remainder accommodated in the form of distributed deformation. Modified from Freeman et al., 2008 (A), and Povey, 2010 (B).

Porosity	**0.2**
Permeability	50 mD
VClay	0.1

Table 7.1. Petrophysical properties of the reservoir interval for the models shown in figure 7.6.

The models have been constructed so that the mean fault throw is greater than the reservoir interval thickness for cases where no normal drag has been included. This is to emphasise the importance of relay zones for across-fault flow (Manzocchi et al., 2010). The displacement minima at the relay zones hence act to enhance across-fault juxtaposition and provide potential connectivity pathways. Including normal drag has a similar effect, essentially leading to a reduction in the discrete displacement and enhanced self-juxtaposition of the reservoir across the faults (figures 7.8, 7.9).

The impact of varying the relay zone geometry on across-fault fluid flow has been tested using a simple streamline fluid flow simulation setup (FrontSim), with a single injection well in the hangingwall and production well in the footwall. This setup encourages fluid to flow across the relay zone allowing the impact of the different geometries to be easily assessed. Selected parameters used during simulation modelling are detailed in table 7.2. Although a number of

publications have previously explored the impact of relay zones on fluid flow, these have tended to be based upon single geometric examples (Rotevatn et al., 2009; Rotevatn and Fossen 2011) or for multiple faults within hydrocarbon fields (Manzocchi et al., 2008, 2010).

Grid cell dimension	**5 x 5 m**
Fluid phases present	Water, Oil
Oil Density	875 Kg/m^3
Bubble point pressure	80 bar
Water Salinity	30000 ppm
Oil-water contact	-3245 m
Pressure at contact	320 bar
Min water saturation	0.2
Max Oil relative permeability	0.9
Simulation length	3 years
Initial Oil production rate	175 sm^3/day
Maximum water production rate	175 sm^3/day
Maximum water injection rate	175 sm^3/day

Table 7.2. Parameters used during simulation modelling. For more details see chapters 6, 8.

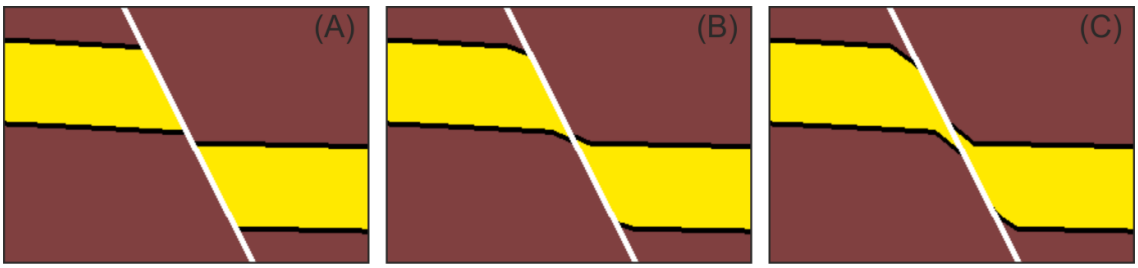

Figure 7.8. Cross-sections through modelled geometry showing the different amounts of normal drag which have been incorporated. (A) No normal drag. (B) Normal drag accounts for 20% of total displacement (i.e. discrete offset is 80% of displacement). (C) Normal drag accounts for 50% of displacement. Increasing the proportion of normal drag effectively reduces the discrete displacement, hence leading to greater across-fault juxtaposition of the reservoir interval (shown in yellow).

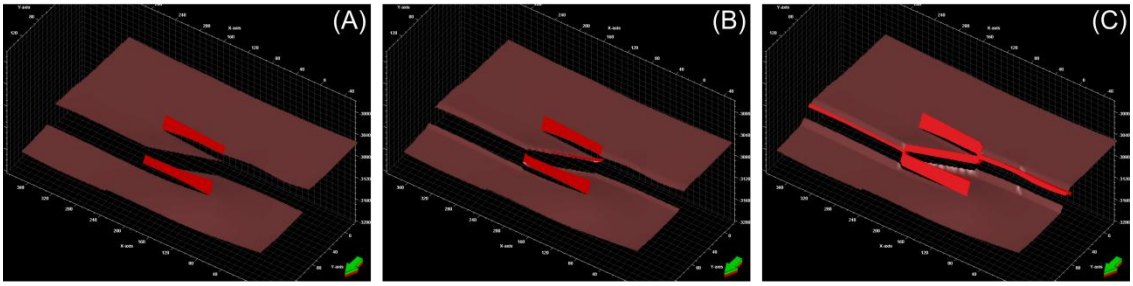

Figure 7.9. Oblique views of areas where the reservoir interval is self-juxtaposed across the faults, for the 'linking fault' geometry (figure 7.6). (A) no normal drag. (B) 20% normal drag. (C) 50% normal drag.

7.5 Results

Figure 7.10 summarises the results for the case of a relay zone with a linking fault geometry and 20% of the deformation accommodated through ductile drag. The results for all the simulations across each geometry are summarised in terms of oil production rate and cumulative produced volume of oil in figure 7.11. For all of the geometries the cumulative produced volume is greater where a larger proportion of the displacement is accommodated through distributed deformation (i.e. normal drag), rather than discrete offsets. The reason for this becomes clear when the water saturations are observed (figure 7.12). The mean fault displacement is greater than the reservoir thickness, hence where displacement is entirely accommodated through discrete offset, the reservoir interval is not self-juxtaposed across the fault. Consequently fluid is forced to flow along the fault and across the relay zone. In contrast, where a proportion of fault displacement is accommodated through distributed deformation, the throw is effectively reduced. This results in the reservoir interval being self-juxtaposed along the entire length of the fault (figure 7.9). In turn, and depending on the local fault rock properties, across-fault fluid flow is not restricted to relay zones, leading to a greater proportion of the reservoir interval being swept of oil. This is also evident from the preferred flow pathways mid-way through the simulations (figure 7.13). Where offsets are accommodated entirely through discrete deformation streamlines are restricted to relay ramps, whereas the inclusion of distributed deformation in the form of normal drag leads to streamlines being located along the entire length of a fault.

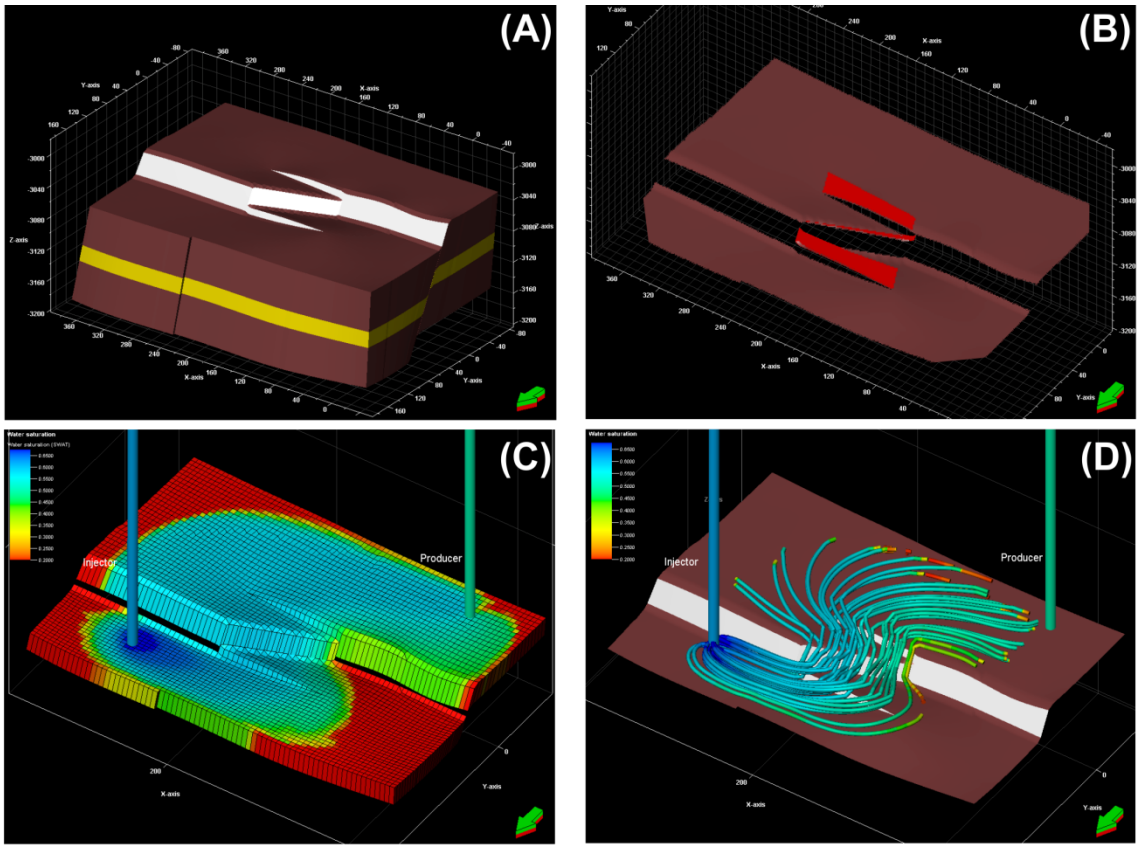
(A)
(B)
(C)
(D)
Injector
Producer
Injector
Producer

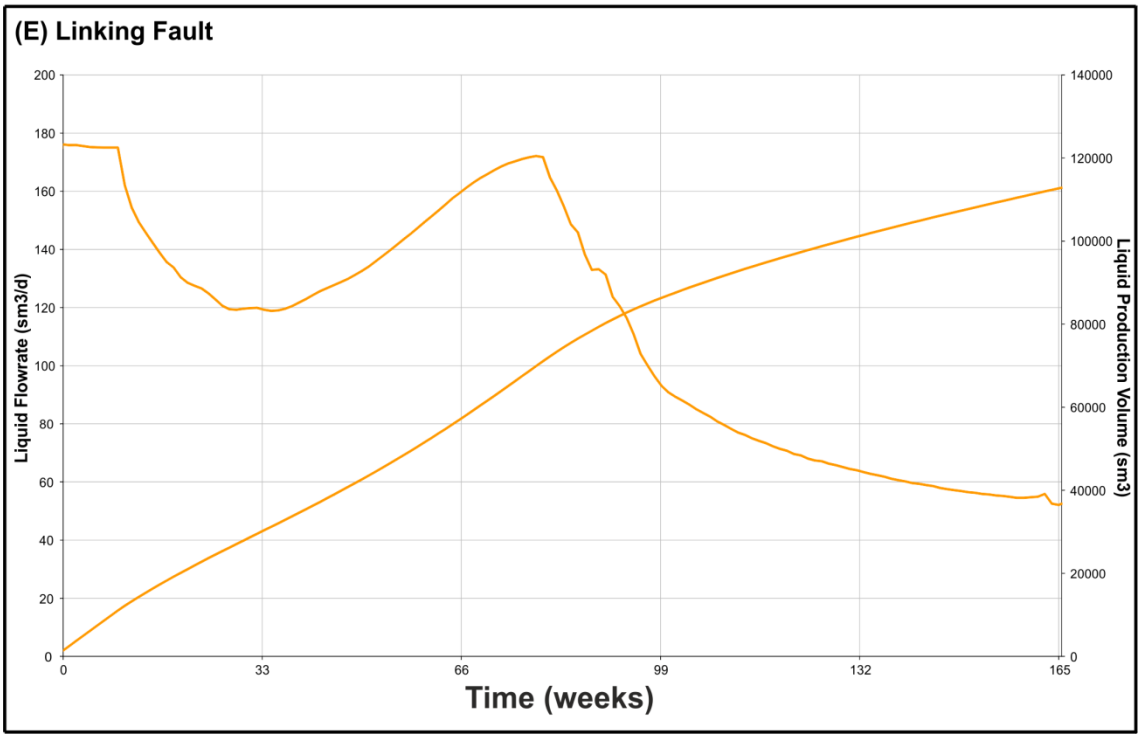
(E) Linking Fault
Liquid Flowrate (sm3/d)
Liquid Production Volume (sm3)
Time (weeks)
0
20
40
60
80
100
120
140
160
180
200
0
20000
40000
60000
80000
100000
120000
140000
0
33
66
99
132
165

Figure 7.10 (Previous page). Summary figure illustrating the inputs and results for the case of a relay zone geometry including a linking/breaching fault, and with 20% of the fault displacement accommodated through distributed deformation (i.e. normal drag). (A) Relay zone geocellular model with stratigraphy coloured by reservoir (yellow) and non-reservoir (brown). (B) Base reservoir surface with areas of across-fault self juxtaposition of the reservoir interval shown in red. These represent the available fluid flow pathways. (C) Water saturation at the final simulation timestep. High water saturation is shown in blue, whilst high oil saturations are in red. (D) Streamlines at the mid simulation timestep describing the flow pathways from the injection well in the hangingwall to the production well in the footwall. The streamlines path illustrates how the reservoir juxtaposition across the low-throw linking fault is crucial in controlling the flow across the relay zone. (E) Plot of oil production rate and cumulative oil production versus time for the linking fault geometry

For some examples, specifically for the 'linking fault' and a 'single fault plane' geometries (figure 7.6), the impact of including distributed deformation is instrumental in controlling across-fault flow. For these geometries, where discrete offsets accommodate 100% of the deformation, displacement is greater than the thickness of the reservoir interval, and hence there is little to no across fault self-juxtaposition. Consequently no across fault flow can occur. Including a proportion of normal drag leads to significantly enhanced connectivity and across-fault flow (figure 7.11, 7.12, 7.13).

Figure 7.11 (Next page). Simulation results for the different fault relay zone geometries shown in figure 7.6. Oil production rate is shown as the solid lines, whilst cumulative produced volumes are as dashed lines. The graphs are colour coded by the amount of normal drag which has been included, with green being no drag, orange being 20% drag and red being 50% drag. (A) Unbreached relay, (B) Unbreached relay, short tips (i.e. fault tip monoclines), (C) Single linking fault, (D) Singly breached relay, (E) Doubly breached relay, (F) Single fault.

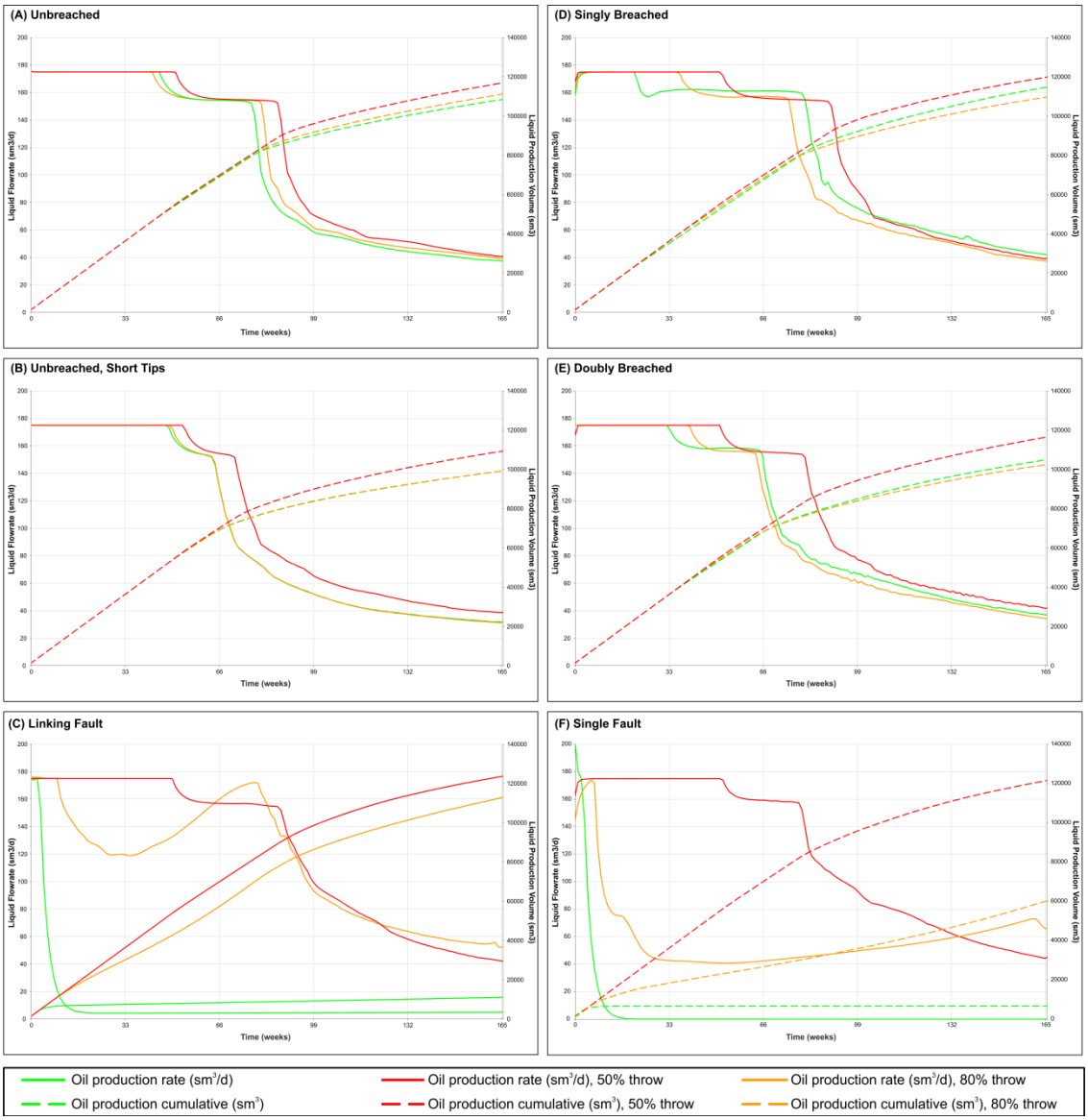

Figure 7.12 (Next page). Water saturation for the reservoir interval at the final simulation timestep for the different relay geometries and proportions of normal drag as shown in figure 7.6. High oil saturations are shown in red, whilst high water saturations are in blue. The injection and production wells are shown in the hangingwall and footwall respectively.

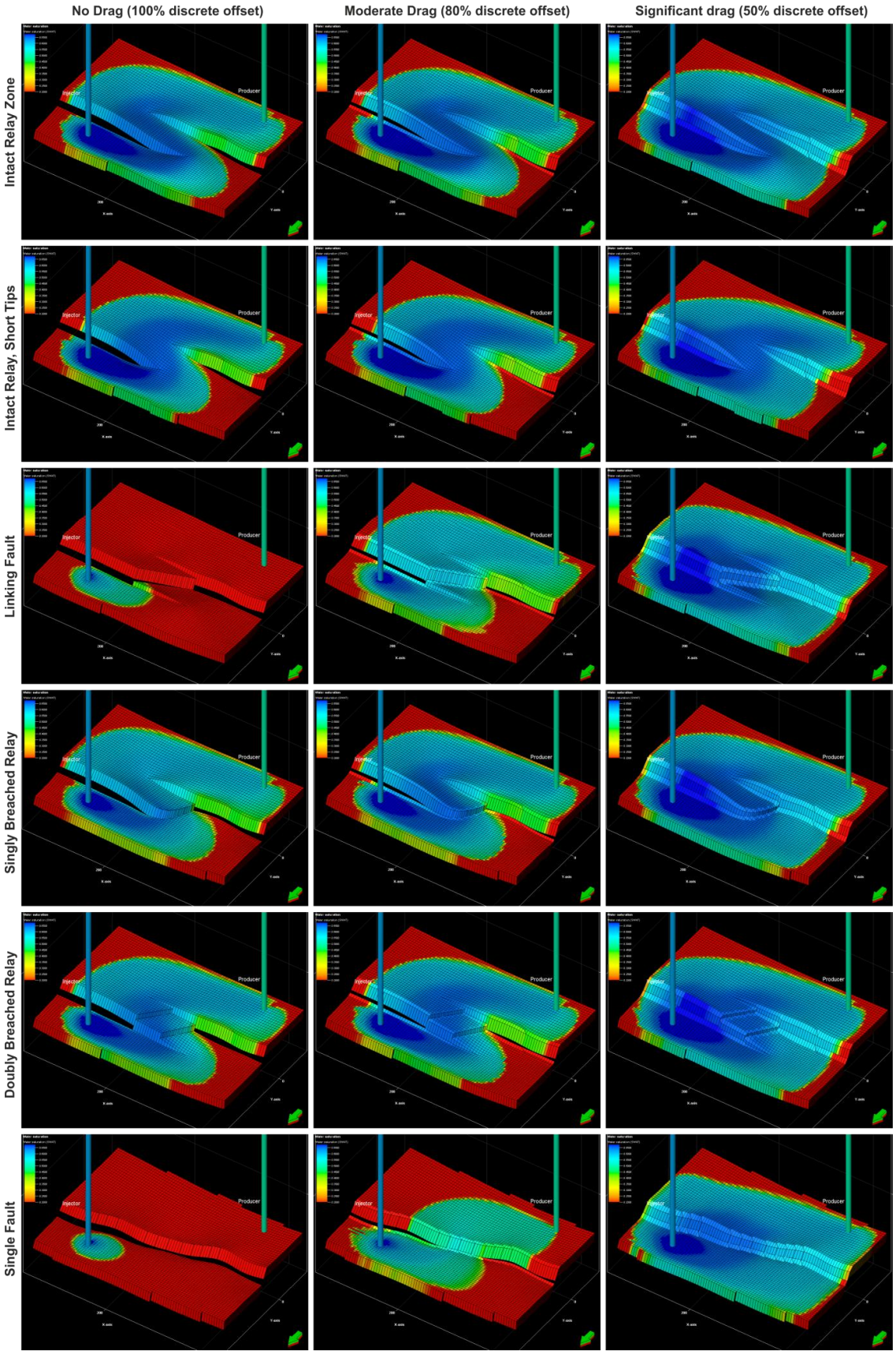
No Drag (100% discrete offset)
Moderate Drag (80% discrete offset)
Significant drag (50% discrete offset)
Intact Relay Zone
Intact Relay, Short Tips
Linking Fault
Singly Breached Relay
Doubly Breached Relay
Single Fault
Injector
Producer

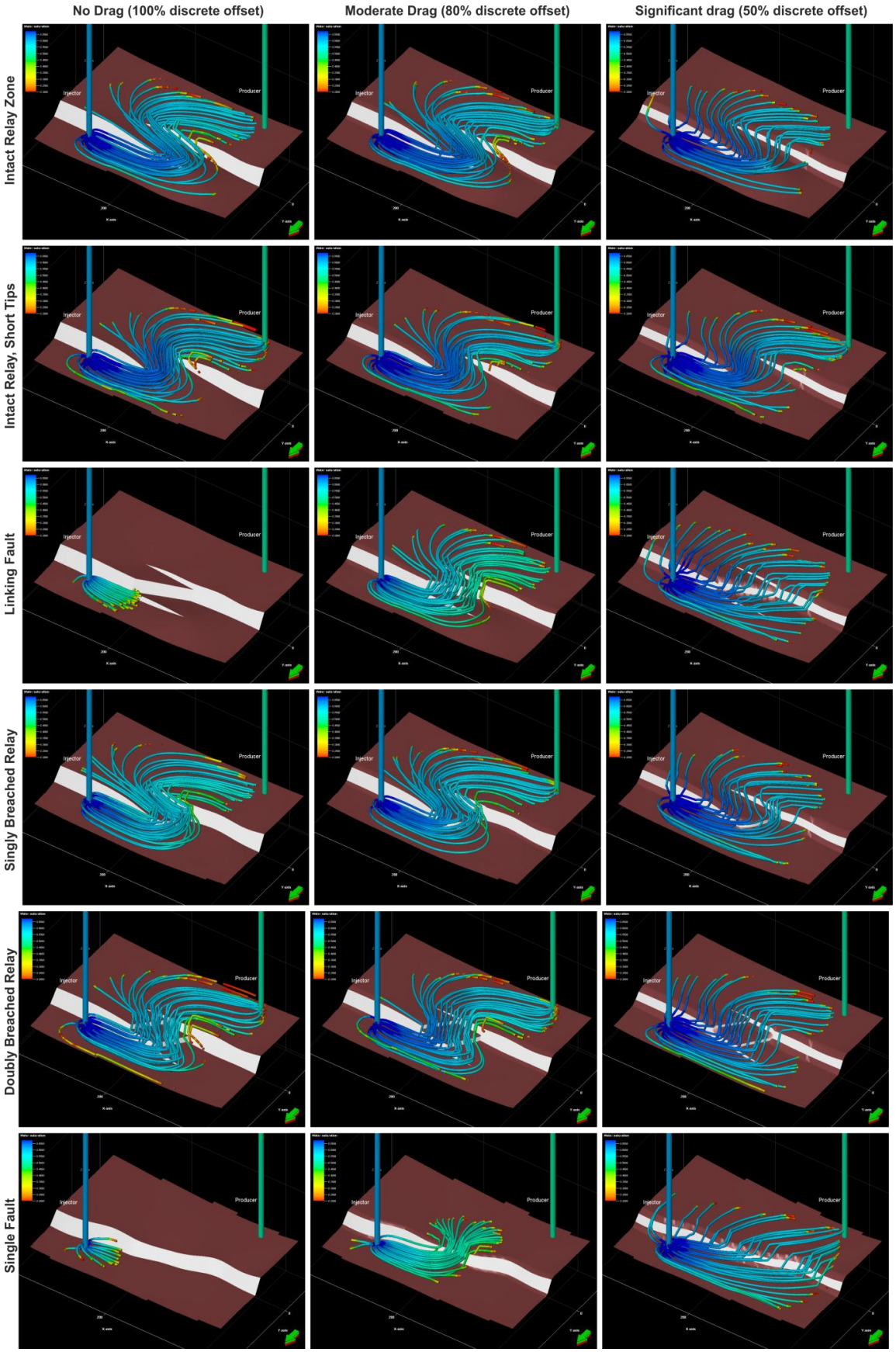

Figure 7.13. Fluid flow pathways in the form of streamlines for midway through the simulation for the different geometries shown in figure 7.6. Streamlines are coloured by water saturation and are filtered to exclude values of 0.2 or less. This hence illustrates the progression of the water flood front from the injection well.

7.6 Discussion

Simulation results presented above suggest that the inclusion of distributed deformation may enhance predicted hydrocarbon recovery from faulted reservoirs. This is especially the case where the thickness of the reservoir interval is similar to the mean fault throw. Standard industry workflows generally tend to exclude normal drag from reservoir models since it is not directly imaged due to limitations in the resolution of seismic data. This is contradictory to observations of faults from this (figure 7.2), and other studies (Freeman et al., 2010), which suggest that distributed deformation may accommodate up to 50% of a faults total displacement. It would therefore be prudent to generate multiple realisations of fault displacement when constructing reservoir models to be taken forward for predictive fluid flow simulation.

The differences in the results for the different relay zone geometries are minimal where the same proportion of distributed deformation has been assigned (figure 7.11). This suggests that simply including across-fault juxtapositions in any form (either via a relay zone or reduced throw through distributed deformation), has a similar impact on across-fault flow and reservoir production performance, where other variables (e.g. production strategy, fault rock properties, etc) remain constant. Determining the presence or absence of a relay zone is therefore more influential on across-fault fluid flow (Manzocchi et al., 2008; Rotevatn et al., 2009a, b, Rotevatn and Fossen, 2011).

The simulations run here are designed so that fluid is forced to flow across the faults, either at the relay zones or where the reservoir is self-juxtaposed. Combined with the restricted grid dimensions acting as a lateral boundary to flow, this may distort the flow behaviour relative to a larger, more complex grid geometry. Despite this the observation that relay zones are critical for across-fault flow at the production scale corresponds with similar studies using full field simulations (Manzocchi et al., 2008).

With this study distributed deformation has been accommodated as normal drag, essentially a ductile deformation style. However the impact on displacement, and hence across-fault juxtaposition, is similar whether distributed deformation is manifested as normal drag or as multiple discrete slip surfaces (figure 7.14), or as a combination of the two. Nevertheless a conceivable difference between these two scenarios would be that in the case of multiple slip surfaces the fault-normal harmonic average permeability would be reduced relative to the normal drag geometry due to the development of multiple zones of fault rock (figure 7.14). This would result in reduced fault flow across the fault zone for a given pressure gradient. Predicting whether deformation is accommodated through a single or multiple slip surfaces or

ductile normal drag hence has significant consequences for predicting across-fault fluid flow behaviour. This quantitative prediction is however outwith the scope of this research.

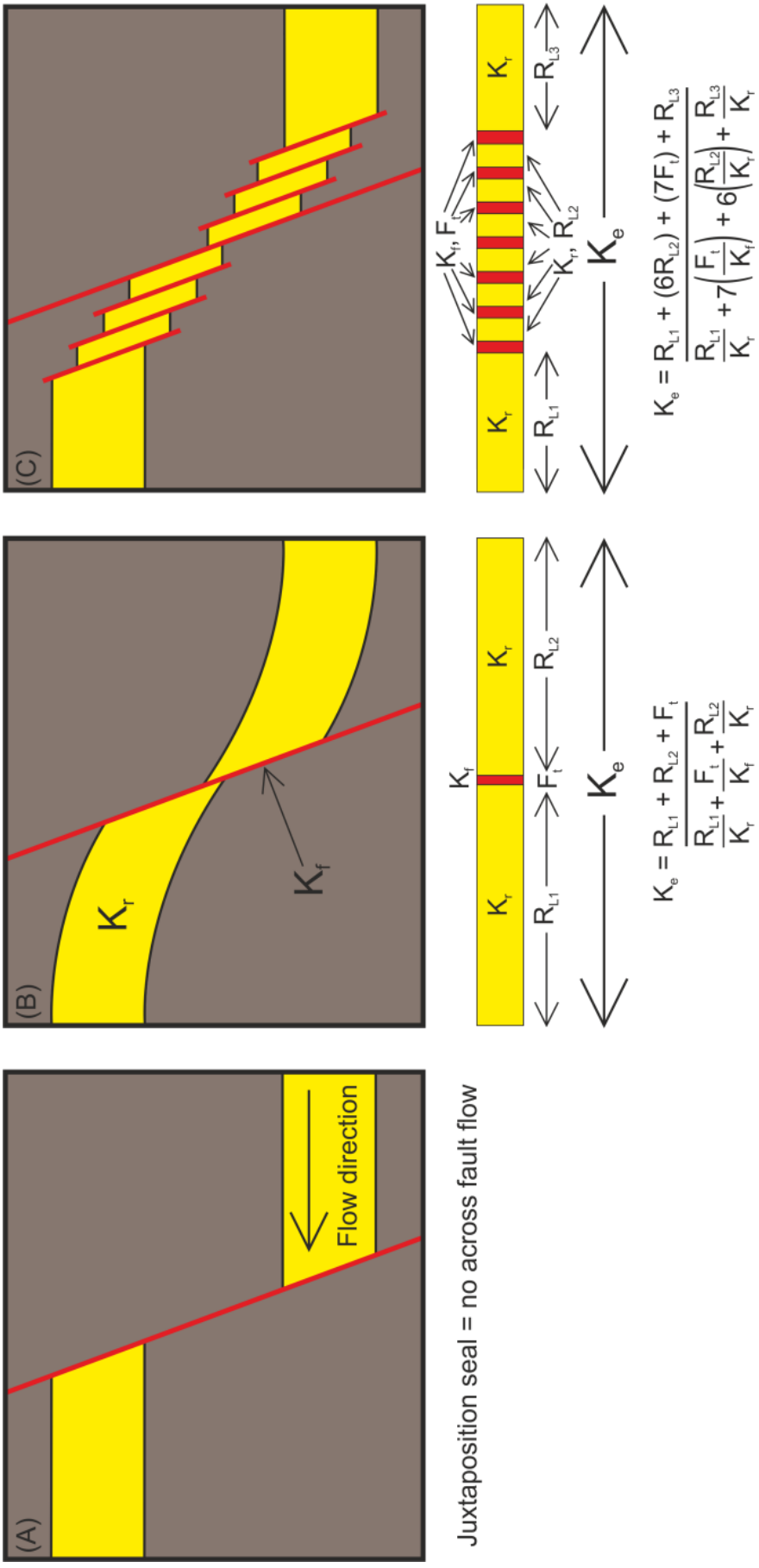

Figure 7.14 (Previous page). Conceptual diagrams illustrating the impact of different styles of deformation accommodation on across fault flow properties in 2D. (A) A single discrete slip surface accommodates all displacement. This leads to a juxtaposition seal being present. (B) A proportion of the total deformation is accommodated by ductile drag. This results in cross fault juxtaposition of the reservoir interval being maintained. (C) Multiple slip surfaces accommodate the deformation. Across-fault self-juxtaposition is maintained although multiple zones of (low permeability) fault rock are developed, leading to a reduction in the overall harmonically averaged effective permeability (K_e). K_r = reservoir permeability, K_f = Fault rock permeability, $R_{L1, 2, 3}$ = reservoir length, F_t = fault rock thickness.

7.7 Conclusions

Fault-relay and drag geometries observed in the Gulf of Corinth provide structural analogues for hydrocarbon production settings located within similar extensional provinces. By running fluid flow simulations across models based on geometries observed in the field, the influence of their geometry on across-fault flow behaviour can be quantified.

• The incorporation of distributed deformation in the form of normal drag may significantly influence sweep patterns, production rates and cumulative produced volumes of hydrocarbon across relay zones, however the precise relay zone geometry is of less importance. Correctly determining whether a relay zone is present or not is a significantly more influential uncertainty.

• In all cases of relay geometries modelled herein, accommodating a proportion of the total displacement as normal drag, as observed at outcrop (chapter 3), increases the area of across-fault reservoir self-juxtaposition.

• Increased juxtaposition area enhances across fault flow leading to longer periods of high production rate (i.e. a later onset of production decline), and correspondingly greater production volumes.

• The initial interpretation of fault and fault-relay geometries in seismic data is a major uncertainty and has significant implications for simulated reservoir performance.

Chapter 8

Comparing Simulated Production Response Across Realistic and Seismically Forward Modelled Fault Geometries

8.1 Abstract

The impact of geometric uncertainty on across-fault flow behaviour at the scale of individual intra-reservoir faults is investigated within this chapter, following from field-scale work in chapters 5, 6 and similar fault-scale analysis in chapter 7. A high resolution digital elevation model (DEM) is used to construct and subsequently populate an outcrop-scale geocellular grid capturing realistic fault geometries. Seismic forward modelling of this grid allows generation of a 3D synthetic seismic cube, which reveals the corresponding seismically resolvable fault geometries. Construction of a second geocellular model, based upon the seismically resolvable fault geometries, allows comparison with the original outcrop geometries. Running fluid flow simulations across both models allows the impact of the different geometries to be quantified. Results suggest that seismically resolvable faults significantly underestimate the area of across-fault juxtaposition relative to realistic fault geometries. In turn this leads to overestimates in sealing ability of faults, and inaccurate calculation of fault plain properties such as transmissibility multipliers (TMs).

8.2 Introduction and Aims

The use of outcrop analogues for understanding geological uncertainty in hydrocarbon reservoirs has been a common practice for many years, and with the advent, and widespread use of geological modelling software significant work has been conducted aiming to better integrate analogue data within subsurface models (Bryant et al., 2000; McCaffrey et al., 2005; Jones et al., 2009; Pringle et al., 2010). Although this work has considerably aided our understanding of geological uncertainty, it has remained largely qualitative when assessing the effect of outcrop-scale heterogeneity on hydrocarbon recovery. It is common industry practice to define a range of possible production outcomes through the use of multiple realisations of petrophysical property distributions. Increasingly, the impact of sub-surface structural uncertainty is also being quantified through the use of reservoir simulations (Tveranger et al., 2008; Manzocchi et al., 2008a, b; Freeman et al., 2010). This allows uncertain parameters to be varied within a set range of geologically reasonable values, and the impact on production rates and volumes measured permitting efficient scenario ranking. The integration of geological and reservoir engineering disciplines has lead to a number of studies characterising the flow response across specific outcrops (Howell et al., 2008; Jackson et al., 2009; Rotevatn et al.,

2009, 2011; Adams et al., 2011), with the aim of constraining the range of possible simulation responses and hence improving field development strategies. However, a quantitative comparison of the simulation response of outcrop- and seismically-resolvable fault geometries has so far been lacking.

Structural geometry is a key uncertainty in subsurface geological modelling. Precise fault-horizon intersections, fault zone complexity and fault linkage geometries are often difficult to resolve using seismic data due to effects such as amplitude deterioration and diffraction (Townsend et al., 1998). As a result, faults are generally incorporated within geological modelling software as geometrically simple two-dimensional planes separating host cells containing the petrophysical properties of the reservoir. Numerous outcrop examples suggest that this simplistic planar fault geometry is unrealistic and contradictory to theories of fault growth and evolution. Modelling faults in this manner may lead to inaccurate representations of across-fault reservoir juxtaposition and erroneous calculations of the associated fault plane properties, with potentially major implications for the simulated production response. To quantify the impact of these simplifications of fault architecture, the technique of seismic forward modelling has been combined with fluid flow simulation modelling within this chapter.

Forward modelling the seismic response of geological outcrops can be applied as a tool for understanding the constraints that the finite resolution of seismic data places on our interpretation of subsurface geology. Previously, it has primarily been used for understanding facies architectural geometries (Hodgetts and Howell, 2000; Janson et al., 2007; Bakke et al., 2008; Armitage and Stright, 2010; Falivene et al., 2010; Tomasso et al., 2010), although it can also be applied to structural uncertainty (Johansen et al., 1994; Townsend et al., 1998; Alaei and Petersen 2007; Frankowicz et al., 2009). Seismic forward modelling allows the derivation of the seismic response generated by realistic, outcrop-derived fault geometries. The aim of this chapter is to compare the simulated production across both the realistic and seismically resolvable fault geometries. This allows the identification of instances when disparities between the different geometries lead to significant variations in the production response. A high resolution Digital Elevation Model (DEM) has been used to construct and petrophysically populate a fine scale structural model capturing fault architectures at a 0.5 m resolution, up to two orders of magnitude greater than that observable in typical seismic data. This geocellular grid can be forward modelled to generate a 3D synthetic seismic cube of the response expected from a 3D seismic survey. A second structural model, at the scale resolvable in the synthetic seismic data, can be constructed and identically populated. Running production simulations across the two geometries allows quantification of the impact of the difference between realistic and seismically resolvable fault architectures.

8.2.1 Fault Evolution and Structure

The geometries, and hence the fluid flow properties, of faults are a function of their evolution and growth. Hence, an understanding of the processes of this evolution is important when trying to accurately predict the flow properties of faults in seismic data, where fine scale architecture may not be resolvable.

The evolution of rifts as a response to an extensional stress regime proceeds through the processes of fault initiation, growth, interaction and linkage (Peacock & Sanderson, 1991; Cartwright et al., 1996; Cowie et al., 2000). The accommodation of strain across a fault results in modification of the local stress field, with stress intensification at the fault tips, and a region of reduced stress in the footwall and hangingwall within which the growth of other faults is inhibited (Willemse, 1997; Gupta et al., 1998; Gupta & Scholz, 2000). This region of reduced stress is proportional in size to the length and displacement of the fault (Ackermann & Schlische, 1997), hence as individual fault segments link via relay zones their stress reduction regions expand. Smaller structures within these stress reduction regions become inactive with strain tending to become localised onto the larger, linked structures (Willemse, 1997; Cowie, 1998; Gupta et al., 2000; Walsh et al., 2001). As a rift evolves it will hence contain fewer active faults, but their average size will increase (Cowie et al., 2000). This process occurs across a range of scales, and has been documented from outcrop- (Schlische et al., 1996; Ackermann & Schlische, 1997), through to rift-scale (Cowie et al., 2000; McLeod et al., 2000). This growth model implies that faults across a range of dimensions and at varying stages of evolution are likely to be present within hydrocarbon reservoirs. Their potential impact on fluid flow is determined both by their geometry and their petrophysical properties.

At the Intra-reservoir scale the complex growth of fault systems due to stress interactions and the continual formation and destruction of relay zones is compounded by local heterogeneities in the mechanical properties of the faulted stratigraphy (Ferrill & Morris, 2008; Welch et al., 2009). These linked processes of fault growth and geomechanics result in significant vertical and lateral variability in fault zone structure manifested as multiple slip surfaces, fault bound lenses, rotated blocks and normal drag (Childs et al, 1997, 2009). This complexity leads to a net reduction in fault displacement relative to the simple, single slip surface case commonly observed in seismic data and implemented within reservoir modelling workflows. Consequently, the modelled across-fault reservoir juxtapositions may differ significantly from those which are present in the subsurface, hence impacting the accuracy of production simulations.

In addition to the uncertainty in across-fault juxtaposition as considered in cross section, complex fault linkage geometries can also represent a significant uncertainty in along-strike fault continuity and displacement variation. Seismic resolution may prevent distinguishing between different relay zone geometries or even from identifying their presence, with potentially significant implications for reservoir and hydraulic connectivity and estimated recoverables. By seismically forward modelling detailed fault- and fault-relay geometries observed in outcrops we can assess the impact of the discrepancy between realistic sub-seismic fault architecture and the modelled approximation upon hydrocarbon flow during simulated production.

8.2.2 Fault Properties

Fault transmissibility multipliers (TMs) are the numerical representation of faults and fault rock petrophysical properties within fluid flow simulators (Knai & Knipe, 1998; Manzocchi et al., 1999). They are a function of fault rock permeability and thickness as well as grid cell permeability and length. In silisiclastic sequences fault rock permeability is typically calculated as a function of fault rock clay content, often defined by the Shale Gouge Ratio (SGR, Yielding et al., 1997), itself defined by the fault throw and the volume of clay within the stratigraphy. Fault rock thickness is also routinely defined as a linear function of fault throw, despite numerous studies questioning this definition (e.g. Childs et al., 2009). Since, then, the calculation of fault transmissibility multipliers is inextricably linked to fault geometry, the fault transmissibility multipliers calculated assuming single slip-surface fault geometries will show significant discrepancies compared to those calculated using the complex geometries observed at outcrop.

8.3 Methodology

8.3.1 DEM Data

To characterise the detailed fault geometries present at outcrop a high resolution digital elevation model (DEM) from the Afar Rift system has been used (figure 8.1). The Afar depression in northern Ethiopia began to form at approximately 30 Ma (Barberi & Varet, 1977) at the triple junction between the Gulf of Aden, Red Sea and East African Rifts (figure 8.1). The depression hosts a range of tectonic regimes including the Dabbahu magmatic segment (Hayward & Ebinger., 1996; Rowland et al., 2007) where the DEM is located.

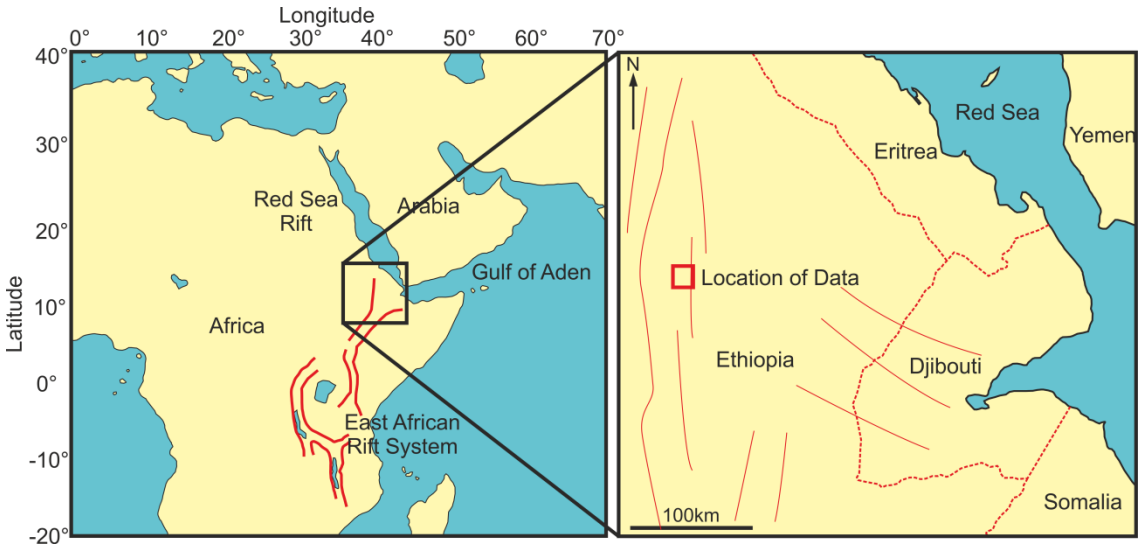

Figure 8.1. Location map for the digital elevation data used to generate realistic fault architectures. The data is located within the Afar rift system, Ethiopia. A number of the rift elements are shown for reference. See Rowland et al., 2007; Barberi & Varet, 1977 for details.

The DEM is derived from an airborne Lidar survey with a spatial resolution of approximately 0.5m, which is at least an order of magnitude greater resolution than high quality reflection seismic data. This level of resolution reveals outcrop-scale detail which would be obscured by Fresnel zone effects in seismic data, hence allowing fault structure and displacement to be accurately captured. Numerous 'reservoir scale' fault sets with displacements of up to approximately 40m are present in the area. The individual segments comprising each fault set are laterally connected via relay zone linkages displaying various stages of evolution, from soft-linked open relays through to fully breached relays with almost continuous displacements. Fault architectural complexity is greatest in the vicinity of relay zones where significant partitioning of displacement across multiple slip surface occurs. Displacement partitioning requires that the mean displacement on each individual slip surface is significantly reduced relative to that of a single slip surface scenario, leading to enhanced self-juxtaposition of lithological units across the fault set. The inference is that relay zones, whether open, partially- or fully-breached, represent the areas with the highest probability of across-fault juxtaposition, and hence of hydraulic continuity, of the reservoir intervals. Indeed, previous work by Manzocchi et al (2008) has shown that relay zones are the single most important structural factor in influencing recovery from faulted reservoirs. Fault growth models (Cowie, 1998; Childs et al., 2009) suggest that relays are almost ubiquitous in the subsurface across a range of scales, hence they are where this study is concentrated.

8.3.2 Seismic Forward Modelling and Geocellular Grid Construction

The process of deriving a synthetic seismic cube from the DEM and comparing simulated production across the outcrop and seismically resolvable fault geometries involves a four-stage workflow (figure 8.2). Two separate relay zone examples at reservoir scale have been identified and focussed upon, representing both partially- and fully-breached geometries (figure 8.3). The DEM is imported as a spatially referenced points set into industry standard geo-modelling software, where it is translated to a depth typically analogous to a hydrocarbon reservoir (3500m). A convergent interpolation algorithm is applied to generate a surface from the points data which is then cropped around the different geometries to a size of approximately 400m x 400m. These separate surfaces are then used as the basis for constructing high resolution fault models capturing the outcrop derived fault structure. Surface attributes such as dip angle and azimuth, and edge detection are employed to aid identification of small scale structures which are then used to condition the generation of a geo-cellular grid. To avoid prohibitively long simulation runs later in the workflow the grid is constructed with horizontal cell dimensions of 5m. Loss of resolution associated with this grid cell dimension is minimised by careful location of cell nodes using the higher resolution DEM as a guide. Vertical grid dimensions are set at 1.5m, with two different reservoir interval thicknesses of either 10m or 30m, which are over- and under-lain by impermeable shales (Figure 8.4). These thicknesses represent scenarios where the reservoir is thinner and thicker than the mean cumulative fault throw respectively, and henceforth are correspondingly referred to as high and low thickness to throw ratios (Th:tw). Each interval thickness is populated with two separate sets of petrophysical properties (Porosity, Permeability, VClay), representing both a homogenous clean sandstone, and a vertically heterogeneous stratigraphy based on proprietary North Sea well data through a Brent group reservoir (figure 8.4). The distributions of these properties relative to the fault geometries are then used to calculate the fault rock properties used during reservoir simulation, assuming that fault clay content as defined by the SGR algorithm (Yielding et al., 1997) is the primary control on fault rock permeability reduction relative to the host stratigraphy. Other mechanisms such as clay smearing and cataclasis are not considered. Low-, mid- and high-seal case fault transmissibility multipliers (Knai & Knipe, 1998; Manzocchi et al., 1999) are calculated by employing three separate clay content to permeability functions based on those of Manzocchi et al (1999), Jolley et al (2007) and Sperrevik et al (2002) respectively. These represent high-, mid-, and low-fault rock permeability respectively. Fault threshold pressures of 5.9 bar have been assigned based on mean SGR values for the suite of models, and the relationship defined by Bretan et al

(2003). To avoid introducing complicating variables this value has been kept constant for all faults across all models.

Figure 8.2 (Next page). Generalised workflow used for comparing simulation results for outcrop derived and seismically forward modelled fault geometries. (A) High resolution LIDAR DEM is used to construct a detailed fault model and geocellular grid at a depth of 3500m. This grid is subsequently populated with appropriate petrophysical properties. (B) The populated geocellular grid is exported to forward modelling software where the elastic and reflectivity properties are calculated. These properties are used in conjunction with a background model and seismic survey design to generate a 3D synthetic pre-stack depth migrated seismic cube. (C) The forward modelled seismic cube is interpreted and the seismically resolvable fault geometries used to construct a second geocellular grid. This grid is populated with the same petrophysical properties as the original, outcrop derived models. (D) Fluid flow simulation results for both the outcrop derived and the seismically resolvable geometries allows the differences in across-fault flow which result due to the discrepancies in fault architecture to be identified.

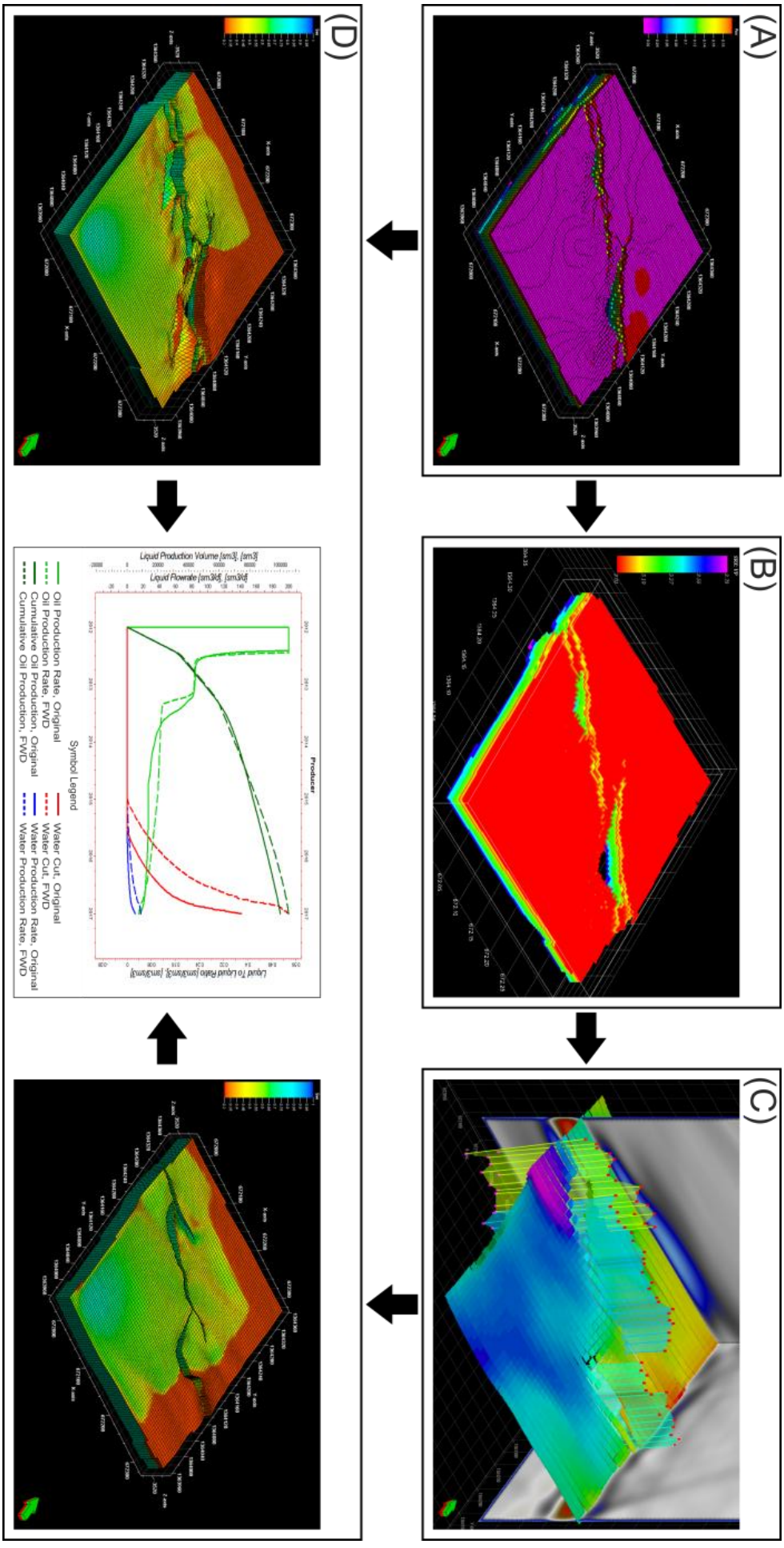
(A)
(B)
(C)
(D)
Liquid Production Volume [sm3], [sm3]
Liquid Flowrate [sm3/d], [sm3/d]
Liquid To Liquid Ratio [sm3/sm3], [sm3/sm3]
Producer
Symbol Legend
Oil Production Rate, Original
Oil Production Rate, FWD
Cumulative Oil Production, Original
Cumulative Oil Production, FWD
Water Cut, Original
Water Cut, FWD
Water Production Rate, Original
Water Production Rate, FWD

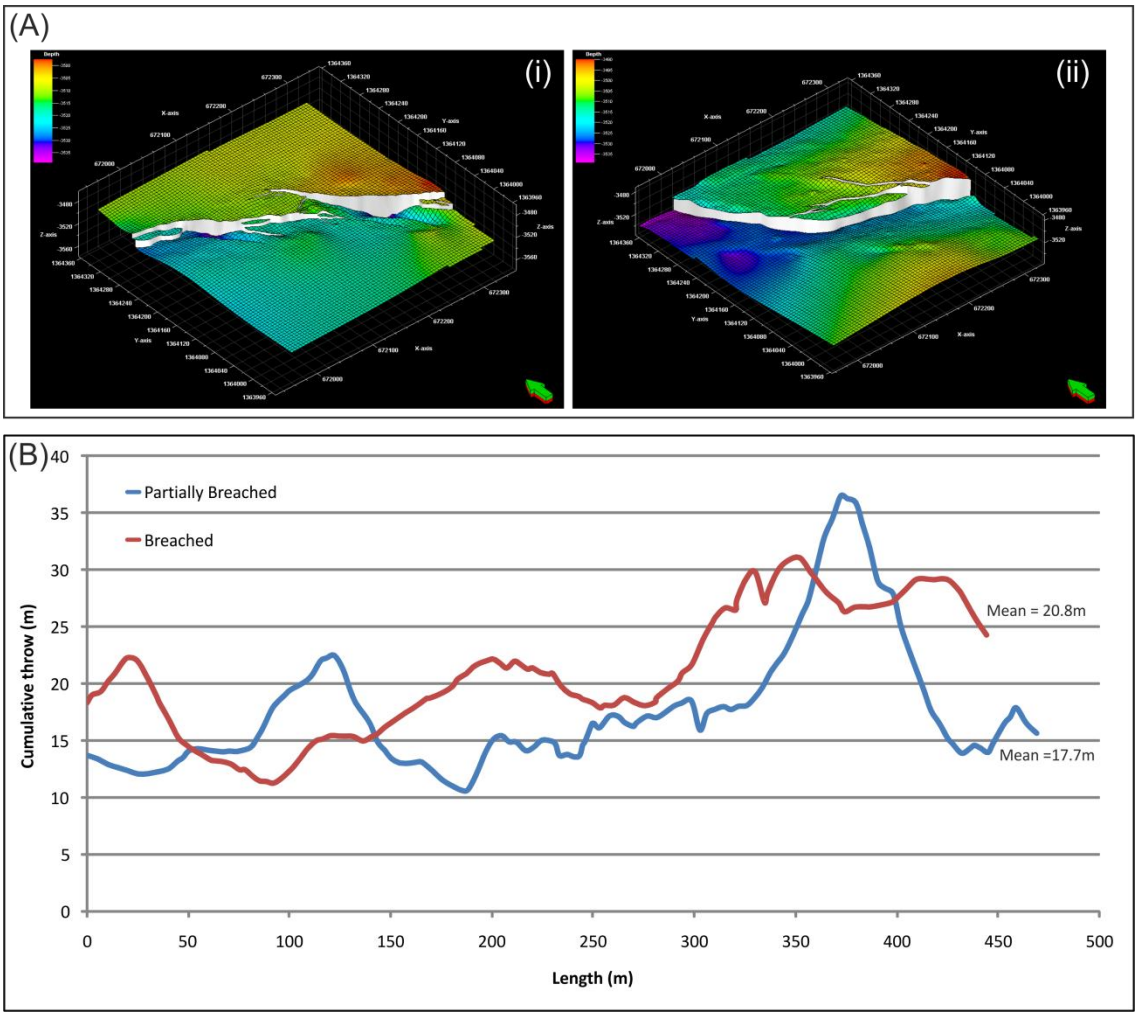

Figure 8.3. Summary of the detailed architectures used to generated the outcrop derived models. (A) Partially breached (i) and fully breached (ii) relay zone architectures as modelled from the high resolution DEM. (B) Cumulative throw profiles for the outcrop-derived fault geometries in (A).

Figure 8.4 (Next page). Well log views of petrophysical properties used to populate the geometries in figure 8.3. The reservoir interval is either thicker (A, B) or thinner (C, D) than the mean fault throws shown in figure 8.3 The stratigraphies are either homogenous (A, C) or derived from North Sea well data (B, D).

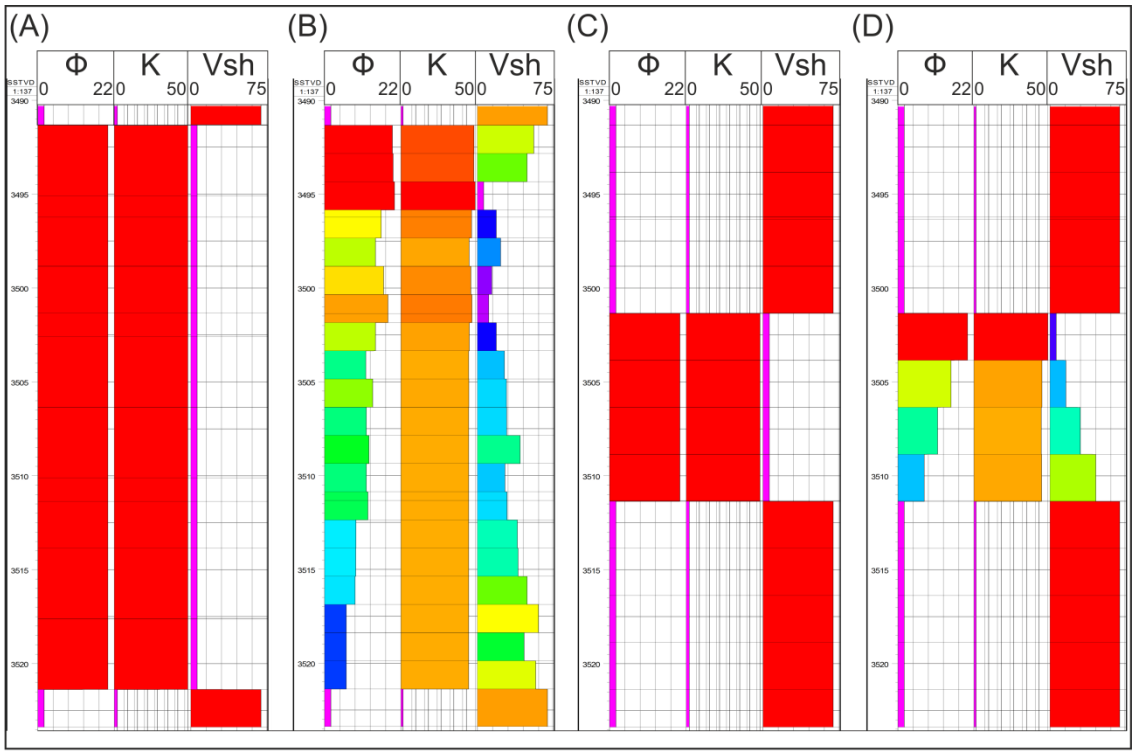

In addition to the petrophysical properties required for reservoir simulation a number of additional properties required for the seismic forward modelling process are defined within the geo-cellular grid. These properties include mineralogical volumetric fractions such VSand and VShale as well as pore pressure and fluid saturations. These properties have again been derived from proprietary well data where possible, with pore pressure defined as being approximately 22 Mpa above the hydrostatic gradient. This value is based on proprietary data from the Penguins oilfield (chapters 5, 6). The populated geo-cellular grids are exported to seismic forward modelling software where the mineralogical compositions and porosity are used to calculate the solid density assuming a Reuss mixing model (Reuss, 1929). Gassmann's theory (Gassmann, 1951) is then applied along with the fluid properties (Table 8.1) and saturation distribution to determine the elastic properties of the model, with reflectivity subsequently calculated using the Zoeppritz equations (Zoeppritz, 1919). A 3D seismic survey geometry is defined and a coarser resolution overburden model is constructed so as to account for wave propagation through the subsurface for a given input wavelet. The geological, elastic and reflectivity properties are combined with the background model and survey design and a simulated prestack local imaging (SimPLI^{TM}) algorithm (Gjøystdal et al., 2007) is applied to generate a synthetic pre-stack depth migrated 3D seismic cube (figure 8.2). This process is repeated for the eight configurations of fault geometry and property distribution which have been modelled.

PROPERTY	VALUE
Shale density	2.6 g/cm^3
Sand density	2.65 g/cm^3
Shale bulk modulus	21 GPa
Sand bulk modulus	37 GPa
Shale shear modulus	7 GPa
Sand shear modulus	44 GPa
Water density	1.02 g/cm^3
Water bulk modulus	2.78 GPa
Oil density	0.65 g/cm^3
Oil bulk modulus	1.45 GPa

Table 8.1. Physical properties used for generation of elastic and reflectivity cubes used in the seismic forward modelling process.

Reflectors within the synthetic seismic volumes which correspond to key horizons are interpreted in geo-modelling software with a range of surface attributes such as coherency, edge detection and dip azimuth applied to aid fault interpretation and modelling (Townsend et al., 1998, Freeman et al., 2010). Faults have been picked on every trace (approximately 10m spacing) in order to maximise lateral resolution and to maintain a consistent interpretation methodology. The seismically resolvable fault and horizon geometries are used to construct geo-cellular grids at the same dimensions and populated with the same properties as the detailed grids from which they are derived (figure 8.5). Fault transmissibility multipliers are re-calculated using the property distributions as defined by the forward modelled geometries.

Figure 8.5 (Next page). Oblique view of a selection of the high resolution, outcrop derived input models, synthetic seismic with 'Top Reservoir' horizon and faults shown, and the resulting geocellular grid based upon the seismically resolvable fault geometries. (A) Thickness < Throw, homogenous stratigraphy, partially breached relay. (B) Thickness > Throw, heterogeneous stratigraphy, partially breached relay. (C) Thickness < Throw, homogenous stratigraphy, fully breached relay. (D) Thickness > Throw, heterogeneous stratigraphy, fully breached relay.

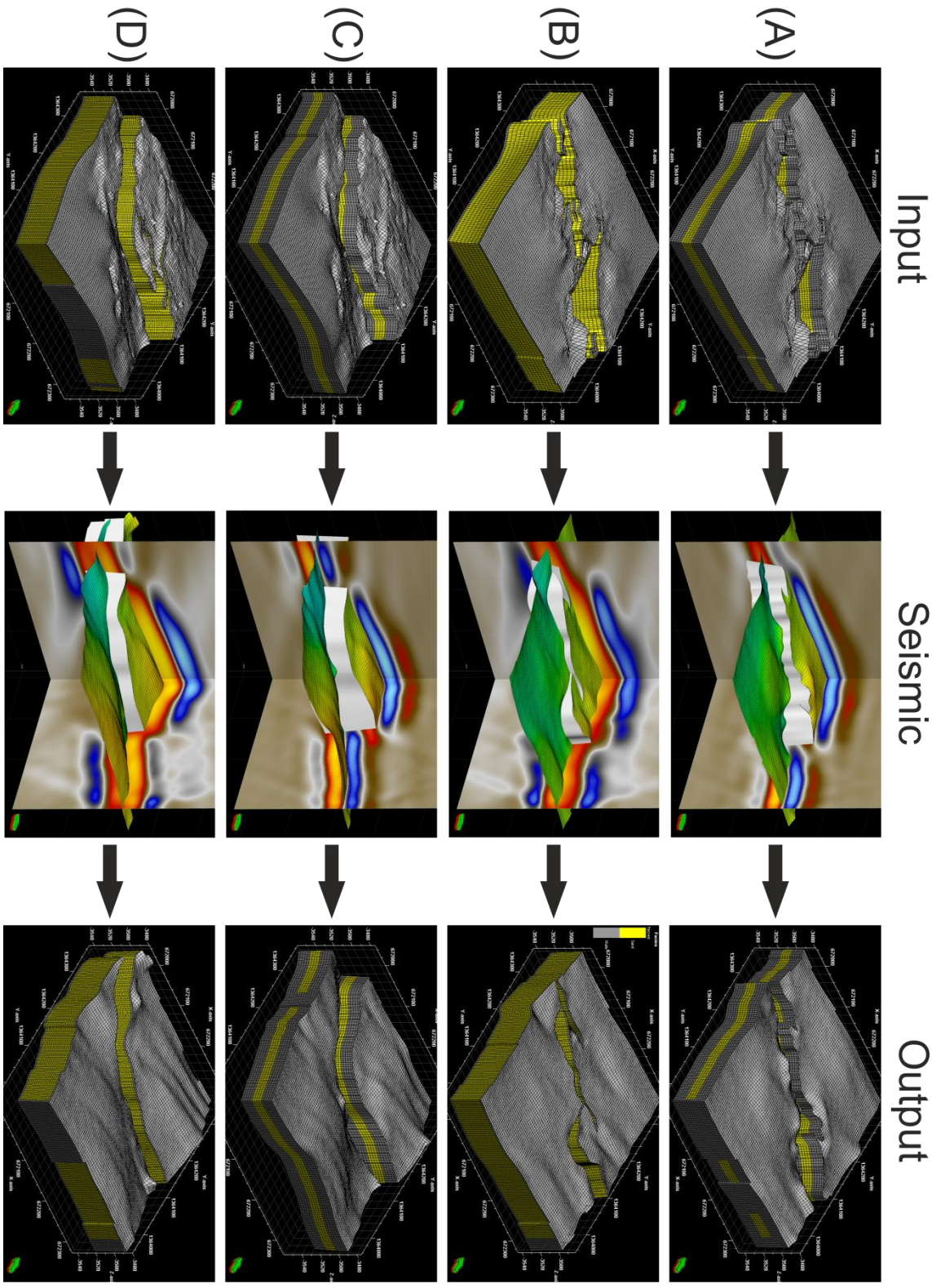
Input
Seismic
Output
(A)
(B)
(C)
(D)

8.3.3 Simulation

Following generation of both outcrop derived and seismically resolvable grids, the effect of the discrepancies between the two geometries upon across fault flow can be quantified using flow simulations. Simulation is performed using the Eclipse^{TM} black oil simulator (Schlumberger, 2008), with a 12 year waterflood development strategy consisting of a single injection well in the hangingwall and a single production well in the footwall. Maximum production rates have been set as 50 sm^3/day for oil and 250sm^3/day for produced water (i.e. an 83% water cut), with injection rates set to match oil production rates (Table 8.2). These rates are broadly inline with both the production data from proprietary dataset used to populate the stratigraphy, and similar simulation bases studies (Rotevatn et al., 2009a, b, Rotevatn and Fossen., 2011). To minimise compositional effects the bottom hole pressure has been set to prevent the bubble point pressure from being reached during pressure depletion of the reservoir. Aquifer support consists of a Carter-Tracy aquifer (Batycky et al., 2007) with drive from the down-dip hangingwall, as would be expected for a tilted fault block trap geometry.

8.4 Simulation Results

Key parameters highlighting the differences between the flow response across outcrop and seismically-resolvable fault geometries include the oil production rate, cumulative oil production volume and fluid saturation. Instances where fault geometry and fault properties play a significant role in controlling oil production can be identified by plotting the standard deviation of the simulated results against time (figure 8.6). For a particular stratigraphy there are 12 possible different structural configurations (figure 8.7). These encompass breached and partially breached relay zone geometries, their forward modelled counterparts, as well as the low-, mid- and high-case fault TM scenarios for each fault geometry. A high standard deviation of the simulation results indicates that the structural variability is significantly influencing the production response. Where the reservoir thickness is less than the mean cumulative fault throw there is an initially high degree of variability between the different fault geometries for the oil production rate (figure 8.6 A), which decreases as the reservoir becomes depleted and production rates tend towards zero. Similarly, there is considerable variability in the cumulative oil production volume between the different fault configurations (figure 8.6 B). In contrast, for cases where the stratigraphic thickness of the reservoir interval is greater than the mean cumulative fault throw (high Th:tw) the variability of simulated production results for the different structural configurations is minimal.

Reservoir Conditions	
Min Pressure	145 Bar
Max Pressure	580 Bar
Temperature	100 °C
Reference Pressure	557 Bar
Datum depth	-3540 m
Fluid Properties	
Oil density	650 kg/m^3
Bubble point pressure	142 Bar
Water Salinity	30000 ppm
Rock physics functions	
Residual oil saturation to water (Sorw)	0.25
Critical water saturation (Swcr)	0.35
Corey correlation (water)	4
Corey correlation (oil-water)	3
Max relative permeability of water	1
Max relative permeability of oil	0.8
Aquifer properties	
Aquifer type	Carter Tracy
Drive direction	Grid edge (090-270°)
Initial pressure	557 Bar
Permeability	100 mD
Porosity	0.2
External radius	150 m
Thickness	50 m
Development strategy	
Simulation run time	12 years
Reporting frequency	10 days
Target oil production rate	50 sm^3/day
Injection replacement fraction target	1
Min bottom hole pressure (producer)	175 Bar
Water injection rate	250 sm^3/day (max)

Table 8.2. Properties used during reservoir simulation. Many of these properties are derived from similar studies (e.g. Manzocchi et al., 2008; Rotevatn et al., 2009; Rotevatn and Fossen 2011).

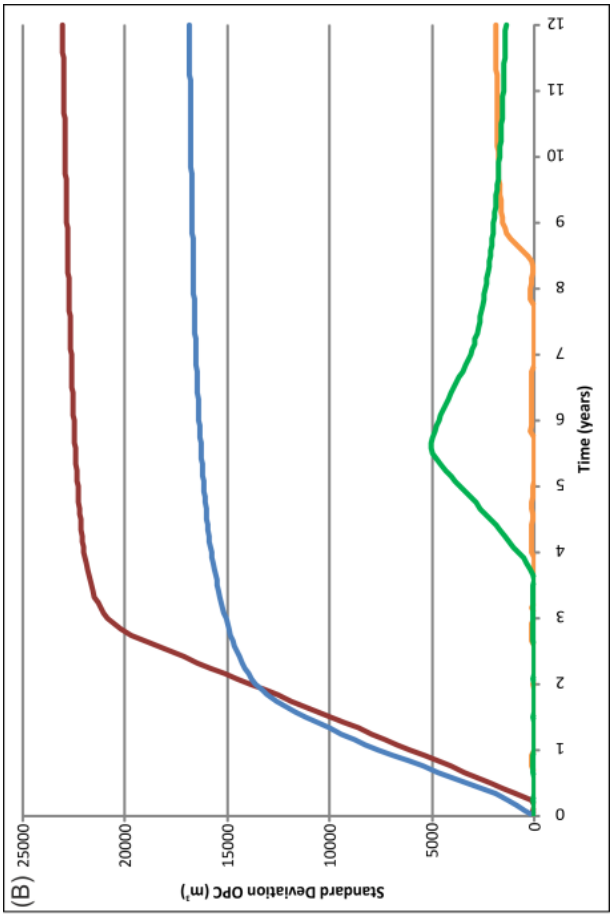
(B)
Standard Deviation OPC (m³)
25000
20000
15000
10000
5000
0
Time (years)
0
1
2
3
4
5
6
7
8
9
10
11
12

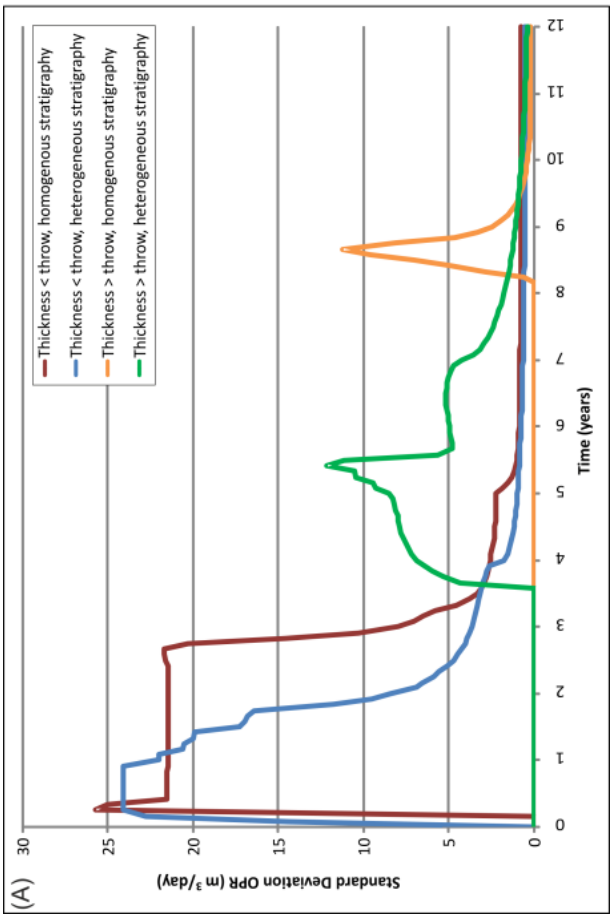
(A)
Standard Deviation OPR (m ³/day)
30
25
20
15
10
5
0
Time (years)
0
1
2
3
4
5
6
7
8
9
10
11
12
Thickness < throw, homogenous stratigraphy
Thickness < throw, heterogeneous stratigraphy
Thickness > throw, homogenous stratigraphy
Thickness > throw, heterogeneous stratigraphy

Figure 8.6 (Previous page). Plots of standard deviation against time for the different fault geometries, stratigraphies and fault properties modelled. For a particular stratigraphy the standard deviation of the simulated results for the different fault geometries and properties, and their seismically resolvable counterparts is represented. A high standard deviation indicates that the across fault flow is significantly influenced by the fault geometry and properties. (A) Oil production rate (OPR), (B) Cumulative oil production (OPC). For both OPR and OPC the faults have a significantly greater impact when the reservoir interval is less than the mean fault throw (low Th:tw).

Figure 8.7 (Next page). Figure illustrating the 12 different simulation runs for each individual stratigraphy. Each stratigraphy is populated within either a partially breached, or fully breached relay zone geometry. Each of these geometries is then seismically forward modelled. The resultant outcrop-derived and seismically resolvable geometries are used to calculate high-, mid- and low-case fault TMs based on the original stratigraphy (albeit populated within the resulting grids). Since there are four different stratigraphies used, the total number of simulation runs is 48.

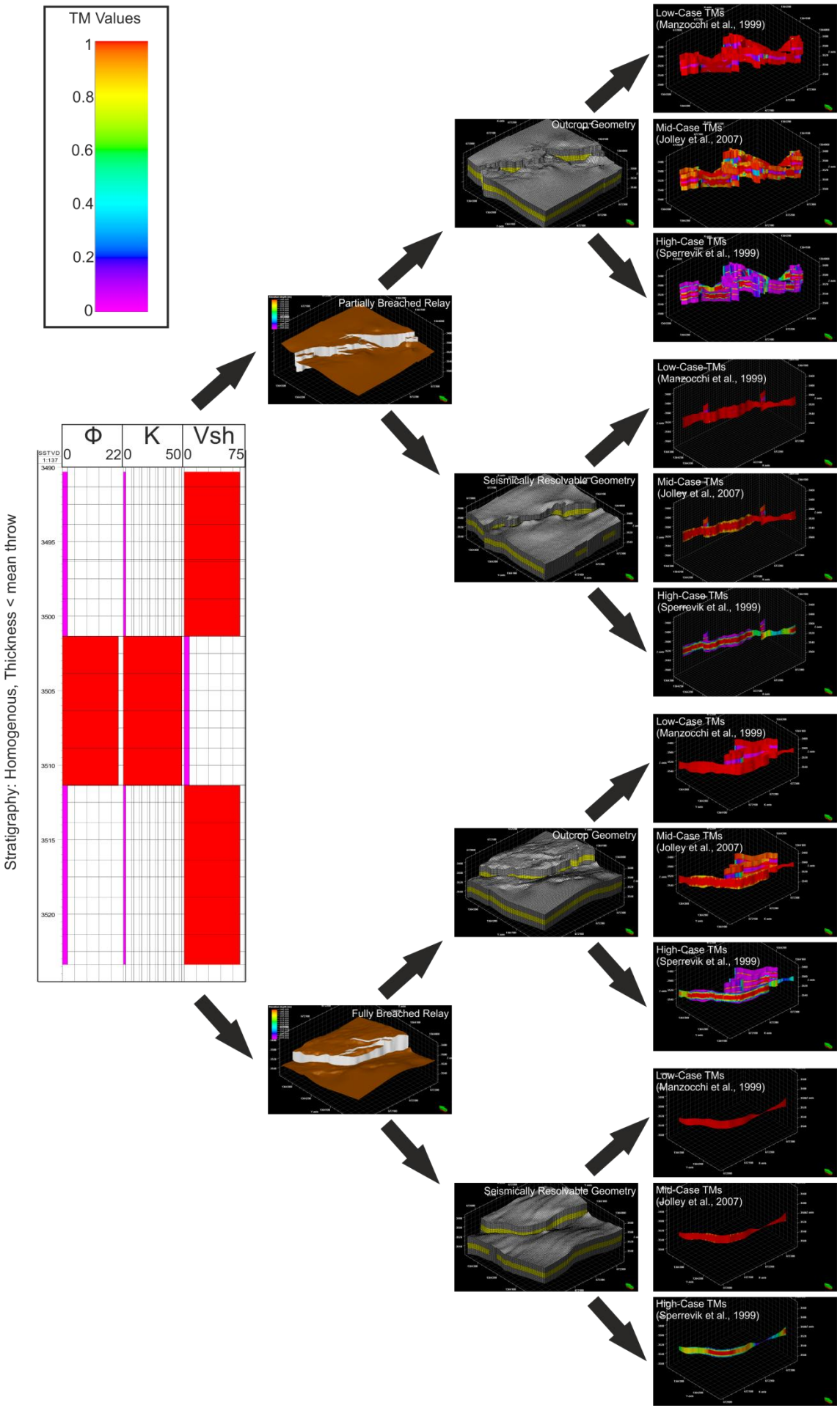
TM Values
1
0.8
0.6
0.4
0.2
0
Stratigraphy: Homogenous, Thickness < mean throw
Φ
K
Vsh
0
22
0
50
0
75
3490
3495
3500
3505
3510
3515
3520
Partially Breached Relay
Fully Breached Relay
Outcrop Geometry
Seismically Resolvable Geometry
Low-Case TMs (Manzocchi et al., 1999)
Mid-Case TMs (Jolley et al., 2007)
High-Case TMs (Sperrevik et al., 1999)

The simulation results for the different geometries, stratigraphies and fault rock permeabilities are summarised in figure 8.8. For a high Th:tw, varying the fault TMs only leads to significant variations in simulation results where a clay rich stratigraphy has been combined with the high-case (Sperrevik et al., 2002) fault TMs (i.e. low permeability fault rocks) (figure 8.8B). In contrast, where the stratigraphic thickness is less than the mean cumulative fault throw (low Th:tw) there are major differences in the results between the outcrop and seismically resolvable geometries (figure 8.8E, G). These effects are magnified where the well-derived stratigraphy, with its higher clay content, has been modelled and has hence resulted in higher clay-content, lower permeability fault rocks. Where a low Th:tw has been modelled with a fully breached relay zone there is no across-fault juxtaposition of the reservoir interval and hence no across-fault hydrocarbon flow or pressure support from the aquifer (8.8F, H). In these situations the footwall suffers rapid pressure depletion with minimal hydrocarbon production before the production well reaches its minimum bottom hole pressure and ceases to flow.

Figure 8.8 (Next page). Summary of simulation results segregated according to relay geometry (partially or fully breached) and stratigraphy. Both oil production rate (OPR) and cumulative oil production (OPC) are plotted, with results colour coded by the fault TMs used. Outcrop derived fault geometries are in solid lines whilst forward modelled geometries are in dashed lines.

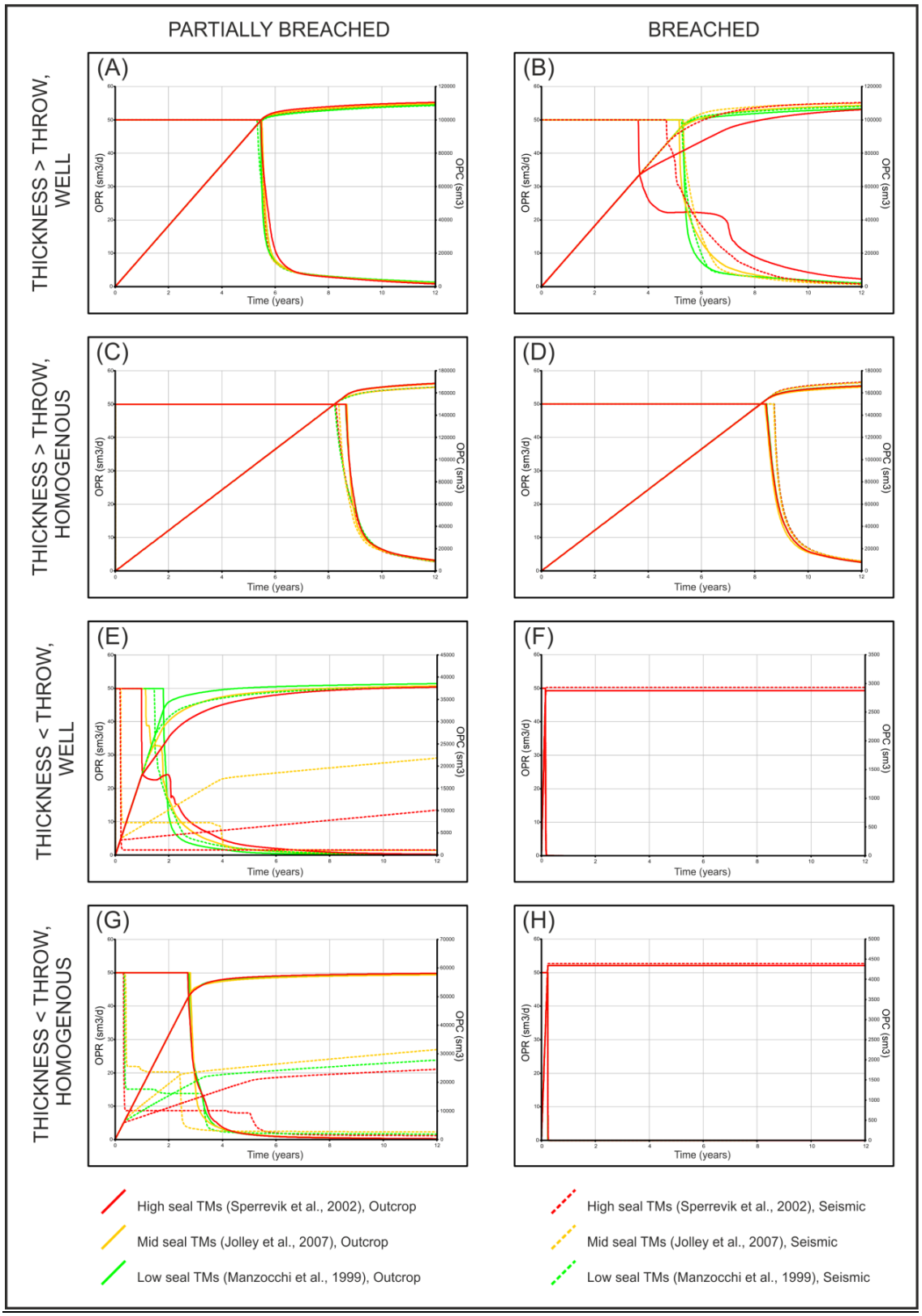
PARTIALLY BREACHED
BREACHED
THICKNESS > THROW, WELL
THICKNESS > THROW, HOMOGENOUS
THICKNESS < THROW, WELL
THICKNESS < THROW, HOMOGENOUS
(A)
(B)
(C)
(D)
(E)
(F)
(G)
(H)
OPR (sm3/d)
OPC (sm3)
Time (years)
High seal TMs (Sperrevik et al., 2002), Outcrop
Mid seal TMs (Jolley et al., 2007), Outcrop
Low seal TMs (Manzocchi et al., 1999), Outcrop
High seal TMs (Sperrevik et al., 2002), Seismic
Mid seal TMs (Jolley et al., 2007), Seismic
Low seal TMs (Manzocchi et al., 1999), Seismic

8.4.1 Impact of Across-Fault Juxtaposition Area

The occurence of disparities in production results between the different fault geometries can be explained in terms of the effective juxtaposition area. The effective juxtaposition area is defined as the area of across-fault self juxtaposition of the reservoir interval that provides a direct or indirect flow pathway between the hangingwall and footwall (figure 8.9). Juxtaposition area across parts of faults contained entirely within either the footwall or hangingwall (e.g. fault tips and splays) does not contribute (although they may still effect the overall sweep pattern of the reservoir).

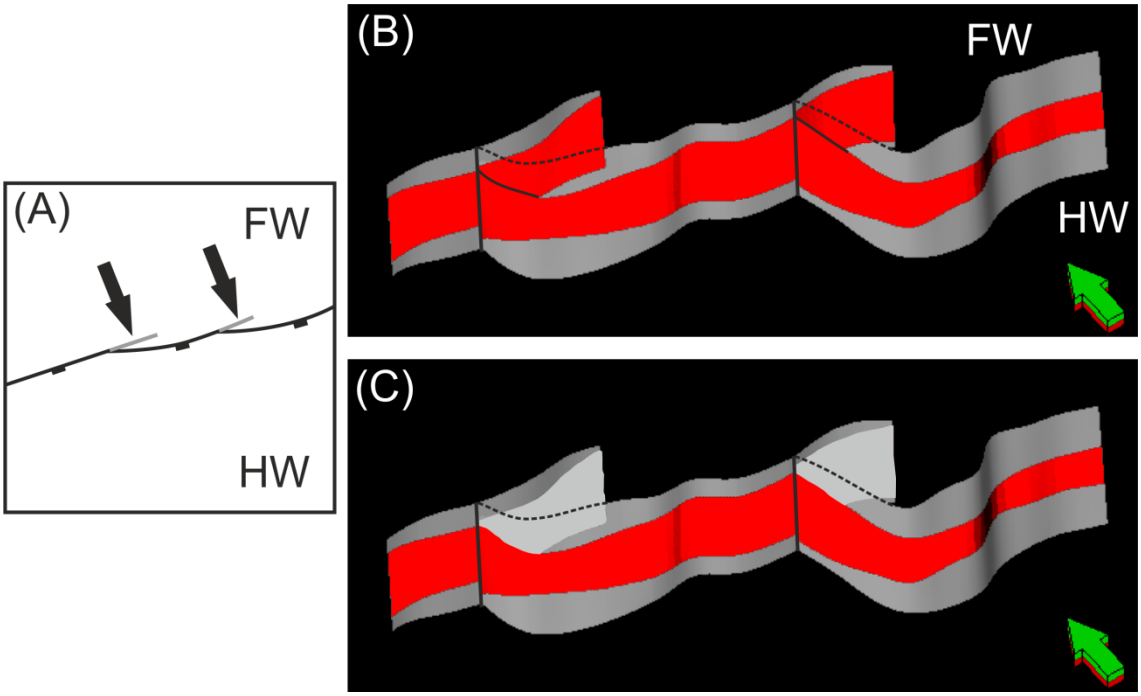

Figure 8.9. (A) Schematic aerial view illustrating the concept of the effective juxtaposition area across a fault or fault set. The effective juxtaposition area is the area of juxtaposition which connects the footwall and hangingwall blocks across a fault. Splays (arrowed, and shown in grey) contained entirely within a single fault block do not contribute, since they do not connect the footwall and hangingwall. (B) Example from seismically forward modelled geometries. Across-fault juxtaposition is shown in red. (C) As (B) but with non-contributing splays greyed-out.

Figure 8.10 shows how the effective juxtaposition area varies between the outcrop-derived and the forward modelled, seismically resolvable, fault geometries. The plots are normalised relative to the outcrop-derived fault geometry, and are also annotated with the absolute effective juxtaposition area in square meters. For both partially breached and fully breached geometries the effective juxtaposition area is significantly lower for the seismically resolvable fault geometries than the outcrop geometries. This is a function of the limited resolution of the seismic data. Fault zones are poorly imaged due to diffraction effects (Townsend et al., 1998) leading to uncertainty in the fault zone architecture and in the position of fault-horizon intersections. Geometries such as slip partitioning, lenses and relay zones resulting from the growth processes of faults (Childs et al., 2009) are often not observed. Consequently faults are modelled as single surfaces leading to a reduced juxtaposition area (figure 8.11). The magnitude of the difference in juxtaposition area is amplified where there is a low Th:tw, since a lower throw is required to completely offset the reservoir and result in a juxtaposition seal. The absolute values of effective juxtaposition area are higher for the partially breched geometries than the fully breached geometries. Again, this is a result of fault growth processes, with profile readjustment of the hard linked faults leading to increased throw across the relay and hence lower juxtaposition areas being maintained. In addition, as throw localises onto the through-going structure small-scale faults and splays are abandoned in the footwall or hangingwall and hence do not contribute to the effective juxtaposition area.

Figure 8.10 (Next page). Effective juxtaposition areas for the different stratigraphies for the partially breached (A) and fully breached (B) relay zone geometries. The juxtaposition areas for the seismically resolvable geometries are normalised against the outcrop derived juxtaposition area. The absolute value for effective juxtaposition area is also shown in m^3. Seismically resolvable geometries have a consistently lower across-fault juxtaposition area than their realistic counterparts, with the effect magnified for instances where the reservoir thickness is less than the mean fault throw.

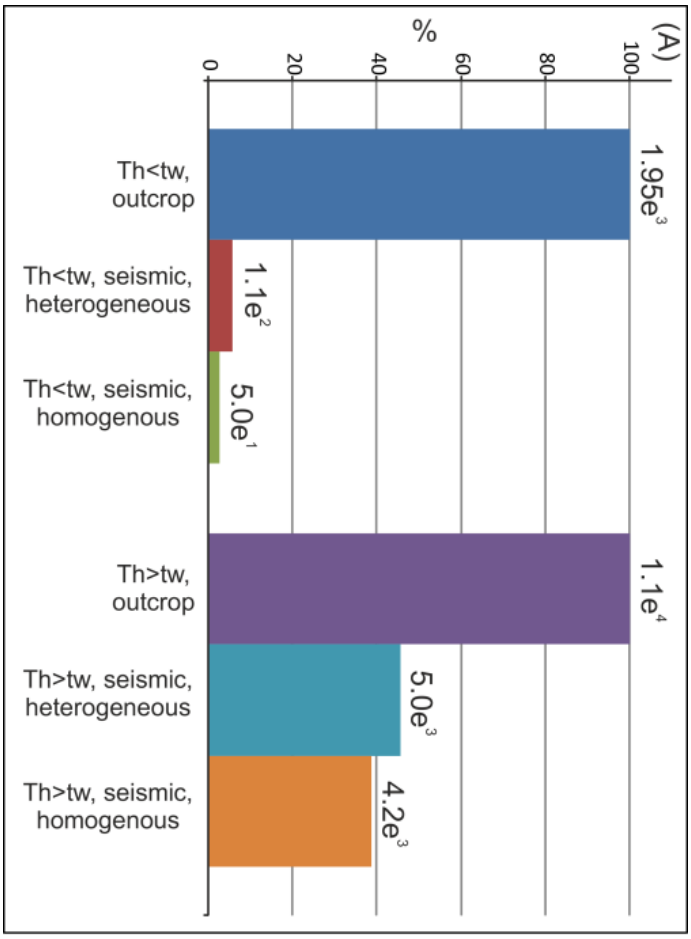
(A)
%
0
20
40
60
80
100
Th<tw, outcrop
Th<tw, seismic, heterogeneous
Th<tw, seismic, homogenous
Th>tw, outcrop
Th>tw, seismic, heterogeneous
Th>tw, seismic, homogenous
1.95e3
1.1e2
5.0e1
1.1e4
5.0e3
4.2e3

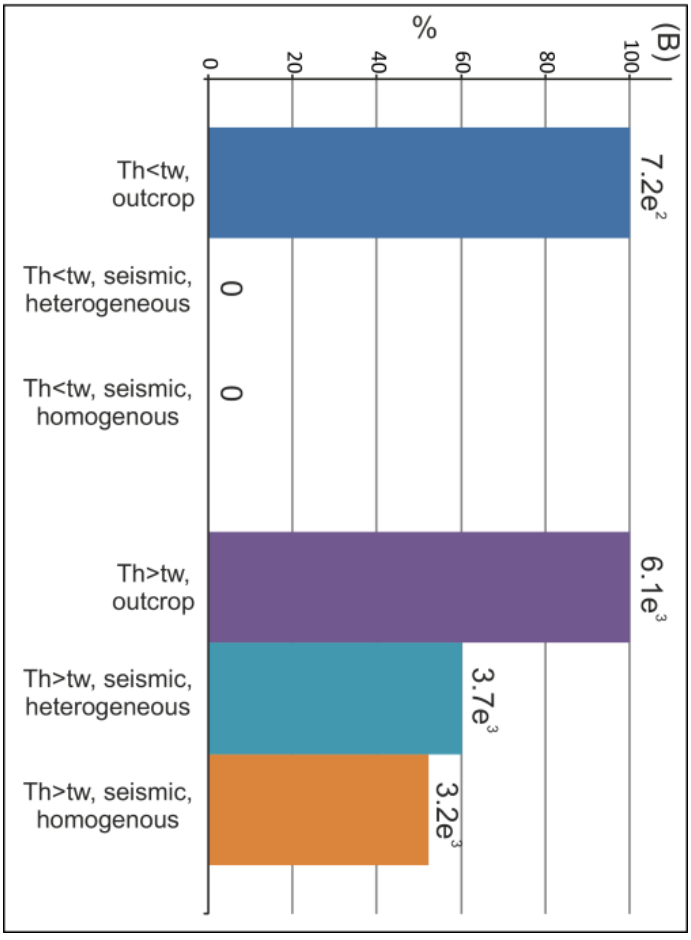
(B)
%
0
20
40
60
80
100
Th<tw, outcrop
Th<tw, seismic, heterogeneous
Th<tw, seismic, homogenous
Th>tw, outcrop
Th>tw, seismic, heterogeneous
Th>tw, seismic, homogenous
7.2e2
0
0
6.1e3
3.7e3
3.2e3

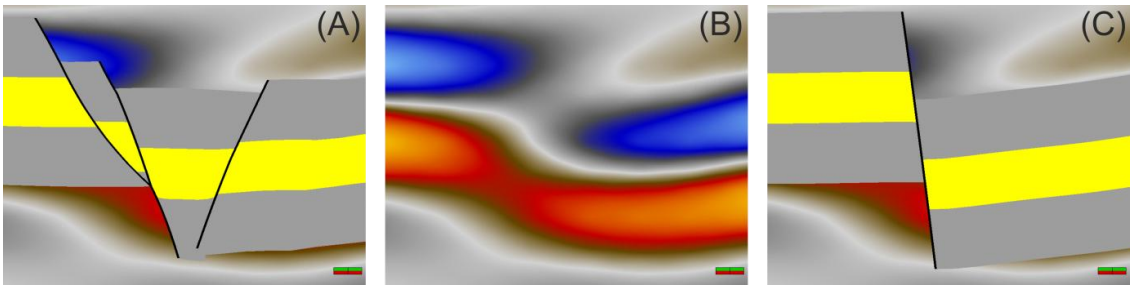

Figure 8.11. Cross sections illustrating the differences between the outcrop derived fault geometry and the seismically resolvable geometry. The model geometry is superimposed onto the forward modelled seismic volume. (A) Outcrop derived geometry. Displacement partitioning on multiple slip surfaces leads to maintenance of across fault juxtaposition of the reservoir interval (yellow) despite the cumulative fault throw being greater than the reservoir thickness. (B) Image of the forward modelled seismic volume. Very few details of the fault architecture are resolved. (C) Seismically resolvable fault geometry. Only single slip plane can be positively interpreted from the forward modelled seismic (B). This leads to the reservoir interval being completely offset and hence a juxtaposition seal being present.

The effects on simulated production of the disparities in juxtaposition area can be significant, with final cumulative produced volumes varying by over a factor of 4 (figure 8.12, 8.13). Figure 8.12 shows an expanded version of the simulation results shown in figure 8.8 (A, E) which illustrates the differences between outcrop and seismically resolvable geometries for low-, mid- and high-case fault rock permeability, and for both high and low Th:tw ratios. Also shown are fault-normal views displaying the area of across-fault self juxtaposition of the reservoir interval. Where a high Th:tw is modelled the effective juxtaposition areas are on the same order of magnitude for both outcrop- (figure 8.12A) and seismically-resolvable (figure 8.12B) geometries, leading to virtually no differrence in the simulated production results regardless of the different fault TMs. In contrast where a low Th:tw is modelled, the effective juxtaposition area is over an order of magnitude lower for the seismically-resolvable geometry (figure 8.12D) than the outcrop-derived geometry (figure 8.12C), leading to significant variations in the simulation results. The architectural complexity of the outcrop geometry leads to in excess of an order of magnitude greater effective juxtaposition area than the seismically resolvable geometry, and hence to multiple potential flow pathways being preserved. For the outcrop derived fault geometries with a low Th:tw the influence of varying the fault TMs is not as pronounced as for the seismically resolvable geometry. Although the different TMs do lead to variations in the onset of production decline, over the course of the simulations the cumulative

produced volumes are similar. This differs to the seismically resolvable geometries, where production rates and hence cumulative volumes vary significantly over the course of the simulations. The high-case fault TMs (low permeability) lead to restricted across fault flow and hence low production rates compared to the mid- and low- case TMs. This is reflected in the cumulative produced volumes which vary by up to factor of 7 between the different fault TMs over the course of the simulation runs (figure 8.13).

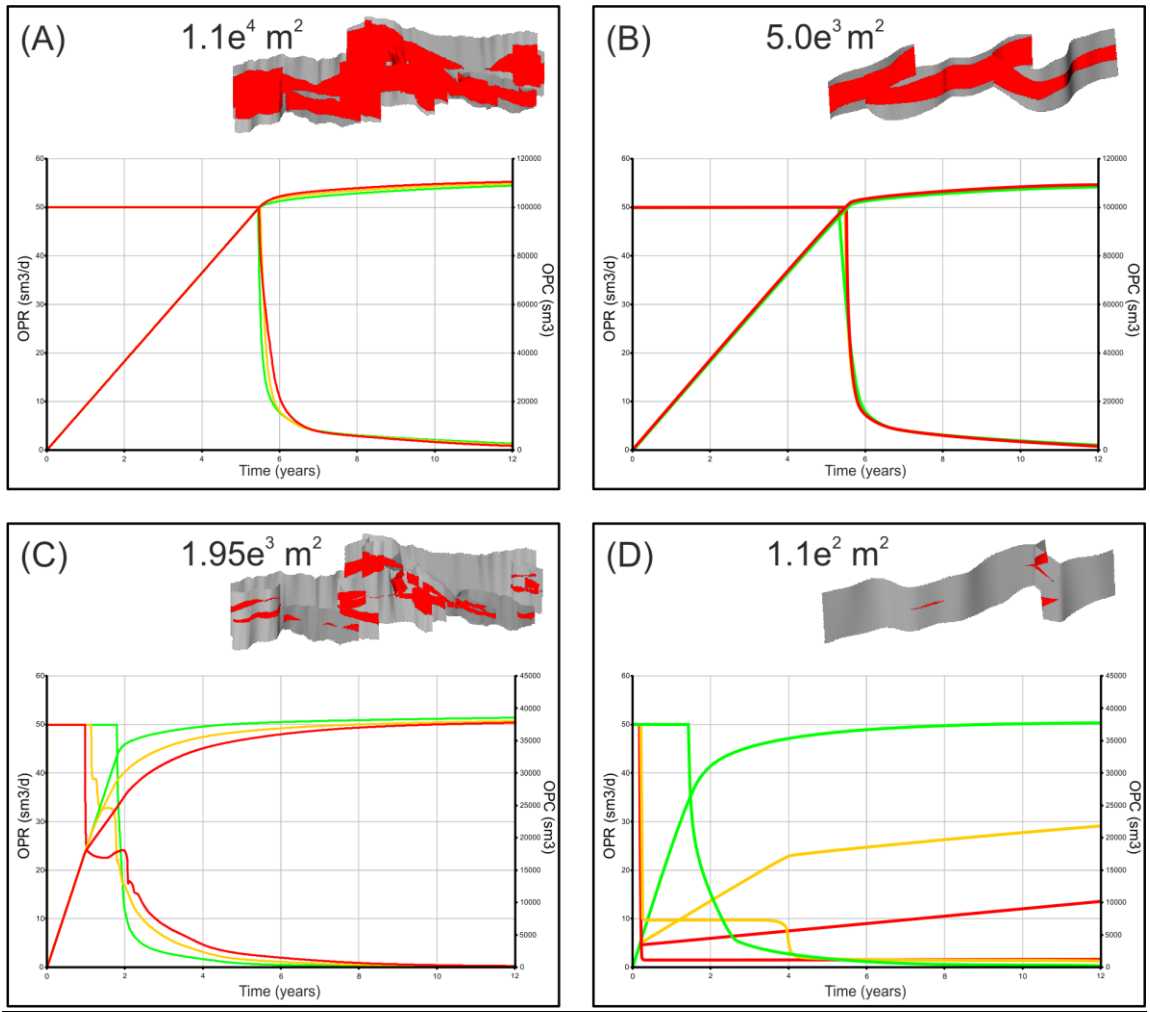

Figure 8.12. Simulation results highlighting the importance of the ratio of stratigraphic thickness to fault throw (Th:tw) in terms of the effective juxtaposition area (shown) for a partially breached relay zone geometry. Colour coding is as figure 8.8. The well-derived petrophysical properties are used in all cases. (A) High Th:tw, outcrop fault geometry. (B) High Th:tw, seismically resolvable geometry. (C) Low Th:tw, outcrop fault geometry. (D) Low Th:tw, seismically resolvable geometry. For discussion see text. OPC = Oil Production Cumulative, OPR = Oil Production Rate.

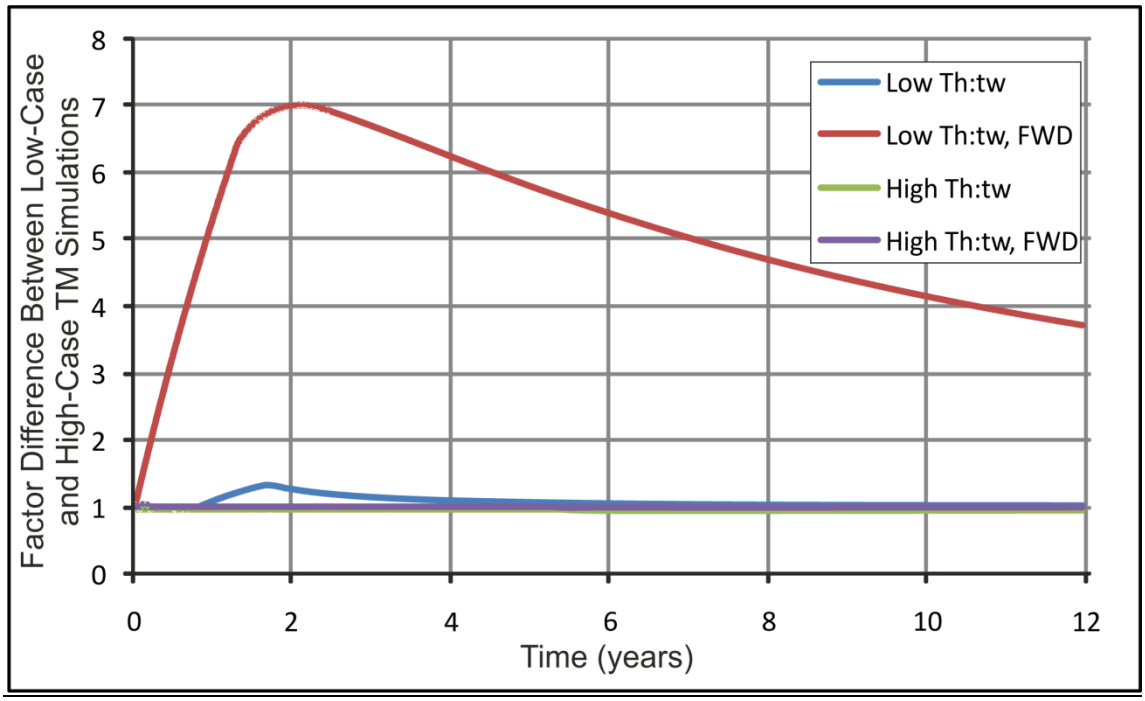

Figure 8.13. Plot illustrating the magnitude in the difference between cumulative produced volume for the different fault TM cases modelled for each geometry shown in figure 8. For the low Th:tw, forward modelled case varying the fault TMs has a significant impact with the produced volume varying by up to a factor of 7 between the low and high cases. In contrast varying the fault TMs for a high Th:tw configuration has little impact on the cumulative produced volume.

The impact of varying the juxtaposition area and the fault TMs is also manifested by the fluid saturation distribution (figure 8.14). For the outcrop-derived geometries there is increased focussing of flow up the relay zone with decreasing fault rock permeability (high-case TMs), since the relay zone offers the path of least resistance. This is true for both high and low Th:tw, although is more apparent for low Th:tw. Despite this, for the outcrop derived geometries the saturation distributions are broadly consistent irresepective of the fault TMs used (figure 8.14). Conversely the saturations for the geometries resolvable in the seismic data vary vastly at any one timestep depending on the different fault geometries (and hence juxtaposition area) and the different fault TMs. Where a high Th:tw is modelled varying the fault TMs has very little impact, whereas a low Th:tw leads to significant variation in the simulated saturation distribution. In this situation the high-, and mid-case TMs reduce across fault flow and hence impede the replacement of oil with water in the hangingwall. The low-case TMs however have little impact on flow retardation, with production simulation results being very similar to the outcrop derived geometry.

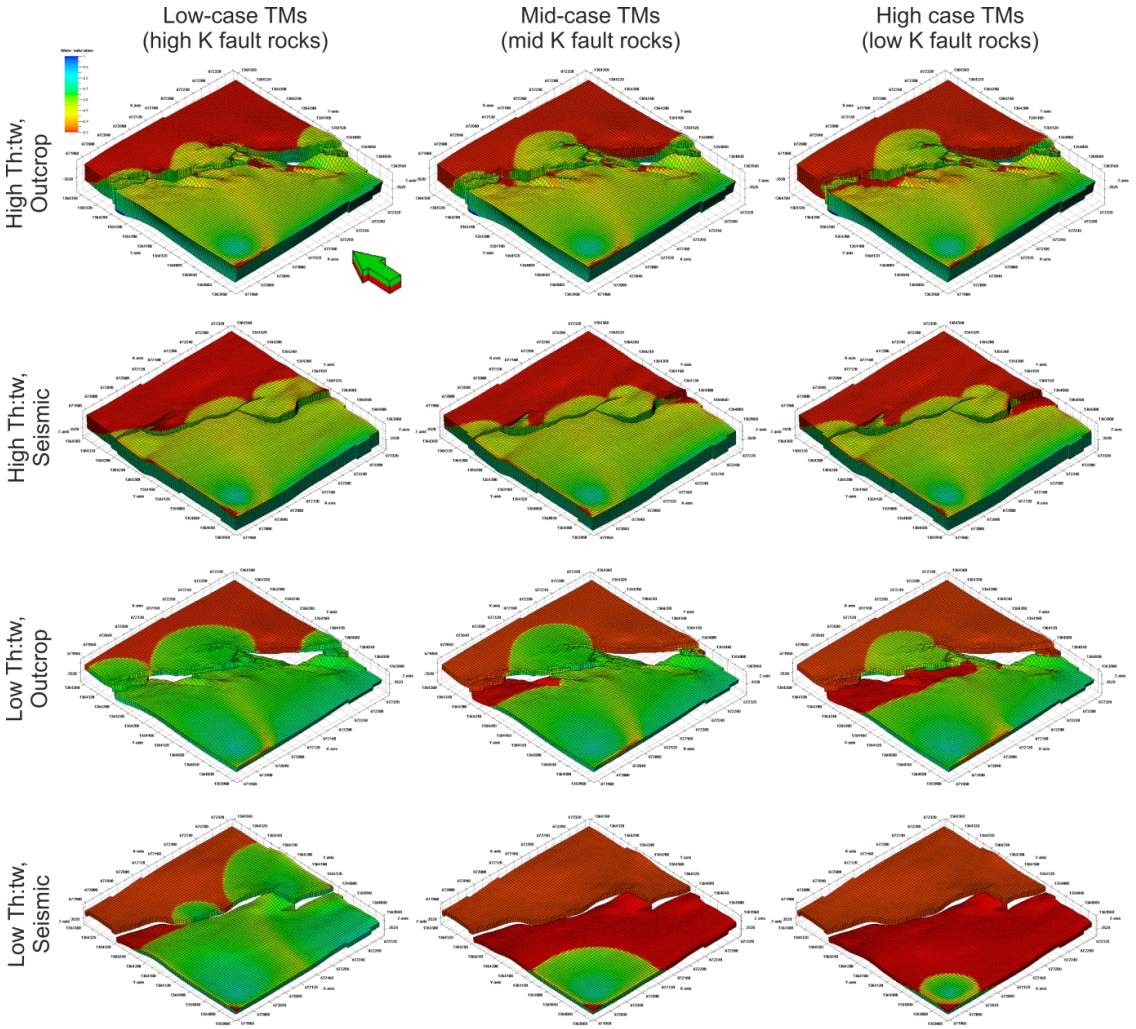

Figure 8.14. Images of fluid saturation part way through the simulation runs for the models shown in figure 8. There are limited differences in fluid distribution between the outcrop and seismically resolvable fault geometries and the different fault TMs where there is a high Th:tw, and hence a large juxtaposition area. In contrast the low Th:tw cases show significant differences in fluid saturation distribution for the different fault geometries and different fault TMs.

8.4.2 Impact of Fault Rock Properties

The results imply that the impact of fault TMs is limited above a critical amount of across-fault juxtaposition area being maintained. To illustrate this a number simulations have been performed using constant fault TMs and a homogenous stratigraphy (figure 8.15). Using constant fault TMs is geologically unrealistic, however it ensures that a single variable (juxtaposition area) is influencing the results. Figure 8.15 shows that for the outcrop-derived geometry with its high amount of across-fault juxtaposition there is little difference in the cumulative produced volumes despite the TMs spanning 3 orders of magnitude. In contrast, for the seismicaly resolvable geometry with low juxtaposition area, varying the fault TMs makes a significant difference to the cumulative production volume. TMs of 0.001 and 0.01 significantly impede across-fault fluid flux and hence reduce the cumulative produced volume of hydrocarbon. However, the less flow-retardent TM values have limited impact, with simulation results being similar to those of the outcrop-derived geometry with its larger juxtaposition area. These results confirm that the juxtaposition area is critical in controlling across-fault flow, with high juxtaposition areas negating the impact of low permeability fault rocks. An alternative viewpoint is based on the observation that the results for the low juxtaposition area, seismically resolvable, geometry have very similar production respones to that of the high juxtaposition area, outcrop-derived, geometry where the less sealing fault TMs have been applied. This suggests that even very small juxtaposition windows can control cross fault flow in situations where the fault rock is relatively permeable (e.g. low clay content).

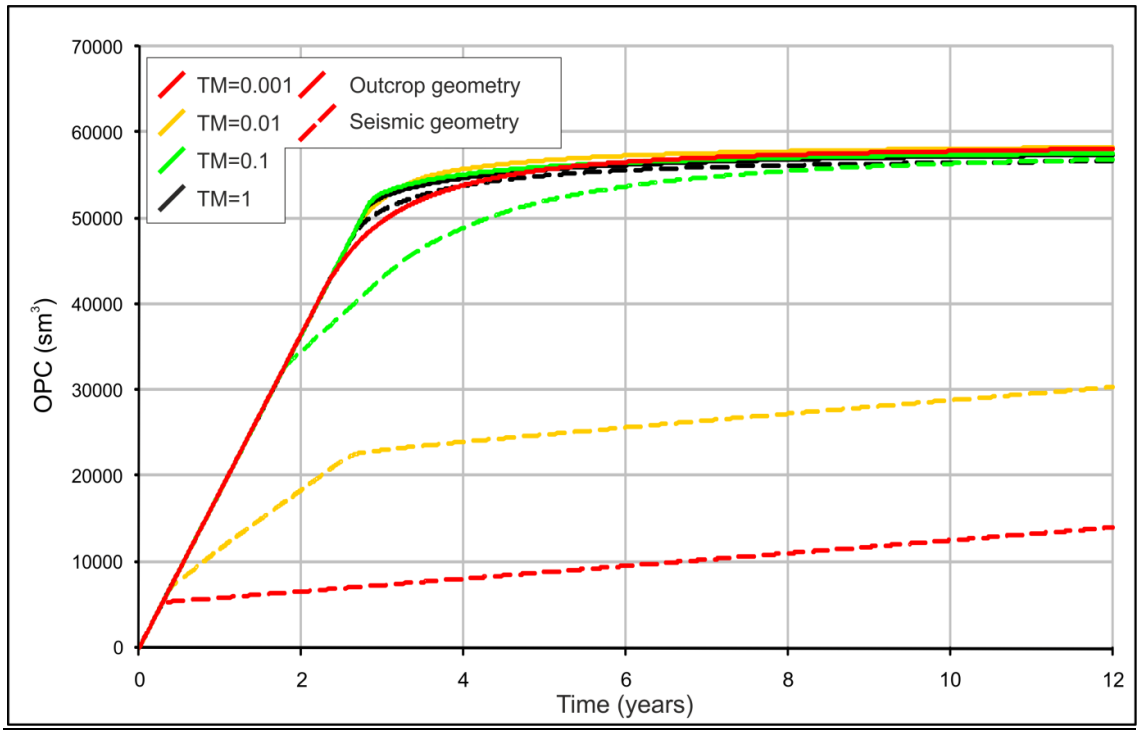

Figure 8.15 (Previous page). Comparison of the simulated cumulative produced volume of oil where constant fault TMs are specified. Limited differences exist in the results for the outcrop geometry (solid lines) irrespective of the fault TMs applied. In contrast the low juxtaposition area of the seismically resolvable geometries leads to significant variations in cumulative production between the different fault TMs. This illustrated the importance of correctly modelling fault geometry and across-fault juxtaposition area and indicates that seismically resolvable fault geometries will tend to result in overly sealing faults being modelled during reservoir simulation. Interestingly, where high permeability fault rocks (e.g. TMs = 1, 0.1), the simulated response for low and high juxtaposition areas are similar. This suggests that under these conditions (high permeability fault rocks) even very small juxtaposition windows can dominate the across fault flow of hydrocarbons.

The results have a number of implications. Firstly, as expected, fault geometries resolvable in seismic data are significantly simplified relative to outcrop examples. Complex fault architectures which are below seismic resolution lead to displacement partitioning across multiple slip surfaces, with this partitioning and complexity being a direct a result of fault growth processes. The result is that seismically resolvable fault geometries have significantly lower across fault juxtaposition area than that likely to be present for relaistic, outcrop-derived geometries. The magnitude of this effect is significantly greater where the vertical thickness of the reservoir interval is less than the mean cummulative fault throw (low Th:tw), although the single dataset examined here does not allow a general estimate of this disparity to be confidently made. Seismically resolvable fault geometries generaly consist of a single fault plane which accomodates all of the fault displacement. As a consequence, low Th:tw configurations are often modelled with the reservoir interval being completely offset, hence resulting in widespread juxtaposition sealing. In contrast the architectural complexity of realisitic fault geometries, as defined by our outcrop examples, leads to maintanence of across-fault juxtaposition, even for low Th:tw situations (figure 8.11, 8.12).

Our simulation results suggest that it is the juxtaposition area which is the most critical factor in controlling across-fault fluid flow, with fault rock properties being of subordinate importance (figures 8.12, 8.13, 8.14, 8.15). For realistic fault geometries, with high juxtaposition areas, there is minimal difference in simulated results irrespective of the fault TMs which are apllied. Converesely the seismically resolvable geometries, with low juxtaposition areas, display significant variation between different fault TM scenarios. This leads to the most important implication, that seismically resolvable fault geometries are often

modelled as being too sealing, since they underestimate the juxtaposition area available to across-fault flow. This also leads to erroneous emphasis being placed on the influence of fault rock properties on fluid flow. Indeed, since the calculation of SGR-based fault TMs is dependent on fault throw, it is likely that the fault TMs applied to seismically resolvable fault geometries may be inappropriate.

8.5 Stratigraphic Permeability Structure

Our initial results have largely focussed on how the geometric disparity between realistic and seismically resolvable fault geometries effects across-fault fluid flow for different fault TMs. There are however a number of additional stratigraphic factors that also contribute to these disparities.

8.5.1 Vertical Permeability

Although a number of our models utilise a well-derived, vertically layered permeability distribution, within each individual layer the permeability values are isotropic. It is common however for vertical to horizontal permeability ratios (Kv:Kh) to be significantly lower than 1 due to compaction and preferential alignment of grains during burial. This leads to the impediment of layer-perpendicular fluid flow which hence restricts hydraulic connectivity of vertically separated layers. Previous work (Manzocchi et al., 2010) has shown the importance of fault structure in enhancing vertical connectivity in low Kv:Kh sequences. The relative impact of varying the Kv:Kh on the simulated production response of outcrop and seismically resolvable fault geometries has been assessed by running simulations across 6 orders of magnitude of Kv:Kh (Manzocchi et al., 2010) (figure 8.16). Mid-case fault TMs have been assigned for all scenarios. For both geometries a lower Kv:Kh results in a lower cumulative production volume, with the absolute produced volumes being lower for the seismically resolvable geometry compared to the outcrop-derived geometry. The results for the seismically resolvable geometry also display significantly more variation than those of the outcrop-derived geometry. As already seen, outcrop fault geometries are significantly more complex than those resolved within seismic data. This complexity enhances vertical connectivity by allowing across-fault juxtaposition of otherwise vertically separated areas, and hence leads to less disparity between high and low ratio Kv:Kh stratigraphies. As a result, the limited across fault juxtaposition area of the seismically resolvable geometries restricts the vertical connectivity and leads to greater variability between the different Kv:Kh ratio stratigraphies. This suggests that determining the correct Kv:Kh may be less important than simulations based upon seismically resolvable fault geometries would imply.

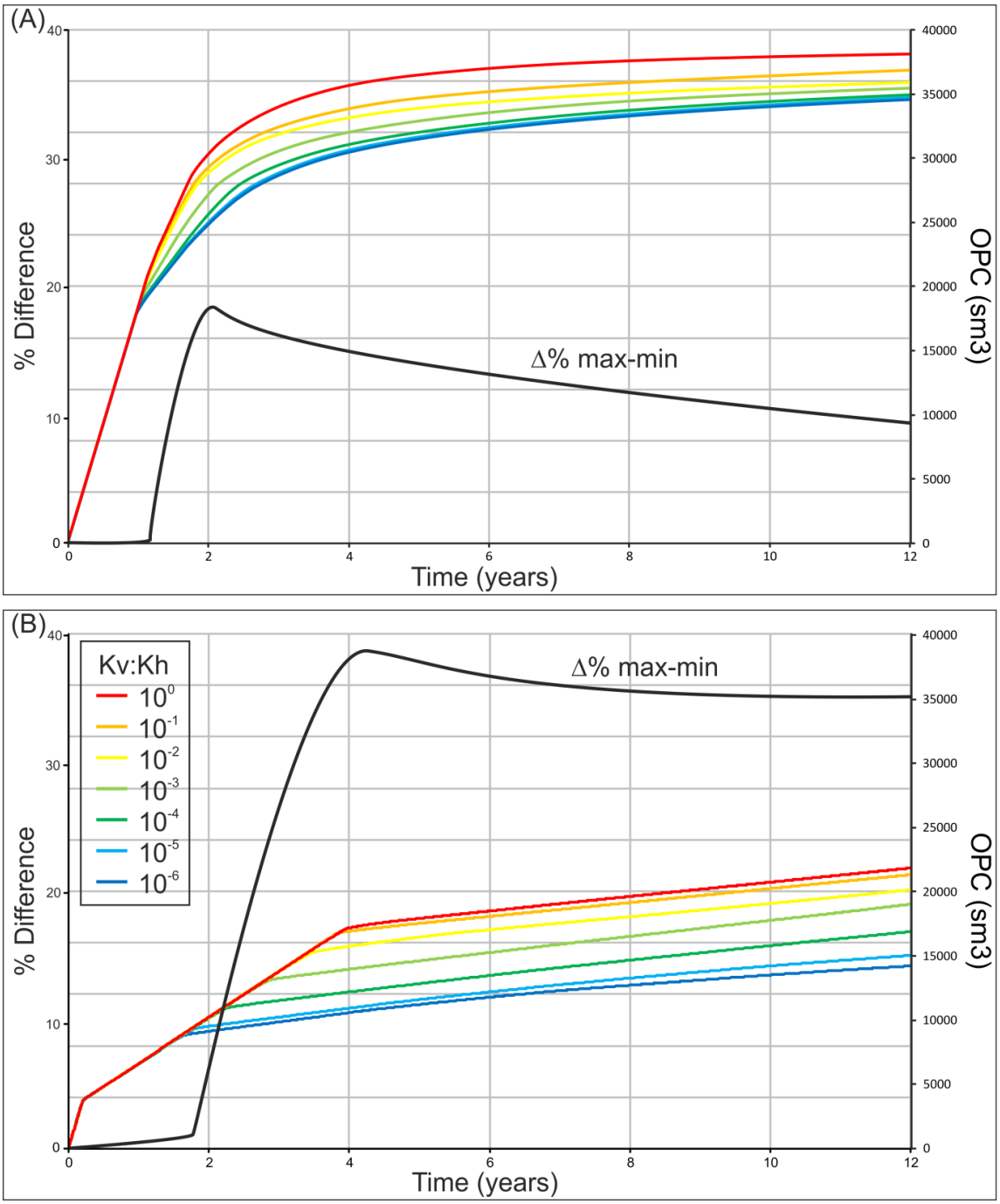

Figure 8.16. Plots illustrating the impact of vertical to horizontal permeability ratio (Kv:Kh) on cumulative hydrocarbon production for (A) Outcrop derived fault geometry and (B) Forward modelled, Seismically resolvable fault geometry. The percentage difference between the highest and lowest Kv:Kh ratios is shown by the solid black lines. In both cases lower Kv:Kh results in lower cumulative hydrocarbon production over the course of the simulation runs. The difference between the highest and lowest produced volumes however is significantly greater for the seismically resolvable fault geometries (B, approx 40%) than the outcrop derived fault geometries (A, approx 20%). Note that the absolute produced volumes are also significantly lower for the seismically resolvable geometry (B).

8.5.2 Net:Gross Ratio

The initial models employed a stratigraphy where the reservoir interval had a constant net to gross ratio of 1. Vertical connectivity was hence not as restricted as would be the case for an interbedded sequence of permeable and impermeable layers. In such vertically stratified sequences faults can significantly enhance vertical permeability by juxtaposing otherwise separate layers (Manzocchi et al., 2010). To test the impact of fault geometric uncertainty in these situations a series of models for both outcrop and seismically resolvable geometries have been constructed with the net:gross ratio ranging between 0.14 and 0.46 (figure 8.17). The effect of varying the net:gross ratio upon the effective juxtaposition area available for across-fault flow is shown in figure 8.18. For both outcrop and seismically resolvable geometries the effective juxtaposition area increases with net:gross. Intuitively it would be expected that the mean SGR values on these juxtaposition windows would decrease with increasing net:gross since overall there is less shale within the sequence, however this is not the case. Instead a more complex, less predictable pattern of mean SGR values emerges, especially for the outcrop-derived geometry. At the lowest values of net:gross the majority of juxtaposition windows occur where the throw is less than the thickness of the individual layers, for example towards fault tips (figure 8.19). A minimal volume of shale has therefore passed the fault and hence low SGR values result. In contrast, where moderate net:gross ratios have been modelled, a greater amount of juxtaposition area occurs, however a larger proportion of shale has passed these windows and resulted in a higher SGR value (figure 8.18).

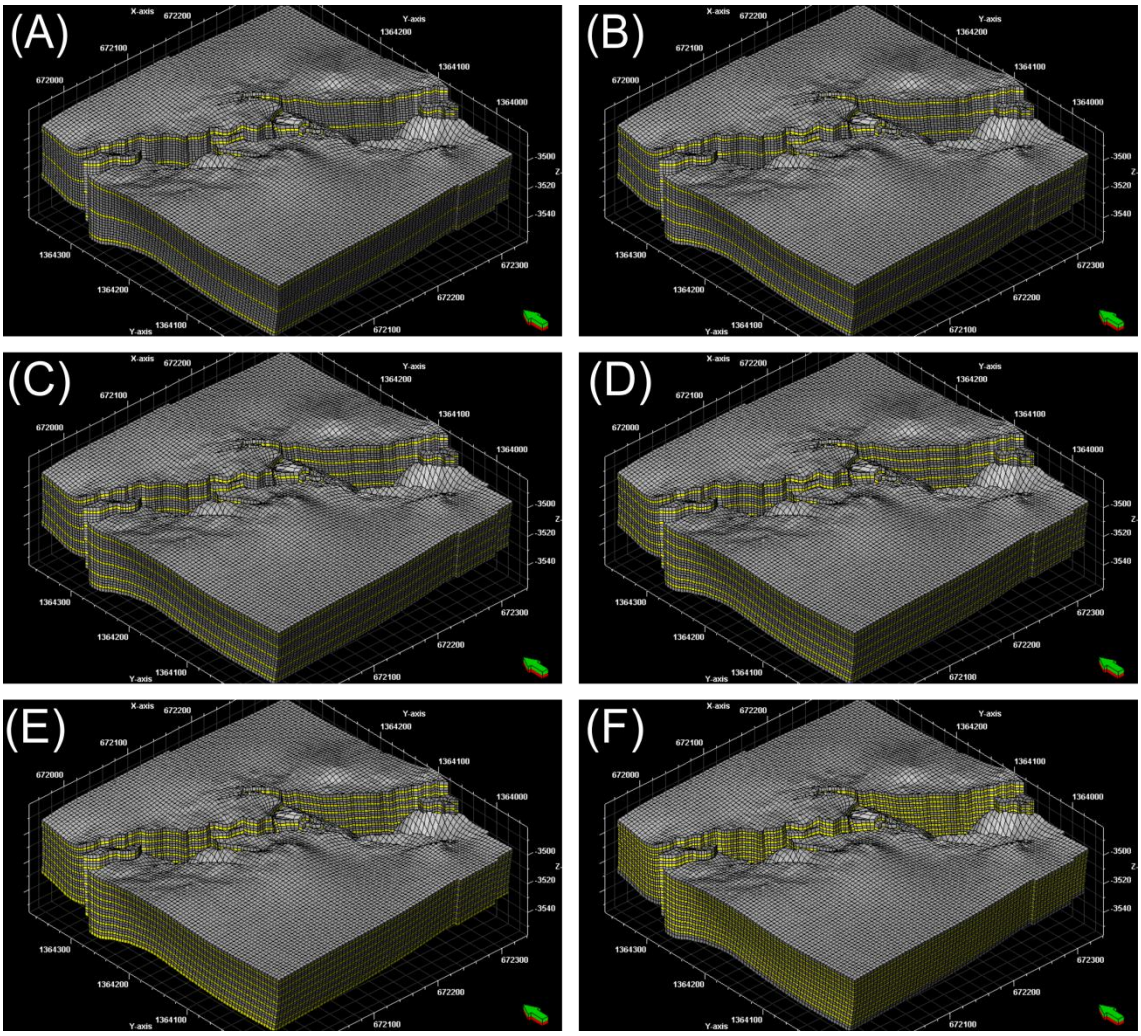

Figure 8.17. Oblique view of partially breached outcrop geometry populated with varying net to gross ratios (N:G). Brown represents shale, whilst yellow represents sand. (A) N:G = 0.14, (B) N:G = 0.18, (C) N:G = 0.23, (D) N:G =0.27, (E) N:G = 0.36, (F) N:G = 0.46.

Figure 8.18 (Next page). Variation of effective juxtaposition area and mean SGR values with Net:Gross ratio. The SGR values are restricted to the values where the reservoir interval is self juxtaposed. (A) Outcrop derived geometry, (B) Seismically resolvable geometry. Note the different scales for effective juxtaposition area. For explanation see text.

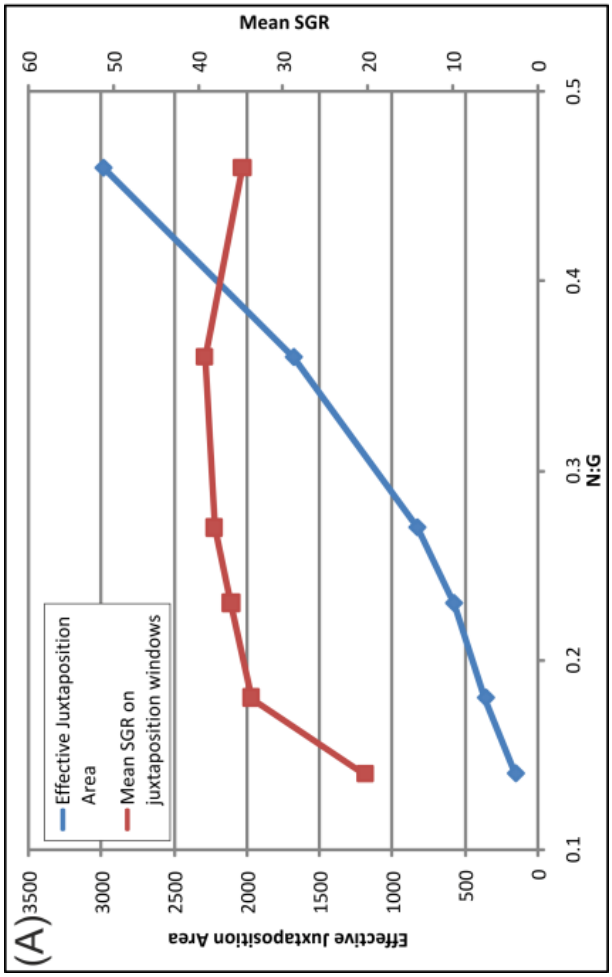
(A)
Mean SGR
Effective Juxtaposition Area
N:G
Effective Juxtaposition Area
Mean SGR on juxtaposition windows
0
500
1000
1500
2000
2500
3000
3500
0
10
20
30
40
50
60
0.1
0.2
0.3
0.4
0.5

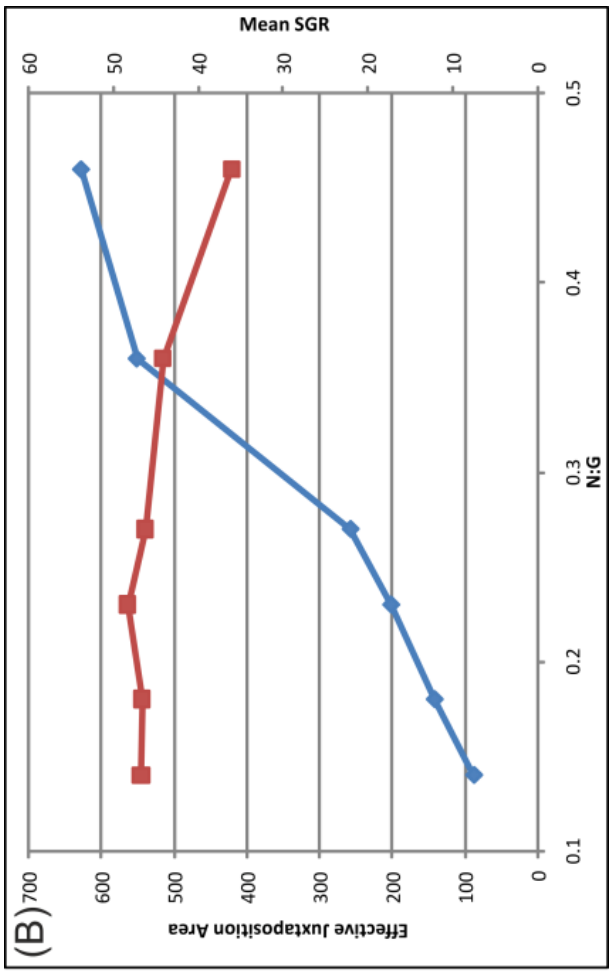
(B)
Mean SGR
Effective Juxtaposition Area
N:G
0
100
200
300
400
500
600
700
0
10
20
30
40
50
60
0.1
0.2
0.3
0.4
0.5

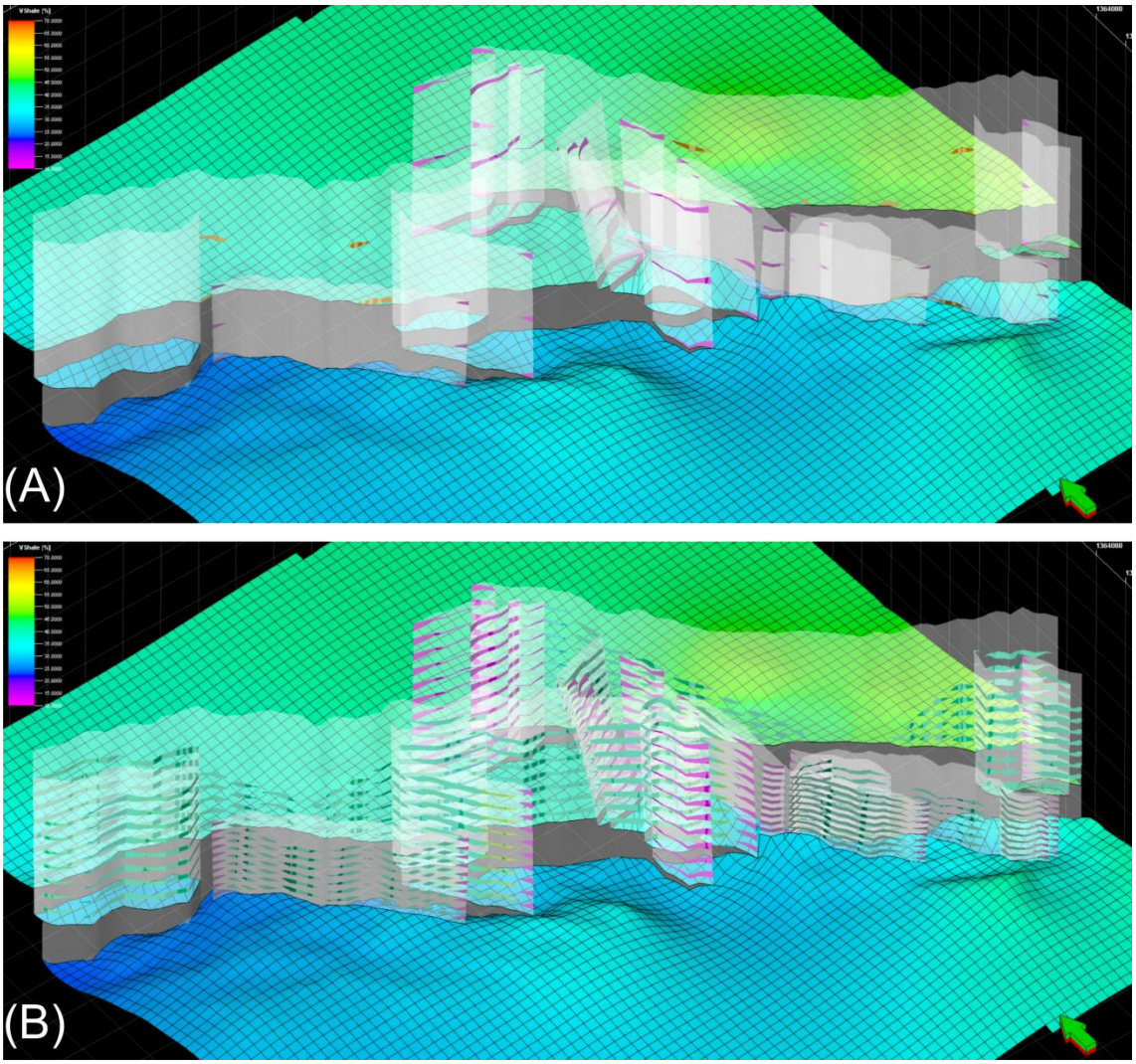

Figure 8.19. Oblique view of outcrop-derived fault geometries illustrating the disparity in SGR values between low (A) and high (B) net:gross. Faults are shown as a transparency with SGR values superimposed where the reservoir interval is self juxtaposed. The base reservoir horizon is also shown. (A) Low N:G (0.14) results in the reservoir only being self-juxtaposed at areas of very low displacement, i.e. at the fault tips. Since these areas have passed little shale during deformation, their corresponding SGR values are low. (B) In contrast a higher N:G (0.46) leads to multiple sections of the reservoir interval being self-juxtaposed. Many of these intervals have passed shale during deformation and hence have higher SGR values.

The 'net' portions of the simulation models have a constant horizontal permeability of 50mD with Kv:Kh of 0.0001. Figure 8.20 shows the cumulative production volume of the forward modelled geometry as a percentage of the cumulative production volume for the outcrop

geometry for low-, mid- and high-case fault TMs (figure 8.20A, B and C respectively). In all cases the higher net:gross stratigraphies lead to a greater similarity in the cumulative produced volume between the outcrop and the seismically resolvable fault geometries. Similarly, the more permeable the fault rock (i.e. low-case TMs), the closer the results for the seismically resolvable geometry are to the outcrop geometry (figure 8.20A), although with significantly more variability than for the less permeable cases (Figure 8.20C) (high-case TMs).

As we have seen, juxtaposition area increases with net:gross for both outcrop-derived and seismically resolvable geometries, but it remains consistently lower for the seismically resolvable geometry (figure 8.18). Where low-case (high permeability) fault TMs are specified (figure 8.20A) the disparity in juxtaposition area between the two geometries has less impact on the simulated production, since the low-case fault TMs do not excessively restrict across-fault flow. Therefore, for any given net:gross ratio the difference between the outcrop-derived and seismically resolvable geometries is less than for the cases with lower permeability fault rocks (figure 8.20C). Since the low-case fault TMs do not overly influence across-fault flow, the disparity in the juxtaposition area of the different net:gross stratigraphies is more pronounced. In contrast where high-case TMs are employed (figure 8.20C) the cumulative production volume is consistently lower for the seismically resolvable geometry than the outcrop-derived geometry irrespective of the net:gross of the stratigraphy. This indicates that the low permeability of the fault rocks, combined with the lower juxtaposition areas of the seismically resolvable geometry, is severely restricting across fault flow. This emphasises that the predicted impact of faults within reservoirs based upon their seismically resolvable geometries may vary significantly compared to their impact when realistic geometries (and hence juxtaposition areas) are accounted for.

Figure 8.20 (Next page). Cumulative produced volume of seismically resolvable geometries as a percentage of that of the outcrop geometry for varied NTG ratios. (A) low case TMs, (B) mid case, (C) high case. Higher fault rock permeability (A) leads to less disparity between seismically resolvable and outcrop derived fault geometries than less permeable fault rocks (C). For discussion see text.

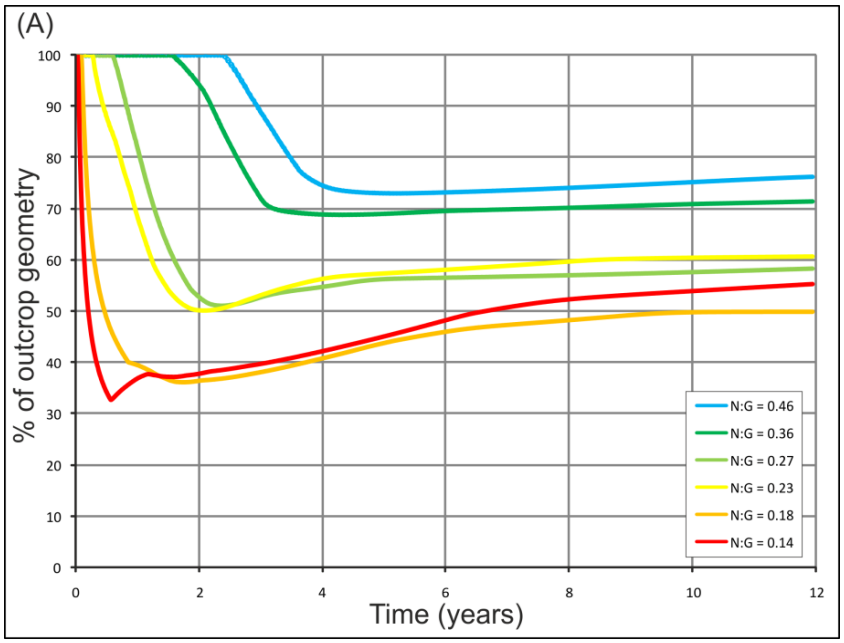
(A)
% of outcrop geometry
Time (years)
N:G = 0.46
N:G = 0.36
N:G = 0.27
N:G = 0.23
N:G = 0.18
N:G = 0.14

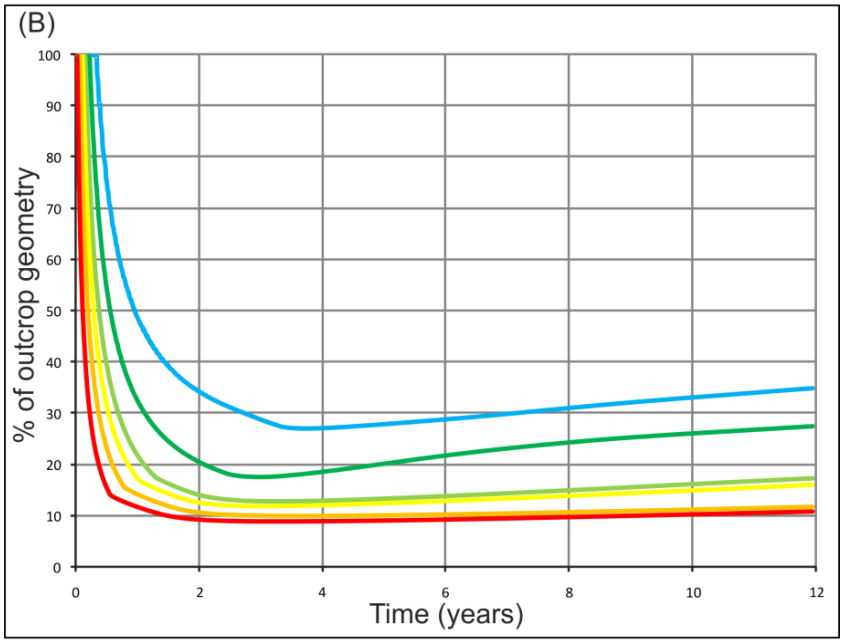
(B)
% of outcrop geometry
Time (years)

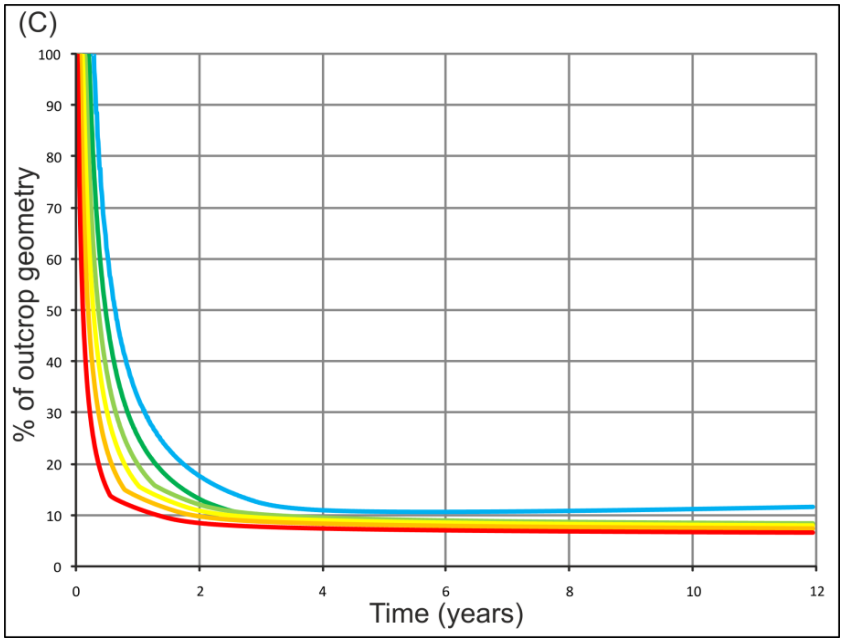
(C)
% of outcrop geometry
Time (years)

8.5.3 Effective Permeability

Although the differences in flow response between realistic- and seismically-resolvable fault geometries are evident from the results presented, they are for a specific, rather than a general case. It is recognised that the relative impact of faults upon fluid flow for a generalised case is a function of the effective permeability (Pickup et al., 1994; Manzocchi et al., 1998; Freeman et al., 2010). The effective permeability is the harmonically averaged permeability of the system as a whole, which includes the permeabilities of the host on the upstream and downstream sides of a fault, the path-length from the injection well (if present) across the fault(s) and to the production well, as well as the fault permeability and thickness. In numerical flow simulators these properties are represented as grid-cell transmissibilities and dimensionless fault transmissibility multipliers, however it is perhaps easier to visualise as effective permeability. As a consequence of effective permeability the properties of the stratigraphic model, the placement of wells, and the production strategy employed all influence the relative impact of faults upon fluid flow. Fluid flow in the subsurface follows Darcy's law (EQ1, Darcy, 1856). If a constant pressure gradient, fluid viscosity and path length (i.e. well spacing) is assumed then the fluid flux becomes proportional to the permeability, K, and cross sectional area, A (EQ2). Where flow is across a fault the cross sectional area is restricted and is proportional to the juxtaposition area (figure 8.21, for a more in-depth explanation see e.g., Yaxley, 1987; Manzocchi et al., 1999; Schlumberger Eclipse 2008). This equation implies that for a given path length (i.e. $L_1+L_2+L_3$), the effect that a fault has on flow is determined by both its own properties (juxtaposition area, thickness and permeability), and the permeability of the host rock.

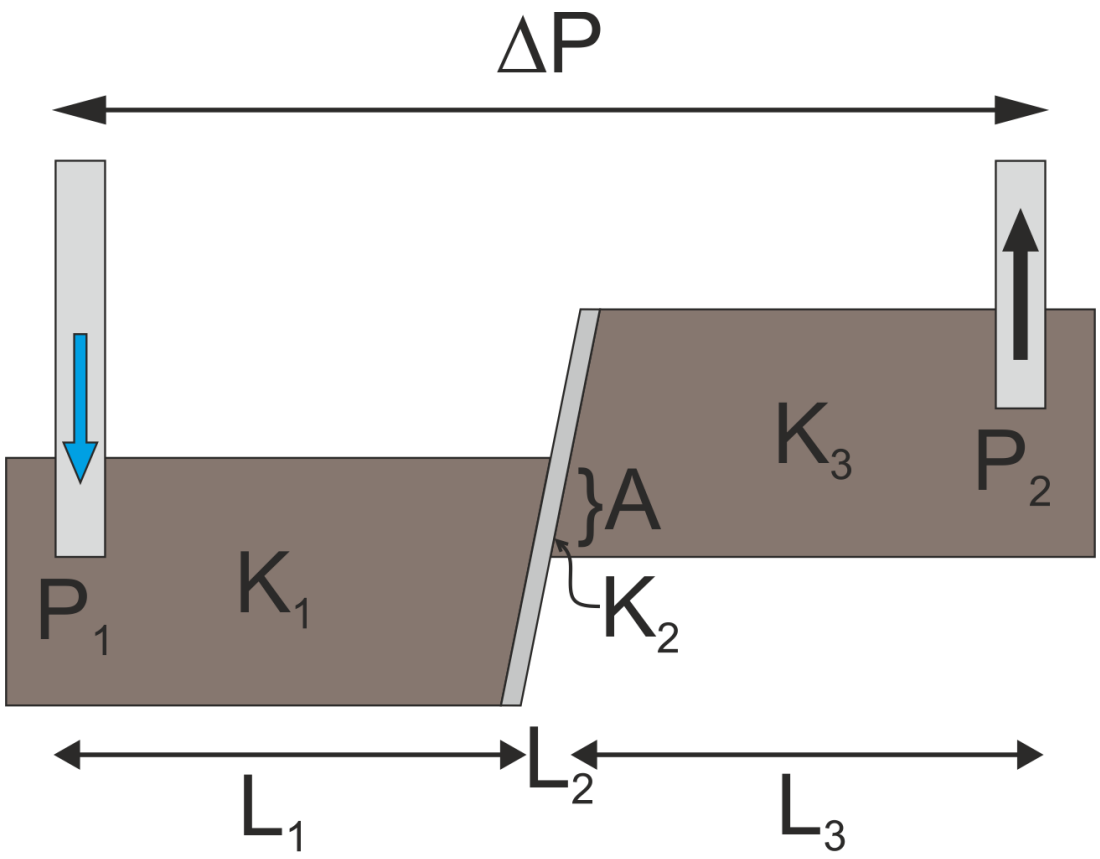

Figure 8.21. Schematic illustrating the concept and of effective permeability in terms of Darcy's law in two dimensions. P = pressure, K = permeability, A = cross sectional area, L = length.

$$\textbf{e.q. (1)} \quad \mathbf{Q} = \frac{\mathbf{K_{eff} A \Delta P}}{\mu \mathbf{L}}$$

$$\textbf{e.q. (2)} \quad \mathbf{Q} \propto \mathbf{K_{eff} A}$$

$$\textbf{e.q. (3)} \quad \mathbf{K_{eff}} = \frac{\mathbf{L_1 + L_2 + L_3}}{\frac{\mathbf{L_1}}{\mathbf{K_1}} + \frac{\mathbf{L_2}}{\mathbf{K_2}} + \frac{\mathbf{L_3}}{\mathbf{K_3}}}$$

To demonstrate the effect of varying the effective permeability a number of simulations have been performed with the host permeability being the altered variable, rather than, as with our previous examples, the fault permeability. Figure 8.22 shows the simulated cumulative production volume for the outcrop and seismically resolvable fault geometries for a low Th:tw. The host permeabilities have been varied across three orders of magnitude and high-, mid- and low-case fault TMs have been assigned. For the outcrop-derived fault geometry (figure 8.22A) with its large area of juxtaposition the host permeability is the controlling factor for the produced volume, with the results clustered according to the value of the host permeability (line style). The standard deviation between the different TMs for each host permeability

grouping is relatively low (figure 8.22B), suggesting that the fault permeability plays a minor role. In contrast the results for the seismically resolvable, low juxtaposition area fault geometries (figure 8.22C) are broadly clustered according to the fault TMs (line colour). Within each host permeability grouping there is a large difference in the simulated results depending on the fault TM values assigned, and hence there is a high standard deviation (figure 8.22D). The explanation for these differences is reconcilable with the concept of effective permeability. As previously stated the across fault fluid flux is proportional to the product of the effective permeability and the juxtaposition area. Where the juxtaposition area is high, the differences in the effective permeability caused by varying the fault permeability has only a limited effect on the across fault flow. In this situation the host permeability is significantly more important the fault permeability in respect to controlling fluid flow. Where juxtaposition area is low, the variations in the effective permeability caused by the fault permeability are large enough to influence the flux rate and hence the cumulative production values. Again, this suggests that since seismically resolvable fault geometries will tend to underestimate juxtaposition area, faults will tend to be modelled as overly sealing, and too great an emphasis placed on the relative importance of fault rock properties. In reality, since the area of juxtaposition is significantly larger than can be imaged, the fault rock petrophysical properties do not as strongly influence across-fault flow as they would based upon seismically resolvable juxtaposition area.

Figure 8.22 (Next page). The influence of varying the effective permeability (by varying the host permeability) on simulated cumulative production results for Outcrop and seismically resolvable fault geometries. For the outcrop geometry, with its high juxtaposition area, the simulation results are controlled by the host permeability rather than the fault rock permeability (A). This leads to a relatively low standard deviation (B) in the results when different fault TMs are applied for a specific host rock permeability. Where the seismically resolvable fault geometries are modelled (C) the cumulative production is controlled by the fault rock permeability due to the low juxtaposition area. This leads to a large standard deviation in the results when the fault TMs are varied.

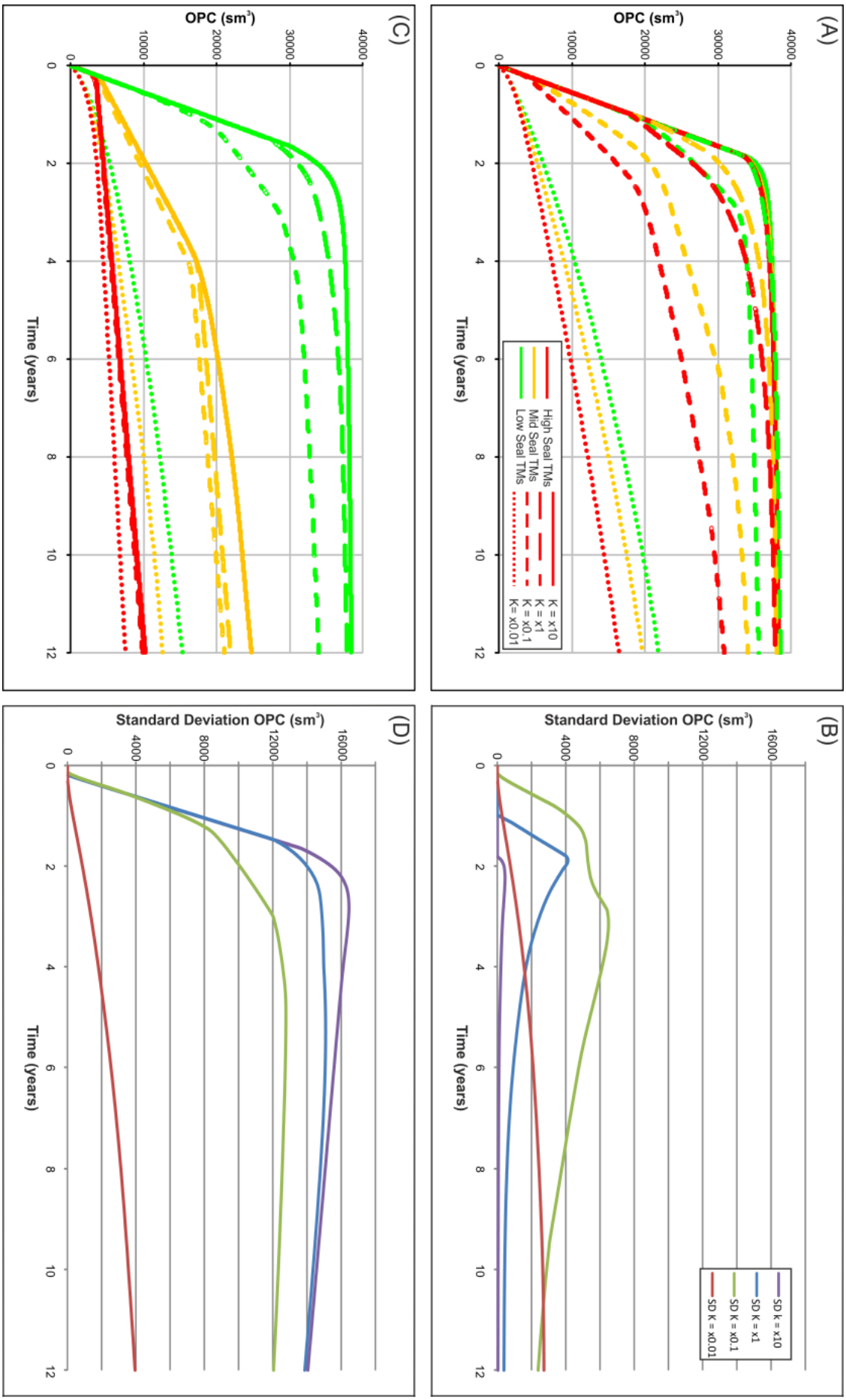
(A)
OPC (sm³)
Time (years)
High Seal TMs
Mid Seal TMs
Low Seal TMs
K = x10
K = x1
K = x0.1
K= x0.01
(B)
Standard Deviation OPC (sm³)
Time (years)
SD k = x10
SD K = x1
SD K = x0.1
SD K = x0.01
(C)
OPC (sm³)
Time (years)
(D)
Standard Deviation OPC (sm³)
Time (years)

8.6 Discussion

Faults are almost universally represented within fluid flow simulators as simple, single slip-surfaces. The reason for this is both an issue of data resolution, and the mechanisms for incorporating faults within geocellular grids. However, fault growth processes necessitate that fault architecture is significantly more complex than the geometries resolvable in, and modelled from, seismic data. As a result, simulation models which are constructed based upon seismically resolvable fault geometries are unlikely to behave in the same way as would the complex fault geometries present in the subsurface.

A number of different approaches may aid and improve the accuracy of simulations where faults are present. A number of tools exist for predicting fault architecture based upon the burial history and geomechanical properties of the stratigraphy, however these are generally restricted to two dimensions (e.g. Welch et al., 2012). However, difficulties arise in incorporating this complexity into large reservoir models, where horizontal grid-cell dimensions may typically be on the order of 200m. Locally refining the grid to a level of detail which allows the complexity to be captured often leads to prohibitively long simulation run times (Manzocchi et al., 2008). Incorporating the vertical heterogeneity in fault structure is even less straightforward given the way geo-cellular grids are constructed in the majority of reservoir modelling software packages. Indeed, since our models are based on surface data (albeit at a high resolution), they are consequently not fully 3D, rather they could be described as being 2.5D. Where it possible to capture and subsequently model the full 3D geometry of faults it is likely that the additional heterogeneity encountered would lead to even greater levels of across-fault juxtaposition than our 2.5D approximations.

An alternative approach to that of deterministically including fault geometries and properties may be to incorporate complexity in relation to juxtaposition area and fault rock permeability via a conditioned semi-stochastic or probabilistic methodology (Odling et al., 2005; Rivenæs et al., 2005; Childs et al., 2007; Manzocchi et al., 2008; Yielding, 2012). Although this approach has a number of potential pitfalls, especially where a laterally heterogeneous stratigraphy is present, it may provide more accurate predictive simulations of fluid flow. Perhaps the simplest approach to account for geometric complexity is to stochastically include sub-seismic relay zones (Manzocchi et al., 2008) which provide across-fault flow pathways. Geometric ‘rules’ based on variables such as displacement: length ratios could be used to geologically condition the stochastic population of such features.

Our results have indicated that across-fault juxtaposition area is likely to be severely underestimated when based on seismically resolvable fault geometries, potentially leading to

faults being modelled as overly retardant to flow. However under certain conditions, such as marginal, low net:gross reservoirs will indeed promote juxtaposition limited across fault. Under these conditions the relative importance of the fault rock properties on influencing across-fault transmissibility increases with significant variability observed where different clay content to permeability transforms are applied (e.g. figure 8.12D). These permeability transforms are dependent on a number of variables including the specific burial history, hence applying a locally calibrated clay content to permeability transform is critical where limited across-fault juxtaposition area exists.

We have purposely focussed on clay mixing (SGR) in terms of permeability reduction across faults rather than other processes such as smearing, cataclasis and cementation. This is partially for the sake of brevity, since it demonstrates our arguments clearly, and partially because it is generally the most prevalent methodology within the hydrocarbon industry for generating estimates of fault permeability. Although there is some degree of depth dependency on the processes of fault rock formation they are not entirely mutually exclusive and hence a number of fault rock types are likely to be present in any single area. This notwithstanding, and despite its original inception as a deterministic approach (yielding et al., 1997), SGR can to some degree be treated as a probabilistic indicator of likely fault permeability independent of the actual processes involved in fault rock formation (Childs et al., 2007; Yielding, 2012). This is in part a reflection of the architectural complexity of fault zones- they are not single slip surfaces of homogenous composition, but discontinuous zones of heterogeneous deformation across multiple slip planes. Appropriate in-situ calibration of permeability (for production purposes, Childs et al., 2007), or column height and/or across pressure differential (for exploration purposes, Yielding et al., 2010) accounts for this heterogeneity. As such SGR can be treated as a proxy for fault properties, rather than as a direct deterministic representation.

Although the complexity in fault architecture is largely controlled by fault growth processes, the geomechanical properties of the stratigraphy also influence the resulting geometries. The complex fault geometries which we have modelled are hosted in basalt and formed at, or close to, the free surface of the earth, and hence under limited confining pressure. Both the lithology and stress conditions are therefore a-typical of those found in conventional hydrocarbon reservoirs. This raises a question as to the applicability of these geometries to faults found at depth within silisiclastic sequences. However as depth, and hence confining pressure, increases the contrast between the mechanical properties of different lithologies is reduced due to compaction and cementation effects. A ‘strong’ lithology under low confining stress will therefore deform in a broadly similar manner to a ‘weaker’ lithology at depth. In

addition, sedimentary sequences are by their nature mechanically heterogeneous and are hence likely to result in even greater fault geometric complexity than more mechanically homogenous lithologies such as basalt. In addition, the geometries modelled herein appear (at least qualitatively) to be similar to the types of fault and relay geometries observed in silisiclastic sediments, for example in Canyonlands (Cartwright et al., 2005). Although the geometries modelled here may not be exactly identical to those in the subsurface, it is the inherent complexity which is the relevant variable. As seen, this complexity, in the form of features such as fault bound lenses and displacement partitioning across multiple slip surfaces, leads to enhanced across-fault juxtaposition relative to the single slip surface fault geometries typically employed in hydrocarbon reservoir models. It is the presence, rather than the exact geometry, of this juxtaposition which is the important factor in controlling across-fault fluid flow.

The concept of effective permeability for reconciling the relative impact of the stratigraphic and the fault properties, as well as their respective uncertainties, on across-fault hydrocarbon flow is potentially a powerful tool during field development. The influence of faults on hydrocarbon flow reduces as the contrast in permeability between host rock and fault rock decreases (figure 8.22). Similarly, increasing the path length for given fault and host permeability values will increase the effective permeability, since the ratio of high permeability values (host rock) to low permeability values (fault rock) will increase. This suggests that production from wells which are further away from faults will be less attenuated than for wells in close proximity of faults. Understanding effective permeability therefore has important consequences for well placement decisions during hydrocarbon field development of faulted reservoirs. This is however complicated somewhat by a number of factors. The stratigraphies we have modelled to illustrate the influence of effective permeability are horizontally homogenous, and as a result fluid can follow a direct path from injection well to production well via the faults. In reality stratigraphic property distribution is far from homogenous, with flow pathways often being highly convoluted. Our models have been designed to force fluid to flow across the faults, however the necessity for across-fault flow depends on the connectivity of the fault network as a whole. Property distributions within lower connectivity fault networks may result in fluids flowing around, rather than across faults. In a similar manner well connected fault networks are highly likely to have a significant level of subseismic geometric heterogeneity, such as relay zones, which will act as fluid conduits and control the across-fault flux of fluids.

8.7 Conclusions

A high resolution DEM has been used to capture realistic fault geometries from outcrop and model them within the framework of a geocellular grid. These models have been populated with petrophysical properties typical of a conventional hydrocarbon reservoir and forward modelled to generate 3D synthetic seismic cubes. The fault geometries resolvable in the seismic data have formed the basis of a second set of geocellular grids. Both the outcrop-derived and forward modelled geometries have been subject to flow simulations with the impact on hydrocarbon production of their geometrical differences being assessed. Furthermore the influence of varying the petrophysical properties of the stratigraphy on across-fault flow has also been considered, and the following conclusions drawn.

● Fault geometries identifiable in seismic data are significantly simplified relative to those observed at outcrop. The limited resolution of seismic data leads to an absence of the complex geometries such as displacement partitioning across multiple slip surfaces that characterise fault geometries observed at outcrop. In turn this leads to a severe underestimate in the area of across-fault self-juxtaposition of reservoir intervals for seismically resolvable fault geometries. The magnitude of this disparity is amplified where reservoir thickness is less than mean fault throw.

● Large juxtaposition areas lead to limited differences in the across flux of hydrocarbon irrespective of the fault transmissibility multipliers which are applied. This is the case for the realistic, outcrop-derived fault geometries, and for high thickness to throw ratio configurations. Conversely, where low thickness to throw ratios are combined with low juxtaposition area, seismically resolvable geometries, significant differences arise in simulated results when different TMs are assigned. Across-fault fluid flow is therefore, in this situation at least, controlled by a combination of both juxtaposition area and fault permeability. Fault geometries modelled from seismic data will underestimate the juxtaposition area available for across-fault flow, often leading to faults being modelled as overly sealing even when appropriate fault permeabilities are included.

• Where the fault rock is defined as being relatively permeable, only a small juxtaposition ‘window’ is required to dominate across-fault fluid flow and lead to a similar production response to situations with significantly larger juxtaposition areas. Identifying potential juxtaposition ‘windows’ is therefore critical when attempting to predict across-fault flow behaviour.

• Varying the fault TMs does influence the simulated production results where the across fault juxtaposition area is low. It is important however to distinguish between instances when there is actually a low across-fault juxtaposition area, and instances where low juxtaposition area it is simply an artefact of the seismically resolvable, simplistic fault architecture. This emphasises the importance of carefully mapping fault geometries in as much detail as is feasible when trying to anticipate their effect on reservoir performance. Ideally multiple, rather than a single, realisation of fault geometry would be included in reservoir uncertainty analysis.

• The reduced juxtaposition area of seismically resolvable fault geometries relative to realistic geometries leads to reduced vertical connectivity for low net:gross and low Kv:Kh stratigraphies. As Kv:Kh and Net:gross decrease the disparity in simulated production between the outcrop and seismically resolvable fault geometries increases. This disparity also increases when combined with lower permeability fault rocks.

• The concept of effective permeability can be used to explain the differences in simulated production between outcrop and seismically resolvable fault geometries. It also illustrates that the effect of faults on reservoir performance is not just a function of the fault geometry and properties, but also on the petropyhsical properties of the host stratigraphy. The combination of the low juxtaposition area of seismically resolvable fault geometries with a lack of appreciation for the consequences of effective permeability may often lead to faults being incorrectly labelled as overly sealing to fluid flow.

Chapter 9

Stability of Sub-Seismic Scale Faults During Fluid Injection

9.1 Abstract

This chapter applies the concepts of sub-seismic fault geometry investigated in chapter 8 to the issue of fault reactivation due to pressure perturbations during hydraulic fracturing. The increased range in fault orientations of a realistic fault geometry compared to a simple seismically resolvable geometry results in a greater probability that some fault segments will become unstable during fluid injection. This may lead to induced seismicity occurring at lower pore fluid pressures than that predicted when solely seismically resolvable geometries have been modelled.

9.2 Introduction and Aims

The recent rapid increase in the application of hydraulic fracturing techniques to release hydrocarbons from shales has raised concerns about the potential associated risks (Howarth et al., 2011), including that of induced seismicity (Green et al., 2012). A key variable when assessing fault stability and the likelihood of inducing seismicity is the orientation of faults relative to the in situ stress field. Fault orientation is often characterised using reflection seismic surveys, however the limited spatial resolution of reflection seismic data leads to uncertainty in, and simplification of fault geometries and orientations (Townsend et al., 1998). In this chapter seismic forward modelling is used to generate the 3D synthetic response of realistic, outcrop-derived geometries with the aim of highlighting when seismic and geomechanical uncertainties can lead to uncertainty in fault stability calculations. The observed disparity between seismically resolvable and realistic geometries likely to be present in the subsurface suggests that unstable faults may often remain unidentified, potentially resulting in induced seismicity during hydraulic fracturing.

Induced seismicity has previously been reported for geothermal projects (Majer et al., 2007), disposal of waste fluids (Healy et al., 1968) and conventional hydrocarbon production (Suckale, 2010) whilst it is also a concern for potential $C0_2$ sequestration sites (Lucier et al., 2006). Seismic events as a result of hydraulic fracturing have generally thought to be of a low magnitude ('microseismic', M=<1, Shapiro et al., 2010), and have been associated with the disposal of waste fluids used during the hydraulic fracturing process, (Frohlich et al., 2011; Horton, 2012) rather than the fracturing process itself. Some notable exceptions to this are the recent seismic events in Oklahoma, USA (Keranen et al., 2013) and in NW England (maximum magnitude 2.3, de Pater and Baisch, 2011). A follow-up study to the latter of these events (de

Pater and Baisch, 2011) concluded that the seismicity was indeed related to the hydraulic fracturing operations, caused by injection of fluids directly into a critically stressed fault plane (de Pater and Baisch, 2011). This fault had not been identified in the well data and no seismic survey had been conducted. The rupture area required to generate the magnitudes observed approximates to $1x10^4$ m^2 (Kanamori and Anderson, 1975; de Pater and Baisch, 2011). Published relationships between fault displacement and length (Kim and Sanderson, 2005) and earthquake rupture dimensions and rupture displacement (Kanamori and Anderson, 1975; Wells and Coppersmith, 1994) suggest that it is entirely conceivable that a fault hosting a rupture of this size could be of dimensions which would be below the resolution of a 3D seismic survey. Fault planes are rarely directly imaged with reflection seismic surveys, their presence instead identified by the offset of reflection events (Townsend et al., 1998), with fault offsets below the minimum resolution not resolved. The minimum resolution is dependent on a number of factors, primarily the seismic wavelength at the specific depth of observation, but will typically be on the order of 10m. This limited resolution and the potential presence of acquisition and processing artefacts results in the introduction of uncertainty, leading to non-unique interpretations of the sub-surface structural geometry and stratigraphic architecture (Bond et al., 2012). Geological models derived from seismic datasets are therefore inevitably simplified compared to the true geometries and property distributions which are present in the sub-surface. Since, by their nature, the presence and orientation of any sub-seismic faults is unknown, their potential for reactivation under conditions of increased pore fluid pressure is uncertain. Hydraulic fracturing techniques induce the formation of fractures by raising the pore fluid pressure via the injection of fluids. The increase in pore fluid pressure reduces the effective normal stress leading to tensile failure in the form of fractures (figure 9.1), increasing the permeability and facilitating the flow of gas to the well bore. The seismicity associated with fracture formation is generally of very low magnitudes (M=<1 Shapiro et al., 2010), however larger magnitude seismicity may occur if the increase in pore fluid pressure leads to the reactivation of pre-existing fault planes. This raises the question as to whether uncertainty in seismic data could lead to unstable fault surfaces remaining unidentified even where seismic coverage exists.

Low differential stress (σ_1-σ_3)
High differential stress (σ_1-σ_3)
Formation of new fractures
Reactivation of pre-existing fractures
(A)
(B)
(C)
(D)
(τ)
(σ_n)
Tensile fracture
Mohr-Coulomb criterion
Dilatant shear fracture
Reactivated fracture
Frictional sliding criterion
p_fp
σ_1
σ_3
T
C_r
C_f

Figure 9.1 (Previous page). Schematic Mohr diagrams illustrating the effect on fracture formation and reactivation of increased pore fluid pressure (pfp) under different conditions. τ = Shear stress, σn = normal stress, Cr = Intact rock cohesion, Cf = Fracture cohesion, σ1 = Maximum principal stress, σ3 = Minimum principal stress, T = Rock tensile strength. (A) A low differential stress (σ1 - σ3). No pre-existing fractures are present therefore the Mohr-Coulomb failure criterion is applicable. Increasing the pore pressure reduces the effective stress, shifting the Mohr circle to the left into the tensile failure region. If the minimum stress (σ3) is negative, tensile fractures will form perpendicular to σ3. (B) As (A) but with a higher differential stress. Increasing the pore pressure leads to the Mohr circle intersecting the failure envelope whilst σ3 is still positive, leading to the formation of shear fractures, although a smaller pfp increase is required for fracture formation than for low differential stress. (C) Low differential stress. The presence of pre-existing fractures means that the friction sliding criterion is applicable, and a lower pfp increase is required in order to reactivate the fractures. (D) A higher differential stress requires a smaller pfp increase for fracture reactivation. It is assumed that the effective horizontal stress remains constant during fluid injection induced pore pressure changes (Zoback, 2007).

It is a common practice to use relevant outcrop analogues to help understand and constrain the characteristics of sub-surface geology (Bryant et al., 2000; Moraes et al., 2004; McCaffrey et al., 2005; Jones et al., 2009; Pringle et al., 2010; Guerriero et al., 2011). Outcrop data captures a larger degree of heterogeneity at a higher resolution than can be observed in seismic data. This data may be directly incorporated into, (Enge et al., 2007; Paton et al., 2007; Sech et al., 2009) or stochastically applied to condition geological models (Hodgetts et al., 2004; Howell et al., 2008) or used to enhance our understanding of geological processes (Nicol et al., 2010; Sumner et al., 2012). Seismic forward modelling has been used previously for understanding stratigraphic architectural and sedimentary facies distribution uncertainties (Hodgetts and Howell, 2000; Janson et al., 2007; Bakke et al., 2008; Armitage and Stright, 2010; Falivene et al., 2010; Tomasso et al., 2010). However, its application to structural geology has been relatively limited, generally being restricted to two-dimensional (Johansen et al., 1994; Townsend et al., 1998; Alaei and Petersen 2007; Frankowicz et al., 2009) or crustal scale (Mackenzie et al., 2005) sections. Nevertheless seismic forward modelling presents a highly beneficial tool for constraining structural uncertainty across a range of situations, with this chapter highlighting how the technique can be applied to aid our understanding of induced seismicity during hydraulic fracturing operations.

As described and illustrated in chapters 1, 4, and 7, fault geometries are significantly more complex than can be imaged using seismic data (figure 9.2). As discussed this is largely due to the process of fault growth and of the influences of the mechanical properties of the faulted medium. Complex fault geometries lead to a greater range in orientations and dips relative to those observed and modelled from seismic data. In turn this influences the magnitude of the local stress field which is resolved onto each part of a fault surface, and hence its proximity to the failure envelope (figure 9.2).

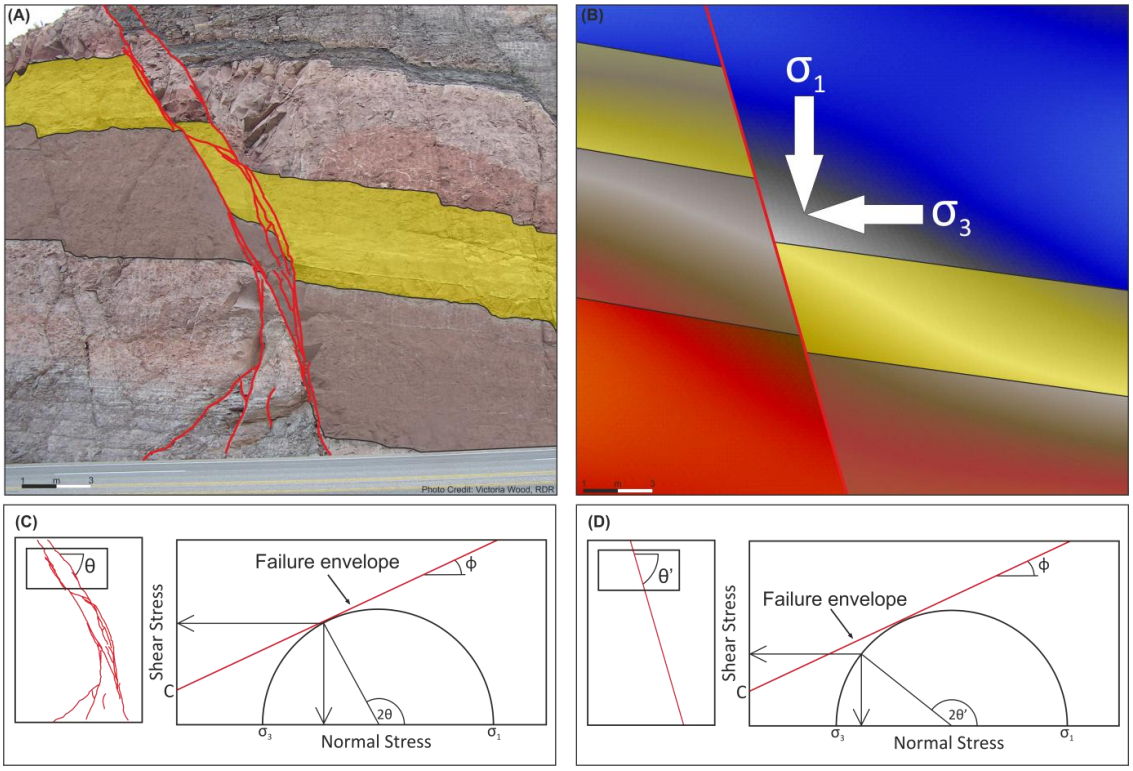

Figure 9.2. Outcrop example of how seismic data leads to underestimates in the complexity of fault geometry, and the influence that this has on fault stability during fluid injection. (A) View of road cutting showing significant geometric complexity. (B) The seismically resolvable version of the same geometry. A single fault plane is imaged effecting how the local stress field is predicted to be resolved onto the fault plane. (C) The outcrop geometry has a shallower dip than the seismically resolvable geometry (D). For a constant local stress field, the complex outcrop geometry is closer to the failure envelope than the seismically resolvable geometry. A lower pore pressure increase is hence required to induce failure and induce seismicity.

9.3 Methodology

A high resolution airborne-LIDAR derived digital elevation model (DEM) from the Afar rift, Ethiopia, with a spatial resolution of 0.5m has been used as the basis for capturing detailed fault geometries. The relatively recent timing of the initiation of tectonic activity (Rowland et al., 2007) and the arid climate result in minimal erosive degradation of the outcrop, and therefore excellent preservation of fault geometries. This DEM has been used to construct a detailed fault model and geocellular grid for a fault relay zone (Larsen, 1988; Peacock and Sanderson, 1991) using industry standard geological modelling software (Petrel, Schlumberger Limited, 2011). A fault relay zones has been modelled since they typically represent areas of increased fault geometric complexity induced by linkage processes which is generally not resolved within seismic datasets. The model has been constructed assuming a depth of 2500m, and has been populated with petropysical properties appropriate to this depth, with pressure and fluid saturation properties assigned based upon those of the Barnett Shale, Texas (Palmer et al., 2007., Figure 9.3 and Table 9.1). The geocellular grid is then exported to seismic forward modelling software (SeisRox, Norsar, 2011, see chapter 1) where elastic and reflectivity properties are calculated (Reuss, 1929; Gassmann, 1951; Shuey, 1985). Full 3D ray tracing with realistic source-reciever offsets are combined with the subsurface petrophysical properties to generate pre-stack depth migrated synthetic seismic cubes (Gjoystdal et al., 2007; Lecomte, 2008). The seismically resolvable fault geometries can then be identified using seismic interpretation software and compared to the outcrop geometry used in their generation (figure 9.4). This allows quantification of the stability of both the realistic and the resolvable fault geometries under specific subsurface stress conditions.

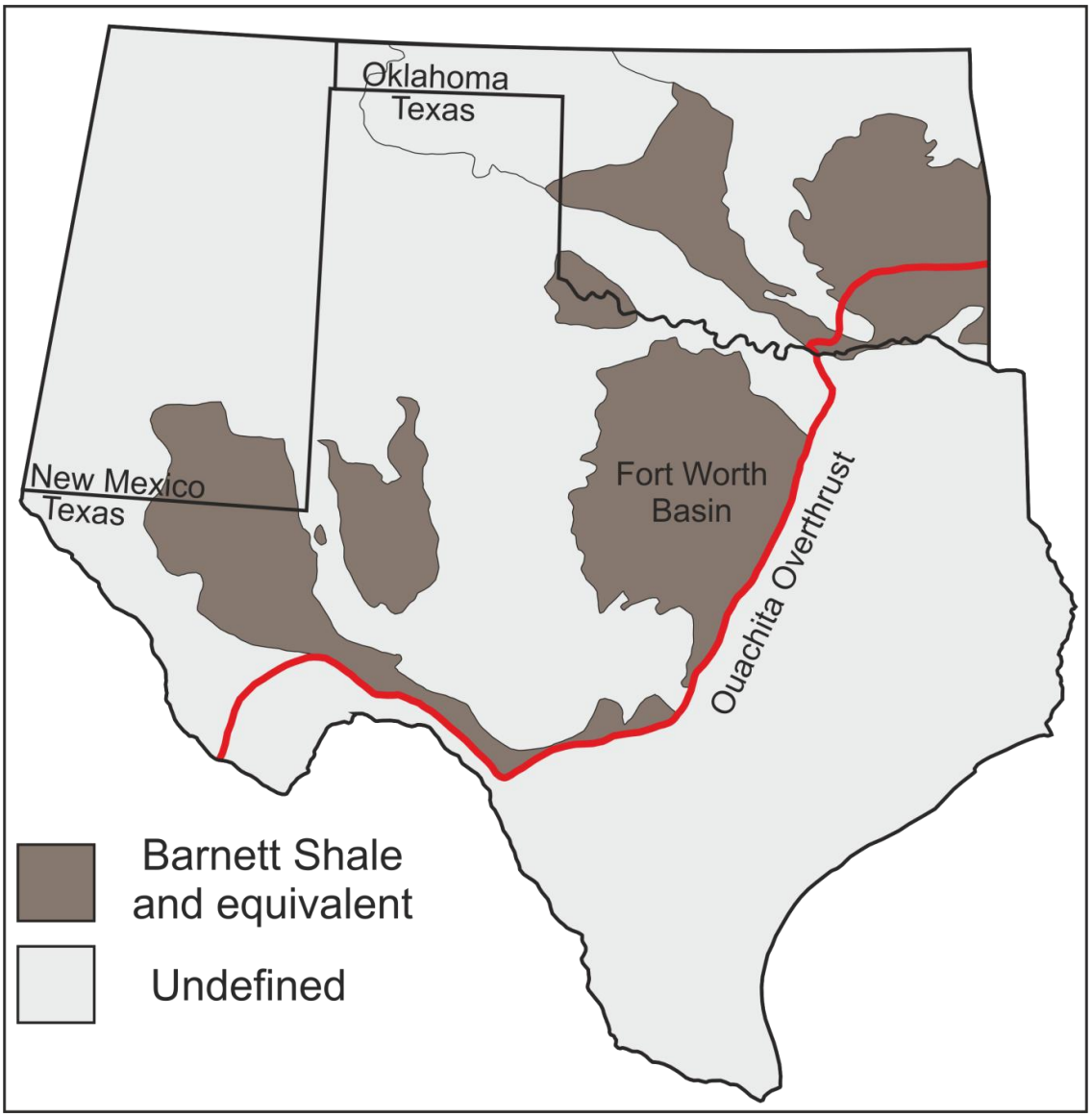

Figure 9.3. Map of the Barnett Shale distribution across Texas, and location of the Fort Worth Basin. The Fort Worth Basin is a prolific shale gas producing province, with a number of recent seismic events being attributed to hydraulic fracturing operations (Frohlich et al., 2011).

	Barnett Shale
Vertical Stress (σV)	8200psi (56.5 MPa)
Maximum Horizontal Stress (σH)	6286psi (43.3 MPa)
Minimum Horizontal Stress (σh)	5658psi (39 MPa)
Stress Regime	Extensional
Initial Pore Pressure (P)	4100psi (28.3 MPa)
Fault Cohesion (C)	100psi (0.69 MPa)
Fault Friction Angle (ϕ)	31°

Table 9.1. In-situ stress conditions prior to fluid injection and geomechanical properties defining the failure envelope for the faults present. These properties are typical to those found in the Barnett Shale (Palmer et al., 2007), a shale gas producing formation found in Texas, USA.

Figure 9.4 (Next page). Comparison of outcrop-derived geometry and the geometry resolvable within forward modelled seismic data. (A) High resolution LiDAR derived fault and surface geometry used for generation of forward modelled seismic cube. (B) Section through forward modelled seismic. The outcrop fault and surface geometry is superimposed. (C) Fault and surface geometry resolvable within the forward modelled seismic cube. (D) Section through forward modelled seismic data with resolvable fault geometry superimposed. The realistic, outcrop-derived geometries are significantly more complex compared to the geometries which can be resolved from the forward modelled seismic data.

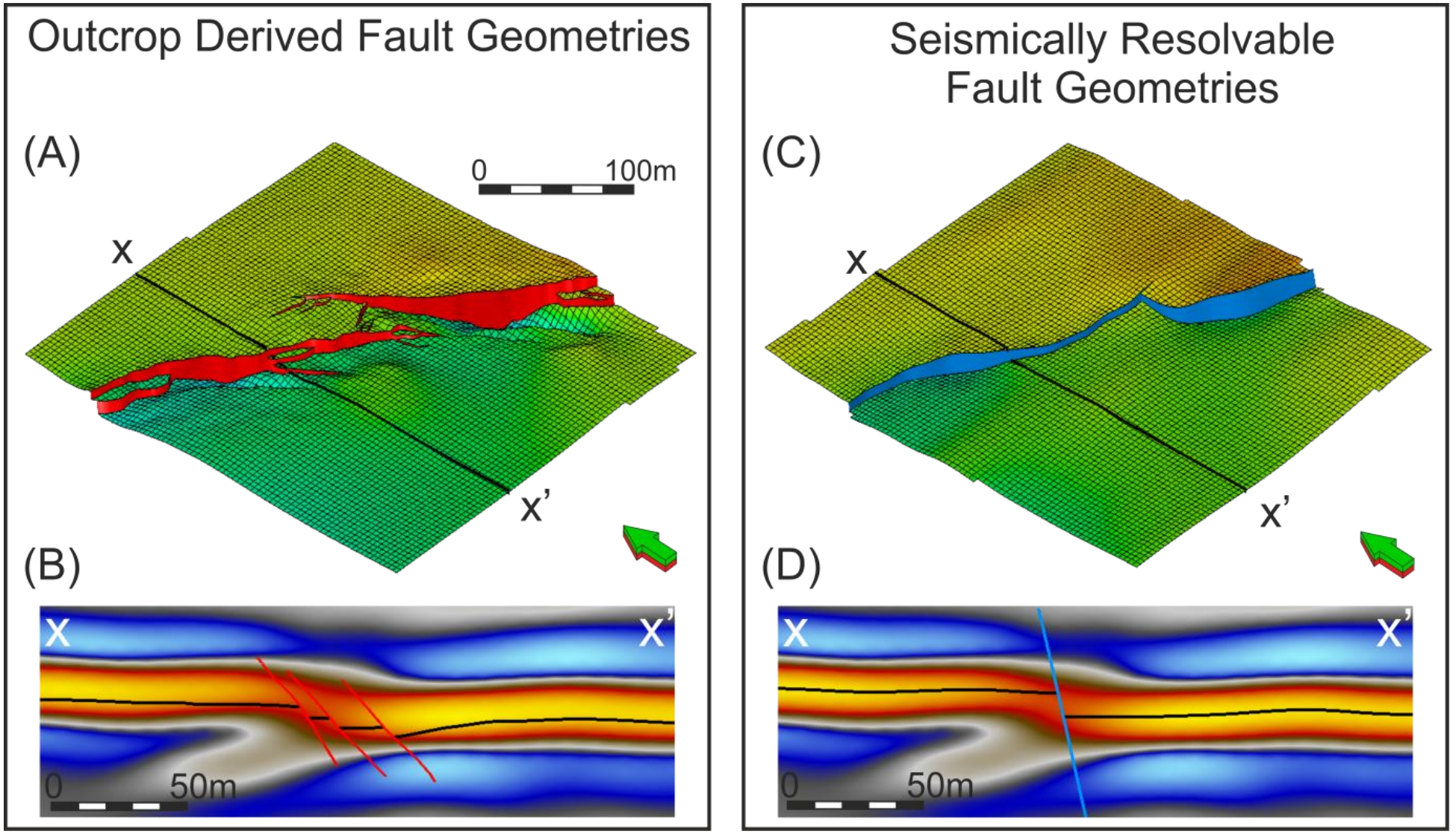
Outcrop Derived Fault Geometries
(A)
0
100m
X
X'
(B)
X
X'
0
50m
Seismically Resolvable
Fault Geometries
(C)
X
X'
(D)
X
X'
0
50m

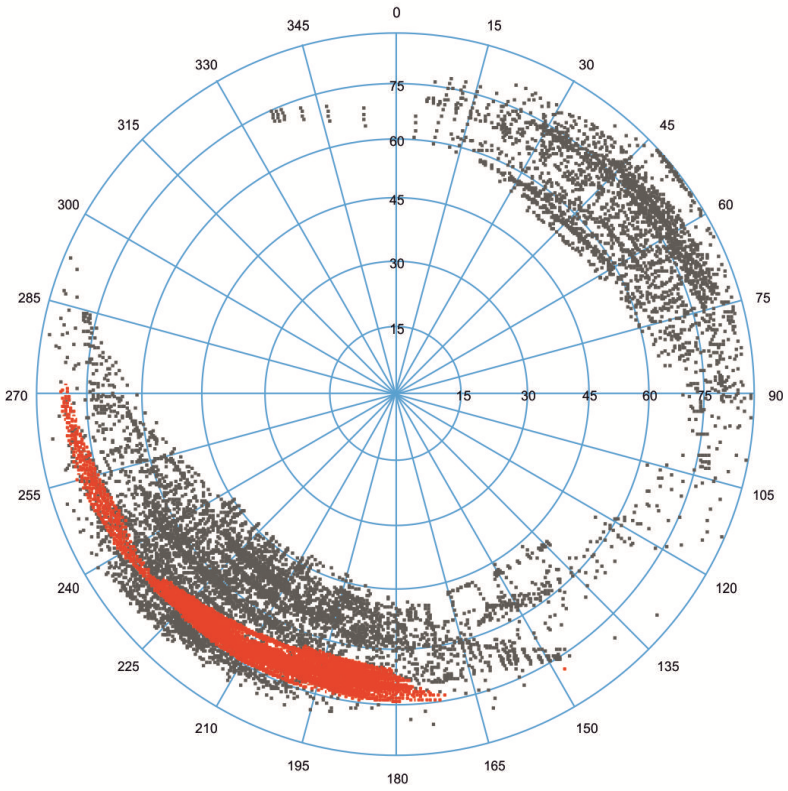

Figure 9.5. Stereographic plot of dip angle and dip azimuth for each node on the fault surfaces. The outcrop-derived faults (grey) display a much broader range of orientations compared to the seismically resolvable faults (red), indicating that they are more likely to include unstable portions within a given stress field orientation.

9.4 Modelling Fault Stability

The stability of a pre-existing fault depends upon its geomechanical properties (cohesion, angle of internal friction), the pore pressure and the in situ stress field. The orientation of a fault relative to the regional stress field is critical since this determines the magnitude of the stresses which are resolved onto the fault plane, and hence the distance that a fault of a particular orientation is to the Mohr-Coulomb failure envelope.

It is clear from forward modelling that substantially less detail than is present can be resolved in the seismic data, with significant disparities in the local fault orientations between the two geometries (figures 9.4, 9.5). The stability during hydraulic fracturing of both the outcrop and seismic resolvable fault geometries have been assessed under stress conditions found in parts of the Barnett Shale (Palmer et al., 2007; Table 9.1, Figure 9.3), a prolific shale gas formation found in the Bend Arch-Fort Worth Basin, Texas (Montgomery et al., 2005). Under these conditions both the seismic and outcrop geometries are stable. However if the pore pressure is

raised to represent the injection of fluids during the hydraulic fracturing process the faults state of stress begins to approach the failure envelope (figure 9.6). The pore pressure at which failure would initially occur varies significantly between the two geometries. Whereas the geometry resolvable in the seismic data would not fail until pore fluid pressure had increased by 720 psi (4.96 MPa), the outcrop geometry from which it is defined would experience initial failure at a pore fluid pressure increase of 530 psi (3.65 MPa). Pore fluid pressure increases required for hydraulic fracturing of the Barnett Shale vary between 100 and 900 psi (0.69-6.21 MPa), with the majority of values lying in the range of 400-600 psi (2.76-4.14 MPa) The value at which failure through fault reactivation occurs is therefore well below the estimated upper bound of pore pressure increase required to induce hydraulic fracturing in this region (900psi, Palmer et al., 2007). Figure 9.6 shows the stress distribution across the outcrop and seismically resolvable geometries for a pore fluid pressure increase of 600 psi (4.14 MPa), a typical value for the region (Palmer et al., 2007). If fault stability is calculated using the geometry identified in the seismic data then failure would not be expected at this value of pore pressure increase, however parts of the outcrop geometry would have already passed into an unstable state of stress, potentially failing and resulting in seismicity.

Figure 9.6 (Next page). Aerial view of fault planes shown in figure 9.4. Faults are coloured by the increase in pore fluid pressure required for the Mohr-Coulomb failure envelope to be reached. Initial in-situ stress conditions and pore fluid pressures are as table 9.1. Under these conditions both the outcrop (A) and seismically resolvable (B) fault geometries are stable. Increasing the pore fluid pressure by 600 psi (4.14 MPa), a typical fracturing pressure, results in parts of the outcrop geometry becoming unstable (C). This is in contrast to the seismically resolvable fault geometry (D), which remains stable. Induced seismicity may therefore occur at lower pore fluid pressures than anticipated based on seismically resolvable fault geometries.

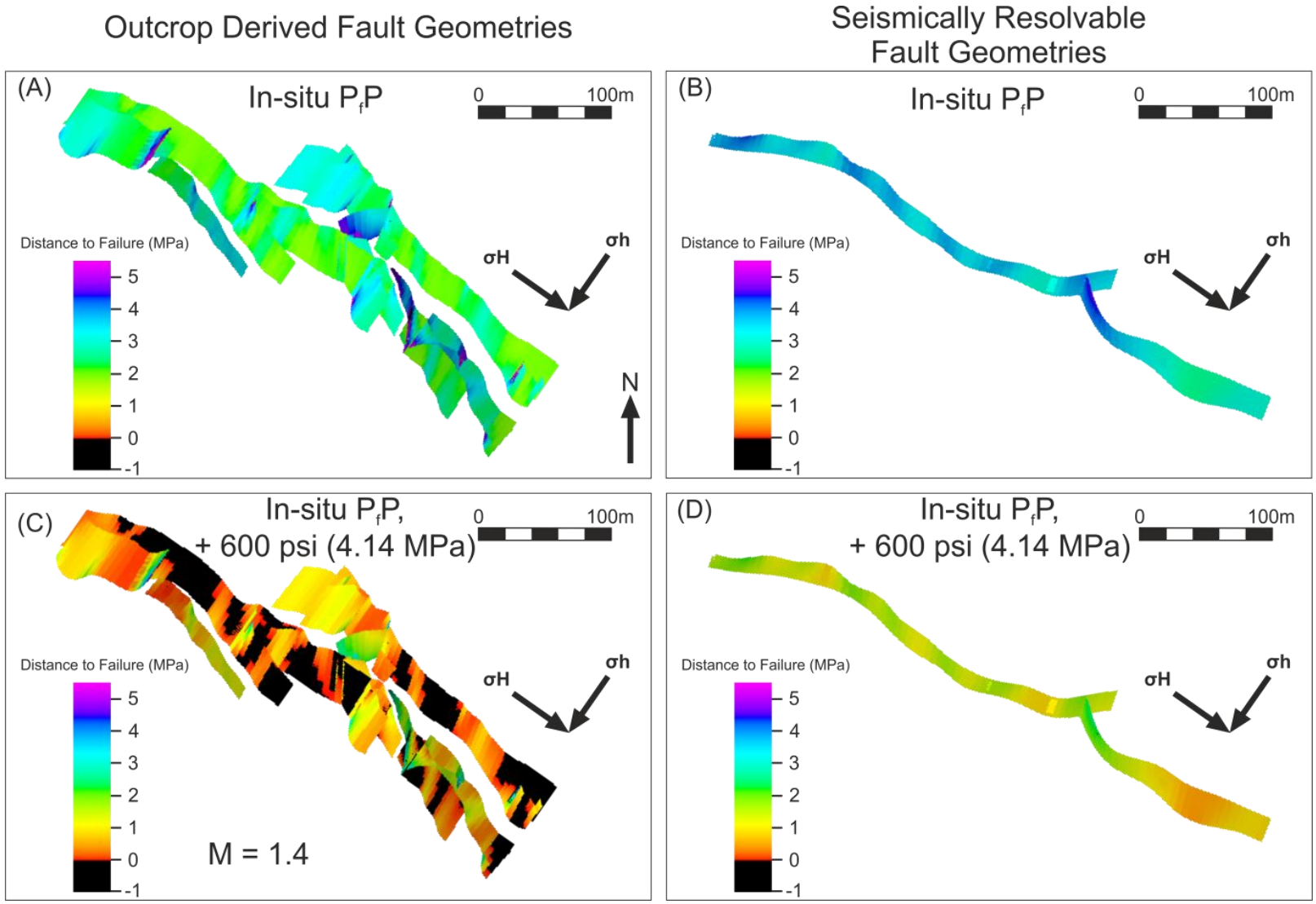
Outcrop Derived Fault Geometries
Seismically Resolvable Fault Geometries
(A)
In-situ PfP
0
100m
Distance to Failure (MPa)
5
4
3
2
1
0
-1
σH
σh
N
(B)
In-situ PfP
0
100m
Distance to Failure (MPa)
5
4
3
2
1
0
-1
σH
σh
(C)
In-situ PfP,
+ 600 psi (4.14 MPa)
0
100m
Distance to Failure (MPa)
5
4
3
2
1
0
-1
σH
σh
M = 1.4
(D)
In-situ PfP,
+ 600 psi (4.14 MPa)
0
100m
Distance to Failure (MPa)
5
4
3
2
1
0
-1
σH
σh

Initially conservative values for the geomechanical properties have been applied, with a fault friction angle of 31°. To illustrate the importance of accounting for geomechanical uncertainty a more moderate fault friction angle of 23° has also been used to assess fault stability (figure 9.7). Under these conditions the amount of unstable fault surface at a pore fluid pressure increase of 600 psi (4.14 MPa) is significantly greater than at a higher angle of friction (figure 9.8). This is the case for both realistic and seismically resolvable geometries, with the potential result being increased seismic magnitudes should fault reactivation occur.

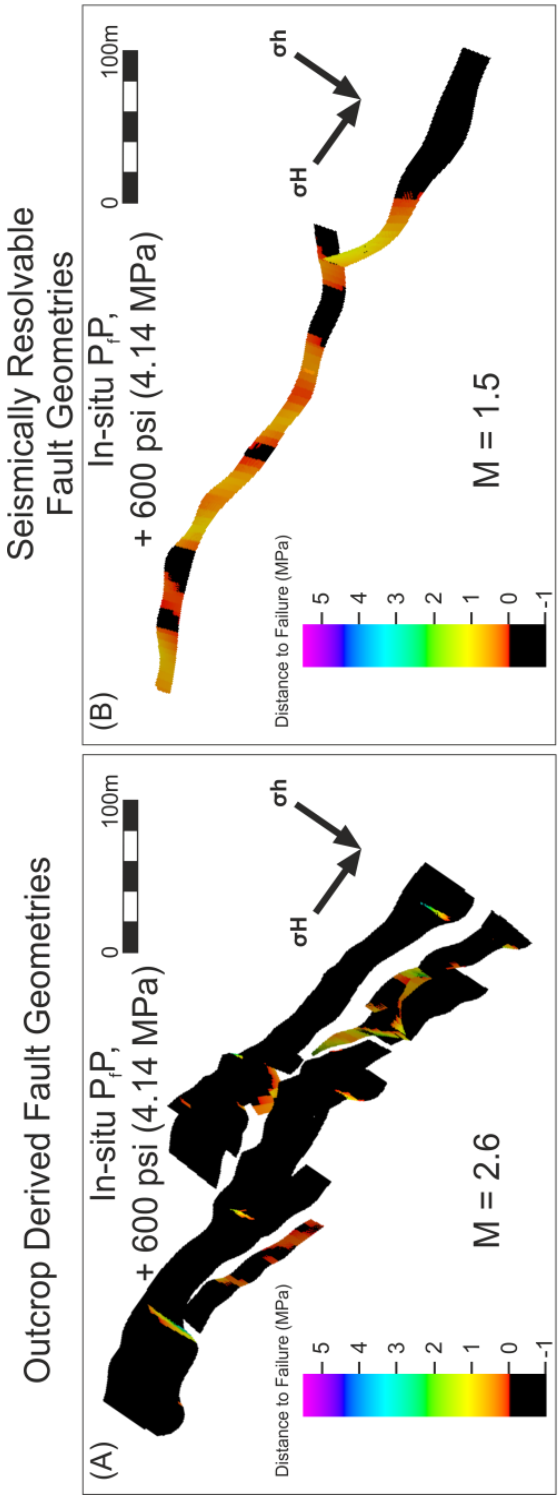

Figure 9.7 (Previous page). A less conservative estimate of a fault friction angle of 23° leads to a greater proportion of the faults becoming unstable. At this lower friction angle almost all of the outcrop-derived geometry (A) is unstable for a pore fluid pressure increase of 600 psi (4.14 MPa) In contrast significantly less of the seismically resolvable fault geometry (B) is unstable. The area of unstable fault surface for the outcrop-derived geometry would be sufficient to generate seismicity of magnitude M=2.6.

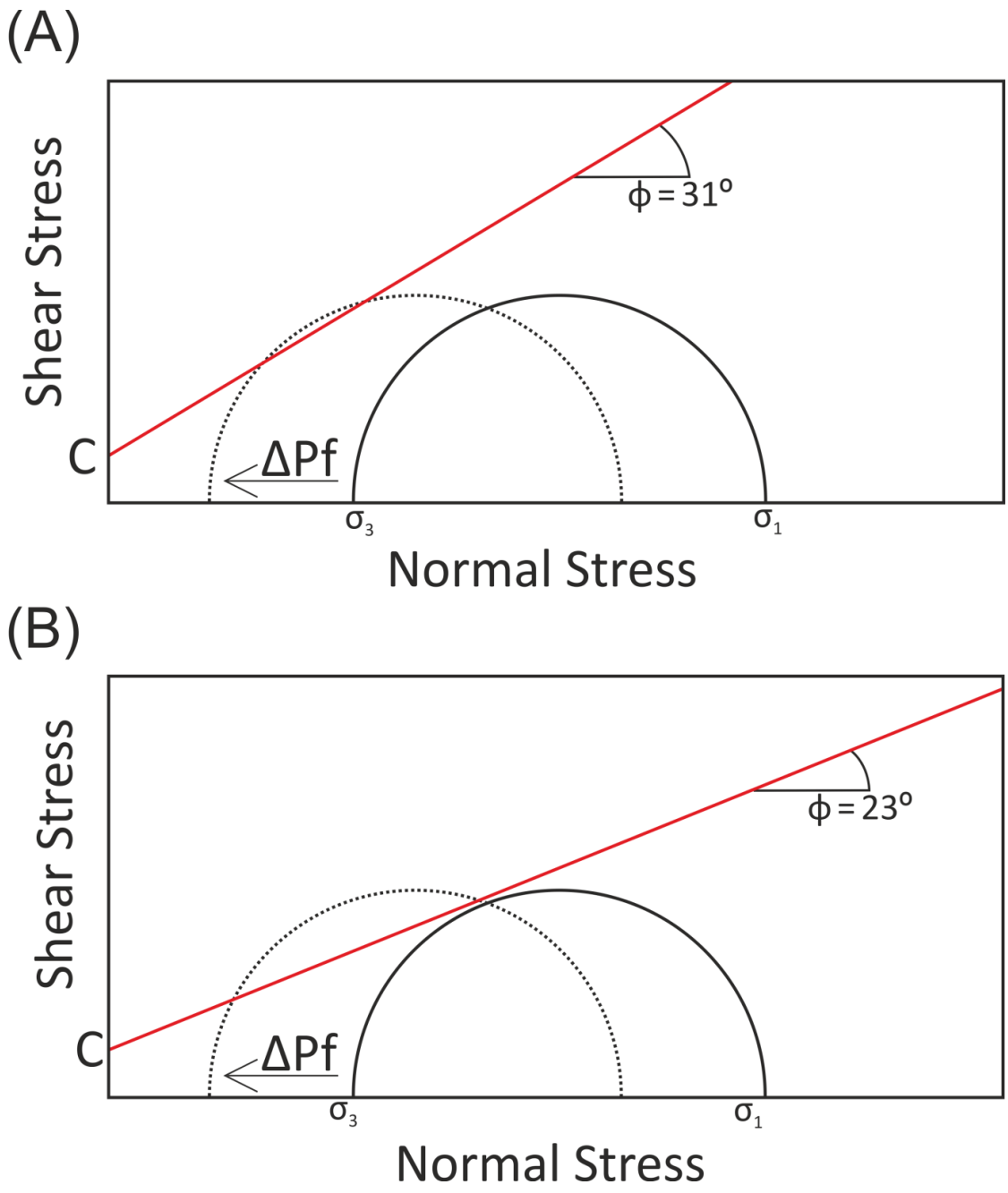

Figure 9.8 (Previous page). Mohr circles schematically illustrating the impact of geomechanical uncertainty on estimates of fault stability. (A) A conservative value of the fault rock friction angle (31°) as used to define fault stability in figure 9.6. (B) The same parameters as (A), except that the fault rock friction angle has been changed to 23° as in figure 9.7. This results in favourably orientated faults becoming unstable at significantly smaller increases of the pore fluid pressure.

9.5 Magnitude of Induced Seismicity

Predicting the magnitude of any seismicity associated with reactivation of the structures modelled in Figures 9.6 and 9.7 has significant uncertainty. It is widely recognised that the seismic moment (M_0) of an earthquake event is related to the area of the rupture, the average displacement and the shear modulus (1), (Kanamori and Anderson, 1975). The average displacement expected can be estimated using the empirical relationship between surface rupture length and average rupture displacement (2) defined by Wells and Coppersmith (1994). Note that we have modified this relationship to account for their observation that the length of a rupture observed at the surface is approximately 75% of its sub-surface length. We use a shear modulus for shale of 1.5×10^{11} dynes/cm^2 (Warpinski et al., 2012), however values may be up to an order of magnitude lower (Horsrud, 2001). Seismic moment can be converted to moment magnitude (M) using equation (3). The dimensions used are schematically illustrated in figure 9.9.

(1) $M_0 = \mu AD$, where μ=Shear Modulus in dynes/cm^2, A = Rupture length x down dip rupture width in cm and D=average displacement of rupture in cm (Kanamori and Anderson, 1975)

(2) Log (D) = -1.43 + 0.88 log (0.75L), where D = average displacement in m, L = rupture length in km (Modified from Wells and Coppersmith, 1994)

(3) $M = 2/3 \log M_0 - 10.7$, (Hanks and Kanamori, 1979)

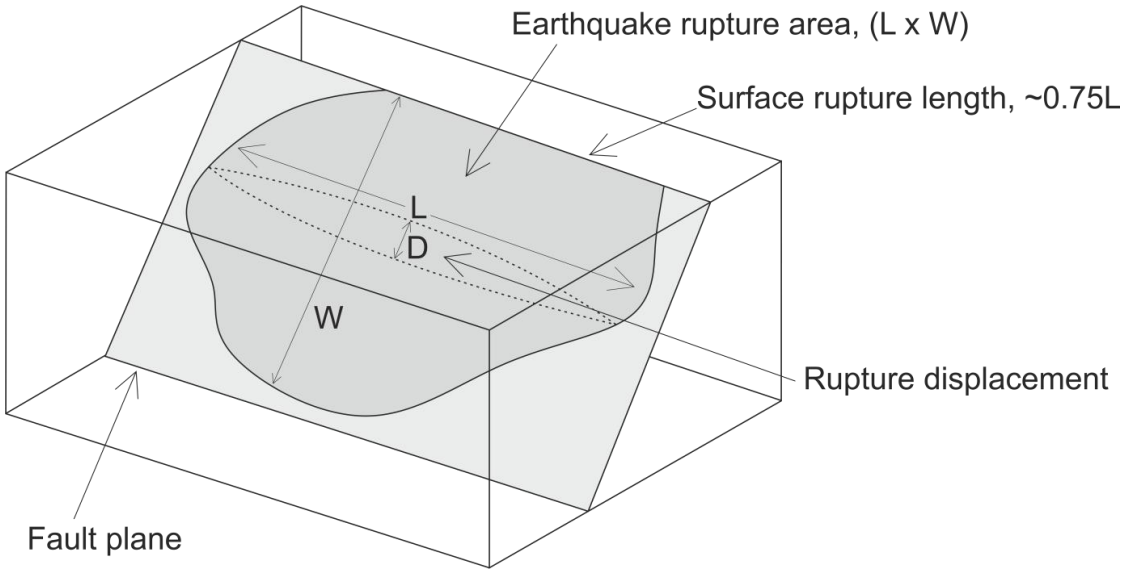

Figure 9.9. Schematic illustration of the fault dimensions used to calculate earthquake magnitude.

The maximum length of instability in our dataset is approximately 70m for a pore pressure increase of 600psi (Figure 9.6), and a friction angle of 31°. Data compiled by Wells and Coppersmith (1994) suggests that on average, rupture dimensions have down-dip width to length ratios of approximately 0.66, placing an upper bound on rupture area for our data of approximately 3250m^2. This equates to a magnitude for the geometries modelled here of approximately M=1.39 (assuming μ=1.5x10^{11}dynes/cm^2, and D=0.28cm). This value is significantly greater than the M=0.5 maximum threshold for the cessation of hydraulic fracturing operations recommended by Green et al (2012) in relation to induced seismicity in NW England. If however, the less conservative value of fault friction angle is applied (23°, figure 9.7), then the length of instability increases to 300m for a pore fluid pressure increase of 600 psi. In turn this leads to a potential seismic magnitude of M=2.6 should reactivation occur. Friction angles may in fact be as low as 6° (de Pater and Baisch, 2011), possibly leading to even larger magnitude seismicity occurring for a given pore fluid pressure.

9.6 Discussion

Seismically forward modelling outcrop-based fault geometries confirms that geometries observed in seismic data are significantly simplified, and contain a large degree of uncertainty relative to realistic fault geometries. The accuracy of the forward modelling procedure

depends upon how well constrained the petrophysical and elastic properties of the sub-surface are for the target area, as well as the properties of the background model, and the definition of the seismic survey and input wavelet. Since rock properties are rarely isotropic there will inevitably be discrepancies between the modelled properties and those present in the subsurface, although due to the low energy environment typical for shale deposition it is anticipated that this variation will be relatively limited. Although the ray tracing algorithm does account for diffractions in a heterogeneous overburden, it does not include noise which may be present during seismic acquisition. Resolution in a forward modelled seismic cube will therefore be slightly better than for a 'real' seismic cube. The most important uncertainty when generating the seismically resolvable fault geometries is the interpretation of the synthetic cube. Interpretation is highly subjective, with significant differences even when those performing the interpretation are defined as experts (Bond et al., 2012). Although a number of surface and volume algorithms have been applied to the data to ensure that the maximum possible detail has been captured with the minimum geometric error, fault interpretations are nevertheless still non-unique, potentially leading to variation in the magnitude of stresses that may be resolved onto the modelled fault plains.

The modelled geometries are derived from faults hosted in mechanically strong, brittle basaltic rocks deformed at the earth's surface (Rowland et al., 2007). The applicability of these geometries to faults within shale gas reservoirs will depend upon the conditions under which deformation of the shale occurred. The geomechanical properties of shales vary with the confining pressure, temperature, density, consolidation and chemical composition (Magara, 1968; Hoshino et al., 1972; Bolton et al., 1998; Ingram and Urai, 1999; Bjørlykke, 1999; Petley, 1999; Nygård et al., 2006). The specific conditions control whether a shale responds to stress through ductile or brittle deformation, and hence the occurrence and geometry of any faults which may be present. If the shale formation has not been subjected to brittle failure then the presence of fault planes susceptible to reactivation during hydraulic fracturing is unlikely, although slip along favourably orientated planes, such as dipping bedding, is possible (Donath, 1961). Since faults are not always resolvable in seismic data reconciling the subsurface mechanical properties with the tectonic history is therefore crucial in assessing the likelihood of brittle failure having occurred, and hence the presence of any discrete fault structures liable to be reactivated during fluid injection.

Assuming that an entire fault can be ruptured in a single event places an intrinsic upper limit on the maximum magnitude which can be generated from that fault. The faults modelled here have small horizontal dimensions and surface areas and hence have a low maximum potential magnitude. Faults with dimensions sufficient to host much larger ruptures, and therefore

higher magnitude seismicity, may however also be undetectable within seismic data, since it is fault displacement rather than fault size which is the identifiable dimension. Horizontal displacement gradients on faults range between 0.1 and 0.001m/m, with vertical gradients approximately double this (Walsh and Watterson, 1988). Therefore a fault plain with a maximum displacement just below the typical limit of seismic resolution (~10m) could foreseeably have an area on the order of $5x10^7 m^2$ if the minimum displacement gradients are used to calculate its area. This would correspond to a maximum magnitude approaching M=5.44 if the entire fault surface should rupture. Nevertheless such a fault would have a down dip width dimension of approximately 5km, significantly larger than the thickness of sediment that would be subject to increase pore pressures during fluid injection. Indeed, the value calculated here of a potential magnitude of M=2.6 resulting from reactivation of the sub-seismic faults modelled here can be treated as approaching a maximum value. This is because it relies on the supposition that a 600psi pore pressure increase during fluid injection is instantaneous and isotropic, and that rupture occurs along the entire zone of instability simultaneously. In reality fluid is typically injected over the course of a few hours or days leading to a more gradual increase in pressure and distributed microseismicity with a higher frequency of occurrence but considerably lower magnitudes (Shapiro et al., 2009). Heterogeneity in the host permeability and the presence of pre-existing fractures are likely to result in pressure increases during hydraulic fracturing varying non-linearly both spatially and temporally (Figure 9.10) (Shapiro & Dinske, 2010), leading to uncertainty in constraining the distributions of stress across any fault plains which may be present.

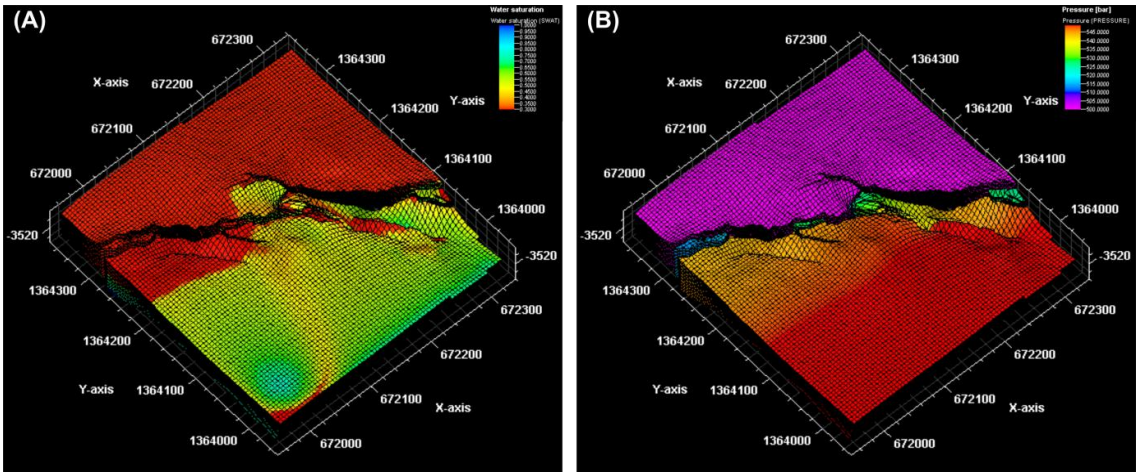

Figure 9.10. Illustration of how fluid saturation (A) and pressure (B) vary non-linearly during fluid injection. The implication is that different parts of a fault set will become critically stressed and will hence fail at different times, rather than simultaneously.

There remains uncertainty in the geomechanical properties of faults within shales, leading to uncertainty when defining their stability under specific stress conditions. For the purposes of assessing the potential for reactivation, faults are often assumed to be cohesionless (e.g. Morris et al., 1996), however this is likely to be influenced by the deformation processes and the resultant fault rocks, as well as any post deformation healing (Morrow et al., 1982; Dewhurst and Jones, 2002). The friction angle of faults within shale is also uncertain, with de Pater and Baisch (2011) reporting polished surfaces possibly representing shear plains to have friction angles potentially as low as 6°. Incorrect definition of the failure envelope will lead to erroneous predictions of the pore pressure at which failure will occur. To maximise the accuracy of fault stability predictions additional research constraining the geomechanical properties of fault rocks within shale sequences is required.

An additional uncertainty regarding the stability of faults during fluid injection relates to the degree to which the pore pressure is coupled to the effective stress. A pore pressure increase will lead to a decrease in the total horizontal stress within a reservoir, and hence a reduction in the effective stress (Hillis, 2001). In turn this reduces the diameter of the Mohr circle describing the state of stress in the sub-surface (figure 9.11). This will tend to the reduce the likelihood of shear failure, whilst increase the likelihood of tensile failure occurring.

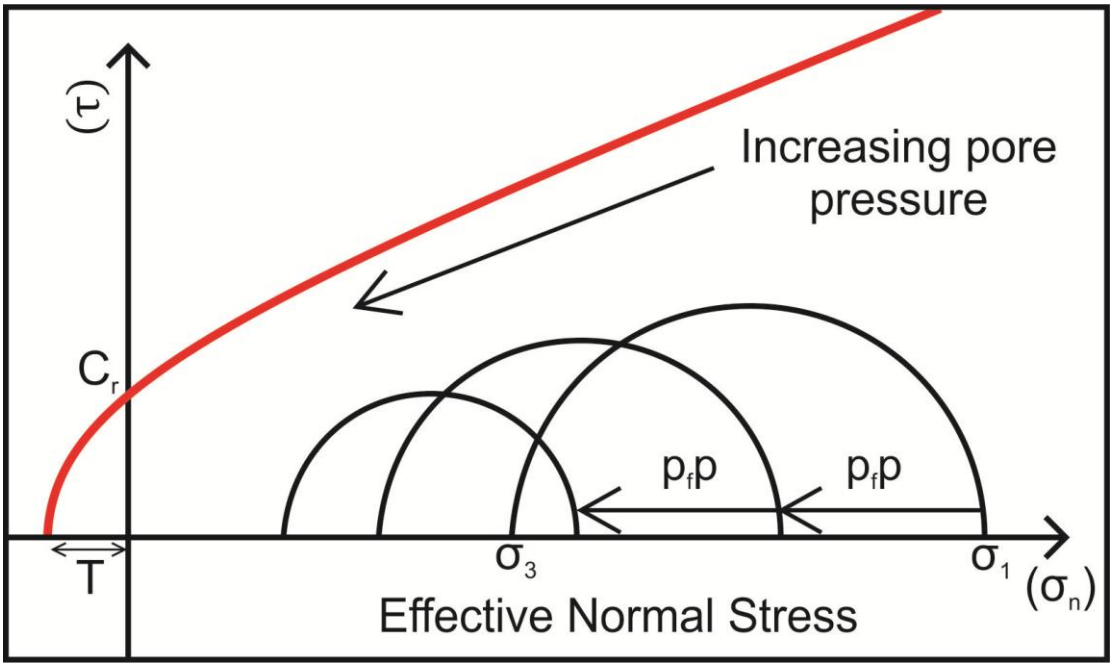

Figure 9.11 (Previous page). Schematic Mohr circle plot illustrating the effect of pore-pressure/stress coupling during fluid injection. The increase in pore pressure increases the minimum horizontal stress (hence decreasing the differential stress), whilst at the same time reducing the maximum stress (assumed to be vertical, i.e. extensional faulting regime). This leads to the Mohr circle decreasing in diameter and moving to the left, as shown above. In turn this reduces the likelihood of shear failure whilst increasing the likelihood of tensile failure occurring.

It has been demonstrated that seismic forward modelling can be employed to limit the structural uncertainty that may influence induced seismicity during hydraulic fracturing, however the technique also has potential to be applied to numerous additional situations to aid the constraint of ambiguous structural data. These include, but are not limited to, calculating sub-seismic strain distribution, improving the accuracy of hydrocarbon production simulations and modelling the seismic response of $C0_2$ injection into the subsurface at potential sequestration sites.

9.7 Conclusions

Fault geometries identifiable within seismic data are significantly simplified and display considerable variations in orientation relative to outcrop geometries. These discrepancies lead to differences in the stress magnitudes which are modelled as being resolved onto fault planes under the specific in-situ stress conditions. As a result significantly lower pore pressure increases than anticipated may induce failure. It is possible that sub-seismic scale faults have sufficient surface areas to generate seismicity exceeding the recommended limit for hydraulic fracturing operations of M = 0.5. Significantly higher values than this would however require an effectively instantaneous large increase of pore pressure with rupture occurring across the entirety of an unstable fault surface simultaneously. Further work is required to characterise the temporal and spatial evolution of pore pressure increases during injection of fluids into low permeability media.

Chapter 10

Discussion and Conclusions

10.1 Introduction

The theme of this thesis has been to investigate fault geometric uncertainty and its effect on fluid flow in the subsurface, primarily from the perspective of the recovery of hydrocarbon reserves. In this context geometric uncertainty stems from the limited resolution of reflection seismic data, the principal source of constraint on subsurface structural architectures. The influence of this uncertainty has been examined across a range of scales from rift-basin through oil-field scale to individual faults, with a deliberate ordering from large to small scale. The tools of investigation have included field data collection, seismic interpretation, 3D geocellular modelling, fluid flow simulation and forward seismic modelling, and have been coupled with an extensive review and integration of the existing literature. The structure of the thesis has been for the individual Chapters to be largely independent, although linked by the over-arching theme of geometric uncertainty. Consequently the main points of discussion have largely been covered therein. This Chapter therefore aims to link and summarise, rather than repeat, the points already discussed.

10.2 Summary

As mentioned the thesis can be broadly divided by the scale to which each Chapter relates. A brief summary is here provided for Rift (Chapters 3 and 4), Field (Chapters 5 and 6), and Fault scale (Chapters 7, 8, 9). The majority of figures are referred to although a number of key figures are reproduced.

10.2.1 Rift Scale

Data from the Gulf of Corinth (Chapter 3) indicate that initial rift activity and fault growth may have occurred over a relatively broad area prior to localisation onto more dominant structures (e.g. Cowie et al., 2000). Nevertheless ambiguity in the precise nature of the evolution of the rift still exists since observations also indicate strain being accommodated along strike by both multiple and single fault sets (Figure 10.1). This may be related to a possible rotation of the extension direction (figure 3.27), although further work is required to verify this hypothesis. These uncertainties illustrate the potential dangers in applying a single model for rift evolution.

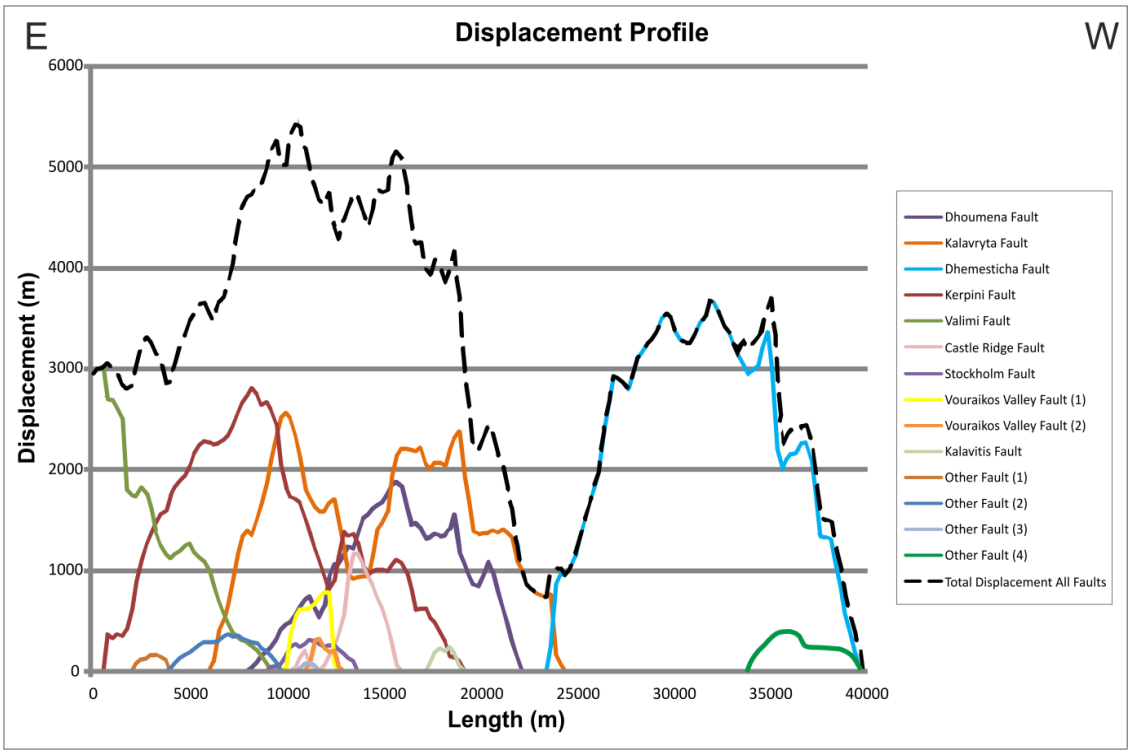

Figure 10.1. Mid-case displacement-length plots for Gulf of Corinth faults with displacement projected onto a strike-parallel plane (approximately E-W). The disparity in cumulative displacement between the east and west areas is clearly seen. In the eastern area to the north of the Kalavryta fault, strain is partitioned across multiple faults, whereas further west a single fault, the Dhemesticha fault, accommodates almost all of the strain.

Multiple phases of discreet activity on individual fault sets indicate that the evolution of the Gulf of Corinth Rift did not occur as a sequential northwards progression of faulting as has previously been proposed (e.g. Sorel, 2000). A more complex pattern locally superimposed onto a more generalised migration towards the rift axis is observed. It remains unclear as to whether this more complex rift evolution is a phenomenon local to the Gulf of Corinth rift, or whether it can be identified in multiple areas. Major internal unconformities within syn-rift strata indicative of multiple phases of rifting may be coupled with facies changes, with implications for the distribution of reservoir units.

The uncertainty inherent in seismic data limits the detail to which faults can be resolved (see Chapter 4). In terms of hydrocarbon exploration, where 2D seismic is the primary data source, this leads to uncertainty in along-strike displacement continuity. This is often exacerbated since the position of displacement minima and/or maxima is unlikely to correspond with the position of potentially disparate seismic lines. Pragmatism, and an understanding of fault

evolution (Figure 4.2) are hence required when correlating faults between seismic lines (Figures 4.10, 4.11, 4.12, 10.2). Structural spill points, trap crests and maximum column heights estimated using 2D data are hence subject to the non-unique nature of seismic data and its interpretation (Figure 4.15). This geometric uncertainty has other implications since it also influences pore pressure predictions (Figure 4.16, 10.3, 10.4) and fault rock property calculations (Figure 4.22).

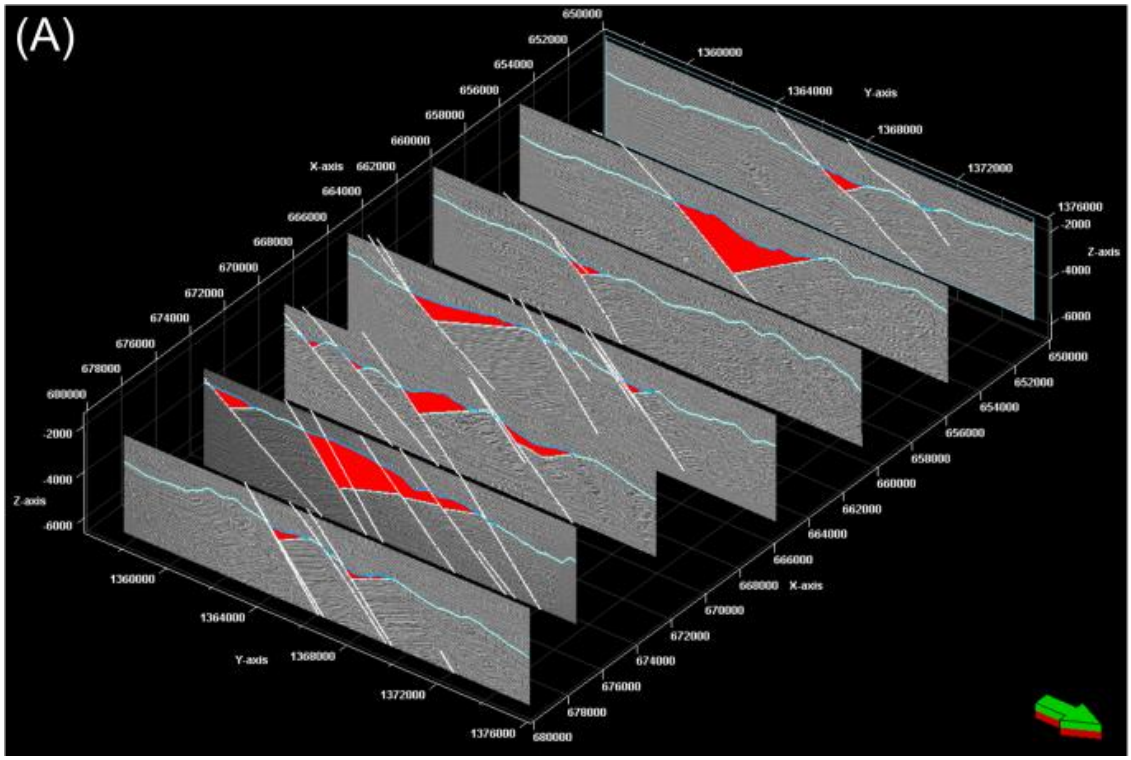

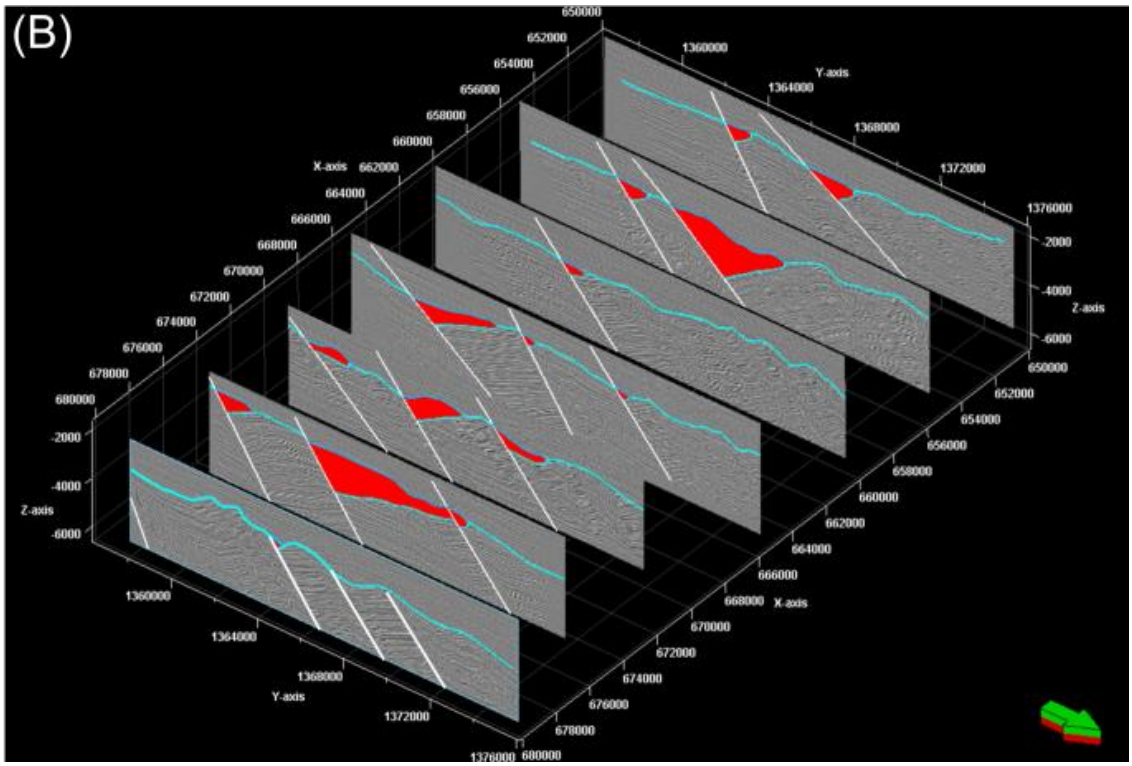

Figure 10.2. Synthetic seismic sections through the Gulf of Corinth rift geometry defined from field data in Chapter 3. (A) The syn-rift distribution, top pre-rift surface and fault geometries defined from field data are superimposed onto the seismic sections. (B) The syn-rift distribution as defined by the interpreted surface and fault geometries. 2D sections have a spacing of 5 km.

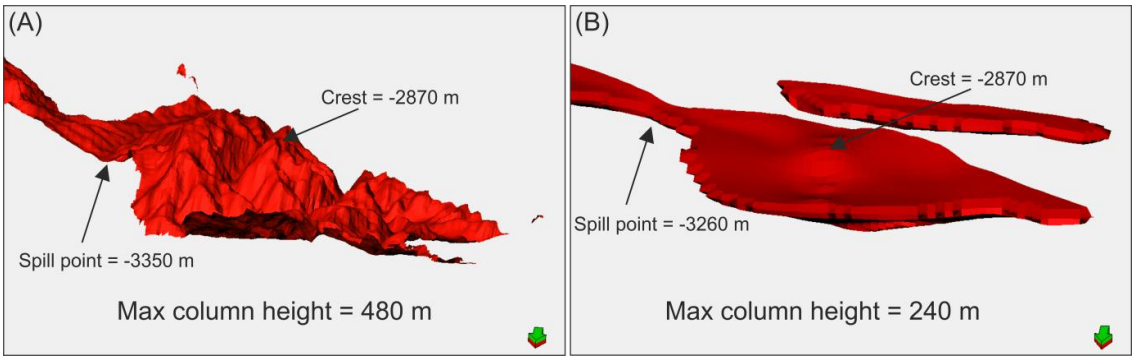

Figure 10.3. Oblique views of the modelled syn-rift fill in the Dhemesticha sub-basin shown in Chapter 4. The figure illustrates the difference in the depth of the structural crest, the spill point and the corresponding difference in predicted maximum column height for the outcrop-derived (A), and seismically resolvable (B) geometries.

Figure 10.4 (Next page). Plot of pressure versus depth for the outcrop derived and seismically resolvable prospect geometries shown in Chapter 4. The difference in predicted column height leads to an underestimate in pore fluid pressure for the seismically resolvable geometry relative to the outcrop derived geometry.

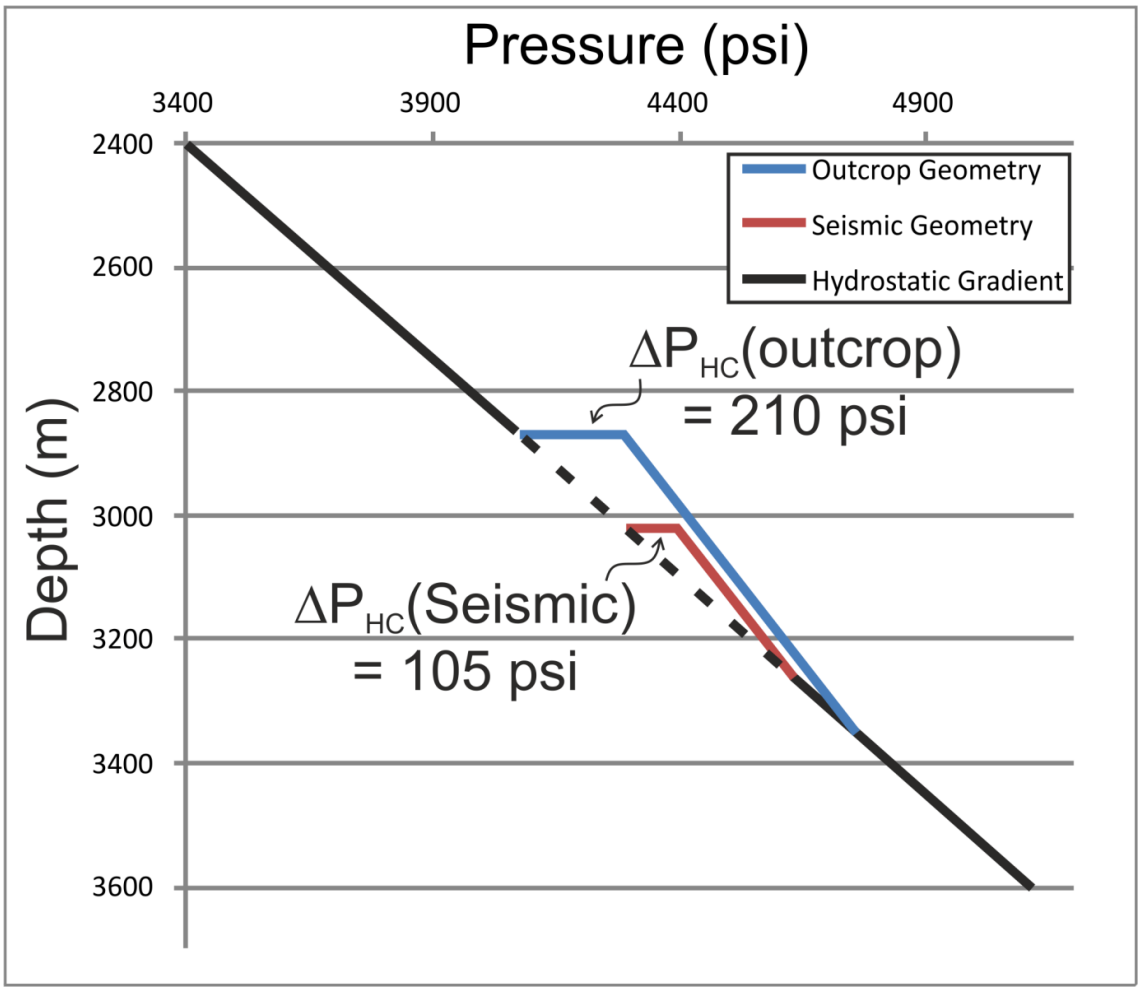

10.2.2 Field Scale

At the scale of individual oilfields, where 3D seismic data is available, the limitations in seismic resolution have different impacts on structural uncertainties. The primary concern regarding intra-reservoir scale faults is whether or not they pose a barrier or baffle to across-fault flow of hydrocarbons during production, and hence cause any degree of reservoir compartmentalisation.

The impact of two aspects of sub-seismic fault geometries has been investigated. Chapter 5 shows how sub-seismic fault geometries, in the form of fault tips and relay-zone breaching faults can be predicted from seismically resolvable parameters (figures 5.6, 5.7, 5.8, 5.9, 5.19, 10.5, 10.6). Incorporating these features may lead to enhanced fault network connectivity (figures 5.15, 5.16) and corresponding reservoir segmentation. Despite this enhanced connectivity the impact on oil production is relatively limited, at least for the example of the Penguin oilfield used herein (Chapter 6, figures 6.6, 6.8, 6.10). The simulation results suggest that increasing fault connectivity may result in a moderate enhancement of overall recovery

due to a more efficient hydrocarbon sweep pattern, an observation in agreement with a number of other studies (Manzocchi et al., 2008a, b). In contrast to oil production, increased connectivity significantly reduces the volume of produced water (figures 10.7, 10.8). Since the processing of produced water is a significant cost during production, the implication is that, contrary to the common perception, connectivity and segmentation of a reservoir by faults may in fact be economically beneficial in certain situations.

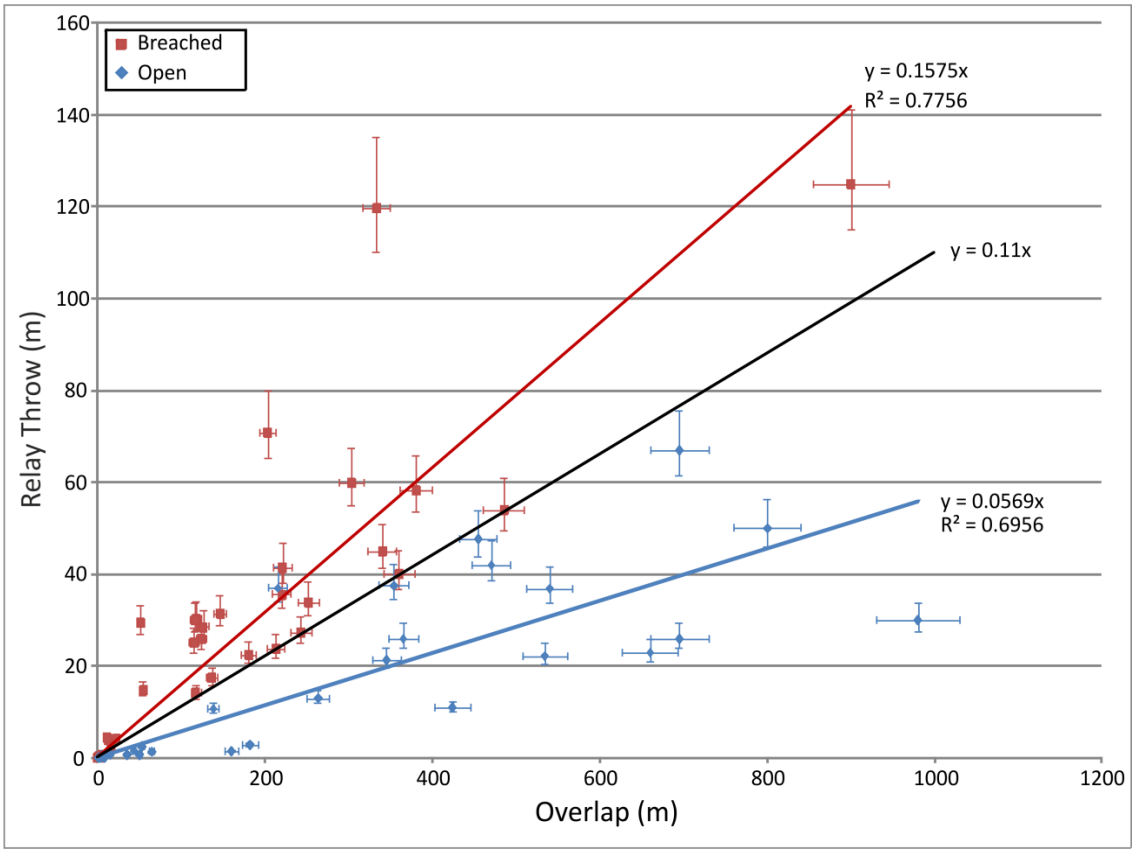

Figure 10.5. Cross plot of cumulative relay throw against overlap for 88 relay zones. Breached and open relays are clearly clustered in separate fields, with low relay throw:overlap ratios indicating intact relays, and high ratios indicating breached relays. 5% error bars are included for fault length measurements, and vertical error bars representing 10° to account for variation in fault dip are also included. Data compiled from; Walsh and Watterson, 1990; Peacock and Sanderson, 1991, 1994; Cowie et al, 1994; Childs et al, 1995; Huggins et al, 1995; Cartwright et al, 1996; Schlische et al, 1996; Willemse et al, 1996; Davies et al, 1997; Bohnenstiehl and Kleinrock, 1999, 2000; Mansfield and Cartwright, 2001; Imber et al, 2004; Soliva and Benedicto, 2004; Taylor et al, 2004; Mirabella et al, 2005; Hus et al, 2006; Rotevatn et al, 2007; Polit et al, 2009; Long, 2011. See figures 5.12, 5.13, 5.14 for examples from this study.

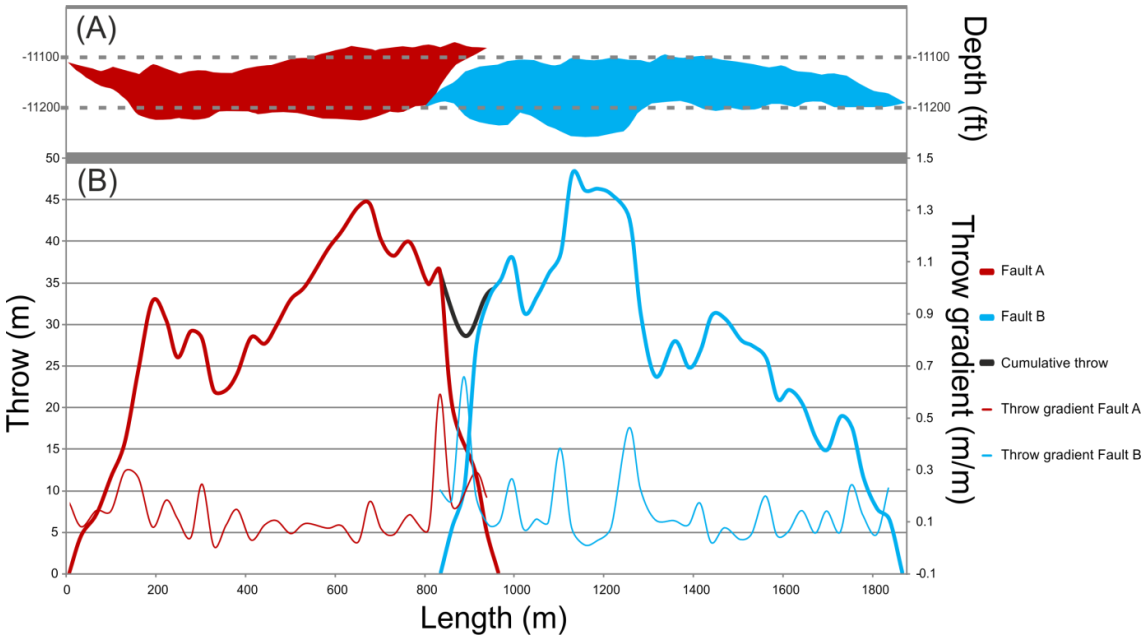

Figure 10.6. (A) Perpendicular view of two interacting faults from our dataset as defined by top reservoir footwall and hangingwall cut-offs. Vertical exaggeration is x3. (B) Throw and throw gradient profiles of the shown faults in (A). An increase in the throw gradient is observed where the faults overlap and interact. Fault interaction and tip restriction has resulted in migration of the position of maximum throw on the two fault segments towards the relay zone. The breaching criteria (figure 5.10) suggest that a sub-seismic breaching fault should link the two fault segments.

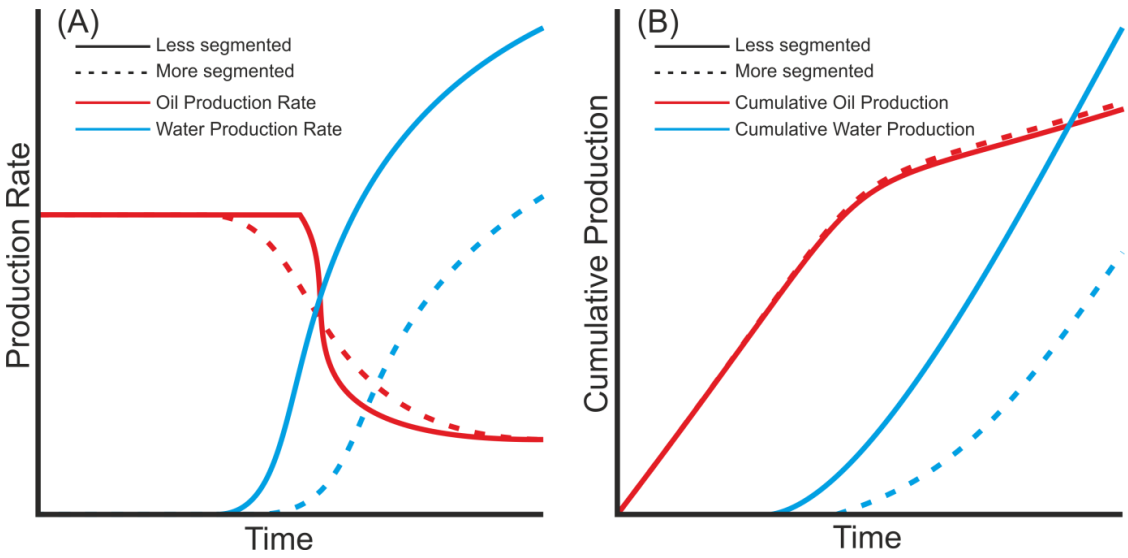

Figure 10.7. Schematic summary of the influence of including relay zone breaching faults and sub-seismic fault tips on production rates (A) and production volumes (B).

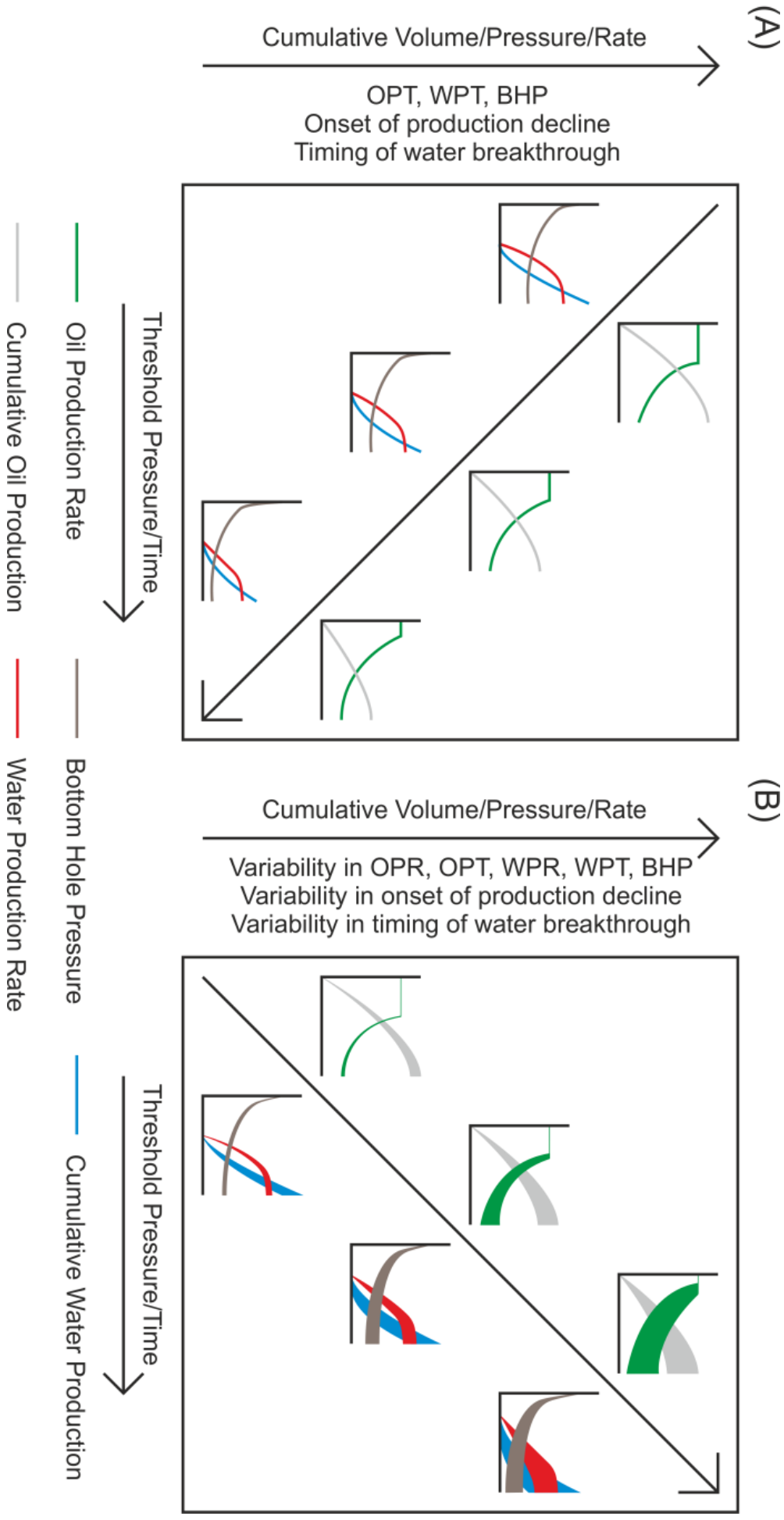
(A)
Cumulative Volume/Pressure/Rate
OPT, WPT, BHP
Onset of production decline
Timing of water breakthrough
Threshold Pressure/Time
Oil Production Rate
Cumulative Oil Production
(B)
Cumulative Volume/Pressure/Rate
Variability in OPR, OPT, WPR, WPT, BHP
Variability in onset of production decline
Variability in timing of water breakthrough
Threshold Pressure/Time
Bottom Hole Pressure
Water Production Rate
Cumulative Water Production

Figure 10.8 (Previous page). Schematic graphs summarising the impact of varying the fault threshold pressure during simulation. (A) General trends. The onset of production decline occurs earlier for higher threshold pressures, leading to a lower cumulative produced volume. The water production rate, cumulative volume of produced water and bottom hole pressure at the production well are all lower for higher fault threshold pressures. (B) Variability of simulation results between different structural configurations for increased fault threshold pressure. At low threshold pressures the simulation results for the ten different fault network configurations (Chapter 6) are relatively similar. However, as threshold pressure is increased the variability of the simulation results also increases. This indicates that fault network connectivity becomes more important when attempting to achieve a realistic forward prediction or accurate history match when fault threshold pressures are expected to be high. OPT = Oil Production Total, OPR = Oil Production Rate, WPT = Water Production Total, WPR = Water Production Rate, BHP = Bottom Hole Pressure.

10.2.3 Fault Scale

The impact of uncertainty in the geometry of individual faults upon across fault flow has been assessed in Chapters 7 and 8. The presence or absence of relay zones is critical in controlling the flow behaviour of faults, especially where the mean reservoir interval is less than the mean fault throws (figures 7.11, 7.12, 7.13). In these instances the low-displacement at relay zones represent the only areas of reservoir:reservoir juxtaposition, and hence of potential across-fault fluid and pressure communication. The specific geometry of a relay zone is of secondary importance compared to the incorporation of discrete deformation, here modelled as normal drag (figures 7.6, 7.11, 10.9). This has the effect of reducing the effective displacement of a fault, and hence leads to enhanced across-fault juxtaposition, a parameter which is critical in controlling across-fault flow during hydrocarbon production (Chapter 8).

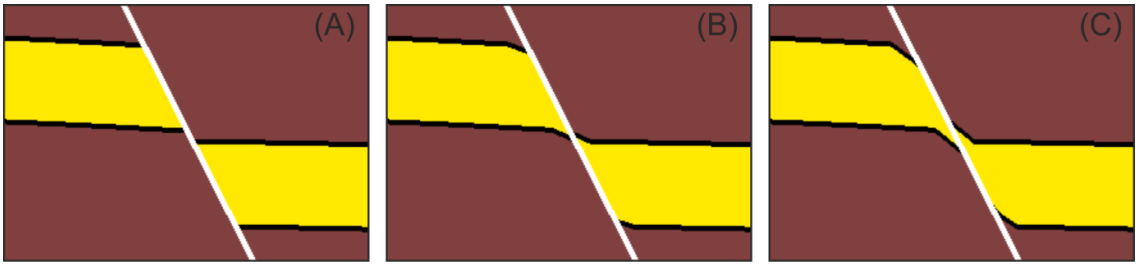

Figure 10.9 (Previous page). Cross-sections through modelled geometry showing the different amounts of normal drag which have been incorporated. (A) No normal drag. (B) Normal drag accounts for 20% of total displacement (i.e. discrete offset is 80% of displacement). (C) Normal drag accounts for 50% of displacement. Increasing the proportion of normal drag effectively reduces the discrete displacement, hence leading to greater across-fault juxtaposition of the reservoir interval (shown in yellow).

Seismic forward modelling allows the comparison of the flow properties of realistic, outcrop-derived fault geometries, with those geometries observable within seismic data. The complexity of realistic fault geometries leads to significantly greater juxtaposition area compared with the planar faults imaged in seismic data (figures 8.10, 10.10, 10.11). Consequently the impact of faults upon reservoir compartmentalisation may be regularly overestimated when sub-seismic fault complexity is not accounted for (Chapter 8).

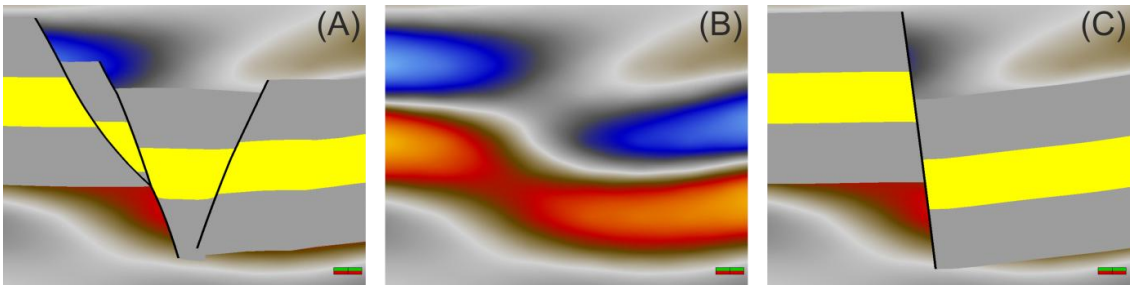

Figure 10.10. Cross sections through illustrating the differences between the outcrop derived fault geometry and the seismically resolvable geometry. The model geometry is superimposed onto the forward modelled seismic volume. (A) Outcrop derived geometry. Displacement partitioning on multiple slip surfaces leads to maintenance of across fault juxtaposition of the reservoir interval (yellow) despite the cumulative fault throw being greater than the reservoir thickness. (B) Image of the forward modelled seismic volume. Very few details of the fault architecture are resolved. (C) Seismically resolvable fault geometry. Only single slip plane can be positively interpreted from the forward modelled seismic (B). This leads to the reservoir interval being completely offset and hence a juxtaposition seal being present.

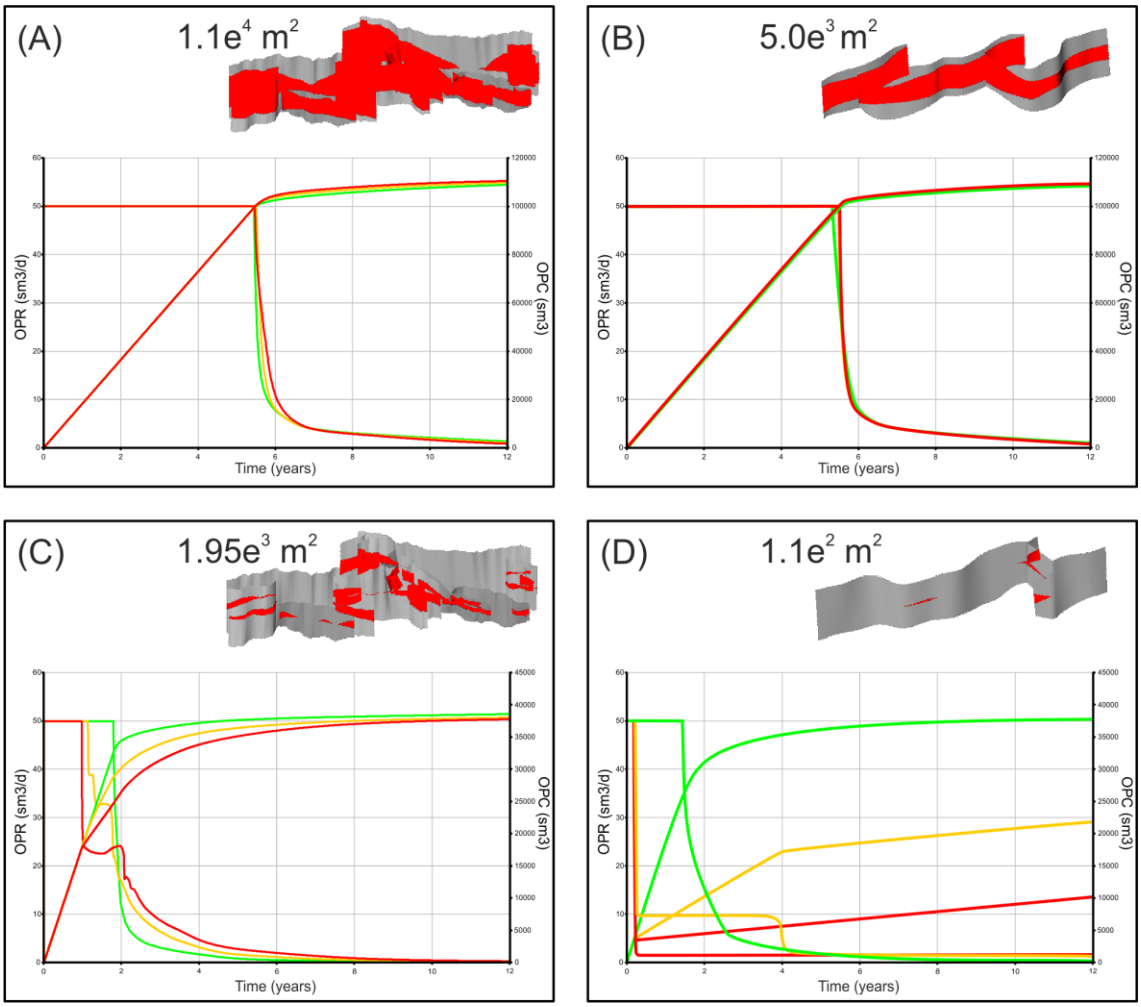

Figure 10.11. Simulation results highlighting the importance of the ratio of stratigraphic thickness to fault throw (Th:tw) in terms of the effective juxtaposition area (shown) for a partially breached relay zone geometry. Red = High case TMs, Yellow = mid-case TMs, Green = low-case TMs. The well-derived petrophysical properties are used in all cases. (A) High Th:tw, outcrop fault geometry. (B) High Th:tw, seismically resolvable geometry. (C) Low Th:tw, outcrop fault geometry. (D) Low Th:tw, seismically resolvable geometry. For discussion see text. OPC = Oil Production Cumulative, OPR = Oil Production Rate.

The sub-seismic complexity of fault zones also influences the way that local and regional stresses are resolved onto the fault planes (figure 10.12). In turn this affects estimates of fault stability under conditions of deviated pore fluid pressure, such as during hydraulic fracturing. The potential for induced seismicity may underestimated when fault stability is calculated using solely the seismically resolvable fault geometries (figures 9.6, 10.13).

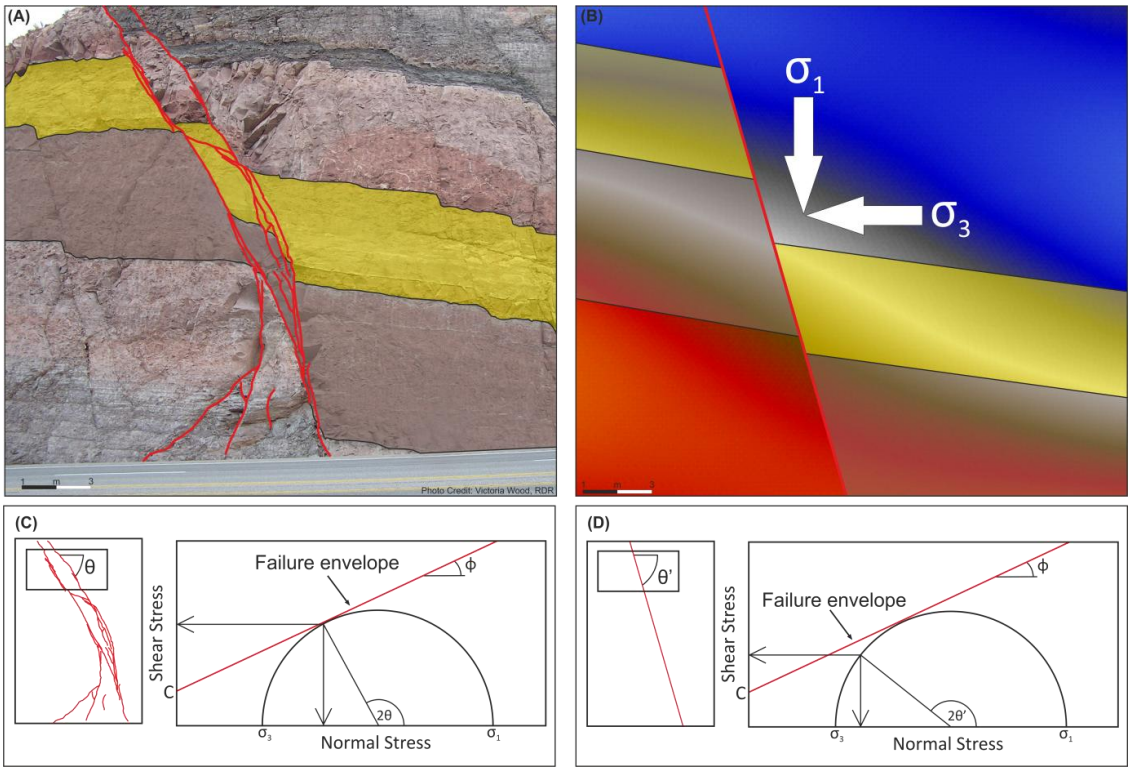

Figure 10.12. Outcrop example of how seismic data leads to underestimates in the complexity of fault geometry, and the influence that this has on fault stability during fluid injection. (A) View of road cutting showing significant geometric complexity. (B) The seismically resolvable version of the same geometry. A single fault plane is imaged effecting how the local stress field is predicted to be resolved onto the fault plane. (C) The outcrop geometry has a shallower dip than the seismically resolvable geometry (D). For a constant local stress field, the complex outcrop geometry is closer to the failure envelope than the seismically resolvable geometry. A lower pore pressure increase is hence required to induce failure and induce seismicity.

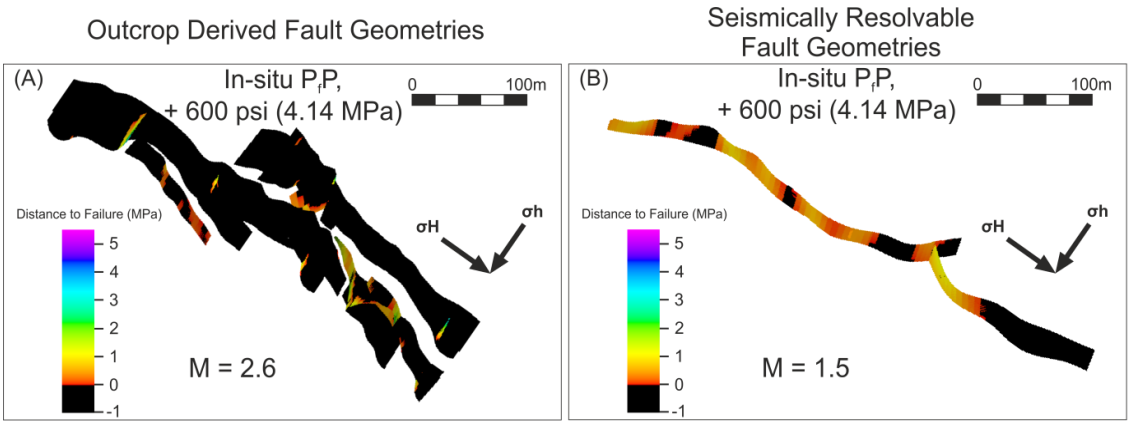

Figure 10.13 (Previous page). Fault stability assuming a fault friction angle of 23°. This leads to a greater proportion of the faults becoming unstable than for a more conservative estimate of 31°. At this lower friction angle almost all of the outcrop-derived geometry (A) is unstable for a pore fluid pressure increase of 600 psi (4.14 MPa) In contrast significantly less of the seismically resolvable fault geometry (B) is unstable. The area of unstable fault surface for the outcrop-derived geometry would be sufficient to generate seismicity of magnitude M=2.6.

10.3 Geometric Uncertainty

It is at the production-scale where the disparity between seismically resolvable fault geometries and those geometries developed through the processes of fault growth, interaction and linkage becomes most apparent (Chapters 5, 6, 7, 8). Faults, as resolvable in seismic data and subsequently modelled within geocellular grids, do not geometrically resemble faults that can be resolved in the field or in higher resolution data such as DEMs (e.g. figure 10.12). They are almost universally modelled as simple planar structures, a geometric simplification which completely ignores the processes of fault growth (Peacock and Sanderson, 1991; Cartwright et al., 1995; Cowie et al., 2000; Walsh et al., 2003; Childs et al., 2009). Faults are composed of multiple segments which gradually coalesce as a response to strain through a continuous, three dimensional, process of interaction, linkage and further interaction. This process occurs at all scales and hence the associated structures which accommodate fault interaction (i.e. relay zones) are ubiquitous at all scales (e.g. Childs et al., 2009). This process of growth leads to faults being significantly more complex than the planar structures which are typically modelled during hydrocarbon exploration and production. The reasons for this conflict is a matter of resolution: firstly the fine scale complexity of faults is often not imaged within seismic data and secondly, even if it were then the limitations of geocellular modelling would prevent an accurate 3D representation from being constructed and advantageously used. As a result there is a disparity between the 'real' geometry of faults, and the resolvable, modelled geometry. This disparity leads to inaccurate modelling of parameters critical for efficient hydrocarbon reservoir management such as across-fault juxtapositions and fault connectivity (and hence reservoir segmentation and possibly compartmentalisation). Furthermore the petrophysical properties of faults used within reservoir simulators are calculated using algorithms which have a significant geometric component (e.g. SGR, Yielding et al., 1997, Fault TMs, Knai and Knipe, 1998; Manzocchi et al., 1999). Since the resolvable geometry is inaccurate, the absolute output from these algorithms is often erroneous if

treated deterministically, although may still be valid as a locally calibrated proxy for fault-fluid behaviour, at least at the exploration/rift scale (Yielding, 2012).

Results presented in Chapter 8 illustrate the relative importance of fault geometry and fault properties. Correctly modelling (or at least modelling in a way that accounts for) fault geometric complexity is significantly more important than the values of fault transmissibility multipliers for the majority of situations that have been modelled. TMs which have been calculated for seismically resolvable geometries may have limited influence or predictive value since they refer to a spurious fault geometry with incorrect representations of the across fault juxtapositions. The complex nature of 'real' fault geometries leads to displacement partitioning across multiple slip surfaces, with a significantly greater amount of across fault reservoir:reservoir juxtaposition being maintained when compared to seismically resolvable fault geometries (e.g. figure 10.11). This leads to enhanced across-fault communication and flow potential, often irrespective of the fault rock properties. This leads to the observation that the importance of fault rock properties in flow simulation is significantly overstated when compared to geometric uncertainty. Fault rock properties may be relatively unimportant, except in cases where NTG of a reservoir interval is low, with a high shale content, or where thick, continuous shale layers are present (e.g. Childs et al., 2002). This scenario also implies a low quality reservoir, hence also implying that a correct understanding of structural uncertainty becomes increasingly more important as hydrocarbon fields become more marginal and more complex.

Since fault geometric complexity is a function of the processes which drive fault growth and interaction, an understanding of these processes is critical in understanding the relative importance of faults on fluid flow in reservoirs. Although this complexity may not be resolvable it can have a significant impact, hence recognising the disparity between seismically resolvable and realistic fault geometries is critical. Accounting for this complexity is a challenging process, as it cannot currently be modelled deterministically due to gridding and computational limitations. Reconciling what we know the fault structure should be like, with resolvable geometries and the capability to incorporate this within existing modelling frameworks requires the use of methodologies which are proxies for the geometric reality. For example, this may take the form of reducing the modelled fault throw by a certain percentage to account for sub-seismic displacement partitioning, or continuous deformation (Chapter 7). Whilst this is unlikely to represent the real sub-surface architecture, it will allow the maintenance of across-fault juxtapositions leading to a more accurate prediction of the impact of the faults on fluid flow. Similar approaches may include stochastic, or semi-stochastic,

population of displacement minima representing relay zones (Manzocchi et al., 2008), and extending the length of fault tips (Chapters 5 and 6).

As shown in Chapters 5 and 6, extending the faults to include their sub-seismic tips may lead to increased reservoir segmentation and fault connectivity, especially in areas where there is a range in fault orientations. An important distinction to note, however, is that this increased segmentation does not necessarily mean increased compartmentalisation. Fault related reservoir compartmentalisation implies that adjacent fault blocks are not in pressure communication, due to the presence of sealing faults or other impermeable barriers. Segmentation simply implies that faults are connected, with no allusion towards their sealing, or non-sealing nature. This division is often overlooked, with the potential result being that segmented, but non-sealing, fault networks are vilified as compartmentalising, and hence having a negative impact on field development. As the results from Chapter 6 show, this may be a misnomer, with increased fault connectivity often leading to enhanced sweep efficiency and decrease in the volume of produced water (also shown by Manzocchi et al 2008). This segmentation versus compartmentalisation issue is further emphasised by the results from Chapter 8, which highlight the role of fault geometric complexity in reducing the perceived sealing capacity of faults. It could be argued that fault compartmentalisation is only likely in situations where a juxtaposition seal is present, a scenario which, due to geometric complexity (i.e. displacement partitioning) requires the mean fault throw to be greater than the mean reservoir thickness. Even in such situations, the presence of relay zones would potentially lead to enhanced connectivity and hydraulic continuity due to the localised maintenance of across-fault juxtapositions.

10.4 Fault Rock Properties

The majority of the results presented herein have focussed on shale gouge (yielding et al., 1997) as the primary permeability reducing mechanism across faults. This is simply because it is relatively easy to model using standard software, rather than it being a preferred mechanism or proxy. Other mechanisms, or combinations of mechanisms, such as disaggregation, cataclasis, cementation and clay smearing (Fisher and Knipe, 1998) are also capable of reducing fault permeability, leading to pressure compartmentalisation under certain circumstances (Childs et al., 2002). The spatial variability of these processes is however often poorly constrained, and may display significant localisation.

The modelled permeability of fault rock used in production-scale simulations often relies upon deterministically assigning a fault permeability based on laboratory measurements calibrating the estimated clay content (e.g. as defined by the SGR algorithm) against sample permeability

(e.g. Sperrevik et al., 2002). This approach assumes invariance between core-scale and reservoir-scale fault permeability. As seen in Chapters 8 and 9, faults have significant geometric complexity, deviating from a simple planar structure; it is therefore reasonable to assume that there is significant heterogeneity in the lateral distribution of their petrophysical properties. Therefore applying a core-derived permeability will tend to underestimate the bulk permeability of a fault (i.e. overestimate its sealing capacity), whilst not accounting for geometric complexity. At a single point on a fault this approach may be valid, but for the fault as a whole such a deterministic methodology becomes unreliable. A preferred approach, which would account for the effects of geometric and special variability of permeability-reducing processes, would be that of stochastic or probabilistic fault property population (Childs et al., 2007; Manzocchi et al., 2007), coupled with more realistic fault geometries than are currently employed.

At the exploration scale, at least where pressure data is available, the modelled clay content of a fault can be calibrated against the across-fault pressure differential (e.g. Bretan et al., 2003). The derived relationship can then be modified to predict maximum potential column heights for specific SGR values. Since this approach is calibrated against fault-scale, rather than sample-scale variables, it implicitly accounts for geometric and petrophysical heterogeneity of faults, and can hence be viewed as good proxy for fault sealing capacity at the exploration scale (Yielding, 2012).

10.5 Sealing or Non-Sealing?

An issue that has come to light over the course of this project is that of the definition of a sealing fault. Where a juxtaposition seal is present, this is relatively straight forward, with across-fault hydrocarbon leakage prevented by the presence of an adjacent impermeable lithology (excluding the possibility of fault parallel flow). In situations where a juxtaposition seal is not present, the sealing nature of a fault is dependent on the petrophysical properties of the fault rock, and their contrast relative to the host rock adjacent to the fault. Results from Chapters 6, 7 and 8 suggest that for geometrically realistic faults, the petrophysical properties of the fault rock alone are rarely, if ever, sufficient to form a seal over production timescales. Although a pressure differential may develop across a fault, it is acting as a baffle, rather than a barrier (seal) to flow. This pressure differential is often incorrectly assumed to represent a sealing, rather than baffling, fault (Manzocchi et al., 2012). The term sealing is therefore somewhat ambiguous and misleading, inferring as it does an impermeable barrier over geological timescales.

An associated concept is that of the effective transmissibility and effective permeability of a system as a whole (Chapters 4, 8, Freeman et al., 2010). This concept couples the fault and reservoir properties with the development strategy to be employed (e.g. well positioning, expected induced pressure perturbations). It is essentially based upon Darcy's law, and illustrates that for across-fault fluid flow, the absolute fault properties become less important as the reservoir permeability, well-spacing and across-fault pressure differentials increase (e.g. due to varying the production rate of a well). This is due to the fault permeability contributing relatively less to the bulk permeability of the system as a whole. This concept is considered to be under-utilised, however it could significantly improve the efficiency of well placement decisions. As an example, the production rate of a well located adjacent to a low permeability fault will be influenced by the presence of that fault to a greater extent than if the well were placed a greater distance away.

10.6 Conclusions

Initially a number of structural uncertainties pertinent to either the hydrocarbon exploration or production scale were highlighted (table 1.1). Results from the individual chapters has allowed these uncertainties have been ranked as either having a high, medium or low impact (Table 10.1).

	Structural Uncertainty	Impact of Uncertainty	
EXPLORATION	● Linkage Geometry	High	(Chapters 3, 4)
	● Along-Strike Displacement Continuity	High	(Chapters 3, 4)
	● Syn-Rift Reservoir Facies Distribution	High	(Chapter 4)
	● Fault Rock Properties	Low-Medium	(Chapter 4)
PRODUCTION	● Linkage Geometry	Medium	(Chapters 5, 6, 7, 8)
	● Sub-Seismic Fault Tips	Medium	(Chapters 5, 6)
	● Sub-Seismic Fault Complexity	High	(Chapter 8)
	● Juxtaposition Uncertainty	High	(Chapters 7, 8)
	● Fault Rock Properties	Low-Medium	(Chapters 6, 8)
	● Presence of Relay Zones	High	(Chapters 5, 6, 7, 8)
	● Fault Stability	Medium-High	(Chapter 9)

Table 10.1. Summary table highlighting structural uncertainties at either hydrocarbon exploration or production scale. Results from the thesis have allowed the relative impact of these uncertainties to be ranked.

Each Chapter contains a number of conclusions specific to the work present therein. Here the main points are re-iterated.

● Fault activity in the Gulf of Corinth rift has not preceded in a sequential, basin-wards manner as has previously been reported. Although a general basin-wards trend is observed, a more disparate rift history is superimposed onto this.

● Three stages of rifting are observed in the Gulf of Corinth, with an initial distributed stage giving way to localisation of strain onto larger fault-sets. Late stage rifting is observed as angular unconformities within hangingwall syn-rift sediments.

● Synthetic seismic modelling of rift-scale outcrop analogues highlights the uncertainty in fault geometries extrapolated from 2D data. Structurally important features such as relay zones, trap crests and spill points may remain unidentified leading to uncertainty in pore pressure and fault property predictions and calculation of hydrocarbon column heights.

● Using a statistical approach for calculating sub-seismic fault tip length does not account for fault growth processes. Using the local displacement gradient significantly enhances the accuracy of predictions by accounting for the effects of fault interaction.

● The displacement gradient at pairs of overlapping fault tips can be used to estimate the integrity of the intervening relay ramp. High displacement gradients imply high strain, and hence a higher likelihood that a relay ramp is breached.

● The impact of extending fault tip length upon reservoir segmentation is dependent on the range of strikes present within the fault network. Where only parallel to sub-parallel faults are present, increased segmentation is heavily reliant upon the presence of breached relay ramps between overlapping faults.

● Reservoir segmentation is not the same as reservoir compartmentalisation. A segmented fault network only compartmentalises a reservoir where the across-fault juxtapositions and fault rock properties act to restrict across-fault flow significantly over a production timescale.

● Increasing reservoir segmentation, at least for the Penguin C field modelled in Chapter 6, effects oil production to a lesser extent than water production. Earlier onsets of oil production decline for more segmented reservoirs are offset by a lower rate of decline, due to an enhanced sweep pattern, and a lower volume of produced water when compared to less segmented cases.

● The influence of sub-seismic fault tips and relay zones on production increases as fault threshold pressures are increased, with simulation results also increasing in their variability as fault network segmentation is increased. Increased fault threshold pressures also tend to effect water production to a greater extent than oil production.

● The interpretation of fault-relay geometries in seismic data influences the fluid flow behaviour during production. Since relay zones allow hydraulic conductivity to be maintained across a fault set, correctly identifying their presence is crucial although the absolute relay zone geometry has limited impact on how fluid flows across it.

● Decreasing fault throw to account for the distribution of deformation, in the form of multiple slip surfaces or continuous deformation-'drag', can significantly increase the across-fault fluid flux. Not including these sub-seismic geometries may lead to overestimates in the compartmentalising nature of faults.

● Fault geometries identified in seismic data are significantly simplified in comparison to those observed at outcrop. Complex geometries such as displacement partitioning across multiple slip surfaces are hence not incorporated within reservoir models. This leads to the area of across-fault reservoir:reservoir juxtaposition being severely underestimated.

● The disparity in juxtaposition area between seismically resolvable and realistic fault geometries is greatest where the thickness of the reservoir interval is less than the mean fault throw. In this situation seismically resolvable geometries will tend towards the presence of a juxtaposition seal, whereas in reality geometric complexities such as displacement partitioning will lead to the maintenance of across-fault juxtapositions.

● Where realistic (i.e. larger) areas of across-fault juxtaposition are modelled, varying the fault transmissibility multipliers has less impact upon across-fault hydrocarbon flux. For cases where a very small amount of across-fault juxtaposition area is modelled, fault TMs begin to exert an increased influence on across-fault flow.

● The differences in across-fault flow of hydrocarbons between seismically resolvable and realistic fault geometries are magnified as Kv:Kh and Net:gross decrease. This is due to the lower vertical connectivity of stratigraphic layers across faults for the simple, planar, seismically resolvable fault geometries.

● In production scale reservoir models, the simplistic fault geometries resolvable in seismic data lead to the importance of fault rock properties being overstated. Fault geometry is significantly more influential on the across-fault flow behaviour of hydrocarbons.

● Across-fault juxtaposition of reservoir facies is the primary control on the impact of faults during hydrocarbon production.

10.7 Further Work

Through the course of conducting and documenting the work which contributes to this thesis a number of ideas have been formulated which time constraints have prevented from being validated or refuted. Here, a number of these ideas for future work are briefly outlined.

Seismic forward modelling is relatively under-represented in the scientific literature, with the majority of studies relating to qualitative modelling of outcrop analogues. By adopting a multidisciplinary approach a more quantitative result can be obtained, as is the case in Chapter 8. Significant aspects of geophysics, petrophysics and reservoir engineering are required in addition to geological knowledge, although integrating these aspects opens the door to many possible applications.

CO_2 sequestration is a topic currently under scientific review at numerous institutions. Predicting and monitoring the migration of injected CO_2 is important to ensure that the integrity of storage sites is maintained (e.g. Tueckmantel et al., 2012). By coupling reservoir modelling with 4D seismic forward modelling, the flow of CO_2 from injection wells could be predicted, allowing for optimisation of well positioning. This would allow minimisation of the occurrence of pressure build-ups, which could compromise top- or fault-seals.

Seismic forward modelling can also be used as a tool for quantifying the contribution of sub-seismic scale faults to regional strain. Using high resolution data, such as the DEM from the Afar rift used in Chapters 8 and 9, allows the identification and incorporation into geological models of small-scale faults. By comparing the structurally restored bed-length of outcrop and seismically forward modelled geometries, the amount of sub-seismic strain could be quantified.

Recent work has highlighted the potential role of fluid injection in triggering seismicity (Davies et al., 2013; Keranen et al., 2013). This has been explored to some extent in Chapter 9. Forward modelling the injection of gas or water in conventional and unconventional reservoirs would allow 4D monitoring of the predicted pressure perturbations. In turn, the modification of the effective stress around faults would allow quantitative prediction of the likelihood of reactivation. This methodology could possibly also be adapted to predict subsidence in hydrocarbon fields where no artificial pressure support mechanisms are used.

Work presented in Chapter 8, as well as recent discussions regarding fault structure and the impact of faults on hydrocarbon flow (Manzocchi et al., 2010; Childs et al., 2012; Manzocchi et al., 2012), have opened a dialogue questioning the notion of faults being able to form a seal over production time-scales. It may be possible to develop a methodology to predict the

sealing behaviour of a fault with a realistic (rather than seismically resolvable) geometry, over longer timescales, such as those relevant to hydrocarbon exploration. By coupling migration models with long run-time fluid flow simulations the leakage rate across faults may be modelled.

The impact on oil recovery of extending fault tips is explored in Chapter 6, with results indicating that increasing tip length has a greater impact on water, rather than oil flow. One explanation discussed was that of the effect of the saturation and relative permeability of the two phases impacting their respective mobility, and hence flow velocity. This is an aspect which requires further investigation.

Simulations of hydrocarbon flow across realistic fault geometries (Chapter 8) have highlighted the role of the effective permeability of a system as a whole. One variable in the effective permeability is the path-length between injection and production wells. The impact of this factor could be highlighted by performing simulations with geological grids with a range of lengths and populated with identical petrophysical properties. Although this has been attempted, time constraints prevented a suitable approach for accounting for the effects of increased pore volume associated with increasing the grid dimensions.

The piece of additional work with potentially the highest impact would involve generating high resolution geocellular models of multiple (rather than single) detailed faults from the Afar DEM dataset (Chapters 8 and 9). This could be initiated as a full-field simulation model incorporating realistic fault geometries. Seismically forward modelling this grid, and re-running simulations with the seismically resolvable fault geometries would allow the impact of the disparity in fault geometries to be quantified at the field scale. Furthermore, the seismically resolvable geometries could be modified using approaches such as probabilistic relay zone population, fault tip extension and throw modification. These are approaches that can be applied to try attempt to represent detailed fault architectures within the limitations of geological and simulation software. By simulating these modified models, the impact, and effectiveness, of these different approaches could be quantified by performing a history match against the original, realistic grid. This would allow the most appropriate methodologies for accounting for fault geometric complexity to be implemented in order to enhance the predictive nature of flow simulations and aid hydrocarbon recovery.

Reference List

ACKERMANN, R. V. & SCHLISCHE, R. W. 1997. Anticlustering of small normal faults around larger faults. *Geology,* 25, 1127-1130.

ADAMS, E. W., GRÉLAUD, C., PAL, M., CSOMA, A. É., AL JA'AIDI, O. S. & HINAI, R. A. 2011. Improving reservoir models of Cretaceous carbonates with digital outcrop modelling (Jabal Madmar, Oman): static modelling and simulating clinoforms. *Petroleum Geoscience,* 17, 309-332.

AHMED, T. 2010. *Reservoir Engineering Handbook (4th edition)*, Gulf Professional Publishing.

AL-HINAI, S. M., FISHER, Q. J., GRATTONI, C. A., HARRIS, S. D. & AL-BUSAFI, B. 2007. Recent Advances in the Understanding and Incorporation of the Multiphase Fluid Flow Properties of Fault Rocks into Production Simulation Models. *SPE Middle East Oil and Gas Show and Conference*.

ALAEI, B. & PETERSEN, S. A. 2007. Geological modelling and finite difference forward realization of a regional section from the Zagros fold-and-thrust belt. *Petroleum Geoscience,* 13, 241-251.

ALLAN, U., S. 1989. Model for hydrocarbon migration and entrapment within faulted structures. *AAPG Bulletin,* 73, 803-811.

APLIN, A. C. & MACQUAKER, J. H. S. 2011. Mudstone diversity: Origin and implications for source, seal, and reservoir properties in petroleum systems. *AAPG Bulletin,* 95, 2031-2059.

ARMIJO, R., MEYER, B., HUBERT, A. L. & BARKA, A. 1999. Westward propagation of the North Anatolian fault into the northern Aegean: Timing and kinematics. *Geology,* 27, 267-270.

ARMIJO, R., MEYER, B., KING, G. C. P., RIGO, A. & PAPANASTASSIOU, D. 1996. Quaternary evolution of the Corinth Rift and its implications for the Late Cenozoic evolution of the Aegean. *Geophysical Journal International,* 126, 11-53.

ARMITAGE, D. A. & STRIGHT, L. 2010. Modeling and interpreting the seismic-reflection expression of sandstone in an ancient mass-transport deposit dominated deep-water slope environment. *Marine and Petroleum Geology,* 27, 1-12.

ARMITAGE, P. J., FAULKNER, D. R., WORDEN, R. H., APLIN, A. C., BUTCHER, A. R. & ILIFFE, J. 2011. Experimental measurement of, and controls on, permeability and permeability anisotropy of caprocks from the CO2 storage project at the Krechba Field, Algeria. *Journal of Geophysical Research: Solid Earth,* 116, B12208.

ATHMER, W., GROENENBERG, R. M., LUTHI, S. M., DONSELAAR, M. E., SOKOUTIS, D. & WILLINGSHOFER, E. 2010. Relay ramps as pathways for turbidity currents: a study combining analogue sandbox experiments and numerical flow simulations. *Sedimentology,* 57, 806-823.

ATHMER, W. & LUTHI, S. M. 2011. The effect of relay ramps on sediment routes and deposition: A review. *Sedimentary Geology,* 242, 1-17.

AYDIN, A. & SCHULTZ, R. A. 1990. Effect of mechanical interaction on the development of strike-slip faults with echelon patterns. *Journal of Structural Geology,* 12, 123-129.

BACKERT, N., FORD, M. & MALARTRE, F. 2010. Architecture and sedimentology of the Kerinitis Gilbert-type fan delta, Corinth Rift, Greece. *Sedimentology,* 57, 543-586.

BAILEY, W. R., MANZOCCHI, T., WALSH, J. J., KEOGH, K., HODGETTS, D., RIPPON, J., NELL, P. A. R., FLINT, S. & STRAND, J. A. 2002. The effect of faults on the 3D connectivity of

reservoir bodies: a case study from the East Pennine Coalfield, UK. *Petroleum Geoscience,* 8, 263-277.

BAILEY, W. R., WALSH, J. J. & MANZOCCHI, T. 2005. Fault populations, strain distribution and basement fault reactivation in the East Pennines Coalfield, UK. *Journal of Structural Geology,* 27, 913-928.

BAKKE, K., GJELBERG, J. & AGERLIN PETERSEN, S. 2008. Compound seismic modelling of the Ainsa II turbidite system, Spain: Application to deep-water channel systems offshore Angola. *Marine and Petroleum Geology,* 25, 1058-1073.

BARBERI, F. & VARET, J. 1977. Volcanism of Afar: Small-scale plate tectonics implications. *Geological Society of America Bulletin,* 88, 1251-1266.

BARNETT, J. A. M., MORTIMER, J., RIPPON, J. H., WALSH, J. J. & WATTERSON, J. 1987. Displacement geometry in the volume containing a single normal fault. *AAPG Bulletin,* 71, 925-937.

BARR, D. 1987. Lithospheric stretching, detached normal faulting and footwall uplift. *Geological Society, London, Special Publications,* 28, 75-94.

BATYCKY, R.P., THIELE, M.R., COATS, K.H., GRINDHEIM, A., PONTING, D., KILLOUGH, J.E., SETTARI, T., THOMAS, K.L., WALLIS, J., WATTS, J.W. & WHITSON C.H. 2007. Reservoir Engineering and Petrophysics. 17 Reservoir Simulation. V-1399. In: Petroleum Engineering Handbook, Volume V, Holstein, E.D. (ed). 2007. Society of Petroleum Engineers.

BELL, R. E., MCNEILL, L. C., BULL, J. M. & HENSTOCK, T. J. 2008. Evolution of the offshore western Gulf of Corinth. *Geological Society of America Bulletin,* 120, 156-178.

BELL, R. E., MCNEILL, L. C., BULL, J. M., HENSTOCK, T. J., COLLIER, R. E. L. & LEEDER, M. R 2009. Fault architecture, basin structure and evolution of the Gulf of Corinth Rift, central Greece. *Basin Research,* 21, 824-855.

BELL, R. E., MCNEILL, L. C., HENSTOCK, T. J. & BULL, J. M. 2011. Comparing extension on multiple time and depth scales in the Corinth Rift, Central Greece. *Geophysical Journal International,* 186, 463-470.

BENSE, V. F. & VAN BALEN, R. 2004. The effect of fault relay and clay smearing on groundwater flow patterns in the Lower Rhine Embayment. *Basin Research,* 16, 397-411.

BERNARD, P., BRIOLE, P., MEYER, B., LYON-CAEN, H., GOMEZ, J.-M., TIBERI, C., BERGE, C., CATTIN, R., HATZFELD, D., LACHET, C., LEBRUN, B,. DESCHAMPS, A., COURBOULEX, F., LARROQUE, C., RIGO, A., MASSONNET, D., PAPADIMITRIOU, P., KASSARAS, J., DIAGOURTAS, D., MAKROPOULOS, K., VEIS, G., PAPAZISI, E., MITSAKAKI, C., KARAKOSTAS, V., PAPADIMITRIOU, E., PAPANASTASSIOU, D., CHOULIARAS, M., & STAVRAKAKIS, G. 1997. The *M*s=6.2, June 15, 1995 Aigion earthquake (Greece): evidence for low angle normal faulting in the Corinth rift. *Journal of Seismology,* 1, 131-150.

BJØRLYKKE, K. 1999. Principal aspects of compaction and fluid flow in mudstones. *Geological Society, London, Special Publications,* 158, 73-78.

BOHNENSTIEHL, D. R. & KLEINROCK, M. C. 1999. Faulting and fault scaling on the median valley floor of the trans-Atlantic geotraverse (TAG) segment, ~26°N on the Mid-Atlantic Ridge. *J. Geophys. Res.,* 104, 29351-29364.

BOHNENSTIEHL, D. R. & KLEINROCK, M. C. 2000. Evidence for spreading-rate dependence in the displacement-length ratios of abyssal hill faults at mid-ocean ridges. *Geology,* 28, 395-398.

BOLTON, A. J., MALTMAN, A. J. & CLENNELL, M. B. 1998. The importance of overpressure timing and permeability evolution in fine-grained sediments undergoing shear. *Journal of Structural Geology,* 20, 1013-1022.

BOND, C. E., LUNN, R. J., SHIPTON, Z. K. & LUNN, A. D. 2012. What makes an expert effective at interpreting seismic images? *Geology,* 40, 75-78.

BOUVIER, J. D., KAARS-SIJPESTEIJN, C. H., KLUESNER, D. F., ONYEJEKWE, C. C., AND VAN DER PAL, R. C. 1989. Three-dimensional seismic interpretation and fault sealing investigations, Nun River field, Nigeria: AAPG Bulletin, v. 73, p. 1397–1414.

BREHM, J. A. 2003. The North Brae and Beinn Fields, Block 16/7a, UK North Sea. *Geological Society, London, Memoirs,* 20, 199-209.

BRETAN, P., YIELDING, G. & JONES, H. 2003. Using calibrated shale gouge ratio to estimate hydrocarbon column heights. *AAPG Bulletin,* 87, 397-413.

BRIOLE, P., RIGO, A., LYON-CAEN, H., RUEGG, J. C., PAPAZISSI, K., MITSAKAKI, C., BALODIMOU, A., VEIS, G., HATZFELD, D. & DESCHAMPS, A. 2000. Active deformation of the Corinth rift, Greece: Results from repeated Global Positioning System surveys between 1990 and 1995. *Journal of Geophysical Research: Solid Earth,* 105, 25605-25625.

BROWN, A. 2003. Capillary effects on fault-fill sealing. *AAPG Bulletin,* 87, 381-395.

BRYANT, I., CARR, D., CIRILLI, P., DRINKWATER, N., MCCORMICK, D., TILKE, P. & THURMOND, J. 2000. Use of 3D digital analogues as templates in reservoir modelling. *Petroleum Geoscience,* 6, 195-201.

BÜRGMANN, R., POLLARD, D. D. & MARTEL, S. J. 1994. Slip distributions on faults: effects of stress gradients, inelastic deformation, heterogeneous host-rock stiffness, and fault interaction. *Journal of Structural Geology,* 16, 1675-1690.

CARTWRIGHT, J. A., MANSFIELD, C. & TRUDGILL, B. 1996. The growth of normal faults by segment linkage. *Geological Society, London, Special Publications,* 99, 163-177.

CARTWRIGHT, J. A., TRUDGILL, B. D. & MANSFIELD, C. S. 1995. Fault growth by segment linkage: an explanation for scatter in maximum displacement and trace length data from the Canyonlands Grabens of SE Utah. *Journal of Structural Geology,* 17, 1319-1326.

CAUSSE, C., MORETTI, I., ESCHARD, R., MICARELLI, L., GHALEB, B. & FRANK, N. 2004. Kinematics of the Corinth Gulf inferred from calcite dating and syntectonic sedimentary characteristics. *Comptes Rendus Geosciences,* 336, 281-290.

CHILDS, C., MANZOCCHI, T., NELL, P. A. R., WALSH, J. J., STRAND, J. A., HEATH, A. E. & LYGREN, T. H. 2002. Geological implications of a large pressure difference across a small fault in the Viking Graben. *In:* ANDREAS, G. K. & ROBERT, H. (eds.) *Norwegian Petroleum Society Special Publications.* Elsevier.

CHILDS, C., MANZOCCHI, T., WALSH, J. J., BONSON, C. G., NICOL, A. & SCHÖPFER, M. P. J. 2009. A geometric model of fault zone and fault rock thickness variations. *Journal of Structural Geology,* 31, 117-127.

CHILDS, C., WALSH, J. J., MANZOCCHI, T., STRAND, J., NICOL, A., TOMASSO, M., SCHOPFER, M. P. J. & APLIN, A. C. 2007. Definition of a fault permeability predictor from outcrop studies of a faulted turbidite sequence, Taranaki, New Zealand. *Geological Society, London, Special Publications,* 292, 235-258.

CHILDS, C., WALSH, J. J. & WATTERSON, J. 1997. Complexity in fault zone structure and implications for seal prediction. *In:* MØLLER-PEDERSEN, P. & KOESTLER, A. G. (eds.) *Hydrocarbon Seals: Importance for Exploration and Production.*

CHILDS, C., WATTERSON, J. & WALSH, J. J. 1995. Fault overlap zones within developing normal fault systems. *Journal of the Geological Society,* 152, 535-549.

CHILDS, C., MANZOCCHI, T., WALSH, J.J. & SCHÖPFER M.P.J. Fault core/damage zone; an unhelpful description of fault zone structure? Fault and Top Seals, EAGE Conference, Montpellier, October 2012.

CLARKE, P. J., DAVIES, R. R., ENGLAND, P. C., PARSONS, B., BILLIRIS, H., PARADISSIS, D., VEIS, G., CROSS, P. A., DENYS, P. H., ASHKENAZI, V., BINGLEY, R., KAHLE, H. G., MULLER, M. V. & BRIOLE, P. 1998. Crustal strain in central Greece from repeated GPS measurements in the interval 1989–1997. *Geophysical Journal International,* 135, 195-214.

CLAYTON, C., J. & HAY, S., J. 1994. Gas migration mechanisms from accumulation to surface. *Bulletin of the Geological Society of Denmark,* 41, 12-23.

COLLIER, R. E. L. 1990. Eustatic and tectonic controls upon Quaternary coastal sedimentation in the Corinth Basin, Greece. *Journal of the Geological Society,* 147, 301-314.

COLLIER, R. E. L. & DART, C. J. 1991. Neogene to Quaternary rifting, sedimentation and uplift in the Corinth Basin,Greece. *Journal of the Geological Society,* 148, 1049-1065.

COLLIER, R. E. L. & GAWTHORPE, R. L. 1995. Neotectonics, drainage and sedimentation in central Greece: insights into coastal reservoir geometries in syn-rift sequences. *Geological Society, London, Special Publications,* 80, 165-181.

COLLIER, R. E. L. & JONES, G. 2004. Rift Sequences of the Southern Margin of the Gulf of Corinth (Greece) as Exploration / Production Analogues. *AAPG International Conference Extended Abstract, Barcelona, Spain, Sept 2003.*

COWIE, P. A. 1998. A healing-reloading feedback control on the growth rate of seismogenic faults. *Journal of Structural Geology,* 20, 1075-1087.

COWIE, P. A., GUPTA, S. & DAWERS, N. H. 2000. Implications of fault array evolution for synrift depocentre development: insights from a numerical fault growth model. *Basin Research,* 12, 241-261.

COWIE, P. A., MALINVERNO, A., RYAN, W. B. F. & EDWARDS, M. H. 1994. Quantitative fault studies on the East Pacific Rise: A comparison of sonar imaging techniques. *J. Geophys. Res.,* 99, 15205-15218.

COWIE, P. A. & SCHOLZ, C. H. 1992a. Displacement-length scaling relationship for faults: data synthesis and discussion. *Journal of Structural Geology,* 14, 1149-1156.

COWIE, P. A. & SCHOLZ, C. H. 1992b. Physical explanation for the displacement-length relationship of faults using a post-yield fracture mechanics model. *Journal of Structural Geology,* 14, 1133-1148.

COWIE, P. A. & SHIPTON, Z. K. 1998. Fault tip displacement gradients and process zone dimensions. *Journal of Structural Geology,* 20, 983-997.

DART, C. J., COLLIER, R. E. L., GAWTHORPE, R. L., KELLER, J. V. A. & NICHOLS, G. 1994. Sequence stratigraphy of (?)Pliocene-Quaternary synrift, Gilbert-type fan deltas, northern Peloponnesos, Greece. *Marine and Petroleum Geology,* 11, 545-560.

DAVIES, R., ENGLAND, P., PARSONS, B., BILLIRIS, H., PARADISSIS, D. & VEIS, G. 1997a. Geodetic strain of Greece in the interval 1892–1992. *Journal of Geophysical Research: Solid Earth,* 102, 24571-24588.

DAVIES, R. K., CRAWFORD, M., DULA, W. F., COLE, M. J. & DORN, G. A. 1997b. Outcrop interpretation of seismic-scale normal faults in southern Oregon; description of

structural styles and evaluation of subsurface interpretation methods. *The Leading Edge,* 16, 1135-1141.

DAWERS, N. H., ANDERS, M. H. & SCHOLZ, C. H. 1993. Growth of normal faults: Displacement-length scaling. *Geology,* 21, 1107-1110.

DAWERS, N. H. & UNDERHILL, J. R. 2000. The Role of Fault Interaction and Linkage in Controlling Synrift Stratigraphic Sequences: Late Jurassic, Statfjord East Area, Northern North Sea. *AAPG Bulletin,* 84, 45-64.

DE MARTINI, P. M., PANTOSTI, D., PALYVOS, N., LEMEILLE, F., MCNEILL, L. & COLLIER, R. 2004. Slip rates of the Aigion and Eliki Faults from uplifted marine terraces, Corinth Gulf, Greece. *Comptes Rendus Geosciences,* 336, 325-334.

DE PAOLA, N., HOLDSWORTH, R. E. & MCCAFFREY, K. J. W. 2005. The influence of lithology and pre-existing structures on reservoir-scale faulting patterns in transtensional rift zones. *Journal of the Geological Society,* 162, 471-480.

DE PATER, C. J. B., S. 2011. Geomechanical Study of Bowland Shale Seismicity. UK.

DEGNAN, P. J. & ROBERTSON, A. H. F. 1998. Mesozoic-early Tertiary passive margin evolution of the Pindos ocean (NW Peloponnese, Greece). *Sedimentary Geology,* 117, 33-70.

DENNIS, H., BERGMO, P. & HOLT, T. 2005. Tilted oil–water contacts: modelling the effects of aquifer heterogeneity. *Geological Society, London, Petroleum Geology Conference series,* 6, 145-158.

DEWHURST, D. N. & JONES, R. M. 2002. Geomechanical, Microstructural, and Petrophysical Evolution in Experimentally Reactivated Cataclasites: Applications to Fault Seal Prediction. *AAPG Bulletin,* 86, 1383-1405.

DOMÍNGUEZ, R. 2007. Structural evolution of the Penguins Cluster, UK northern North Sea. *Geological Society, London, Special Publications,* 292, 25-48.

DONATH, F. A. 1961. EXPERIMENTAL STUDY OF SHEAR FAILURE IN ANISOTROPIC ROCKS. *Geological Society of America Bulletin,* 72, 985-989.

DORE, A. G., LUNDIN, E. R., FICHLER, C. & OLESON, O. 1997. Patterns of basement structure and reactivation along the NE Atlantic margin. *Journal of the Geological Society,* 154, 85-92.

The Corinth-Patras rift as the initial stage of continental fragmentation behind an active island arc (Greece), 1988. Directed by DOUTSOS, T., KONTOPOULOS, N. & POULIMENOS, G.: Blackwell Publishing Ltd.

DOUTSOS, T. & POULIMENOS, G. 1992. Geometry and kinematics of active faults and their seismotectonic significance in the western Corinth-Patras rift (Greece). *Journal of Structural Geology,* 14, 689-699.

EBINGER, C. J., JACKSON, J. A., FOSTER, A. N., HAYWARD, N. J., MCKENZIE, D., KUSZNIR, N., LOUDEN, K. E., WATTS, A. B., MENZIES, M. & ROBERTS, A. 1999. Extensional Basin Geometry and the Elastic Lithosphere [and Discussion]. *Philosophical Transactions: Mathematical, Physical and Engineering Sciences,* 357, 741-765.

EBNER, M., KOEHN, D., TOUSSAINT, R., RENARD, F. & SCHMITTBUHL, J. 2009. Stress sensitivity of stylolite morphology. *Earth and Planetary Science Letters,* 277, 394-398.

EHRENBERG, S. N. & NADEAU, P. H. 2005. Sandstone vs. carbonate petroleum reservoirs: A global perspective on porosity-depth and porosity-permeability relationships. *AAPG Bulletin,* 89, 435-445.

ENGE, H. D., BUCKLEY, S. J., ROTEVATN, A. & HOWELL, J. A. 2007. From outcrop to reservoir simulation model: Workflow and procedures. *Geosphere,* 3, 469-490.

FALIVENE, O., ARBUÉS, P., LEDO, J., BENJUMEA, B., MUÑOZ, J. A., FERNÁNDEZ, O. & MARTÍNEZ, S. 2010. Synthetic seismic models from outcrop-derived reservoir-scale three-dimensional facies models: The Eocene Ainsa turbidite system (southern Pyrenees). *AAPG Bulletin,* 94, 317-343.

FAUPL, P., PAVLOPOULOS, A. & MIGIROS, G. 2007. Chapter 30 Provenance of Flysch Sediments and the Palaeogene-Early Miocene Geodynamic Evolution of the Hellenides: A Contribution from Heavy Mineral Investigations. *In:* MARIA, A. M. & DAVID, T. W. (eds.) *Developments in Sedimentology.* Elsevier.

FERRILL, D. A. & MORRIS, A. P. 2001. Displacement gradient and deformation in normal fault systems. *Journal of Structural Geology,* 23, 619-638.

FERRILL, D. A. & MORRIS, A. P. 2008. Fault zone deformation controlled by carbonate mechanical stratigraphy, Balcones fault system, Texas. *AAPG Bulletin,* 92, 359-380.

FISHER, Q. J., HARRIS, S. D., MCALLISTER, E., KNIPE, R. J. & BOLTON, A. J. 2001. Hydrocarbon flow across faults by capillary leakage revisited. *Marine and Petroleum Geology,* 18, 251-257.

FISHER, Q. J. & KNIPE, R. J. 1998. Fault sealing processes in siliciclastic sediments. *Geological Society, London, Special Publications,* 147, 117-134.

FISHER, Q. J., KNIPE, R. J. & WORDEN, R. 2000. The microstructure of deformed and undeformed sandstones from the North Sea: its implications for the origin of quartz cement. *In:* MORAD, S. & WORDEN, R. (eds) *Quartz Cement. Origin and Effects on Hydrocarbon Reservoirs.* International Association of Sedimentology, Special Publication.

FLETCHER, K. J. 2003. The South Brae Field, Blocks 16/07a, 16/07b, UK North Sea. *Geological Society, London, Memoirs,* 20, 211-221.

FLETCHER, R. C. & POLLARD, D. D. 1981. Anticrack model for pressure solution surfaces. *Geology,* 9, 419-424.

FLOTTÉ, N., PLAGNES, V., SOREL, D. & BENEDICTO, A. 2001. Attempt to date Pleistocene normal faults of the Corinth Patras Rift (Greece) by U/Th Method, and tectonic implications. *Geophys. Res. Lett.,* 28, 3769-3772.

FORD, M., LE CARLIER DE VESLUD, C. & BOURGEOIS, O. 2007. Kinematic and geometric analysis of fault-related folds in a rift setting: The Dannemarie basin, Upper Rhine Graben, France. *Journal of Structural Geology,* 29, 1811-1830.

FORD, M., ROHAIS, S., WILLIAMS, E. A., BOURLANGE, S., JOUSSELIN, D., BACKERT, N. & MALARTRE, F. 2012. Tectono-sedimentary evolution of the western Corinth rift (Central Greece). *Basin Research*, n/a-n/a.

FORD, M., ROHAIS, S., WILLIAMS, E. A., BOURLANGE, S., JOUSSELIN, D., BACKERT, N. & MALARTRE, F. 2013. Tectono-sedimentary evolution of the western Corinth rift (Central Greece). *Basin Research,* 25, 3-25.

FOSSEN, H. & HESTHAMMER, J. 1997. Geometric analysis and scaling relations of deformation bands in porous sandstone. *Journal of Structural Geology,* 19, 1479-1493.

FOSSEN, H., SCHULTZ, R. A., RUNDHOVDE, E., ROTEVATN, A. & BUCKLEY, S. J. 2010. Fault linkage and graben stepovers in the Canyonlands (Utah) and the North Sea Viking Graben, with implications for hydrocarbon migration and accumulation. *AAPG Bulletin,* 94, 597-613.

FRANKOWICZ, E. & MCCLAY, K. R. 2010. Extensional fault segmentation and linkages, Bonaparte Basin, outer North West Shelf, Australia. *AAPG Bulletin,* 94, 977-1010.

FREEMAN, S. R., HARRIS, S. D. & KNIPE, R. J. 2008. Fault seal mapping – incorporating geometric and property uncertainty. *Geological Society, London, Special Publications,* 309, 5-38.

FREEMAN, S. R., HARRIS, S. D. & KNIPE, R. J. 2010. Cross-fault sealing, baffling and fluid flow in 3D geological models: tools for analysis, visualization and interpretation. *Geological Society, London, Special Publications,* 347, 257-282.

FROHLICH, C., HAYWARD, C., STUMP, B. & POTTER, E. 2011. The Dallas–Fort Worth Earthquake Sequence: October 2008 through May 2009. *Bulletin of the Seismological Society of America,* 101, 327-340.

FULLJAMES, J. R., L. J. J. ZIJERVELD, R. C. M. W. FRANSSEN, G. M. INGRAM, AND P. D. RICHARD. 1996. Fault seal processes, *in* Norwegian Petroleum Society, eds., Hydrocarbon seals—importance for exploration and production (conference abstracts): Oslo, Norwegian Petroleum Society, p. 5.

GADALLAH, M. R. & FISHER, R. L. 2004. *Applied Seismology: A Comprehensive Guide to Seismic Theory and Application,* Tulsa, OK, USA, Pennwell Books.

GASSMANN, F. 1951. On the Elasticity of Porous Media. *Vierteljahrsschrift der Naturforschenden Gesellschaft in Zurich,* 96, 1-23.

GAUTHIER, B. D. M. & LAKE, S. D. 1993. Probabilistic modeling of faults below the limit of seismic resolution in Pelican Field, North Sea, offshore United Kingdom. *AAPG Bulletin,* 77, 761-777.

GAWTHORPE, R. L., FRASER, A. J. & COLLIER, R. E. L. 1994. SEQUENCE STRATIGRAPHY IN ACTIVE EXTENSIONAL BASINS - IMPLICATIONS FOR THE INTERPRETATION OF ANCIENT BASIN-FILLS. *Marine and Petroleum Geology,* 11, 642-658.

GAWTHORPE, R. L. & HURST, J. M. 1993. Transfer zones in extensional basins: their structural style and influence on drainage development and stratigraphy. *Journal of the Geological Society,* 150, 1137-1152.

GHISETTI, F. & VEZZANI, L. 2004. Plio-Pleistocene sedimentation and fault segmentation in the Gulf of Corinth (Greece) controlled by inherited structural fabric. *Comptes Rendus Geosciences,* 336, 243-249.

GHISETTI, F. & VEZZANI, L. 2005. Inherited structural controls on normal fault architecture in the Gulf of Corinth (Greece). *Tectonics,* 24, TC4016.

GJØYSTDAL, H., DROTTNING, Å., LECOMTE, I. & BRANSTON, M. 2007. Advances in quantitative model-assisted seismic interpretation. *First Break,* 25, 95-102.

GOLDSWORTHY, M. & JACKSON, J. 2001. Migration of activity within normal fault systems: examples from the Quaternary of mainland Greece. *Journal of Structural Geology,* 23, 489-506.

GRAS, R. & THUSU, B. 1998. Trap architecture of the Early Cretaceous Sarir Sandstone in the eastern Sirt Basin, Libya. *Geological Society, London, Special Publications,* 132, 317-334.

GREEN, C. A. S., PETER; BAPTIE, BRIAN J. 2012. Preese Hall Shale Gas Fracturing: Review and Recommendations for Induced Seismic Mitigation. *In:* CHANGE, D. O. E. A. C. (ed.). UK.

GROSS, M. R., GUTIÉRREZ-ALONSO, G., BAI, T., WACKER, M. A., COLLINSWORTH, K. B. & BEHL, R. J. 1997. Influence of mechanical stratigraphy and kinematics on fault scaling relations. *Journal of Structural Geology,* 19, 171-183.

GUERRIERO, V., VITALE, S., CIARCIA, S. & MAZZOLI, S. 2011. Improved statistical multi-scale analysis of fractured reservoir analogues. *Tectonophysics,* 504, 14-24.

GUPTA, UNDERHILL, SHARP & GAWTHORPE 1999. Role of fault interactions in controlling synrift sediment dispersal patterns: Miocene, Abu Alaqa Group, Suez Rift, Sinai, Egypt. *Basin Research,* 11, 167-189.

GUPTA, A. & SCHOLZ, C. H. 2000. A model of normal fault interaction based on observations and theory. *Journal of Structural Geology,* 22, 865-879.

GUPTA, S., COWIE, P. A., DAWERS, N. H. & UNDERHILL, J. R. 1998. A mechanism to explain rift-basin subsidence and stratigraphic patterns through fault-array evolution. *Geology,* 26, 595-598.

HANKS, T. C. & KANAMORI, H. 1979. A Moment Magnitude Scale. *J. Geophys. Res.,* 84, 2348-2350.

HAYWARD, N. J. & EBINGER, C. J. 1996. Variations in the along-axis segmentation of the Afar Rift system. *Tectonics,* 15, 244-257.

HEALY, J. H., RUBEY, W. W., GRIGGS, D. T. & RALEIGH, C. B. 1968. The Denver EarthquakeS. *Science,* 161, 1301-1310.

HILLIS, R. R. 2001. Coupled changes in pore pressure and stress in oilfields and sedimentary basins. Petroleum Geoscience, 7, 419-425.

HODGETTS, D., DRINKWATER, N. J., HODGSON, J., KAVANAGH, J., FLINT, S. S., KEOGH, K. J. & HOWELL, J. A. 2004. Three-dimensional geological models from outcrop data using digital data collection techniques: an example from the Tanqua Karoo depocentre, South Africa. *Geological Society, London, Special Publications,* 239, 57-75.

HODGETTS, D. & HOWELL, J. A. 2000. Synthetic seismic modelling of a large-scale geological cross-section from the Book Cliffs, Utah, USA. *Petroleum Geoscience,* 6, 221-229.

HORSRUD, P. 2001. Estimating mechanical properties of shale from empirical correlations. *SPE Drilling and Completion,* 16, 68-73.

HORTON, S. 2012. Disposal of hydrofracking waste water fluid by injection into subsurface aquifers triggers earthquake swarm in Central Arkansas with potential for damaging earthquake. *Seismological Research Letters* 83, no. 2: 250–260.

HOSHINO, K. 1972. *Mechanical Properties of Japanese Tertiary Sedimentary Rocks Under High Confining Pressures*, Geological Survey of Japan.

HOWARTH, R. W., INGRAFFEA, A. & ENGELDER, T. 2011. Natural gas: Should fracking stop? *Nature,* 477, 271-275.

HOWELL, J. A., SKORSTAD, A., MACDONALD, A., FORDHAM, A., FLINT, S., FJELLVOLL, B. & MANZOCCHI, T. 2008. Sedimentological parameterization of shallow-marine reservoirs. *Petroleum Geoscience,* 14, 17-34.

HUGGINS, P., WATTERSON, J., WALSH, J. J. & CHILDS, C. 1995. Relay zone geometry and displacement transfer between normal faults recorded in coal-mine plans. *Journal of Structural Geology,* 17, 1741-1755.

HUS, R., DE BATIST, M., KLERKX, J. & MATTON, C. 2006. Fault linkage in continental rifts: structure and evolution of a large relay ramp in Zavarotny; Lake Baikal (Russia). *Journal of Structural Geology,* 28, 1338-1351.

IMBER, J., TUCKWELL, G. W., CHILDS, C., WALSH, J. J., MANZOCCHI, T., HEATH, A. E., BONSON, C. G. & STRAND, J. 2004. Three-dimensional distinct element modelling of relay growth and breaching along normal faults. *Journal of Structural Geology,* 26, 1897-1911.

INGRAM, G. M. & URAI, J. L. 1999. Top-seal leakage through faults and fractures: the role of mudrock properties. *Geological Society, London, Special Publications,* 158, 125-135.

JACKSON, C. A. L., GAWTHORPE, R. L. & SHARP, I. R. 2006. Style and sequence of deformation during extensional fault-propagation folding: examples from the Hammam Faraun and El-Qaa fault blocks, Suez Rift, Egypt. *Journal of Structural Geology,* 28, 519-535.

JACKSON, J. 1999. Fault death: a perspective from actively deforming regions. *Journal of Structural Geology,* 21, 1003-1010.

JACKSON, J. & MCKENZIE, D. 1983. The geometrical evolution of normal fault systems. *Journal of Structural Geology,* 5, 471-482.

JACKSON, J. & MCKENZIE, D. 1988. The relationship between plate motions and seismic moment tensors, and the rates of active deformation in the Mediterranean and Middle East. *Geophysical Journal,* 93, 45-73.

JACKSON, J. A. 1987. Active normal faulting and crustal extension. *Geological Society, London, Special Publications,* 28, 3-17.

JACKSON, M. D., HAMPSON, G. J. & SECH, R. P. 2009. Three-dimensional modeling of a shoreface-shelf parasequence reservoir analog: Part 2. Geologic controls on fluid flow and hydrocarbon recovery. *AAPG Bulletin,* 93, 1183-1208.

JANSON, X., KERANS, C., BELLIAN, J. A. & FITCHEN, W. 2007. Three-dimensional geological and synthetic seismic model of Early Permian redeposited basinal carbonate deposits, Victorio Canyon, west Texas. *AAPG Bulletin,* 91, 1405-1436.

JERVEY, M. T. 1988. QUANTITATIVE GEOLOGICAL MODELING OF SILICICLASTIC ROCK SEQUENCES AND THEIR SEISMIC EXPRESSION. *Sea-Level Changes.* SEPM (Society for Sedimentary Geology).

JOHANSEN, S. E., KIBSGAARD, S., ANDRESEN, A., HENNINGSEN, T. & GRANLI, J. R. 1994. Seismic modeling of a strongly emergent thrust front, West Spitsbergen fold belt, Svalbard. *AAPG Bulletin,* 78, 1018-1027.

JOLIVET, L. 2001. A comparison of geodetic and finite strain pattern in the Aegean, geodynamic implications. *Earth and Planetary Science Letters,* 187, 95-104.

JOLLEY, S. J., DIJK, H., LAMENS, J. H., FISHER, Q. J., MANZOCCHI, T., EIKMANS, H. & HUANG, Y. 2007a. Faulting and fault sealing in production simulation models: Brent Province, northern North Sea. *Petroleum Geoscience,* 13, 321-340.

JOLLEY, S. J., FISHER, Q. J. & AINSWORTH, R. B. 2010. Reservoir compartmentalization: an introduction. *Geological Society, London, Special Publications,* 347, 1-8.

JOLLEY, S. J., STUART, G. W., FREEMAN, S. R., KNIPE, R. J., KERSHAW, D., MCALLISTER, E., BARNICOAT, A. C. & TUCKER, R. F. 2007b. Progressive evolution of a late orogenic thrust system, from duplex development to extensional reactivation and disruption: Witwatersrand Basin, South Africa. *Geological Society, London, Special Publications,* 272, 543-569.

JONES, R. R., MCCAFFREY, K. J. W., CLEGG, P., WILSON, R. W., HOLLIMAN, N. S., HOLDSWORTH, R. E., IMBER, J. & WAGGOTT, S. 2009. Integration of regional to outcrop digital data: 3D visualisation of multi-scale geological models. *Computers & Geosciences,* 35, 4-18.

KANAMORI, H. & ANDERSON, D. L. 1975. Theoretical basis of some empirical relations in seismology. *Bulletin of the Seismological Society of America,* 65, 1073-1095.

KATZ, O., RECHES, Z. & ROEGIERS, J. C. 2000. Evaluation of mechanical rock properties using a Schmidt Hammer. *International Journal of Rock Mechanics and Mining Sciences,* 37, 723-728.

KERANEN, K. M., SAVAGE, H. M., ABERS, G. A. & COCHRAN, E. S. 2013. Potentially induced earthquakes in Oklahoma, USA: Links between wastewater injection and the 2011 Mw 5.7 earthquake sequence. *Geology*.

KIM, Y.-S. & SANDERSON, D. J. 2005. The relationship between displacement and length of faults: a review. *Earth-Science Reviews,* 68, 317-334.

KING, G. C. P., OUYANG, Z. X., PAPADIMITRIOU, P., DESCHAMPS, A., GAGNEPAIN, J., HOUSEMAN, G., JACKSON, J. A., SOUFLERIS, C. & VIRIEUX, J. 1985. The evolution of the Gulf of Corinth (Greece): an aftershock study of the 1981 earthquakes. *Geophysical Journal of the Royal Astronomical Society,* 80, 677-693.

KNIPE, R. J. 1997. Juxtaposition and seal diagrams to help analyze fault seals in hydrocarbon reservoirs. *AAPG Bulletin,* 81, 187-195.

KNIPE, R. J., JONES, G. & FISHER, Q. J. 1998. Faulting, fault sealing and fluid flow in hydrocarbon reservoirs: an introduction. *Geological Society, London, Special Publications,* 147, vii-.

KOMINZ, M. A. & PEKAR, S. F. 2001. Oligocene eustasy from two-dimensional sequence stratigraphic backstripping. *Geological Society of America Bulletin,* 113, 291-304.

KUSZNIR, N. J., MARSDEN, G. & EGAN, S. S. 1991. A flexural-cantilever simple-shear/pure-shear model of continental lithosphere extension: applications to the Jeanne d'Arc Basin, Grand Banks and Viking Graben, North Sea. *Geological Society, London, Special Publications,* 56, 41-60.

KUSZNIR, N. J., ROBERTS, A. M. & MORLEY, C. K. 1995. Forward and reverse modelling of rift basin formation. *Geological Society, London, Special Publications,* 80, 33-56.

LAMBIASE, J. J. & BOSWORTH, W. 1995. Structural controls on sedimentation in continental rifts. *Geological Society, London, Special Publications,* 80, 117-144.

LARSEN, G. & CHILINGAR, G.V., 1983. Diagenesis in Sediments and Sedimentary Rocks (Developments in Sedimentology 25B): Elsevier Publ. Co., 572 p.

LARSEN, P.-H. 1988. Relay structures in a Lower Permian basement-involved extension system, East Greenland. *Journal of Structural Geology,* 10, 3-8.

LECOMTE, I. 2008. Resolution and illumination analyses in PSDM. *The Leading Edge,* 27, 650-663.

LINDSAY, N. G., MURPHY, F. C., WALSH, J. J., AND WATTERSON, J. 1993. Outcrop studies of shale smear on fault surfaces: International Association of Sedimentologists Special Publication 15, p. 113–123.

LONG, J. J. 2011. Geometry, evolution and scaling of fault relay zones in 3D using detailed observations from outcrops and 3D seismic data. *Doctoral Thesis,* Durham University.

LONG, J. J. & IMBER, J. 2010. Geometrically coherent continuous deformation in the volume surrounding a seismically imaged normal fault-array. *Journal of Structural Geology,* 32, 222-234.

LONG, J. J. & IMBER, J. 2011. Geological controls on fault relay zone scaling. *Journal of Structural Geology,* 33, 1790-1800.

LUCIER, A., ZOBACK, M., GUPTA, N. & RAMAKRISHNAN, T. S. 2006. Geomechanical aspects of CO2 sequestration in a deep saline reservoir in the Ohio River Valley region. *Environmental Geosciences,* 13, 85-103.

LYON-CAEN, H., PAPADIMITRIOU, P., DESCHAMPS, A., BERNARD, P., MAKROPOULOS, K., PACCHIANI, F. & PATAU, G. 2004. First results of the CRLN seismic network in the

western Corinth Rift: evidence for old-fault reactivation. *Comptes Rendus Geosciences,* 336, 343-351.

MACKENZIE, G. D., THYBO, H. & MAGUIRE, P. K. H. 2005. Crustal velocity structure across the Main Ethiopian Rift: results from two-dimensional wide-angle seismic modelling. *Geophysical Journal International,* 162, 994-1006.

MAERTEN, L., MAERTEN, F. 2006. Chronologique modeling of faulted and fractured reservoirs using geomechanically based restoration: Technique and industry applications: American Association of Petroleum Geologist Bulletin, v. 90, p. 1201-1226

MAGARA, K. 1968. Compaction and migration of fluids in Miocene mudstone, Nagaoka plain, Japan. *AAPG Bulletin,* 52, 2466-2501.

MAJER, E. L., BARIA, R., STARK, M., OATES, S., BOMMER, J., SMITH, B. & ASANUMA, H. 2007. Induced seismicity associated with Enhanced Geothermal Systems. *Geothermics,* 36, 185-222.

MALARTRE, F., FORD, M. & WILLIAMS, E. A. 2004. Preliminary biostratigraphy and 3D geometry of the Vouraikos Gilbert-type fan delta, Gulf of Corinth, Greece. *Comptes Rendus Geosciences,* 336, 269-280.

MANSFIELD, C. & CARTWRIGHT, J. 2001. Fault growth by linkage: observations and implications from analogue models. *Journal of Structural Geology,* 23, 745-763.

MANZOCCHI, T., CARTER, J. N., SKORSTAD, A., FJELLVOLL, B., STEPHEN, K. D., HOWELL, J. A., MATTHEWS, J. D., WALSH, J. J., NEPVEU, M., BOS, C., COLE, J., EGBERTS, P., FLINT, S., HERN, C., HOLDEN, L., HOVLAND, H., JACKSON, H., KOLBJORNSEN, O., MACDONALD, A., NELL, P. A. R., ONYEAGORO, K., STRAND, J., SYVERSVEEN, A. R., TCHISTIAKOV, A., YANG, C., YIELDING, G. & ZIMMERMAN, R. W. 2008a. Sensitivity of the impact of geological uncertainty on production from faulted and unfaulted shallow-marine oil reservoirs: objectives and methods. *Petroleum Geoscience,* 14, 3-15.

MANZOCCHI, T., CHILDS, C. & WALSH, J. J. 2010. Faults and fault properties in hydrocarbon flow models. 10, 94-113.

MANZOCCHI, T., HEATH, A. E., PALANANTHAKUMAR, B., CHILDS, C. & WALSH, J. J. 2008b. Faults in conventional flow simulation models: a consideration of representational assumptions and geological uncertainties. *Petroleum Geoscience,* 14, 91-110.

MANZOCCHI, T., HEATH, A. E., WALSH, J. J. & CHILDS, C. 2002. The representation of two phase fault-rock properties in flow simulation models. *Petroleum Geoscience,* 8, 119-132.

MANZOCCHI, T., MATTHEWS, J. D., STRAND, J. A., CARTER, J. N., SKORSTAD, A., HOWELL, J. A., STEPHEN, K. D. & WALSH, J. J. 2008c. A study of the structural controls on oil recovery from shallow-marine reservoirs. *Petroleum Geoscience,* 14, 55-70.

MANZOCCHI, T., WALSH, J. J., NELL, P. & YIELDING, G. 1999. Fault transmissibility multipliers for flow simulation models. *Petroleum Geoscience,* 5, 53-63.

MANZOCCHI, T., WALSH, J. J., TOMASSO, M., STRAND, J., CHILDS, C. & HAUGHTON, P. D. W. 2007. Static and dynamic connectivity in bed-scale models of faulted and unfaulted turbidites. *Geological Society, London, Special Publications,* 292, 309-336.

MANZOCCHI, T. & CHILDS, C. Production-induced capillary fault seal failure: How common is it? Fault and Top Seals, EAGE Conference, Montpellier, October 2012.

MARCHAL, D., GUIRAUD, M. & RIVES, T. 2003. Geometric and morphologic evolution of normal fault planes and traces from 2D to 4D data. *Journal of Structural Geology,* 25, 135-158.

MARRETT, R. & ALLMENDINGER, R. W. 1991. Estimates of strain due to brittle faulting: sampling of fault populations. *Journal of Structural Geology,* 13, 735-738.

MARTEL, S. J. 1999. Mechanical controls on fault geometry. *Journal of Structural Geology,* 21, 585-596.

MCCAFFREY, K. J. W., JONES, R. R., HOLDSWORTH, R. E., WILSON, R. W., CLEGG, P., IMBER, J., HOLLIMAN, N. & TRINKS, I. 2005. Unlocking the spatial dimension: digital technologies and the future of geoscience fieldwork. *Journal of the Geological Society,* 162, 927-938.

MCCLAY, K. R., DOOLEY, T., WHITEHOUSE, P. S. & ANADON-RUIZ, S. 2005. 4D analogue models of extensional fault systems in asymmetric rifts: 3D visualizations and comparisons with natural examples. *Geological Society, London, Petroleum Geology Conference series,* 6, 1543-1556.

MCCLUSKY, S., BALASSANIAN, S., BARKA, A., DEMIR, C., ERGINTAV, S., GEORGIEV, I., GURKAN, O., HAMBURGER, M., HURST, K., KAHLE, H., KASTENS, K., KEKELIDZE, G., KING, R., KOTZEV, V., LENK, O., MAHMOUD, S., MISHIN, A., NADARIYA, M., OUZOUNIS, A., PARADISSIS, D., PETER, Y., PRILEPIN, M., REILINGER, R., SANLI, I., SEEGER, H., TEALEB, A., TOKSÖZ, M. N. & VEIS, G. 2000. Global Positioning System constraints on plate kinematics and dynamics in the eastern Mediterranean and Caucasus. *J. Geophys. Res.,* 105, 5695-5719.

MCKENZIE, D. 1972. Active Tectonics of the Mediterranean Region. *Geophysical Journal of the Royal Astronomical Society,* 30, 109-185.

MCKENZIE, D. 1978. Some remarks on the development of sedimentary basins. *Earth and Planetary Science Letters,* 40, 25-32.

MCKENZIE, D. P. 1970. Plate Tectonics of the Mediterranean Region. *Nature,* 226, 239-243.

MCKIE, T., JOLLEY, S. J. & KRISTENSEN, M. B. 2010. Stratigraphic and structural compartmentalization of dryland fluvial reservoirs: Triassic Heron Cluster, Central North Sea. *Geological Society, London, Special Publications,* 347, 165-198.

MCLEOD, A. E., DAWERS*, N. H. & UNDERHILL, J. R. 2000. The propagation and linkage of normal faults: insights from the Strathspey–Brent–Statfjord fault array, northern North Sea. *Basin Research,* 12, 263-284.

MCNEILL, L. C. & COLLIER, R. E. L. 2004. Uplift and slip rates of the eastern Eliki fault segment, Gulf of Corinth, Greece, inferred from Holocene and Pleistocene terraces. *Journal of the Geological Society,* 161, 81-92.

MCNEILL, L. C., COLLIER, R. E. L., MARTINI, P. M. D., PANTOSTI, D. & D'ADDEZIO, G. 2005. Recent history of the Eastern Eliki Fault, Gulf of Corinth: geomorphology, palaeoseismology and impact on palaeoenvironments. *Geophysical Journal International,* 161, 154-166.

MCNEILL, L. C., COTTERILL, C. J., BULL, J. M., HENSTOCK, T. J., BELL, R. & STEFATOS, A. 2007. Geometry and slip rate of the Aigion fault, a young normal fault system in the western Gulf of Corinth. *Geology,* 35, 355-358.

MILLER, K. G., KOMINZ, M. A., BROWNING, J. V., WRIGHT, J. D., MOUNTAIN, G. S., KATZ, M. E., SUGARMAN, P. J., CRAMER, B. S., CHRISTIE-BLICK, N. & PEKAR, S. F. 2005. The Phanerozoic Record of Global Sea-Level Change. *Science,* 310, 1293-1298.

MIN, B., SHU, L., YIN, H., XIN, W. & ZHANG, D. 2007. Conglomeratic reservoir characterization in the Caiyu field of the Langgu sag, North China. *Marine and Petroleum Geology,* 24, 579-590.

MIRABELLA, F., BOCCALI, V. & BARCHI, M. R. 2005. Segmentation and interaction of normal faults within the Colfiorito fault system (central Italy). *Geological Society, London, Special Publications,* 243, 25-36.

MOLLIEX, S., BELLIER, O., TERRIER, M., LAMARCHE, J., MARTELET, G. & ESPURT, N. 2011. Tectonic and sedimentary inheritance on the structural framework of Provence (SE France): Importance of the Salon-Cavaillon fault. *Tectonophysics,* 501, 1-16.

MONTGOMERY, S. L., JARVIE, D. M., BOWKER, K. A. & POLLASTRO, R. M. 2005. Mississippian Barnett Shale, Fort Worth basin, north-central Texas: Gas-shale play with multi–trillion cubic foot potential. *AAPG Bulletin,* 89, 155-175.

MORAES, M. A. S., BLASKOVSKI, P. R. & JOSEPH, P. 2004. The Gres d'Annot as an analogue for Brazilian Cretaceous sandstone reservoirs: comparing convergent to passive-margin confined turbidites. *Geological Society, London, Special Publications,* 221, 419-437.

MORLEY, C. K., HARANYA, C., PHOOSONGSEE, W., PONGWAPEE, S., KORNSAWAN, A. & WONGANAN, N. 2004. Activation of rift oblique and rift parallel pre-existing fabrics during extension and their effect on deformation style: examples from the rifts of Thailand. *Journal of Structural Geology,* 26, 1803-1829.

MORLEY, C. K., NELSON, R. A., PATTON, T. L. & MUNN, S. G. 1990. Transfer zones in the East African Rift system and their relevance to hydrocarbon exploration in rifts. *AAPG Bulletin,* 74, 1234-1253.

MORRIS, A., FERRILL, D. A. & HENDERSON, D. B. 1996. Slip-tendency analysis and fault reactivation. *Geology,* 24, 275-278.

MORRIS, A. P., FERRILL, D. A. & MCGINNIS, R. N. 2009. Mechanical stratigraphy and faulting in Cretaceous carbonates. *AAPG Bulletin,* 93, 1459-1470.

MORROW, C. A., SHI, L. Q. & BYERLEE, J. D. 1982. Strain Hardening and Strength of Clay-Rich Fault Gouges. *J. Geophys. Res.,* 87, 6771-6780.

NEEDHAM, D. T., YIELDING, G. & FREEMAN, B. 1996. Analysis of fault geometry and displacement patterns. *Geological Society, London, Special Publications,* 99, 189-199.

NELSON, R. A., PATTON, T. L. & MORLEY, C. K. 1992. Rift-segment interaction and its relation to hydrocarbon exploration in continental rift systems. *AAPG Bulletin,* 76, 1153-1169.

NICOL, A., WALSH, J. J., VILLAMOR, P., SEEBECK, H. & BERRYMAN, K. R. 2010. Normal fault interactions, paleoearthquakes and growth in an active rift. *Journal of Structural Geology,* 32, 1101-1113.

NICOL, A., WALSH, J. J., WATTERSON, J. & GILLESPIE, P. A. 1996. Fault size distributions — are they really power-law? *Journal of Structural Geology,* 18, 191-197.

NYGÅRD, R., GUTIERREZ, M., BRATLI, R. K. & HØEG, K. 2006. Brittle–ductile transition, shear failure and leakage in shales and mudrocks. *Marine and Petroleum Geology,* 23, 201-212.

ODLING, N. E., HARRIS, S. D., VASZI, A. Z. & KNIPE, R. J. 2005. Properties of fault damage zones in siliclastic rocks: a modelling approach. *Geological Society, London, Special Publications,* 249, 43-59.

ORI, G. G. 1989. Geologic history of the extensional basin of the Gulf of Corinth (?Miocene-Pleistocene), Greece. *Geology,* 17, 918-921.

ORI, G. G., ROVERI, M. & NICHOLS, G. 1991. ARCHITECTURAL PATTERNS IN LARGE-SCALE GILBERT-TYPE DELTA COMPLEXES, PLEISTOCENE, GULF OF CORINTH, GREECE. *The Three-Dimensional Facies Architecture of Terrigenous Clastic Sediments and Its Implications for Hydrocarbon Discovery and Recovery.* SEPM (Society for Sedimentary Geology).

PALMER, I. M., ZISSIS; CAMERON, JOHN. 2007. Modelling Shear Failure and Stimulation of the Barnett Shale After Hydraulic Fracturing. *SPE Hydraulic Fracturing Technology Conference.* College Station, Texas, USA: SPE.

PAOLA, C. & MOHRIG, D. 1996. Palaeohydraulics revisited: palaeoslope estimation in coarse-grained braided rivers. *Basin Research,* 8, 243-254.

PAPANICOLAOU, C., DEHMER, J. & FOWLER, M. 2000. Petrological and organic geochemical characteristics of coal samples from Florina, Lava, Moschopotamos and Kalavryta coal fields, Greece. *International Journal of Coal Geology,* 44, 267-292.

PATON, D., CARR, M., TRUDGILL, B., ORTNER, H. & MEDWEDEFF, D. A. 2007. Alpine-scale 3D geospatial modeling: Applying new techniques to old problems. *Geosphere,* 3, 527-549.

PATON, D. A. 2006. Influence of crustal heterogeneity on normal fault dimensions and evolution: southern South Africa extensional system. *Journal of Structural Geology,* 28, 868-886.

PATON, D. A. & UNDERHILL, J. R. 2004. Role of crustal anisotropy in modifying the structural and sedimentological evolution of extensional basins: the Gamtoos Basin, South Africa. *Basin Research,* 16, 339-359.

PE-PIPER, G. & PIPER, D. J. W. 1984. Tectonic setting of the Mesozoic Pindos basin of the Peloponnese, Greece. *Geological Society, London, Special Publications,* 17, 563-567.

PEACOCK, D. C. P. & AZZAM, I. N. 2006. Development and scaling relationships of a stylolite population. *Journal of Structural Geology,* 28, 1883-1889.

PEACOCK, D. C. P. & SANDERSON, D. J. 1991. Displacements, segment linkage and relay ramps in normal fault zones. *Journal of Structural Geology,* 13, 721-733.

PEACOCK, D. C. P. & SANDERSON, D. J. 1994. Geometry and development of relay ramps in normal fault systems. *AAPG Bulletin,* 78, 147-165.

PEACOCK, D. C. P. & SANDERSON, D. J. 1996. Effects of propagation rate on displacement variations along faults. *Journal of Structural Geology,* 18, 311-320.

PERISSORATIS, C., PIPER, D. J. W. & LYKOUSIS, V. 2000. Alternating marine and lacustrine sedimentation during late Quaternary in the Gulf of Corinth rift basin, central Greece. *Marine Geology,* 167, 391-411.

PETLEY, D. N. 1999. Failure envelopes of mudrocks at high confining pressures. *Geological Society, London, Special Publications,* 158, 61-71.

PICKERING, G., PEACOCK, D. C. P., SANDERSON, D. J. & BULL, J. M. 1997. Modeling tip zones to predict the throw and length characteristics of faults. *AAPG Bulletin,* 81, 82-99.

PICKUP, G. E., RINGROSE, P. S., JENSEN, J. L. & SORBIE, K. S. 1994. Permeability tensors for sedimentary structures. *Mathematical Geology,* 26, 227-250.

PIPER, D. J. W. 2006. Sedimentology and tectonic setting of the Pindos Flysch of the Peloponnese, Greece. *Geological Society, London, Special Publications,* 260, 493-505.

POLIT, A. T., SCHULTZ, R. A. & SOLIVA, R. 2009. Geometry, displacement–length scaling, and extensional strain of normal faults on Mars with inferences on mechanical stratigraphy of the Martian crust. *Journal of Structural Geology,* 31, 662-673.

POULIMENOS, G., ALBERS, G., & DOUTSOS, T. 1989. Neotectonic evolution of the central section of the Corinth graben. *Z. dt. geol. Ges,* 140, 173-182.

POVEY, D., 2010. Integrating uncertainties in fault zone architecture and distributed throw into fault modelling. Unpublished MSc thesis, University of Leeds.

PRINGLE, J. K. B., R. L.; HODGSON, D. M.; FLINT, S. S. 2010. Capturing stratigraphic and sedimentological complexity from submarine channel complex outcrops to digital 3D models, Karoo Basin, South Africa. *Petroleum Geoscience,* 16, 307-330.

PURCELL, W., R. 1949. Capillary Pressures-Their Measurement Using Mercury and the Calculation of Permeability. *Journal of Petroleum Technology,* 1, 39-48.

RAILSBACK, L. B. 1993. Lithologic controls on morphology of pressure-dissolution surfaces (stylolites and dissolution seams) in Paleozoic carbonate rocks from the mideastern United States. *Journal of Sedimentary Research,* 63, 513-522.

REDMANN JR, K. P. 1991. Understanding Kick Tolerance and its Significance in Drilling Planning and Execution. *SPE Drilling Engineering,* 6, 5.

REUSS, A. 1929. Berechnung der Fließgrenze von Mischkristallen auf Grund der Plastizitätsbedingung für Einkristalle. *ZAMM - Journal of Applied Mathematics and Mechanics / Zeitschrift für Angewandte Mathematik und Mechanik,* 9, 49-58.

RIETBROCK, A., TIBERI, C., SCHERBAUM, F., LYON-CAEN, H. 1996. Seismic slip on a low angle normal fault in the Gulf of Corinth: Evidence from high-resolution cluster analysis of microearthquakes. *Geophysical Research Letters,* 23, 1817–1820.

RIGO, A., LYON-CAEN, H., ARMIJO, R., DESCHAMPS, A., HATZFIELD, D., MAKROPOULOS, K., PAPADIMITRIOU, P. & KASSARAS, I. 1996. A Microseismic study in the Western part of the Gulf of Corinth (Greece): Implications for large scale normal faulting mechanisms. *Geophysical Journal International,* 126, 663-688.

RIVENÆS, J. C., OTTERLEI, C., ZACHARIASSEN, E., DART, C. & SJØHOLM, J. 2005. A 3D stochastic model integrating depth, fault and property uncertainty for planning robust wells, Njord Field, offshore Norway. *Petroleum Geoscience,* 11, 57-65.

ROBERTS, A. M., YIELDING, G., KUSZNIR, N. J., WALKER, I. M. & DORN-LOPEZ, D. 1995. Quantitative analysis of Triassic extension in the northern Viking Graben. *Journal of the Geological Society,* 152, 15-26.

ROBERTS, G. P. 1996. Variation in fault-slip directions along active and segmented normal fault systems. *Journal of Structural Geology,* 18, 835-845.

ROBERTS, G. P. & GAWTHORPE, R. L. 1995. Strike variation in deformation and diagenesis along segmented normal faults: an example from the eastern Gulf of Corinth, Greece. *Geological Society, London, Special Publications,* 80, 57-74.

ROBERTS, S. & JACKSON, J. 1991. Active normal faulting in central Greece: an overview. *Geological Society, London, Special Publications,* 56, 125-142.

ROHAIS, S., ESCHARD, R., FORD, M., GUILLOCHEAU, F. & MORETTI, I. 2007. Stratigraphic architecture of the Plio-Pleistocene infill of the Corinth Rift: Implications for its structural evolution. *Tectonophysics,* 440, 5-28.

ROTEVATN, A., BUCKLEY, S. J., HOWELL, J. A. & FOSSEN, H. 2009a. Overlapping faults and their effect on fluid flow in different reservoir types: A LIDAR-based outcrop modeling and flow simulation study. *AAPG Bulletin,* 93, 407-427.

ROTEVATN, A. & FOSSEN, H. 2011. Simulating the effect of subseismic fault tails and process zones in a siliciclastic reservoir analogue: Implications for aquifer support and trap definition. *Marine and Petroleum Geology,* 28, 1648-1662.

ROTEVATN, A., FOSSEN, H., HESTHAMMER, J., AAS, T. E. & HOWELL, J. A. 2007. Are relay ramps conduits for fluid flow? Structural analysis of a relay ramp in Arches National Park, Utah. *Geological Society, London, Special Publications,* 270, 55-71.

ROTEVATN, A., TVERANGER, J., HOWELL, J. A. & FOSSEN, H. 2009b. Dynamic investigation of the effect of a relay ramp on simulated fluid flow: geocellular modelling of the Delicate Arch Ramp, Utah. *Petroleum Geoscience,* 15, 45-58.

ROWLAND, J. V., BAKER, E., EBINGER, C. J., KEIR, D., KIDANE, T., BIGGS, J., HAYWARD, N. & WRIGHT, T. J. 2007. Fault growth at a nascent slow-spreading ridge: 2005 Dabbahu rifting episode, Afar. *Geophysical Journal International,* 171, 1226-1246.

ROYDEN, L. H. 1993. The tectonic expression slab pull at continental convergent boundaries. *Tectonics,* 12, 303-325.

SCHLISCHE, R. W., YOUNG, S. S., ACKERMANN, R. V. & GUPTA, A. 1996. Geometry and scaling relations of a population of very small rift-related normal faults. *Geology,* 24, 683-686.

SCHOWALTER, T. 1979. Mechanics of Secondary Hydrocarbon Migration and Entrapment. *AAPG Bulletin,* 63, 723-760.

SCHULTZ, R. A. & FOSSEN, H. 2002. Displacement–length scaling in three dimensions: the importance of aspect ratio and application to deformation bands. *Journal of Structural Geology,* 24, 1389-1411.

SECH, R. P., JACKSON, M. D. & HAMPSON, G. J. 2009. Three-dimensional modeling of a shoreface-shelf parasequence reservoir analog: Part 1. Surface-based modeling to capture high-resolution facies architecture. *AAPG Bulletin,* 93, 1155-1181.

SHAPIRO, S. A. & DINSKE, C. 2009. Fluid-induced seismicity: Pressure diffusion and hydraulic fracturing. *Geophysical Prospecting,* 57, 301-310.

SHAPIRO, S. A., DINSKE, C., LANGENBRUCH, C. & WENZEL, F. 2010. Seismogenic index and magnitude probability of earthquakes induced during reservoir fluid stimulations. *The Leading Edge,* 29, 304-309.

SHAW, D. B. & WEAVER, C. E. 1965. The mineralogical composition of shales. *Journal of Sedimentary Research,* 35, 213-222.

SHUEY, R. T. 1985. A simplification of the Zoeppritz equations. *Geophysics,* 50, 609-614.

SIBSON, R. H. 1995. Selective fault reactivation during basin inversion: potential for fluid redistribution through fault-valve action. *Geological Society, London, Special Publications,* 88, 3-19.

SKOURTSOS, E. & KRANIS, H. 2009. Structure and evolution of the western Corinth Rift, through new field data from the Northern Peloponnesus. *Geological Society, London, Special Publications,* 321, 119-138.

SOLIVA, R. & BENEDICTO, A. 2004. A linkage criterion for segmented normal faults. *Journal of Structural Geology,* 26, 2251-2267.

SOLIVA, R., BENEDICTO, A. & MAERTEN, L. 2006. Spacing and linkage of confined normal faults: Importance of mechanical thickness. *J. Geophys. Res.,* 111.

SOREL, D. 2000. A Pleistocene and still-active detachment fault and the origin of the Corinth-Patras rift, Greece. *Geology,* 28, 83-86.

SPERREVIK, S., GILLESPIE, P. A., FISHER, Q. J., HALVORSEN, T. & KNIPE, R. J. 2002. Empirical estimation of fault rock properties. *In:* KOESTLER, A. G. & HUNSDALE, R. (eds.) *Hydrocarbon Seal Quantification.*

STRUIJK, A. P. & GREEN, R. T. 1991. The Brent Field, Block 211/29, UK North Sea. *Geological Society, London, Memoirs,* 14, 63-72.

SUCKALE, J. 2010. Moderate-to-large seismicity induced by hydrocarbon production. *The Leading Edge,* 29, 310-319.

SUMNER, E. J., TALLING, P. J., AMY, L. A., WYNN, R. B., STEVENSON, C. J. & FRENZ, M. 2012. Facies architecture of individual basin-plain turbidites: Comparison with existing models and implications for flow processes. *Sedimentology*, no-no.

SWARBRICK, R. E., LAHANN, R. W., O'CONNOR, S. A. & MALLON, A. J. 2010. Role of the Chalk in development of deep overpressure in the Central North Sea. *Geological Society, London, Petroleum Geology Conference series,* 7, 493-507.

SYMEONIDIS, N., THEODOROU, G., SCHUTT, H. & VELITZELOS, E. 1986. Paleontological and stratigraphic observations in the area of Achaia and Etoloakarnania (W. Greece). *Annls Geol. Pays Hellen,* 33, 329-365.

TADA, R. & SIEVER, R. 1989. Pressure solution during diagenesis. Annual Review of Earth Planetary Sciences 17, 89–118.

TAYLOR, B., WEISS, J. R., GOODLIFFE, A. M., SACHPAZI, M., LAIGLE, M. & HIRN, A. 2011. The structures, stratigraphy and evolution of the Gulf of Corinth rift, Greece. *Geophysical Journal International,* 185, 1189-1219.

TAYLOR, S. K., BULL, J. M., LAMARCHE, G. & BARNES, P. M. 2004. Normal fault growth and linkage in the Whakatane Graben, New Zealand, during the last 1.3 Myr. *J. Geophys. Res.,* 109, B02408.

TOMASSO, M., BOUROULLEC, R. & PYLES, D. R. 2010. The use of spectral recomposition in tailored forward seismic modeling of outcrop analogs. *AAPG Bulletin,* 94, 457-474.

TOWNSEND, C., FIRTH, I. R., WESTERMAN, R., KIRKEVOLLEN, L., HARDE, M. & ANDERSEN, T. 1998. Small seismic-scale fault identification and mapping. *Geological Society, London, Special Publications,* 147, 1-25.

TRUDGILL, B. & CARTWRIGHT, J. 1994. Relay-ramp forms and normal-fault linkages, Canyonlands National Park, Utah. *Geological Society of America Bulletin,* 106, 1143-1157.

TSIKALAS, F., INGE FALEIDE, J. & ELDHOLM, O. 2001. Lateral variations in tectono-magmatic style along the Lofoten-Vesterålen volcanic margin off Norway. *Marine and Petroleum Geology,* 18, 807-832.

TUCKER, M. E. & BATHURST, R. G. C. (eds) 1990. Carbonate Diagenesis. Reprint Series Volume 1 of the International Association of Sedimentologists. viii + 312 pp.

TUECKMANTEL, C., FISHER, Q. J., GRATTONI, C. A. & APLIN, A. C. 2012a. Single- and two-phase fluid flow properties of cataclastic fault rocks in porous sandstone. *Marine and Petroleum Geology,* 29, 129-142.

TUECKMANTEL, C., FISHER, Q. J., KNIPE, R. J., LICKORISH, H. & KHALIL, S. M. 2010. Fault seal prediction of seismic-scale normal faults in porous sandstone: A case study from the eastern Gulf of Suez rift, Egypt. *Marine and Petroleum Geology,* 27, 334-350.

TUECKMANTEL, C., FISHER, Q. J., MANZOCCHI, T., SKACHKOV, S. & GRATTONI, C. A. 2012b. Two-phase fluid flow properties of cataclastic fault rocks: Implications for CO2 storage in saline aquifers. *Geology,* 40, 39-42.

TVERANGER, J., CARDOZO, N., KJELDAAS, G.C., NØTTVEIT, H. AND RØE, P. 2008: Volumetric fault zone modelling using fault facies. Fault zones: structure geomechanics and fluid flow conference. The Geological Society, London 2008.

WALSH, J. J., BAILEY, W. R., CHILDS, C., NICOL, A. & BONSON, C. G. 2003. Formation of segmented normal faults: a 3-D perspective. *Journal of Structural Geology,* 25, 1251-1262.

WALSH, J. J., CHILDS, C., MEYER, V., MANZOCCHI, T., IMBER, J., NICOL, A., TUCKWELL, G., BAILEY, W. R., BONSON, C. G., WATTERSON, J., NELL, P. A. & STRAND, J. 2001. Geometric controls on the evolution of normal fault systems. *Geological Society, London, Special Publications,* 186, 157-170.

WALSH, J. J., NICOL, A. & CHILDS, C. 2002. An alternative model for the growth of faults. *Journal of Structural Geology,* 24, 1669-1675.

WALSH, J. J. & WATTERSON, J. 1987. Distributions of cumulative displacement and seismic slip on a single normal fault surface. *Journal of Structural Geology,* 9, 1039-1046.

WALSH, J. J. & WATTERSON, J. 1988. Analysis of the relationship between displacements and dimensions of faults. *Journal of Structural Geology,* 10, 239-247.

WALSH, J. J. & WATTERSON, J. 1990. New methods of fault projection for coalmine planning. *Proceedings of the Yorkshire Geological and Polytechnic Society,* 48, 209-219.

WARPINSKI, N. R. D., J; ZIMMER, U. 2012. Measurements of Hydraulic-Fracture-Induced Seismicity in Gas Shales. *SPE Hydraulic Fracturing Technology Conference.* The Woodlands, Texas, USA: SPE.

WATTS, N. L. 1987. Theoretical aspects of cap-rock and fault seals for single- and two-phase hydrocarbon columns. *Marine and Petroleum Geology,* 4, 274-307.

WELCH, M. J., DAVIES, R. K., KNIPE, R. J. & TUECKMANTEL, C. 2009. A dynamic model for fault nucleation and propagation in a mechanically layered section. *Tectonophysics,* 474, 473-492.

WELCH, M., FRISCHBUTTER, A., & . KNIPE, R.J. 2012. The Value of Geomechanical Modelling of Fault Properties for Trap Analysis. Fault and Top Seals Conference, 2012, Montpellier.

WELLS, D. L. & COPPERSMITH, K. J. 1994. New empirical relationships among magnitude, rupture length, rupture width, rupture area, and surface displacement. *Bulletin of the Seismological Society of America,* 84, 974-1002.

WIBBERLEY, C.A.J., PETIT, J.P. & RIVES, T. 2000. Micromechanics of shear rupture and the control of normal stress. *Journal of Structural Geology,* 4, 411-427.

WIBBERLEY, C.A.J., KURZ, W., IMBER, J., HOLDSWORTH, R.E. & COLLETTINI, C. 2008. The Internal Structure of Fault Zones: Implications for Mechanical and Fluid-Flow Properties. Geological Society Publishing House.

WILLEMSE, E. J. M. 1997. Segmented normal faults: Correspondence between three-dimensional mechanical models and field data. *J. Geophys. Res.,* 102, 675-692.

WILLEMSE, E. J. M., POLLARD, D. D. & AYDIN, A. 1996. Three-dimensional analyses of slip distributions on normal fault arrays with consequences for fault scaling. *Journal of Structural Geology,* 18, 295-309.

WILSON, R. W., HOLDSWORTH, R. E., WILD, L. E., MCCAFFREY, K. J. W., ENGLAND, R. W., IMBER, J. & STRACHAN, R. A. 2010. Basement-influenced rifting and basin development: a reappraisal of post-Caledonian faulting patterns from the North Coast Transfer Zone, Scotland. *Geological Society, London, Special Publications,* 335, 795-826.

YASUHARA, H., MARONE, C. & ELSWORTH., D. 2005. Fault Zone Restengthening and Frictional Healing: The Role of Pressure Solution. *Journal of Geophysical Research*, 110, 1-11.

YAXLEY, L. M. 1987. Effect of a Partially Communicating Fault on Transient Pressure Behavior. *SPE Formation Evaluation*.

YIELDING, G. 2012. Using probabilistic shale smear modelling to relate SGR predictions of column height to fault-zone heterogeneity. *Petroleum Geoscience,* 18, 33-42.

YIELDING, G., BRETAN, P. & FREEMAN, B. 2010. Fault seal calibration: a brief review. *Geological Society, London, Special Publications,* 347, 243-255.

YIELDING, G., FREEMAN, B. & NEEDHAM, D. T. 1997. Quantitative fault seal prediction. *AAPG Bulletin,* 81, 897-917.

YIELDING, G. & ROBERTS, A. 1992. Footwall uplift during normal faulting - implications for structural geometries in the North Sea. *Structural and Tectonic Modelling and its Application to Petroleum Geology, Norwegian Petroleum Society (NPF) Special Publication* No.1, p. 289-304.

YIELDING, G., WALSH, J. J. & WATTERSON, J. 1992. The prediction of small-scale faulting in reservoirs. *First Break,* 10, 449-460.

ZHANG, Z. & GHASSEMI, A. 2011. Simulation of hydraulic fracture propagation near a natural fracture using virtual multidimensional internal bonds. *International Journal for Numerical and Analytical Methods in Geomechanics,* 35, 480-495.

ZOBACK, M. D. 2007. Reservoir Geomechanics. Cambridge University Press.

ZOEPPRITZ, K. 1919. Erdbebenwellen VII. VIIb. Über Reflexion und Durchgang seismischer Wellen durch Unstetigkeitsflächen. Nachrichten von der Königlichen Gesellschaft der Wissenschaften zu Göttingen, Mathematisch-physikalische Klasse, 66-84.

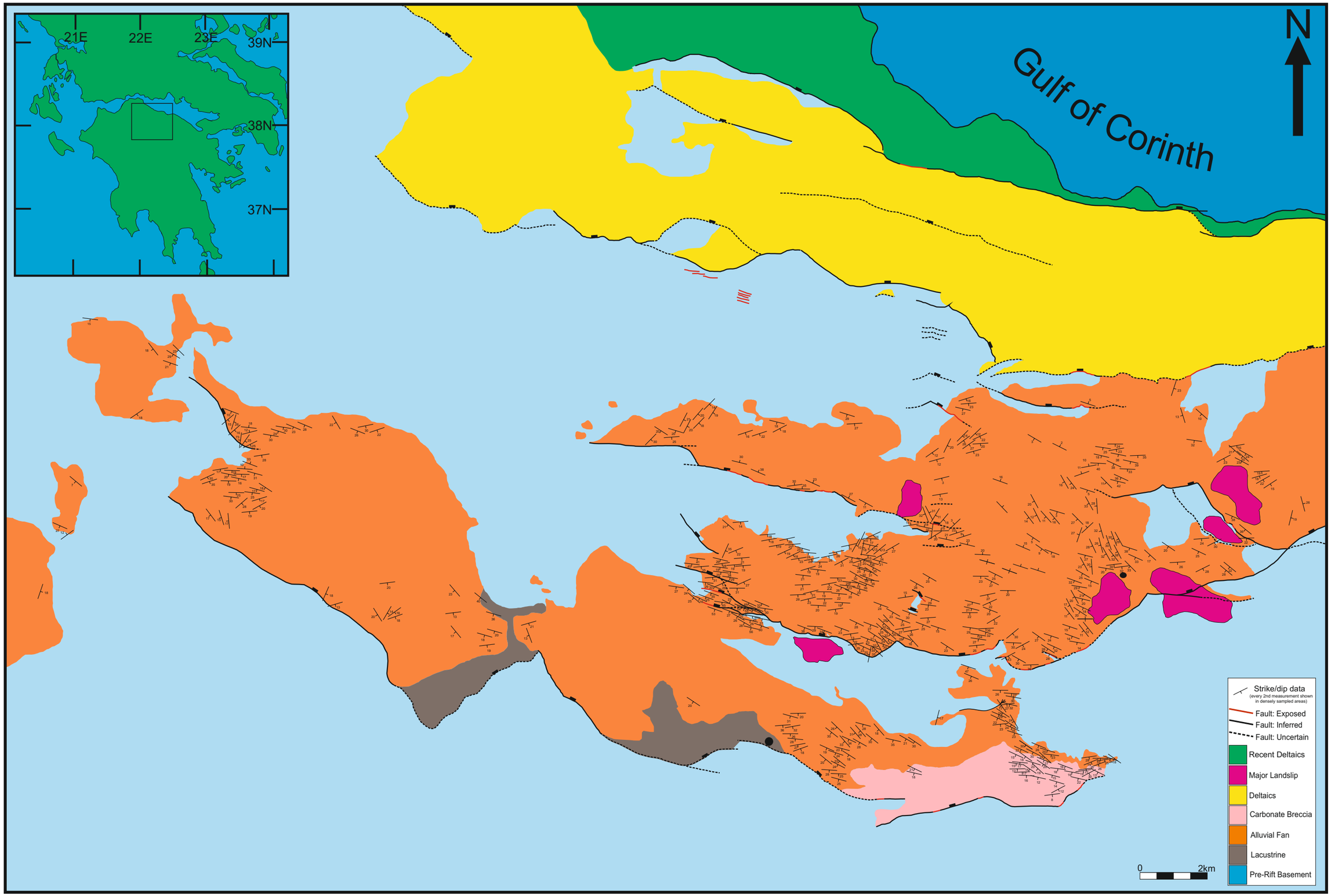
21E
22E
23E
39N
38N
37N
N
Gulf of Corinth
Strike/dip data
(every 2nd measurement shown in densely sampled areas)
Fault: Exposed
Fault: Inferred
Fault: Uncertain
Recent Deltaics
Major Landslip
Deltaics
Carbonate Breccia
Alluvial Fan
Lacustrine
Pre-Rift Basement
0
2km

(A)

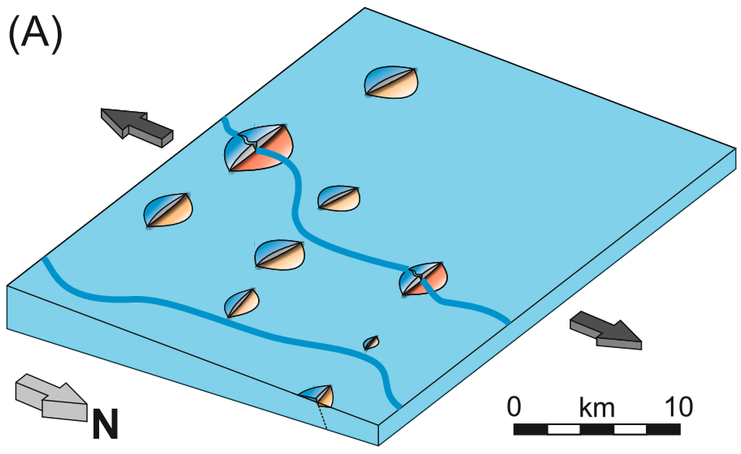

(B)

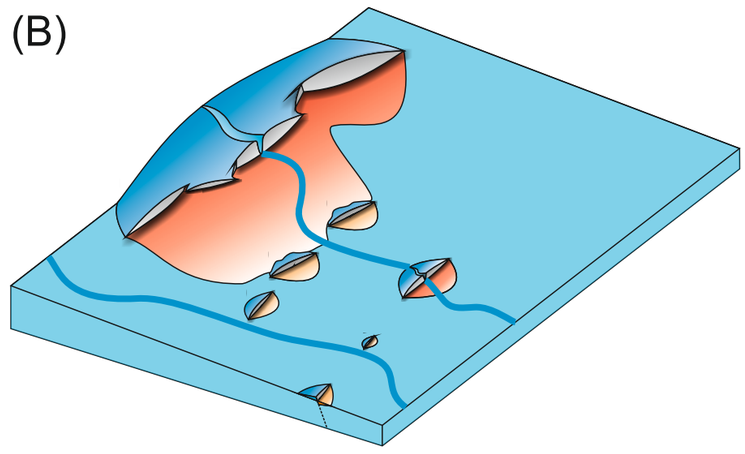

(C)

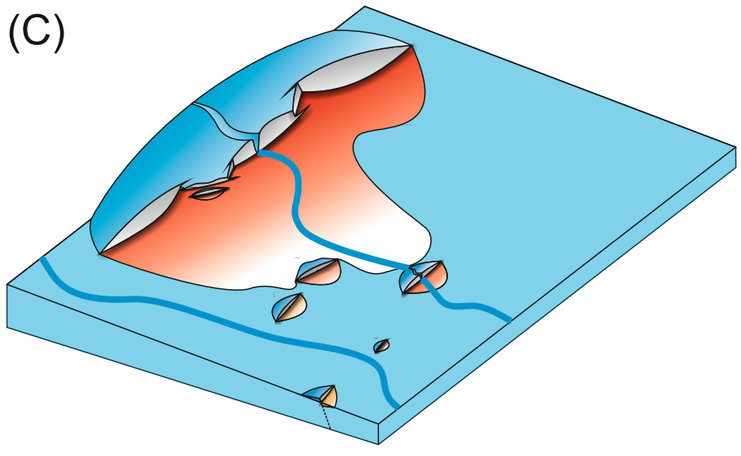

(D)

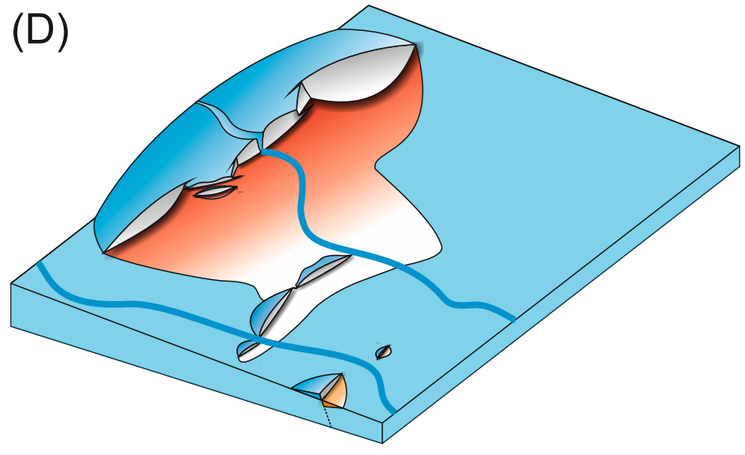

(E)

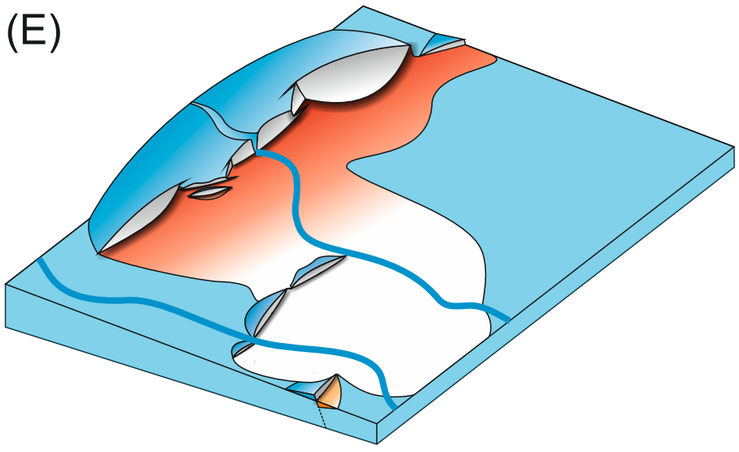

(F)

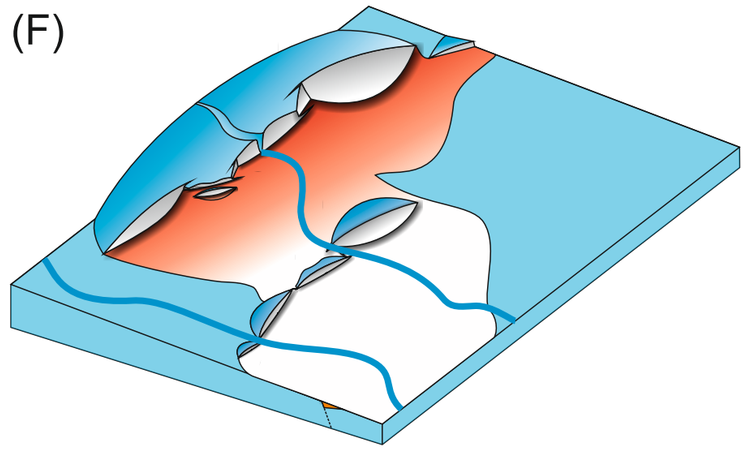

(G)

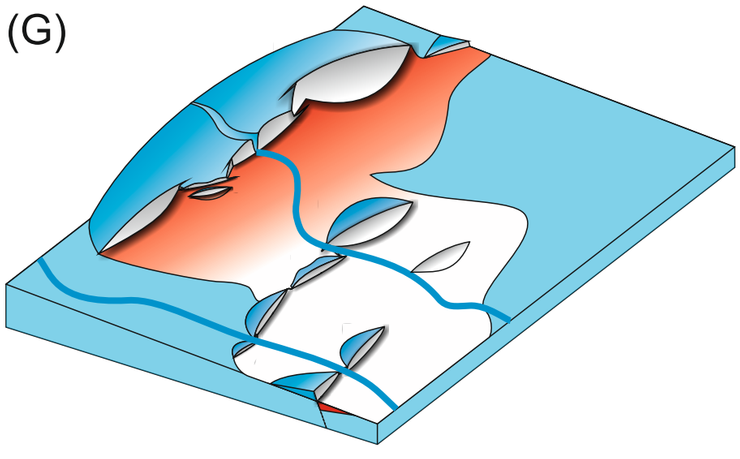

(H)

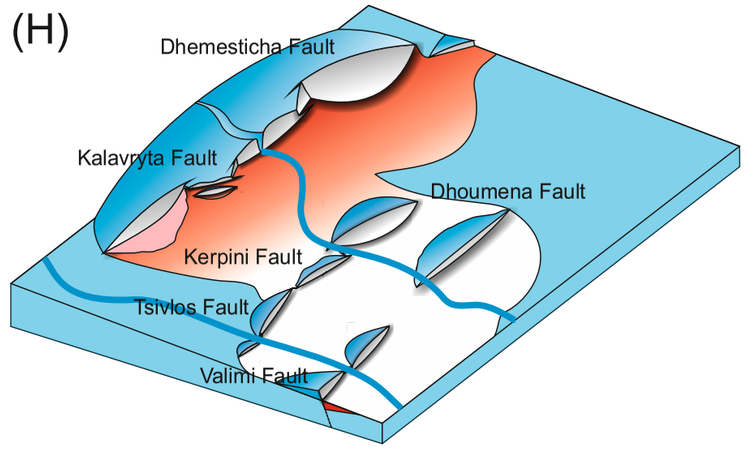

Late stage Carbonate Breccia
Basement Carbonate
Main Alluvial Fan
Early basin fill
Fault plane
Vouraikos/Krathis river

Normal Fault Relay Zone Geometries in the Early Gulf of Corinth Rift (Greece) and its Application as a Hydrocarbon Exploration and Production Analogue

Alan Wood*, Douglas Paton and Richard Collier

Basin Structure Group (http://bsg.leeds.ac.uk), School of Earth and Environment, University of Leeds, Leeds, LS2 9JT, United Kingdom. *ee08amw@leeds.ac.uk

Introduction

Within extensional hydrocarbon provinces the style of deformation and of fault linkages which are developed has major implications for hydrocarbon exploration and production, influencing maturation, migration, reservoir distribution, trap integrity and reservoir performance (Dou and Chang, 2003). Seismic resolution often does not allow imaging and full constraint of fault and fault linkage geometries, hence leading to uncertainty in cross-fault juxtapositions and fault rock properties. Volumetric estimations, spill point locations and the extent of reservoir compartmentalisation are strongly influenced by these uncertainties, with major implications for recovery rates and economic viability. It is therefore crucial to fully assess the potential effects of geometric uncertainty during both the appraisal and development stage.

The onshore Gulf of Corinth Rift presents a high quality study area in which basin- to reservoir-scale fault systems encompassing a range of relay geometries are exposed. Detailed field mapping and integration into the three dimensional geological modelling environment has constrained relay and deformation geometries and allowed a conceptual model describing the evolution of the area to be developed.

Limitations of seismic resolution often permit multiple, equally valid, interpretations of fault and fault relay geometries to be constructed, however it is common that only a single geometry is modelled and taken forward as the base case for simulation. Here we apply geometries observed in the field to an analogous North Sea seismic dataset to show the effect that geometric uncertainty can have on simulated reservoir performance.

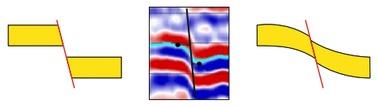

Correctly modelling the amount of normal drag adjacent to a fault has significant impacts on the cross-fault juxtapositions and hence on cross fault fluid flow during reservoir simulation.

Field Observations

Above. Location map showing the Peloponnese's location within the eastern Mediterranean

Left. Close up of the Peloponnese peninsula. The field area covered by this study is highlighted by the red box.

Right. Geological map of field area with inset representative cross sections showing the general structure (no vertical exaggeration). Numbers refer to the locations of the annotated field photographs.

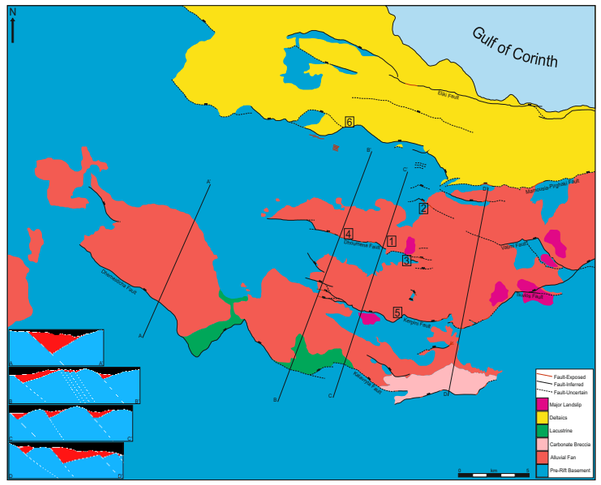

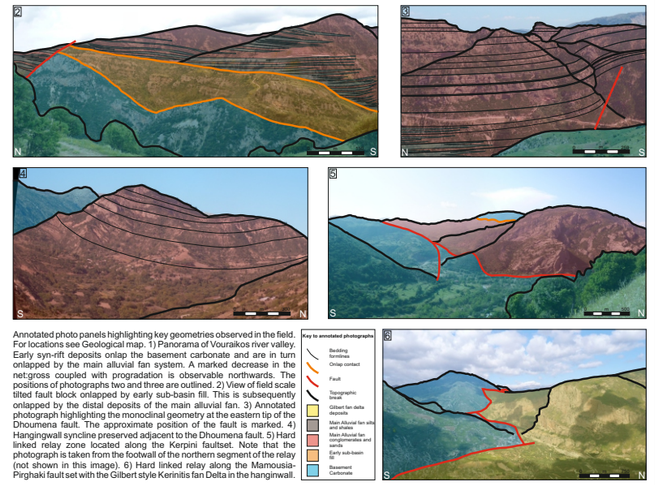

Annotated photo panels highlighting key geometries observed in the field. For locations see Geological map. 1) Panorama of Vouraikos river valley. Early syn-rift deposits onlap the basement carbonate and are in turn onlapped by the main alluvial fan system. A marked decrease in the net:gross coupled with progradation is observable northwards. The positions of photographs two and three are outlined. 2) View of field scale tilted fault block onlapped by early sub-basin fill. This is subsequently onlapped by the distal deposits of the main alluvial fan. 3) Annotated photograph highlighting the monoclinal geometry at the eastern tip of the Dhoumena fault. The approximate position of the fault is marked. 4) Hangingwall syncline preserved adjacent to the Dhoumena fault. 5) Hard linked relay zone located along the Kerpini faultset. Note that the photograph is taken from the footwall of the northern segment of the relay (not shown in this image). 6) Hard linked relay along the Mamousia-Pirghaki fault set with the Gilbert style Kerinitis fan Delta in the hanginwall.

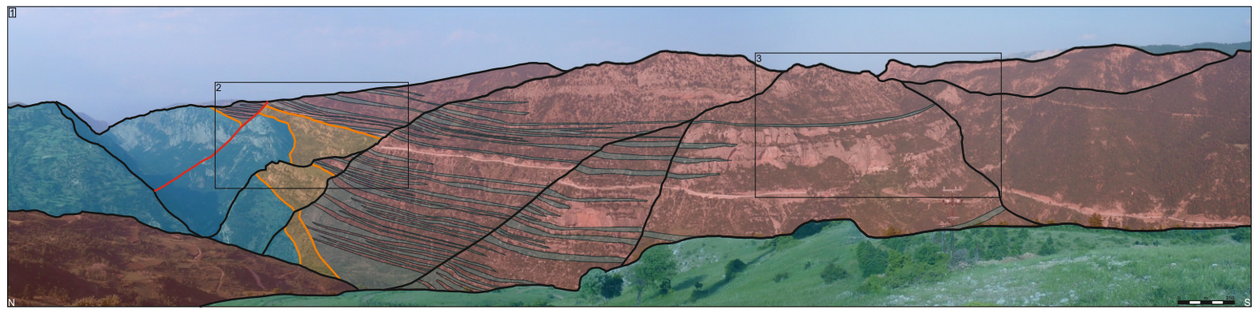

Background

The eastern Mediterranean has long been recognised as an area of active tectonism with the region dominated by the collision of the African and Arabian plates with the Eurasian plate. Subduction of the African plate at the Hellenic arc is occurring at a faster rate than the northwards movement of the plate itself leading to slab pull and southwards migration of the arc relative to the Eurasian plate. This leads to backarc extension and continental rifting of mainland Greece to the north (Doutsos et al., 1988). It is thought that rifting commenced at about 15 Ma and was initially distributed across the Aegean region (Armijo et al., 1996). The Gulf of Corinth rift initiated at approximately 5 Ma and is currently the most active with extension rates averaging 5 to 15mm/yr (Bell et al., 2008).

The modern day Gulf of Corinth is a large E-W orientated inlet in central Greece approximately 120km in length with a maximum width of 27km and maximum water depth of almost 900m. It separates the Peloponnese in the south from Central mainland Greece to the north. The area is actively extending and is characterised by high extension rates which are accommodated on a number of major north dipping and minor south dipping faults. Broadly speaking these faults run ENE-WSW, cross-cutting pre-existing NNE-SSW orientated thrusts within the pre-rift basement. This basement consists of Mesozoic age shelf carbonates, radiolarites, flysch and ophiolites derived from the Tethys Ocean and deformed during Alpine Collision. Early dispersed rifting in the northern Peloponnese resulted in the formation of a number of isolated sub-basins prior to strain localisation onto the southernmost fault sets. The main phase of onshore syn-rift sedimentation consisted of continental alluvial fan deposits, with subsidence on later faults to the north leading to deltaic sedimentation at the margin of the Gulf and turbidite deposition along its axis. Younger faults developed in the hangingwalls to older faults suggesting a generalised trend of northwards migration of

The stratal architecture of the continental alluvial fan sediments provides a tool for estimating along-strike throw variations of the fault systems and constraining fault timing and basin development. Geometries mapped in the field can be integrated with digital elevation, structural and sedimentological data within the modelling environment to characterise their three dimensional expression and to consider their relevance as analogues to exploration and production settings.

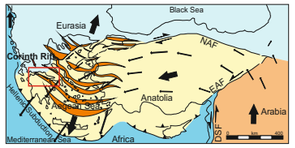

Tectonic setting of the eastern Mediterranean. The Anatolian plate is extruded westwards away from the Arabia-Eurasia collision zone and towards the Hellenic subduction zone with lateral strike-slip movement accommodated along the North Anatolian Fault (NAF) and East Anatolia Fault (EAF). Large block arrows represent mean plate motions whilst small arrows represent movement vectors. Localised rifting in the Aegean region over the last 15Ma is indicated by the orange areas with the Corinth Rift highlighted by a red box. DSF=Dead Sea Fault. Modified from Armijo et al., 1999.

Normal Fault Relay Zone Geometries in the Early Gulf of Corinth Rift (Greece) and its Application as a Hydrocarbon Exploration and Production Analogue

Alan Wood*, Douglas Paton and Richard Collier
Basin Structure Group (http://bsg.leeds.ac.uk), School of Earth and Environment, University of Leeds, Leeds, LS2 9JT, United Kingdom. *ee08amw@leeds.ac.uk

Model for Structural Evolution

Subtle structural and stratigraphic relationships have been used to develop a conceptual model for the evolution of the onshore portion of the rift. This model illustrates how timing of fault activity is significantly more complex than indicated by previously published models (e.g. Sorel, 2000).

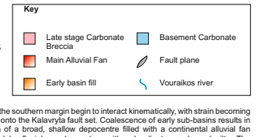

(1)

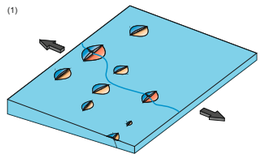

Initial extensional stress across the area accommodated through dispersed rifting on a number of isolated faults. Small sub-basins develop in the hangingwalls to these faults with the associated fill being composed of both local footwall derived material and more compositionally varied river transported sediments with a hinterland provenance.

It is likely that established fluvial systems existed with their positions controlled by the pre-existing, approximately N-S orientated structural fabric of the Hellenide Mountain range. Whether or not the courses of these river systems were influenced by early fault growth is unclear and is largely dependent on the relative rates of deformation and incision. However it is suggested that the broad positions of these antecedent river systems changed little after the initiation of rifting.

(2)

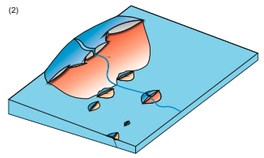

Faults at the southern margin begin to interact kinematically, with strain becoming localised onto the Kalavryta fault set. Coalescence of early sub-basins results in formation of a broad, shallow depocentre filled with a continental alluvial fan dominated by fluvial conglomerates, with subordinate sands and silts. The compositionally variable nature of the sediment suggests a largely hinterland provenance.

The main sediment input point is the palaeo-Vouraikos river, with incision exceeding the rate of footwall uplift, and hence maintaining its antecedent course. It is likely that secondary input systems were also present along strike, potentially controlled by the positions of early relay zones or the pre-existing structural fabric.

High sediment input rates coupled relatively with low displacement rates across the fault set result in rapid progradation, with onlap onto the topographic highs of the footwall crests of the proto-Kerpini fault set reveals their presence due to dispersed rifting in the initial stage of evolution.

(3)

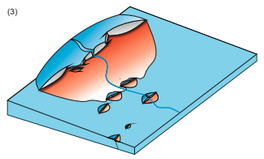

Fault profile re-adjustment results in a rapid increase in the deformation rate around displacement minima associated with relay zones. This increasing displacement results in high strain and breaching of relays. In turn the rate of accommodation creation in the hangingwall increases, limiting progradation of the fan system. Footwall uplift is now occurring along the entire fault set potentially re-directing secondary rivers and limiting sediment input into the basin, possibly resulting in aggradation rather than progradation.

Sub-basins in the hangingwall to the proto-Kerpini fault set preserved from the initial stage of dispersed rifting may become filled with distal alluvial fan deposits. It is unclear as to whether or not the footwall crests to these early faults became buried at this stage.

(4)

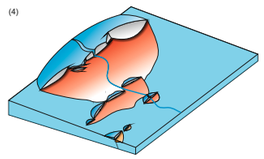

Extensional deformation moves northwards, concentrating onto the Kerpini and Tsivlos fault sets, with an associated decrease in displacement rates across the Kalavryta fault set where overlap of fault sets occurs. Further west where no overlap occurs, on the segment of the Kalavryta fault set known as the Dhemesticha fault, displacement continues unimpeded. Similarly, to the northeast of the Kerpini-Tsivlos fault set extension is accommodated by movement on the Valimi fault set.

The majority sedimentation is now within the newly forming basin in the hangingwall to the Kerpini-Tsivlos fault set. This results in a similar pattern as observed in stage 2, with rapid early progradation fed by the palaeo-Vouraikos and subsidiary rivers flowing through soft-linked relay zones. This progradation is observable as a diachronous decrease in net:gross in the Vouraikos river valley to the north of the Kerpini Fault.

(5)

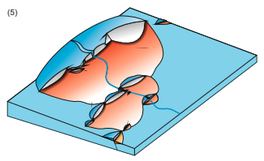

Kinematic linkage and profile re-adjustment of the Kerpini-Tsivlos fault set results in a rapid increase in displacement at relay zones and subsequent breaching and hard linkage. Minor variations in the displacement along this, as well as other fault sets can be explained by 'displacement shadows' where two or more faults are located in close proximity in a direction normal to strike.

Displacement continues on the Dhemesticha fault, with local stresses leading to the formation of a subsidiary fault to the north west of the main fault.

(6)

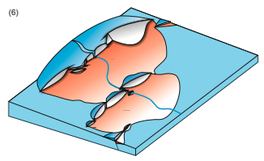

Eastwards propagation of the Kerpini-Tsivlos fault set is limited by strain being accommodated instead on the Valimi fault set to the North. Westwards propagation is also limited, with additional strain being accommodated by a number of splays. The reason for this stalling in westwards propagation of the Kerpini fault set is as yet unclear, however we speculate that a mechanical barrier, or pre-existing structure may be the cause.

The alluvial fan continues to prograde, first onlapping and then burying the footwall crest of the proto-Dhoumena fault.

(7)

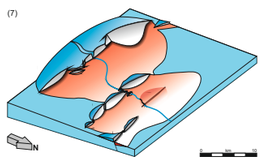

The deformation front moves northwards with strain accommodation switching to the Valimi fault set. Removal of the 'displacement shadow' caused by the Kerpini-Tsivlos fault set allows westwards propagation and hard linkage of the Valimi fault set.

To the west strain is accommodated through reactivation of the now buried Dhoumena fault. A monocline forms over the fault as it propagates upwards through the syn-rift strata in the hangingwall to the Kerpini-Tsivlos fault set.

(8)

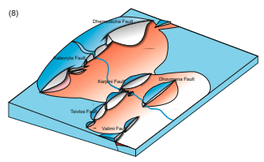

The Dhoumena fault propagates up through the monocline formed above it revealing a footwall crest composed of the basement carbonate. A broad monocline is preserved at the present day erosion surface to the east of the Megaspillion monastery, the lateral extent of which marks the approximate expression of the Dhoumena fault beneath the surface. The Valimi fault set is also propagating westwards potentially beginning to link at depth with the Dhoumena fault. Prior to hard linkage occurring at surface the deformation front again steps northwards, with displacement nucleating onto the Mamoussia-Pirgahki fault set. This marks a transition from continental to marine deposition, with the hangingwall basin of the Mamoussia-Pirghaki fault set being filled with deltaic sediments such as those observed at the Kerinitis Gilbert style fan delta to the north.

An area of uncertainty with our model stems from the continued movement of the Kalavryta fault set. A secondary fan composed solely of local footwall derived carbonate outcrops in the hangingwall to the eastern portion of the Kalavryta fault set (see diagram 8). This onlaps the main alluvial fan with the respective dips indicating that at the time of the secondary fans deposition the main alluvial fan dipped at approximately 8 degrees towards the fault. The entire area was subsequently rotated by a further 17 degrees. This implies two things; 1) That a significant amount of displacement (equivalent to 8 degrees of rotation) occurred on the Kalavryta fault following cessation of deposition of alluvial deposits in the immediate hangingwall. 2) That an additional 17 degrees of rotation, almost 70% of the total observable at the present day land surface, occurs subsequent to deposition of the secondary fan. Although this secondary fan is only preserved at the eastern end of the Kalavryta fault set the dips of the underlying alluvial fan are consistent along the entire strike of the fault, indicating that this late movement was not simply restricted to the eastern segment.
This has major implications for the evolution of the rift system. Continuous and/or late activity on the Kalavryta fault set necessitates a more complex model than the simple northwards progression previously proposed. In analogous settings late stage fault movement and associated deposition may significantly modify fairway distribution, as well as compromising seal integrity.

3D Modelling and Structural Analysis

Field data such as bedding and fault orientations, outcrop patterns, palaeocurrents, mechanical properties and sedimentary logs can be integrated with DEM data within geological modelling software. This provides a tool for constraining the three dimensional fault geometry and along strike variations in throw associated with relay zones.

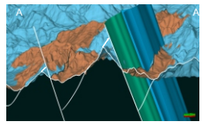

Above. Cut out view of model construction. A digital elevation model (DEM) is draped with map data. Structural field data is used to construct fault and top-basement surfaces. Arrows indicate where footwall cutoffs have been projected to account for fault scarp degredation.

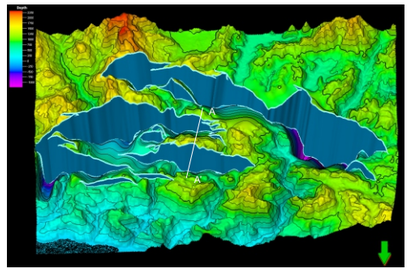

Right. View of horizon representing the top of the pre-rift basement. Fault surfaces between footwall and hangingwall cut-offs are shown in blue. Displacement minima are associated with relay zones and 'displacement shadows' where strain is accommodated across multiple faults which overlap in a direction normal to strike. x2 vertical exaggeration.

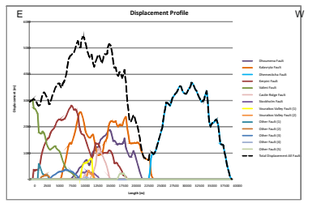

Displacement profiles of faults extracted from the 3D geological model. Displacement minima are observed at relay zones and within 'displacement shadows'. Displacement is partitioned between the east and the west of the area, with extension in the west accommodated across a single fault, whilst extension in the east is accommodated by a number of faults. The reason for this disparity is unclear.

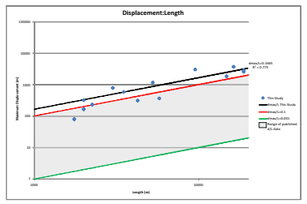

Displacement-length plots for the modelled faults. The red and green lines represent the upper and lower bounds of published d/L data (Kim and Sanderson, 2005). The majority of the modelled faults fall above this range indicating a high d/L ratio. This may be a result of interaction with the pre-existing basement fabric limiting lateral fault propagation.

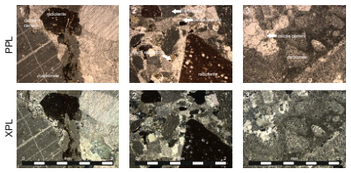

Plane and cross polarised light photographs illustrating the variation in composition of different stages of basin fill. Coloured boxes refer to evolutionary diagrams.

1) Initial dispersed rifting resulted in depocentres filled with both hinterland and locally derived material.

2) The main progradational alluvial fan is compositionally varied, dominated by sediments with a hinterland provenance. This includes sandstone, chert, radiolarite and carbonate lithologies.

3) The breccia stratigraphically above the main alluvial fan in the hangingwall to the Kalavryta fault is composed entirely of carbonate material derived from the local footwall.

All stages display carbonate cementation to varying degrees, with both vadose and phreatic cements observed.

Application for Quantifying Geometric Uncertainty

When a high quality geological model honouring all available data has been constructed and populated with appropriate properties it is taken forward for reservoir simulation. However, the subsurface environment is non-unique, with multiple structural, sedimentological and petrophysical uncertainties requiring consideration (Manzocchi et al., 2008). These uncertainties can have significant impacts on the validity of a prospect or the performance of a field. Here we examine the effects that a single structural uncertainty, fault-relay geometry, has on simulated hydrocarbon production.

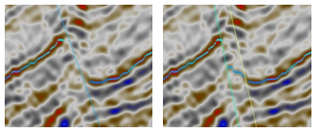

Uncertainty in reflector positioning leads to multiple interpretations of fault geometry being equally valid.

During geological modelling it is standard practise to project key stratigraphic horizons towards faults from a set distance. This removes all drag, whether a processing artefact or a genuine geometry. Geometries observed in the field show that normal drag does occur at multiple scales and can have significant implications for cross-fault juxtapositions, and hence cross-fault flow and reservoir compartmentalisation.

Six separate fault geometry interpretations based on seismic data from the North Sea have been modelled (1-6). Each fault model has been populated with three distinct horizon geometries (1a, b and c). The fault intersections of the horizons have been modified to incorporate varying degrees of normal drag, consistent with geometries observed in the field. This results in each fault model having horizons showing no drag, moderate drag and an intact monocline at the level of the uppermost stratigraphic layer. All other parameters are constant between the models with a simple, homogenous reservoir stratigraphy uniformly populated with reservoir properties. Effectively impermeable layers have been modelled above and below the reservoir interval with a standard SGR algorithm used to calculate fault rock properties.

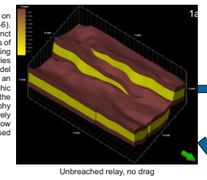

Unbreached relay, no drag

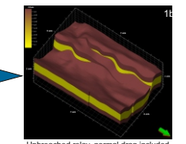

Unbreached relay, normal drag included

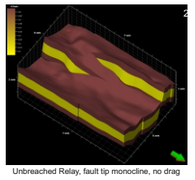

Unbreached Relay, fault tip monocline, no drag

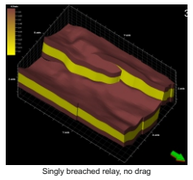

Singly breached relay, no drag

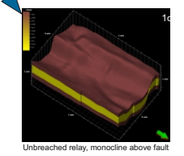

Unbreached relay, monocline above fault

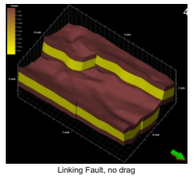

Linking Fault, no drag

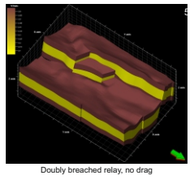

Doubly breached relay, no drag

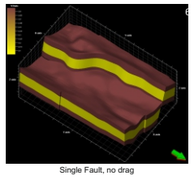

Single Fault, no drag

Normal Fault Relay Zone Geometries in the Early Gulf of Corinth Rift (Greece) and its Application as a Hydrocarbon Exploration and Production Analogue

Alan Wood*, Douglas Paton and Richard Collier
Basin Structure Group (http://bsg.leeds.ac.uk), School of Earth and Environment, University of Leeds, Leeds, LS2 9JT, United Kingdom. *ee08amw@leeds.ac.uk

Reservoir Simulation Results

A total of seventeen different geometries were simulated using a dead oil fluid model. A production well was positioned in the footwall and an injection well in the hangingwall. Two separate water flood production strategies were employed, a constant injection rate set to the initial production rate, and a variable injection rate set to maintain a minimum bottom hole pressure (BHP) at the production well.
Although maintaining the BHP lead to a higher cumulative production in most cases, it also resulted in high injection rates, earlier water breakthrough and a high water cut when compared to a constant injection strategy.
For the same production strategy, the oil production rate for the different geometries is highly variable. The highest variability is observed for geometries where an element of drag, as observed in the field, is included in the geological model.

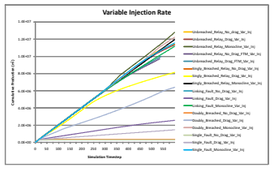

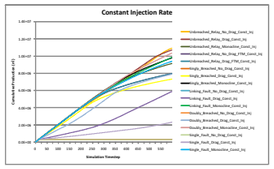

Cumulative oil production for variable and constant water injection rates. Although using a variable injection rate results in a larger cumulative oil production, a higher water cut is observed for many of the structural geometries. Where the fault geometries limit cross fault flux, pressure compartmentalisation occurs requiring an unfeasibly high injection rate to maintain the BHP.

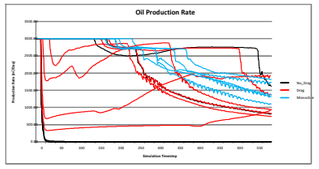

Oil production rates for the different fault relay geometries using a constant injection rate strategy. The different models are colour coded by the amount of drag incorporated. Where no drag is included cross-fault communication is limited to the models where the relay ramp is intact. Breached ramps result in a lack of cross-fault reservoir:reservoir juxtapositions, hence leading to rapid pressure depletion in the footwall. Monoclinal geometries result in large areas with reservoir:reservoir juxtaposition, reducing the impact that different relay geometries have on production. Where normal drag is included production rates are highly variable for the different fault relay geometries, and significantly different to the models where no drag is included.

Shown below are simulation results using a constant injection rate strategy for the six different fault relay geometries modelled, with normal drag included in each.

	Unbreached Relay	Unbreached Relay, Fault Tip Monocline	Singly Breached Relay	Linking Fault	Doubly Breached Relay	Single Fault
Streamlines mid-way through the simulations. Streamlines are displayed from the injection well and filtered to display high water saturations, hence showing the advancement of the water front and sweep pattern at this timestep. The base reservoir horizon is shown in white and faults in blue. The injection well is blue and the production well red. Vertical exaggeration x5.	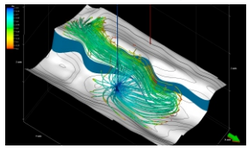	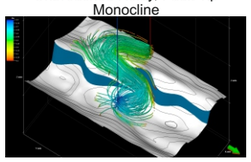	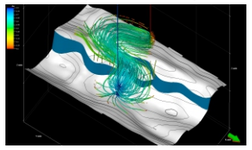	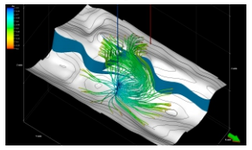	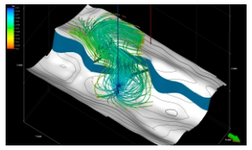	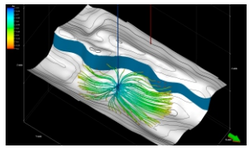
Water saturation within the reservoir interval at the final timestep of the simulations. By this stage the majority of models have seen water breakthrough at the production well, although large volumes remain un-swept. Vertical exaggeration x5	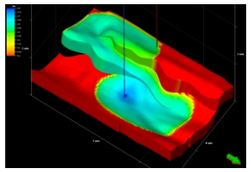	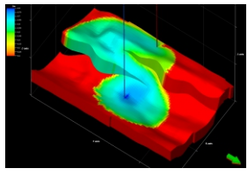	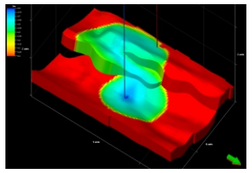	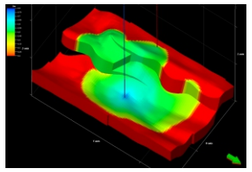	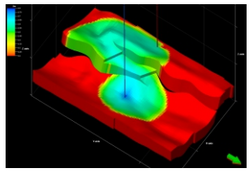	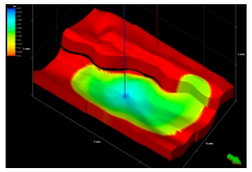
Plots of Oil Production Rate and Water Cut over the course of the simulations. Increasing the complexity of the relay zone geometry increases the variability of the production rate.	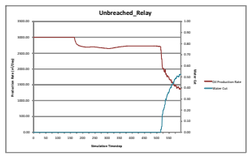	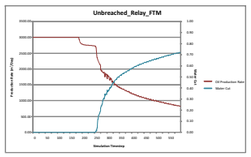	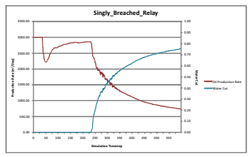	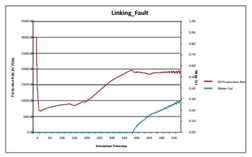	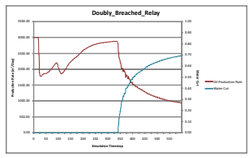	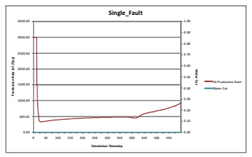
	Discrete offsets at the fault tips increases the path length for water from the injection well, hence improving sweep efficiency and delaying water breakthrough. This geometry is analogous to including sub-seismic displacement at fault tips.	Shorter faults with monoclines at the fault tips rather than discrete offsets provide a shortcut for fluid flow, hence leading to early water breakthrough, a high water cut and remaining un-drained pockets of the reservoir.	Introducing a physical connection across the relay reduces the area of reservoir:reservoir juxtaposition, initially leading to pressure compartmentalisation and a drop in production. Once a sufficient pressure differential is reached production rates increase until water breakthrough occurs.	Having a high throw linking fault initially reduces cross fault flux, causing pressure depletion of the footwall block and decreasing production rates. The distribution of throw leads to multiple along-strike reservoir:reservoir juxtapositions and cross fault flow occurring at multiple positions. This results in a recovery in production rates and a relatively low water cut.	Two negative spikes in production occur as cross flux is reduced across the two breaching faults. Production subsequently increases until rapidly dropping after water breakthrough takes place.	A single fault decreases the probability of cross fault juxtaposition hence increasing the likelihood of reservoir compartmentalisation. Production rates decrease dramatically as pressure depletes in the footwall. Normal drag results in a small area of reservoir:reservoir juxtaposition allowing some pressure communication and cross fault flux.

Conclusions

- Detailed field mapping, data collection and three dimensional geological modelling have allowed the development of a new model for the structural evolution of the onshore Gulf of Corinth. This model describes a more complex evolution of rifting than previously thought, with some faults displaying evidence for multiple phases of activity.
- Displacement profiles of the onshore faults indicate a high displacement-length ratio compared with global studies.
- Fault-relay and drag geometries observed in the field provide structural analogues for both hydrocarbon exploration and production settings located within similar extensional provinces.
- The initial interpretation of fault and fault-relay geometries in seismic data is a major uncertainty and has significant implications later in the workflow for simulated reservoir performance.
- Relay geometry and positioning of wells relative to relay zones can significantly influence sweep patterns and timing of water breakthrough.
- Incorporating a proportion of normal drag reduces the effective throw of faults hence altering cross fault juxtapositions and flow response during simulation.

Further Work

Accounting for, and mitigating against, geometrical uncertainty in flow simulation is currently restricted to statistical population based on a limited number of field observations and numerical models. We wish to further the current understanding and hence reduce this uncertainty by developing models for predicting under what mechanical and stress conditions different relay and drag geometries develop. It is believed that the mechanical heterogeneity of multilayered sequences is a major control on fault propagation and fault damage zone geometries for reservoir scale faults (Welch et al., 2009). We aim to understand the influence that mechanical stratigraphy has on how strain is accommodated at the field to basin scale, and to predict the relative proportions of ductile (i.e. drag) and brittle deformation.

Acknowledgements

The authors would like to thank NERC and Shell for sponsorship of the project, Schlumberger for use of academic licenses for Petrel and FrontSim, and PGS for supply of seismic data to the University of Leeds.

References

Armijo, R., Meyer, B., King, G.C.P., Rigo, A., and Papanastassiou, D. 1996. Quaternary evolution of the Corinth Rift and its implications for the Late Cenozoic evolution of the Aegean. Geophysical Journal International, 126, 11-53.

Armijo, R., Meyer, B., Hubert, A.I., and Barka, A. 1999. Westward propagation of the North Anatolian fault into the northern Aegean: Timing and kinematics. Geology, 27, 267-270.

Bell, R.E., McNeill, L.C., Bull, J.M., and Henstock, T.J. 2008. Evolution of the offshore western Gulf of Corinth. Geological Society of America Bulletin, 120, 156-178.

Dou, L., and Chang, L. 2003. Fault linkage patterns and their control on the formation of the petroleum systems of the Erlian Basin, Eastern China. Marine and Petroleum Geology, 20, 1213-1224.

Doutsos, T., Kontopoulos, N., and Poulimenos, G. 1988. The Corinth-Patras rift as the initial stage of continental fragmentation behind an active island arc (Greece), Volume 1, Blackwell Publishing Ltd, p. 177-190.

Kim, Y.-S. and Sanderson, D. J. 2005. The relationship between displacement and length of faults: a review. Earth-Science Reviews, 68, 317-334.

Manzocchi, T., Carter, J. N., et al. 2008. Sensitivity of the impact of geological uncertainty on production from faulted and unfaulted shallow-marine oil reservoirs: objectives and methods. Petroleum Geoscience, 14, 3-15.

Sorel, D. 2000. A Pleistocene and still-active detachment fault and the origin of the Corinth-Patras rift, Greece. Geology, 28, 83-86.

Welch, M.J., Davies, R.K., Knipe, R.J. and Tueckmantel, C. 2009. A dynamic model for fault nucleation and propagation in a mechanically layered section. Tectonophysics, 474, 473-492.

Determining Relay Zone Linkage Geometry for Faults Close to Seismic Resolution

Alan Wood*, Richard Collier & Douglas Paton

Basin Structure Group (bsg.leeds.ac.uk), School of Earth & Environment, University of Leeds, Leeds, LS2 9JT. *ee08amw@leeds.ac.uk

Introduction

Determining whether overlapping fault segments transfer displacement via a hard or soft linked relay zone is often difficult in seismic data where faults have displacements close to, or below, the limits of resolution. Where hard linkage occurs such faults may act as barriers or baffles to fluid flow in the subsurface, hence impacting on hydrocarbon reservoir performance. We use outcrop, LIDAR and 3D seismic data at a range of scales to develop an empirical relationship for predicting fault linkage geometry within relay zones using parameters which are readily obtainable from seismic data.

The throw of an idealised isolated fault decreases from a maximum at its centre to zero at the fault tips. The portion of a fault where throw is below the seismic resolution will not be observed, hence the low throw fault tips are unresolved and the length of the fault is underestimated (Figure 2). Extending the lengths of faults to include the sub-seismic fault tips may lead to a greater degree of fault connectivity and reservoir segmentation and depending on the petrophysical properties of the fault rock, may lead to increased reservoir compartmentalisation. Here we use a North Sea dataset to compare different methods for predicting the sub-seismic length of faults and, along with sub-seismic fault linkages, investigate their effect on simulated hydrocarbon production.

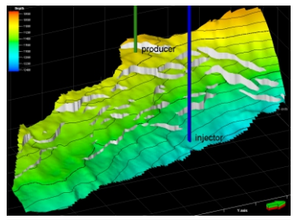

Figure 1. 3D oblique view of the top reservoir horizon and unmodified fault network, along with the positions of the production and injection wells.

North Sea dataset

A sub-set of a seismic dataset covering a currently producing North Sea oilfield has been re-interpreted. To minimise errors the data has been interpreted on every trace resulting in a lateral resolution of approximately 25m. The geological model has been built using a grid of the same dimensions to enure that fault geometries are honoured as accurately as possible (figure 1). This model has formed the basis for the analysis and subsequent modification of the fault population, and for capturing the effects that this has on fluid flow simulation.

Sub-seismic fault tips

Although numerous workers have shown the importance of incorporating sub-seismic faults into simulation models, relatively limited attention has been focussed on predicting and incorporating the sub-seismic tips of seismically resolvable structures (Pickering et al, 1997; Townsend et al, 1998; Rotevatn & Fossen, 2011). Sub-seismic scale fault tips can be defined as the portion of a fault which has a throw less than the limit of resolution of the seismic data (figure 2). Increasing the length of faults to Incorporate their sub-seismic length may lead to greater connectivity of a fault network with implications for recovery from faulted hydrocarbon reservoirs.

Two approaches for estimating the sub-seismic fault tip length are used here, a statistical technique analysing the fault population as a whole, and a geometrical approach using the throw gradient of each individual fault.

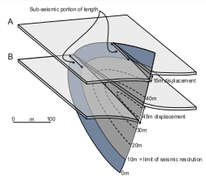

Figure 2. Schematic diagram of half a fault plane with contoured displacement values illustrating the portion of a fault which can be defined as 'sub-seismic'. The position of the horizon relative to the fault influences the sub-seismic length. For horizon A which is oblique to the displacement contours, the fault has a larger sub-seismic length than for horizon B which is perpendicular to the displacement contours. This is a key factor introducing scatter to t_{max}:L plots. Modified after (Gauthier & Lake 1993).

Method 1. Statistical Method

The statistical approach for estimating the length of sub-seismic fault tips is based upon analysis of the relationship between length and maximum throw of a population of faults (Kim & Sanderson, 2005). It is widely accepted that these two geometric parameters have a power law relationship of the form;

$$t_{max}=cL^n,$$

where t_{max} is the maximum displacement, L is the length, n is the exponent value and c relates to the displacement at a unit length. In the case where n=1, a linear relationship applies. Data derived from seismic datasets will generally display a relationship where n<1. This is because, if a constant displacement gradient is assumed, the sub-seismic portion of a faults length will be consistent across a dataset, regardless of the size of an individual fault. Therefore small faults will have a proportionally larger amount of their length below seismic resolution compared to large faults. To correct for this effect a constant length can be added to each fault until a power law trend line reaches the stage where it has an exponent of 1 (Pickering et al, 1997).

Although this methodology is relatively quick, it does not account for factors such as fault interaction and linkage (figure 8), 3D fault geometry (figure 2), and statistical error.

For our North Sea dataset the fault population requires an additional 200m of length (100m at each tip-figure 3) for an exponent of 1 to be reached (figure 5b).

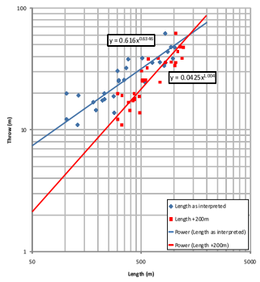

Figure 3. Plot of length against maximum throw for the fault population shown in figure 1. Blue diamonds show the original interpreted lengths, whilst red squares show the population where each fault has an additional 200m of length. This additional length results in a power law exponent of 1, that expected for a linear, scale invariant, relationship between length and throw.

Method 2. Throw gradient

The throw gradient of a fault tells us the rate of change of the fault throw with respect to fault length. It can be calculated from the observable fault dimensions, and where the seismic resolution is known, can be used to predict the sub-seismic tip length (figure 4). Using the throw gradient to predict the sub-seismic length of a fault reduces many of the uncertainties associated with using a statistical approach. Where the stress fields of faults interact their throw profiles become increasingly asymmetrical (Peacock & Sanderson, 1994), leading to variations in throw gradient and hence on the sub-seismic fault tip length. Unlike the statistical method, the throw gradient approach captures this variation and provides a more geologically realistic estimate of sub-seismic tip lengths. Since the length of the sub-seismic fault tips is dependent on the seismic resolution we have included a selection of cases assuming a resolution of 5, 10 and 25m (figure 5).

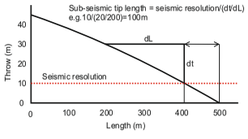

Figure 4. Length-throw plot illustrating how the displacement gradient and seismic resolution can be used to estimate sub-seismic fault tip length.

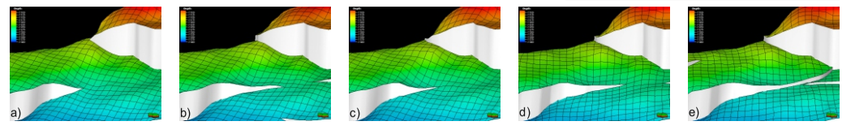

Figure 5. 3D perspective images of the effect of increasing fault length to include sub-seismic tips. a) Original interpretation. b) Statistically elongated. c) Extended based upon throw gradient and seismic resolution of 5m, 10m (d) and 25m (e).

Sub-seismic fault linkages

Fault linkage geometry is another factor which influences hydrocarbon production in faulted reservoirs. Numerous studies over the previous two decades have highlighted the evolution of extensional faults (Peacock & Sanderson, 1991; Childs et al, 1995; Cowie et al, 2000; Gupta & Scholz, 2000; Walsh et al, 2003), from initiation of individual discontinuities as a response to local or regional extension, through stages of growth, interaction, linkage and continued growth (figure 8). Relay zones are ubiquitous at all stages of this process, and their potential influence on hydrocarbon exploration and production is well documented (Peacock & Sanderson, 1994; Athmer & Luthi, 2011; Rotevatn et al, 2007). As is the case for fault tips, sub-seismic breaching faults close to or below the limit of resolution may not be fully resolvable in seismic data. The discrete offsets associated with breached relays as opposed to intact relays may result in unfavourable juxtapositions for cross fault flow and the development of baffling or sealing fault rocks such as clay smears, hence their sub-seismic geometry is a key uncertainty.

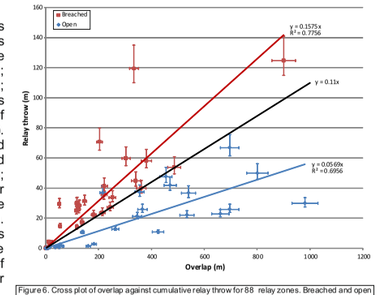

Figure 6. Cross plot of overlap against cumulative relay throw for 88 relay zones. Breached and open relays are clearly clustered in separate fields, with low relay throw:overlap ratios indicating intact relays, and high ratios indicating breached relays. 5% error bars are included for fault length measurements, and vertical error bars representing 10° to account for variation in fault dip are also included.

Figure 6 shows a cross plot of fault relay zone overlap versus relay throw for 88 open and breached relay zones across a range of scales. The data has been compiled from this study and a range of other sources within the literature including seismic, outcrop and LIDAR data. Relay throw is defined as the cumulative throw of the two overlapping faults defining a relay zone, measured at the centre of the relay zone (figure 7). It includes only the throw of the overlapping faults, not any component of ductile deformation associated with rotation of the relay zone. Relay zones which are fully breached, i.e. have undergone profile re-adjustment, are not included. The plot shows a clear distinction between breached and open relays, and therefore provides a criteria which can be used to assess sub-seismic relay integrity from observable geometries. The criteria can also be reconciled with models for relay zone evolution (figures 8 and 9). This criteria has been used to include breached relays in the realisations shown in figure 10.

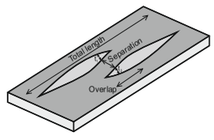

Figure 7. Schematic defining the measurements used in the analysis of relay geometry. Interacting relays are defined as having a separation of less than 15% the total length (Gupta & Scholz, 2000). Cumulative relay throw is $t_1 + t_2$ and, like separation, is measured at the centre of the relay.

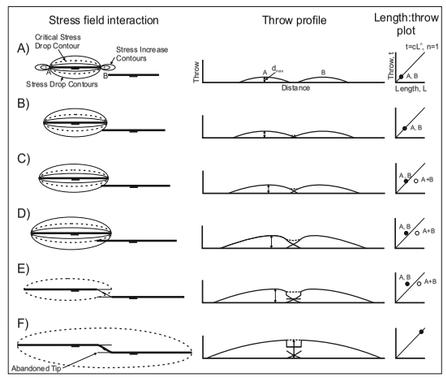

Figure 8. Schematic diagrams describing the evolution of a relay zone in terms of stress field interaction, throw profile and length:throw plots. A) Underlapping faults have little to no stress field interaction. They have symmetrical throw profiles, and plot in the same position on a length:throw plot. B) At the initial stages of overlap the stress fields do not interact sufficiently to effect the fault growth. C) Increasing overlap leads to interaction with the critical stress drop contour (Gupta & Scholz, 2000). This leads to tip restriction and migration of the position of maximum displacement. Depending on whether the faults are defined as separate structures or as a single interacting structure determines where they plot on a length:throw plot. D) Extension continues as does throw accumulation, however stress field interaction prevents lateral tip propagation increasing the throw gradient within the relay zone. The throw profiles become increasingly asymmetrical. E) Above a critical displacement gradient the yield strength of the rock is overcome, and a breaching fault initiates. The position of maximum displacement continues to migrate towards the centre of the linked fault pair. If the faults are defined as being separate, they will appear as short, high throw structures on a length:throw plot. Conversely if they are defined as a single structure they will appear to be a longer, low throw structure. Defining interacting faults as single or separate structures is a major cause of introducing scatter into fault populations. F) Post linkage profile re-adjustment occurs, with the fault now behaving as a single structure. The throw profile is equivalent to the initially isolated faults in (A), with the length:throw plotting along the same relationship.

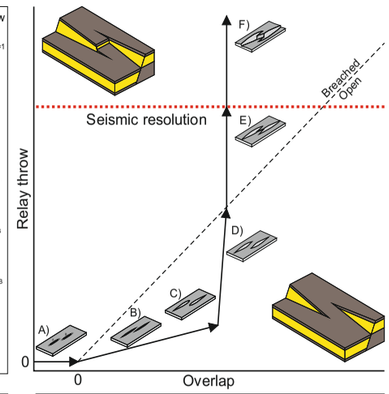

Figure 9. Schematic plot of relay zone evolution relative to relay throw and overlap. Labelling is equivalent to that in figure 8. A) Initially underlapping faults have zero overlap and zero cumulative relay throw. B) As faults overlap, the relay throw begins to increase. C) As the critical stress drop contours are intersected overlap becomes pinned. D) A small increase in overlap is accompanied by a large increase in relay throw as displacement gradients steepen due to interacting stress fields. E) The relay zone becomes breached, with relay throw:overlap ratios increasing into the breached field. F) Profile re-adjustment leads to increased throw on the breaching fault, which becomes visible in seismic data.

Fault connectivity and fluid flow simulation

Following calculation of different fault tip lengths and relay zone geometries a number of realisations have been built to capture their effect on fluid flow simulation. The effect on fault connectivity can be seen in figure 10. Each realisation has been populated with an identical, layer-cake stratigraphy and associated petrophysical properties based upon local well data. Fault plane properties have been calculated using the SGR algorithm (Yielding et al, 1997) and the clay to permeability relationship of Jolley et al, (2007). Threshold pressures of 300psi have been used based upon studies of core data. Simulations have been performed using a single injection and production well, for a period of 40 years. An unfaulted grid has also been simulated for comparison.

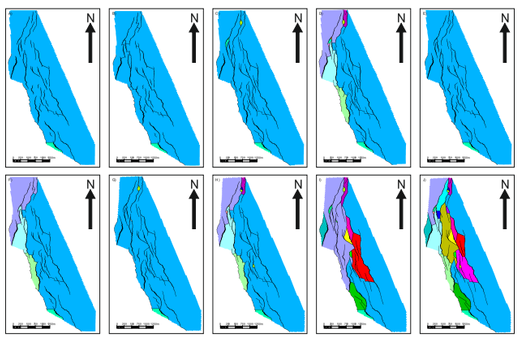

Figure 10. Maps showing the effect of incorporating sub-seismic fault tips and relays on the connectivity of the fault network. Breached relays have been incorporated according to the criteria determined in figure 6. Colours represent isolated fault bound compartments. A) As interpreted. B) As interpreted, with the addition of breached relays according to the breaching criteria in figure 6. C) Statistically elongated fault tips, open relays. D) Statistically elongated fault tips, breached relays. E) Elongated fault tips based on displacement gradient and seismic resolution of 5m, open relays. F) As (E), but with breached relays. G) Elongated fault tips based on displacement gradient and seismic resolution of 10m, open relays. H) As (G), but with breached relays. I) Elongated fault tips based on displacement gradient and seismic resolution of 25m, open relays. J) As (I), but with breached relays.

Simulation results

Results of the simulations show a similar trend for all of the realisations, with oil production rates declining following water breakthrough after approximately 16 years of production (figure 11). Water production however is markedly different. The water production rate decreases with increasing sub-seismic tip length, indicating an improved sweep efficiency. Including sub-seismic breached fault relays also reduces the amount of water produced. Closer inspection of the results (figure 12), shows that including sub-seismic fault tips tends to lead to an earlier onset of production decline, but that decline tends to be slower, with a lower water cut. Including breached relays has a similar effect. Cumulative oil production is similar for all cases, with the disparity in water cut being the major economic factor. Including sub-seismic tips and breaching faults generally decreases the predicted water cut, increasing the economic favourability of a prospect or field.

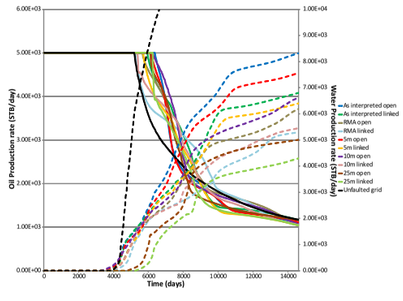

Figure 11. Plot of Oil production rate and Water production rate against simulation time step for all realisations. Oil production rates are similar, however water production rates vary significantly between the different models. Since produced water must be treated and disposed of, estimating the volume that will be produced is a significant factor when considering the economics of a reservoir.

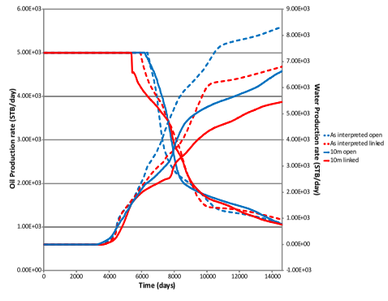

Figure 12. Plot of Oil production rate and water production rate against simulation time step illustrating the general differences between different sub-seismic tip lengths, and including breached relays. Incorporating sub-seismic fault tips generally results in a earlier production rate decline, albeit at a lower rate. A similar result can be observed when breached relays are included. Water production rates tend to be lower where sub-seismic fault tips are included, as is the case for breached relays.

Conclusions

- Using a statistical approach for calculating sub-seismic fault tips does not account for variations resulting from the growth mechanisms of normal faults. Hence using the local throw gradient is favoured.
- A strong relationship exists between cumulative relay throw, overlap and whether a relay zone is intact or breached. This can be used as a predictive tool in seismic interpretation.
- In general, increasing fault tip length leads to an earlier onset of production decline, however the rate of decline is lower compared to shorter faults.
- Incorporating sub-seismic relay zones has a similar response, with linked relays leading to an earlier, but more gradual decline in the production rate.
- Open cases generally have a higher water production rate than their hard linked counterparts, with water production rates being higher for shorter faults.

References

ATHMER, W. & LUTHI, S.M. (2011) The Effect of Relay Ramps on Sediment Routes and Deposition: A Review. Sedimentary Geology, 242, 1-17.
CHILDS, C., WATTERSON, J. & WALSH, J.J. (1995) Fault Overlap Zones within Developing Normal Fault Systems. Journal of the Geological Society, 152, 535-549.
COWIE, P.A., GUPTA, S. & DAWERS, N.H. (2000) Implications of Fault Array Evolution for Synrift Depocentre Development: Insights from a Numerical Fault Growth Model. Basin Research, 12, 241-261.
GAUTHIER, B.D.M. & LAKE, S.D. (1993) Probabilistic Modeling of Faults Below the Limit of Seismic Resolution in Pelican Field, North Sea, Offshore United Kingdom. AAPG Bulletin, 77, 761-777.
GUPTA, A. & SCHOLZ, C.H. (2000) A Model of Normal Fault Interaction Based on Observations and Theory. Journal of Structural Geology, 22, 865-879.
JOLLEY, S.J., DIJK, H., LAMENS, J.H., FISHER, Q.J., MANZOCCHI, T., EIKMANS, H. & HUANG, Y. (2007) Faulting and Fault Sealing in Production Simulation Models: Brent Province, Northern North Sea. Petroleum Geoscience, 13, 321-340.
KIM, Y.-S. & SANDERSON, D.J. (2005) The Relationship between Displacement and Length of Faults: A Review. Earth-Science Reviews, 68, 317-334.
PEACOCK, D.C.P. & SANDERSON, D.J. (1991) Displacements, Segment Linkage and Relay Ramps in Normal Fault Zones. Journal of Structural Geology, 13, 721-733.
PEACOCK, D.C.P. & SANDERSON, D.J. (1994) Geometry and Development of Relay Ramps in Normal Fault Systems. AAPG Bulletin, 78, 147-165.
PICKERING, G., PEACOCK, D.C.P., SANDERSON, D.J. & BULL, J.M. (1997) Modeling Tip Zones to Predict the Throw and Length Characteristics of Faults. AAPG Bulletin, 81, 82-99.
ROTEVATN, A. & FOSSEN, H. (2011) Simulating the Effect of Subseismic Fault Tails and Process Zones in a Siliciclastic Reservoir Analogue: Implications for Aquifer Support and Trap Definition. Marine and Petroleum Geology, 28, 1648-1662.
TOWNSEND, C., FIRTH, I.R., WESTERMAN, R., KIRKEVOLLEN, L., HARDE, M. & ANDERSEN, T. (1998) Small Seismic-Scale Fault Identification and Mapping. Geological Society, London, Special Publications, 147, 1-25.
WALSH, J.J., BAILEY, W.R., CHILDS, C., NICOLI, A. & BONSON, C.G. (2003) Formation of Segmented Normal Faults: A 3-D Perspective. Journal of Structural Geology, 25, 1251-1262.
YIELDING, G., FREEMAN, B. & NEEDHAM, D.T. (1997) Quantitative Fault Seal Prediction. AAPG Bulletin, 81, 897-917.

Acknowledgements

The authors would like to thank Shell for permission to use the seismic and well data and internal reports. Schlumberger are thanked for the provision of academic licenses for Petrel and Eclipse.

Simon Price and Kachi Onyeagoro are thanked for their time and useful discussions during the interpretation and modelling stages of the project, and Victoria Wood is thanked for providing useful advice during reservoir simulation.

Basin Structure Group

Applied Structural Geology

UNIVERSITY OF LEEDS

Quantifying Structural Uncertainty by Forward Modelling the Seismic Response of

Alan M. Wood*, Douglas A. Paton and Richard E.L. Collier

Basin Structure Group (http://bsg.leeds.ac.uk), School of Earth and Environment, University of Leeds, Leeds, LS2 9JT, United Kingdom. *ee08amw@leeds.ac.uk

Abstract

Structural geometry is a key uncertainty in subsurface geological modelling. Precise fault-horizon intersections, fault zone complexity and fault linkage geometries are often difficult to resolve using seismic data due to effects such as amplitude deterioration and diffraction. This inevitably leads to a simplification of structural models when compared to geometries observed in analogous outcrop datasets (Figure 1). In turn this simplification leads to inaccurate representations of cross-fault reservoir juxtapositions and calculation of the associated of fault plane properties with potentially serious implications for the simulated production response.

High resolution digital elevation models (DEMs) have been used to construct detailed geological models of realistic reservoir-scale fault geometries. Simulations have subsequently been performed to assess the predicted cross-fault hydrocarbon flow. Forward modelling the seismic response of these realistic geometries allows construction of geological models based solely upon their seismically resolvable geometries. The simulated production response of the detailed, and of the seismically forward modelled geometries can then be compared.

Our results suggest that for fully open and fully breached relay zones simplification of fault structure has a relatively small impact upon predicted simulation response, regardless of reservoir thickness. Conversely, simplification of the complex fault architecture of partially breached relay

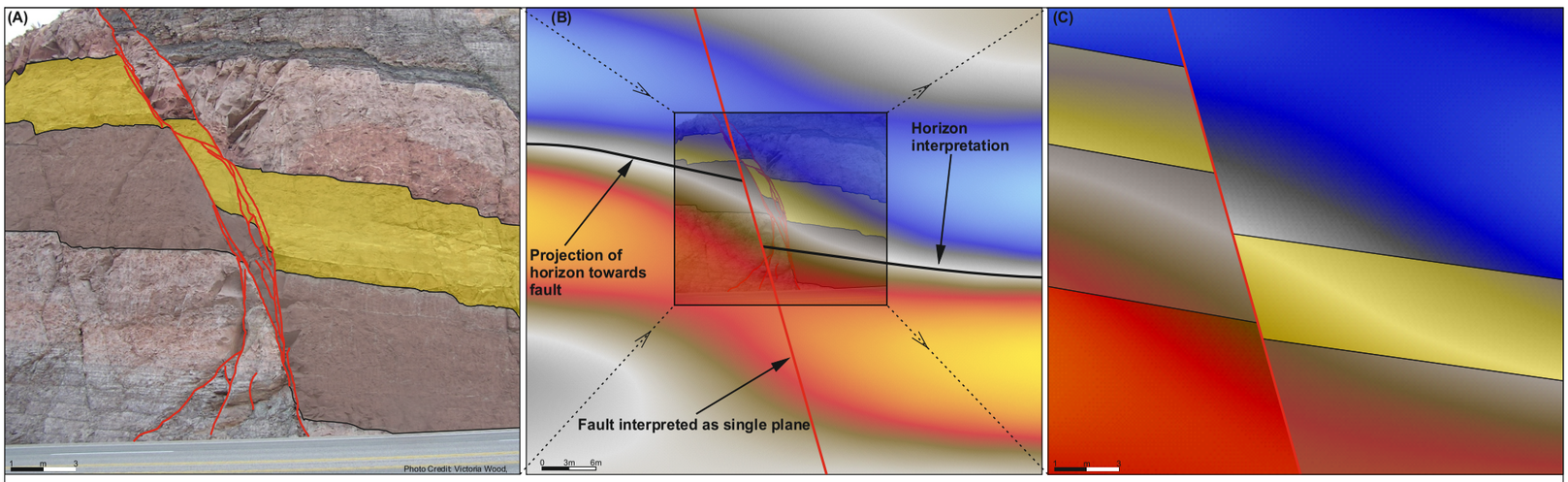

Figure 1. (A) Annotated photograph of reservoir scale faults from Utah, USA. The complex fault geometry results in partitioning of displacement across multiple fault planes, leading to the individual units being self juxtaposed. (B) Typical sub-surface seismic response of the fault structure shown in (A). The image shown in (A) is superimposed for reference. Note the lack of resolvable detail. The preclusion of detailed imaging of fault structure generally leads to faults being modelled as simple two-dimenaional planes. Uncertainty in the position of horizon-fault intersections caused by amplitude deterioration adjacent to faults is tackled by projecting reflectors towards the faults from a set distance. (C) Typical geometry of a geological model constructed from interpretation of the seismic data in (B). Interpreting the fault as a simple plane results in incorrect cross-fault

Introduction

Following their initiation as a response to stress, faults evolve through a process of growth, interaction, linkage and continued growth (Cartwright et al, 1996). For reservoir scale faults this process, along with the heterogeneous mechanical properties of the stratigraphy, results in complex fault architectures consisting of fault lenses, multiple slip surfaces and relay zones (Figure 1). This complexity often leads to a net reduction in fault throw, with the preservation of cross-fault flow pathways. In contrast, poor resolution of faults in seismic data prevents the identification of their detailed structure. Consequently faults are commonly modelled as simple two-dimensional planes. The cross-fault juxtapositions resulting from these simplified geometries may be significantly different to those present in the subsurface, with major implications for predicted cross-fault fluid flow behaviour.

Fault relay zones are often areas of reduced displacement and can hence enhance cross fault connectivity of reservoir units compared to continuous fault structures. The lateral resolution of seismic data may however prevent their identification leading to errors in the modelled cross-fault juxtapositions.

Our aims with this work are as follows;

(1) To construct geological models of detailed fault relay geometries based upon high resolution digital elevation models.

(2) To synthetically generate the seismic response expected from these detailed geometries.

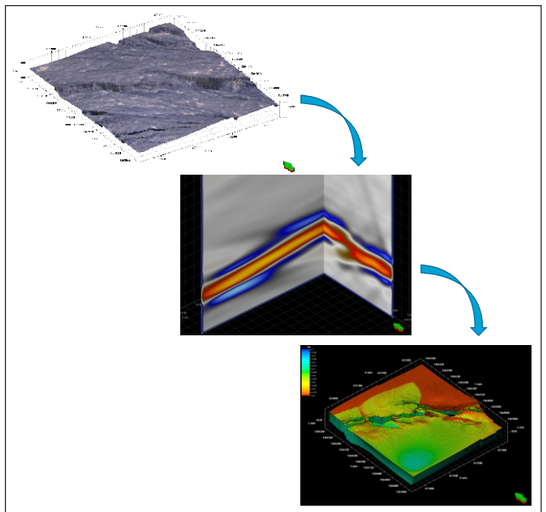

Figure 2. Summary of workflow. Outcrop geometries derived from high resolution DEMs are forward modelled to generate a synthetic seismic cube. The production response of the original, and forward modelled geometries can hence be compared to assess the role of fault

Structural Geometries

To assess the impact of architectural complexity of fault relay zones upon cross-fault fluid flow behaviour high resolution digital elevation data has been used to construct detailed structural models. This data has a resolution of up to 0.5m and is located at outcrops in Utah, USA and Afar, Ethiopia. These areas have little vegetation and have experienced limited erosion and hence allow the full detail of the fault architecture to be resolved. Open, partially breached and fully breached relay geometries of similar dimensions have been selected, all of which are at the scale of intra-reservoir faults (Figure 3). To preserve the maximum feasible detail the structural models have been constructed using a horizontal grid cell geometry of 5m (Figure 3). This is significantly finer than typical geological and simulation grids, generally having cell dimensions of 25 to 250m. Each geocellular grid has been populated with four stratigraphic models prior to seismic forward modelling and reservoir simulation (Figure 4).

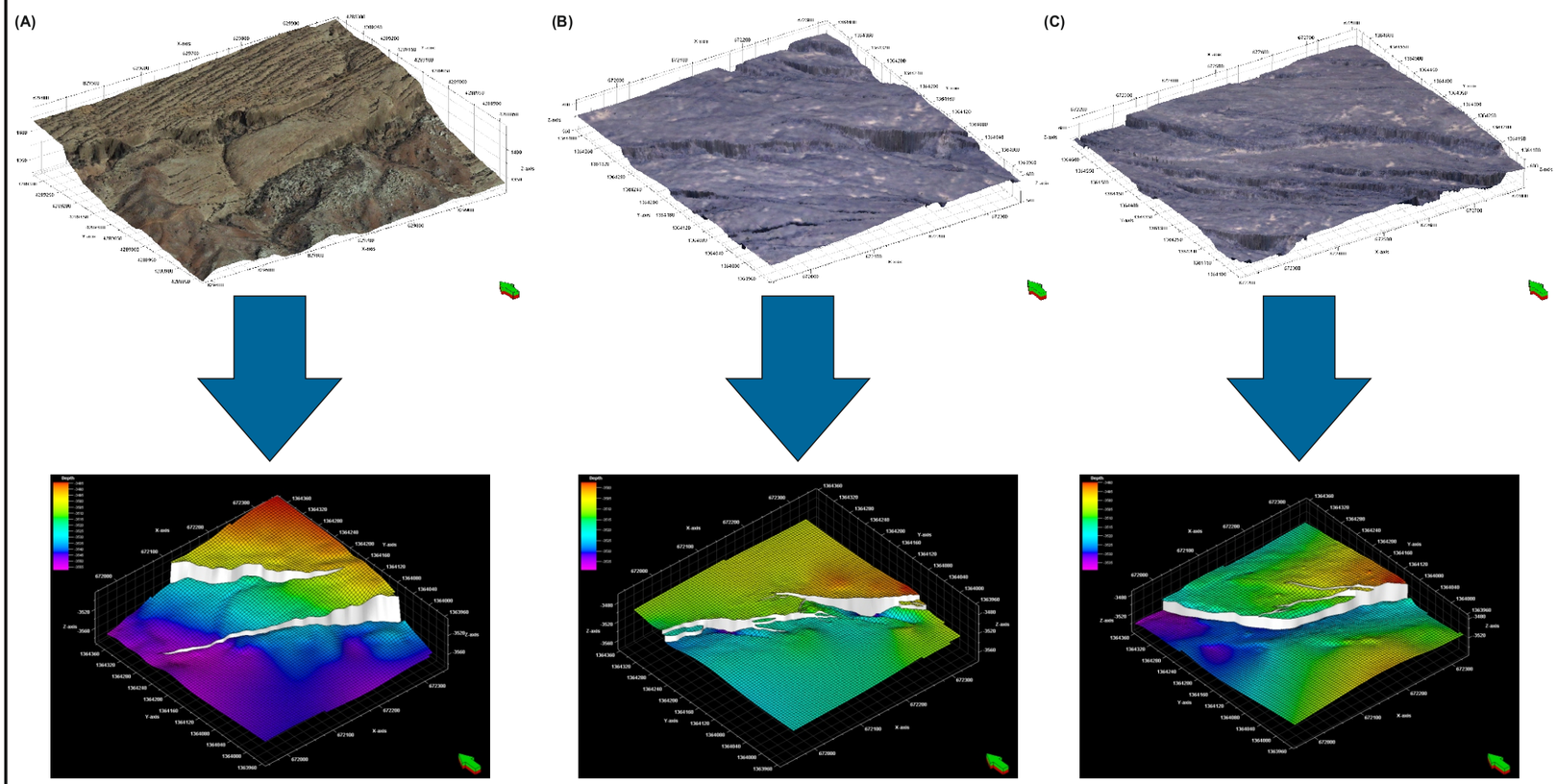

Figure 3. Digital Elevation Models (DEMs) draped with aerial photography with the corresponding structural models shown below. Each DEM surface has been translated to a depth of 3500m. The geocellular grids have horizontal cell dimensions of 5x5m. Faults are shown in white with the horizons coloured by depth. (A) Open relay structure from Utah, USA. (B) Partially breached relay structure from Afar, Ethiopia. (C) Fully breached relay structure from Afar, Ethiopia.

Petrophysical Property Population

Each structural model has been populated with four separate stratigraphic models (Figure 4). These consist of reservoir intervals whose thicknesses either approximate the throw of the faults, or are lower than the fault throws. The rational is to test whether geometric fault complexity, such as multiple slip surfaces, allows self juxtaposition of a thin reservoir interval across a fault (Figure 1). If so then the cross-fault fluid flow characteristics will vary significantly with respect to the seismically resolvable geometry.

The reservoir intervals have been populated with either a homogenous, high permeability reservoir or with a vertically variable stratigraphy derived from an upscaled North Sea exploration well drilled through a typical prograding shoreface sequence (Figure 4b, d). Petrophysical properties used include porosity, permeability and Vshale.

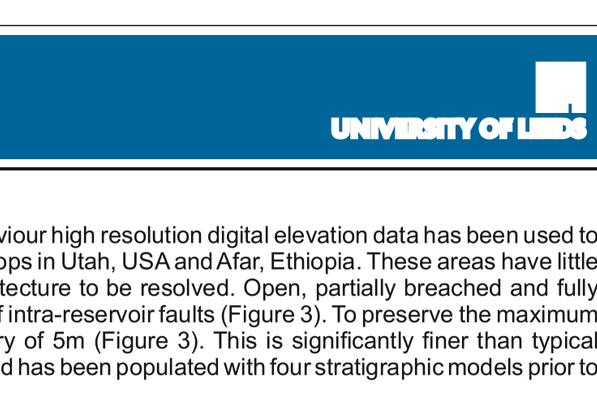

Figure 4. Well sections of properties (porosity, permeability, Vshale) used for petrophysical population. (A) Reservoir interval thickness ≈ fault throw, homogenous stratigraphy. (B) Reservoir interval thickness ≈ fault throw, well stratigraphy. (C) Reservoir interval thickness < fault throw. (D) Reservoir interval thickness < fault throw, well stratigraphy.

Forward Modelling Workflow

The workflow to forward model the seismic response of a DEM surface involves multiple steps and processes. These are outlined below and on the following page.

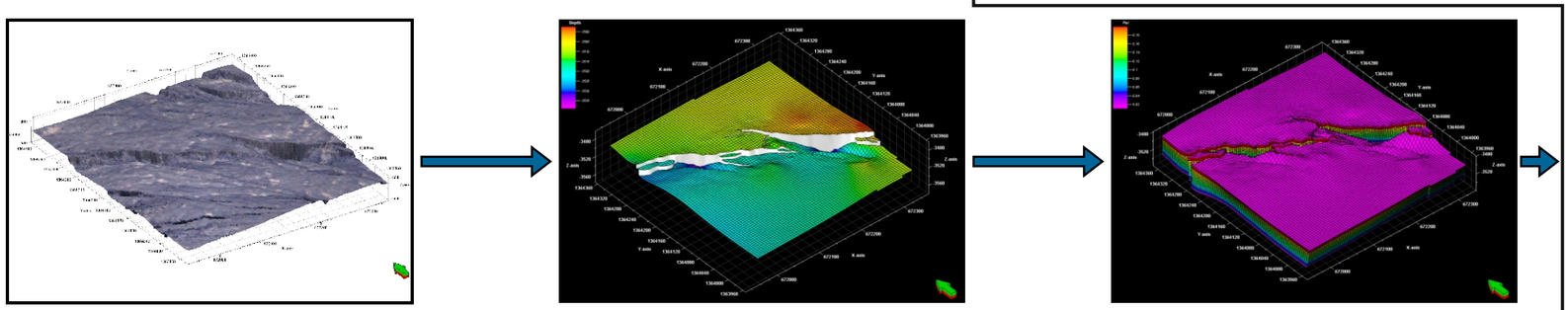

Import of high resolution digital elevation data into geological modelling software.

Digital elevation data is used to construct a fine-scale geocellular grid incorporating the realistic fault-horizon geometries seen at outcrop scale.

The geocellular grid is populated with petrophysical properties including porosity, permeability, Vsand and Vshale. The pore pressure is also modelled as a grid property, as is the fluid saturation.

Basin Structure Group

Applied Structural Geology

UNIVERSITY OF LEEDS

Forward Modelling Workflow, Continued

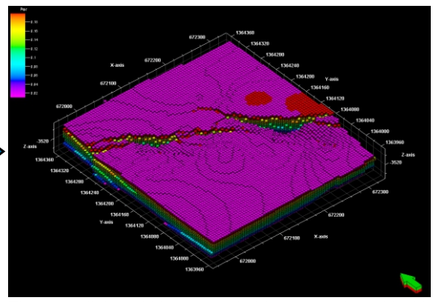

The geocellular grid is re-sampled into a regular grid with uniform cell dimensions prior to export to the forward modelling software.

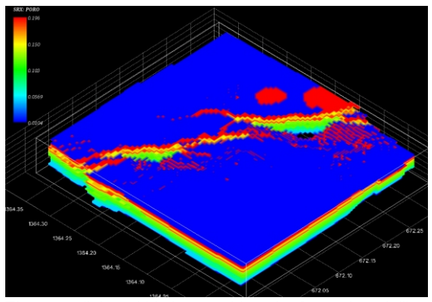

The geocellular grid is imported into the forward modelling software. Vsand and Vshale are used to calculate rock density using values of 2.65g/cm^3 and 2.6g/cm^3 respectively. Pore pressure values are used to calculate the confining and effective pressures assuming a vertical pressure gradient of 22.5 MPa/km.

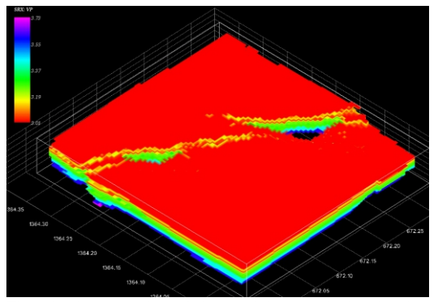

The elastic properties of the model are calculated using Gassmann's theory with the properties of the saturating fluids, and of the individual solid components (i.e. Sand and Shale) as inputs. A Reuss mixing model is assumed.

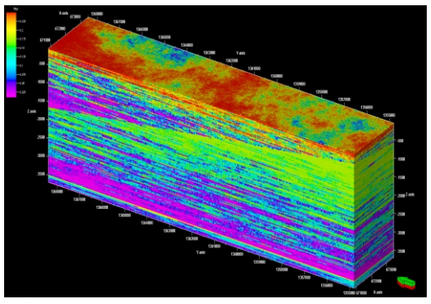

A Background property model is constructed within the geological modelling software (porosity is shown here). This represents the overburden above the detailed target area, and is used to calculate seismic wave propagation effects between the survey source/recievers and the target. It is exported to the forward modelling software where its elastic and reflectivity properties are determined.

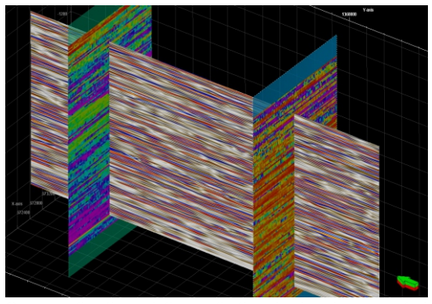

Cross section through the synthetic seismic cube generated using the background model. Sections through the porosity (left) and Vshale (right) models used in its derivation are also shown.

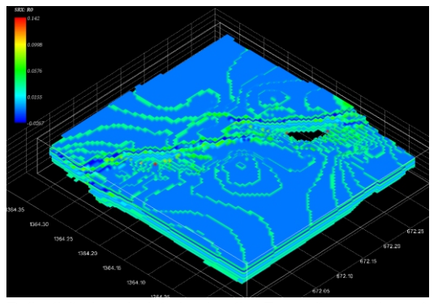

Reflectivity is calculated using the Zoeppritz equations. A target area is defined around the model where the synthetic cube is to be generated.

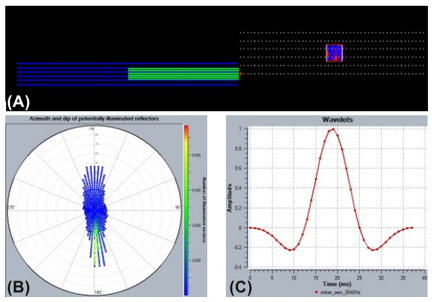

A 3D survey is designed (A), and the dip and azimuth of potentially illuminated reflections calculated (B). This is combined with an input wavelet (C), the elastic and reflectivity properties of the target area, and of the background model, to generate the synthetic seismic cube.

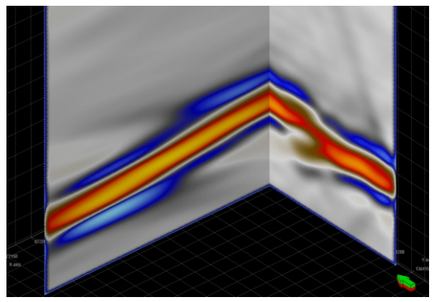

The elastic, reflectivity and background models are combined with the survey design and input wavelet to generate a synthetic prestack depth migrated (PSDM) seismic cube using Simulated Prestack Local Imaging (SimPLI; Gjøystdal et al, 2007). This can be saved as a segy file for visualisation and interpretation.

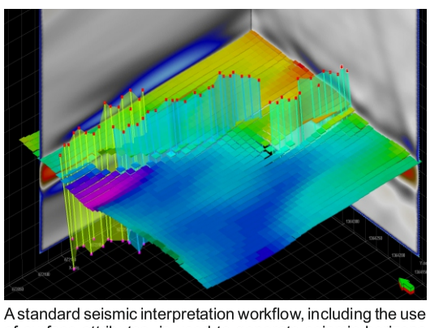

A standard seismic interpretation workflow, including the use of surface attributes, is used to generate seismic horizons and fault interpretations.

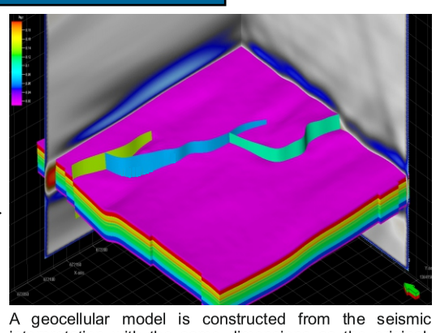

A geocellular model is constructed from the seismic interpretation with the same dimensions as the original, detailed model. It is populated with identical petrophysical properties.

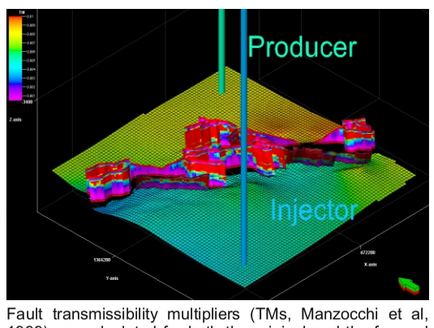

Fault transmissibility multipliers (TMs, Manzocchi et al, 1999) are calculated for both the original and the forward modelled geometries. A simulation case is defined including well design, fluid model, rock physics functions and development strategy.

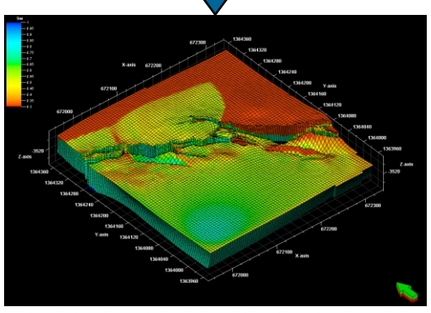

Water Saturation at final simulation timestep for original geometry.

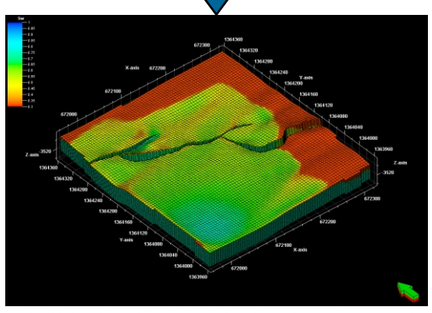

Water Saturation at final simulation timestep using geometry derived from forward modelled seismic data.

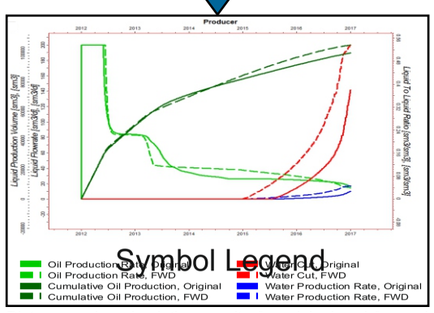

Plot comparing simulation results for original and forward modelled fault geometries.

Forward Modelled Seismic Data

The seismic volumes generated by forward modelling the response of the detailed, outcrop scale geometries observed in the DEM data allow only the coarse scale fault geometry to be resolved (Figure 5). Fault bound lenses, small scale antithetic faults and other minor structures crucial to maintaining cross-fault reservoir:reservoir juxtapositions are identifiable only as a single, planar structure in cross section. In three dimensions the presence of relay zones is elucidated to by abrupt changes in fault strike, with their position and geometry subject to significant uncertainty. However their identification is only possible when the seismic interpretation is performed on a line by line basis, impractical for many industry datasets.

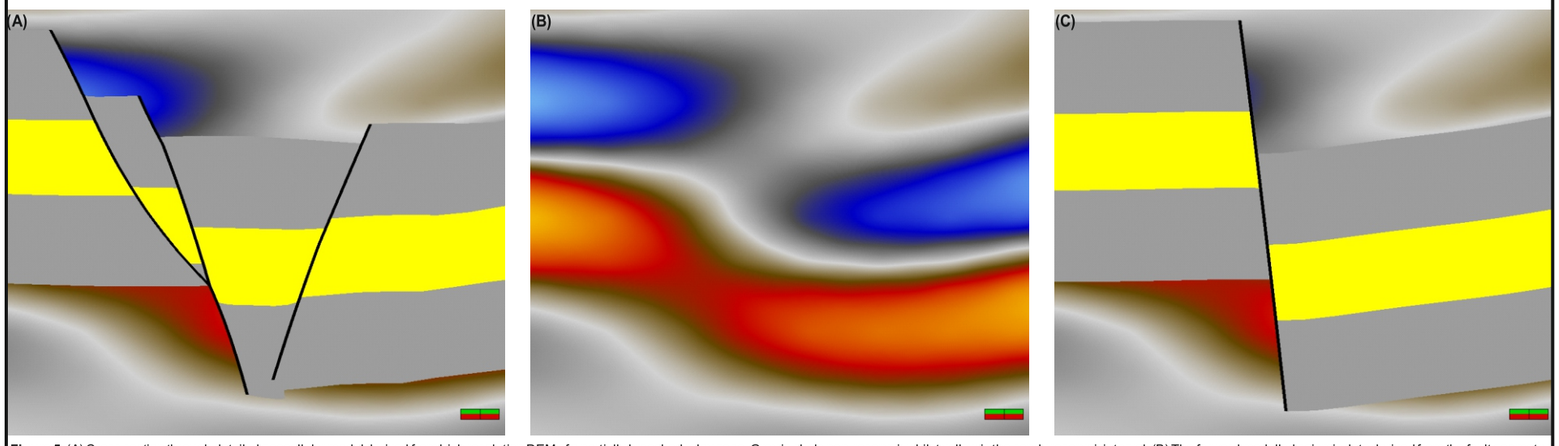

Figure 5. (A) Cross section through detailed geocellular model derived from high resolution DEM of a partially breached relay zone. Grey is shale non-reservoir whilst yellow is the sandy reservoir interval. (B) The forward modelled seismic data derived from the fault geometry and petrophysical properties shown in (A). (C) The geocellular model derived from interpretation of the forward modelled seismic data shown in (B). Note the differences in cross-fault reservoir juxtapositions between the detailed (A), and forward modelled (C) geometries.

Simulation Parameters

To test the impact of the loss of fault resolution inherent in seismic data, production simulations were performed on both the outcrop, and the seismically resolvable geometries.

Fault transmissibility multipliers were calculated using the Shale Gouge Ratio (SGR) mixing algorithm (Yielding et al, 1997), with a mid-range permeability based on the relationship proposed by Jolley et al (2007). Mercury-air fault threshold pressures of 20 Bars (290 psi) were also assigned to each fault.

A waterflood development strategy running over a course of five years was employed. This consisted of single injection and production wells located in the hangingwall and footwall respectively, with an initial production rate of 200 m^3/day (1258 bbl). The results of these simulations are summarised in figure 6.

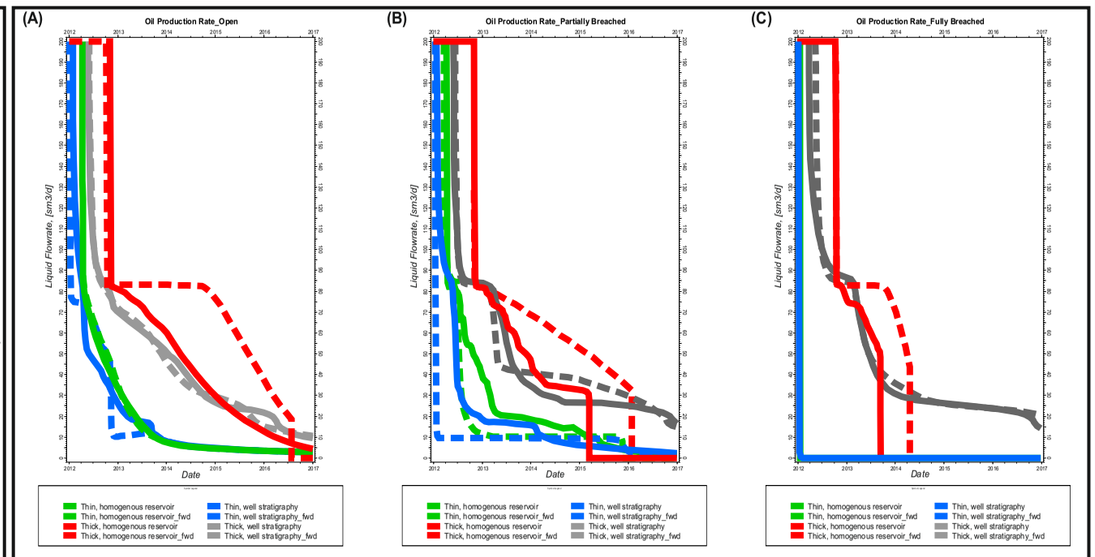

Figure 6. Plots of simulated oil production rate over time for both detailed (solid lines) and seismically resolvable (dashed lines) geometries. results are colour coded by the stratigraphy used. Green=thin, homogenous stratigraphy. Red=thick homogenous stratigraphy. Blue=thin, well stratigraphy. Grey=thick, well stratigraphy. (A) Open relay structure. (B) Partially breached relay structure. (C) Fully breached relay structure. The majority, but not all, of stratigraphies lead to comparable simulation results for the detailed and seismically resolvable geometries for the open (A) and fully breached (C) relay structures. In contrast, for the partially breached relay structure (B) the production responses of the detailed and seismically resolvable geometries are significantly different irrespective of the stratigraphy.

Selected Results

The number of simulations run prohibits reviewing them all here, however a selection are shown below. These encompass when, and when not, incorporating detailed fault geometries as observed at outcrop influences simulated production relative to the seismically resolvable geometries. The water saturation at the final timestep for both detailed and seismically resolvable geometries are shown, along with the cross-fault reservoir:reservoir juxtapositions for each model and the plots of production rate and cumulative production over the course of the simulations.

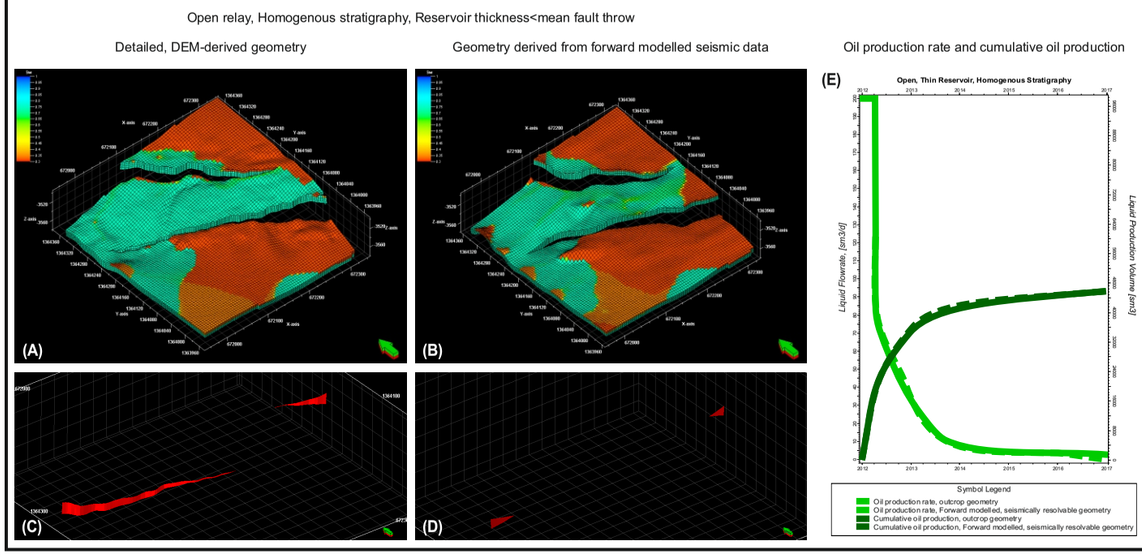

Figure 7. Open relay structure (see figure 3(A)) populated with a homogenous stratigraphy with a lower thickness than the mean fault throw. (A) Water saturation at final timestep, outcrop geometry. (B) Water saturation at final timestep, seismically resolvable geometry. (C) Cross-fault reservoir:reservoir juxtapositions, outcrop geometry. (D) Cross-fault reservoir:reservoir juxtapositions, seismically resolvable geometry. (E) Oil production rate and cumulative oil production versus time.

The water saturation describes a similar pattern in both geometries at the final timestep (A, B). This is reflected in the almost identical production rates and volumes for both the outcrop and forward modelled geometries (E). Since the relay zone is open rather than breached the area of cross-fault reservoir:reservoir juxtaposition is largely irrelevant as the least resistant flow pathway is simply along the un-breached relay ramp. In situations where the relay zone can clearly be identified as being open, the small scale fault geometry is relatively insignificant for cross-fault fluid flow behaviour.

Basin Structure Group

Applied Structural Geology

UNIVERSITY OF LEEDS

Selected Results, Continued

Partially breached relay, Well stratigraphy, Reservoir thickness<mean fault throw

Detailed, DEM-derived geometry | Geometry derived from forward modelled seismic data | Oil production rate and cumulative oil production

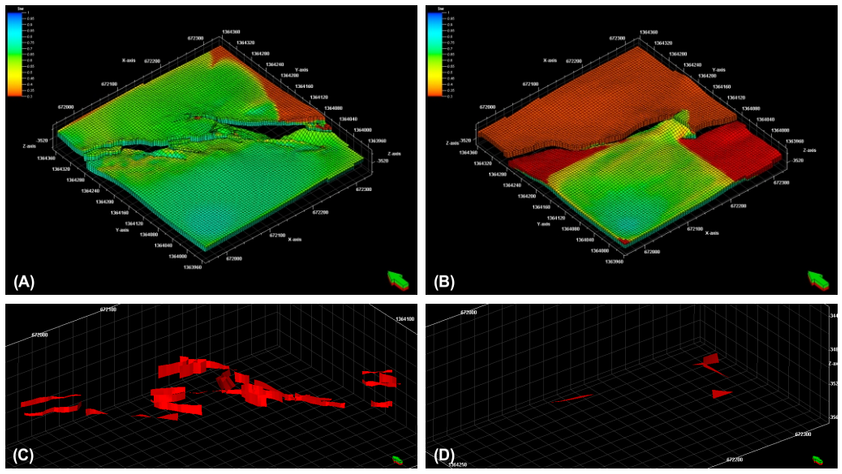

Figure 8. Partially breached relay structure (see figure 3(B)) populated with a well-derived stratigraphy with a lower thickness than the mean fault throw. (A) Water saturation at final timestep, outcrop geometry. (B) Water saturation at final timestep, seismically resolvable geometry. (C) Cross-fault reservoir:reservoir juxtapositions, outcrop geometry. (D) Cross-fault reservoir:reservoir juxtapositions, seismically resolvable geometry. (E) Oil production rate and cumulative oil production versus time.

The difference in the water saturation between the outcrop (A) and the seismically resolvable (B) geometry clearly demonstrates the influence of fault architecture on cross-fault hydrocarbon flow in this scenario. The partitioning of displacement across multiple slip surfaces, together with the presence of fault bound lenses, results in a significant number of cross-fault juxtaposition windows for the outcrop derived model (C). In contrast, the low reservoir thickness, combined with the interpretation of the fault as a single plane, leads to limited cross-fault self juxtaposition for the seismically resolvable geometry (D). The influence on hydrocarbon recovery is evident on the production plot (E). The outcrop geometry maintains a consistently higher production rate than the seismically resolvable geometry, since the cross fault flux is severely restricted in the latter due to the low area of cross fault juxtapositions. As a consequence the cumulative

Fully breached relay, Well stratigraphy, Reservoir thickness=mean fault throw

Detailed, DEM-derived geometry | Geometry derived from forward modelled seismic data | Oil production rate and cumulative oil production

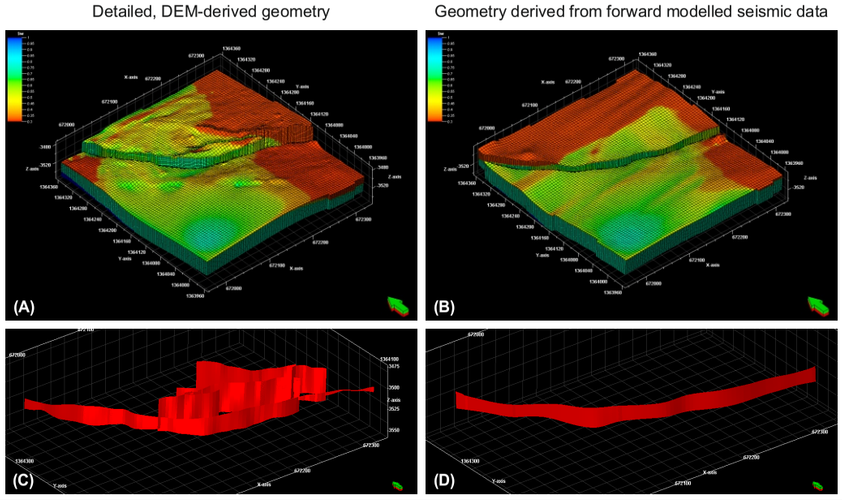

Figure 9. Fully breached relay structure (see figure 3(C)) populated with a well-derived stratigraphy with a thickness approximating the mean fault throw. (A) Water saturation at final timestep, outcrop geometry. (B) Water saturation at final timestep, seismically resolvable geometry. (C) Cross-fault reservoir:reservoir juxtapositions, outcrop geometry. (D) Cross-fault reservoir:reservoir juxtapositions, seismically resolvable geometry. (E) Oil production rate and cumulative oil production versus time.

The water saturations of the outcrop (A) and seismically resolvable (B) geometries show significant differences at the final timestep. Despite this, the production rates and volumes remain very similar (E). The broad scale reservoir:reservoir juxtapositions remain similar (C, D) although the outcrop geometry includes a number of additional small scale faults. These faults do not appear to influence the cross-fault flux as evidenced by the almost identical production rate curves for the two geometries (E). However, these faults do appear to act as moderate baffles, resulting in a deflection of flow around their tips (A). This deflection of the water front by minor faults may be significant in terms of the timing of water breakthrough at production wells.

Conclusions

• Fault architectures and fault relay geometries resolvable in seismic data are substantially less complex than their outcrop equivalents.

• The three dimensional variability in fault geometry and displacement observed from outcrop examples may result in significantly larger areas of cross-fault reservoir:reservoir juxtapositions than can be identified from seismic data. In addition, the difference in the calculated transmissibility multipliers for the different geometries may be non-trivial.

• Additional cross-fault reservoir self-juxtaposition due to fault geometric complexity may lead to flow pathways being present in the subsurface in situations where the seismically resolvable structure appears to form a juxtaposition seal.

• Partially breached relays are often only resolvable as single through-going structures in seismic data. The cross-fault flow characteristics of resolvable versus real geometries may be considerably different. The magnitude of this difference is dependent upon the thickness of the reservoir interval relative to the mean fault displacement, and is most significant for situations where the reservoir thickness approximates, or is less, than the fault displacement.

• There is limited difference in the production response of open and fully breached relays between realistic and seismically resolvable geometries.

• Small scale faults, un-resolvable in seismic data may have the potential to act as baffles during production. Deflection of the water flood front around the tips of such faults may lead to variations in the timing of water breakthrough at production wells.

References

Cartwright, J.A., Mansfield, C. & Trudgill, B. 1996. The Growth of Normal Faults by Segment Linkage. Geological Society, London, Special Publications, 99, 163-177.

Gjøystal, H., Drottning, Å., Lecomte, I. & Branston, M. 2007. Advances in Quantitative Model-Assisted Seismic Interpretation. First Break, 25, 95-102.

Jolley, S.J., Dijk, H., Lamens, J.H., Fisher, Q.J., Manzocchi, T., Eikmans, H. & Huang, Y. 2007. Faulting and Fault Sealing in Production Simulation Models: Brent Province, Northern North Sea. Petroleum Geoscience, 13, 321-340.

Manzocchi, T., Walsh, J.J., Nell, P. & Yielding, G. (1999) Fault Transmissibility Multipliers for Flow Simulation Models. Petroleum Geoscience, 5, 53-63.

Yielding, G., Freeman, B. & Needham, D.T. 1997. Quantitative Fault Seal Prediction. AAPG Bulletin, 81, 897-917.

Acknowledgments

The authors would like to thank the following for contributing support to this work;

Schlumberger

BSG

CiPEG Centre for Integrated Petroleum Engineering and Geoscience

www.bsg.leeds.ac.uk

Comparing Simulated Production Response Across Realistic and Seismically Forward Modelled Fault Geometries

Alan Wood*, Richard Collier, Douglas Paton
Basin Structure Group, University of Leeds

CiPEG | Centre for Integrated Petroleum Engineering and Geoscience

Basin Structure Group

Overview

Concept

Use a range of data and software applications to model the seismic response of complex fault geometries.

Aim

When does the difference between seismically resolvable and sub-seismic fault geometries impact production?

Fault Growth

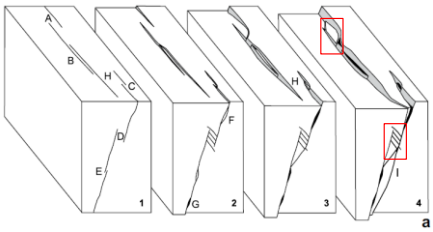

Childs et al, 2009 (JSG)

Faults in Seismic Data

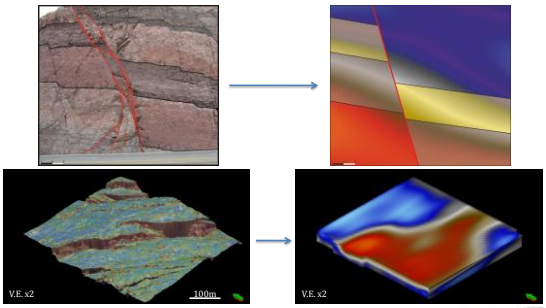

Workflow (1) – Static Model

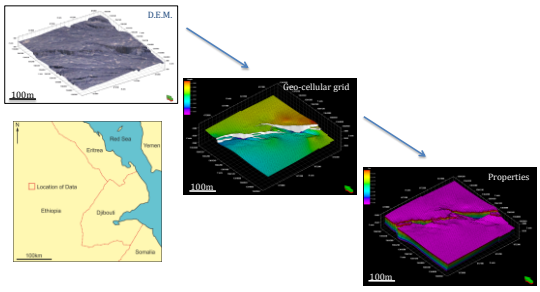

Workflow (2) – Forward Model

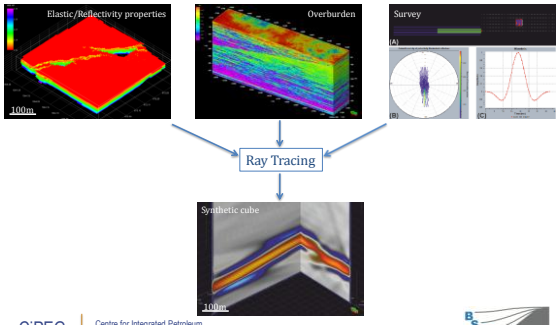

Workflow (3) – Interpretation, Model 2

UNIVERSITY OF LEEDS

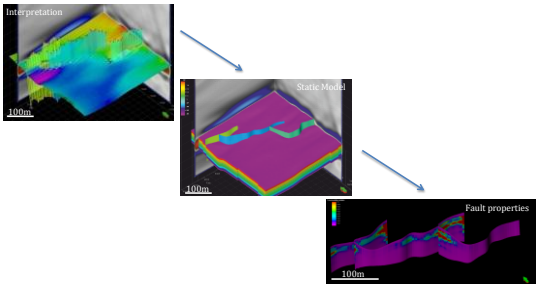

Workflow (4) – Simulation

UNIVERSITY OF LEEDS

Outcrop-Derived Geometry

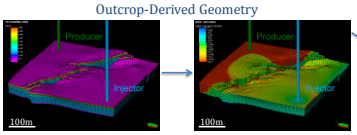

Seismically Resolvable Geometry

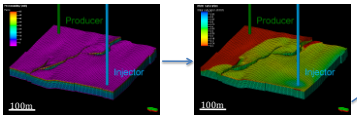

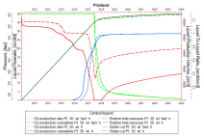

Uncertainty

UNIVERSITY OF LEEDS

Geometry x Stratigraphy x Fault TMs

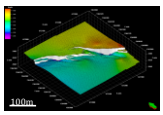

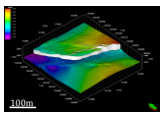

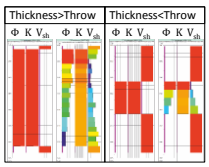

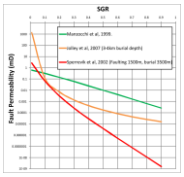

x Forward Modelled Geometries = 48 simulation runs

Results (1) Reservoir Thickness>Mean Throw

UNIVERSITY OF LEEDS

Outcrop-Derived Geometry

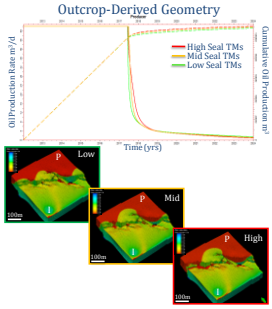

Seismically Resolvable Geometry

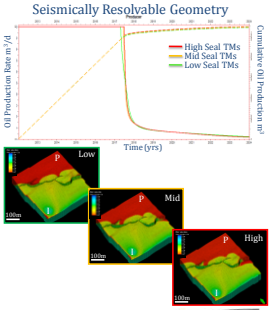

Results (2) Reservoir Thickness<Mean Throw

UNIVERSITY OF LEEDS

Outcrop-Derived Geometry

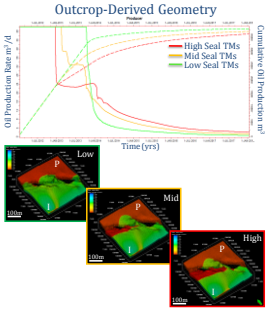

Seismically Resolvable Geometry

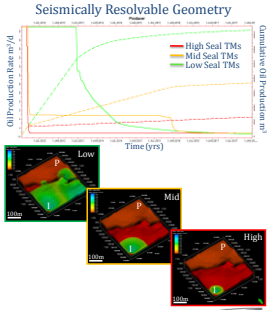

Outcrop v Seismic Juxtapositions

UNIVERSITY OF LEEDS

Outcrop Geometry

Forward Modelled Seismic

Seismically Resolvable Geometry

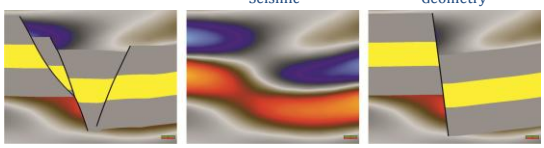

Juxtaposition Area

UNIVERSITY OF LEEDS

Outcrop-Derived Geometry | Seismically Resolvable Geometry

Reservoir Thickness>Mean Fault Throw

Reservoir Thickness<Mean Fault Throw

Results Summary: Outcrop v Seismic

UNIVERSITY OF LEEDS

	Partially Breached	Breached
Thickness>Throw Layered Stratigraphy	Little difference	●
Thickness>Throw Homogenous Stratigraphy	Little difference	Little difference
Thickness<Throw Layered Stratigraphy	● ● ●	No difference
Thickness<Throw Homogenous Stratigraphy	● ● ●	No difference

Implications (1)

UNIVERSITY OF LEEDS

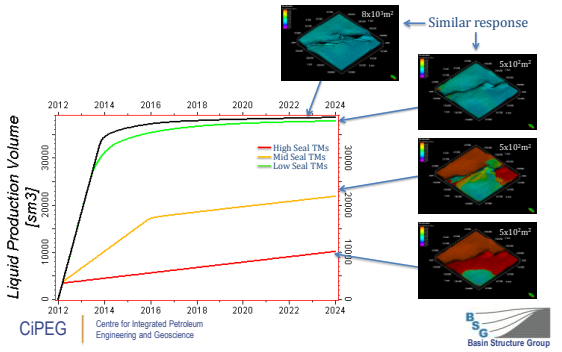

Implications (2)

UNIVERSITY OF LEEDS

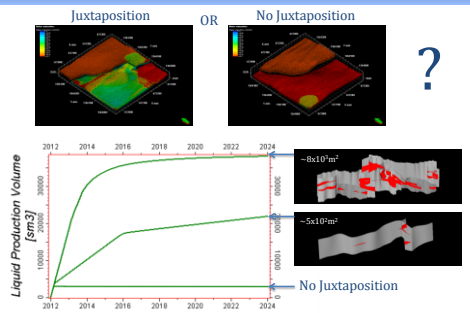

Workflow?

UNIVERSITY OF LEEDS

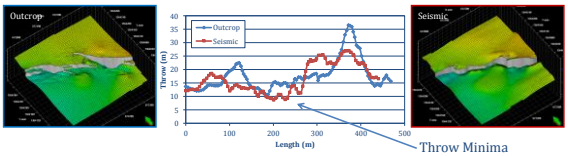

- Identify displacement Minima
- Stochastic population of low-throw areas (e.g. Manzocchi et al, 2008)
- Reduce throw along faults
- Modify TMs

Conclusions: Case Specific

UNIVERSITY OF LEEDS

- Results are specific to grid properties, simulation model etc
- Impact of fault properties on across-fault flow greater where juxtaposition area small
- Small juxtaposition windows can result in large across fault flux
- Relative importance of fault properties tends to decrease with increasing juxtaposition area

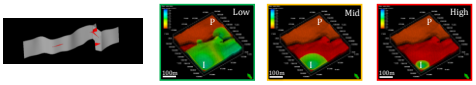

Conclusions: General

UNIVERSITY OF LEEDS

- Significant differences between seismically resolvable and realistic geometries
- Seismically resolvable geometries tend to lead to underestimates in across-fault reservoir juxtaposition, with disparity greater when reservoir thickness is less than mean throw
- Fault juxtaposition is primary control on across-fault flux, fault properties secondary

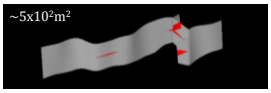

CiPEG | Centre for Integrated Petroleum Engineering and Geoscience

Basin Structure Group

Acknowledgements

UNIVERSITY OF LEEDS

Questions?

Acknowledgements

Schlumberger

NORSAR Innovation AS

RDR

CiPEG | Centre for Integrated Petroleum Engineering and Geoscience

Basin Structure Group

Predicting, Incorporating and Simulating the Effects on Hydrocarbon Production of Sub-Seismic Fault Tips and Breached Relay Zones

Alan Wood[1*], Kachi Onyeagoro[2], Paton, D.A.[1], Marshall, J.D.[2], Price. S.P.[3], Collier, R.E.L.[1].

(1) Basin Structure Group, School of Earth and Environment, University of Leeds, Leeds, UK, LS2 9JT
(2) Shell Upstream International Europe, Aberdeen, UK, AB12 3FY
(3) Shell Global Solutions, Rijswijk, NL, 2288 GS

*Contact email: ee08amw@leeds.ac.uk

CiPEG | Centre for Integrated Petroleum Engineering and Geoscience

Basin Structure Group

Background

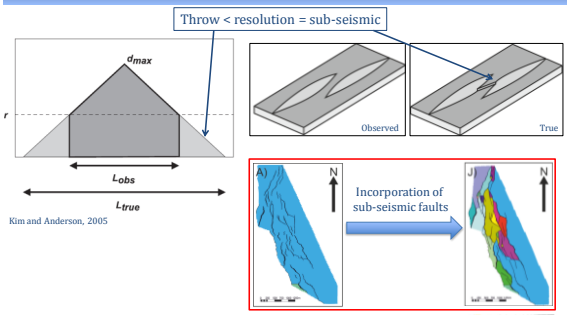

Kim and Anderson, 2005

Aims

(1) Review methodologies of sub-seismic fault tip prediction

(2) Develop predictive tool for identifying sub-seismic breached relays

(3) Assess impact of sub-seismic structure on reservoir segmentation

(4) Assess impact on simulated production

(5) Assess the impact of varying fault threshold pressure

Study area: Sub-set of Penguins Cluster

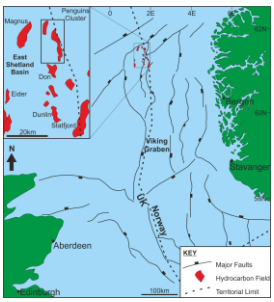

Roberts et al., 1995

Sub-seismic fault tips

Two methodologies;

- Statistical Prediction
- Geometric Prediction

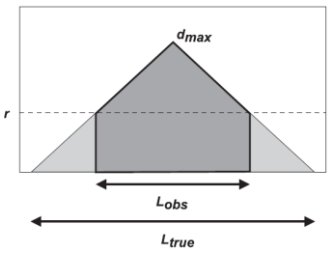

Statistical approach (1)

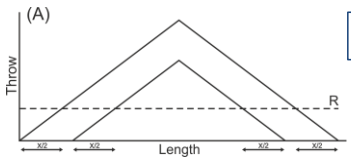

$$t_{max}=cL^{n,\,(n=1)}$$

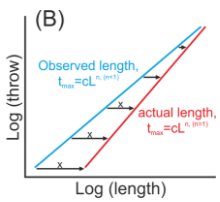

- Assumes faults are fractal
- Small faults have a greater proportion of their length below seismic resolution
- Linear relationship between length and throw

Statistical approach (2)

UNIVERSITY OF LEEDS

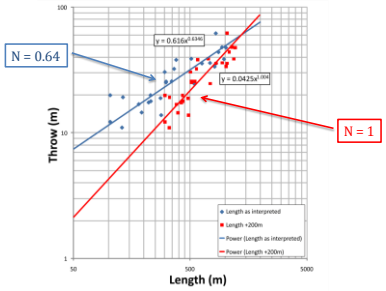

Throw gradient approach (1)

UNIVERSITY OF LEEDS

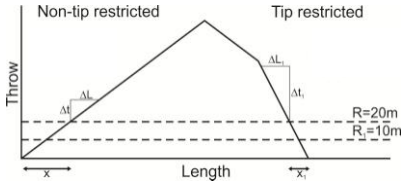

Tip Length = resolution/throw gradient

- Accounts for fault interaction
- Requires estimate of data resolution
- Time consuming
- Uses observable dimensions

Throw gradient approach (2)

UNIVERSITY OF LEEDS

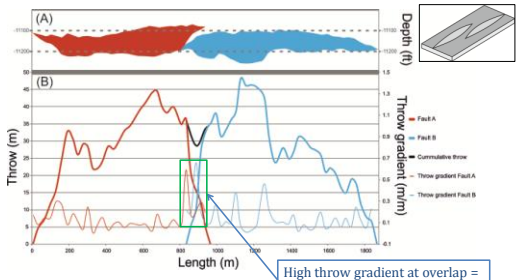

High throw gradient at overlap = shorter sub-seismic tip length

Statistical v Gradient approach

UNIVERSITY OF LEEDS

Pros	Cons
Statistical approach	
Quick	Assumes faults are fractal
	Assumes linear relationship between length and throw
	Does not account for fault interaction and linkage
Gradient approach	
Accounts for fault interaction and linkage	Time consuming
Uses observable dimensions	Requires estimate of resolution of data

Fault Tip Extension

UNIVERSITY OF LEEDS

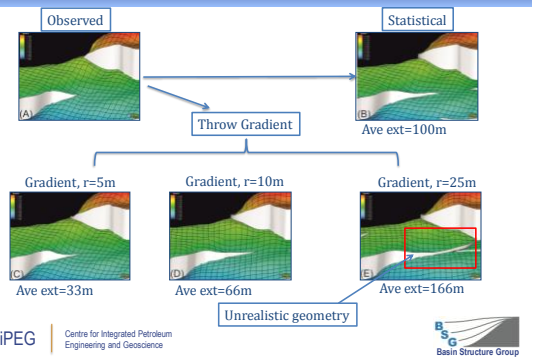

Breached Relays

UNIVERSITY OF LEEDS

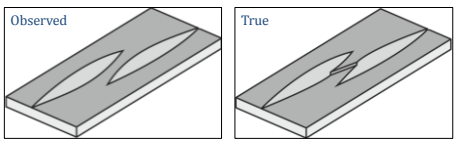

Breached Relays (1)

UNIVERSITY OF LEEDS

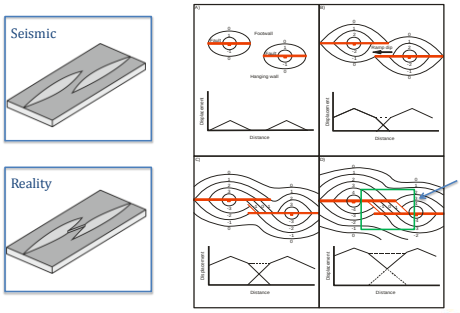

Breached Relays (2)

UNIVERSITY OF LEEDS

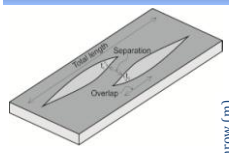

t_1+t_2 = Relay Throw

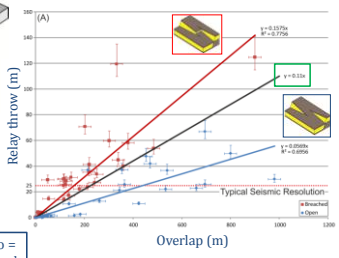

Higher Relay throw:Overlap ratio = more likely for relay to be breached

Effect on Segmentation

UNIVERSITY OF LEEDS

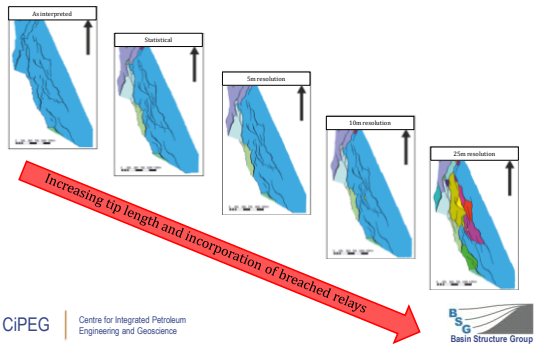

Simulation set-up

UNIVERSITY OF LEEDS

- Well-derived stratigraphy and petrophysical properties
- Locally applicable fault TMs (Jolley et al., 2007)
- Producer-Injector pair, 40yr Simulation run-time
- Low-, Mid-, and High-case fault threshold pressures (Bretan et al., 2003)

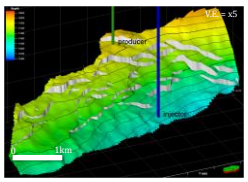

Results (1)

UNIVERSITY OF LEEDS

Lower water production rate with increasing reservoir segmentation

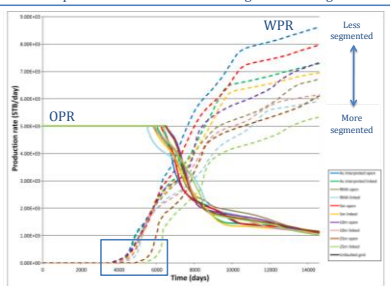

Results (2)

UNIVERSITY OF LEEDS

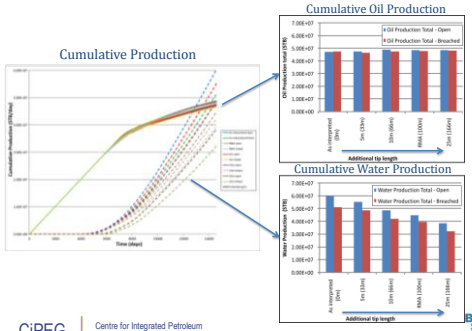

Results Summary

UNIVERSITY OF LEEDS

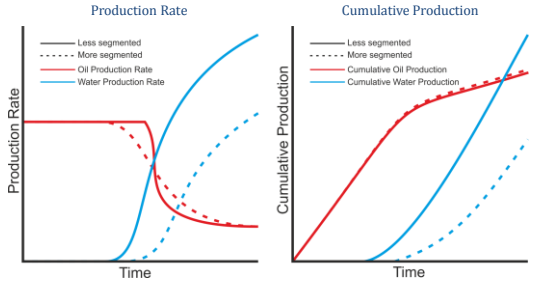

Fault Threshold Pressure

UNIVERSITY OF LEEDS

- Pressure which must be exceeded to allow across-fault flow
- Function of Interfacial tension, contact angle, capillary radius (Schowalter, 1979; Watts, 1987)
- Can be measured in lab and calibrated against clay content (Sperrevik et al., 2002; Bretan et al., 2003)
- High-, mid- and low-cases used (300, 142, 30psi)

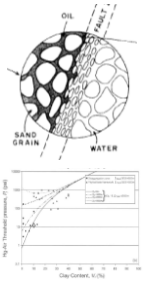

Pressure

UNIVERSITY OF LEEDS

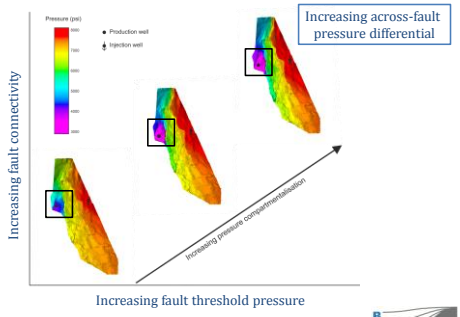

Oil Saturation

UNIVERSITY OF LEEDS

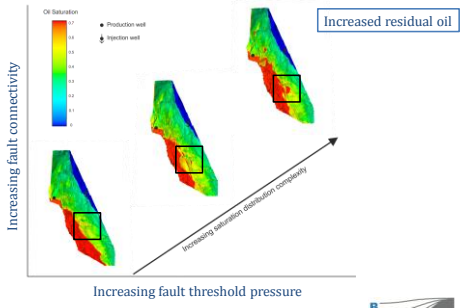

Results Summary

UNIVERSITY OF LEEDS

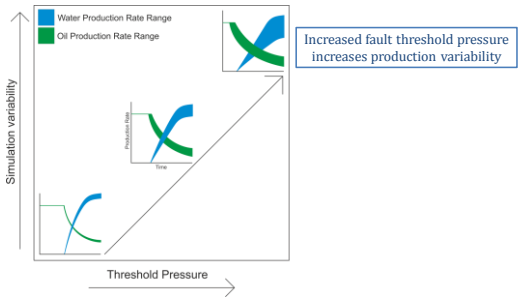

Conclusions

UNIVERSITY OF LEEDS

- Throw gradient approach geologically more reasonable than statistical approach for fault tip estimation
- Relationship between cumulative relay throw/overlap and relay integrity
- Incorporating sub-seismic relay zones and fault tips leads to earlier, but slower production rate decline
- Incorporating sub-seismic structures tends to reduce the water cut of production wells
- Increasing fault threshold pressure leads to greater variability in simulation results

Acknowledgements

UNIVERSITY OF LEEDS

Questions?

Acknowledgements

Schlumberger

CiPEG | Centre for Integrated Petroleum Engineering and Geoscience

Basin Structure Group

Simulated Hydrocarbon Production across Outcrop-Derived Versus Seismically-Resolvable Faults

Alan Wood, Richard Collier, Douglas Paton
Basin Structure Group, University of Leeds

CiPEG | Centre for Integrated Petroleum Engineering and Geoscience

Basin Structure Group

Overview

Aim

When does the difference between seismically resolvable and sub-seismic fault geometries impact production?

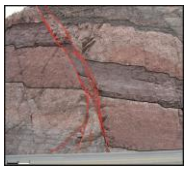

Fault Growth and Complexity

Rift/Basin Scale | Field/Reservoir Scale

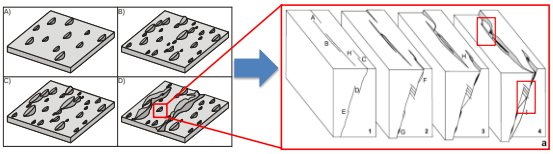

Cowie, 1998 (JSG) | Childs et al, 2009 (JSG)

+ Mechanical Heterogeneity

= Faults are complex!

Faults in Seismic Data

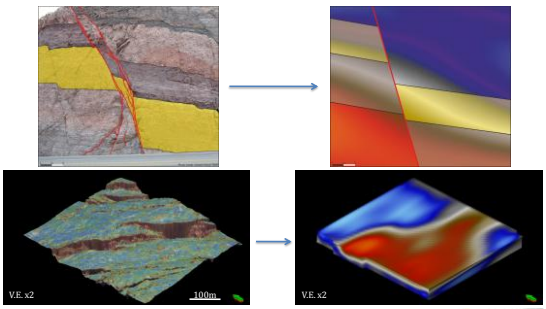

D.E.M.

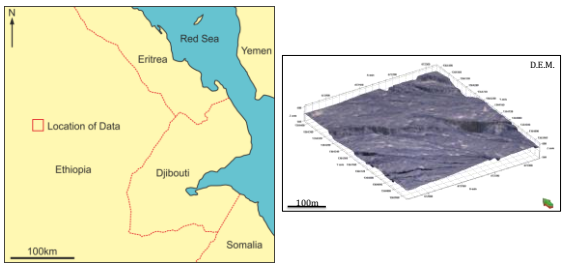

Workflow

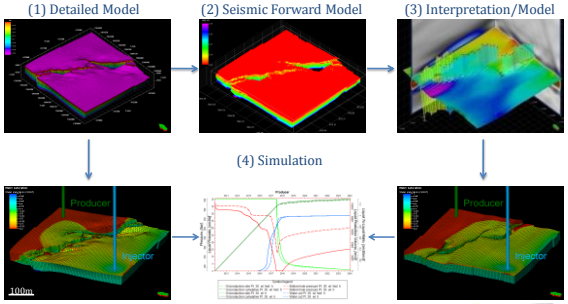

Uncertainty

UNIVERSITY OF LEEDS

Geometry x Stratigraphy x Fault TMs

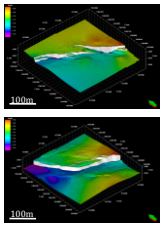

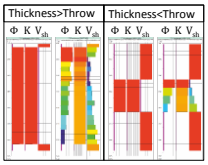

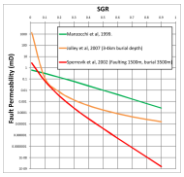

x Forward Modelled Geometries = 48 simulation runs

Results (1) Reservoir Thickness>Mean Throw

UNIVERSITY OF LEEDS

Outcrop-Derived Geometry

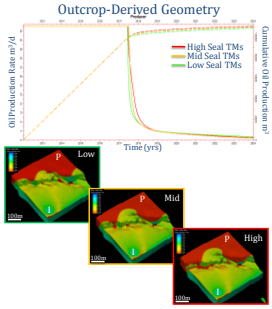

Seismically Resolvable Geometry

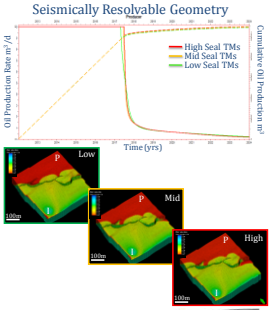

Results (2) Reservoir Thickness<Mean Throw

UNIVERSITY OF LEEDS

Outcrop-Derived Geometry

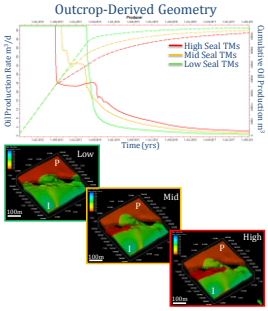

Seismically Resolvable Geometry

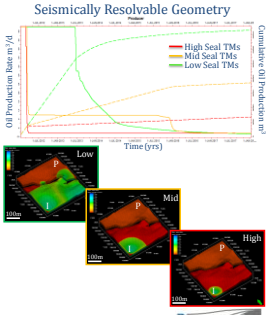

Outcrop v Seismic Juxtapositions

UNIVERSITY OF LEEDS

Outcrop Geometry | Forward Modelled Seismic | Seismically Resolvable Geometry

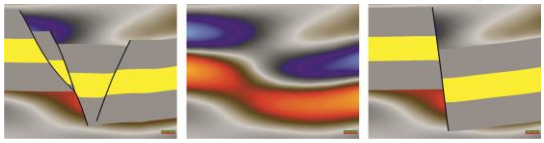

Effective Juxtaposition Area

UNIVERSITY OF LEEDS

Outcrop-Derived Geometry | **Seismically Resolvable Geometry**

Reservoir Thickness>Mean Fault Throw = Similar Simulation Results

Reservoir Thickness<Mean Fault Throw = Varied Simulation Results

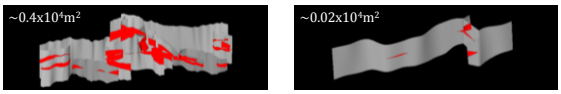

Implications (1)

UNIVERSITY OF LEEDS

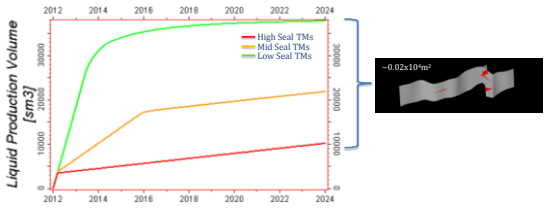

Implications (2)

UNIVERSITY OF LEEDS

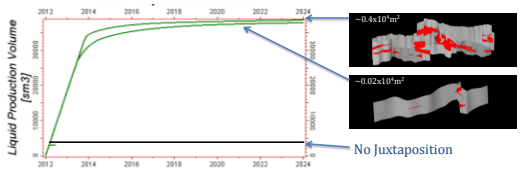

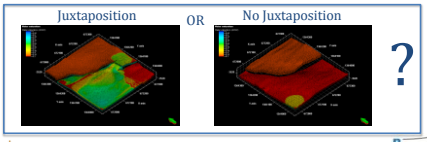

Identification and Incorporation

UNIVERSITY OF LEEDS

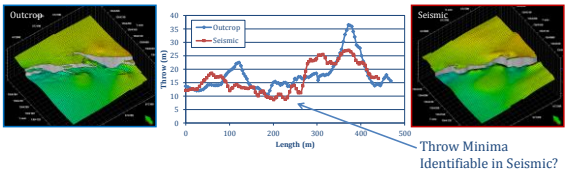

- Identify displacement Minima
- Stochastic population of low-throw areas (e.g. Manzocchi et al, 2008)
- Reduce throw along faults
- Modify TMs

Conclusions

UNIVERSITY OF LEEDS

- Seismically resolvable geometries underestimate across-fault reservoir juxtaposition (overestimate seal?)
- Impact of fault properties greater where juxtaposition area small, decreases with increasing juxtaposition area
- Small juxtaposition windows can result in large across fault flux
- Fault juxtaposition is primary control on across-fault flux, fault properties secondary

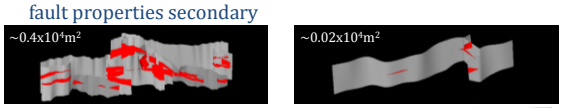

Acknowledgements

UNIVERSITY OF LEEDS

Questions?

Acknowledgements

Schlumberger
NORSAR Innovation AS
RDR

Outcrop Analogue Derived Synthetic Seismic Data: A Tool for Understanding Rift Scale Structural Uncertainty

Alan Wood[(1)]*, Douglas Paton[(1)], Viki Wood[(2)] & Richard Collier[(1)]

(1) Basin Structure Group (bsg.leeds.ac.uk), School of Earth & Environment, University of Leeds, Leeds, LS2 9JT

(2) Rock Deformation Research Limited, West Riding House, Leeds, LS1 5AA

*ee08amw@leeds.ac.uk

ABSTRACT

Much of our understanding of sub-surface rift structure is derived from 2D seismic sections, with 3D coverage generally being restricted to localised areas. Constraining the along strike variation in geometry hence relies on correlating between often widely spaced sections. This results in significant uncertainty in fault displacement distribution and the location and geometry of fault linkages. In turn this limits the degree to which we can constrain 3D rift evolution. Synthetic 2D seismic sections across known outcrop geometries allow us to capture and visualise structural uncertainty in a 3D context. This provides us with a useful tool for understanding the limitations and uncertainties of 2D data.

Detailed field mapping and structural data collection has allowed construction of a 3D geological model of the onshore Gulf of Corinth rift, with fault- and fault-linkage geometries being relatively well constrained. Sample analysis combined with published depth trends have allowed the model to be populated with petrophysical properties appropriate for sub-surface burial conditions. Seismic forward modelling software is used to generate synthetic sections at intervals typical of exploration scale seismic acquisition. Comparison of the synthetic sections with the mapped 3D geometry allows us to constrain the potential uncertainty when predicting 3D rift configuration from 2D data. This work has applications both as a teaching tool and within the hydrocarbon industry, where the inherent limitations of 2D data leads to significant uncertainty in the depth and location of spill points, and hence in potential hydrocarbon column heights and volumes.

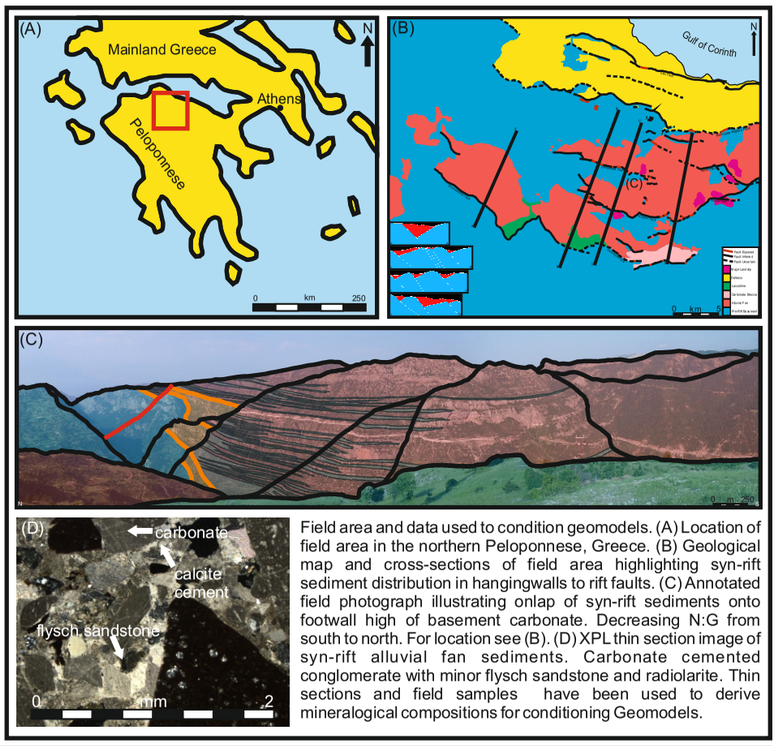

Field area and data used to condition geomodels. (A) Location of field area in the northern Peloponnese, Greece. (B) Geological map and cross-sections of field area highlighting syn-rift sediment distribution in hangingwalls to rift faults. (C) Annotated field photograph illustrating onlap of syn-rift sediments onto footwall high of basement carbonate. Decreasing N:G from south to north. For location see (B). (D) XPL thin section image of syn-rift alluvial fan sediments. Carbonate cemented conglomerate with minor flysch sandstone and radiolarite. Thin sections and field samples have been used to derive mineralogical compositions for conditioning Geomodels.

Forward Modelling Workflow

Structural and Petrophysical Modelling

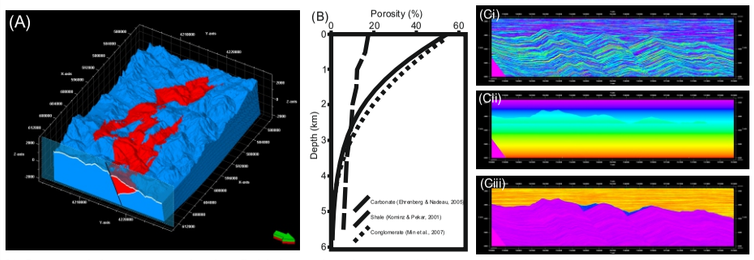

(A) Geo-model constructed using field data, showing pre- (blue) and syn-rift (red) outcrop. (B) Published porosity-depth trends for Carbonate, Conglomerate and Shale used to condition porosity distribution within the model. (C) Cross sections through model showing examples of petrophysical properties used during forward modelling. (i) Porosity, (ii) Pore pressure, (iii) VShale.

Elastic and Reflectivity Modelling

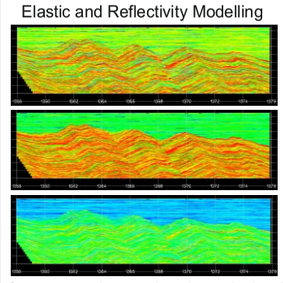

Cross sections showing derived properties used during generation of synthetic seismic sections. (A) Density, (B) Shear Modulus, (C) P-velocity

Forward Modelled Data

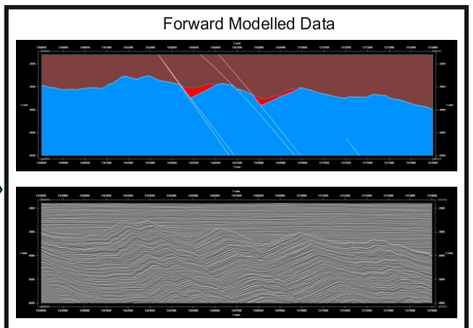

Comparison of model geometry (A) and generated synthetic seismic section (B).

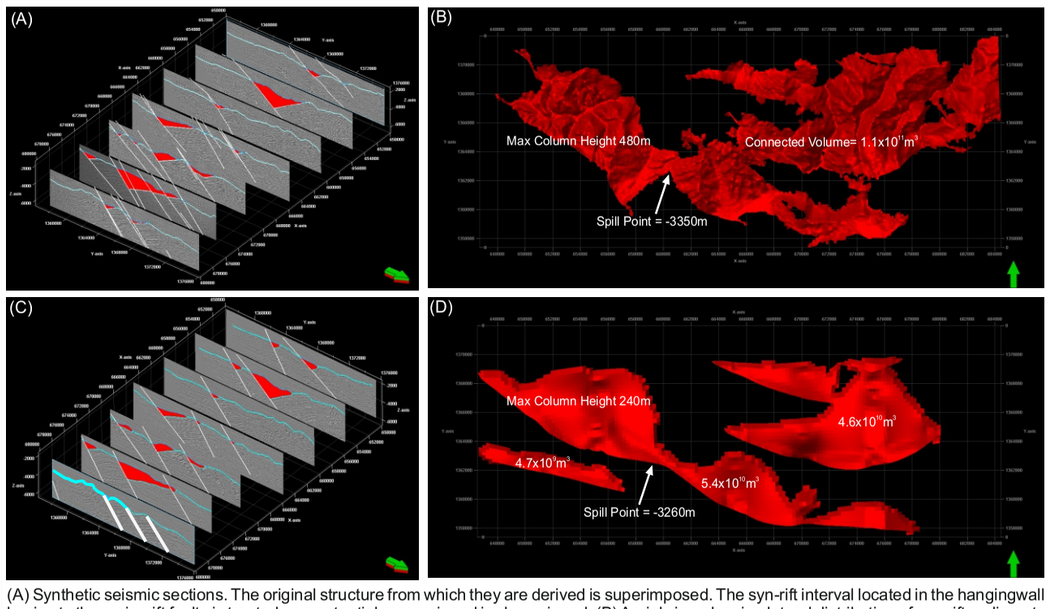

(A) Synthetic seismic sections. The original structure from which they are derived is superimposed. The syn-rift interval located in the hangingwall basins to the major rift faults is treated as a potential reservoir and is shown in red. (B) Aerial view showing lateral distribution of syn-rift sediments as mapped in the field. Note the high degree of connectivity between the different sub-basins. (C) Synthetic seismic sections with interpretation superimposed. (D) Aerial view of extrapolated syn-rift distribution based on interpreted synthetic seismic sections. Note the differences in connectivity and spill point depths.

Application and Implications

To illustrate the uncertainty in predicting 3D geometries from 2D data the synthetic seismic sections have been independently interpreted by an experienced structural geologist. Their initial interpretation (C, D) is reasonably well matched to the original geometry (A, B), with similar 3D interpolation of the syn-rift distribution in the fault hangingwalls. Despite the broad-scale similarities in outcrop pattern, there are a number of significant differences between the original geometry and that which has been interpreted from the forward modelled seismic data. Connected volumes, spill points and trap crests vary appreciably between the different models. As well as influencing reservoir facies distributions, these differences also introduce uncertainty into our understanding and predictions of fault timing and evolution.

The variations in trap crest and spill point depths between the original and seismically resolvable geometries influences the pressure due to buoyancy forces within the reservoir interval. This has major implications for drilling in regions where limited data means that geological contacts are poorly constrained.

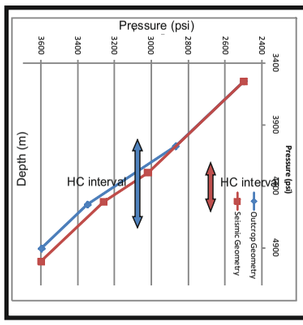

Plot of pressure versus depth for the trap shown in figures C and D. A water pressure of 0.433psi/ft and an oil pressure of 0.3psi/ft have been used. The differences in trap crest and spill points between the outcrop defined and the seismically resolvable geometries leads to significant differences in the pressure. If drilled this trap would have a lower pore pressure than expected if estimates were based on the seismically resolvable geometry, potentially leading to loss of drilling mud.

Conclusions

Synthetic seismic sections across known outcrop geometries highlight the uncertainties when basing 3D understanding on 2D data. This provides a useful tool for both academic and industrial uncertainty analysis and risking.

References

EHRENBERG, S.N. & NADEAU, P.H. (2005) Sandstone Vs. Carbonate Petroleum Reservoirs: A Global Perspective on Porosity-Depth and Porosity-Permeability Relationships. *AAPG Bulletin*, **89**, 435-445.

KOMINZ, M.A. & PEKAR, S.F. (2001) Oligocene Eustasy from Two-Dimensional Sequence Stratigraphic Backstripping. *Geological Society of America Bulletin*, **113**, 291-304.

MIN, B., SHU, L., YIN, H., XIN, W. & ZHANG, D. (2007) Conglomeratic Reservoir Characterization in the Caiyu Field of the Langgu Sag, North China. *Marine and Petroleum Geology*, **24**, 579-590.

Acknowledgments

The authors would like to thank the following for contributing support to this work;

BSG

CiPEG Centre for Integrated Petroleum Engineering and Geoscience

www.bsg.leeds.ac.uk

Using Seismic Forward Modelling to Assess Fault Stability During Fluid Injection

Alan M. Wood*, Douglas A. Paton and Richard E.L. Collier

Basin Structure Group (http://bsg.leeds.ac.uk), School of Earth and Environment, University of Leeds, Leeds, LS2 9JT, United Kingdom. *ee08amw@leeds.ac.uk

Abstract

Secondary hydrocarbon recovery, hydraulic fracturing and CO_2 sequestration require that fluids are injected into the subsurface, with a resulting local increase in pore pressure. A major concern is that this increased pore pressure adversely effects fault stability, potentially leading to reactivation and associated seismicity. The stability of a fault in terms of the Mohr-Coulomb failure criteria is dependent on both the physical properties of the fault and its orientation relative to the in-situ stress field, with the orientation commonly being characterised through the use of seismic imaging. Inherent limitations in seismic resolution result in simplification of the identifiable geometries compared to those present in the subsurface. The disparity between realistic and seismically resolvable fault geometries may lead to incorrect estimates of fault stability under specific stress conditions.

Realistic sub-seismic fault geometries, derived from outcrop data, and those geometries which are resolvable in seismic data are compared using three-dimensional seismic forward modelling. The stability of both geometries has been assessed under stress conditions equivalent to those found at depth within parts of the Fort Worth Basin, a productive shale gas province. Fluid injection is simulated by increasing the pore pressure until the failure envelope is reached. The realistic fault geometries fail at significantly lower pore pressure increases compared to the seismically resolvable fault geometries, suggesting that relying on seismically resolvable geometries may lead to overestimates in fault stability. As a result it is possible that unexpected seismicity may occur during fluid injection into the subsurface.

1. Introduction

Fluid injection, such as during hydraulic fracturing, waste disposal, geothermal energy and CO_2 sequestration raises the pore pressure in the subsurface. The effect of this increased pore pressure is dependent on the magnitude and orientation of the in-situ stress field, the local geomechanical properties and the presence or absence of any pre-existing structures (figure 1).

In the case of hydraulic fracturing the purpose of fluid injection is to initiate the propagation of tensile fractures (figure 1A), hence increasing permeability and enhancing gas flow to the well bore. However, the increased pore fluid pressure may lead to reactivation of pre-existing structures, in turn resulting in the occurrence of induced seismicity (Green et al., 2012; Keranen et al., 2013). A key uncertainty when predicting and mitigating against induced seismicity is sub-seismic fault geometry (figure 2). The limitations of seismic data mean that fault orientations and geometries are often not correctly captured. In turn this leads to inaccurate predictions of how increasing the pore fluid pressure through the injection of fluids will effect fault stability.

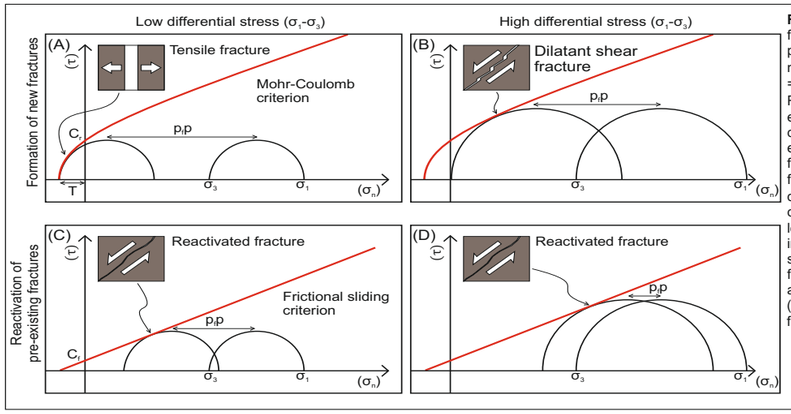

Figure 1. Schematic Mohr diagrams illustrating the effect on fracture formation and reactivation of increased pore fluid pressure (p_fp) under different conditions. = Shear stress, σ_n = normal stress, C_i = Intact rock cohesion, C_t = Fracture cohesion, σ_1 = Maximum principal stress, σ_3 = Minimum principal stress, T = Rock tensile strength. (A) A low differential stress (σ_1 - σ_3). No pre-existing fractures are present therefore the Mohr-Coulomb failure criterion is applicable. Increasing the pore pressure reduces the effective stress, shifting the Mohr circle to the left into the tensile failure region. If the minimum stress (σ_3) is negative, tensile fractures will form perpendicular to σ_3. (B) As (A) but with a higher differential stress. Increasing the pore pressure leads to the Mohr circle intersecting the failure envelope whilst σ_3 is still positive, leading to the formation of shear fractures, although a smaller pfp increase is required for fracture formation than for low differential stress. (C) Low differential stress. The presence of pre-existing fractures means that the friction sliding criterion is applicable, and a lower pfp increase is required in order to reactivate the fractures. (D) A higher differential stress requires a smaller p_fp increase for fracture reactivation.

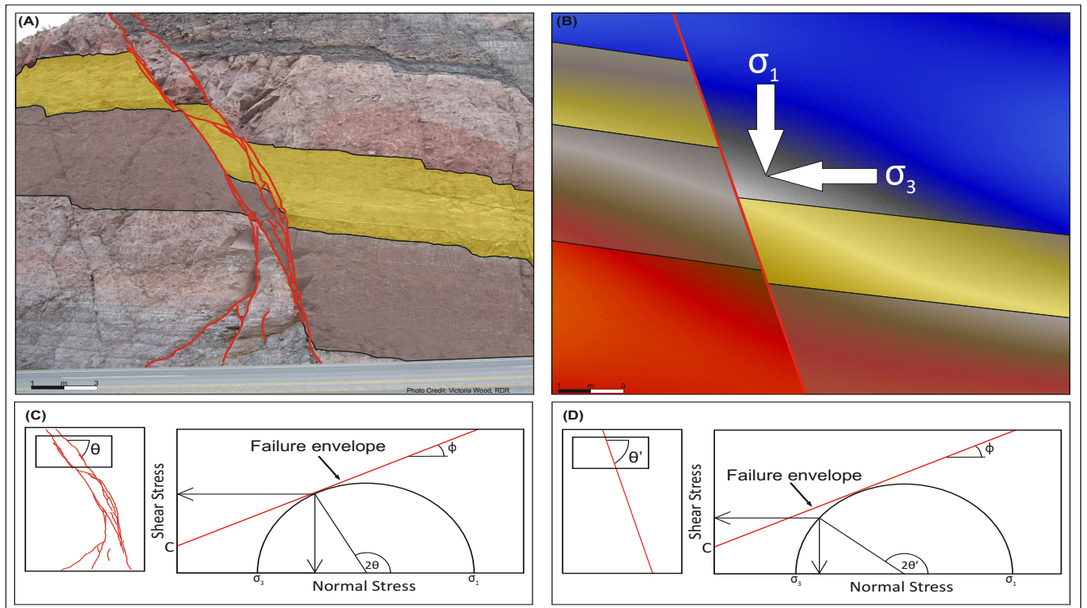

Figure 2. Outcrop example of how seismic data leads to underestimates in the complexity of fault geometry, and the influence that this has on fault stability during fluid injection. (A) View of road cutting showing significant geometric complexity. (B) The seismically resolvable version of the same geometry. A single fault plane is imaged effecting how the local stress field is predicted to be resolved onto the fault plane. (C) The outcrop geometry has a shallower dip than the seismically resolvable geometry (D). For a constant local stress field, the complex outcrop geometry is closer to the failure envelope than the seismically resolvable geometry. A lower pore pressure increase is hence required to induce failure and induce seismicity.

Basin Structure Group

Applied Structural Geology

Using Seismic Forward Modelling to Assess Fault Stability During Fluid Injection

Alan M. Wood*, Douglas A. Paton and Richard E.L. Collier

Basin Structure Group (http://bsg.leeds.ac.uk), School of Earth and Environment, University of Leeds, Leeds, LS2 9JT, United Kingdom. *ee08amw@leeds.ac.uk

UNIVERSITY OF LEEDS

2. Seismic Forward Modelling Methodology

To assess the impact of sub-seismic structural complexity on estimates of fault stability during fluid injection we forward model the synthetic seismic response of outcrop derived fault geometries. The geometries are derived from high resolution (~0.5 m) digital elevation data (DEM) from the Afar rift in Ethiopia (figure 3). Faulting occurred within the last 2 Ma and the area has an arid climate leading to limited erosion and hence excellent preservation of fault geometries.

The DEM data is used to construct a high resolution geocellular grid which is subsequently populated with petrophysical properties typical of the Barnett shale, Texas. Elastic and reflectivity values can be calculated and used to generate a synthetic 3D pre-stack depth migrated seismic volume (figure 4). Interpretation of this volume allows the outcrop derived and seismically resolvable geometries to be compared (figure 5), and their respective geomechanical stability under increased pore fluid pressure to be assessed (figure 8).

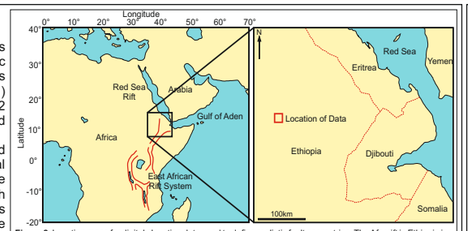

Figure 3. Location maps for digital elevation data used to define realistic fault geometries. The Afar rift in Ethiopia is a result of interaction at the triple junction of the Red Sea rift, the East African rift and the Gulf of Aden rift in East Africa (Rowland et al., 2007).

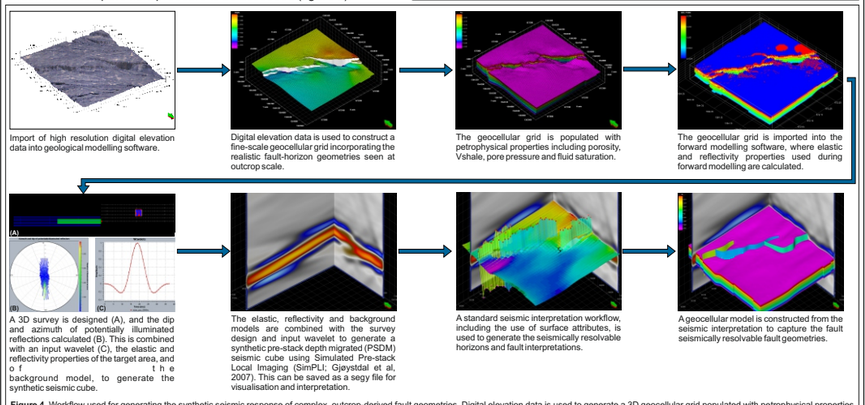

Figure 4. Workflow used for generating the synthetic seismic response of complex, outcrop-derived fault geometries. Digital elevation data is used to generate a 3D geocellular grid populated with petrophysical properties appropriate to a shale gas reservoir. Seismic forward modelling software is used to calculate the elastic and reflectivity values which can be combined with a background model and survey design to generate a synthetic seismic volume. Interpretation of this volume allows identification of the seismically resolvable fault geometries and comparison with the original geometries from which they are derived.

3. Fault Geometry

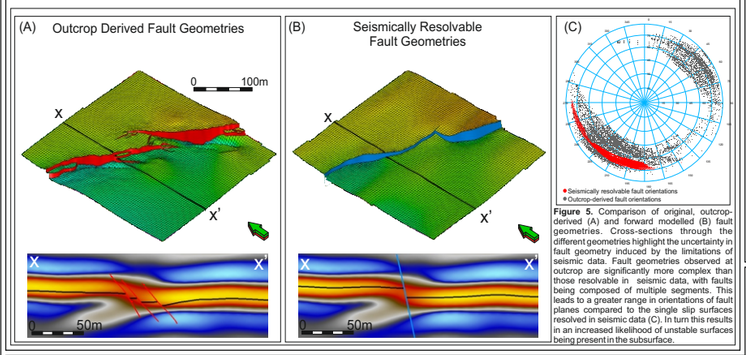

Figure 5. Comparison of original, outcrop-derived (A) and forward modelled (B) fault geometries. Cross-sections through the different geometries highlight the uncertainty in fault geometry induced by the limitations of seismic data. Fault geometries observed at outcrop are significantly more complex than those resolvable in seismic data, with faults being composed of multiple segments. This leads to a greater range in orientations of fault planes compared to the single slip surfaces resolved in seismic data (C). In turn this results in an increased likelihood of unstable surfaces being present in the subsurface.

4. Fault Stability

Following generation of outcrop-derived and seismically resolvable fault geometries, their stability under conditions of increased pore pressure analogous to fluid injection can be examined. We use published values of in-situ stresses and fault rock geomechanical properties for the Barnett Shale of the Fort Worth Basin, a prolific shale gas province in Texas (figure 6). The stability of the different fault geometries can be described by their 'distance to failure', the pore fluid pressure increase required to induce reactivation (figure 7). Fluid injection is simulated by increasing the pore fluid pressure. As the pressure increases the Mohr circles describing the fault stability move closer to the failure envelope. At pressure increases typically applied to induce hydraulic fracturing in the area, the fault stability is significantly reduced with the outcrop geometries failing at much lower pressure increases than the seismically resolvable geometries. This suggests that relying on seismically resolvable fault geometries may lead to overestimates of fault stability.

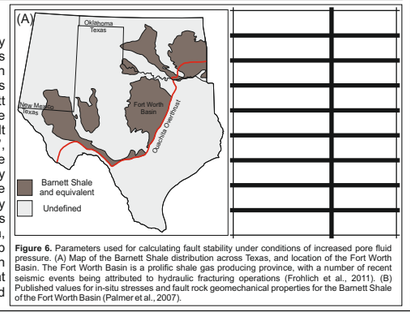

Figure 6. Parameters used for calculating fault stability under conditions of increased pore fluid pressure. (A) Map of the Barnett Shale distribution across Texas, and location of the Fort Worth Basin. The Fort Worth Basin is a prolific shale gas producing province, with a number of recent seismic events being attributed to hydraulic fracturing operations (Frohlich et al., 2011). (B) Published values for in-situ stresses and fault rock geomechanical properties for the Barnett Shale of the Fort Worth Basin (Palmer et al., 2007).

5. Earthquake Magnitude

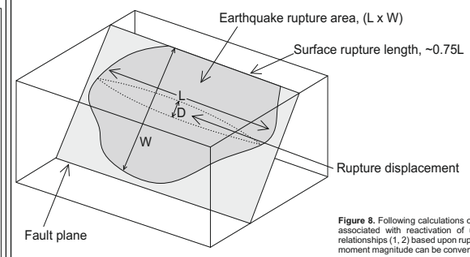

(1) $M_0=\mu AD$, where μ=Shear Modulus in dynes/cm^2, A = Rupture length x down dip rupture width in cm and D=average displacement of rupture in cm (Kanamori and Anderson, 1975)

(2) Log (D) = -1.43 + 0.88 log (0.75L), where D = average displacement in m, L = rupture length in km (Modified from Wells and Coppersmith, 1994)

(3) M = 2/3 log M_0 - 10.7, (Hanks and Kanamori, 1979)

Figure 8. Following calculations of fault stability the potential moment magnitude of induced seismicity associated with reactivation of unstable portions of the faults can be estimated using empirical relationships (1, 2) based upon rupture dimensions and typical values of the shear modulus for shale. The moment magnitude can be converted into the magnitude, a more widespread unit of earthquake strength

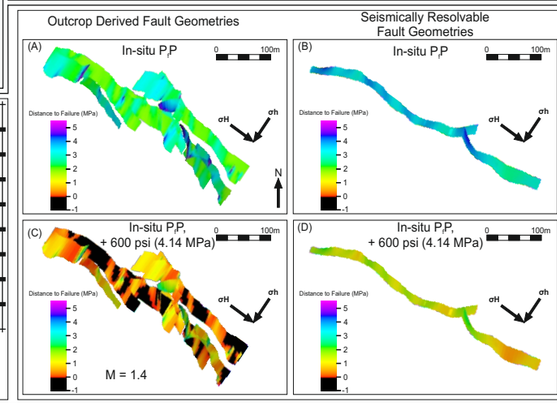

Figure 7. Aerial views of outcrop-derived (A, C) and seismically resolvable (B, D) fault geometries coloured by the distance to failure. At in-situ values of pore fluid pressure both fault geometries are stable (A, B). Simulating fluid injection by increasing the pore fluid pressure leads to parts of the outcrop-derived fault geometry becoming unstable and potentially being reactivated resulting in the occurrence of induced seismicity. This is in contrast to the seismically resolvable geometry which remains stable. The stability of the faults during fluid injection can be illustrated by plotting a Mohr diagram. The increase in pore fluid pressure moves the state of stress on the faults towards the failure envelope (E).

The potential magnitude of induced seismicity associated with fault instability during fluid injection can be calculated using the empirical relationships described in figure 8. In the case of the seismically

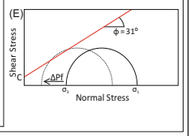

Using Seismic Forward Modelling to Assess Fault Stability During Fluid Injection

Alan M. Wood*, Douglas A. Paton and Richard E.L. Collier

Basin Structure Group (http://bsg.leeds.ac.uk), School of Earth and Environment, University of Leeds, Leeds, LS2 9JT, United Kingdom. *ee08amw@leeds.ac.uk

6. Geomechanical Uncertainty

A major uncertainty with our calculations of fault stability and hence the magnitude of any seismicity which may occur relates to the geomechanical properties applied. Properties such as fault rock friction angle and cohesion are relatively poorly defined for faults within shales. The impact of this uncertainty is illustrated in figure 9, where a lower fault rock friction has been applied.

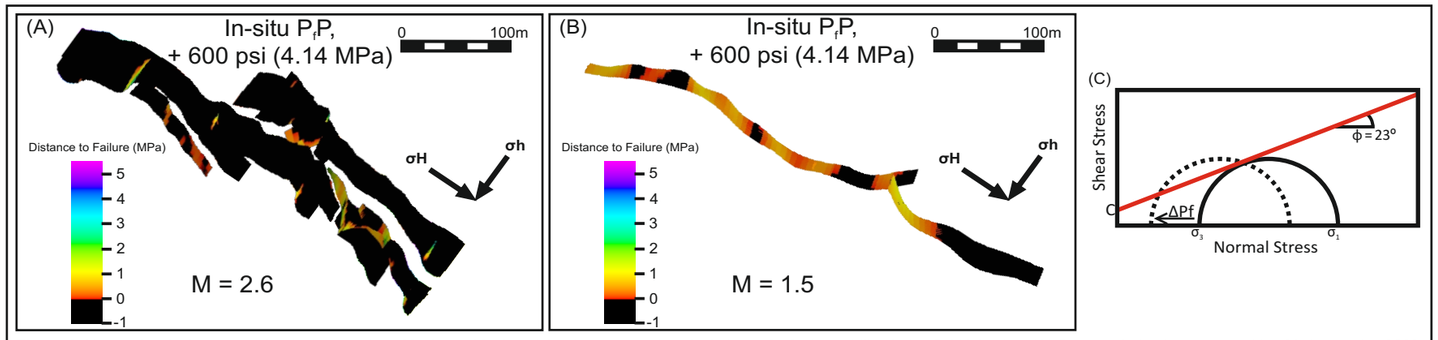

Figure 9. Uncertainty in the geomechanical properties of faults and fault rock leads to uncertain calculations of a faults stability during fluid injection. (A) Outcrop derived geometry with a friction angle of 23°, rather than 31°. This lower angle is within the range of values seen for other fault rocks within shales (6° to 31°, de Pater and Baisch, 2011), and results in a significantly larger area of instability compared to a larger friction angle (figure 7). In turn this larger unstable area has the potential to generate larger magnitude seismicity, up to M = 2.6. (B) Seismically resolvable geometry with the same friction angle. (C) Mohr-circle plot illustrating how reducing the estimate of the friction angle increases the likelihood of fault reactivation during conditions of increased pore fluid pressure.

7. Discussion and Future Work

We have modelled increases in pore fluid pressure associated with fluid injection as occurring effectively instantaneously and isotropically. In reality this is unrealistic since during hydraulic fracturing operations fluid is injected over several hours or days. In addition the permeability structure of the subsurface is unlikely to be homogenous, leading to a non-uniform distribution of injected fluid, and consequently of pore fluid pressure increases (figure 10).

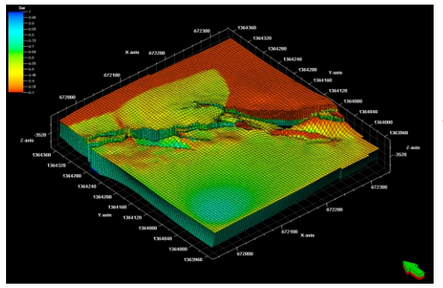

Future work would include integrating geomechanical uncertainty and dynamic fluid injection in order to better constrain the distribution of pore fluid pressure increases, and hence the localisation of fault instability.

Figure 10. Anisotropic fluid distribution during injection as a result of permeability heterogeneity in the subsurface.

8. Conclusions

- Seismic forward modelling of outcrop derived fault geometries illustrates the disparity between realistic fault geometries, and those geometries resolvable in seismic data.
- The greater range in orientations for realistic fault geometries leads to an increased potential for unstable faults, or parts of faults, to be present when compared to the simple geometries resolvable in seismic data.
- Realistic fault geometries may experience failure, reactivation, and induced seismicity at lower increases of pore fluid pressure compared to seismically resolvable geometries.
- Calculations of fault stability using seismically resolvable fault geometries are likely to be overestimated, with realistic geometries more likely to experience failure. The magnitude of any seismicity associated with fault reactivation will also differ between realistic and seismically resolvable geometries.
- Significant uncertainty exists regarding the geomechanical properties of fault rocks within shales. In turn this leads to uncertainty and unpredictability of fault behaviour during phases of increased pore fluid pressure, such as those associated with hydraulic fracturing operations.
- Prediction of the magnitude of induced seismicity relies on a number of uncertain variables. Pore pressure increases associated with fluid injection are likely to be non-linear and hence increase the uncertainty when predicting the occurrence and magnitude of seismicity.

References

Frohlich, C., Hayward, C., Stump, B. & Potter, E. The Dallas–Fort Worth Earthquake Sequence: October 2008 through May 2009. Bulletin of the Seismological Society of America 101, 327-340, doi:10.1785/0120100131 (2011).
Gjeystdal, H., Drothning, Å., Lecomte, I. & Branston, M. Advances in quantitative model-assisted seismic interpretation. First Break 25, 95-102 (2007).
Green, C. A. S., Peter; Baptie, Brian J. (ed Department of Energy and Climate Change) (UK, 2012).
Hanks, T. C. & Kanamori, H. A Moment Magnitude Scale. J. Geophys. Res. 84, 2348-2350, doi:10.1029/JB084iB05p02348 (1979).
Kanamori, H. & Anderson, D. L. Theoretical basis of some empirical relations in seismology. Bulletin of the Seismological Society of America 65, 1073-1095 (1975).
Keranen, K. M., Savage, H. M., Abers, G. A. & Cochran, E. S. Potentially induced earthquakes in Oklahoma, USA: Links between wastewater injection and the 2011 Mw 5.7 earthquake sequence. Geology, doi:10.1130/g34045.1 (2013).
Palmer, I. M., Zissis; Cameron, John. in SPE Hydraulic Fracturing Technology Conference Vol. Paper SPE 106113 (SPE, College Station, Texas, USA, 2007).
de Pater, C. J. B., S. Geomechanical Study of Bowland Shale Seismicity. (UK, 2011).
Rowland, J. V. et al. Fault growth at a nascent slow-spreading ridge: 2005 Dabbahu rifting episode, Afar. Geophysical Journal International 171, 1226-1246, doi:10.1111/j.1365-246X.2007.03584.x (2007).
Wells, D. L. & Coppersmith, K. J. New empirical relationships among magnitude, rupture length, rupture width, rupture area, and surface displacement. Bulletin of the Seismological Society of America 84, 974-1002 (1994).

Acknowledgments

The authors would like to thank the following for contributing support to this work;

Schlumberger

NORSAR Innovation AS

CiPEG Centre for Integrated Petroleum Engineering and Geoscience

www.bsg.leeds.ac.uk